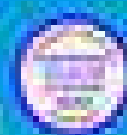
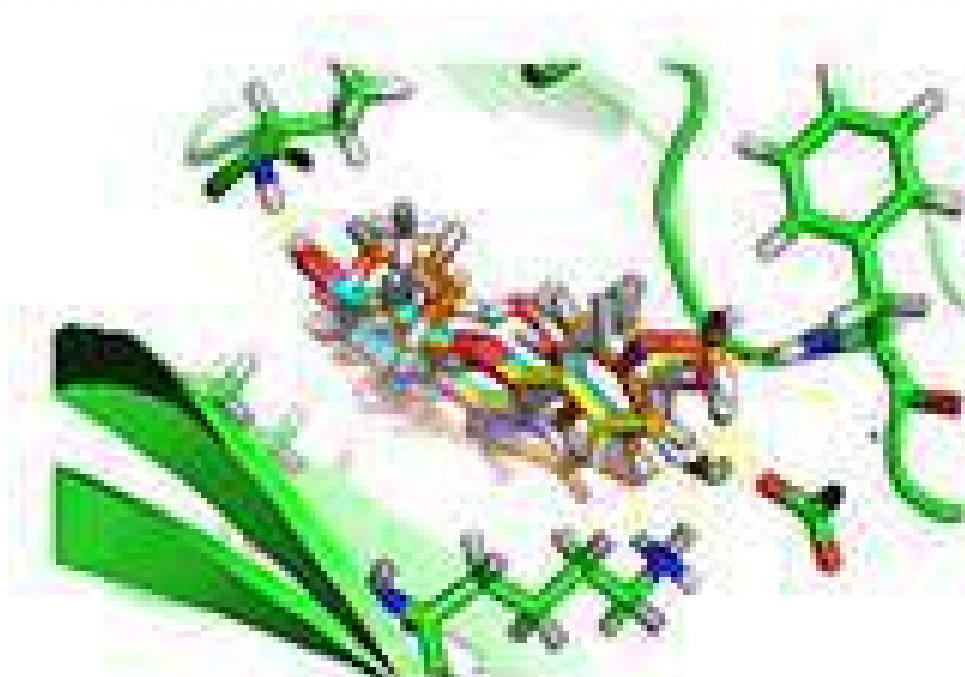


ISSN: 1411-9421 (print) 2462-1578 (online)

Indonesian Journal of Chemistry

Vol. 21, No. 2, April 2021



Google Scholar

Sinta

Crossref

Approved by 2021-2022
by 2020-2021

Antioxidant Activities and Identification of an Active Compound from Rambutan (*Nephelium lappaceum* L.) Peel

Mistriyani^{1,2}, Sugeng Riyanto², Anjar Windarsih³, and Abdul Rohman^{2,4*}

¹Faculty of Pharmacy, Halu Oleo University, Jl. Kampus Hijau Bumi Tridharma, Anduonou, Kendari 93132, Southeast Sulawesi, Indonesia

²Department of Pharmaceutical Chemistry, Faculty of Pharmacy, Universitas Gadjah Mada, Yogyakarta 55281, Indonesia

³Research Division for Natural Product Technology (BPTBA), Indonesian Institute of Sciences (LIPI), Yogyakarta 55861, Indonesia

⁴Center of Excellence Institute for Halal Industry and System (IHIS), Universitas Gadjah Mada, Yogyakarta 55281, Indonesia

* **Corresponding author:**

email: abdul_kimfar@ugm.ac.id

Received: October 7, 2019

Accepted: May 11, 2020

DOI: 10.22146/ijc.50421

Abstract: The consumption of rambutan fruit resulted in a vast amount of peels and seeds waste. Therefore, the exploration of active compounds having beneficial effects on human health, such as antioxidants, is very lucrative. This research was aimed to isolate and to identify the active compound as an antioxidant from rambutan peel. The powdered rambutan peel was extracted with a maceration technique using methanol then fractionated using petroleum ether, chloroform, and ethyl acetate to get the corresponding fractions. The extract and fractions were determined for its antioxidant activities in vitro using 2,2'-diphenyl-1-picrylhydrazyl (DPPH) radical scavenging and metal-chelating assay. The ethyl acetate fraction exhibited the highest antiradical activity with an IC₅₀ value of 26.22 µg/mL and metal-chelating activity, accounting for 12.32%. The antioxidant activities of extract and fractions correlated with its phenolics and flavonoid contents. Identification of active compounds using FTIR, GC-MS, and NMR resulted in the chemical formula of C₇H₆O₄, identified as 3,4-dihydroxybenzoic acid.

Keywords: rambutan peel; DPPH; metal-chelating; 3,4-dihydroxybenzoic acid

■ INTRODUCTION

Rambutan (*Nephelium lappaceum* L.) belonging to *Sapindaceae* family is widely distributed in South East Asian regions such as Indonesia, Malaysia, Thailand, and Vietnam. Rambutan is consumed as the fresh fruit results a vast amount of waste from seeds and peels. Therefore, it is very challenging to take benefits of rambutan waste as natural antioxidant sources. The antioxidant obtained from natural materials usually derived from secondary metabolites of plants like alkaloids, phenols, and flavonoids [1]. An antioxidant is a compound capable of protecting the human body from degenerative diseases caused by oxidative stress such as arteriosclerosis, arthritis, cataract, and premature aging. Free radicals have unpaired electrons that are very highly unstable and very reactive to react with other molecules. They include reactive oxygen species (ROS), reactive nitrogen species

(RNS) and reactive sulfur species (RSS) which able to initiate the reactions that damage organic molecules in the biological systems [2]. These reactions are taken into account to be the cause of some degenerative diseases such as diabetes and aging [3-4].

Rambutan peel has been reported to have antiradical, antioxidant, and antibacterial activities caused by the content of phenolic compounds [5-6]. The ethanol extract of rambutan peel is reported to contain ellagic acid, corilagin, and geraniin [7]. Palanisamy et al. [8] also isolated geraniin in rambutan peel. These compounds were reported to be responsible for antiradical and antioxidant activities. Ethyl acetate fraction of rambutan peel was reported to have radical scavenging activity using 2,2-diphenyl-1-picrylhydrazyl (DPPH) radical with IC₅₀ of 2.73 µg/mL, while quercetin used as a positive control has IC₅₀ of 1.99 µg/mL [9].

However, to obtain more active activities, it is necessary to further fractionation of the ethyl acetate fraction to obtain sub-fraction. Mistriyani et al. [10] also reported that ethyl acetate fraction revealed the highest antioxidant activities as determined by Ferric reducing activity power (FRAP) method. However, Permatasari and Rohman [9] and Mistriyani et al. [10] did not take further fractionation and did not elucidate the active compound responsible for this activity in the fraction of ethyl acetate. Therefore, in this research, the isolation and structure elucidation of the active component contained in the most active fraction of the sub-fraction of ethyl acetate was elucidated. The activity of natural antioxidant was generally attributed to the content of total phenolic and flavonoid contents; therefore, the phenolic and flavonoid contents in rambutan peel extract and fractions were correlated with antioxidant activities [11-13].

■ EXPERIMENTAL SECTION

Materials

Rambutan fruit was obtained from Bantul, Yogyakarta, Indonesia, and the authentication process was determined in the Department of Pharmaceutical Biology, Faculty of Pharmacy, Universitas Gadjah Mada, Yogyakarta, Indonesia.

Procedure

Preparation of methanol extract

The preparation of extract was done according to Permatasari and Rohman [9]. Rambutan peel was cleaned from impurities by using water, then chopped up and dried in an oven at a temperature of 60 °C for 2 × 24 h. Then, the simplicia was powdered and weighed. The powder of rambutan peel was extracted using the maceration method using methanol. The maceration was carried out for 3 days, occasionally stirred, and subjected to re-maceration 2 times. The filtrate obtained was then evaporated using a vacuum rotary evaporator at a temperature of 60 °C to obtain a methanolic extract.

Fractionation of methanolic extract of rambutan peel

The methanolic extract (50 g) was added with warm distilled water (1000 mL), fractionated using petroleum ether (PE) at a ratio (1:1 v/v). The residue of methanol

extract (water fraction) was then fractionated again using chloroform and ethyl acetate to get the fractions of PE, chloroform, ethyl acetate, and water. The initial methanolic extract and the fractions were further used for evaluation of the antioxidant activity

Determination of antioxidant activity using DPPH method

The antiradical activity of extract and fractions toward 2,2-diphenyl-1-picrylhydrazyl (DPPH) was evaluated using a visible spectrophotometer at 517 nm according to Blois method [6]. The stable DPPH radical solution (0.1 mM) in methanol was prepared, and then 1 mL of this solution was mixed with 3 mL of the sample at different concentrations. A control containing 1 mL of DPPH radical solution and 3 mL of methanol was prepared. The mixture was left to stand at ambient temperature for 20 min, and the absorbance was subsequently measured at 517 nm against the blank of methanol.

Determination of metal-chelating activity

The determination of metal-chelating activity was carried out as in Gülçin et al. [14]. A test sample was added with 0.05 mL of FeCl₂ 2 mM. The mixture was added with 0.2 mL of ferrozine 5 mM and vortexed for 10 sec. The absorbance was measured at a wavelength of 562 nm. The inhibition percentage of complexes of Fe²⁺-ferrozine was calculated as follows:

$$\text{Percent (\%)} \text{ inhibition chelating} = \frac{A^0 - A^1}{A^0} \times 100$$

where, A⁰ and A¹ are the absorbances in control and with the presence of the tested sample, respectively. EDTA is used as a positive control.

Determination of total phenolic content

The levels of total phenolic in samples were analyzed using the Colorimetric Method (Folin-Ciocalteu method), according to Chun et al. [15]. Total phenolic contents of samples were expressed as gram of Gallic acid equivalent/100 g of dry samples. Gallic acid for the preparation of the calibration curve was made in the range of 1.0–10.0 mg/100 mL.

Determination of total flavonoid

Flavonoid contents of samples were determined

using the aluminum chloride colorimetric method, according to Zou et al. [16]. Total flavonoid contents of extracts and fractions were expressed as gram rutin equivalent/100 g dry material. Rutin for preparation of calibration curve was made in the range of 1.0–10.0 mg/100 mL.

Fractionation of the most active fraction and identification of the isolate

The fraction of rambutan peel which showed the most active antioxidant (ethyl acetate (EA) fraction) was further fractionated using vacuum liquid using silica gel G 60 GF₂₅₄ (200 g) as in Rohman et al. [12]. The EA fraction was added with anhydrous sodium sulfate previously heated for 2 h at 110 °C, allowed to stand for one night and then filtered using a filter paper. The solvent was evaporated using a vacuum rotary evaporator. Samples were added to the column that has been let stand overnight. The EA fraction was eluted using 250 mL of chloroform, then the mixture of chloroform:EA with the volume ratio of 225:25, 200:50, 175:75, 150:100, 125:125, 100:150, 75:175, 50:200, 25:225, and 0:250 to give total volume of 250 mL. The eluates were collected for each 50 mL and were evaporated using a vacuum rotary evaporator. The isolated compound was identified by FTIR, NMR, and gas chromatography-mass spectrometry (GC-MS) methods [17].

The purity test

The purity of isolate was checked using two methods, namely melting point and thin-layer chromatography (TLC). The melting point of the crystal was checked using Buchi Melting Point B-450. The test was repeated by measuring the temperature of ± 10 °C below the melting point obtained, ramped at 1 °C/min. For purity test using TLC, the isolate was eluted using three eluent systems with a mobile phase having different polarity index, namely acetone: ethyl acetate: chloroform with a ratio of 4:3:3 v/v. The compound is considered to be pure when the TLC spot presents a single spot. The spot detection was performed visually using UV₂₅₄ and UV₃₆₆.

Data analysis

All data of antioxidants and their related data were analyzed in triplicate and expressed as mean \pm standard

deviation using Excel (Microsoft Inc., USA). The statistical analysis, including normality and homogeneity tests, were performed using SPSS software (SPSS Inc., USA).

RESULTS AND DISCUSSION

The evaluation of antioxidant activities in this study was done using several antioxidant assays. Among antioxidant mechanisms, radical scavenging and chelating agent activity were the most reported ones for the evaluation of antioxidant capacity derived from plants. The scavenging activity of DPPH radicals can be employed to measure the antioxidant activities in a relatively short time [18]. The DPPH radical is stable and soluble in polar solvents such as methanol and ethanol. Sharma and Bhat [19] have revisited the use of solvents during DPPH radical scavenging assay, and the results showed that methanol and buffered methanol were selected as solvents due to the capability to provide the highest absorbance value. Therefore, methanol was used in this study.

The results of the antioxidant activity test using DPPH radical assay, as expressed with IC₅₀ were compiled in Fig. 1. It is found that ethyl acetate fraction was the most active fraction with an IC₅₀ value of 26.22 $\mu\text{g/mL}$, followed by MeOH (IC₅₀ 31.56 $\mu\text{g/mL}$), PE and CHCl₃ (IC₅₀ 31.91 $\mu\text{g/mL}$) and then water fraction (IC₅₀ 40.36 $\mu\text{g/mL}$). This can be explained that ethyl acetate fraction contains more active compounds as radical scavenging such as phenolic and flavonoids. The similar results were also reported by Rohman et al. [12], Permatasari and Rohman [9] and Rohman et al. [20] in which ethyl acetate fractions in the methanol extract of Mengkudu, rambutan dan red fruit also revealed the highest antiradical activities among extracts and fractions evaluated. Mistriyani et al. [10] have also previously reported that ethyl acetate also revealed the highest reducing power and antiradical activity toward ABTS radical.

In this study, the IC₅₀ value of ethyl acetate fraction was higher than that of vitamin C (as a positive control) in which vitamin C had an IC₅₀ value of 3.34 $\mu\text{g/mL}$, but the IC₅₀ values of ethyl acetate fraction and other fractions were still categorized as a very strong antioxidant (less

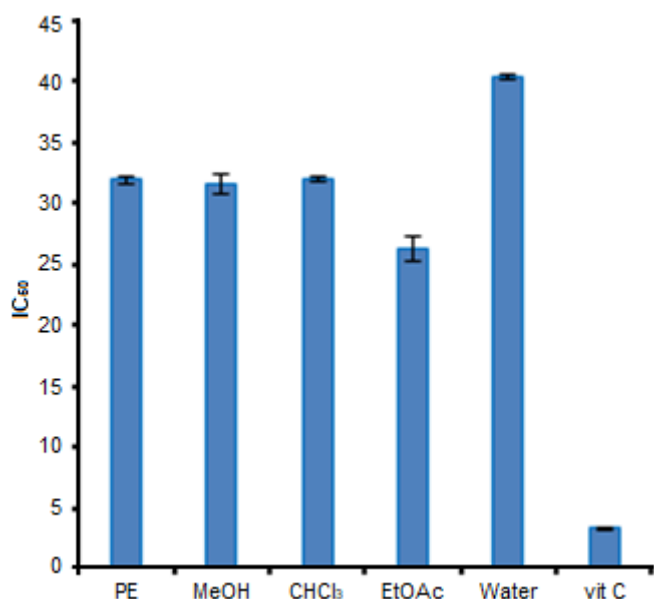


Fig 1. The IC₅₀ values of methanol extract of rambutan peel and its fraction using DPPH radical scavenging assay. PE = petroleum ether fraction; MeOH = methanol extract; CHCl₃ = chloroform fraction; EtOAc = ethyl acetate fraction; water = water fraction; Vit. C = vitamin C

than 50 µg/mL) [21]. Therefore, the ethyl acetate fraction was further fractionated.

The metal-chelating activity test was performed using EDTA as a positive control because EDTA has a strong metal-chelating characteristic [22-23]. The activity of metal-chelating of the methanol extract of rambutan peel and its fraction as well as EDTA was shown in Fig. 2. The water and ethyl acetate fractions have higher metal-chelating activities, accounting for 12.53 and 12.32%, respectively, but lower than that of EDTA, accounting for 35.50%. Based on the results of one-way ANOVA test, it can be shown that water and EA fractions did not differ significantly in a metal-chelating activity.

The antioxidant activity of methanol extract of rambutan peel and its fraction were correlated with phenolics and flavonoid contents. The linear regression equation obtained for the correlation between total phenolic content (TPC) (y-axis) with IC₅₀ values of DPPH radical scavenging (x-axis) has R² of 0.279. This result showed that 27.9% of the antioxidant activities against DPPH were from the contribution of phenolic compounds while 72.1% of the antioxidant activities came from other classes of compounds. It indicated a very low

correlation between IC₅₀ values and TPC. The correlation between TPC with metal-chelating activity had R² of 0.4322, which showed that 43.22% of metal-chelating activities was coming from the contribution of phenolic compounds. This indicated that phenolics compounds present in rambutan peel more active as metal chelator than a radical scavenger. However, the individual phenolics responsible for these activities have not reported yet.

The correlation between the total flavonoid content (TFC) (y-axis) expressed as % w/w RE and IC₅₀ values of methanol extract of rambutan peel and its fraction using DPPH radical scavenging activity having R² of 0.445. This R² value indicated that 44.5% of DPPH radical scavenging activity came from the contribution of flavonoid content contained in rambutan peel, while the correlation between TFC with metal-chelating activities had R² of 0.283, which showed that 28.3% of metal-chelating activities was from the contribution of flavonoid compounds. Based on the results, it can be stated that flavonoid compounds contained in rambutan peel were more active as a radical scavenger than metal chelators.

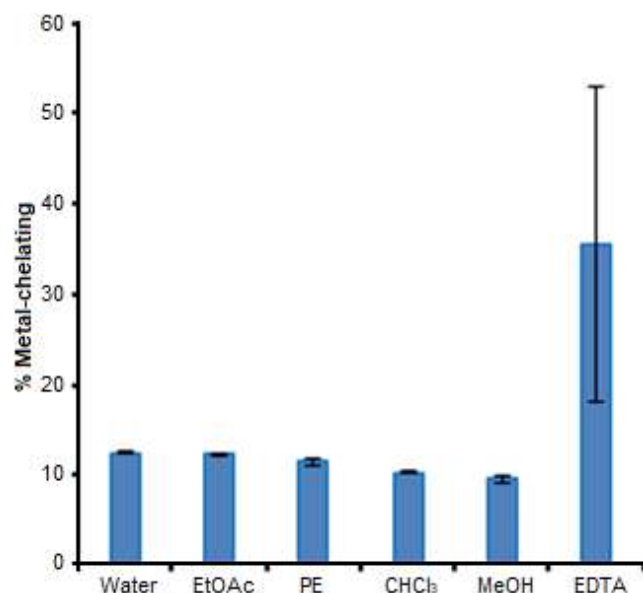


Fig 2. The results of metal chelating activity of methanol extract of rambutan peel and its fraction. The chelating activity data were represented as mean values ± SD, n replication = 3. Water = water fraction; EtOAc = ethyl acetate fraction; PE = petroleum ether fraction; CHCl₃ = chloroform fraction; MeOH = methanol fraction

Isolation and Identification of Active Compounds in Ethyl Acetate Fraction

Isolation of ethyl acetate fraction resulted in 104 sub-fractions. Among these, there was a precipitate of crystalline yellow in sub-fraction 61–65. The combined sub-fraction was subjected to gravity column chromatography (GCC) to obtain more pure compounds. Isolate obtained was yellowish-colored with a crystalline shape resembling small needles. Based on TLC result using three systems of eluents with different polarities, there was one spot with R_f value of 0.7 indicating that the compound has been purified. The melting point of the isolate is 196.3–197.7 °C. The compound was considered pure if it has a melting point with a range of 2 °C [24]. Therefore, the target compound could be further isolated and identified using the spectroscopic method.

The chemical structure of the pure isolate (as analyzed using TLC and melting point) having active antioxidant was identified using spectroscopic methods (UV-Vis, FTIR, GC-MS, and NMR). Identification of functional groups using the IR spectrum (Fig. 3) was as follows: a broad peak at 3400–2400 cm^{-1} indicated the presence of O–H (hydrogen bonding of a carboxylic acid). The peaks at 2924 cm^{-1} indicated asymmetrical stretching vibration CH_2 group whereas the peak at 2863 cm^{-1}

corresponded to the symmetric vibration of CH_3 . Peak at 1667 cm^{-1} originated from C=O stretching vibration, peak at 1597 cm^{-1} revealed C=C benzene, and the peaks at around 1095 cm^{-1} indicated C–O stretching. While peaks at 790 and 760 cm^{-1} indicated aromatic out of plane bending system [25-26].

In order to confirm the chemical formula of isolated compounds, gas chromatography-mass spectrometry (GC-MS) was used. The mass spectrum (Fig. 4) exhibits the base peak at m/z 154 consistent with a molecular formula $\text{C}_7\text{H}_6\text{O}_4$, while the peak at m/z of 137 was formed due to the loss of OH group. The NMR measurement of isolated compounds is presented in Table 1.

The $^1\text{H-NMR}$ spectrum exhibited 2 proton groups that appear at the chemical shift, δ 7.4 and 6.8 ppm with integration 2 and 1, respectively (Fig. 5). The expanded spectra inform clearly that one proton showed peaks at δ 6.8 ppm as a doublet with $J = 8$ Hz was due to signal of H-5. While peaks at δ 7.4 ppm were the signal of 2 protons H-2 and H-6. H-2 rise as a doublet at δ 7.41 ppm $J = 2$ Hz, while H-6 appeared at δ 7.43 ppm as a doublet of doublet $J_{5-6} = 8$ Hz and, $J_{6-2} = 2$ Hz.

The $^{13}\text{C-NMR}$ spectrum of the isolated compound showed signals representing for 7 carbons present in the

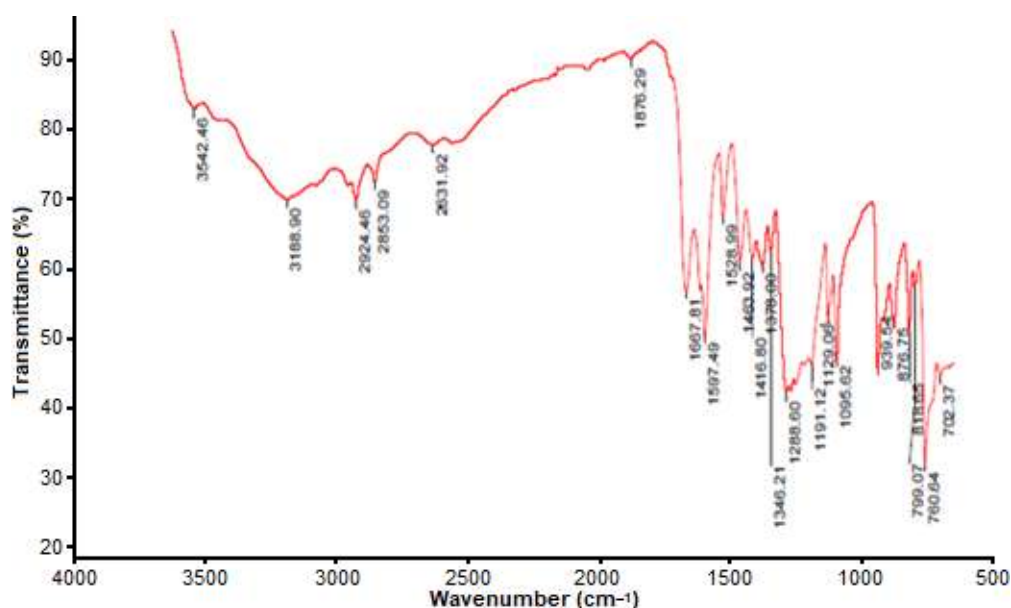


Fig 3. Attenuated total reflectance (ATR)-FTIR spectrum of the target compound, scanned at wavenumbers of 4000–650 cm^{-1}

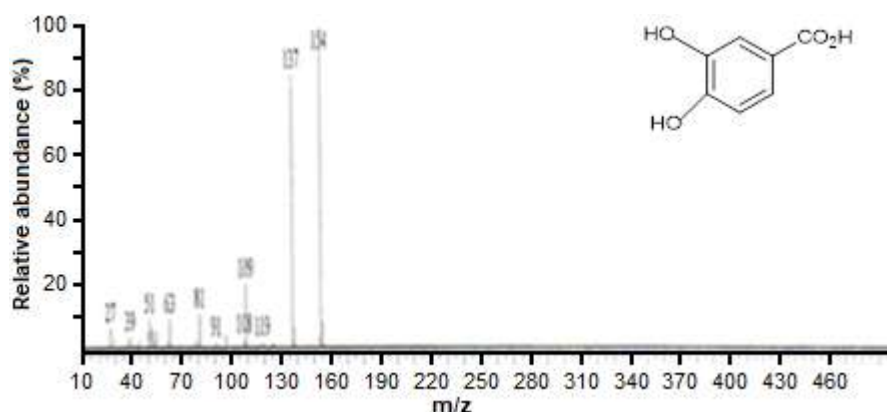


Fig 4. The mass spectrum of the isolated compound

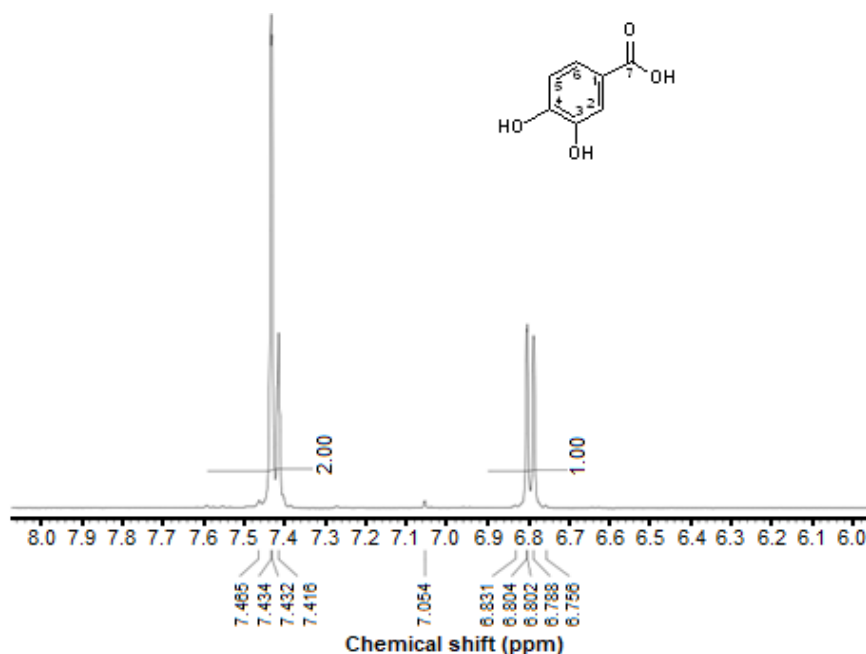


Fig 5. Partial ^1H -NMR spectrum

Table 1. NMR data of isolated compound

Carbon number	^{13}C (ppm, type of carbon)	Proton H (ppm)	HSQC correlation
1	124.03 Cq	-	
2	117.81 Cq	7.43 $d.J = 2$ Hz	H-2
3	146.22 Cq	-	
4	151.16 Cq	-	
5	121.27 Ct	6.8 $d.J = 8$ Hz	H-5
6	115.88 Ct	7.41 $dd.J = 8$ Hz, 2 Hz	H-6
7	170.31 (C=O)	-	

molecule (Fig. 6), namely at δ 170.31 ppm which indicated C (C=O) signal. Signals at δ 151.16 and 146.22 ppm were two C quaternary which attached OH groups those were C4 and C3, respectively. The other quaternary carbons were

C1 and C2; those signals appeared at δ 124.0 and 117.81 ppm, respectively. While tertiary carbon, those were C5 and C6 which resonated at δ 121 and 115.8 ppm. The assignment of the carbon chemical shift was confirmed

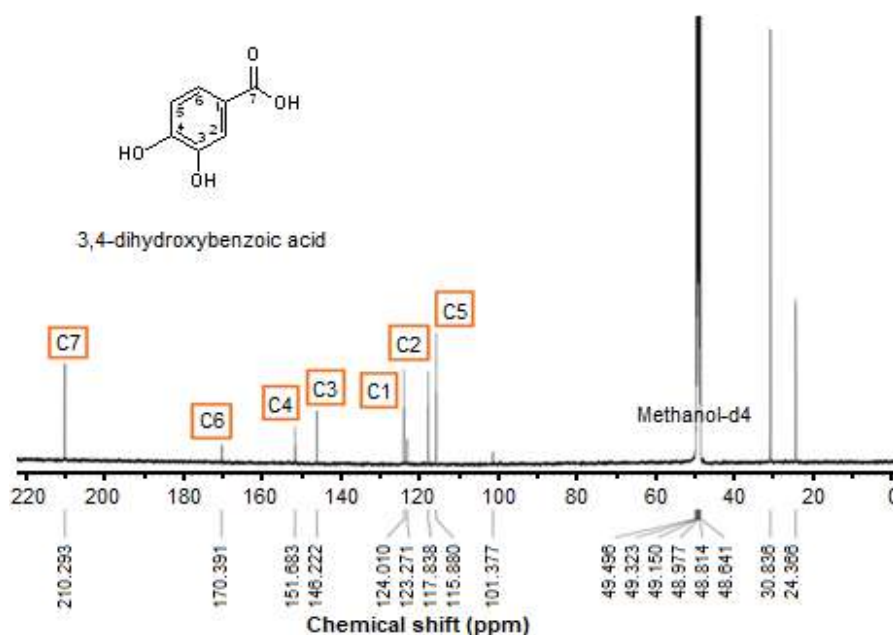


Fig 6. ^{13}C -NMR spectrum of the isolated compound

by DEPT (Suppl. 1). The HSQC spectrum (Suppl. 2) demonstrated that signal H at δ 6.8 ppm attached to C, which resonated at δ 121.27 ppm, while signal H at δ 7.41 ppm correlated to signal C at δ 115.88 ppm. Proton at δ 7.43 ppm attached to C, which resonated at δ 117.81 ppm.

Based on the IR, NMR, and mass spectra of the isolate, it was deduced that the studied compound in isolate had the molecular formula of $\text{C}_7\text{H}_6\text{O}_4$ identified as 3,4-dihydroxybenzoic acid, or protocatechuic acid with chemical structure shown in Fig. 5 and 6. This compound is a phenolic compound. This compound was further used for the evaluation of DPPH radical activity using vitamin C as a positive control. The result showed that the compound had IC_{50} of 5.17 $\mu\text{g}/\text{mL}$, higher than that of vitamin C (IC_{50} of 3.34 $\mu\text{g}/\text{mL}$) [18] indicating that the compound revealed lower antioxidant activity than vitamin C.

■ CONCLUSION

Among the methanolic extract and its fraction, ethyl acetate fraction revealed the highest antiradical activity using DPPH radical with the IC_{50} of 26.22 $\mu\text{g}/\text{mL}$ and the metal chelating activity, accounting of 12.32%. The identification of active compounds using spectroscopic (FTIR, GC-MS, and NMR) analyses resulted in an active

compound identified as 3,4-dihydroxybenzoic acid or protocatechuic acid.

■ ACKNOWLEDGMENTS

The authors thank the Ministry of Research and Technology and the Ministry of Education and Culture, Republic of Indonesia for financial support through scheme World Class Research 2020 with contract number 869/UN1/DITLIT/DIT-LIT/PT/2020.

■ REFERENCES

- [1] Altemimi, A., Lakhssassi, N., Baharlouei, A., Watson, D.G., and Lightfoot, D.A., 2017, Phytochemicals: Extraction, isolation, and identification of bioactive compounds from plant extracts, *Plants*, 6 (4), 42.
- [2] Caroch, M., and Ferreira, I.C.F.R., 2013, A review on antioxidants, prooxidants and related controversy: Natural and synthetic compounds, screening and analysis methodologies and future perspectives, *Food Chem. Toxicol.*, 51, 15–25.
- [3] Kontoghiorghes, G.J., and Kontoghiorge, C.N., 2019, Prospects for the introduction of targeted antioxidant drugs for the prevention and treatment of diseases related to free radical pathology, *Expert Opin. Invest. Drugs*, 28 (7), 593–603.

- [4] Yaribeygi, H., Atkin, S.L., and Sahebkar, A., 2019, A review of the molecular mechanisms of hyperglycemia-induced free radical generation leading to oxidative stress, *J. Cell. Physiol.*, 234 (2), 1300–1312.
- [5] Hernández-Hernández, C., Aguilar, C.N., Rodríguez-Herrera, R., Flores-Gallegos, A.C., Morlett-Chávez, J., Govea-Salas, M., and Ascacio-Valdés, J.A., 2019, Rambutan (*Nephelium lappaceum* L): Nutritional and functional properties, *Trends Food Sci. Technol.*, 85, 201–210.
- [6] Thitilertdecha, N., and Rakariyatham, N., 2011, Phenolic content and free radical scavenging activities in rambutan during fruit maturation, *Sci. Hortic.*, 129 (2), 247–252.
- [7] Yongliang, Z., Qingyu, M., Yan, G., and Liping, S., 2017, Purification and identification of rambutan (*Nephelium lappaceum*) peel phenolics with evaluation of antioxidant and antiglycation activities *in vitro*, *Int. J. Food Sci. Technol.*, 52 (8), 1810–1819.
- [8] Palanisamy, U., Cheng, H.M., Masilamani, T., Subramaniam, T., Ling, L.T., and Radhakrishnan, A.K., 2008, Rind of the rambutan, *Nephelium lappaceum*, a potential source of natural antioxidants, *Food Chem.*, 109 (1), 54–63.
- [9] Permatasari, L., and Rohman, A., 2016, 2,2'-Diphenyl-1-picrylhydrazyl (DPPH) radical scavenging activity of extracts and fractions of rambutan (*Nephelium lappaceum* L.) peel, *Res. J. Phytochem.*, 10 (2), 75–80.
- [10] Mistriyani, Riyanto, S., and Rohman, A., 2018, Antioxidant activities of rambutan (*Nephelium lappaceum* L) peel *in vitro*, *Food Res.*, 2 (1), 119–123.
- [11] Derakhshan, Z., Ferrante, M., Tadi, M., Ansari, F., Heydari, A., Hosseini, M.S., Conti, G.O., and Sadrabad, E.K., 2018, Antioxidant activity and total phenolic content of ethanolic extract of pomegranate peels, juice, and seeds, *Food Chem. Toxicol.*, 114, 108–111.
- [12] Rohman, A., Riyanto, S., and Utari, D., 2006, Antioxidant activities, total phenolic and flavonoid contents of ethyl acetate extract of mengkudu (*Morinda citrifolia*, L) fruit and its fractions, *Indones. J. Pharm.*, 17 (3), 136–142.
- [13] Safdar, M.N., Kausar, T., Jabbar, S., Mumtaz, A., Ahad, K., and Saddozai, A.A., 2017, Extraction and quantification of polyphenols from kinnow (*Citrus reticulata* L.) peel using ultrasound and maceration techniques, *J. Food Drug Anal.*, 25 (3), 488–500.
- [14] Li, Y., Li, Z., Hou, H., Zhuang, Y., and Sun, L., 2018, Metal chelating, inhibitory DNA damage, and anti-inflammatory activities of phenolic from rambutan (*Neppelium lappaceum*) peel and the quantifications of geraniin and corilagin, *Molecules*, 23 (9), 2263.
- [15] Ghafar, F., Tengku Nazrin, T.N.N., Mohd Salleh, M.R., Nor Hadi, N., Ahmad, N., Hamzah, N.A., Mohd Yusof, Z.A., and Azman, I.N., 2017, Total phenolic content and total flavonoid content in *Moringa oleifera* seed, *Sci. Heritage J.*, 1 (1), 23–25.
- [16] Aryal, S., Baniya, M.K., Danekhu, K., Kunwar, P., Gurung, R., and Koirala, N., 2019, Total phenolic content, flavonoid content and antioxidant potential of wild vegetables from western Nepal, *Plants*, 8 (4), 96.
- [17] Mistriyani, 2017, Antioxidant Activity of Rambutan (*Nephelium lappaceum* L.) Peel and Its Structural Elucidation of Active Compound, *Thesis*, Faculty of Pharmacy, Universitas Gadjah Mada, Yogyakarta, Indonesia.
- [18] Talla, E., Tamfu, A.N., Gade, I.S., Yanda, L., Mbafor, J.T., Laurent, S., Elst, L.V., Popova, M., and Bankova, V., 2016, New mono-ether of glycerol and triterpenes with DPPH radical scavenging activity from Cameroonian propolis, *Nat. Prod. Res.*, 31 (12), 1379–1389.
- [19] Sharma, O.P., and Bhat, T.K. 2009, DPPH antioxidant assay revisited, *Food Chem.*, 113 (4), 1202–1205.
- [20] Rohman, A., Riyanto, S., Yuniarti, N., Saputra, W.R., Utami, R., and Mulatsih, W., 2010, Antioxidant activity, total phenolic, and total flavonoid of extracts and fractions of red fruit (*Pandanus conoideus* Lam), *Int. Food Res. J.*, 17, 97–106.
- [21] Paudel, B., Bhattarai, H.D., Kim, I.C., Lee, H., Sofronov, R., Ivanova, L., Poryadina, L., and Yim, J.H., 2014, Estimation of antioxidant, antimicrobial

- activity and brine shrimp toxicity of plants collected from Oymyakon region of the Republic of Sakha (Yakutia), Russia, *Biol. Res.*, 47 (1), 10.
- [22] Ferrero, M.E., 2016, Rationale for the successful management of EDTA chelation therapy in human burden by toxic metals, *Biomed. Res. Int.*, 2016, 8274504.
- [23] Wu, J., Zhou, J. Zhang, S., Alsaedi, A., Hayat, T., Li, J., and Song, Y., 2019, Efficient removal of metal contaminants by EDTA modified MOF from aqueous solutions, *J. Colloid Interface Sci.*, 555, 403–412.
- [24] Akhtar, M.S., Hossain, M.A., and Said, S.A., 2017, Isolation and characterization of antimicrobial compound from the stem-bark of the traditionally used medicinal plant *Adenium obesum*, *J. Tradit. Complement. Med.*, 7 (3), 296–300.
- [25] Jain, P.K., Soni, A., Jain, P., and Bhawsar, J., 2016, Phytochemical analysis of *Mentha spicata* plant extract using UV-Vis, FTIR, and GC-MS technique, *J. Chem. Pharm. Res.*, 8 (2), 1–6.
- [26] Topală, C.M., Tătaru, L.D., and Ducu, C., 2017, ATR-FTIR spectra fingerprinting of medicinal herbs extract prepared using microwave extraction, *AJMAP*, 3 (1), 1–9.

Hydrotreatment of Cellulose-Derived Bio-Oil Using Copper and/or Zinc Catalysts Supported on Mesoporous Silica-Alumina Synthesized from Lapindo Mud and Catfish Bone

Fahri Swasdika, Wega Trisunaryanti*, and Iip Izul Falah

Department of Chemistry, Faculty of Mathematics and Natural Sciences, Universitas Gadjah Mada, Sekip Utara, Yogyakarta 55281, Indonesia

* **Corresponding author:**

email: wegats@ugm.ac.id

Received: October 13, 2019

Accepted: April 19, 2020

DOI: 10.22146/ijc.50558

Abstract: Catalysts comprising copper and/or zinc supported on mesoporous silica-alumina (MSA) with a high Si/Al ratio were prepared by wet impregnation method. This study investigated the preparation, characterization, and catalytic application of the prepared catalysts for hydrotreatment of cellulose-derived bio-oil. The wet impregnation was performed by dispersing $\text{Cu}(\text{NO}_3)_2 \cdot 3\text{H}_2\text{O}$ and/or $\text{Zn}(\text{NO}_3)_2 \cdot 4\text{H}_2\text{O}$ aqueous solution into MSA, followed by calcination and reduction under H_2 gas stream. The acidity test revealed that metal addition on MSA support increases the acidity of catalysts. During hydrotreatment of cellulose-derived bio-oil CuZn/MSA with total acidity, copper loading, zinc loading, and specific surface area of $24.86 \text{ mmol g}^{-1}$, 5.23 wt.%, 3.15 wt.%, and $170.77 \text{ m}^2 \text{ g}^{-1}$, respectively, exhibited the best performance compared to other prepared catalysts with 90.49 wt.% conversion of liquid product.

Keywords: hydrotreatment; bio-oil; catalysis; bifunctional catalyst; mesoporous silica-alumina

■ INTRODUCTION

Lignocellulose biomass is a promising alternative source of petroleum for fuels and chemicals production due to its abundance, non-edible, and relatively low cost [1]. It mainly consists of cellulose (40–60 wt.%), hemicellulose (15–30 wt.%), and lignin (10–25 wt.%) [2]. It could be converted to fuels via a thermochemical process such as pyrolysis. Pyrolysis of biomass usually involves a thermal decomposition of organic materials under an inert atmosphere. Products of biomass pyrolysis mainly consist of bio-oil, char, and gases. Bio-oil produced by biomass pyrolysis has demonstrated as a suitable fuel for heat generation in boiler systems and power generation in some diesel engines [3-4]. However, the produced bio-oil is unusable in internal combustion engines due to its high oxygen content, low heating value, and high acidity [5]. Therefore, an upgrading process to improve the quality of bio-oil is needed.

One of the commonly employed methods for bio-oil upgrading is a hydrotreatment [6-7]. This method

selectively removes oxygen from bio-oil through a catalytic reaction using hydrogen in the presence of a heterogeneous catalyst. Conventional hydrotreating catalysts such as sulfided NiMo and CoMo have been widely used for upgrading bio-oil. However, the sulfided catalysts have problems with sulfur usage and product contamination [8]. Pt-based catalysts have been considered as alternatives due to their high activity for hydrotreatment of bio-oil [9-10]. However, scarcity and the high price of noble metals are the main problems for industrial-scale applications [7]. Other transition metals such as Cu and Zn have attracted considerable attention as hydrotreatment catalysts due to their unique performance in the hydrogenation of esters to alcohol [11-13] and CO_2 [14-15]. However, there is a limited report of Cu-Zn based catalysts for hydrotreatment of bio-oil. The previous study showed that the catalyst containing Cu and Zn metals have good activity in the conversion of cyclic esters into hydrocarbon [16].

Copper-based catalysts exhibit excellent catalytic performance for hydrogenation of esters to alcohols

because they can catalyze selective hydrogenation of carbon-oxygen bonds and are relatively inactive for carbon-carbon bond hydrogenolysis [17]. Copper by itself is usually not active enough, resistant to sintering, nor mechanically stable enough for industrial use [11]. Therefore, promoters such as Zn are needed to improve it. The presence of Zn can promote the dispersion of Cu particles and enhance the reducibility of the copper oxide phase [12].

In a heterogeneous catalyst, a catalyst support also plays an important role in improving the efficiency of hydrotreatment processes. Because the hydrotreatment of aromatics and/or oxygen-containing compounds over bifunctional catalysts involves (de)hydrogenation on metallic centers and isomerization/cracking on acid centers [18]. Porous materials such as zeolite have been widely used as catalyst or catalyst support in the industry due to its unique characteristics such as high surface area, acidity, and thermal stability [19]. However, the application of zeolite is limited to small molecules due to its microporosity. Therefore, porous material with a relatively larger pore would be necessary. Mesoporous silica-alumina (MSA) has received great attention for replacing zeolite as support [9,20-21]. The MSA as catalyst support can be successfully synthesized from natural resources such as Lapindo mud and catfish bone gelatin [22-23]. The high content of Si and Al in Lapindo mud makes great attention to utilize Lapindo mud as a source to produce Si and Al precursor [22-24]. Catfish bone constitutes one of the primary waste associated with industry by-products and is considered as a raw material for gelatin production. Meanwhile, gelatin can be used as an organic template due to its high content of N-H groups which tend to strongly interact with xylanol (Si-OH) group on the silicate species via multiple hydrogen bonding. However, research on the use of gelatin from catfish bone as a template for synthesis of MSA is still rare. Moreover, the utilization of natural resources in the manufacture of MSA may reduce the production cost.

In the present work, the MSA with a high Si/Al molar ratio was synthesized using precursor derived from Lapindo mud and catfish bone. Lapindo mud was used as the source to produce Si and Al precursors, while the

catfish bone was used as the source to produce gelatin as the template precursor. The MSA was used as a support material of copper and/or zinc metals as catalysts for hydrotreatment of bio-oil. α -Cellulose was used as a model of biomass.

■ EXPERIMENTAL SECTION

Materials

Catfish bone waste was collected from Tegalorejo Village, Central Java, Indonesia. Lapindo mud was collected from Sidoarjo Regency, East Java, Indonesia. Hydrochloric acid (HCl 37%) was purchased from Mallinckrodt. Copper nitrate trihydrate ($\text{Cu}(\text{NO}_3)_2 \cdot 3\text{H}_2\text{O}$, purity 99%), zinc nitrate tetrahydrate ($\text{Zn}(\text{NO}_3)_2 \cdot 4\text{H}_2\text{O}$, purity 98.5%), ammonia (NH_3 25%) and sodium hydroxide (NaOH, purity 99%) were purchased from Merck. α -Cellulose was purchased from Sigma-Aldrich. Hydrogen (H_2) and nitrogen (N_2) gas were supplied by PT. Samator Ltd.

Procedure

Extraction of silica and alumina from Lapindo mud

Silica (SiO_2) and alumina (Al_2O_3) extraction had been conducted by the following procedure. The Lapindo mud was dried and sieved up to 100 mesh. 100 g of dried mud was refluxed in 400 mL of 6.0 M HCl (1:4, w/v) at 90 °C and kept under magnetic stirring for 5 h. The Al ions and other soluble metals would be dissolved in the HCl solution. Therefore, it will treat further by adding 150 mL of 6.0 M NaOH (2:3, v/v) up to pH of 8.0, then filtrated to remove the unneeded metals. The Al ions were then precipitated by injecting CO_2 gas into the filtrate. The precipitate was filtered, followed by washing using demineralized water. The slurry was dried at 50 °C and then calcined at 500 °C for 5 h to obtain Al_2O_3 material. Meanwhile, the silica was extracted from Lapindo mud by refluxing the mud residue of aluminium extraction in 400 mL of 6.0 M NaOH (1:4, w/v) at 90 °C and kept this under magnetic stirring for 5 h. The filtrate was then treated by adding a 2.0 M HCl solution to give the solution with a pH of 8. The precipitate was filtered followed by washing using demineralized water. The slurry was dried at 100 °C to obtain solid SiO_2 material.

The chemical composition of silica and alumina was then analyzed using X-Ray Fluorescence (XRF, PANalytical Minipal4).

Extraction of gelatin from catfish bone

Gelatin extraction was carried out according to Marsuki et al. [22] and Kusumastuti et al. [23] with a slight modification. The extraction was prepared by immersing 100 g of catfish bone in 500 mL of 0.1 M NaOH solution (1:5 w/v) for 24 h to remove non-collagenous proteins, then washing with demineralized water to remove the remaining non-collagenous protein until the washed water reached neutral pH. The residue was then immersed with 500 mL of 1.5 M HCl solution (1:5 w/v) for 1 h for demineralization, followed by washing with demineralized water until the wash water reached neutral pH. To produce gelatin, the bone was refluxed with 400 mL of demineralized water (1:4 w/v) at 90 °C for 5 h then evaporated at 50 °C. The dry gelatin was characterized using Fourier Transform-Infrared (FT-IR, Thermo Nicolet iS10).

Preparation of mesoporous silica-alumina

In a typical synthesis of MSA, 0.017 g of alumina and 3.0 g of silica was dissolved in 80 mL of NaOH solution (molar ratio NaOH to (SiO₂ + Al₂O₃) of 1:1) under constant stirring at 40 °C. Meanwhile, 3.0 g of gelatin was dissolved in 80 mL of distilled water under constant stirring at 40 °C, and the solution was slowly added into the silica-alumina solution. Afterward, the mixture was adjusted to pH 10 using 1.0 M HCl solution while stirring process was kept for the next 1 h. The formed gel solution was transferred into an autoclave and hydrothermally treated at 100 °C for 24 h. The solid obtained from hydrothermal treatment was filtered, followed by washing with distilled water. The solid was dried at 80 °C for overnight. Finally, the solid was calcined at 550 °C for 5 h and the resulting solid was labeled as MSA. The MSA has a Si/Al molar ratio of 115.34 based on ICP-AES (Shimadzu ICPE-9820) analysis.

Metal impregnation on MSA

Copper and zinc metals were sequentially impregnated onto the prepared MSA by the wet impregnation method, in which Zn metal was firstly

loaded, followed by Cu metals. The mixture of MSA-salt solution was stirred for 24 h at room temperature and dried at 100 °C for overnight. The catalysts were calcined at 500 °C for 3 h under the N₂ gas stream, followed by a reduction under the H₂ gas stream at 450 °C for 3 h. The obtained catalyst was denoted as CuZn/MSA. Further, ZnCu/MSA (Cu metals was firstly loaded followed by Zn metals), Zn/MSA (only zinc metals), and Cu/MSA (only copper metals) catalysts were synthesized following the same method of synthesis CuZn/MSA.

Catalyst characterization

The acidity of the catalyst was determined using the gravimetric method, with NH₃ as the basic adsorbate. The crystallinity of the catalysts was characterized by X-ray diffractometry (XRD, Rigaku Miniflex 600) with CuKα irradiation (λ = 0.154 nm) in the 2θ range of 2–80°. Pore characteristics of the catalysts were analyzed using a gas sorption analyzer (GSA, Quantachrome Touchwin Series) and evaluated by Brunauer–Emmett–Teller (BET) and Barrett–Joyner–Halenda (BJH) theories. The metal content of the catalysts was analyzed using an inductively coupled plasma atomic emission spectroscopy (ICP-AES, Shimadzu ICPE-9820). TEM images were determined by a JEOL-JEM-1400 microscope with an electron beam of 120 kV.

Hydrotreatment process

Cellulose was pyrolyzed at 600 °C for 2 h under the N₂ gas stream to produce bio-oil. The liquid product (bio-oil) obtained from the pyrolysis of cellulose was treated at 450 °C for 1 h under the H₂ gas stream in a semi-batch stainless steel reactor (id: 4.5 cm, od: 4.8 cm, length: 30 cm) using catalysts synthesized in this study. The catalyst to feed ratio was 1:30 (w/w). The yield percentage was calculated using Eq. (1), (2), and (3).

$$\text{Coke (wt.\%)} = \frac{W_{\text{coke}}}{W_{\text{feed}}} \times 100\% \quad (1)$$

$$\text{Liquid (wt.\%)} = \frac{W_{\text{liquid}}}{W_{\text{feed}}} \times 100\% \quad (2)$$

$$\text{Gas (wt.\%)} = [100 - \text{Liquid} - \text{Coke}] \% \quad (3)$$

The liquid products obtained from hydrotreatment bio-oil were characterized by using Gas Chromatography-Mass Spectroscopy (Shimadzu QP

2010 S). The percentage of the product was calculated using Eq. (4).

$$\text{Product} = (\% \text{ Area}) \times (\% \text{ Liquid}) \quad (4)$$

RESULTS AND DISCUSSION

Characterization of Catfish Bone Gelatin

The FT-IR spectrum of the catfish bone gelatin is presented in Fig. 1. Generally, the FT-IR spectrum of gelatin shows five characteristic polypeptide absorption bands called amide A, B, I, II, and III. Amide A observed at 3392 cm^{-1} corresponds to the stretching vibration of N-H group coupled with hydrogen bonding. A free N-H stretching vibration normally occurs in the range of $3400\text{--}3440 \text{ cm}^{-1}$. When the N-H group of a peptide is involved in a hydrogen bond, the position is shifted to lower frequencies [25]. Amide B was observed at 2939 cm^{-1} which corresponds to the asymmetric stretching vibrations of $=\text{C-H}$ as well as NH_3 [25-26].

Amide I which appears at 1652 cm^{-1} is mainly due to C=O stretching vibration coupled to CN contribution, CCN deformation, and in-plane bending modes [25]. The amide II band exhibited at 1537 cm^{-1} corresponds to an out of phase combination of C-N stretching vibration coupled to in-plane NH deformation modes of peptide group [25]. The amide III band at 1242 cm^{-1} represents the combination between CN stretching vibrations and NH deformation from the amide linkage as well as the absorptions arising from wagging vibrations of CH_2 groups [25-26]. Gelatin which contains a lot of NH groups

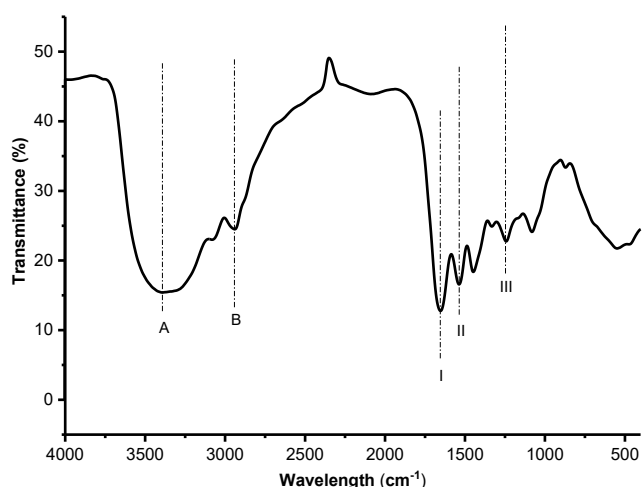


Fig 1. The spectrum of catfish bone gelatin

can be used as a template in preparation of MSA materials. These N-H groups tend to strongly interact with sylanol groups (Si-OH) via multiple hydrogen bonds [27].

Extraction of Silica and Alumina from Lapindo Mud

XRF analysis showed that Lapindo mud contains various kinds of metals such as Fe (36.90%), Si (35.10%), Al (11.00%), Ca (6.95%), K (3.52%), Ti (2.09%), S (1.10%), and others (3.34%). The high content of Si and Al in Lapindo mud makes it one of the resources that can be utilized to produce Si and Al. To produce them, the other metals should be removed by several chemical and physical steps, such as acid leaching and precipitation using an acid or alkaline followed by filtration. In the first step, acid extraction using hydrochloric acid was conducted to destroy the crystalline aluminosilicate phase to release free aluminium ions. Various metals could be dissolved at this condition such as Fe, therefore, the addition of 6.0 M NaOH could be used to remove them. Some impurities will be precipitated into $\text{M}(\text{OH})_n$, while Al remains dissolved in the solution. The Al ions can be precipitated by injecting CO_2 gas into the solution followed by filtration and washing using demineralized water to obtain alumina solid.

The silica was extracted from solid residue alumina extraction by refluxing the solid in 6.0 M NaOH. The silica will be reacted with NaOH to produce $\text{Na}_2\text{SiO}_3(\text{aq})$. The impurities will be removed in the solid residue. By adjusting the pH with the addition of HCl to pH of 8.0, silica could be obtained as the precipitate. In this study, the yield of alumina extraction is 10.83 wt.% with a purity of 84.5 wt.% based on XRF analysis. Meanwhile, the yield of silica extraction is 21.47 wt.% with a purity of 96.3 wt.% based on XRF analysis.

Characterization of MSA and Catalysts Prepared

Fig. 2 shows the FT-IR spectra of MSA before and after calcination. The spectra before calcination indicate the characteristics of the gelatin template. The bands observed around 1547 and 2949 cm^{-1} are corresponding to the amide II and B from the gelatin structure, respectively. This result is in agreement with the previous

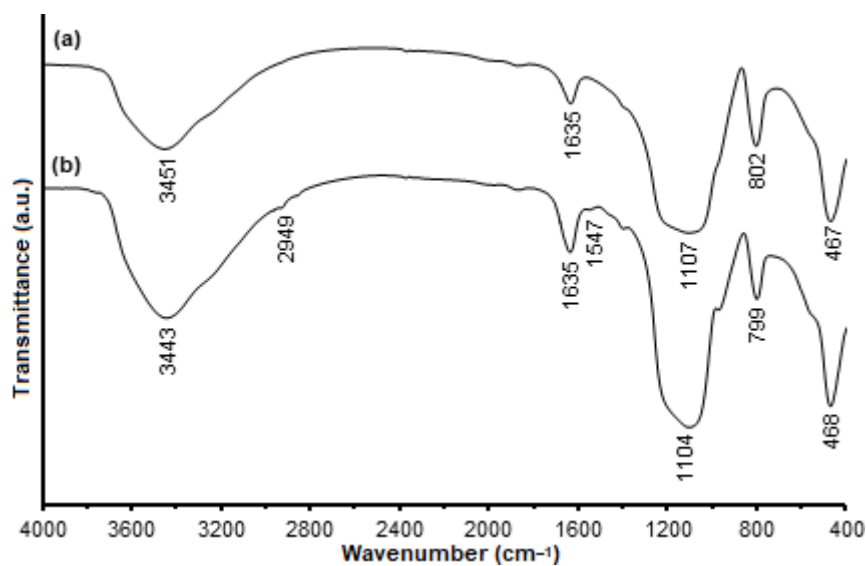


Fig 2. FT-IR spectra of MSA (a) before calcination and (b) after calcination

study that after hydrothermal MSA still contains gelatin [23]. In Fig. 2(b), the bands which correspond to gelatin were not observed. It is proven that the calcination process is effective to eliminate gelatin from the MSA framework. The characteristics of the silica-alumina material were observed in MSA material before calcination as well as after calcination. There are strong bands around at 1100 and 799, which correspond to stretching asymmetric, symmetric stretching of T-O, respectively [28]. The absorption band at 468 cm^{-1} refers to the bending vibration of T-O-T [29]. The band at 3400 cm^{-1} corresponds to OH stretching vibration bound to Si or Al, as well as the adsorbed H_2O molecule on the MSA surface [23]. The molecular vibration of water molecules is confirmed by the presence of an absorption band at 1635 cm^{-1} which corresponds to the bending vibration of O-H.

Fig. 3 shows the XRD patterns of the synthesized MSA and impregnated catalysts. It was observed that MSA is amorphous, as indicated by the single broad peak at 2θ of 21° that arises from the lack of an ordered crystalline structure [30]. The XRD patterns of modified MSA are also presented in Fig. 4. The XRD pattern of Cu/MSA shows peaks at 2θ of 36.2° due to the formation of CuO crystallite. In contrast, ZnCu/MSA and CuZn/MSA show a peak at 2θ of 36.0° indicating the presence of the ZnO phase together with the peaks at 2θ of

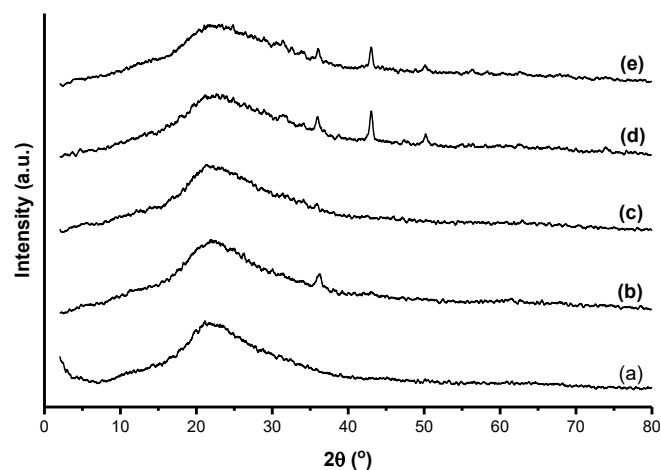


Fig 3. XRD pattern of (a) MSA, (b) Cu/MSA, (c) Zn/MSA, (d) ZnCu/MSA, and (e) CuZn/MSA

43.1 and 50.3° corresponding to the metallic Cu phase [31]. No diffraction of zinc species was found in Zn/MSA samples. This indicates that zinc species are well dispersed at the surface and/or in the channel of MSA [12,32]. The proposed structure of Cu and/or Zn supported on MSA was depicted in Fig. 4. MSA has unbalance charge due to the presence of Al atoms in the structure, therefore naturally it was neutralized with the cation such as Na, Ca, Mg, etc. In this case, the Zn and Cu cation was impregnated on the MSA structure and it can act to balance the charge by binding with the O atom closest to the Al atom.

in each metal act as Lewis acid, which contributes to the total acidity of the catalysts. Herein, it should be noted that CuZn/MSA exhibits higher acidity than other catalysts.

Fig. 7 shows the TEM micrograph of the MSA. The TEM micrograph shows that the MSA has a wormhole-like structure. This result is similar to those of the TEM micrograph of MSA that were synthesized on previous reports [22-23]. The homogeneity of the MSA pore size is relatively low due to the use of a gelatin template which has a wide molecular weight distribution range. The dark spots as shown by the arrow in Fig. 7 were observed in CuZn/MSA, indicating that metal particles are dispersed well in the MSA matrix.

Catalytic Performance

To examine the catalytic properties of synthesized and modified MSA, all samples were tested in the hydrotreatment of bio-oil. Bio-oil was obtained from the pyrolysis of cellulose. Cellulose-derived bio-oil is physically dark brown, thick, and smoke-smell. GC-MS data show that bio-oil contains various oxygenated compounds including ether, aldehyde, ketone, acid, ester, furan, anhydride, and other miscellaneous oxygenates (Table 2). The major product in bio-oil is 1-hydroxy-2-propanone, which is about 20.14%.

Hydrotreatment of cellulose-derived bio-oil was carried out with and without a catalyst. Fig. 8 shows the

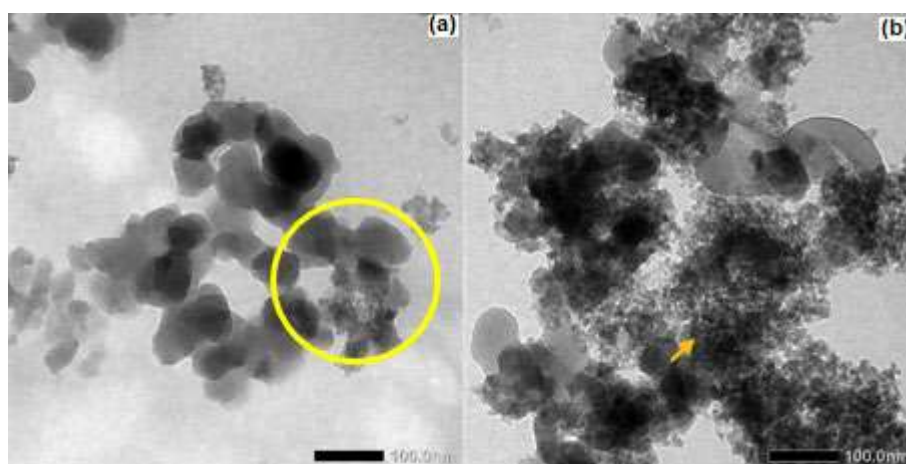


Fig 7. TEM micrograph of MSA (a) and CuZn/MSA (b)

Table 2. Chemical composition of cellulose-derived bio-oil

Compounds	Formula	Content (%)	Compounds	Formula	Content (%)
1-Hidroxy-2-propanone	C ₃ H ₆ O ₂	20.14	1-Acetyloxy-2-propanone	C ₄ H ₆ O ₂	1.16
2,3-Butanedione	C ₄ H ₆ O ₂	13.53	3-Pentanone	C ₅ H ₁₀ O	0.85
Methanoic acid	CH ₂ O ₂	12.72	2-Butanone	C ₄ H ₈ O	0.69
Ethanoic acid	C ₂ H ₄ O ₂	12.34	3-Methyl-1,2-cyclopentadione	C ₆ H ₈ O ₂	0.68
2-Furancarboxaldehyde	C ₅ H ₄ O ₂	10.61	2-Methyl-2-cyclopenten-1-one	C ₆ H ₈ O	0.43
Ethanal	C ₂ H ₄ O	6.34	3-Methyl cyclopentanone	C ₆ H ₁₀ O	0.42
Ethenyl Propanoic	C ₅ H ₈ O ₂	2.58	2-Butenal	C ₄ H ₆ O	0.32
1-Hidroxy-2-propanone	C ₄ H ₈ O ₂	2.56	2,3-Dihydro-1,4-dioxine	C ₄ H ₆ O ₂	0.27
Acetic acid anhydride	C ₄ H ₆ O ₃	2.31	3-Penten-2-one	C ₅ H ₈ O	0.18
Propanal	C ₃ H ₆ O	2.19	2-Pentanone	C ₄ H ₁₀ O	0.17
2,3-Pentanedione	C ₅ H ₈ O ₂	2.16	2,5-Hexanedione	C ₆ H ₁₀ O ₂	0.17
Acetylfuran	C ₆ H ₆ O ₂	1.52	Tetrahydropyran-3-one	C ₅ H ₈ O ₂	0.15
Propanoic acid	C ₃ H ₆ O ₂	1.28	Tetrahydrofuran	C ₄ H ₈ O	0.12
1-Acetyloxy-2-butanone	C ₆ H ₁₀ O ₃	1.20	Methyl succinic anhydride	C ₅ H ₄ O ₃	0.11
2(5H)-Furanone	C ₄ H ₄ O ₂	1.17	2-etoxy propane	C ₅ H ₁₂ O	0.10

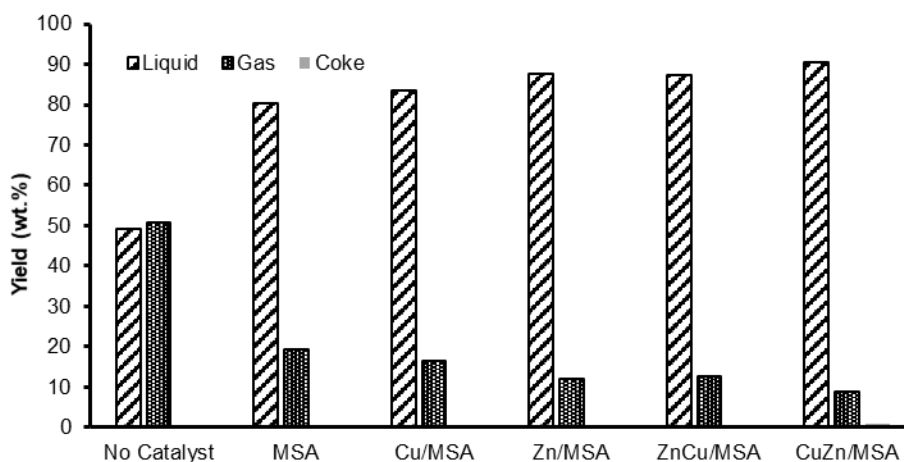


Fig 8. The product distribution of cellulose-derived bio-oil hydrotreatment

product distribution of bio-oil hydrotreatment. It can be shown that many liquid products could be obtained using catalysts more than without catalysts, while gas products could be obtained more without a catalyst. This phenomenon is expected to occur because of the differences in the reaction mechanism involved. Without a catalyst, the reaction occurs through the formation of radical ion triggered by high temperature to produce short-chain carbon compounds, while in the presence of a catalyst, the reaction takes place via the formation of the carbocation to produce longer chain carbon compounds [33]. The short-chain carbon compounds would tend to be in the gaseous phase, while the longer chain carbon compounds would tend to be in the liquid phase.

Among these catalysts, CuZn/MSA catalyst has better performance in producing liquid product than others. This phenomenon was caused by the synergetic effect between Cu and Zn metals. The presence of Zn metals in the bimetallic catalysts electron density on copper and can store or activate hydrogen during the hydrotreatment process [12]. The presence of Zn as the co-promotor can also increase the dispersion of copper particles. The good dispersion of copper particle enhances the effectiveness of the catalyst to produce liquid products.

Comparing to the previous studies, CuZn/MSA catalysts have better performance to produce liquid product. The liquid product that could be obtained using CuZn/MSA catalyst is 90.49 (wt.%). The previous study reported a various hydrotreatments of cellulose-derived

bio-oil using some catalysts, such as Ni/MSA, Mo/MSA, NiMo/MSA, and MoNi/MSA [23]. The highest yield of liquid product of 85.29 (wt.%) could be obtained using MoNi/MSA catalyst. The other previous study also reported hydrotreatment of cellulose-derived bio-oil using Co/MSA, Mo/MSA, and CoMo/MSA catalysts, which the highest yield of liquid product of 82.13 (wt.%) could be obtained using CoMo/MSA catalyst [22].

The chemical composition of the liquid product of bio-oil hydrotreatment was analyzed using GC-MS. It is known that the hydrotreatment of bio-oil involves very complicated reactions, however, the exact mechanism has not been fully understood. These complicated reactions are due to the fact that the bio-oil contains various compounds. Therefore, we focused on the major compounds contained in the liquid product. The major compounds in the liquid product are shown in Table 3. The number of compounds in the upgraded bio-oil was less than in bio-oil. The hydrotreatment of bio-oil significantly reduces several compounds, especially compounds of ketone group such as 2,3-butanedione. Methanoic acid is also reduced during hydrotreatment processes. Reducing the acids could improve the quality of bio-oil because the acids especially formic acid and acetic acid contribute to the acidity of bio-oil [8]. The hydrotreatment process could produce hydrocarbon such as *n*-hexane using MSA catalysts. These results show the MSA catalysts have high selectivity for producing *n*-hexane.

Table 3. Major compounds in bio-oil and upgraded bio-oil

Compound	Product percentage (wt.%)						
	Bio-oil	Catalytic upgrading*					
		No catalyst	MSA	Cu/MSA	Zn/MSA	ZnCu/MSA	CuZn/MSA
<i>n</i> -Hexane	-	-	17.49	-	-	-	-
Ethanal	6.34	4.19	14.41	9.93	9.75	11.28	8.00
2,3-butanadione	13.54	-	-	2.65	-	-	-
Methanoic acid	12.72	-	-	0.45	-	1.15	0.81
Ethanoic acid	12.34	11.90	-	11.23	13.13	12.51	19.79
2-Furancarboxaldehyde	10.61	7.31	13.06	22.51	24.13	18.00	15.07
1-Hydroxy-2-propanone	20.14	11.95	10.78	7.72	6.41	10.73	18.12

■ CONCLUSION

In this study, the preparation of heterogeneous catalysts by a wet impregnation method was successfully carried out. Catalysts comprising Cu and/or Zn supported on MSA denoted as Cu/MSA, Zn/MSA, ZnCu/MSA, and CuZn/MSA were used for hydrotreatment of cellulose-derived bio-oil. The synthesized MSA presented a BET specific surface area of $200.52 \text{ m}^2 \text{ g}^{-1}$, a total pore volume of 0.817 cc g^{-1} , and a pore diameter of 11.44 nm . The acidity of MSA increased after metal loading, which the highest acidity of $24.86 \text{ mmol g}^{-1}$ belonged to CuZn/MSA. During hydrotreatment of cellulose-derived bio-oil CuZn/MSA with total acidity, copper loading, zinc loading, and specific surface area of $24.86 \text{ mmol g}^{-1}$, $5.23 \text{ wt.}\%$, $3.15 \text{ wt.}\%$, and $170.77 \text{ m}^2 \text{ g}^{-1}$, respectively, exhibited the best performance compared to other prepared catalysts with $90.49 \text{ wt.}\%$ conversion of liquid product.

■ ACKNOWLEDGMENTS

This research was conducted under the research grant of PUPT 2018 Universitas Gadjah Mada (Contract No.: 1923/UN1/DITLIT/DIT-LIT/LT/2018). Therefore, the authors thank The Ministry of Research, Technology and Higher Education, the Republic of Indonesia for financial support.

■ REFERENCES

- [1] Cheng, F., and Brewer, C.E., 2017, Producing jet fuel from biomass lignin: Potential pathways to alkyl-benzenes and cycloalkanes, *Renewable Sustainable Energy Rev.*, 72, 673–722.
- [2] Wang, S., Dai, G., Yang, H., and Luo, Z., 2017, Lignocellulosic biomass pyrolysis mechanism: A state-of-the-art review, *Prog. Energy Combust. Sci.*, 62, 33–86.
- [3] Czernik, S., and Bridgwater, A.V., 2004, Overview of applications of biomass fast pyrolysis oil, *Energy Fuels*, 18 (2), 590–598.
- [4] Xiu, S., and Shahbazi, A., 2012, Bio-oil production and upgrading research: A review, *Renewable Sustainable Energy Rev.*, 16 (7), 4406–4414.
- [5] Hossain, A.K., and Davies, P.A., 2013, Pyrolysis liquids and gases as alternative fuels in internal combustion engines - A review, *Renew. Sustain. Energy Rev.*, 21, 165–189.
- [6] Saidi, M., Samimi, F., Karimipourfard, D., Nimmanwudipong, T., Gates, B.C., and Rahimpour, M.R., 2014, Upgrading of lignin-derived bio-oils by catalytic hydrodeoxygenation, *Energy Environ. Sci.*, 7 (1), 103–129.
- [7] Cheng, S., Wei, L., Julson, J., Muthukumarappan, K., Kharel, P.R., and Boakye, E., 2017, Hydrocarbon bio-oil production from pyrolysis bio-oil using non-sulfide Ni-Zn/Al₂O₃ catalyst, *Fuel Process. Technol.*, 162, 78–86.
- [8] He, Z., and Wang, X., 2012, Hydrodeoxygenation of model compounds and catalytic systems for pyrolysis bio-oils upgrading, *Catal. Sustainable Energy*, 1 (2013), 28–52.
- [9] Wang, Y., Wu, J., and Wang, S., 2013, Hydrodeoxygenation of bio-oil over Pt-based supported catalysts: Importance of mesopores and

- acidity of the support to compounds with different oxygen contents, *RSC Adv.*, 3 (31), 12635–12640.
- [10] Lee, H., Kim, H., Yu, M.J., Ko, C.H., Jeon, J.K., Jae, J., Park, S.H., Jung, S.C., and Park, Y.K., 2016, Catalytic hydrodeoxygenation of bio-oil model compounds over Pt/HY catalyst, *Sci. Rep.*, 6, 28765.
- [11] Yuan, P., Liu, Z., Zhang, W., Sun, H., and Liu, S., 2010, Cu-Zn/Al₂O₃ Catalyst for the hydrogenation of esters to alcohols, *Chin. J. Catal.*, 31 (7), 769–775.
- [12] Gao, C., Xiao, X., Mao, D., and Lu, G., 2013, Preparation of L-phenylalaninol with high *ee* selectivity by catalytic hydrogenation of L-phenylalaninate over Cu/ZnO/Al₂O₃ catalyst, *Catal. Sci. Technol.*, 3 (4), 1056–1062.
- [13] Shi, Z., Xiao, X., Mao, D., and Lu, G., 2014, Effects of the preparation method on the performance of the Cu/ZnO/Al₂O₃ catalyst for the manufacture of L-phenylalaninol with high *ee* selectivity from L-phenylalanine methyl ester, *Catal. Sci. Technol.*, 4 (4), 1132–1143.
- [14] Zha, F., Ding, J., Chang, Y., Ding, J., Wang, J., and Ma, J., 2012, Cu-Zn-Al Oxide cores packed by metal-doped amorphous silica-alumina membrane for catalyzing the hydrogenation of carbon dioxide to dimethyl ether, *Ind. Eng. Chem. Res.*, 51 (1), 345–352.
- [15] Chiang, C.L., Lin, K.S., and Chuang, H.W., 2018, Direct synthesis of formic acid via CO₂ hydrogenation over Cu/ZnO/Al₂O₃ catalyst, *J. Cleaner Prod.*, 172, 1957–1977.
- [16] Mascal, M., Dutta, S., and Gandarias, I., 2014, Hydrodeoxygenation of the angelica lactone dimer, a cellulose-based feedstock: Simple, high-yield synthesis of branched C₇-C₁₀ gasoline-like hydrocarbons, *Angew. Chem. Int. Ed.*, 53 (7), 1854–1857.
- [17] Brands, D.S., Poels, E.K., and Blik, A., 1999, Ester hydrogenolysis over promoted Cu/SiO₂ catalysts, *Appl. Catal., A*, 184 (2), 279–289.
- [18] Loricera, C.V., Castaño, P., Infantes-Molina, A., Hita, I., Gutiérrez, A., Arandes, J.M., Fierro, J.L.G., and Pawelec, B., 2012, Designing supported ZnNi catalysts for the removal of oxygen from bio-liquids and aromatics from diesel, *Green Chem.*, 14 (10), 2759–2770.
- [19] Verma, D., Kumar, R., Rana, B.S., and Sinha, A.K., 2011, Aviation fuel production from lipids by a single-step route using hierarchical mesoporous zeolites, *Energy Environ. Sci.*, 4 (5), 1667–1671.
- [20] Vít, Z., Gulková, D., Kaluža, L., Bakardieva, S., and Boaro, M., 2010, Mesoporous silica-alumina modified by acid leaching as support of Pt catalysts in HDS of model compounds, *Appl. Catal., B*, 100 (3-4), 463–471.
- [21] Vít, Z., Gulková, D., Kaluža, L., and Kupčík, J., 2015, Pd–Pt catalysts on mesoporous SiO₂–Al₂O₃ with superior activity for HDS of 4,6-dimethyldibenzo thiophene: Effect of metal loading and support composition, *Appl. Catal., B*, 179, 44–53.
- [22] Marsuki, M.F., Trisunaryanti, W., Falah, I.I., and Wijaya, K., 2018, Synthesis of Co, Mo, Co-Mo and Mo-Co catalysts, supported on mesoporous silica-alumina for hydrocracking of α -cellulose pyrolysis oil, *Orient. J. Chem.*, 34 (2), 955–962.
- [23] Kusumastuti, H., Trisunaryanti, W., Falah, I.I., and Marsuki, M.F., 2018, Synthesis of mesoporous silica-alumina from Lapindo mud as a support of Ni and Mo metals catalysts for hydrocracking of pyrolyzed α -cellulose, *Rasayan J. Chem.*, 11 (2), 522–530.
- [24] Mahardika, I.B.P., Trisunaryanti, W., Triyono, T., Wijaya, D.P., and Dewi, K., 2017, Transesterification of used cooking oil using CaO/MCM-41 catalyst synthesized from Lapindo mud by sonochemical method, *Indones. J. Chem.*, 17 (3), 509–515.
- [25] Ahmad, M., and Benjakul, S., 2011, Characteristics of gelatin from the skin of unicorn leatherjacket (*Aluterus monoceros*) as influenced by acid pretreatment and extraction time, *Food Hydrocolloids*, 25 (3), 381–388.
- [26] Xu, S., Yang, H., Shen, L., and Li, G., 2017, Purity and yield of collagen extracted from southern catfish (*Silurus meridionalis* Chen) skin through improved pretreatment methods, *Int. J. Food Prop.*, 20 (Suppl. 1), S141–S153.
- [27] Trisunaryanti, W., Lisna, P.S., Kartini, I., Sutarno, Falah, I.I., and Triyono, 2016, Extraction of gelatin from bovine bone and its use as template in

- synthesis of mesoporous silica, *Asian J. Chem.*, 28 (5), 996–1000.
- [28] Saraswathi, P., and Makeswari, M., 2017, Preparation and characterization of alumina and silica modified chitosan, *Rasayan J. Chem.*, 10 (3), 759–765.
- [29] Gustian, I., Ghufira, and Oktiarni, D., 2017, Composite membranes based on sulfonated polysulfone and natural zeolite for proton exchange membrane fuel cells, *Rasayan J. Chem.*, 10 (3), 689–694.
- [30] Saber, O., and Gobara, H.M., 2014, Optimization of silica content in alumina-silica nanocomposites to achieve high catalytic dehydrogenation activity of supported Pt catalyst, *Egypt. J. Pet.*, 23 (4), 445–454.
- [31] Wang, X., Ma, K., Guo, L., Tian, Y., Cheng, Q., Bai, X., Huang, J., Ding, T., and Li, X., 2017, Cu/ZnO/SiO₂ Catalyst synthesized by reduction of ZnO-modified copper phyllosilicate for dimethyl ether steam reforming, *Appl. Catal., A*, 540, 37–46.
- [32] Karnjanakom, S., Guan, G., Asep, B., Du, X., Hao, X., Yang, J., Samart, C., and Abudula, A., 2015, A green method to increase yield and quality of bio-oil: Ultrasonic pretreatment of biomass and catalytic upgrading of bio-oil over metal (Cu, Fe and/or Zn)/ γ -Al₂O₃, *RSC Adv.*, 5 (101), 83494–83503.
- [33] Pongsendana, M., Trisunaryanti, W., Artanti, F.W., Falah, I.I., and Sutarno, 2017, Hydrocracking of waste lubricant into gasoline fraction over CoMo catalyst supported on mesoporous carbon from bovine bone gelatin, *Korean J. Chem. Eng.*, 34 (10), 2591–2596.

Influence of Different Annealing Temperatures on the Structural and Optical Properties of TiO₂ Nanoparticles Synthesized via Sol-Gel Method: Potential Application as UV Sensor

Nur Munirah Safiy^{1,2*}, Rozina Abdul Rani³, Najwa Ezira Ahmed Azhar^{1,4}, Zuraida Khusaimi^{1,2}, Fazlena Hamzah⁵, and Mohamad Rusop^{1,4}

¹NANO-SciTech Centre (NST), Institute of Science (IOS), Universiti Teknologi MARA (UiTM), 40450 Shah Alam, Selangor, Malaysia

²Faculty of Applied Sciences, Universiti Teknologi MARA (UiTM), 40450 Shah Alam, Selangor, Malaysia

³Faculty of Mechanical Engineering, Universiti Teknologi MARA (UiTM), 40450 Shah Alam, Selangor, Malaysia

⁴NANO-ElecTronic Centre (NET), Faculty of Electrical Engineering, Universiti Teknologi MARA (UiTM), 40450 Shah Alam, Selangor, Malaysia

⁵Faculty of Chemical Engineering, Universiti Teknologi MARA (UiTM), 40450 Shah Alam, Selangor, Malaysia

* **Corresponding author:**

tel: +603-55444412

email: munirahsafiy@gmail.com

Received: December 6, 2019

Accepted: June 26, 2020

DOI: 10.22146/ijc.52255

Abstract: In this research, TiO₂ thin films were prepared using a simple sol-gel spin coating process. The films were characterized using Field Emission Scanning Electron Microscopy (FE-SEM), Energy Dispersive Ray (EDX), X-ray diffraction (XRD) and Ultraviolet-visible Spectrophotometer in order to investigate the influence of different annealing temperatures to the structural and optical properties of TiO₂. The surface morphology images from FE-SEM display a uniform layer of nanoparticles with a sample of 500 °C possess the most uniform and the visible spherical grain of TiO₂ nanoparticles. EDX spectra confirm the presence of Ti and O elements in the samples. The structural properties from the XRD pattern demonstrate that the films are crystalline at a temperature of 500 and 600 °C and the peak (101) intensity was increased as the annealing temperature increased. They exist in the anatase phase at the preferred plane orientation of (101). The calculated crystallite size for 500 and 600 °C samples is 19.22 and 28.37 nm, respectively. The films also possessed excellent absorption in the ultraviolet (UV) region with optical band gap energy ranging from 3.32 to 3.43 eV. These results can be fundamental for the fabrication of a UV sensing device.

Keywords: TiO₂; annealing; optical; UV; absorption

■ INTRODUCTION

Titanium dioxide (TiO₂) or titania is an n-type semiconductor that existed in three different phases: brookite, anatase, and rutile [1-3]. TiO₂ has gained wide attention due to chemical stability, chemical inertness, non-toxicity, biocompatibility and low cost [4-5]. TiO₂ can be synthesized via the sol-gel method, electrodeposition, hydrothermal, sputtering, Chemical Vapor Deposition (CVD) and the host of others to produce a different type of nanostructures [6-7]. Among

all of the methods, sol-gel synthesis is one of the most preferable methods in synthesizing TiO₂ because it is facile, low cost and easy to control and producing good quality of thin films [8]. Sol-gel spin coating method also provided low temperature synthesis method compared to high temperature synthesis method such as CVD. Hence, this process is more energy saving and environmentally friendly. In producing highly crystalline thin films, treatment is needed. The common treatment method was annealing treatment. Annealing of TiO₂ thin films not only improved the crystallinity but

also the surface morphology. The purpose of annealing also to transform the amorphous structure of the film to a more crystalline structure [9]. It was also reported elsewhere that annealing makes the grain size becomes larger and the surface becomes rougher [9-10].

In this experiment, we discuss the effect of annealing temperature on the structural and optical properties of TiO₂ thin film. Previously, a few types of research suggested an optimum temperature of 450 °C for annealing but in this work, we further optimized the annealing temperature for the fabrication of UV sensor. In the fabrication of the UV sensor, the criteria of the synthesized TiO₂ films needed are high absorptivity in the UV region and have an optical band gap of > 3.00 eV.

■ EXPERIMENTAL SECTION

Materials

Titanium isopropoxide (Ti(OCH(CH₃)₂)₄; 97% purity; Aldrich), absolute ethanol (C₂H₅OH; 99.5% purity; System), glacial acetic acid (CH₃COOH; 99.7% purity; J.T. Baker) and Triton X-100 (C₁₄H₂₂O(C₂H₄O)_n (n = 9-10); 99.9% purity; Aldrich) and DI water.

Instrumentation

The effect of annealing temperatures on the surface morphology of TiO₂ thin films was observed by field emission scanning electron microscope (FESEM; JOEL JSM-7600F). The crystalline property was characterized by X-ray diffraction measurement (XRD; PANalytical X'Pert PRO). The film thickness was measured using a surface profilometer (KLA Tencor P-6). Elemental or compositional analysis was carried out by energy dispersive X-ray spectroscopy (EDX; INCA). The optical property was investigated using an ultraviolet-visible spectrophotometer (UV-Vis; Varian Cary 5000).

Procedures

Firstly, glass substrates (Duran Group) were cut into 1.5 cm × 2 cm in size by using a diamond cutter. Then, for the cleaning process of the glass substrates, they were immersed in a beaker containing acetone and placed in an ultrasonic water bath and sonicated for 10 min. Next, glass substrates were rinsed with deionized (DI) water and then were immersed in methanol and sonicated for

another 10 min. After sonication with methanol, glass substrates were rinsed again with DI water and finally sonicated for another 10 min in a beaker filled with DI water. After the cleaning process, the substrates were blown with nitrogen gas and kept dry in sample containers before the deposition process. The preparation of TiO₂ solution was carried out using titanium isopropoxide, absolute ethanol, glacial acetic acid and Triton X-100 and DI water. Titanium isopropoxide was dissolved in absolute ethanol, which acts as a solvent under continuous stirring on a hot plate. 1.25 mL of glacial acetic acid, 0.09 mL of DI water and 0.01 mL of Triton X-100 was added to the solution as a surfactant and the solution was stirred for 2 h at ambient temperature. The solution was left aging for 24 h prior to the spin coating process. In the spin coating process, deposition speed was fixed at 3000 rpm and deposition time was in 50 sec. The deposition was repeated seven times and each layer was pre-heated at 150 °C for 10 min. Then, the thin films were annealed in a furnace at a different annealing temperature of as-grown, 400, 500 and 600 °C for 1 h.

■ RESULTS AND DISCUSSION

Structural Analysis

Fig. 1 depicts the XRD pattern of the synthesized films of TiO₂ annealed at different temperatures of 400, 500, and 600 °C respectively. The diffraction angles measured were from 10° to 70°. From the XRD pattern, TiO₂ thin films crystallized at a temperature of 500 and 600 °C. Both as-grown and 400 °C films were amorphous. The crystalline samples show the anatase phase (JCPDS 00-004-0477) with a tetragonal crystal structure. From the plots, the anatase phase was confirmed by peaks at $2\theta = 25.2^\circ$ and 48.7° corresponding to the (101) and (200) orientation planes, respectively [9]. The highest intensity of the diffraction peak at around $\sim 25^\circ$ shows a preferred oriented anatase polycrystalline structure for all of the samples. In addition, neither other titania phases, rutile nor brookite were detected in the samples, proving the purity of the anatase phase. The absence of a rutile peak also agrees with the previous report that the transformation of anatase to rutile begins at 1000 °C for

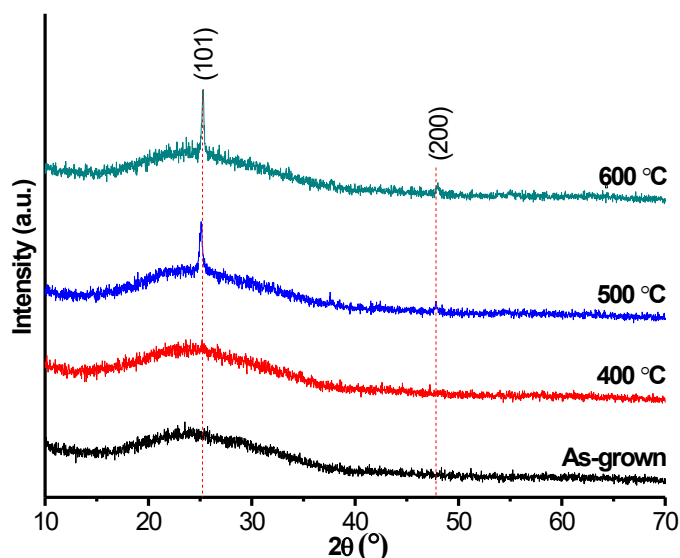


Fig 1. XRD pattern of TiO₂ thin films

sol-gel synthesis [11]. In addition, the crystallinity of the films also increased with increasing annealing temperature. This can be observed by the sharpness of peak intensity at preferred (101) peak. The more intense peaks revealed that the particle size increases at higher annealing temperatures [12].

From the XRD pattern, full-width-at-half-maximum (FWHM) of a peak intensity profile can be determined, which will be used in the Scherrer formula (Eq. (1)) to estimate the average crystallite size [13]:

$$D = \frac{0.94\lambda}{\beta \cos\theta} \quad (1)$$

where D is the crystallite size, λ is the wavelength of X-rays, β is the full width at half maximum of XRD peak and θ is the diffraction angle. The calculated crystallite sizes for 500 and 600 °C were 19.22 and 28.37 nm, respectively. The crystallite size increased when the annealing temperature increased. When the heat was applied to the TiO₂ films, the particles grew because the activation energy of TiO₂ nanoparticles was very minimal [12]. In addition, lattice spacing, lattice strain and dislocation density were also calculated by using Eq. (2), (3) and (4) [7].

$$d_{hkl} = \frac{\lambda}{2\sin\theta} \quad (2)$$

$$\varepsilon = \frac{\beta \cot\theta}{4} \quad (3)$$

$$\delta = \frac{1}{D^2} \quad (4)$$

Here, d_{hkl} is the lattice spacing, ε is the lattice strain, and δ is the dislocation density. The values were tabulated in Table 1. From Table 1, it can be seen that D values were increasing when the annealing temperature increased. This proved that the annealing temperature does play a role in tuning the crystal size [14]. This result also agrees with the previous reports regarding the annealing process which induces diffusion-driven phase segregation hence resulting in a non-homogenous composition and increasing crystal size [14]. The value of the lattice strain is positive (tensile strain). It is well known that the annealing treatment will reduce the tensile strain in thin films. Therefore, the further increase of annealing temperature, the tensile strain tends to change in the opposite direction of strain (compressive), indicating the more tense films [13]. When the lattice strain increase, the dislocation density is also increased.

Surface Morphology

The surface morphology of TiO₂ thin films was characterized by FE-SEM. Fig. 2 represents the surface morphology of all samples at a magnification of 80,000×. The amorphous as-grown film shows that no nanoparticles formed due to the no energy treatment applied to form nanoparticles. In nanotechnology, high energy treatment is needed in the formation of well crystalline nanoparticles. At 400 °C, the grain of nanoparticles was started to form but the spherical shape of nanoparticles still cannot be seen clearly and higher energy is needed to form better surface morphology. At 500 °C, the spherical shape of TiO₂ nanoparticles can be

Table 1. Values for crystallite size, lattice spacing, lattice strain, and dislocation density from XRD analysis

Sample (°C)	2θ at (101) plane (°)	FWHM ₍₁₀₁₎ (°)	Crystallite size, D (nm)	d-spacing (Å)	Lattice Strain, ε (%)	Dislocation Density, δ (× 10 ⁻¹² m ⁻²)
500	25.09	0.442	19.22	0.182	0.236	2.71
600	25.26	0.230	28.37	0.180	0.159	1.24

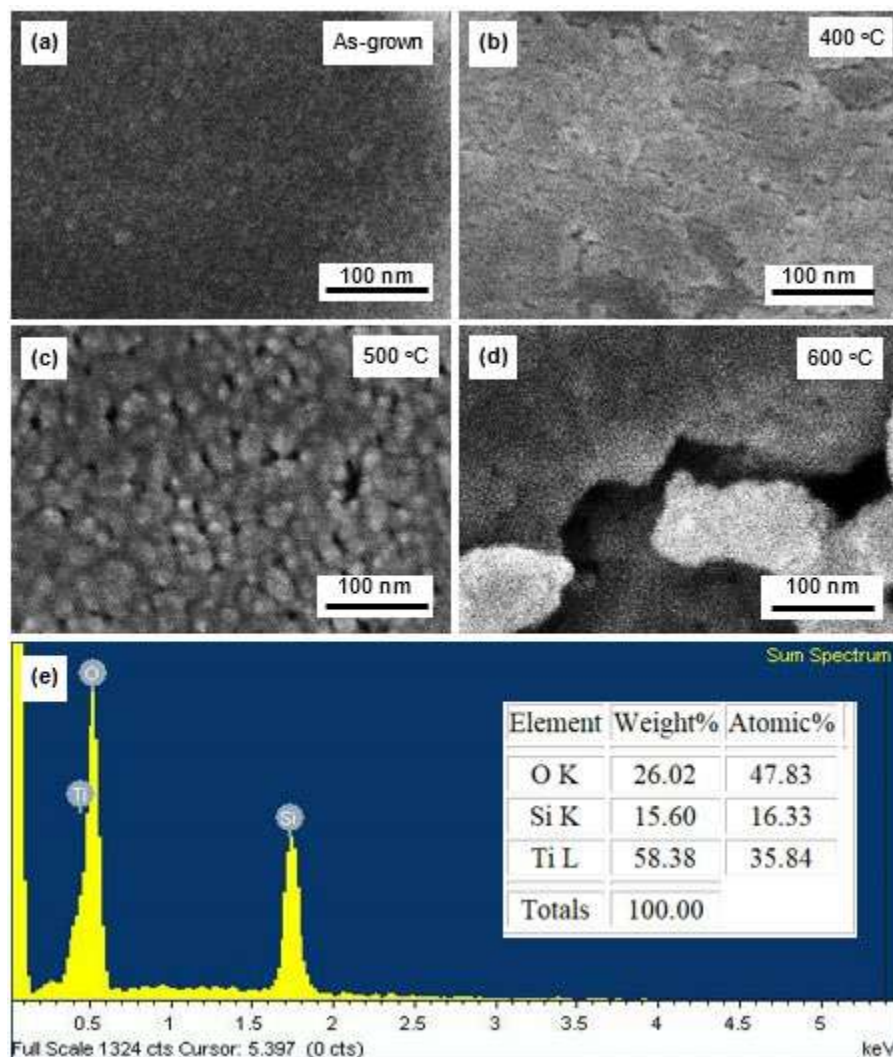


Fig 2. Surface morphology of TiO₂ thin films

observed clearly and the surface of the film was uniform and smooth. When sufficient heat was applied to the TiO₂ films, the particles grew because the activation energy of TiO₂ nanoparticles was very minimal [12]. However, at 600 °C, the film surfaces became rough and crumbled. A previous study reported that the glass substrate started to deform when the annealing temperature at about 600 °C, leading to the deterioration of the film [15].

The elemental analysis of the prepared thin films was examined by EDX as depicted in Fig. 2(e). The EDX result indicated that the TiO₂ sample was mainly composed of Ti and O elements which is consistent with the stoichiometric of TiO₂ [16]. The Ti elements were confirmed by the peak at L α = 0.4522 keV where the

electron from M orbital filled in the hole left by the kicked-out electron in L orbital. Meanwhile, O elements were confirmed by the peak at K α = 0.5249 keV where the electron from L orbital filled in the hole left by the kicked-out electron in K orbital. The additional peaks associated with Si were due to the glass substrate. This EDX analysis assuring that there is no presence of other impurities in the film [17-18].

Optical Analysis

To further obtain information on the light-absorption properties of TiO₂ thin films, UV-Vis analysis was performed. UV-Vis transmittance spectra at room temperature for the samples in the wavelength range from approximately 300 nm to 800 nm illustrated

in Fig. 3. The transmittance spectrum can be divided into two regions i.e. ultra-violet region (< 390 nm) and visible light region (400–800 nm). All samples show average transparency in the visible region and absorbed in the UV range at a wavelength of 300 nm. The abrupt decrease in the transparency of all films in the UV region is due to the fundamental light absorption of TiO₂ [19].

The UV-Vis spectral data are used to obtain the absorption coefficient via Lambert's Law based on Eq. (5) as follows [20]:

$$\alpha = \frac{1}{t} \ln \frac{I_0}{T} \quad (5)$$

where t is the thickness of the film, and T is the transmittance of the film. The absorption coefficients of TiO₂ thin films were displayed in Fig. 4. The plotted graph shows that absorption edges can be observed in the UV region (< 400 nm) for all samples. All films exhibited high absorption of light at the UV region. The 500 °C film produced the best absorption at UV region due to the appearance of fine nanoparticles which magnify the surface area of the film and increase the optical scattering effect, hence exhibited excellent light absorption [21].

In addition, the band gap energies E_g of the synthesized and deposited samples are also calculated based on the Tauc's plot in the measured range using Eq. (6) as follows [20]:

$$(\alpha h\nu)^{1/2} = A(h\nu - E_g) \quad (6)$$

where α is the absorption coefficient, $h\nu$ is the photon energy, A is an absorption constant, and E_g is the band gap.

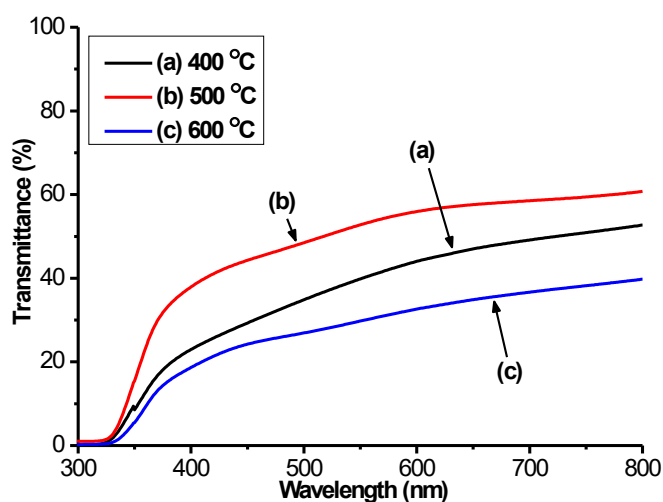


Fig 3. Transmittance spectra of TiO₂ thin films

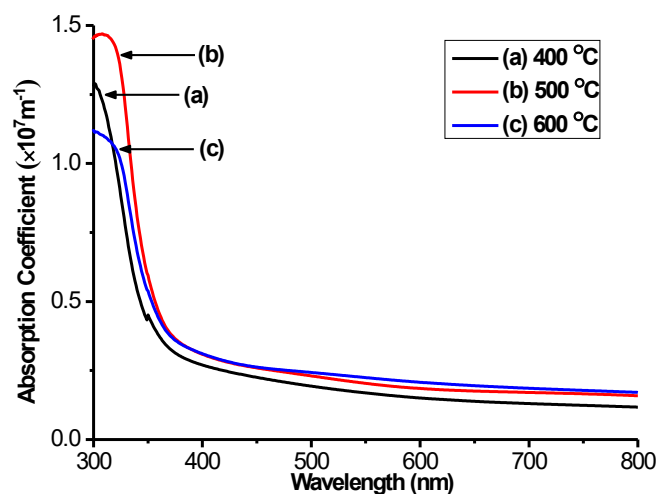


Fig 4. Absorption coefficient spectra of TiO₂ thin films

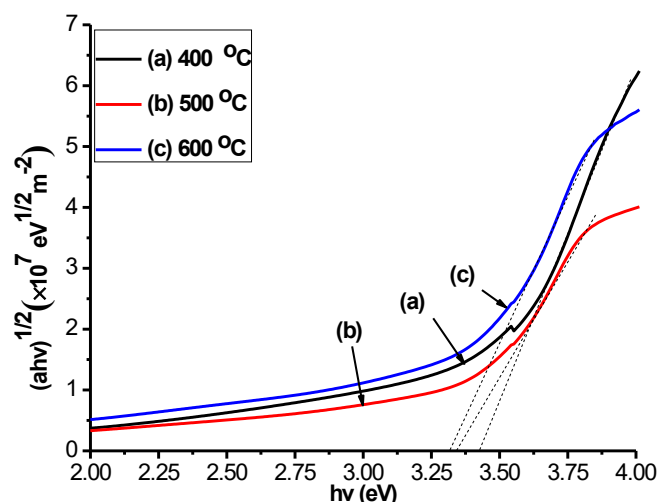


Fig 5. Tauc's plot of TiO₂ thin films

The band gap energy E_g was extrapolated from the linear line on the plotted graph in Fig. 5 of $(\alpha h\nu)^{1/2}$ versus the $h\nu$ curve for the deposited samples. The band gap values obtained were 3.43, 3.35 and 3.32 eV for 400, 500 and 600 °C, respectively. There were no significant changes were observed in E_g .

CONCLUSION

In this work, we successfully synthesized TiO₂ thin films by conducting a simple and low-cost synthesis method using the sol-gel spin coating process. These nanoparticulate thin films were annealed in air at different annealing temperatures for 1 h. XRD pattern confirmed the films show good crystallinity and exist in the anatase phase at temperature 500 °C and above. The

calculated crystallite sizes for 500 and 600 °C were 19.22 and 28.37 nm, respectively. Though higher crystallite size is preferred, 500 °C was chosen as the optimized annealing temperature due to the analysis of other properties. The surface morphology of 500 °C films shows the clearest granular spherical shape of TiO₂ nanoparticles compared to other samples and EDX spectra confirmed the presence of titanium and oxygen elements in the samples. The absorption coefficient also shows 500 °C films to have the highest absorbance in the UV region with an optical band gap energy of 3.35 eV. These results indicate that TiO₂ thin film has a good potential for an optical-based device such as a UV sensor.

■ ACKNOWLEDGMENTS

This work is financially supported by FRGS grant 600-IRMI/FRGS 5/3 (081/2017), Institute of Research Management & Innovation (IRMI), Universiti Teknologi MARA (UiTM).

■ REFERENCES

- [1] Ahmad, I., Usman, M., Zhao, T., Qayum, S., Mahmood, I., Mahmood, A., Diallo, A., Obayi, C., Ezema, F.I., and Maaza, M., 2018, Bandgap engineering of TiO₂ nanoparticles through MeV Cu ions irradiation, *Arabian J. Chem.*, 13 (1), 3344–3350.
- [2] Blanco, E., González-Leal, J.M., and Ramírez-del Solar, M., 2015, Photocatalytic TiO₂ sol–gel thin films: Optical and morphological characterization, *Sol. Energy*, 122, 11–23.
- [3] Zhang, X., Li, W., and Yang, Z., 2015, Toxicology of nanosized titanium dioxide: An update, *Arch. Toxicol.*, 89 (12), 2207–2217.
- [4] Khan, M.M., Ansari, S.A., Pradhan, D., Ansari, M.O., Han, D.H., Lee, J., and Cho, M.H., 2014, Band gap engineered TiO₂ nanoparticles for visible light induced photoelectrochemical and photocatalytic studies, *J. Mater. Chem. A*, 2 (3), 637–644.
- [5] Yazid, S.A., Rosli, Z.M., and Juoi, J.M., 2018, Effect of titanium (IV) isopropoxide molarity on the crystallinity and photocatalytic activity of titanium dioxide thin film deposited via green sol–gel route, *J. Mater. Res. Technol.*, 8 (1), 1434–1439.
- [6] Lourduraj, S., and Williams, R.V., 2017, Effect of molarity on sol–gel routed nano TiO₂ thin films, *J. Adv. Dielectr.*, 7 (6), 1750–1757.
- [7] Desai, N.D., Khot, K.V., Dongale, T., Musselman, K.P., and Bhosale, P.N., 2019, Development of dye sensitized TiO₂ thin films for efficient energy harvesting, *J. Alloys Compd.*, 790, 1001–1013.
- [8] Tahir, M.B., Hajra, S., Rizwan, M., and Rafique, M., 2017, Optical, microstructural and electrical studies on sol gel derived TiO₂ thin films, *Indian J. Pure Appl. Phys.*, 55 (1), 81–85.
- [9] Fazli, F.I.M., Ahmad, M.K., Soon, C.F., Nafarizal, N., Suriani A.B., Mohamed, A., Mamat, M.H., Malek, M.F., Shimomura, M., and Murakami, K., 2017, Dye-sensitized solar cell using pure anatase TiO₂ annealed at different temperatures, *Optik*, 140, 1063–1068.
- [10] Lin, C.P., Chen, H., Nakaruk, A., Koshy, P., and Sorrell, C.C., 2013, Effect of annealing temperature on the photocatalytic activity of TiO₂ thin films, *Energy Procedia*, 34, 627–636.
- [11] Manickam, K., Muthusamy, V., Manickam, S., Senthil, T.S., Periyasamy, G., and Shanmugam, S., 2019, Effect of annealing temperature on structural, morphological and optical properties of nanocrystalline TiO₂ thin films synthesized by sol–gel dip coating method, *Mater. Today: Proc.*, 23 (1), 68–72.
- [12] Nadzirah, S., Hashim, U., Kashif, M., and Shamsuddin, S.A., 2017, Stable electrical, morphological and optical properties of titanium dioxide nanoparticles affected by annealing temperature, *Microsyst. Technol.*, 23 (6), 1743–1750.
- [13] Malek, M.F., Mamat, M.H., Musa, M.Z., Soga, T., Rahman, S.A., Alrokayan, S.A.H., Khan, H.A., and Rusop, M., 2015, Metamorphosis of strain/stress on optical band gap energy of ZAO thin films via manipulation of thermal annealing process, *J. Lumin.*, 160, 165–175.
- [14] Malevu, T.D., Mwankemwa, B.S., Motlounge, S.V., Tshabalala, K.G., and Ocaya, R.O., 2019, Effect of

- annealing temperature on nano-crystalline TiO₂ for solar cell applications, *Physica E*, 106, 127–132.
- [15] Mizuki, T., Matsuda, J.S., Nakamura, Y., Takagi, J., and Yoshida, T., 2004, Large domains of continuous grain silicon on glass substrate for high-performance TFTs, *IEEE Trans. Electron Devices*, 51 (2), 204–211.
- [16] Achoi, M.F., Mamat, M.H., Zabidi, M.M., Abdullah, S., and Mahmood, M.R., 2012, Synthesis of TiO₂ nanowires via hydrothermal method, *Jpn. J. Appl. Phys.*, 51, 06FG08.
- [17] Liu, M., Qiu, X., Hashimoto, K., and Miyauchi, M., 2014, Cu(II) nanocluster-grafted, Nb-doped TiO₂ as an efficient visible-light-sensitive photocatalyst based on energy-level matching between surface and bulk states, *J. Mater. Chem. A*, 2 (33), 13571–13579.
- [18] Singh, S., Sharma, V., and Sachdev, K., 2017, Investigation of effect of doping concentration in Nb-doped TiO₂ thin films for TCO applications, *J. Mater. Sci.*, 52 (19), 11580–11591.
- [19] Safiay, M., Nadzirah, S., Khusaimi, Z., Asib, N.A.M., Hamzah, F., and Rusop, M., 2017, Transmissivity property of nanostructured TiO₂ thin films, *International Conference on Engineering Technology and Technopreneurship (ICE2T)*, 18–20 September 2017, Kuala Lumpur, Malaysia.
- [20] Mamat, M.H., Sahdan, M.Z., Khusaimi, Z., Ahmed, A.Z., Abdullah, S., and Rusop, M., 2010, Influence of doping concentrations on the aluminum doped zinc oxide thin films properties for ultraviolet photoconductive sensor applications, *Opt. Mater.*, 32 (6), 696–699.
- [21] Ismail, A.S., Mamat, M.H., Md. Sin, N.D., Malek, M.F., Zoolfakar, A.S., Suriani, A.B., Mohamed, A., Ahmad, M.K., and Rusop, M., 2016, Fabrication of hierarchical Sn-doped ZnO nanorod arrays through sonicated sol–gel immersion for room temperature, resistive-type humidity sensor applications, *Ceram. Int.*, 42 (8), 9785–9795.

Dual Function of Silver Nanoparticles as Matrix Extracell Removal and Antimicrobial Agent in Polymicrobial Biofilms

Mei Shirli Yasinta, Hera Lisna Ginawati, Nira Ambar Arum, Harini Nur Hikmah, Sri Sumarsih, Mochamad Zakki Fahmi, and Afaf Baktir*

Department of Chemistry, Airlangga University, Kampus C Mulyorejo, Surabaya 60115, Indonesia

* **Corresponding author:**

email: afafi2001@yahoo.com

Received: December 9, 2019

Accepted: August 5, 2020

DOI: 10.22146/ijc.52355

Abstract: *Candida albicans* often form polymicrobial biofilms along with pathogenic microbes. Silver nanoparticles (AgNPs) were well known to have strong antimicrobial activity. However, their effect on polymicrobial biofilms and the mechanism has never been reported. This study aimed to synthesize AgNPs and study their effects on polymicrobial biofilm represented by *C. albicans*-*E. coli* biofilm. Polymicrobial biofilms, formed by clinical isolates of *C. albicans* and *E. coli*, were developed from the standardized suspensions of each strain by culturing flat-bottom 96-well microtiter plates for 48 h then treated with AgNPs. Cell viability was assessed using the tetrazolium salt reduction assay; the extent of biofilm formation was measured by crystal violet staining. AgNPs reduced the polymicrobial biofilm in two ways: by degrading the extracellular matrix and killing both *C. albicans* and *E. coli*. The results showed AgNPs are a potential new approach for developing potent anti-biofilms.

Keywords: silver nanoparticle; polymicrobial biofilm; *C. albicans*; *E. coli*; anti-biofilm

■ INTRODUCTION

Research on biofilms has changed the paradigm of the life of microorganisms. Microorganisms can develop biofilms, which are extracellular matrix-coated communities of microbial cells attached to the host surface [1]. Biofilms are the predominant growth state of many microorganisms [2–4]. According to the National Institute of Health, pathogenic biofilms in the United States played a role in more than 80% of microbial infection cases [4]. Some infection cases related to biofilms included cystic fibrosis, catheter infection, endocarditis, chronic prostatitis, periodontal disease, and ear infections [5,6]. Based on the *in vitro* studies, microorganisms in the form of biofilms can avoid host defense systems, and they are 10^3 – 10^4 times more resistant to antimicrobial agents than their free (planktonic) cells [1,7]. In nature, most microorganisms do not live as single species [8]. They tend to live as a community with other species. Thus, naturally occurring biofilms contain more than one microbial species, called polymicrobial biofilms [8].

Candida albicans (*C. albicans*) is one type of microbe that is capable of building a biofilm and causing infection in humans [9]. It is the most prevalent fungal species in the micro-ecosystem of human microbiota [10]. It is estimated that the polymicrobial biofilms of *C. albicans* cause 27–56% of blood-borne nosocomial infections. *Candida* is often found in the form of polymicrobial biofilms and various types of pathogenic microbes, including *Staphylococcus*, *Pseudomonas*, and *Escherichia coli*. For example, *Candida* interacts with *Streptococcus*, *Lactobacilli*, *Porphyromonas gingivalis* in oral sites. *Candida* and *Cryptococcus* interact with various gram-negative and -positive bacteria in the lower reproductive tract. *Candida* interacts with gram-positive and -negative bacteria (usually *Staphylococcus*) and dermatophyte species on skin sites and vascular catheters. *Candida* also interacts with Enterobacteriaceae and *Enterococcus* in intra-abdominal sites, as well as with Enterobacteriaceae, *Escherichia coli* (*E. coli*), and *Enterobacter faecalis* in the urinary tract [11].

Polymicrobial biofilms have been shown to have several advantages for the multiple species residing within them. These include increased tolerance to antimicrobial agents and increased virulence [12], increasing the difficulty of inhibiting these biofilms. This poses a major clinical issue for human health [2,13]. Previous studies have shown that *E. coli* and *C. albicans* coexist in polymicrobial biofilms isolated from endotracheal tubes and urine catheters [14-15]. This polymicrobial biofilm is thought to increase resistance to the antibiotic ofloxacin [16]. Our current study focuses on identifying a method to inhibit *C. albicans*-*E. coli* biofilms.

For this purpose, we used silver nanoparticles (AgNPs) as they have been reported to have both antibacterial and antifungal activities [16-17]. Moreover, other studies suggest that AgNPs can inhibit the *in vitro* formation of biofilms by various microbial species, such as *P. aeruginosa*, *S. aureus*, *S. epidermis*, *S. pneumonia*, and *S. flexneri* [5,18]. However, the mechanism underlying the activity of AgNPs against polymicrobial biofilms is not understood in detail. Thus, the present study aimed to synthesize AgNPs and study their effects on polymicrobial biofilm represented by *C. albicans*-*E. coli* biofilm.

AgNPs were known less reactive than Ag^+ , making their antibacterial activity lower than AgNO_3 . The inhibitory effect of AgNO_3 on *Pseudomonas putida* mt-2 growth was 1,600 times more than AgNP [19]. On the other hand, extracellular matrix-covered bacterial cells in the biofilm structure more easily penetrated by nanoparticles or nano-sized molecules than that of Ag^+ , which tend to form cluster structures causing low penetration ability. Based on this fact, we will compare the toxicity of AgNPs and AgNO_3 against bacteria and fungi in polymicrobial biofilm protected by wrapped extracellular matrix. Indeed, it is important to compare the effectiveness of AgNPs and AgNO_3 for eradicating *C. albicans*-*E. coli* biofilm.

■ EXPERIMENTAL SECTION

Materials

Silver nitrate (AgNO_3) and tri-sodium citrate ($\text{C}_6\text{H}_5\text{O}_7\text{Na}_3$) were purchased from Sigma Aldrich. The *C.*

albicans (ATCC 10231) and *E. coli* (ATCC 25992) were purchased from the Surabaya Health Laboratory Center (Balai Besar Laboratorium Kesehatan Surabaya). The cultures of *C. albicans* were grown overnight in yeast extract-peptone-dextrose [1% yeast extract (BD Biosciences), 2% peptone (Oxoid Ltd.), and 2% dextrose (Conda Pronadisa)] at 37 °C. The cultures of *E. coli* were grown overnight in Luria Bertani [1% tryptone (Himedia); 0.5% yeast extract (BD bioscience); and 1% NaCl (Merck)] medium at 37 °C. SDB medium was used to create a polymicrobial biofilm in a 96-well microtiter plate. SYTO-59 dye, FITC, and Con A to visualize *E. coli*, *C. albicans* extracellular matrix, respectively.

Procedure

Synthesis of AgNPs

$\text{C}_6\text{H}_5\text{O}_7\text{Na}_3$ and AgNO_3 of analytical grades were used. AgNPs were prepared using a chemical reduction method. Briefly, 100 mL of 1-mM AgNO_3 was heated to the boiling point. Then, 5 mL of 1% $\text{C}_6\text{H}_5\text{O}_7\text{Na}_3$ was added dropwise to this solution. The solution was vigorously stirred during this process. Then the solution was then heated to form a pale-yellow solution. This solution was then stirred until it cooled to room temperature [19].

Growth of *C. albicans*-*E. coli* biofilms

The overnight cultures of *C. albicans* and *E. coli* with optical densities of 0.5 at 600 nm (OD600) were diluted in the SDB medium. Each cell suspension of 75 μL was added to the wells of a round-bottom microtiter plate (TPP, Trasadingen, Switzerland). These *C. albicans*-*E. coli* biofilms in these wells were allowed to grow by adding SDB medium under non-shaking conditions at 37 °C for 48 h. After the incubation period, the culture was further diluted with a fresh SDB medium.

Treatment of *C. albicans*-*E. coli* biofilms with AgNP and AgNO_3

C. albicans-*E. coli* biofilms were divided into three treatment groups. The first group was treated with AgNPs (50 and 100 μL), the second group was treated with AgNO_3 (50 and 100 μL), and the third group was left the untreated group and used as a control. Microtiter plates were incubated for 6 h at 37 °C. After incubation,

the wells were washed twice with 0.2 mL of PBS (pH 7.2) to remove non-adherent cells.

Crystal violet assay

C. albicans-*E. coli* biofilms that were adhered to the walls and bottoms of the wells were stained with 0.01% crystal violet for 30 min. Subsequently, the excess stain was washed off twice with sterile water. The wells were then fixed with 30% acetate acid for 20 min; the solution (100 μ L) was transferred to a new microtiter plate for obtaining absorbance readings. The optical densities (ODs) of the stained and adherent *C. albicans*-*E. coli* biofilms were collected using a micro ELISA auto reader at a wavelength of 595 nm. The average OD of the sterile medium was calculated and subtracted from all the treatment groups' ODs. All steps were conducted at room temperature.

Tetrazolium salt reduction (XTT) assay

After all treatments, the XTT assay was performed as a measure of metabolic activity to estimate the burden of viable cells. Using a multichannel pipette, 40 μ L of XTT solution was added along with 2 μ L of menadione and 158 μ L of PBS to each well containing a pre-washed *C. albicans*-*E. coli* biofilm. Plates were then covered in aluminum foil and incubated in the dark for 2 h at 37 °C. Subsequently, the plates were then uncovered, and a multichannel pipette was used to remove 80 μ L of the resulting colored supernatant from each well. This supernatant was transferred into the corresponding wells of a new microtiter plate. All plates were read in a microtiter plate reader at 490 nm.

Characterizations

Using a UV-1800 spectrophotometer (Shimadzu, Japan), a specific ultraviolet (UV)-Vis spectrum was obtained for AgNPs at a wavelength of 300–600 nm. AgNPs size distribution was assessed using a Zeta Sizer (Malvern Zeta Sizer Nano ZS90). For the visual observation of *C. albicans*-*E. coli* biofilms, biofilm samples were analyzed using SEM and CLSM (Olympus type FV1000). For this, both control and treated *C. albicans*-*E. coli* biofilms were prepared according to the methods described above with modifications in spider medium for growing *C. albicans*-*E. coli* biofilms on

cellulose nitrate filter membranes. The samples were dried overnight at 37 °C. Samples were then dehydrated through a series of graded ethanol (50% for 10 min, 70% for 10 min, and 96% for 20 min). The dried *C. albicans*-*E. coli* biofilms were finally coated with palladium, and their surface was observed using SEM. For CLSM, samples were washed with PBS, stained with SYTO stains for *E. coli* (red); concanavalin A (Con A) for *C. albicans*-*E. coli* biofilm matrix (green); tetramethylrhodamine for *C. albicans* (red); and fluorescein isothiocyanate (FITC) for *C. albicans* (green).

RESULTS AND DISCUSSION

Naturally occurring biofilms contain more than one microbial species and are known as polymicrobial biofilms. Such biofilms are more harmful than monomicrobial biofilms. An antimicrobial agent must be able to degrade and penetrate the extracellular matrix to reach bacterial and fungal cells coexisting in these biofilms to incapacitate polymicrobial biofilms. To solve this problem, in our study, we synthesized AgNPs for use as antimicrobial agents.

AgNPs were successfully synthesized using a chemical reduction method. A change in the solution color characterized AgNPs formation from clear to pale yellow. Thus, the AgNPs formed were stable for 3 weeks, as confirmed by a weekly absorbance examination using a UV-Vis spectrophotometer. AgNPs characterized using a UV-Vis spectrophotometer showed a maximum wavelength at 431.5 nm (Fig. 1(c)), indicating the formation of AgNPs [19]. DLS conducted to determine AgNPs size revealed that the average size of synthesized AgNPs was 20 nm.

The IR spectrum of AgNPs determined using FTIR in Fig. 1(b) revealed some peaks that were following that of AgNPs in a previous study [20]. A peak observed at 3431.36 nm^{-1} corresponded to the OH functional group from H₂O (solvent). A peak at 1614.42 nm^{-1} corresponded to the C=O functional group of C₆H₅O₇Na₃. Briefly, C₆H₅O₇Na₃ acts as a reducing agent and a stabilizing agent to prevent the agglomeration of AgNPs [21].

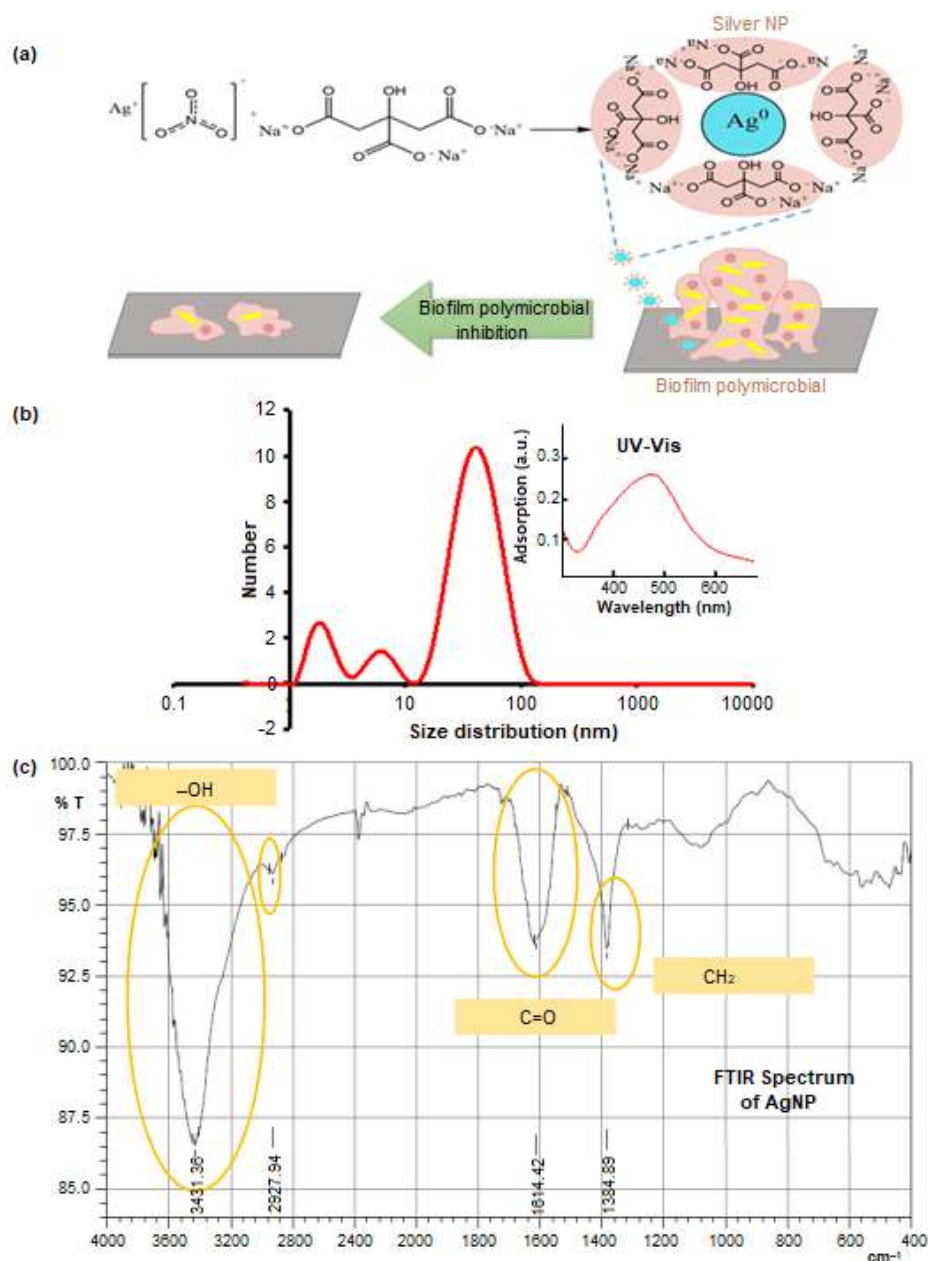


Fig 1. Synthesis, characterization, and application of AgNPs. (a) A schematic process on synthesis AgNPs and its application on biofilm polymicrobial inhibition. Characterization of AgNPs (b) FTIR of AgNPs (c) size distribution and UV-Vis spectra of AgNPs

AgNPs produced in this research were used for the treatment of polymicrobial biofilms. AgNPs can penetrate polymicrobial biofilms to hinder the growth of or eliminate residing microorganisms (Fig. 1). The ability of silver salts $AgNO_3$ and AgNPs, to act as anti-biofilms against *C. albicans*-*E. coli* biofilms were also examined. Crystal violet assay was used to assess the efficacy of

AgNPs and $AgNO_3$ against *C. albicans*-*E. coli* biofilms. Crystal violet provides a good measure of biofilm mass; it stains both bacteria cells and the extracellular matrix [22]. The crystal violet assay indicated that AgNPs was significantly effective in eliminating *C. albicans*-*E. coli* biofilms. The assay demonstrated the inhibition percentages of *C. albicans*-*E. coli* biofilms were 22.15%

and 67.49% following the addition of 50 and 100 μL of AgNPs, and 27.98% and 39.63% following the addition of 50 and 100 μL of AgNO_3 , respectively. AgNPs and AgNO_3 decreased *C. albicans*–*E. coli* biofilms compared with controls. AgNO_3 and AgNPs were able to inhibit extracellular matrix growth, as shown in Fig. 2.

Furthermore, the XTT assay revealed that both AgNO_3 and AgNPs reduced the number of constituent bacterial and fungal cells (Fig. 3). The XTT assay is the most commonly used assay to estimate viable cell count in biofilms and examine the impact of biofilm therapies [21]. As shown in Fig. 3, AgNPs and AgNO_3 could decrease cell viability compared with controls. Cell viability was reduced as the concentrations of AgNPs and AgNO_3 increased, with AgNPs being the most effective. Our data revealed that the inhibition percentages of cell viability were 53.14% and 96.53% following treatment with 50 and 100 μL of AgNPs, and 51.46% and 60.51% following treatment with 50 and 100 μL of AgNO_3 , respectively. These results were also supported by the CLSM assay data.

The CLSM assay demonstrated that the viable cell count of *C. albicans* and *E. coli* was reduced by penetrating AgNO_3 and AgNPs in the extracellular matrix (Fig. 5 and 6). These assays indicated that the higher inhibition ability was proportional to the higher concentration of silver salts used. Thus, both AgNO_3 and AgNPs have the potential to inhibit polymicrobial biofilms.

A noteworthy part of this research was the fact that AgNPs demonstrated more efficient antibiofilm activity compared with AgNO_3 . Also, the inhibition percentage of *C. albicans*–*E. coli* biofilms following treatment with 100 μL of AgNPs was 67.49% compared with 96.53% on AgNO_3 treatment. Furthermore, at a lower concentration, AgNPs showed better antibiofilm activity than AgNO_3 . This may be caused by several factors, including the size of AgNPs compare to that of Ag^+ .

Silver ions form a variety of size and motif clusters [23], which causes the formation of big-size structures. On the other hand, AgNPs comprise nano-sized structures formed of silver atoms that are metallicly

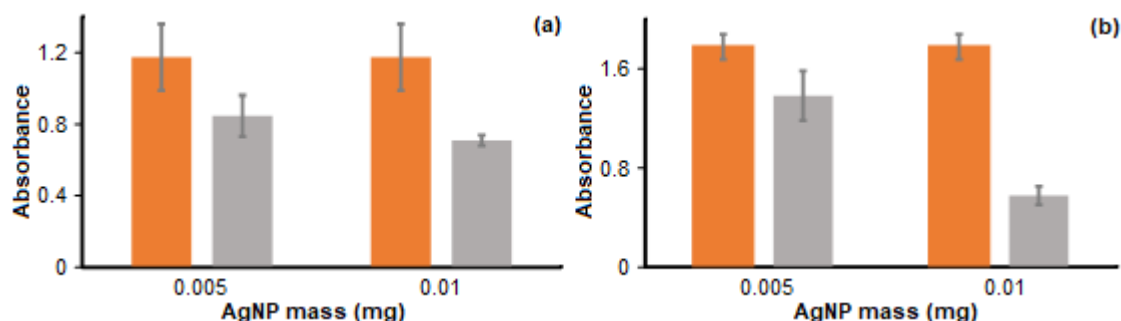


Fig 2. The crystal violet assay of (a) AgNPs and (b) AgNO_3 against *C. albicans*–*E. coli* biofilm. The orange bar indicates the control group, and the grey bar indicates the treatment group. The measurement was performed in triplicates

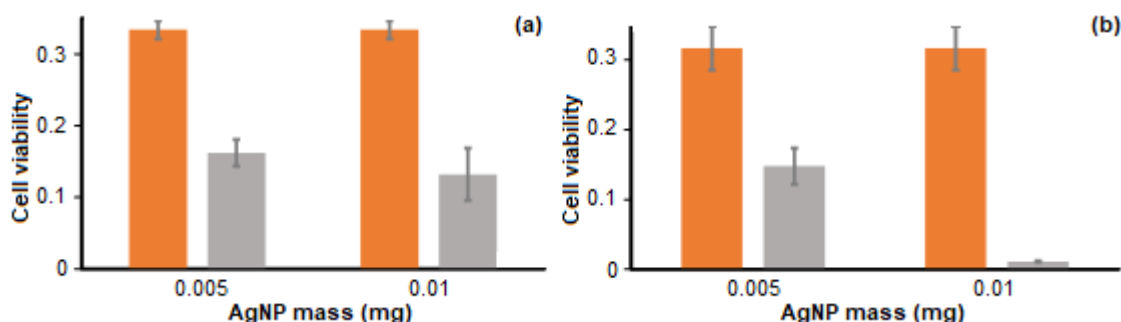


Fig 3. XTT assay of AgNPs (a) and AgNO_3 (b) against *C. albicans*–*E. coli* biofilm. The orange bar indicates the control group, and the grey bar indicates the treatment group. The measurement was performed in triplicates

bonded together and restricted in diameter from 1 to 100 nm by using a matrix. The silver ion will release from the matrix and easily entry to the extracellular matrix of biofilm to access microbial cells inside.

Microbes in a biofilm stay protected from external environmental threats owing to the presence of an extracellular matrix composed of polysaccharides and proteins. Thus, smaller antibiofilm molecules are needed to eliminate biofilms to penetrate the extracellular matrix. A previous study has reported that AgNPs are less toxic to humans compared with AgNO₃. At low concentrations that are non-toxic to humans, the antibacterial ability of AgNPs is highlighted. Meanwhile, the AgNO₃ concentration required to act as an antibacterial agent is toxic to humans [24].

Based on our previous description, we found that AgNPs were able to reduce the cell viability of *C. albicans*–*E. coli* biofilms to a greater extent than AgNO₃. Thus, we further analyzed AgNPs data using SEM. This assay was used to observe biofilm morphology with or without treatment with AgNPs. The typical morphology of *C. albicans*–*E. coli* biofilms was determined using the control group (Fig. 4(a)). *C. albicans*–*E. coli* biofilms that were grown on the cellulose nitrate membrane had aggregated cells covered by the extracellular matrix. Although both *C. albicans* and *E. coli* displayed a normal cell morphology, *C. albicans* was strongly associated with and aggregated to *E. coli* and was covered by the extracellular matrix. In accordance with previous research [25], SEM

analysis in the present study verified that AgNPs are effective in degrading *C. albicans*–*E. coli* biofilms. Moreover, the treated *C. albicans*–*E. coli* biofilms demonstrated a decrease in the extracellular matrix compared to the untreated ones (Fig. 4(b)).

The degraded matrix and debris cells had holes that were formed as the result of matrix degradation. It has been reported that AgNPs can prevent extracellular matrix synthesis. This may explain the inability of certain microorganisms to form biofilms [25] (Scheme 1). In addition, no *C. albicans* and *E. coli* cells were found in *C. albicans*–*E. coli* biofilms treated with AgNPs (see Fig. 3(b)). This result followed that of the XTT assay, demonstrating the ability of AgNPs to reduce cell viability by approximately 96.53%. This was because AgNPs possess the antimicrobial ability, which is mediated by the attachment of AgNPs to the microorganism's cell wall, penetrating it and killing the cells by cell membrane disruption [26]. SEM profile (Fig. 4) and crystal violet assay data (Fig. 2(a)) revealed the ability of AgNPs as extra cell-matrix removal. As for XTT assay, it has revealed the ability of AgNPs to act as antimicrobial toward both bacteria (*E. coli*) and fungi (*C. albicans*). We conclude the dual function of AgNPs as an excellent extracellular matrix removal and cell killer in polymicrobial biofilms.

CLSM analysis was used to compare the differences among fluorescence intensities of *C. albicans*, *E. coli*, and the extracellular matrix from the AgNPs treatment and

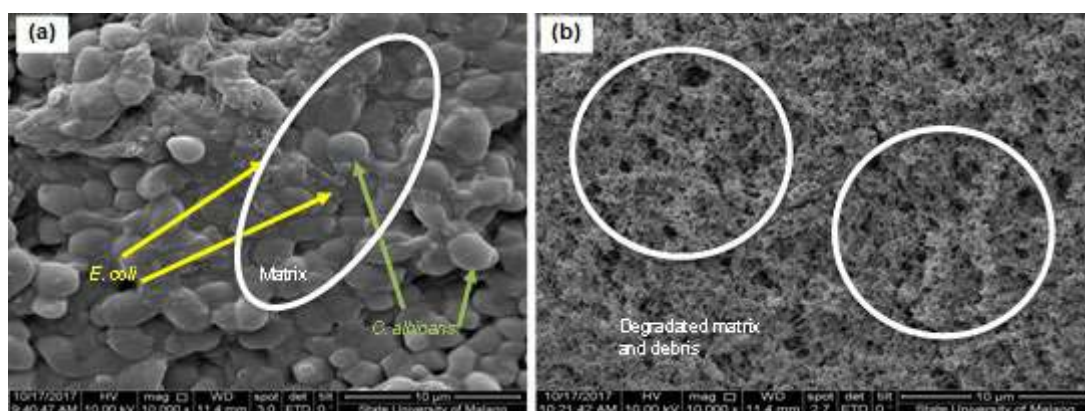


Fig 4. Scanning electron microscopy images of *C. albicans*–*E. coli* biofilm. (a) Control and (b) AgNP treatment. The surface of the extracellular matrix is circled in white. The degraded matrix and debris cells are circled in orange. The green arrows indicate *C. albicans*. The yellow arrows indicate hyphae

control groups. Using CLSM assay, we observed the direct impact of AgNPs on *C. albicans*-*E. coli* biofilm components, including *C. albicans*, *E. coli*, and the extracellular matrix. This assay allowed us to reconstruct a three-dimensional structure of the biofilm by allowing the observation of all layers at different depths with spatial resolution in the order of micrometers [25]. This allowed the visualization of the state of each *C. albicans*-*E. coli* biofilm component using various dyes.

The AgNPs treatment group showed a decrease in fluorescence intensity, which can be observed as a weak

fluorescence on the confocal image of the treatment group (Fig. 5 and 6) and in the quantitative data of mean intensity, which was decreased in the treatment group (Fig. 7(a) and 7(b)). This reduced intensity was proportional to decreased cell numbers, as fluorescence was a consequence of specific binding between the dye and target. We used double staining with the SYTO-59 dye to visualize *E. coli*, with FITC to visualize *C. albicans*, and with Con A to visualize the extracellular matrix. Con A binds to mannose residues, producing a green color indicating the extracellular matrix [25]. Cell numbers are

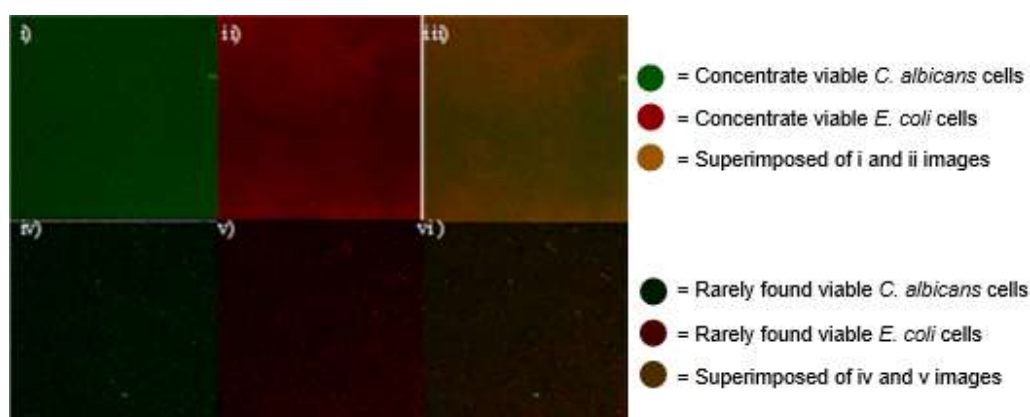


Fig 5. Confocal image of *C. albicans*-*E. coli* biofilms treated with AgNPs. SYTO-59 dye, FITC and Con A were used to visualize *E. coli*, *C. albicans* extracellular matrix, respectively. Control biofilm without treatment (i-iii) showed concentrate light dots of viable cells; As for AgNPs treated biofilm (iv-vi) showed only several light dots of viable cells; Therefore three images at the top (control biofilms without treatment) were far more luminescent than three images at the bottom AgNPs treated biofilms

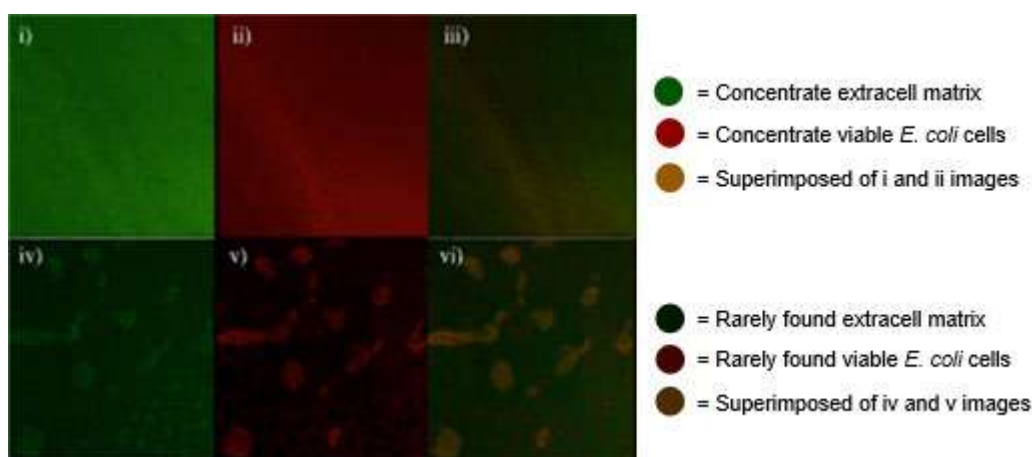


Fig 6. Confocal image of extra cell matrix and *E. coli* cells of *C. albicans*-*E. coli* biofilms treated with AgNPs. SYTO-59 dye to visualize *E. coli* and Con A to visualize the extracellular matrix. Control group without treatment (i-iii) showed concentrate light dots of extra cell matrix; As for treated biofilm (iv-vi) showed only several light dots of extra cell matrix and viable *E. coli* cells

reflected by the intensity of fluorescence observed. We also observed the effect of treating *E. coli* cells and the extracellular matrix in *C. albicans*–*E. coli* biofilms using confocal imaging. We noted a decrease in *E. coli* cells and the extracellular matrix in the treatment group, as demonstrated by reduced staining intensities on the confocal image, compared with those in the control group (Fig. 6).

The existing water channels can explain the presence of dark areas within the biofilm, the heterogeneous production of the extracellular matrix, and the types of exopolysaccharides within the biofilm, and the absence of Con A–FITC binding to the matrix [25]. When CLSM images with red and green fluorescent intensities were superimposed, yellow-colored areas (green + red) revealed that the extracellular-Con A–FITC-reactive polysaccharide (green) was produced in intracellular spaces (red), indicating that extracellular polysaccharides were formed as a capsular component in these biofilms [25].

In addition, we identified that in the AgNPs treatment group, the cell numbers of *C. albicans* and *E. coli* reduced (Fig. 5), as assessed using reduced fluorescence intensities, compared with that in the control group (Fig. 4(a)); this finding was further supported by quantitative data (Fig. 7), showed the cell numbers of *C. albicans* and *E. coli* in the AgNPs treatment group decreased by 57.93 and 50.54%, respectively, compared with that in the control group. In the control group, the cell numbers of *C. albicans* were less than those of *E. coli*. This is possibly due to the difference in the growth abilities of *C. albicans* and *E. coli* within the same period.

Fig. 6 shows *E. coli* and the extracellular matrix in

C. albicans–*E. coli* biofilm. The decreased cell number and extracellular matrix (Fig. 7(b)) observed in the AgNPs treatment group were due to reduced fluorescence intensity compared with that in the control group. This result was also following our quantitative data. The extracellular matrix and the cell number of *E. coli* decreased by 41.89 and 56.81%, respectively. Thus, we conclude that AgNPs can reduce both the number of bacterial cells and the extracellular matrix. The extracellular matrix acts as a protective structure in the biofilm, making it resistant to treatment. The extracellular matrix remains a factor contributing to biofilm resistance against antibiotics and other drugs. According to our quantitative data, AgNPs may be a potential alternative solution to eliminate the extracellular matrix and act as an antimicrobial agent. This dual function of AgNPs confers it with excellent antibiofilm abilities. AgNPs may act via attachment to biofilms, thus inhibiting their growth.

Furthermore, AgNPs can pass through the biofilm water channel. Biofilm water channels play a role in transferring nutrition from the outer environment to the cells beneath the extracellular matrix. AgNPs may pass through these channels due to their small particle size, thus allowing microbial cell access to implement antimicrobial effect and inhibit biofilm formation [25–26]. In addition, AgNPs have a high affinity to microbial cell membranes, thus penetrating and accumulating inside cells and continuously releasing silver ions and damaging the cells [27]. These features of AgNPs contribute to their roles in degrading the extracellular matrix and eliminating *E. coli* and *C. albicans*.

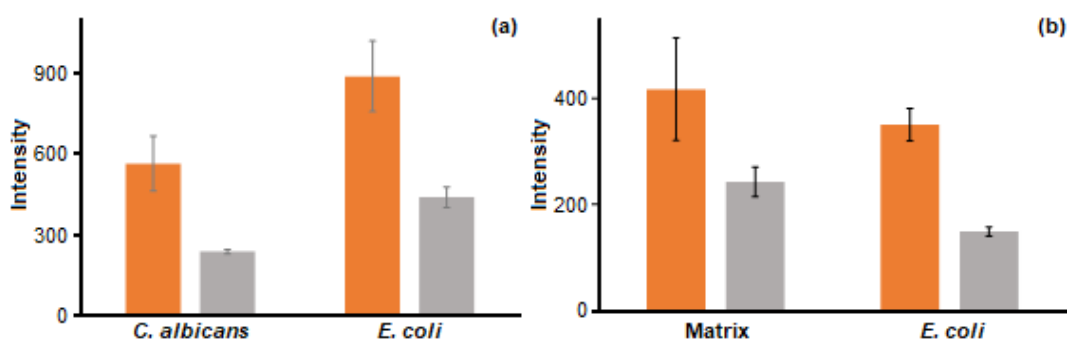


Fig 7. Quantitative data obtained using the CLSM of *C. albicans*–*E. coli* biofilm. The orange bar indicates the control group, and the grey bar indicates the treatment group. The measurements were performed in triplicates

■ CONCLUSION

AgNPs can reduce the number of bacterial cells (acts as cells killer) and degrade the extracellular matrix (extracellular matrix removal). As a cell killer, the percent inhibition cell viability of *C. albicans*–*E. coli* inside matrix biofilms following treatment with 100 μ L of AgNPs was 96.53%. As matrix extra cell removal, AgNPs remove 56.81% of the extracellular matrix covering the cells. These findings suggest that AgNPs can be developed to become potent anti-biofilms towards polymicrobial biofilm consist of *C. albicans* and other pathogenic bacteria. AgNPs can omit tight and thick extracellular matrices that blocking antibiotics reaches their target in the cell, which is one of the triggers of multidrug resistance.

■ ACKNOWLEDGMENTS

The authors thank the Ministry of Research, Technology, and Higher Education for financial support on this study and Airlangga University for the meaningful supports.

■ REFERENCES

- [1] Rabin, N., Zheng, Y., Opoku-Temeng, C., Du, Y., Bonsu, E., and Sintim, H.O., 2015, Biofilm formation mechanisms and targets for developing antibiofilm agents, *Future Med. Chem.*, 7 (4), 493–512.
- [2] Gulati, M., and Nobile, C.J., 2016, *Candida albicans* biofilms: Development, regulation, and molecular mechanisms, *Microbes Infect.*, 18 (5), 310–321.
- [3] Burmølle, M., Ren, D., Bjarnsholt, T., and Sørensen, S.J., 2014, Interactions in multispecies biofilms: Do they actually matter?, *Trends Microbiol.*, 22 (2), 84–91.
- [4] Nobile, C.J., Johnson, A.D., 2015, *Candida albicans* biofilms and human disease, *Annu. Rev. Microbiol.*, 69, 71–92.
- [5] Bandara, H.M.H.N., Yau, J.Y.Y., Watt, R.M., Jin, L.J., and Samaranayake, L.P., 2009, *Escherichia coli* and its lipopolysaccharide modulate *in vitro* *Candida* biofilm formation, *J. Med. Microbiol.*, 58 (12), 1623–1631.
- [6] Palanisamy, N.K., Ferina, N., Amirulhusni, A.N., Mohd-Zain, Z., Hussaini, J., Ping, L.J., and Durairaj, R., 2014, Antibiofilm properties of chemically synthesized silver nanoparticles found against *Pseudomonas aeruginosa*, *J. Nanobiotechnol.*, 12 (1), 2.
- [7] Monroe, D., 2007, Looking for chinks in the armor of bacterial biofilms, *PLoS Biol.*, 5 (11), e307.
- [8] Peters, B.M., Jabra-Rizk, M.A., O'May, G.A., Costerton, J.W., and Shirtliff, M.E., 2012, Polymicrobial interactions: Impact on pathogenesis and human disease, *Clin. Microbiol. Rev.*, 25 (1), 193–213.
- [9] dos Santos, J.D., Piva, E., Vilela, S.F.G., Jorge, A.O.C., and Junqueira, J.C., 2016, Mixed biofilms formed by *C. albicans* and non-*albicans* species: A study of microbial interactions, *Braz. Oral Res.*, 30, e23.
- [10] Baktir, A., Masfufatun, Hanum, G.R., Amailia, K.R., and Purkan, 2014, Construction and characterization of the intestinal biofilm model of *Candida* spp, *Res. J. Pharm., Biol. Chem. Sci.*, 5 (1), 204–211.
- [11] Harriott, M.M., and Noverr, M.C., 2011, Importance of *Candida*-bacterial polymicrobial biofilms in disease, *Trends Microbiol.*, 19 (11), 557–563.
- [12] Røder, H.L., Sørensen, S.J., and Burmølle, M., 2016, Studying bacterial multispecies biofilms: Where to start?, *Trends Microbiol.*, 24 (6), 503–513.
- [13] Fox, E.P., and Nobile, C.J., 2012, A sticky situation: Untangling the transcriptional network controlling biofilm development in *Candida albicans*, *Transcription*, 3 (6), 315–22.
- [14] Vandecandelaere, I., Matthijs, N., Nelis, H.J., Depuydt, P., and Coenye, T., 2013, The presence of antibiotic-resistant nosocomial pathogens in endotracheal tube biofilms and corresponding surveillance cultures, *Pathog. Dis.*, 69 (2), 142–148.
- [15] Samaranayake, Y.H., Bandara, H.M.H.N., Cheung, B.P.K., Yau, J.Y.Y., Yeung, S.K.W., and Samaranayake, L.P., 2014, Enteric gram-negative bacilli suppress *Candida* biofilms on Foley urinary catheters, *APMIS*, 122 (1), 47–58.
- [16] De Brucker, K., Tan, Y., Vints, K., De Cremer, K., Braem, A., Verstraeten, N., Michiels, J., Vleugels, J., Cammue, B.P.A., and Thevissen, K., 2015, Fungal

- β -1,3-glucan increases ofloxacin tolerance of *Escherichia coli* in a polymicrobial *E. coli/Candida albicans* biofilm, *Antimicrob. Agents Chemother.*, 56 (9), 3052–3058.
- [17] Ansari, M.A., Khan, H.M., Khan, A.A., Cameotra, S.S., and Pal, R., 2013, Antibiofilm efficacy of silver nanoparticles against biofilm of extended spectrum β -lactamase isolates of *Escherichia coli* and *Klebsiella pneumoniae*, *Appl. Nanosci.*, 4 (7), 859–868.
- [18] Panáček, A., Kolář, M., Večeřová, R., Prucek, R., Soukupová, J., Kryštof, V., Hamal, P., Zbořil, R., and Kvítek, L., 2009, Antifungal activity of silver nanoparticles against *Candida* spp., *Biomaterials*, 30 (31), 6333–6340.
- [19] Li, W.R., Xie, X.B., Shi, Q.S., Zeng, H.Y., Ou-Yang, Y.S., and Chen, Y.B., 2010, Antibacterial activity and mechanism of silver nanoparticles on *Escherichia coli*, *Appl. Microbiol. Biotechnol.*, 85 (4), 1115–1122.
- [20] Abishek, B., and Hemlata, C., 2014, Antibacterial activity of silver nanoparticles conjugated with antibiotics, *Bionano Front.*, 7, 32–35.
- [21] McGillicuddy, E., Murray, I., Kavanagh, S., Morrison, L., Fogarty, A., Cormican, M., Dockery, P., Prendergast, M., Rowan, N., and Morris, D., 2017, Silver nanoparticles in the environment: Sources, detection and ecotoxicology, *Sci. Total Environ.*, 575, 231–246.
- [22] Manikprabhu, D., and Lingappa, K., 2013, Microwave assisted rapid and green synthesis of silver nanoparticles using a pigment produced by *Streptomyces coelicolor* klmp33, *Bioinorg. Chem. Appl.*, 2013, 341798.
- [23] Blom, M.N., Schooss, D., Stairs, J., and Kappes, M.M., 2006, Experimental structure determination of silver cluster ions (Ag_n^+ , $19 \leq n \leq 79$), *J. Chem. Phys.*, 124 (24), 244308.
- [24] Kvítek, L., Panacek, A., Prucek, R., Soukupova, J., Vanickova, M., Kolar, M., and Zboril, R., 2011, Antibacterial activity and toxicity of silver – nanosilver versus ionic silver, *J. Phys. Conf. Ser.*, 304, 012029.
- [25] Welch, K., Cai, Y., and Strømme, M., 2012, A method for quantitative determination of biofilm viability, *J. Funct. Biomater.*, 3 (2), 418–431.
- [26] Nett, J.E., Cain, M.T., Crawford, K., and Andes, D.R., 2011, Optimizing a *Candida* biofilm microtiter plate model for measurement of antifungal susceptibility by tetrazolium salt assay, *J. Clin. Microbiol.*, 49, 1426–33.
- [27] Ansari, M.A., Khan, H.M., Khan, A.A., Cameotra, S.S., and Alzohairy, M.A., 2015, Anti-biofilm efficacy of silver nanoparticles against MRSA and MRSE isolated from wounds in a tertiary care hospital, *Indian J. Med. Microbiol.*, 33 (1), 101–109.

Fabrication and Performance of a Microbial Fuel Cell: Utilization of Modified Nafion Membrane with Carbon Powder as Separator and Bio-Anode

Mustapha Abdeldjabar Charef^{1,2*}, Hakima Kebaili¹, Mostefa Kameche¹, and Christophe Innocent³

¹Laboratory of Physico-Chemistry of Materials, Catalysis, and Environment, University of Sciences and Technology of Oran-Mohammed-Boudiaf, M'Nouar, BP 1505, Oran, Algeria

²University Hassiba Benbouali of Chlef, B.P. 78C, Ouled Fares Chlef 02180, Algeria

³European Institute of Membranes, University of Montpellier, CC 047, Place Eugene Battalion, 34095 Montpellier Cedex 5, France

*** Corresponding author:**

email: charefmustapha31000@hotmail.com

Received: December 20, 2019

Accepted: September 21, 2020

DOI: 10.22146/ijc.52728

Abstract: A Microbial Fuel Cell (MFC) was conceived by using garden soil as a source to culture. It was then utilized as a bio-catalyst to decompose waste organic matter, reduce pollution from the soil, and produce energies. The MFC was composed of a bio-anode inoculated with a mixture of garden compost leachate and an abiotic stainless steel cathode. Besides, the bio-anode consisted of a Nafion membrane modified with carbon. The microorganisms agglomerated under polarization and formed electroactive bio-film onto bio-anode. In the preliminary test of MFC, potassium hexacyanoferrate has been utilized as catholyte, to enhance the reduction of proton and electrons resulting in a higher voltage. However, this electrolyte is toxic and oxidized rapidly, thus substituted by the hydrochloric acid. The results showed that the MFC with modified Nafion, gave relatively high current-density 379 mA/m² in two days, whereas the conventional biofuel cell without modification attained the current-density 292 mA/m² in four days. Nevertheless, both cells yielded almost the same current density of 20 mA/m² during 60 days. Although it has been used for a long time, the modified Nafion has not been corroded and preserved its physicochemical properties.

Keywords: microbial fuel cell; garden soil leachate; Nafion117 membrane; carbon powder; surface modification; bioenergy; electrochemical characterization

■ INTRODUCTION

Microbial fuel cells (MFCs) are devices that can generate electricity from biomass using bacteria as the catalyst [1-5]. Future applications of MFCs include wastewater treatment and bioelectricity generation for example biosensors [6]. Research on MFCs was started by using low-molecular-weight molecules such as glucose and acetate as fuels [7-8]. Complex substrates such as cellulose and chitin were then tested to extend MFC applicability [9]. Wastes and wastewaters of different origins: food wastewaters [10], meat [11] dairy [12] industries, farm wastes such as farm manure [12], and corn stover [13] have been also investigated for MFC application. When MFC's were tested, the higher

performance was obtained for the more complex substrates: acetate generated 506 mW/m² [7], while hydrolyzed corn stover generated 971 mW/m² [14].

In the anode compartment of the MFC, microorganisms oxidize the substrates (such as glucose [15] and acetate [16]) to generate electrons and protons. The electrons are transported to the anode and they travel through a resistor to the cathode. Protons migrate to the cathode compartment through a proton-exchange membrane. At the cathode (the electron acceptor), the oxygen is reduced to yield water droplets. By this process, the biodegradable organics are removed in the anode chamber, and current is generated as electrons flow from the anode to the cathode [17].

The purpose of this study is to modify the cation-exchange membrane (Nafion117) with carbon graphite powder to avoid corrosion of the bio-anode for a long-time usage (3 months). The modified membrane was also used as a separator between the two compartments of MFC, to stimulate the proton conduction and the oxidation of the fuel at its surface. In addition, the physicochemical properties of the used membrane were also determined to see if the membrane has preserved its characteristics. We determined the transport number of the counter-ions and the limiting current density respectively by using Hittorf and volt-amperometry methods.

■ EXPERIMENTAL SECTION

Materials

The materials used to elaborate the MFC were garden compost (Neuhaus-France), potassium chloride (KCl, Aldrich or Fluka), Sodium acetate (CARLO ERBA), osmosis demineralized water; potassium hexacyanoferrate(III) (Sigma-Aldrich), carbon felt (Alfa Aesar, 6.35 mm thick, anode), carbon powder (TIMREX KS 6 GRAPHITE), Nafion117 membrane (DuPont de Nemours-USA), and Stainless steel 316 (cathode).

Procedure

Preparation of garden compost

The microbial flora was extracted by lixiviation, from the mixture of 500 g of garden soil (Neuhaus) and 1 L of a KCl solution. The mixture was placed in an Erlenmeyer flask and stirred for 72 h. Then the mixture was filtered using a paper filter to give the garden compost that having an ionic conductivity of 4.5 mS/cm and pH 5.

Electrochemical characterization

The device used in the electrochemical experiments (i.e. cyclic voltammetry and impedance spectroscopy) consisted of a cell with three electrodes: working electrode (carbon felt), reference electrode (Ag/AgCl₂), and counter-electrode (Pt). The electrochemical analysis was carried out under experimental conditions controlled by the potentiostat-galvanostat Voltalab-40 functioning with the Volta-Master operating software. The potentiostat allows the potential of the working electrode to be checked against the potential of the reference electrode and the

passage of electric current between the working electrode and the counter electrode.

Anodes were made of carbon felt. Meanwhile, the counter-electrode was made of platinum because of its resistance to corrosion in the electrolytic solution. Working and counter-electrodes were connected to the electrical circuit by copper wires. Silver chloride electrode was used as a reference and the potentials were monitored with a multi-channel provided in the potentiostat-galvanostat apparatus. The electrochemical cell was filled with 80 mL of KCl (60 mM). When the current started, an acetate was added to recover the 20 mM initial concentration to prevent any substrate limitation.

Cyclic voltammetry curves (CV) were recorded at 10 mVs⁻¹. Polarization was interrupted after a polarization depending on the experimental run, and the anode potential was relaxed. It took about 10 min for the anodes to reach a stable open circuit potential (OCP) and perform successive cycles. The potential of the working electrode was scanned from the value used during polarization to the upper limit of 1 V down to -0.1 V and finally back to the starting value. The third and the fourth cycle curves were generally perfectly superimposed thus only the fourth cycle was reported here. Current densities were expressed concerning the projected surface area.

In this work, EIS was used to study the evolution of biofilm formed from garden compost leachate on anodes polarized at a constant potential (+ 0.1 V/ESH) during a certain time. Characterization of the working electrode used, a piece of carbon felt is first recorded. A biofilm was then grown on carbon felt anode system and characterized. The EIS measurement was automatically performed giving an open circuit voltage (OCV) of + 0.1 V/ESH. The parameters adjusted into the Volta-Master software were amplitude of 10 mV (i.e. 10% OCV) and a frequency range from 100 kHz to 100 MHz. The Nyquist impedance spectra were analyzed by fitting experimental data with theoretical data using the Z fit tool provided in the software. Randomization was added before the fitting to select the most suitable set of parameter values.

Surface analysis using scanning electron microscopy.

To visualize the formation of the electroactive biofilm onto the surface of carbon felt bio-anode, scanning electron microscopy was performed. In effect, a small sample of the biofilm was sliced from the surface of the electrode and transferred to a glass substrate to analyze. Therefore, before and at the end of polarization at 0.1 V/ESH, the bio-anode was extracted from the reactor and imaged by scanning microscopy. In some electroactive biofilms, the association of Gram-negative and Gram-positive bacteria has led to better electroactivity than the strains alone [18].

Preparation of modified membrane

The modified membrane was used both as a bio-anode and a separator between the anode and cathode compartments in MFC. The mixture was prepared from carbon powder and deionized water. This mixture was placed in an Erlenmeyer flask and stirred with a magnetic stirrer for 24 h. The Nafion117 was immersed in the carbon solution under stirring for 24 h and then dried in an oven for 5 min at 30 °C. It was immersed again in carbon solution under stirring for 24 h and dried. The chemical modification of the membrane enables the formation of a thin layer containing carbon graphite. Fig.

1 and 2 show the images of pristine and modified membranes.

MFC construction

Following our previous experiments on the conception of bio-electrochemical devices, we have carried on other experiments with newly designed MFCs [4]. These latter consist of two parallel 100 mL sized chambers, separated with the Nafion membrane. The types of MFCs are grouped in Table 1. The bio-anode was immersed into the leachate of the compost garden mixed with 20 mM sodium acetate (used as fuel) and KCl (60 mM) as support conducting electrolyte. The cathode was dipped into the hydrochloride acid solution of potassium hexacyanoferrate(III) at open-air, where oxygen and electrons produced by oxidation are combined into a proton to yield water droplets. The MFC electrical circuit was closed with an external resistance of 1000 Ω to allow the electron transfer from anode to cathode, while protons were exchanged through the Nafion membrane inside the cell. The voltmeter (GEF G 49) was plugged in parallel to follow the evolution of the voltage during the time. The pH meter (Hanna) and conductometer (Hanna) were utilized to control the transfer of ionic species from one compartment to another.



Fig 1. Image of Nafion117



Fig 2. Image of modified Nafion117

Table 1. Limiting current densities of Nafion117 in aqueous solutions (0.1 M)

Limiting Current Density (mA/cm ²)	H ⁺	K ⁺	Na ⁺
Nafion117	32.59	7.33	5.83
Nafion117 modified with carbon powder	20.02	4.83	3.96
Nafion117 used 10 months	26.23	6.01	4.92

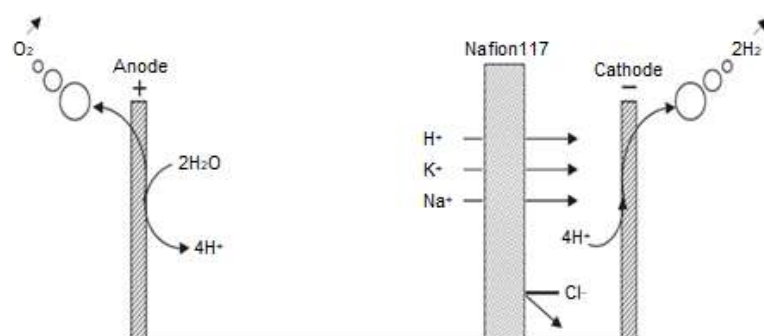


Fig 3. Determination of transport number of counter ions through a cation exchange membrane using the Hittorf method

MFC characteristics

Polarization curves for the MFCs were obtained by changing the external resistance in the range (100–10000 Ω). Values of the external resistance (R) and corresponding voltages (V) were measured by a digital multimeter. The current density (J) was calculated as $J = V/(RA)$, and the power density as $P = iV/A$, where A is the projected surface area of the anode. The internal resistance of the MFC was obtained as the gradient of the polarization curve over the range excluding concentration and activation polarization. The maximum power output was determined from the power curve.

Membrane characterization

Transport number of counter-ion. The permselectivity of a cation exchange membrane is characterized by measurements of the transport number of the counter-ion. This latter may be defined as the fraction of the current transported by the counter-ion, through the membrane when an electric field is applied. In a perfect selective membrane, the transport number of the counter-ion is equal to unity, while that of the co-ion is supposed to be zero. Theoretically, the sum of transport numbers is equal to 1. The transport number of a counter-ion crossing a cation exchange membrane may be given by Faraday's 2nd law [19]:

$$t_{A^+} = \frac{Z_{A^+} n_{A^+} F}{It} \quad (1)$$

where Z_{A^+} is the valence of counter-ion, n_{A^+} is the number of moles crossing the membrane, F refers to Faraday's constant, I represents the electrical current applied, and t is the time of electro dialysis. The measurements of ion

transport numbers were carried out using Hittorf's method as shown in Fig. 3.

Current-voltage measurements. Current-voltage curves were obtained using the cell represented by Fig. 4. It is made of Plexiglas and consists of two symmetrical compartments ($V = 75$ mL). The feed electrodes consist of titanium sheets coated with platinum. The effective area of the membrane was 5 cm². In addition to the feed platinized-titanium electrodes, two silver-silver chloride electrodes were placed nearby the membrane sides, for measurement of the transmembrane potential difference for each value of the applied current. To control both the current intensity and the voltage, two digital multimeters were placed in series and parallel respectively.

Limiting current density. The influence of each electrolytic salt concentration on the current-voltage curve

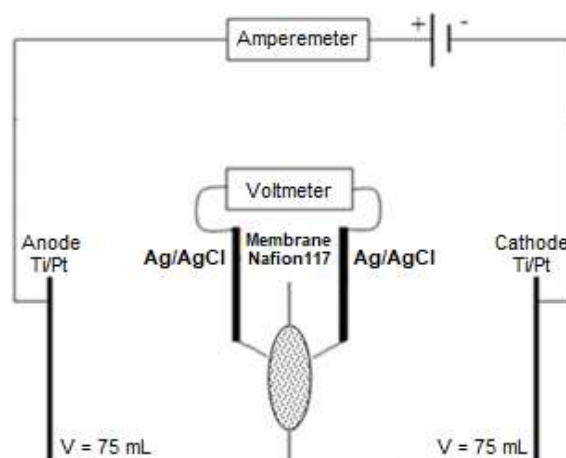


Fig 4. Schematic diagram of a two-compartment electrolytic cell used for current-voltage measurements

was studied and the results are shown in Fig. 6 and 7, respectively. It is also observed that the value of the limiting current density increases with increasing bulk solution concentration. The limiting current density i_{lim} can be calculated according to the following formula [16,31].

$$i_{lim} = \frac{FDC^b}{\Delta t^+ \delta} \quad (2)$$

where F is the Faraday constant, C^b is the concentration of the bulk solution, D is the salt diffusion coefficient, δ is the diffusion boundary layer thickness, and Δt^+ is the being the difference between the transport number in membrane and solution. Eq. (2) assumes that a concentration gradient exists only in the direction perpendicular to the membrane surface, that is, the flow assuming that D , δ , and Δt^+ remain constant. Eq. (2) predicts a proportional relationship between the limiting current density and the bulk solution concentration.

RESULTS AND DISCUSSION

Current-Voltage Curves

The current-voltage (I-V) curves of the Nafion117 membrane are presented in Fig. 6 and 7 for various aqueous electrolytic solutions. These figures show a typical example of a measured current-voltage curve. Three regions can be distinguished. The first region is a linear relationship obtained between the applied current and the voltage drop (generally referred to as the Ohmic region). As the current density increases, the

concentration polarization becomes more pronounced. The concentration in the dilute boundary layer decreases rapidly and the resistance rises. As a result, a deviation of the linear behavior occurs and a limiting current density is reached (represented by a current plateau). Beyond this point, the current density increases again, yielding an over limiting density (due to water dissociation). The figures show that the first two regions are smooth, while the over limiting region is characterized by a considerable scatter, resulting from hydrodynamic instabilities in this region.

The values of related electrical parameters are extracted from these curves and are given in Table 1. They

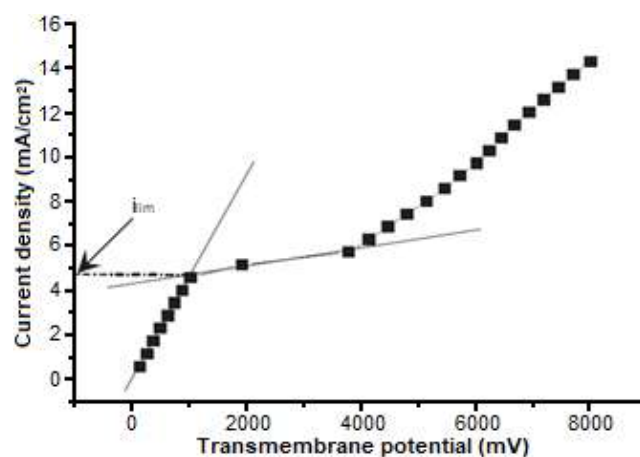


Fig 5. Determination of the limiting current density of Nafion117 membrane using Cross-Section of Tangents method

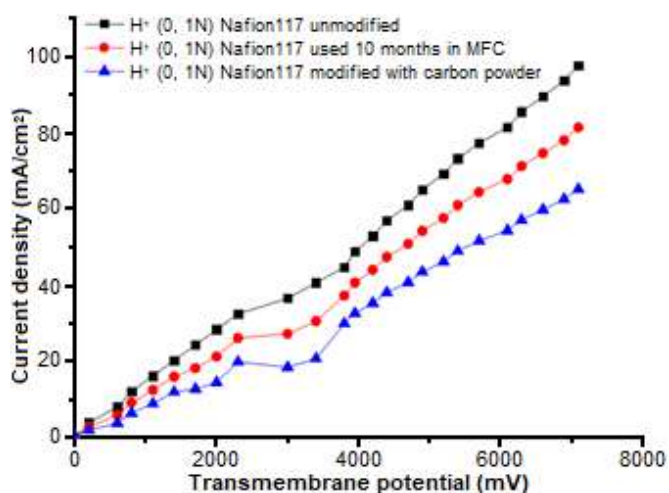


Fig 6. I-V curves of the different membranes conditioned with H^+

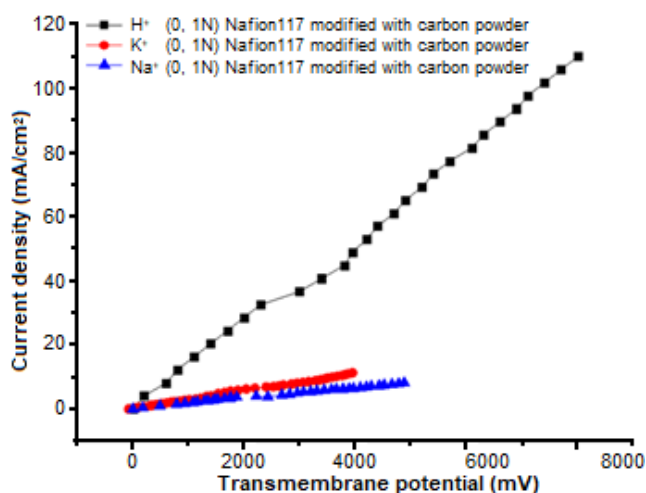


Fig 7. I-V curves of the different membrane conditioned with H^+ , Na^+ , and K^+ separately

are following the concentration polarization and electroconvection phenomena, as mentioned earlier. They are similar to those previously reported in the literature [20] and seem to reflect differences of counterion diffusion coefficients through the membrane and also the ionic conductivity of the solution.

The limiting current density can be determined from the relationship between the current and corresponding potential [21-22]. It is obtained by measuring the transmembrane potential as a function of the applied current. Three graphical methods can be used to determine this limiting current density. We used the method of Cross-Section of Tangents (CST). The limiting current is determined in the relationship between the potential and the current in the characteristic (I-V), where the slope (the reciprocal of the resistance) is changed, following water dissociation on the surface of the ion exchange membrane [23-25]. As shown in Fig. 5, the limiting current density can be determined by drawing the two slopes of the Ohmic region and plateau that intersect at the limiting current. Table 1 shows limiting current densities for 3 membranes in several aqueous electrolytes.

The characterization results show that the modification of the Nafion117 membrane with carbon powder causes an increase in its transport performance, especially in the case of H⁺ transport. In effect, as we reported in the paper, the modification of the Nafion membrane with the carbon did allow the better ionic conduction of the proton. As shown in Table 1, the current-voltage (I-V) characteristic of the modified membrane, shows a limiting current density (20.02 mA/cm²) less than the pristine membrane (without modification, i.e. 32.59 mA/cm²), which is quite reasonable. In effect, with the modified membrane, the coefficient diffusion of the proton in the diffusion layer immediately adjacent to the membrane is less than that of the pristine, which leads to a rapid depletion of the proton from the diffusion layer, and thus a quick transfer through the membrane. Compared to metal cations present in the anode compartment, the proton moves more rapidly, in agreement with previous data reported in the literature. The presence of carbonaceous support (carbon powder)

in the membrane suggests that it may be capable of conducting electrons. For this, we characterized the Nafion117 membrane using cyclic volt-amperometry with three electrodes.

Cyclic voltammetry of Nafion membrane and carbon felt

Cyclic voltammetry (CV) is now used almost routinely to characterize bio-anodes and advance in understanding electron transport and transfer mechanisms. The main objective of a catalytic CV is to characterize the bio-electrode properties in particular oxidation and reduction, by exploiting the substrate. Catalytic CVs are generally performed in stationary mode only, i.e. with a potential scan rate low enough for reactions and electron transport/transfer steps to balance each other. Experimentally, a low scan rate is most often used to ensure such a condition. The stationary catalytic CVs give the current that the electrode could provide under the applied potential over the whole range of scanned potentials, and thus provides a complete characterization of the electroactive biofilm electrocatalytic behavior [26].

The modification of the Nafion membrane with the carbon powder has been made in evidence by CV. Fig. 8 shows that the redox signal of K₃Fe(CN)₆ is visible on the carbon modified Nafion117 membrane with the appearance of the two oxidation and reduction peaks in cycle IV. This demonstrates that modified-Nafion117 is a good electronic conductor. Whilst, Fig. 9 illustrates the oxidation of the substrate by the biofilm on the carbon felt [31].

Electrochemical impedance spectroscopy (EIS) of membranes and carbon felt

EIS is a powerful method to understand and study electron-transfer mechanisms and different properties of pure and heterogeneous biofilms. Many works studied the various parameters that influence impedance in Microbial Fuel Cells (MFCs) on biofilm electrodes. The first studies were only focused on determining the internal resistance of MFCs with a basic interpretation of impedance spectra. Other parameters investigated were the electrode material [28]. Recently, the electrochemical impedance experiments were also used

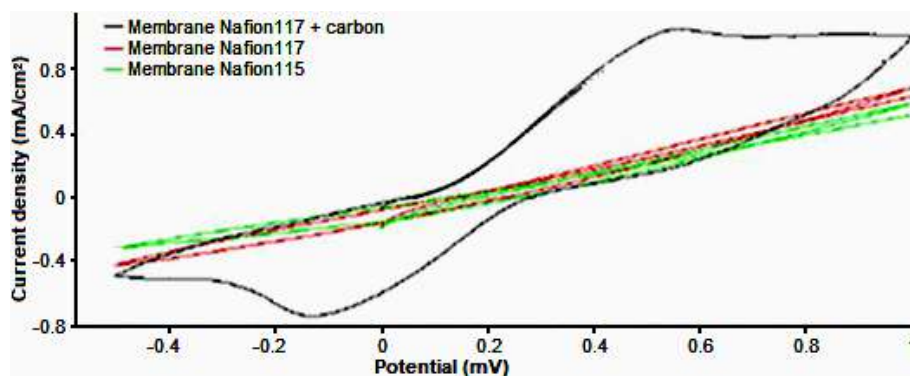


Fig 8. Cyclic voltammetry of the Nafion117 membrane modified with carbon

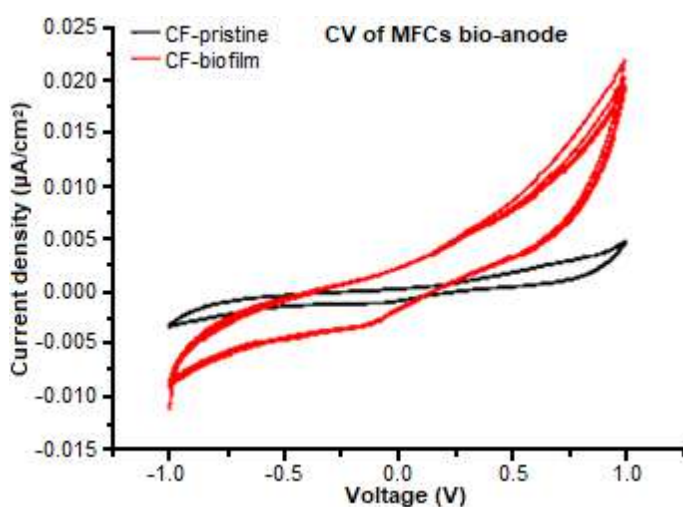


Fig 9. CV of carbon felt

to understand the phenomena related to bioelectrochemistry, such as the ionic strength of the medium [29] effects of the pH, and the presence of microbially secreted mediators [30].

EIS using a Nyquist plot is one of some methods used for evaluating the internal resistance of an MFC. This method is preferred compared to the others as the dynamic response of the system is measured, even though it requires the use of a potentiostat with EIS software. EIS is based on superimposing the applied potential of a working electrode to result in a sinusoidal signal with a small amplitude. By varying the frequency of the sinusoidal signal and plotting the measured electrode impedance, detailed information can be obtained on the system [31].

To confirm the electron conduction of the carbon modified Nafion117 membrane, we performed a characterization by three-electrode impedance

spectroscopy. The EIS Nyquist diagrams have been removed to extract the values of the electric resistance of electrolyte by extrapolation of the Nyquist diagram to infinite frequency [32]. The values are summarized in Table 2. As can be seen, the membrane modified with three thin films of CP displays the smallest electric resistance i.e. the highest electric conductivity. Besides, Fig.10 and 11 show the Nyquist diagrams and SEM image of carbon felt with and without biofilm.

Table 2. Surface electrolyte resistances of the three modified membranes (MM) with carbon powder (CP) extracted from Nyquist diagrams

MM with CP	Re (Ohm cm ⁻²)
One thin film	0.85
Two thin films	0.77
Three thin films	0.26

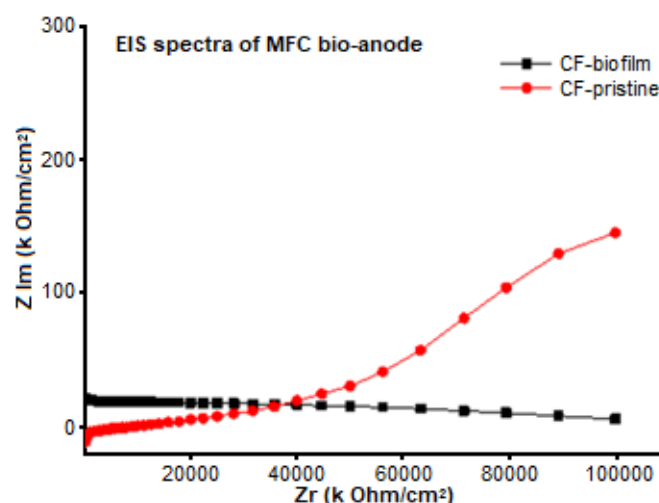


Fig 10. EIS of carbon felt

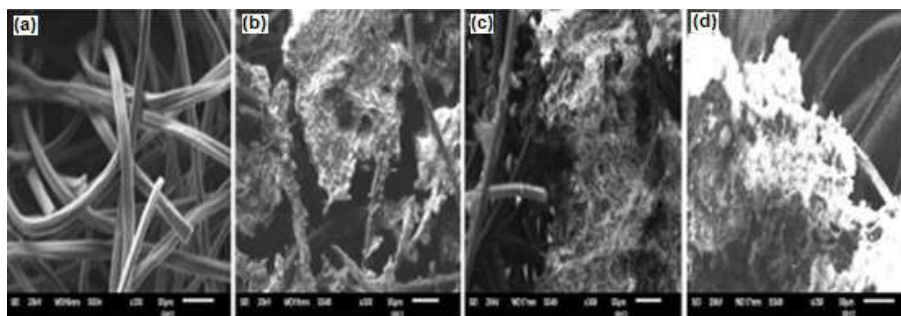


Fig 11. SEM images (magnification 50 μm) confirm reformation of biofilms resulting from sonication of successive generations: (a) pristine CF; (b) biofilm of 1st G; (c) biofilm of 2nd G; (d) biofilm of 3rd G

The values of the electric resistance confirm that the increase in the amount of carbon deposited on the polymer matrix of Nafion117 causes the decrease of resistance of this membrane (used as bio-anode). However, it becomes electrically more conductive [33-35]. The carbon dioxide modified Nafion117 membrane can be used as a bio-anode in the MFC. This latter becomes capable to allow the connection of biofilm on its surface. Since the modified membrane becomes a highly electronic conductor, it can satisfactorily be used as a bio-anode in the conception of a novel MFC device for the production of small bio-energy and depollution of the environment [33-35].

Power Generation of MFCs

The constituents of different MFCs is presented in Table 3 and illustrated schematically in Fig. 12. The performance of the MFC1 was monitored during prolonged operation using bio-anode carbon felt, cathode stainless steel plate, and separator (membrane Nafion117)

[36-37]. The cell was operated over an external load resistance of 1000 Ω . The current Density across the external resistance reached a maximum of more than 290 mA/m^2 approximately 120 h after the beginning of the experiment and falling to about 60% of its first maximum value after a further 50 h (Fig. 13) [38-40]. The addition of extra nutrients (5 mL of sodium acetate added as indicated by the first squared blue symbol) restored the current density to the second maximum value (250 mA/m^2), showing that the decline in current had been due to exhaustion of nutrients in the medium. After the potential had subsequently fallen again, another addition of the same amount of sodium acetate increased the current density. However, after 700 h the current density decreases despite the addition of fuel. At last, it reached the minimum value (30 mA/m^2), after 1200 h.

The MFC2 followed the same behavior as the MFC1, but with a large difference between their current densities (50%) in the beginning. This difference decreased with time. However, the current densities of

Table 3. Constituents of different MFCs

Type of MCF	Bio-anode	Cathode	Separator
MCF1	-Carbon felt -6.5 cm^2	-Stainless Steel 316 -8 cm^2	Nafion117
MCF2	-Carbon felt -6.5 cm^2	-Stainless Steel 316 -8 cm^2	Nafion117 modified with carbon powder KS6
MCF3	-Nafion117 modified with carbon powder KS6 -6.5 cm^2	-Stainless Steel 316 -8 cm^2	Nafion117
MCF4	-Nafion117 modified with carbon powder KS6 -6.5 cm^2	-Stainless Steel 316 -8 cm^2	Nafion117 modified with carbon powder KS6

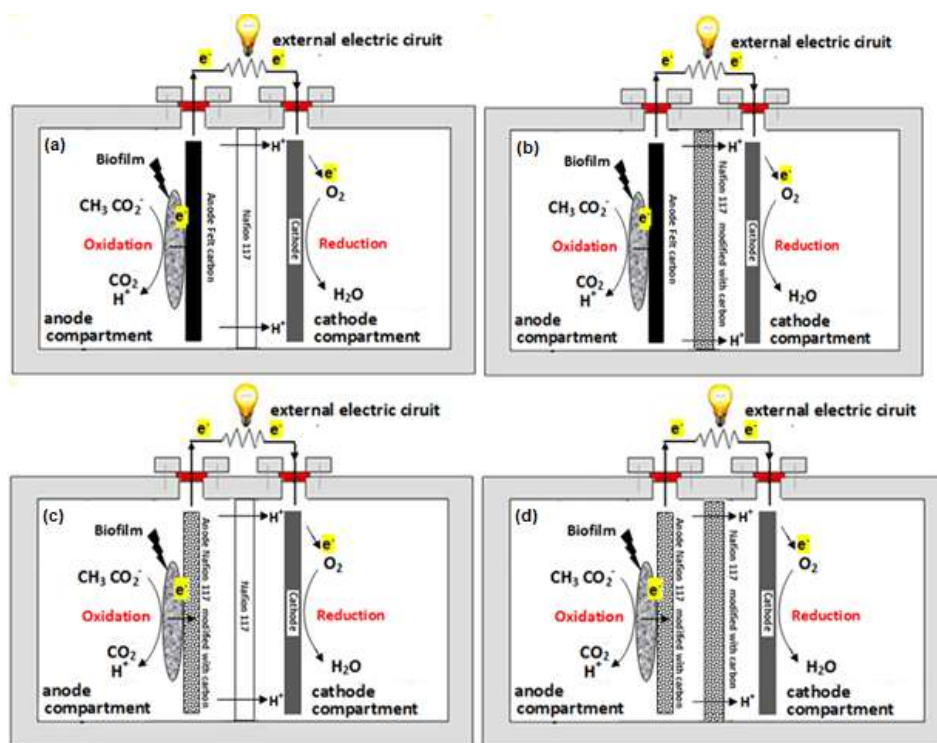


Fig 12. Schemes of MFCs according to Table 3 (a–d); (a) MFC1, (b) MFC2, (c) MFC3, (d) MFC4

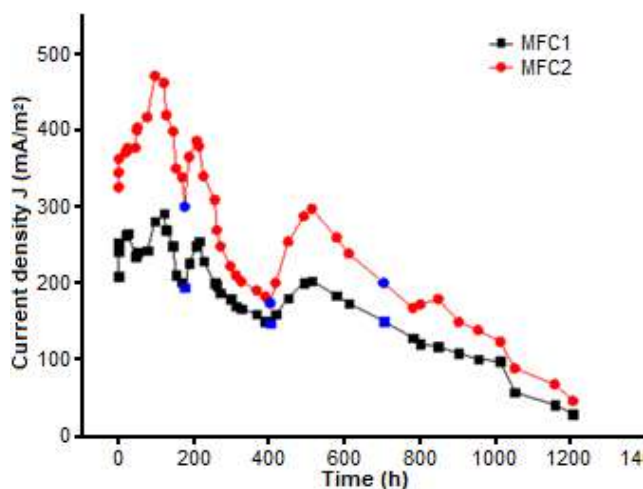


Fig 13. (■) Evolution of current density of MFC1 (membrane separator Nafion117 unmodified), (●) Evolution of current density of MFC2 (membrane separator Nafion117 modified with carbon powder), (■) Indicate additions of 5 mL of sodium acetate; with an external resistance of (1000 Ω)

both MFCs tended towards the same minimum value (50 mA/m²) after 1200 h. It may be concluded that the modification of the membrane with carbon powder enhances its proton conduction.

The performance of the MFC1 was studied for a long time. It reaches the maximum value (290 mA/m²) after 120 h. About 60% of this density is lost after 50 h (Fig. 13). The performance of MFC1 increases to 250 mA/m² after the addition of 5 mL sodium acetate. The value of J decreases 30 mA/m² after 1200 h even with the addition of a carburant. The MFC2 follows the same pace as the MFC1 but with a higher current density of about 50%, so the MFC2 modified with carbon gives more energy.

This increase may be due to the change in the material caused by the modification of the membrane with carbon. On the other hand, the two current densities approach each other as the time is running out. This phenomenon can be explained by the fact that the carbon powder is detached from the modified membrane. This phenomenon can be explained by the fact that the carbon powder is detached from the modified membrane. Despite this, carbon-modified MFC2 remains the most energy-efficient biopile. To confirm this conclusion, it was necessary to use electrochemical characterization techniques such as volt-ampmetry, cyclic voltammetry, and electrochemical impedance spectroscopy.

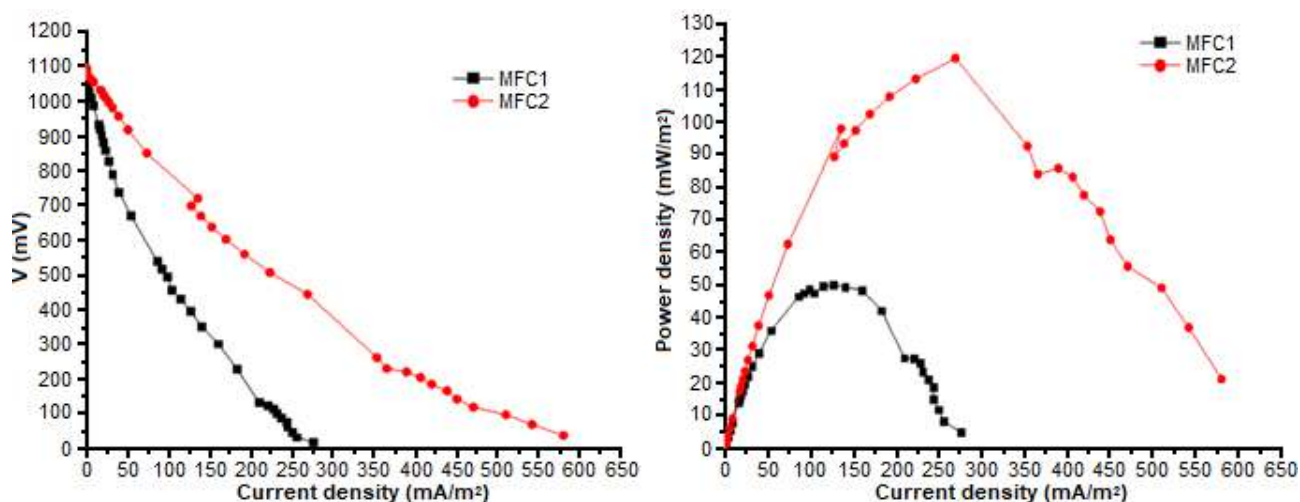


Fig 14. Polarization curves of MFC1 and MFC2

Polarization and Power Curves

Fig. 14 shows the polarization and power curves of the studied MFC. It can be obtained from the polarization curve that the internal resistance of the MFC was 1000Ω . From the power curves, it was observed that the MFC1 generated a maximum power density of 50 mW/m^2 , which corresponded to a density current of 126 mA/m^2 at the cell voltage 400 mV . The MFC2 followed the same behavior as the MFC1, but with a large difference between their power densities of 120 mW/m^2 which corresponds to a current density of 270 mA/m^2 at the cell voltage 450 mV . It may be concluded that the modification of the membrane with carbon powder enhances its performance.

Modified Nafion Membrane as Bio-Anode in MFC

As the membrane demonstrated high electronic conductivity, we considered the MFC device with this membrane. The difference between these two MFCs is the separator between the two compartments. In MFC3, the bio-anode is the Nafion117 membrane modified with carbon powder, the separator is the virgin Nafion117 membrane and the cathode used is stainless steel 316. In MFC4, the bio-anode used is Nafion117 membrane modified with the carbon powder, the separator is the modified Nafion117 membrane with carbon and the cathode used is stainless steel 316.

Stability of MFC3 and MFC4

In the case where the modified membrane was used both as separator and bio-anode, we obtained similar behavior and approximately the same current density as MFC1 and MFC2. The advantage of using the MFC4 was to avoid the corrosion of the bio-anode. It may

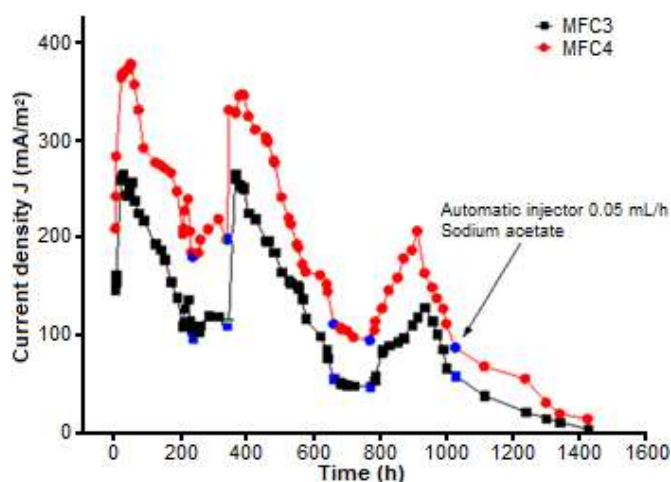


Fig 15. (■) Evolution of current density of MFC3 (anode Nafion117 modified with carbon powder membrane separator Nafion117 unmodified), (■) Evolution of current density of MFC4 (anode Nafion117 modified with carbon powder membrane separator Nafion117 modified with carbon powder), (■) indicate additions of 5 mL of sodium acetate with an external resistance of (1000Ω)

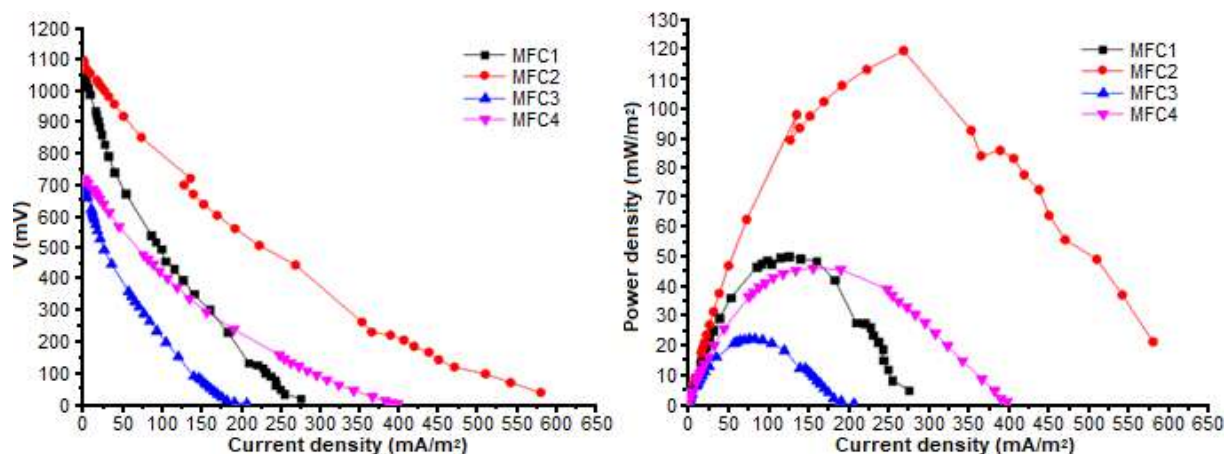


Fig 16. Polarization curves of 4 MFCs

Table 4. Comparison between performances of MFCs

Type of MFC	Initial Current Density (mA/m ²)	Maximum Current Density (mA/m ²)	Power Density (mW/m ²)
MFC1	210	292	50
MFC2	327	470	119
MFC3	145	265	22
MFC4	209	379	45

be concluded that the modification of the membrane with carbon powder used either as bio-anode and separator, enhances its proton conduction and electron production.

Fig. 16 shows the characterizations of the MFC3 and MFC4. A current increase has been observed, indicating the formation of a biofilm and its connection to the anode. This confirms both the good conduction of the Nafion117 membrane modified with graphite carbon, as electrode, but also its ability to connect the microbial biofilm. Moreover, it was noticed that the MFC with a modified membrane either as separator or bio-anode, was stable and kept its form. Its role was to improve the electronic conduction as far as the modified Nafion membrane with carbon powder is known as proton/electron conductor.

Besides, as shown in Table 4 and Fig. 16, the comparison between the four MFCs reveals that the effect of the modification of the membrane on the performances of the microbial fuel cell indicating the possibility of using this membrane as an electrode, even if in the latter two MFC3 and MFC4. The power results are lower and the capacity of the membrane is made conductive. It establishes an electrical connection between the bacterial

medium and the bio-anode. This point is certainly the explanation of the increase in the performance of the biopiles in the presence of membrane modified with the carbon powder (MFC1 and MFC2). The membrane acts as an electrode and behaves like an anode at the same time. This property is at the cause of the performances observed. We have shown by the voltammetric technique that the membrane permeability was not modified to explain the increase in observed power.

CONCLUSION

The characterization of the Nafion117 membrane used in a microbial fuel cell was carried out under the operating conditions. The results showed moderate differences in membrane permeability which lead to the conclusion that this material could be used as a microbial fuel cell separator. Moreover, the modification of the Nafion117 membrane with carbon powder made it possible to obtain a mixed conductive membrane material (ionic and electronic) which we were able to characterize. The integration of this modified membrane in a microbial fuel cell has shown its ability

to increase device power. According to our first analyzes, it seems that the properties of electronic conductivity associated with the capacity of connection of a biofilm by the membrane explain this performance. The preliminary results should be supplemented by analyzes of the presence of biofilm on the membrane. In the absence of biofilm, this would demonstrate a moderate transfer of electrons from the bacterial to the electrode via redox mediators secreted by microbial cells.

■ REFERENCES

- [1] Cheng, S., Xing, D., Call, D.F., and Logan, B.E., 2009, Direct biological conversion of electrical current into methane by electro methanogenesis, *Environ. Sci. Technol.*, 43, 3953–3958.
- [2] Logan, B.E., 2009, Exoelectrogenic bacteria that power microbial fuel cells, *Nat. Rev. Microbiol.*, 7 (5), 375–381.
- [3] Kato, S., 2016, Microbial extracellular electron transfer and its relevance to iron corrosion, *Microb. Biotechnol.*, 9 (2), 141–148.
- [4] Djellali, M., Kameche, M., Kebaili, H., Bohent, M.M., and Benhamou, A., 2019, Synthesis of nickel-based layered double hydroxide (LDH) and their adsorption on carbon felt fibers: Application as low-cost cathode catalyst in microbial fuel cell (MFC), *Environ. Technol.*, 0 (0), 1–13.
- [5] Kebaili, H., Kameche, M., Innocent, C., Benayyad, A., Kosimaningrum, W.E., and Sahraoui, T., 2019, Scratching and transplanting of electro-active biofilm in fruit peeling leachate by ultrasound: Re-inoculation in new microbial fuel cell for enhancement of bio-energy production and organic matter detection, *Biotechnol. Lett.*, 42 (6), 965–978.
- [6] Zhang, X., Cheng, S., Liang, P., Huang, X., and Logan, B.E., 2011, Scalable air cathode microbial fuel cells using glass fiber separators, plastic mesh supporters, and graphite fiber brush anodes, *Bioresour. Technol.*, 102 (1), 372–375.
- [7] Cheng, S., Liu, H., and Logan, B.E., 2006, Increased performance of single-chamber microbial fuel cells using an improved cathode structure, *Electrochem. Commun.*, 8 (3), 489–494.
- [8] Ouis, M., Kameche, M., Innocent, C., Charef, M., and Kebaili, H., 2018, Electro-polymerization of pyrrole on graphite electrode: Enhancement of electron transfer in bioanode of microbial fuel cell, *Polym. Bull.*, 75 (2), 669–684.
- [9] Niessen, J., Schröder, U., Harnisch, F., and Scholz, F., 2005, Gaining electricity from in situ oxidation of hydrogen produced by fermentative cellulose degradation, *Lett. Appl. Microbiol.*, 41 (3), 286–290.
- [10] Gil, G.C., Chang, I.S., Kim, B.H., Kim, M., Jang, J.K., Park, H.S., and Kim, H.J., 2003, Operational parameters affecting the performance of a mediator-less microbial fuel cell, *Biosens. Bioelectron.*, 18 (4), 327–334.
- [11] Heilmann, J., and Logan, B.E., 2006, Production of electricity from proteins using a microbial fuel cell, *Water Environ. Res.*, 78 (5), 531–537.
- [12] Zhang, B.G., Zhou, S.G., Zhao, H.Z., Shi, C.H., Kong, L.C., Sun, J.J., Yang, Y., and Ni, J.R., 2010, Factors affecting the performance of microbial fuel cells for sulfide and vanadium (V) treatment, *Bioprocess. Biosyst. Eng.*, 33 (2), 187–194.
- [13] Kondaveeti, S., Choi, K.S., Kakarla, R., and Min, B., 2014, Microalgae *Scenedesmus obliquus* as renewable biomass feedstock for electricity generation in microbial fuel cells (MFCs), *Front. Environ. Sci. Eng.*, 8 (5), 784–791.
- [14] Cercado-Quezada, B., Delia, M.L., and Bergel, A., 2010, Treatment of dairy wastes with a microbial anode formed from garden compost, *J. Appl. Electrochem.*, 40 (2), 225–232.
- [15] Chaudhuri, S.K., and Lovley, D.R., 2003, Electricity generation by direct oxidation of glucose in mediatorless microbial fuel cells, *Nat. Biotechnol.*, 21 (10), 1229–1232.
- [16] Cheng, S., Liu, H., and Logan, B.E., 2006, Increased performance of single-chamber microbial fuel cells using an improved cathode structure, *Electrochem. Commun.*, 8 (3), 489–494.
- [17] Zhu, X., and Ni, J., 2009, Simultaneous processes of electricity generation and *p*-nitrophenol degradation in a microbial fuel cell, *Electrochem. Commun.*, 11 (20), 274–277.

- [18] Read, S.T., Dutta, P., Bond, P.L., Keller, J., and Rabaey, K., 2010, Initial development and structure of biofilms on microbial fuel cell anodes, *BMC Microbiol.*, 10 (1), 98.
- [19] Zerrouki, A., Kameche, M., Kebaili, H., Boukoussa, I.S., Flitti, M.A., Ilikti, H., and Innocent, C., 2018, An investigation on polymer ion exchange membranes used as separators in low energy microbial fuel cells, *Polym. Bull.*, 75 (11), 4947–4965.
- [20] Hamani, H., Bouamrane, R., Kameche, M., Innocent, C., and Derriche, Z., 2013, Transport number and current voltage of a cation exchange membrane equilibrated in aqueous and organic solutions, *Phys. Chem. Liq.*, 51 (3), 265–280.
- [21] Choi, J.H., Lee, H.J., and Moon, S.H., 2001, Effects of electrolytes on the transport phenomena in a cation-exchange membrane, *J. Colloid Interface Sci.*, 238 (1), 188–195.
- [22] Lachachi, Z., Kameche, M., Bendjeda, S., Meddah, K., Hamani, H., Boumediene, H., and Innocent, C., 2016, Study of proton leakage at interface of anion exchange membrane in solutions of acids, salts and solvents using current-voltage characteristics, *Chem. Eng. Commun.*, 203 (4), 566–574.
- [23] Choi, Y.J., Park, J.M., Yeon, K.H., and Moon, S.H., 2005, Determination of the limiting current density in electro dialysis desalination as an empirical function of linear velocity, *Desalination*, 190 (1-3), 43–50.
- [24] Choi, Y.J., Park, J.M., Yeon, K.H., and Moon, S.H., 2002, Direct measurement of concentration distribution within the boundary layer of an ion-exchange membrane, *J. Colloid Interface Sci.*, 251 (2), 311–317.
- [25] Grosse, W., Champavert, J., Gambhir, S., Wallace, G.G., and Moulton, S.E., 2013, Aqueous dispersions of reduced graphene oxide and multi wall carbon nanotubes for enhanced glucose oxidase bioelectrode performance, *Carbon*, 61, 467–475.
- [26] Rousseau, R., Délia, M.L., and Bergel, A., 2014, A theoretical model of transient cyclic voltammetry for electroactive biofilms, *Energy Environ. Sci.*, 7 (3), 1079–1094.
- [27] Varanasi, J.L., Nayak, A.K., Sohn, Y., Pradhan, D., and Das, D., 2016, Improvement of power generation of microbial fuel cell by integrating tungsten oxide electrocatalyst with pure or mixed culture biocatalysts, *Electrochim. Acta*, 199, 154–163.
- [28] Ouitrakul, S., Sriyudthsak, M., Charojrochkul, S., and Kakizono, T., 2007, Impedance analysis of bio-fuel cell electrodes, *Biosens. Bioelectron.*, 23 (5), 721–727.
- [29] Aaron, D., Tsouris, C., Hamilton, C.Y., and Borole, A.P., 2010, Assessment of the effects of flow rate and ionic strength on the performance of an air-cathode microbial fuel cell using electrochemical impedance spectroscopy, *Energies*, 3 (4), 592–606.
- [30] Ramasamy, R.P., Gadhamshetty, V., Nadeau, L.J., and Johnson, G.R. 2009, Impedance spectroscopy as a tool for non-intrusive detection of extracellular mediators in microbial fuel cells, *Biotechnol. Bioeng.*, 104 (5), 882–891.
- [31] Logan, B.E., Hamelers, B., Rozendal, R., Schröder, U., Keller, J., Freguiac, S., Aelterman, P., Verstraete, W., and Rabaey, K., 2006, Microbial fuel cells: Methodology and technology, *Environ. Sci. Technol.*, 40 (17), 5181–5192.
- [32] Zhang, S., You, J., Kennes, C., Chang, Z., Ye, J., Chen, D., Chen, J., and Wang, L., 2018, Current advances of VOCs degradation by bioelectrochemical systems: A review, *Chem. Eng. J.*, 334, 2625–2637.
- [33] Sanjuan, B., Millot, R., Innocent, C., Dezayes, C., Scheiber, J., and Brach, M., 2016, Major geochemical characteristics of geothermal brines from the Upper Rhine Graben granitic basement with constraints on temperature and circulation, *Chem. Geol.*, 428, 27–47.
- [34] Xu, F., Kameche, M., and Innocent, C., 2013, Transport of ions and solvent through a Nafion membrane modified with polypyrrole, *J. Membr. Sep. Technol.*, 1 (2), 108–116.
- [35] Kebaili, H., Kameche, M., Innocent, C., Ziane, F.Z., Sabeur, S.A., Sahraoui, T., Ouis, M., Zerrouki, A., and Charef, M.A., 2021, Treatment of fruit waste leachate using microbial fuel cell: Preservation of

- agricultural environment, *Acta Ecol. Sin.*, 41 (2), 97–105.
- [36] Djellali, M., Kameche, M., Kebaili, H., Benhamou, A., Bouhent, M., and Innocent, C., 2020, “Utilization of double-layered hydroxides for enhancement of dissolved oxygen reduction in microbial fuel cell: An approach for the evaluation of coulomb efficiency” in *ICREEC 2019*, Eds. Belasri, A., and Beldjilali, S., Springer Proceedings in Energy, Springer, Singapore, 239–244.
- [37] Zerrouki, A., Kameche, M., Kebaili, H., Amer, A.A., and Innocent, C., 2020, “Electro-catalytic electrodes and ionic exchange membranes in microbial fuel cell” in *ICREEC 2019*, Eds. Belasri, A., and Beldjilali, S., Springer Proceedings in Energy, Springer, Singapore, 211–217.
- [38] Kebaili, H., Kameche, M., Innocent, C., Kosimaningrum, W.E., and Sahraoui, T., 2020, “Growth of electroactive biofilm onto carbon felt bioanode in microbial fuel cell: Enhancement of bioenergy production” in *ICREEC 2019*, Eds. Belasri, A., and Beldjilali, S., Springer Proceedings in Energy, Springer, Singapore, 205–210.
- [39] Benayyad, A., Kameche, M., Kebaili, H., and Innocent, C., 2021, “Design of a microbial fuel cell used as a biosensor of pollution emitted by oxidized organic matter” in *Advances in Renewable Hydrogen and Other Sustainable Energy Carriers*, Eds. Khelaff, A., Springer Proceedings in Energy, Springer, Singapore, 279–284.
- [40] Ci, J., Cao, C., Kuga, S., Shen, J., Wu, M., and Huang, Y., 2017, Improved performance of microbial fuel cell using esterified Corn cob cellulose nanofibers to fabricate air-cathode gas diffusion layer, *ACS Sustainable Chem. Eng.*, 5 (11), 9614–9618.

In Vitro and In Silico Studies of Quercetin and Daidzin as Selective Anticancer Agents

Muhammad Sulaiman Zubair^{1*}, Syariful Anam¹, Saipul Maulana¹, and Muhammad Arba²

¹Department of Pharmacy, Faculty of Mathematics and Natural Sciences, Tadulako University, Palu 94118, Indonesia

²Department of Pharmacy, Faculty of Pharmacy, Universitas Halu Oleo, Kendari 93231, Indonesia

* **Corresponding author:**

email: sulaiman_zubair80@yahoo.co.id

Received: January 19, 2020

Accepted: November 2, 2020

DOI: 10.22146/ijc.53552

Abstract: Quercetin and daidzin are flavonoid and flavonoid glycoside type compounds that have been found in many plants and nutraceuticals. This study aims to examine the in vitro cytotoxic and selectivity properties of quercetin and daidzin on breast and cervical cancers and to study their molecular interaction and stability on epidermal growth factor receptor tyrosine kinase (EGFR-TK) by applying molecular docking and molecular dynamics (MD) simulations. In vitro anticancer activity was performed by 3-(4,5-dimethylthiazol-2-yl)-2,5-diphenyltetrazolium bromide (MTT) method on breast cancer cell (T47D), cervical cancer cells (HeLa), and Vero normal cells, while molecular docking and MD simulation were done by using AutoDock Vina and Amber18 package software, respectively. Quercetin and daidzin showed potent cytotoxic and high selectivity on both cell lines. Daidzin was found to have a higher IC₅₀ and selectivity index than quercetin. Docking and MD results showed that both compounds prefer to interact with epidermal growth factor receptor tyrosine kinase (EGFR-TK). Daidzin showed better interaction than quercetin with a docking score of -9.6 kcal/mol. Also, daidzin was found more stable than quercetin with low RMSD and RMSF values.

Keywords: quercetin; daidzin; T47D; HeLa; docking; molecular dynamics

■ INTRODUCTION

In recent times, computational applications for predicting the molecular interactions on the biological system are broadly used to study molecular recognition or design more potent bioactive compounds. Molecular docking and molecular dynamics are two kinds of recent computational methods that can provide molecular interactions between receptor proteins and drugs and how they stabilize the interaction. These methods focused on protein–drugs (ligands) complexes to study how the drugs bind to the protein receptor, which is very important for discovering or developing new bioactive compounds in fighting against diseases. Besides, the methods for identification of protein-ligand interaction fingerprints that featuring how strong the interaction has developed as well [1-2].

In terms of cancer diseases, many molecular mechanisms of cell proliferation inhibition have been reported so far. The advanced technique of molecular

assay on cancer research has led to the increasing knowledge of the molecular basis of carcinogenesis that opens the possibility of discovering a more selective chemopreventive agent, mostly from the natural product. Attention has been focused on natural substances capable of inhibiting carcinogenesis via the apoptosis mechanism [3].

Quercetin and daidzin (Fig. 1) are two natural anticancer compounds that have been given much attention at this time. Quercetin is a flavonoid found mainly in various vegetables and fruits, such as capers, lovage, dill, cilantro, and onions. It was reported to suppress the HeLa cells by blocking the phosphatidylinositol 3-kinase (PI3K)-Akt/PKB (protein kinase B) pathway. Quercetin also induces apoptosis by activation of intrinsic apoptotic pathway associated with upregulation of Bax, Bad, Bid, caspase-9, -3, downregulation of Bcl-2; Bcl-xL, and cytochrome c release and inhibit NF- κ B, PKC- δ , ERK1/2 along with

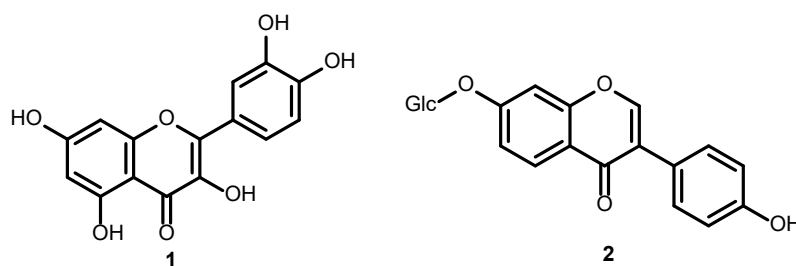


Fig 1. Quercetin (1) and daidzin (2)

AMPK activation and downregulation of uPA/uPAR, MMP-9, and -2 for cell inhibition of migration and invasion [4-7]. Meanwhile, daidzin, an ingredient of soy isoflavones, is a glycoside form of daidzein flavonoid. It has also been reported to possess anticancer activity in early prostate cancer development stages and reduce postmenopausal breast cancer risk. It can inhibit telomerase activity by hydrogen bonding with the base of G-quadruplex as well [8-10].

To obtain more insight into the selectivity and stability properties of the anticancer mechanism of quercetin and daidzin, in this present study, they were in vitro tested on breast and cervical cancers along with the normal cells and in silico molecular docking, and molecular dynamics on epidermal growth factor receptor tyrosine kinase (EGFR-TK) were also performed. EGFR-TK has been known as a target for flavonoids and flavonoid glycoside on their activity in inhibiting cancer cell proliferation and transformation [11]. This study is the first report regarding the molecular docking and MD simulations of quercetin and daidzin on EGFR-TK.

■ EXPERIMENTAL SECTION

Materials

Quercetin and daidzin were purchased from Sigma Aldrich. RPMI-1640, Streptomycin, Penicillin, Fetal Bovine Serum (FBS), Dimethylsulphoxide (DMSO), and MTT were purchased from Merck.

Human ductal breast epithelial tumor cell line (T47D), human cervical cancer cell line (HeLa), and green African monkey renal epithelial cell (Vero) were obtained from Laboratory of Parasitology, Faculty of Medicine, Universitas Gadjah Mada. Cells were maintained in RPMI-1640 medium supplemented with 100 µg/mL

streptomycin, 100 units/mL penicillin, and 10% fetal bovine serum (FBS) in 5% CO₂ atmosphere at 37 °C.

Procedure

Cytotoxicity test

Cytotoxic activity was applied to the Human ductal breast epithelial tumor cell line (T47D), human cervical cancer cell line (HeLa), and green African monkey renal epithelial cell (Vero) cell lines by the MTT method as described in our previous study [12]. The stock samples were briefly diluted with RPMI-1640 medium to desired concentrations of 25, 12.5, 6.25, 3.125, 1.5625, 0.7812, and 0.3906 µg/mL. The final concentration of dimethylsulphoxide (DMSO) in each sample was 1% v/v. The cancer cells were batch cultured for 10 days, then seeded in 96 well plates of 1 × 10⁴ cells/well in fresh complete growth medium in 96-well microtiter plastic plates at 37 °C for 24 h under 5% CO₂ using a water-jacketed carbon dioxide incubator (CelCulture, Esco Medical ApS, Denmark). The medium (without serum) was added, and cells were incubated either alone (negative control) or with different sample concentrations. After 48 h of incubation, cells were added with 10 µL/well of MTT (5 mg/mL) and incubated for 4 h in an incubator at 37 °C in a 5% CO₂ humidified atmosphere. The reaction was stopped by 100 µL dimethylsulfoxide (DMSO). The plate was then incubated for 15 min. Each well's absorbance was read at 550 nm wavelength in Elisa Reader (Infinite M200 pro NanoQuant, Tecan, Switzerland), using wells without cells as blanks. All experiments were performed in triplicate. The effect of compounds on the proliferation of cancer cells was expressed as the % cytoviability, using the following formula:

$$\% \text{ Cytoviability} = \frac{\text{Absorbance of treated cells}}{\text{Absorbance of control cells}} \times 100\%$$

The IC₅₀ calculation was done statistically by probit analysis using SPSS 17.0 (SPSS Inc., Chicago IL, USA), in which the series of dose-response data and the percentage of cytoviability were plotted together.

Molecular docking

Molecular docking was performed using AutoDock Vina [13]. EGFR-TK protein target was obtained from the Brookhaven Protein Data Bank (www.rcsb.org) with the code 1M17. BIOVIA Discovery Studio 2017 was used to separate water, native ligand, and other non-standard residues and visualizes the docking result [14]. AutoDock Tools (ADT) was used to optimize and prepare the required files to be docked. The grid spacing of 0.375 Å and the grid points in X, Y, and Z-axis were set at 42 × 40 × 40 points. The grid center coordinates were placed at X: 21.697, Y: 0.303, and Z: 52.093. ChemDraw (ACDLabs, Netherland) was used to build quercetin and daidzin chemical structures and converted to the 3D structure after optimization using the MM2 method. Docking methods and parameters were validated by redocking the co-crystallized ligands erlotinib into the protein structure. The root-mean-square deviation (RMSD) value was calculated using the rms_cur module in PyMol [15]. The default settings of each software were used if no further explanation. Docking was performed on Linux operating system with Intel(R) Core™2 Duo CPU T5800 @ 2 GHz as a processor and 1.93 GB of RAM.

Molecular dynamics

Molecular dynamics (MD) simulation was carried out for quercetin and daidzin on EGFR-TK employing the AMBER18 package [16]. Leap module was used to prepare each complex using the ff99SB force field for protein and GAFF force field and AM1-BCC for ligands [17-19]. Counterions were added to the neutralized complex. Each complex was placed inside a truncated octahedron TIP3P water model with a 12 Å distance between the complex and the box's edge. Each complex underwent two-step minimization. In the first step, minimization was performed for water and ions while protein-ligand was restrained with a 500 kcal mol⁻¹ Å⁻² and to heat the system ligand-protein in 300 K. Next, only

backbone atoms of the protein were restrained with a force constant of 500 kcal mol⁻¹ Å⁻².

Further, following the minimization step, each complex underwent a heating step for 120 ps with 1000 steps minimization, and backbone atoms of protein were restrained with a force constant of 500 kcal/mol Å⁻². The system was then equilibrated at 300 K, and the density was 1 g/mL for 60.000 steps each with a 2 fs time step giving simulation lengths of 120 ps. The production MD simulation was performed for 8 ns in the NPT ensemble without any restraint employing PMEMD (Particle Mesh Ewald Molecular Dynamics). The Cuda module under a periodic boundary condition with a non-bonding cutoff distance of 12.0 Å. The SHAKE algorithm was used to constrain all bonds involving hydrogen atoms with a 2 fs integration time step [20]. The particle-mesh Ewald algorithm method was used to treat long-range electrostatic interactions of a periodic box with a non-bonding cutoff distance of 12.0 Å [21]. The Langevin thermostat was used to control the Langevin thermostat with a collision rate of 1.0 ps⁻¹. The coordinate files were saved every 1 ps. The Root Mean Square Deviation (RMSD) and Root Mean Square Fluctuation (RMSF) were analyzed with the CPPTRAJ module of AMBER18 [22], while visualization and hydrogen bond occupancy in the protein-ligand system was conducted using the Visual Molecular Dynamics (VMD) software [23].

RESULTS AND DISCUSSION

In Vitro Cytotoxicity

Cytotoxic activity of quercetin and daidzin was tested on the breast (T47D) and cervical (HeLa) cancer cell lines. It was found that daidzin has more potent cytotoxic activity than quercetin on T47D and HeLa cell lines with the IC₅₀ of 0.04 and 0.54 µg/mL, respectively. Moreover, daidzin did not toxic on Vero cell lines (normal cells) at the concentration of 100 µg/mL. Meanwhile, quercetin showed IC₅₀ of 41.57 µg/mL on Vero cell lines. Therefore, the selectivity index can be calculated by the formula; IC₅₀ of a compound on Vero cells/IC₅₀ of a compound on cancer cells. Selectivity index > 3 can be categorized as having high selectivity [24].

Table 1. Cytotoxic activity of quercetin and daidzin against cancer cell lines

Compounds	IC ₅₀ (µg/mL)			Selectivity Index (SI)	
	T47D	HeLa	Vero	T47D	HeLa
Quercetin	9.58 ± 2.34	3.66 ± 0.84	41.57 ± 26.33	4.34	11.36
Daidzin	0.04 ± 0.04	0.54 ± 0.07	> 100 (NT)	S	S

NT: No Toxicity at 100 µg/mL, S: Selective (High selectivity index, SI > 3.0)

Based on this, daidzin can be considered to have high selectivity. Meanwhile, quercetin showed to be more selective on the HeLa cell than the T47D cell (Table 1).

The different anticancer activity and selectivity properties of quercetin and daidzin might be caused by glucose unit presence, forming a glycosidic bond with the daidzin hydroxyl group [25]. Daidzin was reported as a potent tyrosinase inhibitor based on the glycoside moieties, and mostly the glycoside form of flavonoids was absorbed in the small intestine [26-27].

Molecular Docking and Molecular Dynamics

Molecular docking and molecular dynamics of both compounds were performed on epidermal growth factor receptor tyrosine kinase (EGFR-TK) responsible for breast and cervical cancer cell proliferation. EGFR (also known as Erb-B1 or HER-1) is a tyrosine kinase receptor that able to activate different signaling cascades involved in the pathogenesis of carcinomas, such as phosphatidylinositol 3-kinase (PI3K)/Akt and mitogen-activated protein kinase (MAPK) [28]. Docking protocol was validated by redocking native ligand erlotinib to EGFR-TK receptors (PDB Id: 1M17). It can be seen from Table 2, that native ligand erlotinib has an RMSD value < 2 Å, which means the protocol used has prospectively validated [29-30]. It is interesting to note that daidzin showed good interaction on the EGFR-TK receptor target that might be responsible for the high cytotoxicity on cancer cells. Daidzin has lower docking energy on epidermal growth factor receptor – tyrosine kinase (EGFR-TK) proteins than quercetin, indicating a higher binding affinity of daidzin compared to quercetin.

Quercetin was found to interact with the catalytic residue of MET769 by hydrogen bonding and showed hydrophobic interaction with several amino acids of LEU 820, LEU694, ALA719, VAL702, and LYS721 in the hydrophobic pocket of EGFR-TK protein. Meanwhile,

Table 2. Docking score of quercetin and daidzin on EGFR-TK receptor target

Compounds	Docking Energy (Kcal/mol)	RMSD (Å)
Quercetin	-9.0	-
Daidzin	-9.6	-
Native Ligand Erlotinib	-7.1	1.912

daidzin did not show that kind of interactions where the hydrogen bonding was found only between the glycoside group and amino acid residues of ALA719, LYS721, LEU764, THR830, and ASP831 located on the EGFR phosphate-binding region along with the sugar pocket. Besides, the aglycone part of daidzin also showed hydrophobic interaction with amino acids of LEU820, VAL702, and LEU694 (Fig. 2).

Further study was carried out by employing molecular dynamics (MD) simulation to investigate the stability of the interaction between quercetin and daidzin on the EGFR-TK binding pocket. Based on quercetin and daidzin are well-known natural compounds with anticancer activity, the MD simulation was done for 8 ns [31-33]. Root mean square deviation (RMSD) value was used to monitor interaction stability (Fig. 3). It can be seen that quercetin, daidzin, and native ligand erlotinib maintained stable interaction on the EGFR-TK binding pocket with an overall RMSD value lower than 3 Å. However, quercetin (blue) was found to have a high RMSD value (> 3 Å) at the end of the simulation, indicating less stability of quercetin than daidzin and native ligand erlotinib during 8 ns of simulation time.

Further evaluation of the fluctuation of amino acid residues of EGFR-TK during the dynamics run can be seen on the root mean square fluctuation (RMSF) graph (Fig. 4). A similar pattern of amino acid fluctuation was seen in the whole region of EGFR-TK, indicating a

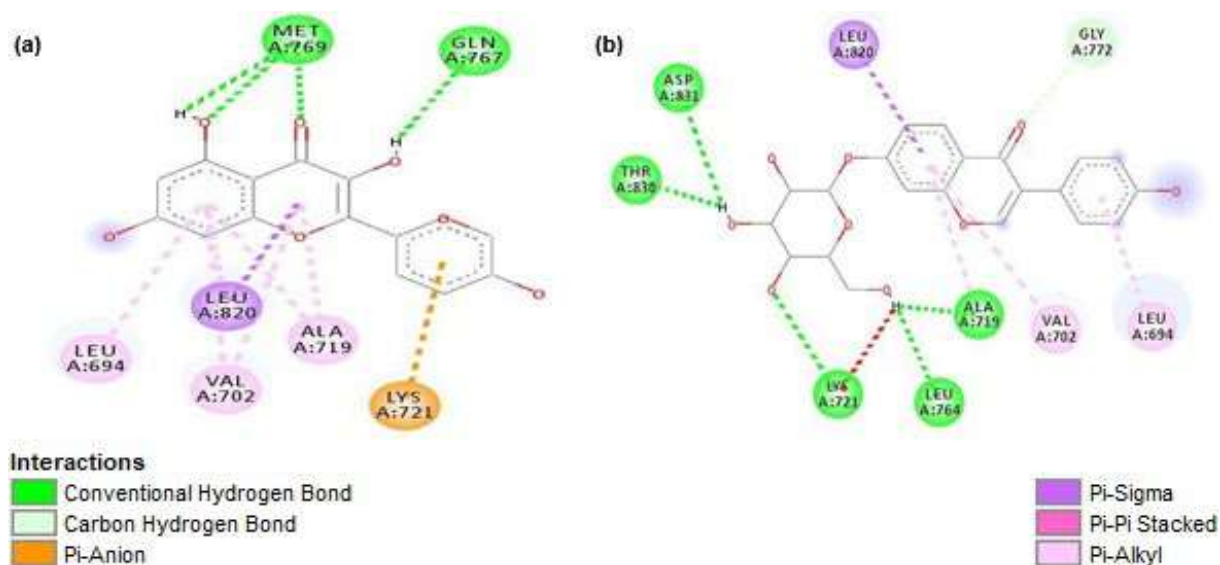


Fig 2. Molecular interaction between quercetin (a), and daidzin (b) on active site of EGFR-TK (pdb code 1M17)

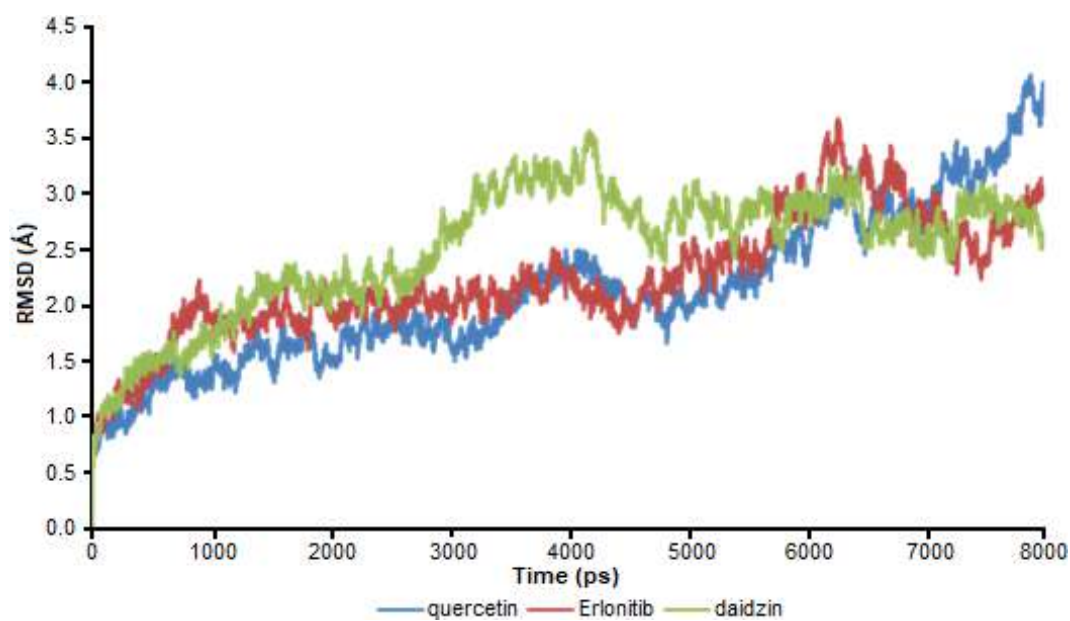


Fig 3. RMSD value of ligands on EGFR-TK during 8 ns MD calculated for quercetin (blue), Daidzin (green), and native ligand erlotinib (red)

similar pattern of binding interaction of native ligand erlotinib, quercetin, and daidzin. However, quercetin was found to have a higher RMSF value than daidzin and native ligand erlotinib, indicating that quercetin more fluctuated during 8 ns MD simulation, affording the less stable interaction. Hydrogen bond interactions of docked conformations of quercetin and daidzin were not observed after 8 ns MD simulation, indicating that the

most stable interaction was caused by van der Waals and hydrophobic type interactions.

From this study, molecular docking and molecular dynamics of quercetin and daidzin showed that epidermal growth factor receptors tyrosine kinase (EGFR-TK) was the potential target of the compounds, and this target was well-marked to have a contribution to the development and malignancy of breast cancer and

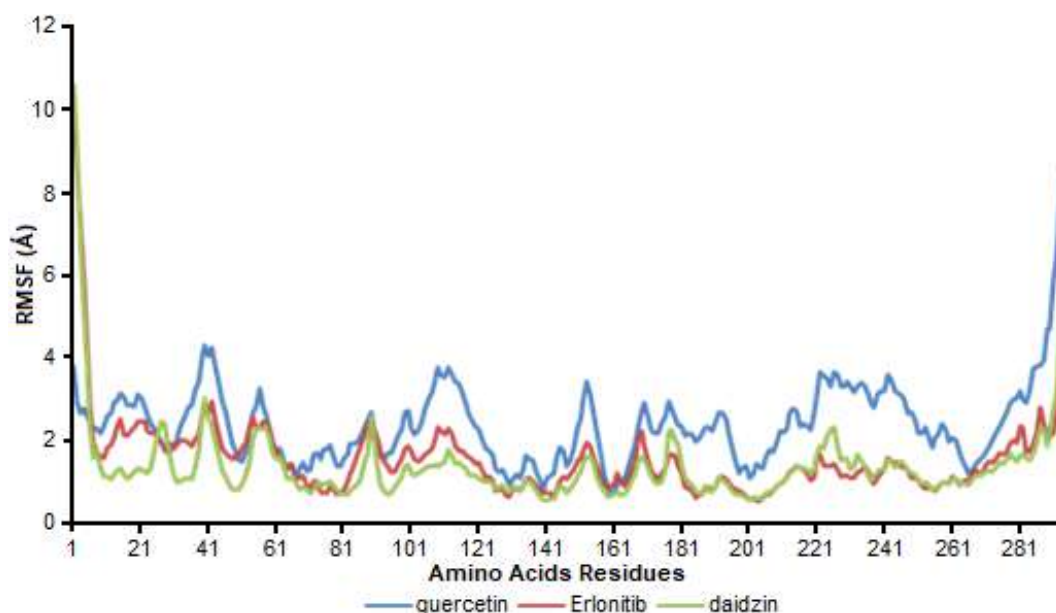


Fig 4. RMSF plotting during 8 ns MD simulation for quercetin (blue), daidzin (green), and native ligand erlotinib (red)

cervical cancers [34-35]. Daidzin is suggested to be a chemical scaffold for the development of epidermal growth factor receptors tyrosine kinase (EGFR-TK) protein inhibitor based on the high cytotoxicity, selectivity, and stability properties.

■ CONCLUSION

In conclusion, daidzin is more cytotoxic and selective on T47D and HeLa cell lines than quercetin by in vitro assay. The presence of glucose units in daidzin might be responsible for this activity. The docking result showed that daidzin has lower energy than quercetin, attributed by glucose unit in daidzin that possessing the interaction by hydrogen bonding with the amino acid residues of ALA719, LYS721, LEU764, THR830, and ASP831. Molecular dynamics simulation exhibited that daidzin also has lower RMSD and RMSF values than quercetin, indicating more stability during interaction on EGFR-TK protein in 8 ns MD simulation.

■ ACKNOWLEDGMENTS

The authors would like to acknowledge the Ministry of Research, Technology, and Higher Education, Republic of Indonesia, for supporting this study as part of the INSINAS 2015 (RD-2015-0106) grant.

■ REFERENCES

- [1] Vasseur, R., Baud, S., Steffanel, L.A., Vigouroux, X., Martiny, L., Krajecki, M., and Dauchez, M., 2015, Inverse docking method for new proteins targets identification: A parallel approach, *Parallel Comput.*, 42, 48–59.
- [2] Istyastono, E.P., 2017, Binary quantitative structure-activity relationship analysis to increase the predictive ability of structure-based virtual screening campaigns targeting cyclooxygenase-2, *Indones. J. Chem.*, 17 (2), 322–329.
- [3] Phosrithong, N., and Ungwitayatorn, J., 2010, Molecular docking study on anticancer activity of plant-derived natural products, *Med. Chem. Res.*, 19 (8), 817–835.
- [4] Teekaraman, D., Elayapillai, S.P., Viswanathan, M.P., and Jagadeesan, A., 2019, Quercetin inhibits human metastatic ovarian cancer cell growth and modulates components of the intrinsic apoptotic pathway in PA-1 cell line, *Chem. Biol. Interact.*, 300, 91–100.
- [5] Li, H., and Chen, C., 2018, Quercetin has antimetastatic effects on gastric cancer cells via the interruption of uPA/uPAR function by modulating

- NF- κ b, PKC- δ , ERK1/2, and AMPK α , *Integr. Cancer Ther.*, 17 (2), 511–523.
- [6] Khan, F., Niaz, K., Maqbool, F., Hassan, F.I., Abdollahi, M., Venkata, K.C.N., Nabavi, S.M., and Bishayee, A., 2016, Molecular targets underlying the anticancer effects of quercetin: An update, *Nutrients*, 8 (9), 529.
- [7] Xiang, T., Fang, Y., and Wang, S.X., 2014, Quercetin suppresses HeLa cells by blocking PI3K/Akt pathway, *J. Huazhong Univ. Sci. Technol., Med. Sci.*, 34 (5), 740–744.
- [8] Wang, Q., Ge, X., Tian, X., Zhang, Y., Zhang, J., and Zhang, P., 2013, Soy isoflavone: The multipurpose phytochemical (Review), *Biomed. Rep.*, 1 (5), 697–701.
- [9] Boucher, B.A., Cotterchio, M., Anderson, L.N., Kreiger, N., Kirsh, V.A., and Thompson, L.U., 2012, Use of isoflavone supplements is associated with reduced postmenopausal breast cancer risk, *Int. J. Cancer*, 132, 1439–1450.
- [10] Shan, C., Tan, J.H., Ou, T.M., and Huang, Z.S., 2013, Natural products and their derivatives as G-quadruplex binding ligands, *Sci. China Chem.*, 56 (10), 1351–1363.
- [11] Chen, H., Yao, K., Nadas, J., Bode, A.M., Malakhova, M., Oi, N., Li, H., Lubet, R.A., and Dong, Z., 2012, Prediction of molecular targets of cancer preventing flavonoid compounds using computational methods, *PLoS ONE*, 7 (5), e38261.
- [12] Zubair, M.S., Anam, S., and Lallo, S., 2016, Cytotoxic activity and phytochemical standardization of *Lunasia amara* Blanco wood extract, *Asian Pac. J. Trop. Biomed.*, 6 (11), 962–966.
- [13] Trott, O., and Olson, A.J., 2010, AutoDock Vina: Improving the speed and accuracy of docking with a new scoring function, efficient optimization and multithreading, *J. Comput. Chem.*, 31 (2), 455–461.
- [14] Dassault Systèmes BIOVIA, 2016, *Discovery Studio Modeling Environment Release 2017*, Dassault Systèmes, San Diego, USA.
- [15] Seeliger, D., and de Groot, B.L., 2010, Ligand docking and binding site analysis with PyMOL and Autodock/Vina, *J. Comput.-Aided Mol. Des.*, 24 (5), 417–422.
- [16] Arba, M., Ruslin, Kalsum, W.U., Alroem, A., Muzakkar, M.Z., Usman, I., and Tjahjono, D.H., 2018, QSAR, molecular docking and dynamics studies of quinazoline derivatives as inhibitor of phosphatidylinositol 3-kinase, *J. Appl. Pharm. Sci.*, 8 (5), 1–9.
- [17] Maier, J.A., Martinez, C., Kasavajhala, K., Wickstrom, L., Hauser, K.E., and Simmerling, C., 2015, ff14SB: Improving the accuracy of protein side chain and backbone parameters from ff99SB, *J. Chem. Theory Comput.*, 11 (8), 3696–3713.
- [18] Wang, J.M., Wolf, R.M., Caldwell, J.W., Kollman, P.A., and Case, D.A., 2004, Development and testing of a general amber force field, *J. Comput. Chem.*, 25 (9), 1157–1174.
- [19] Jakalian, A., Jack, D.B., and Bayly, C.I., 2002, Fast, efficient generation of high-quality atomic charges. AM1-BCC model: II. Parameterization and validation, *J. Comput. Chem.*, 23 (16), 1623–1641.
- [20] Elber, R., Ruymgaart, A.P., and Hess, B., 2011, SHAKE parallelization, *Eur. Phys. J. Spec. Top.*, 200 (1), 211–223.
- [21] Darden, T., York, D., and Pedersen, L., 1993, Particle mesh Ewald: An N-log(N) method for Ewald sums in large systems, *J. Chem. Phys.*, 98 (12), 10089–10092.
- [22] Roe, D.R., and Cheatham III, T.E., 2013, PTRAJ and CPPTRAJ: Software for processing and analysis of molecular dynamics trajectory data, *J. Chem. Theory Comput.*, 9 (7), 3084–3095.
- [23] Humphrey, W., Dalke, A., and Schulten, K., 1996, VMD: Visual molecular dynamics, *J. Mol. Graphics*, 14 (1), 33–38.
- [24] Mahmoud, A.M., and El-Shemy, H.A., 2012, Efficacy assessment for several natural products with potential cytotoxic activity against breast and cervix cancers, *J. Arid Land Stud.*, 22, 107–110.
- [25] Kim, D.H., Jung, H.A., Park, S.J., Kim, J.M., Lee, S., Choi, J.S., Cheong, J.H., Ko, K.H., and Ryu, J.H., 2010, The effects of daidzin and its aglycon, daidzein, on the scopolamine-induced memory impairment in male mice, *Arch. Pharmacol. Res.*, 33 (10), 1685–1690.

- [26] Liu, H., Zhu, Y., Wang, T., Qi, J., and Liu, X., 2018, Enzyme-site blocking combined with optimization of molecular docking for efficient discovery of potential tyrosinase specific inhibitors from *Puerariae lobatae* Radix, *Molecules*, 23 (10), 2612.
- [27] Heim, K.E., Tagliaferro, A.R., and Bobilya, D.J., 2002, Flavonoid antioxidants: Chemistry, metabolism and structure-activity relationships, *J. Nutr. Biochem.*, 13 (10), 572–584.
- [28] Wee, P., and Wang, Z., 2017, Epidermal growth factor receptor cell proliferation signaling pathways, *Cancers*, 9 (5), 52.
- [29] Fajrin, F.A., Nugroho, A.E., Susilowati, R., and Nurrochmad, A., 2018, Molecular docking analysis of ginger active compound on transient receptor potential cation channel subfamily V member 1 (TRPV1), *Indones. J. Chem.*, 18 (1), 179–185.
- [30] Zubair, M.S., Anam, S., Khumaidi, A., Susanto, Y., Hidayat, M., and Ridhay, A., 2016, Molecular docking approach to identify potential anticancer compound from *Begonia* (*Begonia sp.*), *AIP Conf. Proc.*, 1755 (1), 080005.
- [31] Prasasty, V.D., and Istyastono, E.P., 2020, Structure-based design and molecular dynamics simulations of pentapeptide AEYTR as a potential acetylcholinesterase inhibitor, *Indones. J. Chem.*, 20 (4), 953–959.
- [32] Liu, K., and Kokubo, H., 2017, Exploring the stability of ligand binding modes to proteins by molecular dynamics simulations: A cross-docking study, *J. Chem. Inf. Model.*, 57 (10), 2514–2522.
- [33] Arba, M., and Tjahjono, D.H., 2015, The binding modes of cationic porphyrin-anthraquinone hybrids to DNA duplexes: *in silico* study, *J. Biomol. Struct. Dyn.*, 33 (3), 657–665.
- [34] Masuda, H., Zhang, D., Bartholomeusz, C., Doihara, H., Hortobagyi, G.N., and Ueno, N.T., 2012, Role of epidermal growth factor receptor in breast cancer, *Breast Cancer Res. Treat.*, 136 (2), 331–345.
- [35] Viswanath, L., Naveen, T., Siddanna, P., Chetana, P., Geethasree, M., Pasha, S.C.R.T., Bindhu, J., Pramod, K.P.R., Ashalatha, D., Priyadarshni, V., Ajai, G.V., Ashwini, V., Mahalakshmi, A., Riach, T., Sugashwaran, S., and Yeshaswini, T., 2014, Epidermal growth factor receptor (EGFR) overexpression in patients with advanced cervical cancer, *J. Clin. Oncol.*, 321 (Suppl. 15), e16538.

Characterization and Utilization of Sulphuric Acid and Bitter Leaf Extract Activated Carbon from Rice Husk for Zn(II) Adsorption

Ilesanmi Osasona* and Ujiro Bestow Kanuhor

Department of Chemical Sciences, Afe Babalola University, Km 8.5, Afe Babalola Way, P.M.B. 5454, Ado-Ekiti, Nigeria

* **Corresponding author:**

tel: +234-8030656679

email: oosasona@yahoo.com

Received: March 10, 2020

Accepted: October 9, 2020

DOI: 10.22146/ijc.54786

Abstract: The world is clamoring for green synthetic modes of scientific and technological operations. From this point of view, an attempt was made to prepare activated carbon from rice husk using aqueous bitter leaf extract and a mineral acid (H_2SO_4) separately. The surface characteristics and the adsorption properties of the activated carbons from both methods were compared. The effects of adsorption variables on the adsorption of Zn(II) by bitter leaf extract activated carbon (RHAC1) and H_2SO_4 activated carbon (RHAC2) were conducted through batch studies. The morphological characterization revealed RHAC1 to be fibrous, more porous and contained finer particles than the chemical-activated counterpart. The role of hydroxyl and carbonyl groups in the adsorption of Zn(II) was pivotal. The optimum pH values for the adsorption of Zn(II) by both samples was 7. The adsorption kinetics and equilibrium isotherm obeyed Elovich and Freundlich models respectively while the evaluated Langmuir q_{max} were 71.47 and 67.12 $mg\ g^{-1}$ for RHAC1 and RHAC2 respectively. The thermodynamic parameters revealed that the process was endothermic and spontaneous at all evaluated temperatures. Therefore, bitter leaf aqueous extract, as an activating agent for carbon production, could serve as a better or close substitute for the less environment-friendly H_2SO_4 .

Keywords: adsorption; green synthesis; rice husk; bitter leaf; activated carbon

■ INTRODUCTION

Advances in global technology and knowledge have their inherent merits and demerits. Of course, the advantages derivable from technological advancement outweigh its disadvantages, yet technologies involving the use of chemicals, metals, and metalloids have grave consequences on the sustainability of the environment. An unhealthy environment will breed unhealthy life. Hence, to maintain the sustainability of the global environment, the influx of pollutants must be controlled. Water is a major component of our physical environment that contributes greatly to life sustenance. However, its life-sustaining ability is constantly being threatened as a result of the introduction of harmful substances through various human technological endeavors [1]. The chief among these harmful substances are heavy metals contained in industrial wastewater. Some heavy metals commonly contained in industrial wastewater include:

lead, chromium, mercury, uranium, selenium, zinc, arsenic, cadmium, silver, gold, and nickel [2].

Zinc belongs to the Group IIB elements alongside the highly toxic cadmium and mercury. It is a trace element known to play a key role in human health. It is important for the physiological functions of living tissues and regulates many biochemical processes. Zn(II) is involved in the function of enzymes in several different areas of metabolism. For example, enzymes involved in carbohydrate and energy metabolism, acid/base balance, protein biosynthesis and degradation, nucleic acid biosynthesis, cellular protection against free radicals (superoxide dismutase), inter-conversion of trans-retinal with retinol, heme biosynthesis, dihydrotestosterone production, and several other reactions that are reported to be associated with zinc [3-4]. In spite of its important biochemical roles in the human body, excessive ingestion of zinc, can bring about serious health problems, which include stomach cramps, abdominal

pains, skin irritations, vomiting, nausea, and anemia [5-6]. There are three major ways a man can be exposed to zinc: through inhalation, through the skin, or by ingestion [6].

To avoid excessive exposure/intake and concomitant accumulation of zinc in the human body, the need to reduce the concentration of zinc present in wastewater becomes imperative. To achieve this, many conventional methods are available to remove heavy metal ions from industrial effluents. Among these methods are: the use of chemical precipitation, crystallization, reverse osmosis, electrophoresis, coagulation, floatation, ultrafiltration, ion exchange, etc. [3,7]. All these methods are associated with different drawbacks such as: sludge production, high cost of operation, ineffectiveness/poor efficiency at low metal concentration, etc. Adsorption, particularly using commercial activated carbon (CAC) is a better alternative to heavy metal sequestration from wastewater [8-9]. However, the use of CAC is constrained by high cost and requirement of chelating agent to increase its performance which definitely increases its cost of operation [10].

The high cost associated with the use of commercial activated carbon gave birth to the search for less expensive and better efficient alternatives. To this end, researchers have beamed their searchlight on the production of activated carbon from cheap and readily available materials. The use of activated carbons from various precursors has been reported for heavy metals removal. Among these are activated carbon from: spent barley husks [11], *Spartina alterniflora* [12], almond husk [13], apricot stones [14], activated coconut shell [15], etc. In particular, some of the precursors that have been exploited for Zn(II) removal are activated carbon from: mesembryanthemum [16], olive stone [17], bamboo [18], *Xanthoceras sorbifolia* bunge hull [19], eucalyptus seeds [20], olive branches [21], saw dust [22], oil palm mill effluent [23], etc.

Rice husk is a fibrous agricultural by-product obtained from the rice paddy processing after harvest. Rice processing involves several steps: removal of the husks, milling the shelled rice to remove the bran, and an additional whitening step to meet market expectations for the appearance of the rice kernels. This process leads to the generation of different by-products which include:

husks, bran, and milled rice kernel [24]. Rice husk forms about 16–25% by weight of the paddy processed [25]. Heaps of rice husks can be sited around different rice mills in Nigeria.

Nigeria annually generates about 1.1 million tons out of about 120 million tons of rice husk generated globally [25-26]. Rice husk disposal constitutes a great environmental threat to the surroundings of the milling houses. The major disposal method for rice husk is combustion which also constitutes greater environmental pollution. Hence, recycling this agricultural waste and converting it to high-value material is not only beneficial to the environment but also a promising bio-resource technology [27].

Vernonia amygdalina, commonly called bitter leaf because of its bitter taste is a shrub growing to a height of 3 or more meters in the African tropics and other parts of Africa, particularly, Nigeria, Cameroon, and Zimbabwe [28]. The leaves are consumed either as a vegetable (macerated leaves in soup) or aqueous extracts as tonics for the treatment of various illnesses such as anemia, nausea, diabetes, loss of appetite, dysentery, gingivitis, toothache, and gastrointestinal tract problems [29-30]. The biologically-active compounds which have been extracted and isolated from *Vernonia amygdalina* are: saponins and alkaloids, terpenes, steroids, coumarins, flavonoids, phenolic acids, lignans, xanthenes, and anthraquinone, edotides, and sesquiterpenes [28]. The presence of these phytochemicals in *Vernonia amygdalina* could be exploited as activating agents in the production of activated carbon since the phytochemicals, particularly the flavonoids and phenolic compounds, are known for metal chelating activities and redox reactions [31].

Therefore, this study was conducted to compare the adsorptive properties of bitter leaf extract activated carbon (RHAC1) and H₂SO₄ activated carbon (RHAC2) from rice husk for the removal of Zn(II) from aqueous solution. From extensive literature search, no report has been made on the use of plant-derived acids or extracts for the activation or modification of carbons for adsorption purposes. Generally, chemical and physical activation methods that are rather non-eco-friendly and/or expensive to operate and maintain have been

used for a very long time. This study is an attempt to make the environment safer for both humans and animals.

■ EXPERIMENTAL SECTION

Materials

Chemicals and reagents used include: sulphuric acid (H_2SO_4), zinc sulphate heptahydrate ($\text{ZnSO}_4 \cdot 7\text{H}_2\text{O}$), hydrochloric acid (HCl), sodium hydroxide (NaOH) and potassium hydroxide (KOH). All reagents were of analytical grade, hence no further purification was carried out before use.

Procedure

Collection and preparation of materials

Rice husk was collected from a local rice mill industry in Ado-Ekiti, Ekiti State, Nigeria. The husk was thoroughly washed with distilled water and oven-dried at 105 °C to a constant weight. The dried husks were stored in desiccators to avoid exposure to atmospheric moisture and transferred into a well-sealed and air-tight container in preparation for carbonization and activation. Bitter leaves (*Vernonia amygdalina*) were plucked from Afe Babalola University's farm. The leaves were authenticated at the Department of Plant Science, Ekiti State University, Ado-Ekiti, Ekiti State, Nigeria. The leaves were thoroughly washed with distilled water to remove dirt and dust particles. Then the leaves were blended with the addition of 5 mL of distilled water per 10 g of leaves. The aliquot was filtered using a mesh net and the filtrate was collected. The rice husk was carbonized using a muffle furnace (Vecstar Ltd England) which allows little supply of air. Carbonization was done at 350 °C for 30 min. The carbonized sample was then allowed to cool in a desiccator at room temperature [32].

Chemical and bio-activation of carbonized rice husk

The carbonized rice husk was activated using the method described by Osasona et al. [11]. Twenty-five grams of carbonized rice husk (425 μm) was weighed into a beaker containing 500 mL 0.1 M sulphuric acid. The contents of the beaker were thoroughly mixed and heated at 60 °C on a magnetic stirrer with a hot plate until a paste was formed. The paste was transferred to an evaporating

dish which was placed in a furnace and heated at 500 °C for 30 min. The sample was then allowed to cool overnight. It was then neutralized with KOH and washed several times with distilled water until the pH was 6.80 ± 0.1 . The sample was further oven-dried at 105 °C to a constant weight and was kept in an air-tight bottle. Twelve and a half grams (12.5 g) of RH was soaked in 250 mL of *Vernonia amygdalina* extract with intermittent shaking for 12 h. The mixture was then filtered using a mesh net and washed with distilled water several times. The residue was oven-dried at 105 °C for 1 h to obtain the carbonized rice bran treated with *Vernonia amygdalina*. The dried residue was then stored in an airtight container. The bitter leaf extract activated carbon from rice husk was subsequently referred to as RHAC1 while its acid-activated counterpart was tagged as RHAC2.

Characterization of activated carbons from rice husk

The activated carbon samples from rice husk were characterized using Fourier Transform-Infrared Spectroscopy (FTIR), Scanning Electron Microscope (SEM), and Energy Dispersion X-Ray (EDX). FT-IR analysis in solid phase was performed on the samples before and after zinc adsorption at the central research laboratory of Ladoke Akintola University of Technology, Ogbomoso, Oyo State, Nigeria using Fourier Transform Infrared Spectrometer (Shimadzu 100 series spectrometer USA). This analysis was conducted to determine the possible involvement of the surface functional groups on the RH surface in the adsorption process. Five milligrams (5 mg) of each sample was homogeneously mixed with dry potassium bromide and made into pellets in a disc by applying pressure. The spectra of the adsorbents were measured within the wavenumber range of 4000–400 cm^{-1} . The spectra were plotted using the same scale on the transmittance axis for all the adsorbents before and after adsorption. The qualitative and quantitative elemental composition and the morphology of the different activated carbons from rice husk were determined in the Geology laboratory, University of Ibadan, Nigeria using SEM-EDX couple (JEOL JSM-7600F).

Procedure for batch studies

Unless otherwise stated, all experimental runs were carried out in 100 mL conical flasks for 60 min at room temperature. Forty milliliters (40 mL) of 25 mg L⁻¹ Zn solution prepared from a stock solution of ZnSO₄·7H₂O (prepared by dissolving 4.42 g of analytical grade ZnSO₄·7H₂O with distilled water in a 1 L standard flask) was agitated with 0.1 g activated carbon from rice husk on a SearchTech Instrument SHZ-82 Thermostatic water bath shaker (India) operated at a steady speed. The mixture of the activated carbon and Zn(II) solution was filtered using filter paper after agitation and the concentration of residual Zn(II) in the filtrate was determined using Atomic Absorption Spectrometer (Buck Scientific 210 VGP).

Experiments on the variation of pH were conducted by adjusting the pH of different standard solutions (each containing 25 mg L⁻¹ Zn) from pH of 2 to 7 using 0.1 M HCl or 0.1 M NaOH. Subsequent experiments were conducted at the optimum pH obtained from the experiment on pH variation. The effect of contact time was determined by varying the agitation time from 5 to 240 min. Temperatures of 298, 303, 313, and 323 K were used to determine the effect of temperature while the activated carbon dosage range of 0.05–0.25 g was employed to determine the effect of adsorbent dosage on Zn(II) adsorption. Equilibrium isotherm studies were conducted by varying the initial metal concentration from 5 to 100 mg L⁻¹ at 298 K.

The amount of zinc adsorbed per unit mass (q_e) of activated carbon was determined using the following equation:

$$q_e = \left(\frac{C_i - C_f}{m} \right) V \quad (1)$$

Where; m is the mass of activated carbon used (g), V is the volume of the solution (L), C_i is the initial concentration of Zn (mg L⁻¹) and C_f is the equilibrium concentration of Zn(II) (mg L⁻¹) in the filtrate.

The removal efficiency (%R) of each activated carbon was calculated using the following expression:

$$\%R = \frac{(C_o - C_f) \times 100}{C_o} \quad (2)$$

RESULTS AND DISCUSSION

Effect of pH

The effect of pH is the most important parameter affecting adsorption from aqueous medium because it affects the solution chemistry of metals and the functional groups on the adsorbent surface [33-34]. The result of the experiments on the effect of pH on the adsorption of Zn(II) by activated carbon from rice husk is shown in Fig. 1. It was observed that the increase in pH brought about an increase in the percentage of zinc removed. The percentage removal (%R) of Zn(II) increased from 31.2% to 98.96% for RHAC1 (bitter leaf extract activated carbon) and from 18% to 93.60% for RHAC2 (H₂SO₄ activated carbon) when the pH was increased from 2 to 7. This tends to happen because at low pH values, the activated carbon surface is saturated with hydrogen ions, thereby decreasing the percentage of Zn(II) adsorbed because of the electrostatic repulsion existing between the two cations. In addition, the H⁺ ions in the solution compete with Zn(II) ions for the active sites on the adsorbent. By increasing the pH, the number of H⁺ ions will be reduced: the competition between H⁺ ions and Zn(II) for adsorption sites will also be decreased. It is a common phenomenon to observe that the surfaces of adsorbents adsorb cations poorly at low pH values due to the presence of H⁺ ions, whereas,

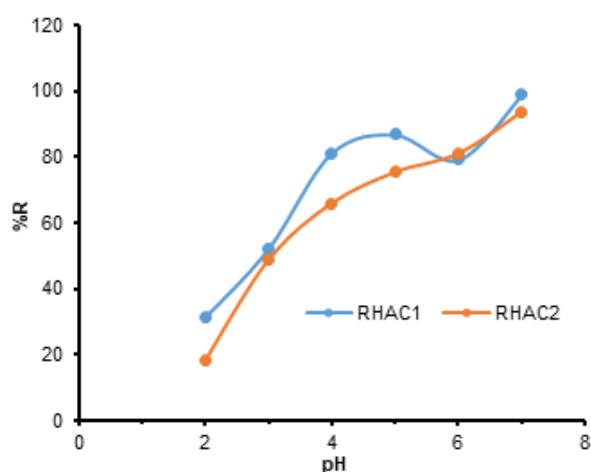


Fig 1. Effect of pH on the adsorption of Zn(II) using RHAC1 and RHAC2

adsorbent surfaces actively adsorb cations at high pH values due to the high concentrations of OH^- ions [35]. It is obvious from Fig. 1 that the adsorption of Zn(II) by RHAC1 was slightly higher than that by RHAC2. The optimum pH level of adsorption was found to be 7 for both RHAC1 and RHAC2. Previous studies have also reported the pH range of 6–7 as the optimum condition for Zn(II) adsorption by activated carbon from different precursors [17,36-39]. However, some authors have also reported the pH range of 4–5 as the optimum condition for Zn(II) removal by certain activated carbons [19-22]. Further experiments were carried out at the optimum pH of adsorption for each of the activated carbon samples.

Effect of Contact Time

Fig. 2 presents the result of the effect of agitation time on the adsorption of Zn(II) by RHAC1 and RHAC2. The figure reveals that the adsorption of Zn(II) was rapid at the initial stage of the contact period, and thereafter became slower near the equilibrium. This is because at the initial stages, the ratio of the unoccupied adsorbent sites to the number of adsorbate particles is higher than at the later stages. This is obvious from the fact that a large number of vacant surface sites are available for adsorption during the initial stage. However, the remaining vacant surface sites are difficult to be occupied due to repulsive forces between the solute molecules on the solid and solution phases [35].

For both RHAC1 and RHAC2, the rate of Zn(II) adsorption was very rapid within the first 5 min of equilibration. The adsorption rate for RHAC1 proceeded gradually after this rapid stage to attain equilibrium after 30 min while the adsorption rate for RHAC2 passed through a steady increase stage between the agitation period of 10 and 60 min before proceeding to equilibrium.

Effect of RHAC1 and RHAC2 Dosage

The effect of activated carbon dosage on the adsorption of Zn(II) is depicted in Fig. 3. It is clear from the figure that the percentage removal of Zn(II) by RHAC1 and RHAC 2 increased with the increase in the mass of the activated carbon. This is expected because as the amount of carbon dose increases, the number of surface active sites for Zn(II) adsorption also increases.

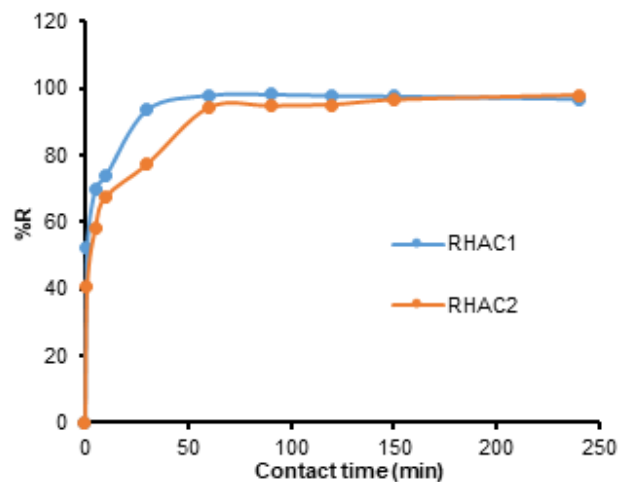


Fig 2. Effect of contact time on the adsorption of Zn(II) from aqueous solution using RHAC1 and RHAC2

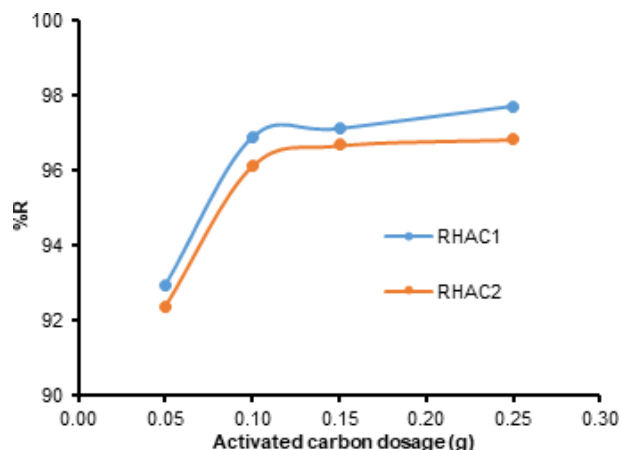


Fig 3. Effect of adsorbent dosage on the adsorption of Zn(II) from aqueous solution using RHAC1 and RHAC2

Characterization

Activated carbon is generally described as an amorphous form of graphite with a random structure of graphite plates; having a highly porous structure with a range of cracks and crevices reaching molecular dimensions [35]. The SEM micrographs of the inactivated carbons, RHAC1 and RHAC2, before and after Zn(II) adsorption are shown in Fig. 4. The figure presents both RHAC1 and RHAC2 as porous materials having different morphological appearances. The bitter leaf activated carbon (RHAC1) appeared to be fibrous, more porous and contained finer particles than RHAC2. The number of pores in RHAC1 was found to be relatively

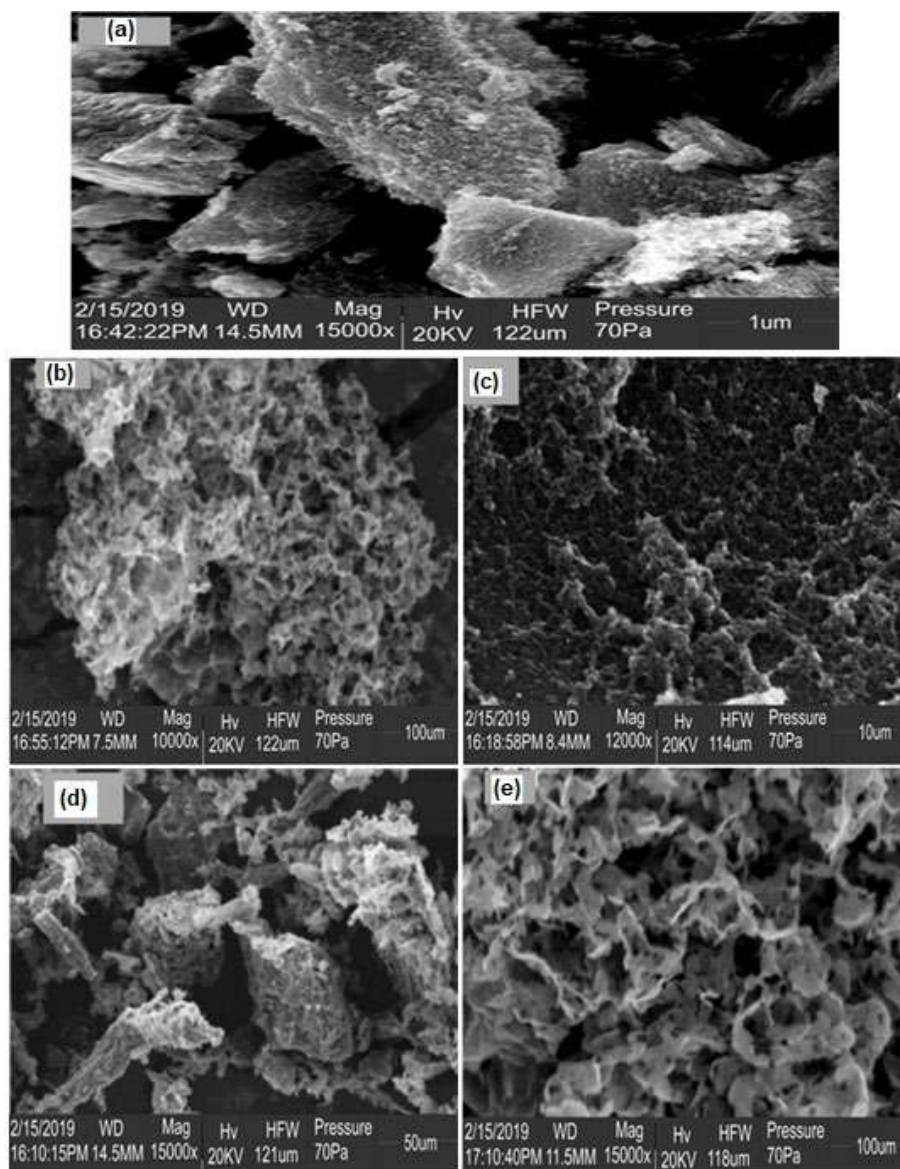


Fig 4. SEM micrographs of: inactivated carbonized rice husk (a), RHAC1 before (b) and after Zn adsorption (c); RHAC2 before (d) and after Zn(II) adsorption (e)

greater than that of RHAC2. Comparing the morphological characteristic of the samples, both bitter leaf (Fig. 4(b)) and H_2SO_4 activated (Fig. 4(d)) samples were more porous than the inactivated sample (Fig. 4(a)). In addition, the inactivated sample appeared in flaky layers while the bitter leaf and H_2SO_4 activated variants were fibrous and porous. It is obvious that the number of pores on the surfaces of both RHAC1 and RHAC2 seemed to decrease after Zn(II) adsorption (Fig. 4(c) and 4(e)). The reduction in the number of pores can be attributed to

the adsorption of Zn(II) ions on the activated carbon surfaces.

Fig. 5 presents the EDX results of the inactivated carbon, RHAC1 and RHAC2 before and after Zn(II) adsorption. It is apparent from the figure that RHAC1 and RHAC2 are carbonaceous. In addition, EDX analysis shows that Zn formed part of the elemental components of both RHAC1 and RHAC2 after adsorption.

In order to determine the possible involvement of functional groups in the adsorption of Zn(II) by RHAC1

and RHAC2, the FTIR analyses of the samples were conducted and the results are presented in Fig. 6 and 7. The peaks at 3537, 3449, 3274 and 3219 cm^{-1} (Fig. 6(a)), recorded for carbonized rice, which are due to the hydroxyl group with hydrogen bonding of OH stretching vibration were respectively shifted to 3536, 3458, 3276 and 3223 cm^{-1} (Fig. 6(b)) after bio-activation with bitter leaf extract. The same set of bands were respectively shifted to 3522, 3443, 3305, and 3253 cm^{-1} (Fig. 7(b)) after activation of rice husk carbon with H_2SO_4 . The absorption band at 3095.2 cm^{-1} for inactivated carbon (Fig. 6(a)) which could be assigned to C–H stretching vibration of the methylene group disappeared after activation with bitter leaf extract (Fig. 6(b)). The same band was found to be reduced to 3013 cm^{-1} after activation with the mineral acid (Fig.

7(b)). The peak at 2887 cm^{-1} , assigned to C–H stretching of the methyl group, which was slightly decreased to 2882 cm^{-1} after chemical activation remained unchanged after bio-activation. The absorption band at 1660 cm^{-1} assigned to the C=O stretching vibration of conjugated ketone was shifted to 1678 cm^{-1} after undergoing chemical activation (Fig. 7(b)) but was left unchanged after bio-activation (Fig. 6(b)). The absorption peak at 1603 cm^{-1} assigned to the C=C stretching vibration of conjugated alkene was shifted to 1621 and 1645 cm^{-1} after bio-activation and chemical activation respectively.

Other important noticeable bands in the carbonized rice husk (Fig. 6(a) and 7(a)) are 1409 cm^{-1} (assigned to C–H out of plane bending vibration),

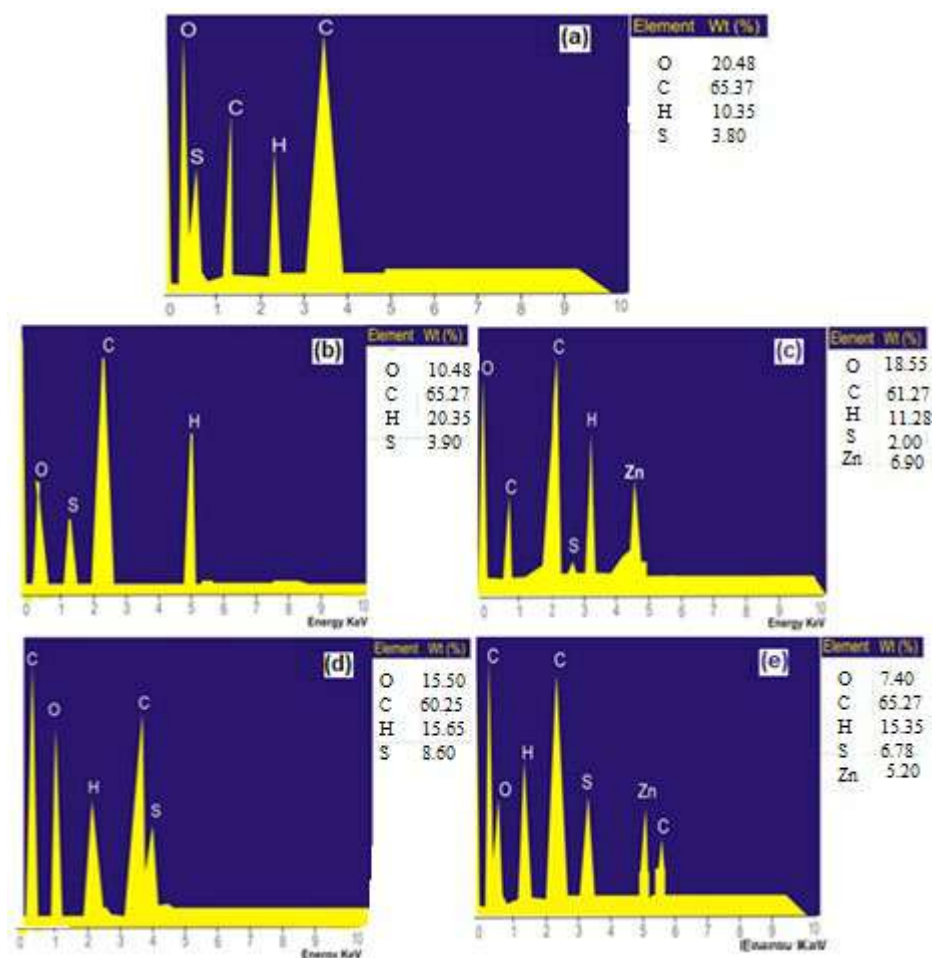


Fig 5. EDX results of: inactivated carbonized rice husk (a); RHAC1 before (b) and after Zn adsorption (c); RHAC2 before (d) and after Zn(II) adsorption (e)

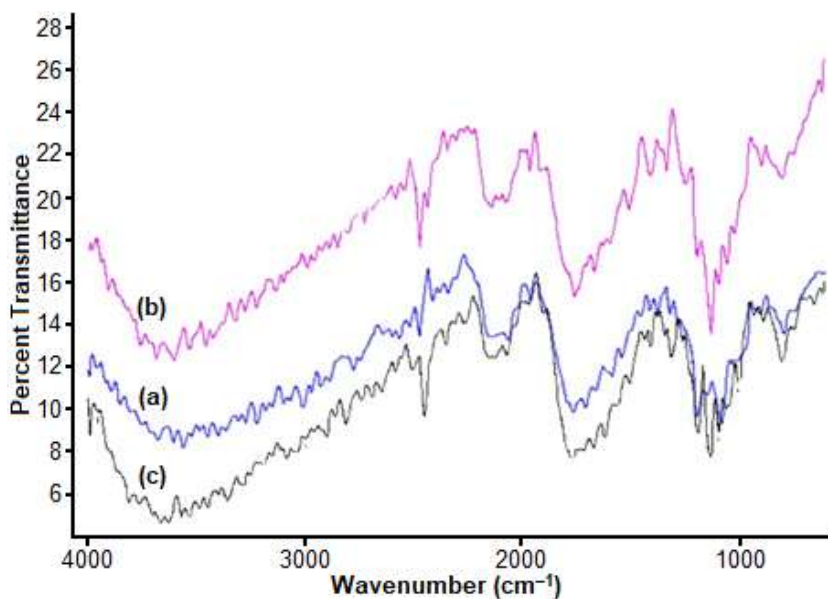


Fig 6. FTIR spectra of: (a) inactivated carbonized rice husk, (b) RHAC1, and (c) RHAC1 after Zn(II) adsorption

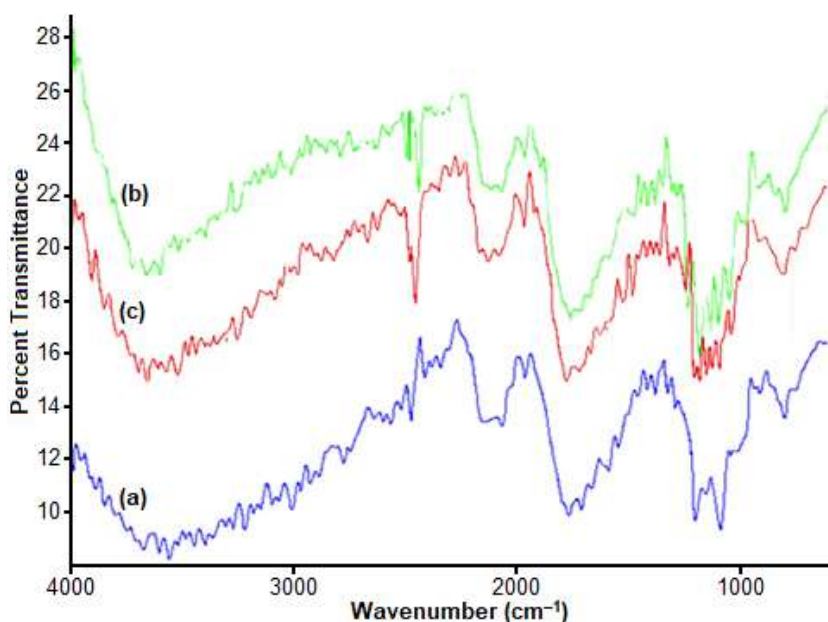


Fig 7. FTIR spectra of: (a) inactivated carbonized rice husk, (b) RHAC2, and (c) RHAC2 after Zn adsorption

1317 cm^{-1} (assigned to OH bending vibration of primary or secondary alcohol) and 1080 cm^{-1} (assigned to C–O stretching of alkyl substituted ether).

All these absorption peaks were also shifted after bio-activation and chemical activation. The changes observed in absorption peaks are a pointer to the influence of both bio-activation and chemical activation on the functional groups at the surface of carbonized rice husk.

For RHAC1, the band at 3458 and 2882 cm^{-1} (Fig. 6(b)) decreased to 3449 and 2862 cm^{-1} (Fig. 6(c)) respectively after Zn(II) adsorption, while the bands at 3276 and 3223 cm^{-1} (Fig. 6(b)) increased to 3286 and 3251 cm^{-1} , respectively after Zn(II) adsorption (Fig. 6(c)). This phenomenon, coupled with the appearance of a new vibrational band at 3486 cm^{-1} revealed that the functional groups on the surface of RHAC1, particularly hydroxyl group, played a prominent role in the

adsorption of zinc by the bitter leaf extract activated carbon from rice husk. For RHAC2, hydroxyl and carbonyl functional groups played a vital role in its adsorption of Zn(II) as reflected in the pronounced shifts observed in the absorption peaks of these groups after Zn(II) adsorption.

Adsorption Thermodynamics

Temperature has two major effects on adsorption processes. Increase in temperature brings about increase in the rate of diffusion of adsorbate molecules across the external boundary layer and in the internal pores of the adsorbent particles. This can be attributed to the decrease in the viscosity of the solution. In addition, changing the temperature will change the equilibrium capacity of the adsorbent for a particular adsorbate [40]. The thermodynamic parameters of the adsorption of Zn(II) by RHAC1 and RHAC2 were determined using the following equations:

$$\Delta G^\circ = -RT \ln K_e \quad (3)$$

where R is the gas constant, T is the temperature in K and K_e is the equilibrium constant given by Eq. (4) [41-43].

$$K_e = -\frac{C_e - C_i}{C_e} \quad (4)$$

According to Van't Hoff equation,

$$\log_{10} K_e = \frac{\Delta S}{2.303R} - \frac{\Delta H}{2.303RT} \quad (5)$$

The values of ΔH° and ΔS° were obtained from the slope and intercept of the plot of $\log K_e$ against $1/T$ while values of ΔG° at different temperatures were obtained using the equation:

$$\Delta G^\circ = \Delta H^\circ - T\Delta S^\circ \quad (6)$$

The results of these parameters are presented in Table 1. The positive values of ΔH° for both RHAC1 and RHAC2 show that the adsorption process was endothermic while the positive ΔS° values evaluated for both adsorbents suggest increased randomness at the solid/solution interface during the adsorption of Zn(II) by both activated carbons from rice husk. The values of evaluated Gibbs free energy change for both RHAC1 and RHAC2 were all negative at all temperatures considered. This is an indication of the spontaneity and feasibility of the adsorption process.

Adsorption Kinetic Study

The adsorption kinetics for RHAC1-Zn(II) and RHAC2-Zn(II) systems was studied using four kinetic models: pseudo first-order, pseudo-second-order, Elovich, and intra-particle models in their natural nonlinear forms. The nonlinear forms were applied because the transformation of nonlinear equations to linear forms, as commonly practiced in most literature reports, may produce bias such as having poor linearity despite high linear regression coefficients, alter their error structure and may also violate the error variance and normality assumptions of standard least-squares method or distort the fit. In addition, linearization can lead to the introduction of error into the independent variable, and alteration of the weight placed on each data point, which often leads to differences in the fitted parameter values between linear and nonlinear versions [44-47].

The pseudo-first-order and pseudo-second-order kinetic models are as presented in Eq. (7) and (8) respectively [48].

Table 1. Thermodynamic parameters for the adsorption of Zn(II) RHAC1 and RHAC2

Sample	T (K)	ΔG° (kJ mol ⁻¹)	ΔH° (kJ mol ⁻¹)	ΔS° (kJ K ⁻¹ mol ⁻¹)
RHAC1	298	-8.80	5.36	0.475
	303	-9.03		
	313	-9.51		
	323	-9.98		
RHAC2	298	-7.08	5.97	0.434
	303	-7.30		
	313	-7.74		
	323	-8.18		

$$q_t = q_e \left[1 - \text{Exp}^{-k_1 t} \right] \quad (7)$$

$$q_t = q_e \left[1 - \frac{1}{1 + q_e k_2 t} \right] \quad (8)$$

where q_e is the amount of solute adsorbed at equilibrium (mg g^{-1}), q_t is the amount of solute adsorbed at time t (mg g^{-1}); k_1 is the pseudo-first order equilibrium rate constant (min^{-1}) and k_2 is the pseudo-second order equilibrium rate constant ($\text{g mg}^{-1} \text{min}^{-1}$).

The Elovich's equation, which has been used to describe the kinetics of chemisorption of gases and metal ions onto solid materials [48-49] takes the non-linear form:

$$q = \frac{1}{\beta} \ln(\alpha \beta t + 1) \quad (9)$$

where α and β are constants. The parameter α represents the rate of chemisorption at zero coverage, the parameter β is related to the extent of surface coverage and to the activation energy for the adsorption.

$$q_t = k_d t^{0.5} + C \quad (10)$$

where k_d is the initial rate of intra particular diffusion ($\text{mg L}^{-1} \text{min}^{-1}$), and C is a constant which is related to the mass transfer across the boundary layer.

The best fitting kinetic model was chosen based on the values of the correlation coefficient (R^2) and the error function. The model that presented the highest R^2 value and the lowest E value was adjudged to best fit the data. The sum of the squares of the error (ERRSQ) and the sum of the absolute errors (EABS) were employed to minimize the error distribution between the experimental data (for both kinetics and equilibrium isotherm) and those predicted by the different models using the *solver* add-in function, Microsoft Excel, Microsoft Corporation.

$$\text{ERRSQ} = \sum_{i=1}^n (q_{e \text{ cal}} - q_{e \text{ exp}})^2 \quad (11)$$

$$\text{EABS} = \sum_{i=1}^n |q_{e \text{ cal}} - q_{e \text{ exp}}| \quad (12)$$

where $q_{e \text{ cal}}$ is each value of q predicted by the fitted model and $q_{e \text{ exp}}$ is each value of q measured experimentally, and n is the number of experiments performed.

From the R^2 and ERRSQ values presented in Table 2, it can be observed that Elovich equation best fitted the adsorption of Zn(II) by both RHAC1 and RHAC2. This

implies that chemisorption played a vital role in the Zn(II) adsorption by activated carbon from rice husk. Literature reports have indicated that Elovich equation is satisfactory in chemical adsorption processes and is suitable for systems with heterogeneous adsorbing surfaces, thus describing many heavy metal adsorption systems [45,50].

Adsorption Isotherms

Equilibrium isotherm data are important to develop an equation that can represent results and for design purposes. The equilibrium data obtained at different initial concentrations of Zn(II) in this study were analyzed using three isotherm models in their non-linear forms, namely, Langmuir, Freundlich, and Dubinin–Radushkevich as represented by Eq. (13–15) respectively.

Table 2. Kinetics parameters for the adsorption of Zn(II) by RHAC1 and RHAC2 at 298 K

	RHAC1	RHAC2
Pseudo-first-order		
q_e (mg g^{-1})	9.76	9.78
K_1 (min^{-1})	0.77	1.01
R^2	0.7779	0.7252
ERRSQ	12.35	33.38
EABS	5.52	12.21
Pseudo-second-order		
q_e (mg g^{-1})	9.39	9.84
K_2 ($\text{g mg}^{-1} \text{min}^{-1}$)	0.13	0.03
R^2	0.9139	0.9622
ERRSQ	4.03	5.18
EABS	4.82	3.91
Elovich		
α ($\times 10^2$)	2.37	0.40
β	1.05	0.88
R^2	0.9596	0.9869
ERRSQ	2.01	0.89
EABS	3.13	1.94
Intra-particle		
K_d ($\text{mg g}^{-1} \text{min}^{-0.5}$)	0.31	0.35
C	6.39	5.63
R	0.8257	0.9012
ERRSQ	7.39	7.14
EABS	6.22	5.79

$$q = \frac{q_m K_L C_e}{1 + K_L C_e} \quad (13)$$

$$q = K_f C_e^{1/n} \quad (14)$$

$$q = q_D \text{Exp} \left[-K \left(RT \ln \left(1 + \frac{1}{C_e} \right) \right)^2 \right] \quad (15)$$

where q is the Zn(II) uptake (mg g^{-1}), C_e is the equilibrium solute concentration, q_m is a constant which denotes the maximum achievable uptake by a system (mg g^{-1}), K_L is the Langmuir constant which defines the affinity between the adsorbate and the adsorbent (L mg^{-1}), K_f is the Freundlich constant which corresponds to the binding capacity ($\text{L}^{1/n} \text{g}^{-1} \text{mg}^{-1/n}$), n which characterizes the affinity between the sorbent and adsorbate, q_D is the Dubinin-Radushkevich model uptake capacity, K is the Dubinin-Radushkevich model constant ($\text{mol}^2 \text{kJ}^{-2}$), R is the gas constant ($\text{kJ K}^{-1} \text{mol}^{-1}$), and T is the temperature (K).

The mean adsorption energy can be determined from the D-R model using the following relationship.

$$E = (-2K_D)^{-1/2} \quad (16)$$

The results of the adsorption isotherms are presented in Table 3. It can be observed that the adsorption process was best described by the Freundlich model based on the R^2 and the error function values. This shows that the adsorption process was largely multi-

layered and the system was heterogeneous. According to the Freundlich theory, the adsorption isotherm becomes linear when $n = 1$, favorable when $n < 1$, and unfavorable when $n > 1$ [47]; hence the adsorption of Zn(II) by both RHAC1 and RHAC2 can be described as favorable. The

Table 3. Isotherm parameters for the adsorption of Zn(II) by RHAC1 and RHAC2 at 298 K

	RHAC1	RHAC2
Langmuir		
q_m (mg g^{-1})	71.47	67.12
K_L (L mg^{-1})	0.069	0.065
R^2	0.9649	0.9814
ERRSQ	71.05	63.19
EAB	17.85	17.98
Freundlich		
K_f ($\text{L}^{1/n} \text{g}^{-1} \text{mg}^{-1/n}$)	3.01	3.01
n	0.97	1.05
R^2	0.9793	0.9876
ERRSQ	55.35	25.01
EABS	8.12	7.23
Dubini-Raduskevich		
q_D (mg g^{-1})	29.29	28.42
E (kJ mol^{-1})	0.62	0.59
R^2	0.9188	0.9341
ERRSQ	198.24	133.57
EABS	27.35	21.79

Table 4. Comparison of maximum adsorption capacity of RHAC1 and RHAC2 for Zn(II) with some other activated carbons reported in literature

S/N	Activated Carbon Precursor	q_{max} (mg g^{-1})	Reference
1.	Mesembryanthemum	52.63	[16]
2.	Olive stone waste	18.95	[17]
3.	Nigerian bamboo	250	[18]
4.	<i>Xanthoceras sorbifolia</i> Bunge hull	100.7	[19]
5.	Eucalyptus seeds	80.37	[20]
6.	Olive branches	34.97	[21]
7.	Birch saw dust	21.44	[22]
8.	Dates stone	10.41	[38]
9.	Capsicum straw	63.3	[39]
10.	Treated green coconut (<i>Cocos nucifera</i>) shells	17.08	[46]
11.	Commercial activated carbon	19.9	[46]
12.	Date pit	111	[51]
13.	RHAC1	71.47	This study
14.	RHAC2	67.12	This study

mean adsorption energy (E) value for the adsorption of Zn(II) on both RHAC1 and RHAC2 fell within the range (< 8 kJ) for physical adsorption. This indicates that physisorption also played some part in the adsorption process.

A comparison of the Langmuir maximum adsorption capacities of RHAC1 and RHAC2 with other activated carbon from other precursors presented in Table 4 indicates that the maximum adsorption capacity values evaluated in this study compare favorably with those previously reported in literature.

■ CONCLUSION

It is practicable and feasible to activate carbonized rice husk with aqueous bitter leaf extract and still obtain a similar or slightly better result than activation using conventional but toxic and non-eco-friendly chemical activating agents (H₂SO₄). This study revealed that bitter leaf extract activated rice husk carbon and its H₂SO₄ activated counterpart had a more porous and finer surface than the inactivated carbonized rice husk. The study further showed that the adsorption of Zn(II) from aqueous solution by the two activated carbon types was temperature, pH, contact time, and adsorbent dosage dependent. The removal of Zn(II) by both activated carbons was spontaneous, feasible, and endothermic. The kinetic evaluation showed that the process followed the Elovich kinetic model while the isotherm parameter analysis showed that the adsorption process followed the Freundlich isotherm model and had Langmuir maximum adsorption capacity of 71.47 (RHAC1) and 67.12 mg g⁻¹ (RHAC2).

■ REFERENCES

- [1] Osasona, I., Ajayi, O.O., and Adebayo, A.O., 2013, Equilibrium, kinetics, and thermodynamics of the biosorption of Zn(II) from aqueous solution using powdered cow hooves, *Int. Sch. Res. Notices*, 2013, 865219.
- [2] Lakherwal, D., 2014, Adsorption of heavy metals: A review, *Int. J. Environ. Res. Dev.*, 4 (1), 41–48.
- [3] Ajjabi, L.C., and Chouba, L., 2009, Biosorption of Cu²⁺ and Zn²⁺ from aqueous solutions by dried marine green macroalga *Chaetomorpha linum*, *J. Environ. Manage.*, 90 (11), 3485–3489.
- [4] Engelking, L.R., 2015, “Zinc” in *Textbook of Veterinary Physiological Chemistry*, 3rd Ed., Academic Press, Boston, US, 309–313.
- [5] Volesky, B., and Holan, Z.R., 1995, Biosorption of heavy metals, *Biotechnol. Progr.*, 11 (3), 235–250.
- [6] Plum, L.M., Rink, L., and Haase, H., 2010, Essential toxin: Impact of zinc on human health, *Int. J. Environ. Res Public Health*, 7 (4), 1342–1365.
- [7] Nomanbhay, S.M., and Palanisamy, K., 2005, Removal of heavy metal from industrial wastewater using chitosan coated oil palm shell charcoal, *Electron. J. Biotechnol.*, 8 (1), 43–53.
- [8] Monser, L., and Adhoum, N., 2002, Modified activated carbon for the removal of copper, zinc, chromium, and cyanide from wastewater, *Sep. Purif. Technol.*, 26 (2-3), 137–146.
- [9] Shim, J.W., Park, S.J., and Ryu, S.K., 2001, Effect of modification with HNO₃ and NaOH on metal adsorption by pitch-based activated carbon fibers, *Carbon*, 39 (11), 1635–1642.
- [10] Ismail, N.E.A., Taha, M.F., and Ramli, A., 2016, Preparation and characterization activated carbon from rice husk and oil palm empty fruit bunches for removal of Zn²⁺ in aqueous solution, *AIC Conf. Proc.*, 1787, 040019.
- [11] Osasona, I., Aiyedatiwa, K., Johnson, J.A., and Faboya O.L., 2018, Activated carbon from spent brewery barley husks for cadmium ion adsorption from aqueous solution, *Indones. J. Chem.*, 18 (1), 145–152.
- [12] Li, K., and Wang, X., 2009, Adsorptive removal of Pb(II) by activated carbon prepared from *Spartina alterniflora*: Equilibrium, kinetics and thermodynamics, *Bioresour. Technol.*, 100 (11), 2810–2815.
- [13] Hasar, H., Cuci, Y., Obek, E., and Dilekoglu, M.F., 2003, Removal of zinc(II) by activated carbon prepared from almond husks under different conditions, *Adsorpt. Sci. Technol.*, 21 (9), 799–808.
- [14] Kobya, M., Demirbas, E., Senturk, E., and Ince, M., 2005, Adsorption of heavy metal ions from aqueous

- solutions by activated carbon prepared from apricot stone, *Bioresour. Technol.*, 96 (13), 1518–1521.
- [15] Amuda, O.S., Giwa, A.A., and Bello, I.A., 2007, Removal of heavy metal from industrial wastewater using modified activated coconut shell carbon, *Biochem. Eng. J.*, 36 (2), 174–181.
- [16] Alkheraz, A.M., Ali, A.K., and Elsherif, K.M., 2020, Equilibrium and thermodynamic studies of Pb(II), Zn(II), Cu(II) and Cd(II) adsorption onto mesembryanthemum activated carbon, *J. Med. Chem. Sci.*, 3, 1–10.
- [17] Sharaf El-Deen, G.E, 2015, Sorption of Cu(II), Zn(II) and Ni(II) from aqueous solution using activated carbon prepared from olive stone waste, *Adv. Environ. Technol.*, 3, 147–161.
- [18] Ademiluyi, F.T., and Abidde, A., 2016, Batch adsorption kinetics of zinc ions using activated carbon from waste Nigerian bamboo, *Int. J. Eng. Appl. Sci.*, 3 (1), 95–99.
- [19] Zhang, X., Hao, Y., Wang, X., and Chen, Z., 2017, Rapid removal of Zinc(II) from aqueous solutions using a mesoporous activated carbon prepared from agricultural waste, *Materials*, 10 (9), 1002.
- [20] Kumar, P.S., Saravanan, A., Kumar, K.A., Yashwanth, R., and Visvesh, S., 2016, Removal of toxic zinc from water/wastewater using eucalyptus seeds activated carbon: Non-linear regression analysis, *IET Nanobiotechnol.*, 10 (4), 244–253.
- [21] Alkheraz, A.M., Ali, A.K., and Elsherif, K.M., 2020, Removal of Pb(II), Zn(II), Cu(II) and Cd(II) from aqueous solutions by adsorption onto olive branches activated carbon: Equilibrium and thermodynamic studies, *Chem. Int.*, 6 (1), 11–20.
- [22] Tuomikoski, S., Kupila, R., Romar, H., Bergna, D., Kangas, T., Runtti, H., and Lassi, U., 2019, Zinc adsorption by activated carbon prepared from lignocellulosic waste biomass, *Appl. Sci.*, 9 (21), 4853.
- [23] Adebisi, G.A., Chowdhury, Z.Z., and Alaba, P.A., 2017, Equilibrium, kinetic, and thermodynamic studies of lead ion and zinc ion adsorption from aqueous solution onto activated carbon prepared from palm oil mill effluent, *J. Cleaner Prod.*, 148, 958–968.
- [24] Ajala, A.S., and Gana, A., 2015, Analysis of challenges facing rice processing in Nigeria, *J. Food Process.*, 2015, 893673.
- [25] James, A., Mamai, E.A., and Bako, T., 2017, Rice waste conversion for economic empowerment in Taraba State, Nigeria: A review, *Int. J. Trend Res. Dev.*, 4 (5), 515–519.
- [26] Abass, A., and Ansumali, S., 2010, Global potential of rice husk as a renewable feedstock for ethanol biofuel production, *BioEnergy Res.*, 3 (4), 328–334.
- [27] Okoro, E.E., Dosunmu, A., Iyuke, S., and Oriji, B., 2016, Production of silicon ethoxide from Nigerian rice husk, *Int. J. Recent Sci. Res.*, 7 (2), 9032–9036.
- [28] Faronmbi, E.O., and Owoeye, O., 2011, Antioxidative and chemopreventive properties of *Vernonia amygdalina* and *Garcinia biflavonoid*, *Int. J. Environ. Res. Public Health*, 8 (6), 2533–2555.
- [29] Alara, O.R., Abdurahman, N.H., Mudalip, S.K.A., and Olalere, O.A., 2017, Phytochemical and pharmacological properties of *Vernonia amygdalina*: A review, *JCEIB*, 2 (1), 80–96.
- [30] Imaga, N.O.A., and Bamigbetan, D.O., 2013, *In vivo* biochemical assessment of aqueous extracts of *Vernonia amygdalina* (Bitter leaf), *Int. J. Nutr. Metab.*, 5 (2), 22–27.
- [31] Seef, L.B., Lindsay, K.L., Bacon, B.R., Kresina, T.F., and Hoofnagle, J.H., 2001, Complementary and alternative medicine in chronic liver disease, *Hepatology*, 34 (3), 595–603.
- [32] Ekpete, O.A., Horsfall Jr., M., and Tarawou, T., 2011, Sorption kinetic study on the removal of phenol using fluted pumpkin and commercial activated carbon, *Int. J. Biol. Chem. Sci.*, 5 (3), 1143–1152.
- [33] Vijayaraghavan, K., and Yun, Y.S., 2008, Bacterial biosorbents and biosorption, *Biotechnol. Adv.*, 26 (3), 266–291.
- [34] Elliott, H.A., and Huang, C.P., 1981, Adsorption characteristics of some Cu(II) complexes on aluminosilicates, *Water Res.*, 15 (7), 849–855.
- [35] Srivastava, V.C., Swamy, M.M., Mall, I.D., Prasad, B., and Mishra, I.M., 2006, Adsorptive removal of phenol by bagasse fly ash and activated carbon:

- Equilibrium, kinetics and thermodynamics, *Colloids Surf., A*, 272 (1-2), 89–104.
- [36] Khademi, Z., Ramavandi, B., and Ghaneian, M.T., 2015, The behaviors and characteristics of a mesoporous activated carbon prepared from *Tamarix hispida* for Zn(II) adsorption from wastewater, *J. Environ. Chem. Eng.*, 3 (3), 2057–2067.
- [37] Fischer, A.R., Sgolik, L., Kreller, A., and Dornack, C., 2018, Zinc(II) adsorption by low-carbon shungite: The effect of pH, *Water*, 10 (4), 422.
- [38] Mouni, L., Merabet, D., Bouzaza, K., and Belkhiri, L., 2010, Removal of Pb²⁺ and Zn²⁺ from the aqueous solutions by activated carbon prepared from Dates stone, *Desalin. Water Treat.*, 16 (1-3), 66–73.
- [39] Yang, C., Girma, A., Lei, T., Liu, Y., and Ma, C., 2016, Study on simultaneous adsorption of Zn(II) and methylene blue on waste-derived activated carbon for efficient applications in wastewater treatment, *Cogent Environ. Sci.*, 2, 1151983.
- [40] Sathishkumar, M., Binupriya, A.R., Kavitha D., Selvakumar, R., Choi, J.G., and Yun, S.E., 2009, Adsorption potential of maize cob carbon for 2,4-dichlorophenol removal from aqueous solutions: Equilibrium, kinetics and thermodynamics modeling, *Chem. Eng. J.*, 147 (2-3), 265–271.
- [41] Al-Rashed, S.M., and Al-Gaid A.A., 2012, Kinetic and thermodynamic studies on the adsorption behavior of Rhodamine B dye on Duolite C-20 resin, *J. Saudi Chem. Soc.*, 16 (2), 209–215.
- [42] Yu, Y., Zhuang, Y.Y., and Wang, Z.H., 2001, Adsorption of water soluble dye onto functionalized resin, *J. Colloid Interface Sci.*, 242 (2), 288–293.
- [43] Malik, A., Khan, A., Anwar, N., and Naeem, M., 2020, Comparative study of the adsorption of Congo Red dye on rice husk, rice husk char and chemically modified rice husk char from aqueous media, *Bull. Chem. Soc. Ethiop.*, 34 (1), 41–54.
- [44] Foo, K.Y., and Hameed, B.H., 2010, Insights into the modeling of adsorption isotherm systems, *Chem. Eng. J.*, 156 (1), 2–10.
- [45] López-Luna, J., Ramírez-Montes, L.E., Martínez-Vargas, S., Martínez, A.I., Mijangos-Ricardez, O.F., González-Chávez, M.C.A., Carrillo-González, R., Solís-Domínguez, F.A., Cuevas-Díaz, M.C., and Vázquez-Hipólito, V., 2019, Linear and nonlinear kinetic and isotherm adsorption models for arsenic removal by manganese ferrite nanoparticles, *SN Appl. Sci.*, 1 (8), 950.
- [46] Mahmoud, D.K., Mohd Salleh, M.A., and Wan Abdul Karim, W.A., 2012, Langmuir model application on solid liquid adsorption using agricultural wastes: Environmental application review, *J. Purity Util. React. Environ.*, 1 (4), 170–199.
- [47] Tran, H.N., You, S.J., Hosseini-Bandegharaei, A., and Chao, H.P., 2017, Mistakes and inconsistencies regarding adsorption of contaminants from aqueous solutions: A critical review, *Water Res.*, 120, 88–116.
- [48] Cheung, C.W., Porter, J.F., and McKay, G., 2000, Sorption kinetics for the removal of copper and zinc from effluents using bone char, *Sep. Purif. Technol.*, 19 (1-2), 55–64.
- [49] Osasona, I., Adebayo, A.O., and Okoronkwo, A.E., 2017, Characterization and utilization of citric acid modified cow hoof for adsorption of cadmium and copper from wastewater, *Chem. Sci. Int. J.*, 21 (1), 32537.
- [50] Wu, F.C., Tseng, R.L., and Juang, R.S., 2009, Characteristics of Elovich equation used for the analysis of adsorption kinetics in dye-chitosan systems, *Chem. Eng. J.*, 150 (2-3), 366–373.
- [51] Aldawsari, A., Khan, M.A., Hameed, B.H., Alqadami, A.A., Siddiqui, M.R., Alothman, Z.A., and Hadj Ahmed, A.Y.B., 2017, Mercerized mesoporous date pit activated carbon- A novel adsorbent to sequester potentially toxic divalent heavy metals from water, *PLoS ONE*, 12 (9), e0184493.

Development of Voltammetry Analysis Method of Copper Metal Ions by Solid-State Membrane with Carbon Nanotube

Suyanta^{1*}, Sunarto¹, Regina Tutik Padmaningrum¹, Karlinda¹, Illyas Md. Isa², and Rahadian³

¹Department of Chemistry Education, Universitas Negeri Yogyakarta, Jl. Colombo No. 1, Yogyakarta 55281, Indonesia

²Nanotechnology Research Centre, Faculty of Science and Mathematics, Universiti Pendidikan Sultan Idris, 35900 Tanjong Malim, Perak, Malaysia

³Department of Chemistry, Faculty of Mathematics and Natural Sciences, Universitas Negeri Padang, Jl. Prof. Dr. Hamka, Padang 25173, West Sumatera, Indonesia

* **Corresponding author:**

tel: +62-81227577355

email: suyanta@uny.ac.id

Received: March 26, 2020

Accepted: November 2, 2020

DOI: 10.22146/ijc.55056

Abstract: This study was aimed to develop a method for metal analysis in continuous integration using voltammetry techniques. The research subject was copper(II) ions. The objects of research were linearity, scan rate, repeatability of readings, and the presence of Cu(II) levels in well water samples. In this study, a selective electrode was developed with a solid membrane voltammetry system using differential pulse voltammetry measurement. The results showed the regression line of voltammetry method, $y = 10.265 \ln(x) + 330.47$, with a correlation value of 0.9654, the optimum scan rate was 10 mV/s, and within five repetitions of each measurement for one electrode, it showed good repeatability. Meanwhile, the result of regression with the UV-Vis spectrophotometric method for Cu(II) was $y = 0.12386x + 0.00879$ with a correlation value of 0.9943. The voltammetry method was found to be much better than the UV-Vis method because it was able to be used for analysis up to a concentration of 6.35×10^{-4} ppm (or 1.00×10^{-11} M), while the UV-Vis method was only able to analyze up to 1.5 ppm (or 2.36×10^{-5} M).

Keywords: copper(II); spectrophotometry; voltammetry; nanotube carbon; solid-state membrane

■ INTRODUCTION

Disposal of both industrial and domestic production processes usually results in environmental pollution. Metals commonly found in chemical industrial wastes are copper, silver, cadmium, cobalt, iron, chromium, nickel, and zinc [1]. Copper (Cu) is extensively used in the chemical industry, particularly in electroplating, textile, and metal industries. Copper(II) sulfate is usually used for chemical analysis reagent, organic compound synthesis, additives in NPK fertilizer, blue dyeing in the textile industry, etc. Copper is one of the heavy metals that is toxic and dangerous [2].

Many techniques have been developed to detect the content of copper (ion) in many samples using instruments such as UV-VIS spectrophotometers, AAS, ICP-MS, and ICP-AES. The AAS method is less sensitive

for the determination of rare earth elements because of the high detection limit, which is 800–900 ppm, while ICP-MS and ICP-AES methods require very expensive devices [3]. Because of the limitations of these methods, another method is needed for better copper determination. The Potentiometry method with the use of ion-selective electrodes as working electrodes is a fairly inexpensive and practical analysis method, that can provide good sensitivity and selectivity. Based on a previous study [4], copper electrodes were found to be quite sensitive with a detection limit reaching 10^{-9} mol/L. Ganjali et al. [5] had synthesized a particular compound made of 4-methyl-hidrazino benzothiazole hydrobromide and hydrazine hydrate. This compound has a complex set of copper and iron, so it was able to selectively react with copper and iron.

The development of the analysis of metal ions including copper(II) using voltammetry has been carried out, both ionically and molecularly in compounds, especially with electrometry systems [6-8]. The development of voltammetry analysis techniques using carbon nanotubes has also been developed. The voltammetric determination of cadmium, iron and lead was carried out by Deswati et al. [9]. The determination of several heavy metal ions by means of differential anodic stripping voltammetry pulse was conducted by Thanh et al. [10] and the development of the analysis of Cd, Cu, Pb, and Zn ions in seawater was carried out by Deswati et al. [11].

The use of carbon nanotubes as an ion selective electrode is not only for the analysis of metal ions, but also for the analysis of non-metals, especially organic compounds. The analysis of phenols and their derivatives by voltammetry using carbon nanotubes was developed by Adekunle et al. [12], while the determination of voltammetric tyrosine, acetaminophen and ascorbic acid compounds with carbon nanotube electrodes was developed by Madrakian et al. [13]. Meanwhile, the detection of glutamate at a biosensor of carbon nanotube electrodes was studied by Khan et al. [14].

Copper determination by UV-VIS technique generally uses various complexing compounds. The complexes used include ferrocene [15], which was researched by Zubair et al. [16]. Another compound that has a similar structure is Na-diethyldithiocarbamate or Na-DDTC with the molecular formula of $(C_2H_5)_2NCS_2Na$. Sirotiak [17] in his research, stated that copper is one of the many elements that can form complexes with sodium diethyldithiocarbamate (Na-DDTC). Therefore, in this study, the copper ion-selective electrode was developed by Na-diethyldithiocarbamate as an active ingredient of the membrane and the basic matrix of carbon nanotubes and analyzed by means of differential pulse voltammetry.

■ EXPERIMENTAL SECTION

The subject of this study was copper(II) ions in well water and the objects were linearity, scan rate, repeatability of readings, and the presence of Cu(II) levels in well water samples.

Materials

All reagents used in this study were of analytical reagent grade. Carbon nanotube powder (Timesnano) and paraffin (Uvasol, Merck), copper(II) sulfate (Sigma-Aldrich), Na-diethyldithiocarbamate (Merck), potassium chloride (Merck), and potassium nitrate (Merck) were used as received. Stock solutions of copper ions were freshly prepared by dissolving an appropriate amount of copper(II) sulfate in distilled deionized water. The samples of well water were collected from some areas in the Yogyakarta State University, Indonesia.

Instrumentation

The differential pulse voltammetry was performed with EDAQ Potentiostat, (Australia). All experiments were carried out in a single compartment electrochemical cell with a carbon-paste working electrode, saturated Ag/AgCl reference electrode and Pt wire counter electrode. The reference and counter electrodes refer to previous research conducted by Farahi et al. [18]. These electrodes were immersed in 40 mL buffer solution (also as supporting electrolytes) at various pH and amount of Cu(II) solution. The pH value was determined using a glass electrode Orion 915600, USA. The spectroscopy method was conducted using Spectrophotometer UV-VIS Shimadzu, 2450 Series.

Procedure

Electrode preparation

The modified carbon paste electrodes were a homogenized mixture of Na-diethyldithiocarbamate, carbon nanotube, and solid paraffin with a ratio of 4:3:3 in mass composition in paste form. The modified carbon paste electrodes were packed firmly into a teflon tubing (id = 4 mm). Electrical contact to the paste was established via a copper wire at one end of the tubing, while the other end acted as the disc electrode. Before measurement, the disc electrode was smoothed on a piece of weighing paper. This method refers to Suyanta [19].

Voltammetry analysis

The copper(II) ion analysis was developed using differential pulse voltammetry. This technique was found to be useful in analyzing metal ions. This

technique was developed by several researchers [20-21]. With differential pulse voltammetry techniques, the current is measured at two points for each pulse, just before the application of the pulse and at the end of the pulse. The difference between the two measured currents for each pulse is plotted against the base potential [22]. Voltammetry data in the form of peak adsorption currents were changed in the current study because of the various scan rate, repeatability and various concentration studied in this research.

The conditions applied during the accumulation of the analyte including accumulation of potential (initial -1000 mV, final 0 mV), accumulation of time, and pH of the solution (7,32) referred to the previous studies by Suyanta [19]. The conditions on the determination of Cu(II) by spectrophotometry (the maximum wavelength of 400–500 nm and pH 5–11) refer to the thesis research by Niken and Sunarto [23].

Data analysis

The results of the study on solutions of various concentrations were determined by the linear concentration region and a calibration curve between the high currents of the peak versus the concentration. This analysis was done to determine the linearity and the correlation between the standard solution calibration curve and its samples. This analysis technique was used for the voltammetry and spectroscopy methods.

RESULTS AND DISCUSSION

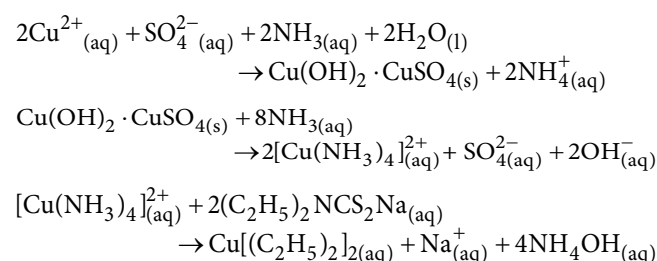
Characterization of Copper(II) Carbon Paste Electrode System in Differential Pulse Voltammetry

The active ingredient sodium diethyldithiocarbamate membrane as the modifier of the carbon paste electrode influenced the copper(II) voltammogram. The results of the voltammogram of the copper ion measurements are shown in Fig. 1.

Fig. 1 shows that the modified electrode of Na-diethyldithiocarbamate carbon paste gave a peak current response to copper(II) solution, at a potential of -0.695 V vs. Ag/AgCl with a current value of 102.636 nA, while an electrode without modification did not give any rise to a peak. Thus the electrode was able to censor the presence of copper(II) ions properly.

Carbon paste electrodes without modification did not produce Cu peaks because no complexation reactions occurred. While the carbon paste electrode with modification caused a complexation reaction between copper with sodium diethyldithiocarbamate (Na-DDTK) which produces a Cu peak.

The complexation reaction mechanism that occurred on the surface of the electrode is proposed as follows:



The formula structure of the complex Cu(DDC)₂ can be depicted as shown in Scheme 1 [24].

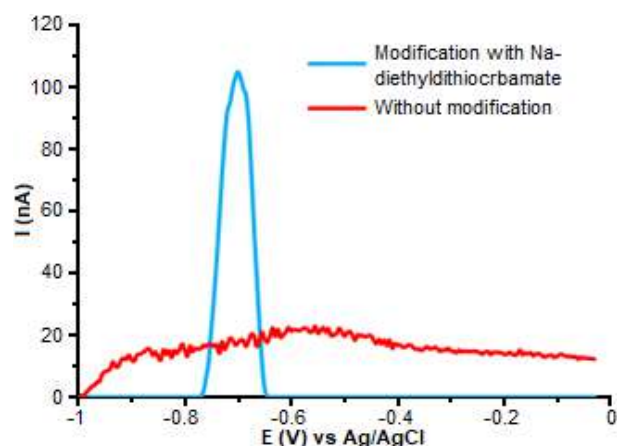
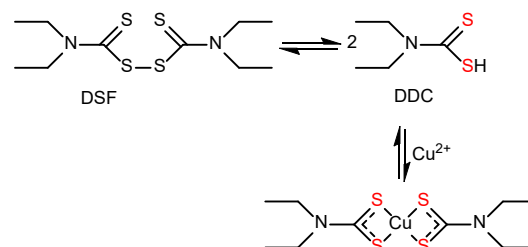


Fig 1. The difference in the voltammogram curve at the working electrode with and without Na-diethyldithiocarbamate modification



Scheme 1. Disulfiram (DSF) in aqueous solutions is reduced to diethyldithiocarbamate (DDC) and in the presence of Cu²⁺ forms bis(diethyldithiocarbamate)copper(II): Cu(DDC)₂

Linearity

The linear concentration area of the modified carbon paste electrode was studied to determine the area (range) of concentration which provided a linear relationship between the height of the peak current and the concentration of copper(II) (10^{-6} – 10^{-10} M). The corresponding voltammograms are shown in Fig. 2.

Based on Fig. 2, it appears that the presence of copper(II) ions at various concentrations can be censored by the electrode properly. The greater the concentration of copper(II) ions, the higher the voltammogram.

If the voltammogram in Fig. 2 created a relationship between the concentration and the measurement current value, a linear graph would be formed. The relationship between the concentration and the current is listed in Table 1.

Based on Table 1, a curve was made between the concentration of copper(II) solution and the height of the peak current produced. The result is shown in Fig. 3.

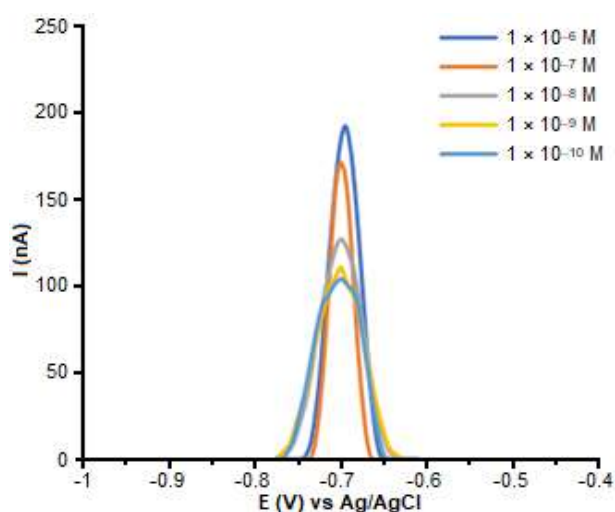


Fig 2. The voltammogram curve of the modified working electrode at various concentrations

Table 1. The measurement results of the copper(II) current at various concentrations

Concentration (M)	Current (nA)
1.0×10^{-6}	192.59
1.0×10^{-7}	171.37
1.0×10^{-8}	127.37
1.0×10^{-9}	111.04
1.0×10^{-10}	104.58

Based on the results of this study, it can be seen that the current is comparable with the concentration. This relationship is mathematically expressed through the regression line equation which is calculated with the value, $y = 10.265 \ln(x) + 330.47$ and the value of $r = 0.9654$. The linearity of the UV-Vis spectroscopy method was expressed by the line equation, $y = 0.12386x + 0.00879$, with the value of $r = 0.9943$, as seen in the calibration curve shown in Fig. 4 [23].

The results of the study show the value of $r \geq 0.95$ which indicates a linear criterion for both techniques. Thus both techniques are good methods of analysis.

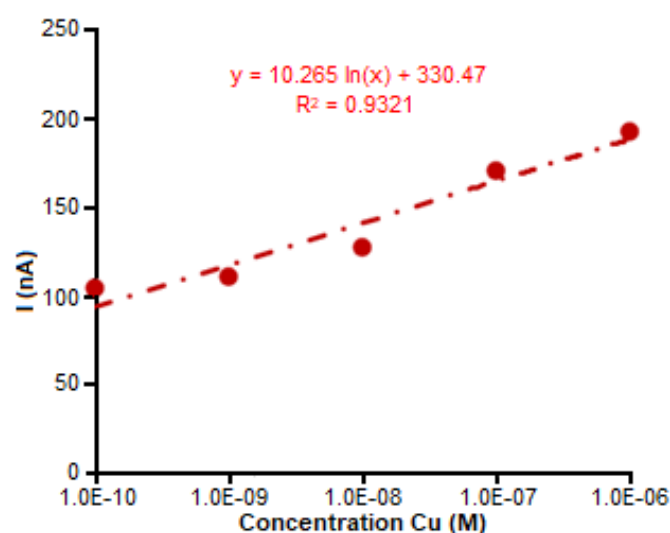


Fig 3. The relationship between the concentration of copper(II) solution and the high current

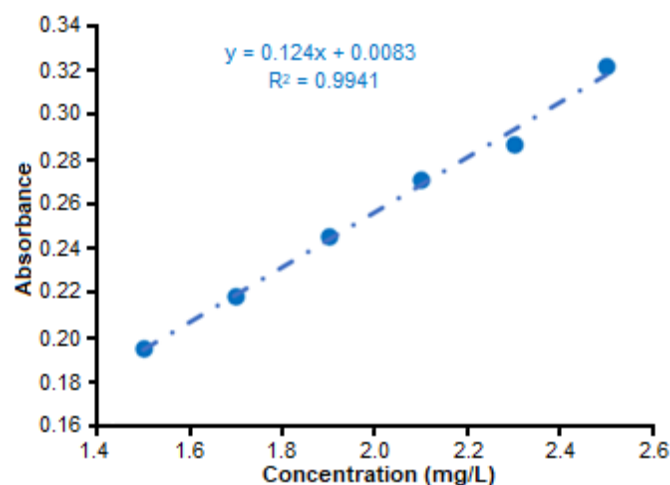


Fig 4. Copper(II)- diethyldithiocarbamate calibration curve

Scan Rate

In differential pulse voltammetry, the height and width of the peak of the current are affected by the speed of reading [25]. The related measurement results are shown in Fig. 5.

Fig. 5 shows that the current produced by a concentration of 10^{-10} M was lower than the data in Table 1 because the determination of maximum current was also different. In Fig. 1 and 2, the maximum current was 100 nA, while in Fig. 5 the maximum current was 50 nA, with 10 nA difference between measurements (10, 20, 30, 40 and 50 nA). The choice of maximum current with a not so large difference between measurements resulted in no significant effect to the current generated. The scan rate selection in Fig. 5 refers to previous research conducted by Suyanta et al. [18]. The peak of the voltammogram in Fig. 5 shifted quite far to the more positive potential. This shows the kinetic limitations in the electrochemical reaction of Cu(II) in Na-DDTK modified carbon paste electrodes.

The results of the current measurements at various scan rates can be seen in Table 2.

Table 2 shows that the higher the scan rate, the smaller the current value obtained. In this study, the optimum reading scan rate was 10 mV/s because the peak obtained was higher and not wider.

Repeatability Results of the Electrode

The repeatability of the modified carbon paste electrodes was studied by comparing the peak currents at optimum conditions. The measurements were carried out 5 times with one electrode under solution conditions and fixed measurements. The measurement results are shown in Fig. 6.

The results of the measurements that were repeated 5 times show that the peak current was stable (constant), indicating that the modified Na-diethyldithiocarbamate carbon paste electrode had a good reproducible repetition. According to Silva et al. [26], the electrodes that presented good precision showed that there was no matrix effect that affected the electrodes for detection.

The Measurement Result of Cu(II) in the Well Water

The Na-diethyldithiocarbamate modified electrode

was applied to determine the content of copper(II) in well water. The results of the well water measurements are shown in Fig. 7.

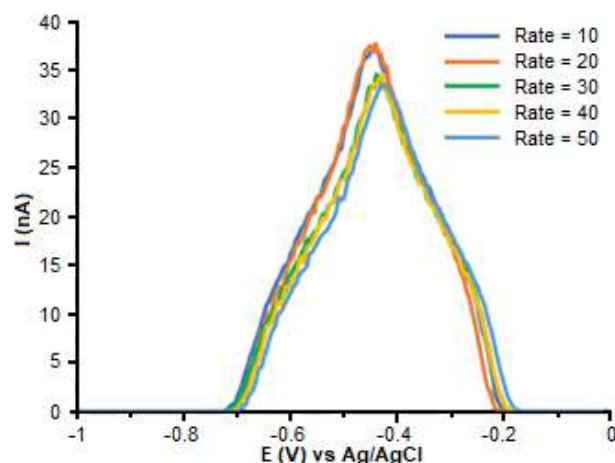


Fig 5. The effect of the difference in the adsorption rate of copper(II) from the modified working electrode at a concentration of 1×10^{-10} M and a maximum current of 50 nA

Table 2. The measurement results of the current at various scan rates

Scan Rate (mV/S)	Current (nA)
10	37.02
20	36.90
30	34.67
40	34.10
50	33.52

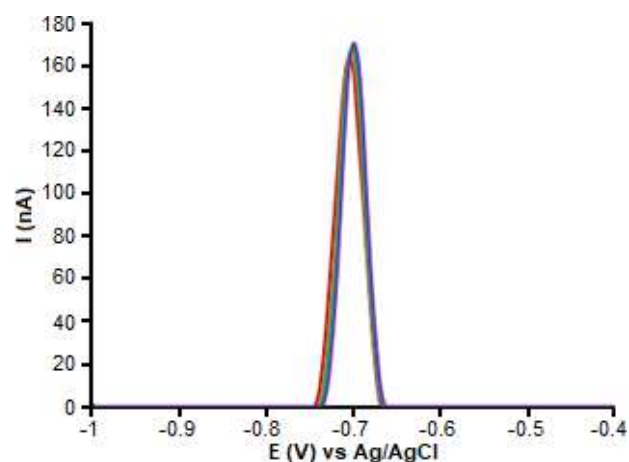
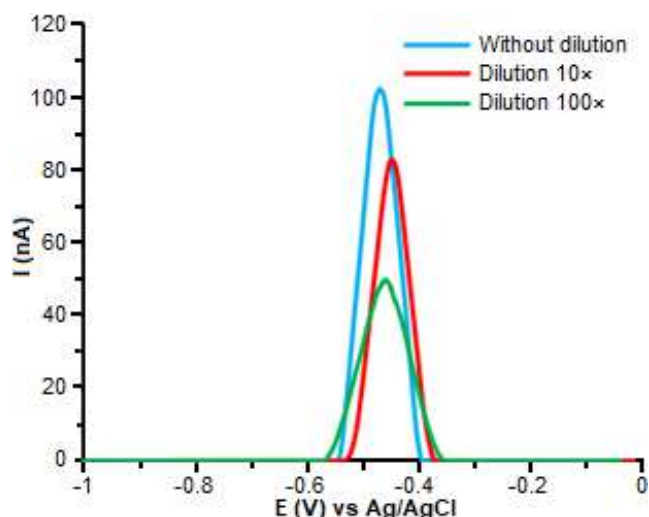


Fig 6. The voltammogram curve of the modified working electrode, measured 5 times at a concentration of 1.00×10^{-7} M and rate of 50 mV/s

Table 3. Comparison of the value of correlation coefficients and the ability of the analysis of copper with UV-Vis spectrophotometry and voltammetry method

Metal Ion	Linear measurement range		Limit detection	
	Voltammetry method	Spectrophotometry method	Voltammetry method	Spectrophotometry method
Copper(II)	0.9654	0.9943	1.00×10^{-11} M	2.36×10^{-5} M

**Fig 7.** Voltammogram of copper(II) content in well water

The results of the measurements of the well water samples show that the copper content in well water was very small. According to the copper voltammogram, the current which was obtained from the analysis was above 100 nA.

Comparison of the Validation Results

The comparison of the validation result was aimed to determine the best method of determining copper(II), between the UV-Vis or the voltammetry spectrophotometry method. Comparison of the correlation coefficient and analytical ability for copper(II) for the UV-Vis spectrophotometry method and the voltammetry method can be seen in Table 3.

The results of the study shows that the voltammetry method was better at measuring the content of copper(II) in solution and also in the well water compared to the UV-Vis spectrophotometry method. The more sensitive method (the lower the detection limit) demonstrate a better analysis process.

CONCLUSION

Based on the current research, it can be concluded

that the modification of the carbon paste electrodes by mixing with the modifier Na-diethyldithiocarbamate shows a very good peak current response to copper(II) solution. This is proven by the low detection limit of 1.00×10^{-11} M and regression line equation $y = 10.265 \ln(x) + 330.47$ with r value of 0.9654, optimum rate of 10 mV/s, and stable repeatability (reproducible). In addition, the voltammetry method was found to be better than the UV-Vis spectrophotometry method for the analysis of copper(II) in solution and well water.

ACKNOWLEDGMENTS

We would like to thank those who have contributed to our research, the team and the research assistants. We would also like to express gratitude to the Yogyakarta State University which was a pleasant place to conduct our research.

AUTHOR CONTRIBUTIONS

Suyanta conducted the experiment and prepared the manuscripts. Ilyas Md. Isa provided the experiment materials. Regina Tutik Padmaningrum analyzed the data. Sunarto, Rahadian, Ilyas Md. Isa, Regina Tutik Padmaningrum revised the manuscript. Karlinda helped in carrying out the experiment. All authors agreed to the final version of this manuscript.

REFERENCES

- [1] Pratiwi, A., Yusuf, B., and Gunawan, R., 2015, Analisis perubahan kadar logam tembaga (Cu) pada penambahan ion perak (Ag) dengan metode elektrokoagulasi, *JKM*, 13 (1), 1–3.
- [2] Parmar, M., and Takur, L.S., 2013, Heavy metal Cu Ni and Zn: Toxicity, health hazards and their removal techniques by low cost adsorbents: A short overview, *Int. J. Plant Anim. Environ. Sci.*, 3 (3), 2231–4490.

- [3] Kooh, M.R.R., Santos, J.H., and Dahri, M.K., 2013, Preparation and evaluation of *Acetabularia*-modified carbon paste electrode in anodic stripping voltammetry of copper and lead ions, *J. Chem.*, 2013, 538012.
- [4] Stankovic, D., Roglic, G., Mutic, J., Andjelkovic, I., Markovic, M., and Manojlovic, D., 2011, Determination of copper in water by anodic stripping voltammetry using Cu-DPABA-NA/GCE modified electrode, *Int. J. Electrochem. Sci.*, 6, 5617–5625.
- [5] Ganjali, M.R., Norouzi, P., Shamsolahrari, L., and Ahmadi, A., 2006, PPb level monitoring of lanthanum by a novel PCV-membrane sensor based on 4-methyl-2-hydrazinobenzothiazole, *Sens. Actuators, B*, 114 (2), 713–719.
- [6] Pandurangachar, M., Swamy, B.E.K., Chandrashekar, B.N., Gilbert, O., Reddy, S., and Sherigara, B.S., 2010, Electrochemical investigations of potassium ferricyanide and dopamine by 1-butyl-4-methylpyridinium tetrafluoro borate modified carbon paste electrode: A cyclic voltammetric study, *Int. J. Electrochem. Sci.*, 5, 1187–1202.
- [7] Ensafi, A.A., and Karimi-Maleh, H., 2010, Modified Multiwall carbon nanotubes paste electrode as a sensor for simultaneous determination of 6-thioguanine and folic acid using ferrocene dicarboxylic acid as a mediator, *J. Electroanal. Chem.*, 640 (1-2) 75–83.
- [8] Putra, B.R., Darusman, L.K., and Rohaeti, E., 2013, Carbon paste electrode hexadecyltrimethyl ammonium bromide modified natural zeolite for chromium(VI) detection, *Indones. J. Chem.*, 13 (2), 122–128.
- [9] Deswati, Suyani, H., Safni, Loekman, U., and Pardi, H., 2013, Simultaneous determination of cadmium, copper and lead in sea water by adsorptive stripping voltammetry in the presence of calcon as a complexing agent, *Indones. J. Chem.*, 13 (3), 236–241.
- [10] Thanh, N.M., Hop, N.V., Luyen, N.D., Phong, N.H., and Toan, T.T.T., 2019, Simultaneous determination of Zn(II), Cd(II), Pb(II), and Cu(II) using differential pulse anodic stripping voltammetry at a bismuth film-modified electrode, *Adv. Mater. Sci. Eng.*, 2019, 1826148.
- [11] Deswati, Suyani, H., and Safni, 2012, The method development of analysis Cd, Cu, Pb and Zn in sea water by absorptive stripping voltammetry (ASV) in the presence of calcon as complexing agent, *Indones. J. Chem.*, 12 (1), 20–27.
- [12] Adekunle, A.S., Arotiba, O.A., Agboola, B.O., Maxakato, N.W., and Mamba, B.B., 2012, Voltammetric and impedance studies of phenols and its derivatives at carbon nanotubes/Prussian blue films platinum modified electrode, *Int. J. Electrochem. Sci.*, 7, 8035–8051.
- [13] Madrakian, T., Haghshenas, E., and Afkhami, A., 2014, Simultaneous determination of tyrosine, acetaminophen and ascorbic acid using gold nanoparticles/multiwalled carbon nanotube/glassy carbon electrode by differential pulse voltammetric method, *Sens. Actuators, B*, 193, 451–460.
- [14] Khan, R., Gorski, W., and Garcia, C.D., 2011, Nanomolar detection of glutamate at a biosensor based on screen-printed electrodes modified with carbon nanotubes, *Electroanalysis*, 23 (10), 2357–2363.
- [15] Skoog, D.A., Holler, F.J., and Crouch, S.R., 2018, *Principles of Instrumental Analysis, Textbook of Instrumental Analysis*, 7th Ed., Thomson Brook/Cole, California.
- [16] Zubair, S., Asghar, F., Badshah, A., Lal, B., Hussain, R.A., Tabassum, S., and Tahir, M.N., 2019, New bioactive ferrocene-substituted heteroleptic copper(I) complex: Synthesis, structural elucidation, DNA interaction, and DFT study, *J. Organomet. Chem.*, 879, 60–68.
- [17] Sirotiak, M., Bartošová, A., and Blinová, L., 2014, UV-Vis Spectrophotometric determinations of selected elements in modelled aqueous solutions, *J. Environ. Prot. Saf. Educ. Manage.*, 3 (2), 75–87.
- [18] Farahi, A., Lahrach, S., Achak, M., El Gaini, L., Bakasse, M., and El Mhammedi, M.A., 2014, Parameters affecting the determination of paraquat at silver rotating electrodes using differential pulse

- voltammetry, *Anal. Chem. Res.*, 1, 16–21.
- [19] Suyanta, Sunarto, Sari, L.P., Wardani, N.I., and Isa, I.M., 2014, Differential adsorptive stripping voltammetric determination of ultra trace lanthanum(III) based on carbon paste electrode modified with 3-methyl-2-hydrazinobenzothiazole, *Int. J. Electrochem. Sci.*, 9, 7763–7772.
- [20] Mohadesi, A., Teimoori, E., Taher, M.A., and Beitollah, H., 2011, Adsorptive stripping voltammetric determination of cobalt(II) on the carbon paste electrode, *Int. J. Electrochem. Sci.*, 6, 301–308.
- [21] Arancibi, V., Nagles, E., García-Beltrán, O., and Hurtad, J., 2018, Adsorptive stripping voltammetric determination of lead and cadmium in natural waters in the presence of rutin using a Nafion–mercury coated film electrode, *Int. J. Electrochem. Sci.*, 13, 8711–8722.
- [22] Wang, H.Y., Pan, M.I., Oliver Su, Y.L., Tsai, S.C., Kao, C.H., Sun, S.S., and Lin, W.Y., 2011, Comparison of differential pulse voltammetry (DPV)-A new method of carbamazepine analysis-with fluorescence polarization immunoassay (FPIA), *J. Anal. Chem.*, 66 (4), 415–420.
- [23] Pratiwi, N.A., and Sunarto, 2018, Perbandingan validasi metode analisis ion tembaga (II) tanpa pengompleks dan dengan pengompleks N-dietilditiokarbamat secara spektrofotometri UV-Vis, *J. Kim. Das.*, 7 (3), 96–104.
- [24] Helsel, M.E., and Franz, K.J., 2015, Pharmacological activity of metal binding agents that alter copper bioavailability, *Dalton Trans.*, 44 (19), 8760–8770.
- [25] Sandford, C., Edwards, M.A., Klunder, K.J., Hickey, D.P., Li, M., Barman, K., Sigman, M.S., White, H.S., and Minter, S.D., 2019, A synthetic chemist's guide to electroanalytical tools for studying reaction mechanism, *Chem. Sci.*, 10 (26), 6404–6422.
- [26] Silva, T.A., Wong, A., and Fatibello-Filho, O., 2020, Electrochemical sensor based on ionic liquid and carbon black for voltammetric determination of Allura red colorant at nanomolar levels in soft drink powders, *Talanta*, 209, 120588.

Identification of the Chemical Constituents of the Selected Fraction of the Dichloromethane Extract of *Syzygium samarangense* Stem Bark Using LC-ESI-MS and Evaluation Its Potential as Antifungal Agent

Tukiran*, Suyatno, and Frisca Nadya Safitri

Department of Chemistry, Faculty of Mathematics and Natural Sciences, Universitas Negeri Surabaya, Jl. Ketintang, Surabaya 60231, Indonesia

* **Corresponding author:**

tel: +62-85607012664

email: tukiran@unesa.ac.id

Received: April 13, 2020

Accepted: February 8, 2021

DOI: 10.22146/ijc.55366

Abstract: Several extracts of *Syzygium* species have been shown to inhibit the growth of some fungal microorganisms implicated in skin diseases, such as *Candida albicans* included *S. samarangense*. However, an antifungal test of *C. albicans* on this plant's stem bark had not been reported. This study aimed to identify chemical constituents of the selected fraction from dichloromethane extracts of the stem bark of *S. samarangense* and determine the antifungal activity of the selected fraction at various concentrations on *C. albicans*. The identification of the chemical constituent of the selected fraction has been performed by the LC-ESI-MS technique. An antifungal test of the selected fraction was carried out using the disk diffusion method. The samples used included the selected fraction with 5 variations of concentration (2.5; 2.0; 1.5; 1.0; and 0.5%), positive control (ketoconazole 1%), and negative control (DMSO). The results showed that the selected fraction has antifungal activity on *C. albicans*. The results showed that the selected fraction contains four flavonoids: pinocembrin, uvangoletin, stercurensin, and aurentiacin. Due to antifungal activity on *C. albicans*, it has moderate activity at a concentration of 2.5%, while concentrations of 2.0, 1.5, 1.0, and 0.5% have weak activity.

Keywords: antifungal; *C. albicans*; flavonoids; LC-ESI-MS; *S. samarangense*

■ INTRODUCTION

Infection can be caused by various microorganisms such as bacteria, viruses, and fungi. Fungal infections affect the skin, hair, or nails, and tend to thrive in the heat and humidity of tropical countries [1], belonging to Indonesia. As known that Indonesia is a country with high humidity which induces easy fungus growth. One of the fungi that can lead to skin infections is *Candida albicans*. *C. albicans* is an opportunistic human fungal pathogen that causes candidiasis. As reported that *C. albicans* has been prominent among the fungal pathogens [2].

Diseases caused by fungal infections of *C. albicans* are usually treated with antibiotics such as amphotericin, nystatin, ketoconazole, and griseofulvin. However, these antibiotics often lead to serious side effects, resistance, complicated rules of use, and the need for doctor supervision. In this regard, it is necessary to look for natural antifungal agents that are more effective and

inexpensive derived from plants, for example, *Syzygium* plants (Myrtaceae), such as leaves of *S. polyanthum* [3] and *S. aromaticum* cloves [4-5].

While other *Syzygium* plants that similar studies have carried out are *S. malaccense*, i.e., the methanolic extract of *S. malaccense* leaves showing effective antimicrobial activity against *C. albicans* [6], essential oils of *S. aromaticum* for their anti-biofilm activity against strong biofilm-forming strains of *C. albicans* [7], hydroalcoholic extracts/fractions of *S. cumini* upon fungal growth of *C. albicans* [8], etc. However, antifungal tests on *C. albicans* from *S. samarangense* stem bark have never been reported till now.

In this antifungal test, the disk diffusion method was chosen to be used because their observations and measurements can be made visually and can detect inner colonies, which may indicate subpopulations that are more resistant and easier and faster in their work. The

antifungal test that had ever been applied to *Syzygium* plants is *S. polyanthum*. Using the disk diffusion method, the ethanolic extract of *S. polyanthum* leaves with various concentrations (0.5; 1.0; 1.5; 2.0; and 2.5%), the results at a concentration of 1.0% the ethanolic extract showed a minimum inhibitory zone against *C. albicans* [9]. It is predicted that the antifungal activity of an extract of plants was influenced by the presence of secondary metabolite compounds such as alkaloids, phenols, flavonoids, saponins, and terpenoids [10-14].

■ EXPERIMENTAL SECTION

Material and Methods

Materials used include: powdered *S. samarangense* stem bark, dichloromethane, *n*-hexane, filter paper, TLC plate, TLC sprayer or viscous agent used saturated solution, stationary phase for vacuum liquid chromatography (VLC) using Merck silica gel 60, stationary phase for gravitational column chromatography (GCC) using Merck silica gel 60, silica gel 60 F-254 for TLC plate, and suitable eluents. The solvents used in the chromatographic techniques included *n*-hexane and dichloromethane (Grade AR), and silica gel purchased from Merck (Germany). Materials (chemicals) for the antifungal test used are Sabouraud Dextrose Broth (SDB) liquid media, Potato Dextrose Agar (PDA) solid media, ketoconazole solution, distilled water, petri dish, filter papers, and *C. albicans* colonies. The stem bark of *S. samarangense* (c.a. 15 kg) was collected from a local area in Kediri, East Java, Indonesia, in October 2018. The plant's identification was performed by the staff of Herbarium-LIPI, Purwodadi, East Java, Indonesia. A voucher sample is kept in the Herbarium of LIPI with Identification No. 1498/IPH.06/HM/X/2018, October 18, 2018.

Equipment and Instruments

The equipment used to do extraction and fractionation were filter paper, Buchner funnel, Hirsch funnel, Erlenmeyer flask, pipette, spatula, measuring flask, vials, containers, separating funnel, and vacuum rotary evaporator type BUCHI Rotavapor R-215. Whereas chromatographic techniques used to fractionate

the chemical constituents from dichloromethane extracts, including Vacuum Liquid Chromatography (VLC) (silica gel 60, 0.200–0.500 mm), Gravitational Column Chromatography (GCC) (silica gel 60, 0.063–0.200 mm or 70–230 mesh ASTM), and TLC analysis were carried out on silica gel 60 F254 chromatoplates with the developing solvent systems. Checking the homogeneity of the fractions was made by TLC on Kieselgel 60 F254 pre-coated sheets (Merck), and the spots were detected by exposure to UV-lamp at 254 or 366 nm.

Equipment used to evaluate antifungal property included refrigerators, incubator, crucible porcelain, desiccator, Biological Safety Cabinet (BSC), Laminar Air Flow (LAF), autoclave, glassware, pipette Pasteur glass, ose needle, microscope, tip, and micropipette, etc. An instrument needed to identify the phytoconstituents for the selected fraction of the dichloromethane extract of *S. samarangense* was ion-trap mass spectrometry in negative ion modes (Shimadzu LCMS-8040 LC/MS analysis).

Procedure

Extraction and separation

The fresh stem bark of *S. samarangense* (c.a. 15 kg) was washed under tap water and dried under sunlight for one week. It was then dried in an oven at a reduced temperature (not more than 50 °C) to make it suitable for grinding purposes. It was then ground to a fine powder using an electric grinder to obtain 9.5 kg and transferred to an airtight container. The dried and powdered stem bark (9.5 kg) of *S. samarangense* was macerated with dichloromethane (c.a. 25 L) at room temperature. The container with its content was sealed by foil and kept for a period of 24 h accompanying occasional shaking and stirring, and carried out three times. The whole mixture was then filtered using the Buchner funnel, and the filtrate was concentrated at 50 °C with a vacuum rotary evaporator. The concentrated extract obtained is termed as a crude extract (60.79 g) of a thick light brown, and this extract will be used to be materials in this study.

As much as 12 g of dichloromethane extract was separated using VLC with eluents (*n*-hexane-

dichloromethane for increasing the polarity) to yield 22 fractions. This way is carried out three times to increase the mass of each fraction. Based on TLC analysis, all fractions that gave the same value of R_f could be combined and grouped into seven significant fractions, namely fraction A (1-4), B (5-6), C (7-9), D (10-12), E (13-14), F (16-18), G (19-22). Furthermore, separation is focused on fraction B and separated using GCC with eluents (*n*-hexane-dichloromethane = 5:5) to yield 35 fractions and can be grouped into five fractions, namely fractions A (1-3), B (4-13), C (14-19), D (20-30), and E (31-35). When looking at the chromatogram profile resulted, it seemed that fraction B contains quite simple spots. The fraction B then was identified its chemical components using the LC-MS method and can be elaborated as follows.

Liquid Chromatography-Mass Spectroscopy (LC-MS) analysis. Analysis for identifying chemical components was performed using an LC system (Shimadzu LCMS - 8040 LC/MS). 1 μ L of a sample was injected into the LC instrument equipped with the column of Shim Pack FC-ODS (2 mm \times 150 mm, 3 μ m particle sizes) and column temperature 35 $^{\circ}$ C. The LCMS separations are carried out with isocratic elution with dichloromethane as a mobile phase at a flow rate of 0.5 mL/min. The parameters for analysis were carried out using a negative ion mode as follows: source temperature 100 $^{\circ}$ C, sampling cone voltage 23 eV, capillary voltage 3.0 kV, desolvation temperature 350 $^{\circ}$ C, and desolvation gas flow 60 mL/h. Mass spectra were detected in the ESI

negative ion mode between m/z 10–1000 with scanning duration (0.6 sec/scan) and running time (25 min).

The chemical components of fraction B (4-13) derived from the dichloromethane extract of *S. samarangense* were further analyzed using the LC-MS method, resulting in a chromatogram profile as shown in Fig. 1. It can be seen that the profile showed four peaks with their respective abundances (composition %), and Table 1 listed all the compounds identified with their chromatographic: retention time and mass spectral data with a similarity index of 92%.

Antifungal test by the disc diffusion method

As the first step before doing an antifungal test, it was necessary to sterilize all the tools that will be used. The whole tools were washed clean, dried, and then wrapped using paper, then sterilized in an autoclave at 121 $^{\circ}$ C for c.a. 15 min. Next was preparing culture media specific for *C. albicans*. In this case, it was used PDA (Potato Dextrose Agar) solid media and SDB (Sabouraud Dextrose Broth) liquid media. The preparation of PDA solid media can be explained as follows. As much as 250 mL of distilled water was prepared to be heated to boiling. When boiling, 9.75 g of PDA powder was put into it and stirred continuously until it dissolves completely. The next step was preparing the SDB liquid media, which can be explained as follows. As much as 100 mL of distilled water was prepared to be heated to boiling. When boiling, 3 g of SDB

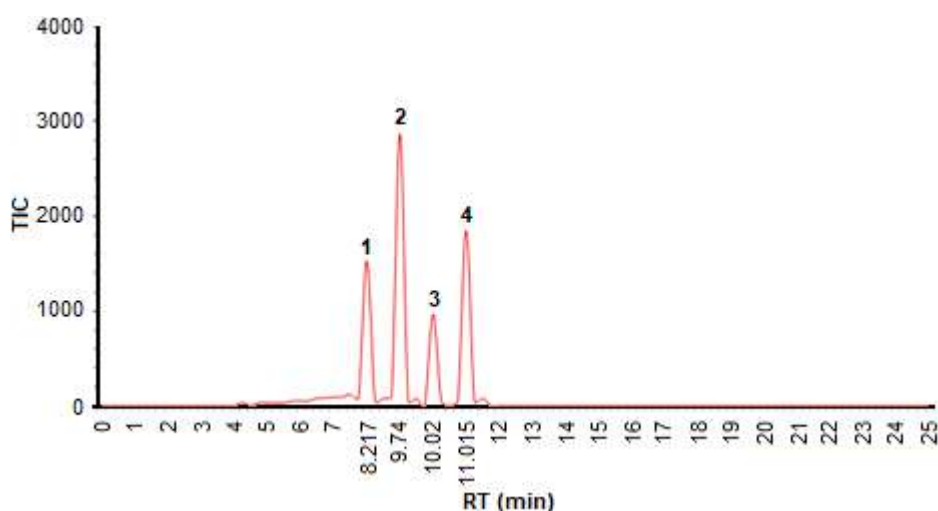


Fig 1. The Chromatogram profile of LCMS for fraction B (4-13)

Table 1. Tentative identification of chemical constituents of fraction B derived from the dichloromethane extract of *S. samarangense* stem bark by using LC-MS technique based on the chromatogram database (library) resume report

Compound No	Rt (min)	Composition (%)	Compound result	
			Analysis	Identified compounds
1	8.217	21.2	Chemical formula: C ₁₅ H ₁₂ O ₄ Exact mass: 256.0736 Molecular weight: 256.2570 m/z: 256.0736 (100.0%), 257.0769 (16.2%), and 258.0803 (1.2%)	Pinocembrin
2	9.740	39.8	Chemical formula: C ₁₆ H ₁₆ O ₄ Exact mass: 272.1049 Molecular weight: 272.3000 m/z: 272.1049 (100.0%), 273.1082 (17.3%), and 274.1116 (1.4%)	Uvangoletin
3	10.020	13.4	Chemical formula: C ₁₇ H ₁₆ O ₄ Exact mass: 284.1049 Molecular weight: 284.3110 m/z: 284.1049 (100.0%), 285.1082 (18.4%), and 286.1116 (1.6%)	Stercurensin
4	11.015	25.6	Chemical formula: C ₁₈ H ₁₈ O ₄ Exact mass: 298.1205 Molecular weight: 298.3380 m/z: 298.1205 (100.0%), 299.1239 (19.5%), and 300.1272 (1.8%)	Aurentiacin

powder was put into it and stirred continuously until it dissolves completely. Both media were stored in sterilized bottles, then sterilized using an autoclave at 121 °C for ± 15 min. PDA solid media that has been sterilized was then allowed to stand at room temperature until the temperature is ± 40 °C and then poured into the petri dish as much as 12–15 mL and allowed to solidify. After solidifying, the PDA media is ready to use.

The next step was making *C. albicans* fungi stock which can be explained as follows. Fungi stock can be prepared by inoculating and scraping one needle of *C. albicans* culture in the PDA media, then incubated for 24–48 h at 37 °C in an incubator. Rejuvenation of *C. albicans* culture was carried out by preparing 50 mL of sterilized SDB liquid media, then supplementing with 1 ose of *C. albicans* taken from the media aseptically and vortex to make it homogeneous. It was then incubated at 37 °C for 24 h.

Testing sample activity against *C. albicans* was carried out using the disk diffusion method, which can be

mentioned. As much as 1 mL of sample (fraction B) from dichloromethane extract of *S. samarangense* stem bark at the various concentration (0.5; 1.0; 1.5; 2.0; and 2.5%), positive control (ketoconazole 1% solution), and negative control (DMSO) prepared was put into a sterilized petri dish, then put 6 mm diameter disk paper on it and saturated for 15 min. Furthermore, the solidified PDA solid media was prepared to be added with a suspension of *C. albicans* fungi stock of 100 µL taken from SDB liquid media with a cell density of 10⁻⁷. It was spread as evenly as possible on top of the media to be affixed with saturated disc paper using an L-pipe. Petri dishes were incubated at 37 °C for 24 h. The inhibition zone was marked by a clear area (zone) around the disc on a solid media surface, then measured using a caliper in millimeters (mm) [15].

Data analysis

Data from the antifungal test results with the disc diffusion method above were analyzed statistically using the SPSS program version 16.0 for the window,

including normality test (Kolmogorov-Smirnov), homogeneity (Levene's test), and continued with the non-parametric Kruskal-Wallis test.

■ RESULTS AND DISCUSSION

LC-ESI-MS Analysis of the Selected Fraction of Dichloromethane Extract from *S. samarangense* Stem Bark

Liquid chromatography coupled with mass spectrometry (LC/MS) is a powerful and new technique for identifying complex botanical extracts [16-17]. It provides information for structural elucidation of the components of these extracts. Therefore, in the present work, the selected fraction of dichloromethane extract of *S. samarangense* was submitted to LC connected with MS spectrometry in negative ion mode. The identification of the chemical components of this fraction was carried out through their retention times, composition (%), and molecular weights (MW), as shown in Fig. 1). By comparing these data with the standards (database (library)), it can be identified the components as shown in Table 1.

Fraction B then was identified its chemical components using LC-ESI-MS, and the result is known to contain four flavonoids, namely pinocembrin (1), uvangoletin (2), stercurensin (3), and aurentiacin (4), as shown in Fig. 2.

The four compounds identified above can be classified into two groups of flavonoids, namely 1)

flavanone derivative (compound 1) and 2) chalcone derivative (compounds 2, 3, and 4). These compounds in the same *Syzygium* plants and others can be explained in detail as follows.

Flavanone derivative

Pinocembrin (1), 5,7-dihydroxyflavanone, is one of the primary flavonoids isolated from various plants [18]. Compound 1 and two phenolic acids: gallic acid and ellagic acid, had been found from the methanolic extracts of the pulp and seeds of the fruits of *S. samarangense* [19]. The compound had also been isolated in the leaf extract of *S. samarangense* [20] and together with 8-methylpinocembrin had been found from *S. samarangense* [21]. Compound 1 along with gallic acid, 3,4,3'-tri-*O*-methylellagic acid, and 3,3'-di-*O*-methylellagic acid had also been isolated from the methanolic extract of *S. polycephalum* stem bark [22].

Chalcone derivatives

Chalcones are a subgroup of flavonoids. They are characterized by the absence of 'ring C' of the basic flavonoid skeleton structure, as shown in Fig. 3. Compounds such as uvangoletin (2), stercurensin (3), and aurentiacin (4) can be grouped to be chalcone derivatives because they have the basic skeleton of chalcones.

Compound 2, for the first time, along with angoletin (dihydrochalcones) and the known *C*-benzylidihydro chalcones, uvaretin, and isouvaretin, had

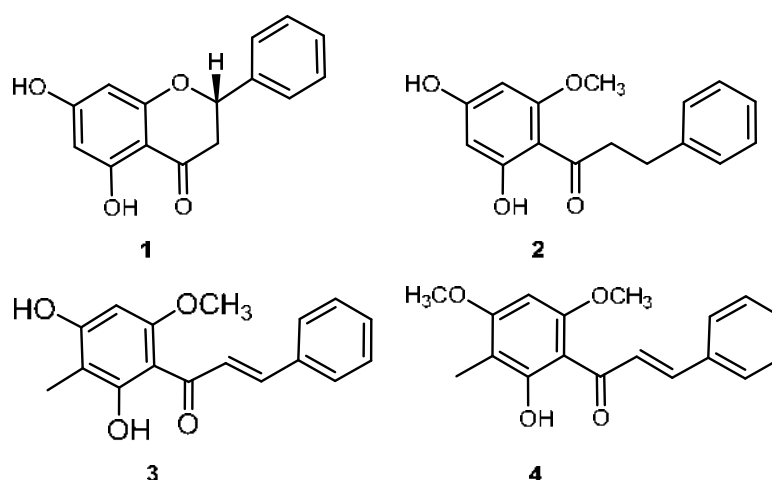


Fig 2. The molecular structure of identified compounds

been isolated from the roots of *Uvaria angolensis* (Annonaceae) [23]. Compound **2**, a 2',4'-dihydroxy-6'-methoxydihydro chalcone, had also been found the roots of *Uvaria acuminata* (Annonaceae) [24]. In Myrtaceous plants, compound **2** had been isolated from the leaves of *S. samarangense* (Myrtaceae) [25].

Compound **3** (called as 2',4'-dihydroxy-6'-methoxy-3'-methylchalcone, stercurensin) along with 2',4'-dihydroxy-6'-methoxy-3',5'-dimethylchalcone, and 2',4'-dihydroxy-6'-methoxychalcone (cardamonin) was isolated from methanolic extracts of the pulp and seeds of the fruits of *S. samarangense* [19,26]. Compound **3**, an active compound isolated from the leaves of *S. samarangense*, was known to have anti-inflammatory activity [27]. Besides, compound **3** together with 2',4'-dihydroxy-6'-methoxy-3'-methylchalcone, 2'-hydroxy-4',6'-dimethoxy-3'-methylchalcone (aurentiacin, **4**), 2',4'-dihydroxy-6'-methoxy-3',5'-dimethylchalcone, and 7-hydroxy-5-methoxy-6,8-dimethylflavanone, had been isolated from the leaves of *S. samarangense* [28].

Compound **4** and flavokawin B were isolated from the frond exudate of *Pityrogramma triangularis* var. *pallida* [29]. Besides, the compound **4**, C-methylated chalcones, and myrigalon-D are the major constituents in leaf glands of *Myrica pensylvanica* (Myrtaceae) [30].

The dichloromethane extract of the leaves of *S. samarangense* afforded compounds **3** and **4** along with 2',4'-dihydroxy-6'-methoxy-3',5'-dimethyl-chalcone, squalene, betulin, lupeol, sitosterol, and a mixture of cycloartenyl stearate, lupenyl stearate, β -sitosteryl stearate, and 24-methylenecycloartenyl stearate [31]. Also, compound **3**

had been isolated from the leaf extract of *S. campanulatum* [32].

Testing of antifungal activity of samples on *C. albicans* was performed three times, and the results of measurement of inhibition zones diameters of the fraction B from dichloromethane extract of *S. samarangense* stem bark can be presented in Table 2. The inhibition zone diameter response (mm) of samples toward the growth of *C. albicans* can be classified as very strong (20–30 mm), strong (10–20 mm), moderate (5–10 mm), and weak (< 5 mm). The inhibition zone's small diameter indicates a low antifungal activity, while the inhibition zone's large diameter indicates a higher antifungal activity [33].

As shown in Table 2, it seemed that fraction B has an antifungal activity to inhibit the growth of *C. albicans*. The lowest inhibition zone diameter is indicated at the concentration of fraction B of 0.5%, an average diameter of 0.50 mm. Simultaneously, the highest inhibition zone is shown at the concentration of fraction B of 2.5%, which is an average diameter of 5.00 mm. Next, on control positive using ketoconazole 1% formed a larger inhibition zone compared to the fraction B, an average diameter of 12.50 mm.

A test using the One way ANOVA through the SPSS program has been applied to know the effect of

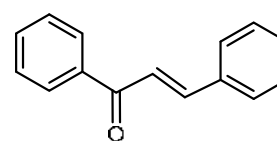


Fig 3. The basic skeleton of chalcone

Table 2. Results of measurement of inhibition zone diameters of several samples

Concentration of samples (%)	The diameter of a clear zone (mm)			Total (mm)	Average (mm)
	I	II	III		
2.5	5.0	5.0	5.0	15.00	5.00
2.0	4.0	3.0	4.0	11.00	3.66
1.5	3.0	2.0	2.0	7.00	2.33
1.0	1.0	1.5	1.5	4.00	1.33
0.5	0.5	0.5	0.5	1.50	0.50
Positive control	12.50	12.50	12.50	37.50	12.50
Negative control	0	0	0	0	0
Total				76	24.99

fraction B inhibition toward *C. albicans*. It was obtained that the data resulted are not homogeneous. Therefore, the test was continued using non-parametric methods. The normality test was carried out using the One-sample Kolmogorov-Smirnov test, and the results can be presented in Table 3.

As presented in Table 3, the normality test obtained showed $p = 0.414$ and $p = 0.917$. As known that data normally distributed is to have $p > 0.05$. Because of the value of $p > 0.05$, the data in this study were stated to be normally distributed. The next is to do a homogeneity test using Levene's test, and the sig results obtained are 0.000. It meant that the data is not homogeneous, so it is necessary to use a non-parametric test that is the Kruskal Wallis test.

The Kruskal Wallis test is a non-parametric test aiming to determine the presence or absence of statistically significant differences between two or more groups of independent variables on the dependent variable with numerical data (interval/ratio scale) and ordinal scale. The test is identical to the One Way ANOVA Test in a parametric test, so the test is an alternative if it does not meet the One Way ANOVA test requirements. The results of the Kruskal Wallis test of data can be shown in Table 4.

In Table 4, it seems that the significance value is 0.003. If the significance value is less than 0.05, so there is a significant influence. It means that fraction B influences inhibiting the growth of fungi *C. albicans*.

Flavonoids are ubiquitous in photosynthesizing cells and are commonly found in fruit, vegetables, nuts, seeds, stems, flowers, tea, wine, propolis, and honey. Many compounds that have isolated and identified their structures possess antifungal activity, including flavonoids [34]. It was shown that the anti-pathogenic effect of flavonoids depends on their structure. It was suggested that the highest antifungal activity is demonstrated by unsubstituted flavones and unsubstituted flavanones (included pinocembrin, **1**). Hydroxyl and methyl groups in these compounds reduce their antifungal properties, though in some cases, methylated flavonoids reveal a higher antifungal effect [35]. In general, flavonoids' mechanism of action in inhibiting fungal growth is by

Table 3. The results of normality test using One-sample Kolmogorov-Smirnov Test

		Diameters (mm)	Treatments
N		21	21
Normal	Mean	3.7619	4.0000
Parameters ^a	Std. Deviation	4.07314	2.04939
Most Extreme Differences	Absolute	0.193	0.121
	Positive	0.193	0.121
	Negative	-0.178	-0.121
Kolmogorov-Smirnov Z		0.885	0.555
Asymp. Sig. (2-tailed)		0.414	0.917

^aTest distribution is Normal

Table 4. The results of the Kruskal Wallis test of data Test Statistics^a

Test Statistics ^a	
Diameter (mm)	
Chi-Square	19.741
Df	6
Asymp. Sig	0.003

^aGrouping variable: Treatment Concentration

disrupting fungal cell membrane permeability. Hydroxyl groups presented in flavonoids cause changes in organic components and transport of nutrients, eventually leading to toxic effects on fungi [36].

■ CONCLUSION

It had been identified by using an LC-ESI-MS technique several compounds from the selected fraction of the dichloromethane extract of *S. samarangense* stem bark, namely pinocembrin, uvangoletin, stercurensin, and aurentiacin. The chosen fraction has moderate activity at a concentration of 2.5%, while concentrations of 2.0, 1.5, 1.0, and 0.5% have weak activity. The higher the concentration of the fraction tested, the greater the inhibition zone diameter formed.

■ ACKNOWLEDGMENTS

We thank the Directorate of Research and Innovation Empowerment, the Ministry of Research, Technology, and the National Research and Innovation Agency to support our project in the National Competitive Fundamental Research Scheme-2020. The

authors also extend thanks to M. Ariesandy PT. Djarum Kudus Malang, East Java, Indonesia for help in LC-ESI-MS measurements.

■ AUTHOR CONTRIBUTIONS

All authors conducted the experiment, Frisca Nadya Safitri sent the sample to PT. Djarum Kudus Malang, Indonesia, for measuring LC-ESI-MS, and all authors wrote and revised the manuscript. All authors agreed to the final version of this manuscript.

■ REFERENCES

- [1] Charles, A.J., 2009, Superficial cutaneous fungal infections in tropical countries, *Dermatol. Ther.*, 22 (6), 550–559.
- [2] Kabir, M.A., Hussain, M.A., and Ahmad, Z., 2012, *Candida albicans*: A model organism for studying fungal pathogens, *Int. Scholarly Res. Not.*, 2012, 538694.
- [3] Kusuma, S.A.F., Purnamasari, E., and Herawati, I.E., 2019, *Syzygium polyanthum* (Wight) Walp. leaves extract as the antifungal agent for oral candidiasis, *Drug Invent. Today*, 12 (7), 1339–1342.
- [4] Yassin, M.T., Mostafa, A.A.F., and Al-Askar, A.A., 2020, In vitro anticandidal potency of *Syzygium aromaticum* (clove) extracts against vaginal candidiasis, *BMC Complementary Med. Ther.*, 20 (1), 25.
- [5] Mansourian, A., Boojarpour, N., Ashnagar, S., Beitollahi, J.M., and Shamshiri, A.R., 2014, The comparative study of antifungal activity of *Syzygium aromaticum*, *Punica granatum* and nystatin on *Candida albicans*; An in vitro study, *J. Mycol. Med.*, 24 (4), e163–e168.
- [6] Purushothaman, A., Sudhir, A.S., Joby, G., Aravind, R., and Varghese, A., 2015, A study on antimicrobial and anthelmintic activity of methanolic leaf extracts of *Syzygium malaccense* (L.) Merr. & Perry, *J. Chem. Pharm. Res.*, 7 (4), 838–841.
- [7] Khan, M.S.A., and Ahmad, I., 2012, Biofilm inhibition by *Cymbopogon citratus* and *Syzygium aromaticum* essential oils in the strains of *Candida albicans*, *J. Ethnopharmacol.*, 140 (2), 416–423.
- [8] Pereira, J.V., Freires, I.A., Castilho, A.R., da Cunha, M.G., Alves, H.S., and Rosalen, P.L., 2016, Antifungal potential of *Sideroxylon obtusifolium* and *Syzygium cumini* and their mode of action against *Candida albicans*, *Pharm. Biol.*, 54 (10), 2312–2319.
- [9] Höfling, J.F., Anibal, P.C., Obando-Pereda, G.A., Peixoto, I.A.T., Furletti, V.F., Foglio, M.A., and Gonçalves, R.B., 2010, Antimicrobial potential of some plant extracts against *Candida* species, *Braz. J. Biol.*, 70 (4), 1065–1068.
- [10] Guevara-Lora, I., Bras, G., Karkowska-Kuleta, J., González-González, M., Ceballos, K., Sidlo, W., and Rapala-Kozik, M., 2020, Plant-derived substances in the fight against infections caused by *Candida* species, *Int. J. Mol. Sci.*, 21 (17), 6131.
- [11] Yusoff, S.F., Haron, F.F., Tengku Muda Mohamed, M., Asib, N., Sakimin, S.Z., Abu Kassim, F., and Ismail, S.I., 2020, Antifungal activity and phytochemical screening of *Vernonia amygdalina* extract against *Botrytis cinerea* causing gray mold disease on tomato fruits, *Biology*, 9 (9), 286.
- [12] Sakander, H., Akhilesh, B., and Koteswara, A.R., 2015, Evaluation of antifungal potential of selected medicinal plants against human pathogenic fungi, *Int. J. Green Pharm.*, 9 (2), 110–117.
- [13] Ribera, A.E., and Zuñiga, G., 2012, Induced plant secondary metabolites for phytopathogenic fungi control: A review, *J. Soil Sci. Plant Nutr.*, 12 (4), 893–911.
- [14] Shakhathreh, M.A.K., Al-Smadi, M.L., Khabour, O.F., Shuaibu, F.A., Hussein, E.I., and Alzoubi, K.H., 2016, Study of the antibacterial and antifungal activities of synthetic benzyl bromides, ketones, and corresponding chalcone derivatives, *Drug Des. Dev. Ther.*, 10, 3653–3660.
- [15] Baharuddin, N.S., Abdullah, H., and Wan Abdul Wahab, W.N.A., 2015, Anti-*Candida* activity of *Quercus infectoria* gall extracts against *Candida* species, *J. Pharm. BioAllied Sci.*, 7 (1), 15–20.
- [16] Septaningsih, D.A., Darusman, L.K., Afendi, F.M., and Heryanto, R., 2018, Liquid chromatography mass spectrometry (LC-MS) fingerprint combined

- with chemometrics for identification of metabolites content and biological activities of *Curcuma aeruginosa*, *Indones. J. Chem.*, 18 (1), 43–52.
- [17] Zhang, A., Wan, L., Wu, C., Fang, Y., Han, G., Li, H., Zhang, Z., and Wang, H., 2013, Simultaneous determination of 14 phenolic compounds in *Grape canes* by HPLC-DAD-UV using wavelength switching detection, *Molecules*, 18 (11), 14241–14257.
- [18] Rasul, A., Millimouno, F.M., Eltayb, W.A., Ali, M., Li, J., and Li, X., 2013, Pinocebrin: A novel natural compound with versatile pharmacological and biological activities, *Biomed Res. Int.*, 2013, 379850.
- [19] Aung, E.E., Kristanti, A.N., Aminah, N.S., Takaya, Y., and Ramadhan, R., 2020, Plant description, phytochemical constituents and bioactivities of *Syzygium* genus: A review, *Open Chem.*, 18 (1), 1256–1281.
- [20] Peter, T., Padmavathi, D., Sajini, R.J., and Sarala, A., 2011, *Syzygium samarangense*: A Review on morphology, phytochemistry and pharmacological aspects, *Asian J. Biochem. Pharm. Res.*, 1 (4), 155–163.
- [21] Majumder, R., Hasnat, N.E., Zaman, M.A.U., and Alam, M.B., 2014, *In vivo* evaluation of the pharmacological activities of *Syzygium samarangense* (Blume) Merr. & L.M. Perry, *Adv. Biol. Res.*, 8 (3), 107–115.
- [22] Tukiran, Wardana, A.P., Hidajati, N., and Shimizu, K., 2019, Chemical components and antioxidant activities of methanol extract of *Syzygium polycephalum* Miq. stem bark (Myrtaceae), *Indian J. Nat. Prod. Resour.*, 10 (2), 127–136.
- [23] Hufford, C.D., and Oguntimein, B.O., 1980, Dihydrochalcones of *Uvaria angolensis*, *Phytochemistry*, 19 (9), 2036–2038.
- [24] Ascherio, A., and Munger, K.L., 2010, Epstein-Barr virus infection and multiple sclerosis: A review, *J. Neuroimmune Pharmacol.*, 5 (3), 271–277.
- [25] Debnath, T., Chakraverty, R., and Chakraborty, P., 2019, Flavonoids from leaves of *Syzygium samarangense* and its pharmacological potential: Some recent insights, *Pharmawave*, 12, 15–19.
- [26] Mukaromah, A.S., 2020, Wax Apple (*Syzygium samarangense* (Blume) Merr. & L.M. Perry): A comprehensive review in phytochemical and physiological perspectives, *Al-Hayat J. Biol. Appl. Biol.*, 3 (1), 40–58.
- [27] Kim, Y.J., Kim, H.C., Ko, H., Amor, E.C., Lee, J.W., and Yang, H.O., 2011, Stercurensin inhibits nuclear factor- κ B-dependent inflammatory signals through attenuation of TAK1-TAB1 complex formation, *J. Cell. Biochem.*, 112 (2), 548–558.
- [28] Amor, E.C., Villaseñor, I.M., Nawaz, S.A., Hussain, M.S., and Choudhary, M.I., 2005, A dihydrochalcone from *Syzygium samarangense* with anticholinesterase activity, *Philipp. J. Sci.*, 134 (2), 105–111.
- [29] Kim, Y.J., Kim, H.C., Ko, H., Amor, E.C., Lee, J.W., and Yang, H.O., 2012, Inhibitory effects of aurenfiacin from *Syzygium samarangense* on lipopolysaccharide-induced inflammatory response in mouse macrophages, *Food Chem. Toxicol.*, 50 (3–4), 1027–1035.
- [30] Wollenweber, E., Kohorst, G., Mann, K., and Bell, J.M., 1985, Leaf gland flavonoids in *Comptonia peregrina* and *Myrica pensylvanica* (Myricaceae), *J. Plant Physiol.*, 117 (5), 423–430.
- [31] Ragasa, C.Y., Franco, F.C., Raga, D.D., and Shen, C.C., 2014, Chemical constituent of *Syzygium samarangense*, *Deer Pharma Chem.*, 6 (3), 256–260.
- [32] Memon, A.H., Ismail, Z., Aisha, A.F.A., Al-Suede, F.S.R., Hamil, M.S.R., Hashim, S., Saeed, M.A.A., Laghari, M., and Abdul Majid, A.M.S., 2014, Isolation, characterization, crystal structure elucidation, and anticancer study of dimethyl cardamonin, isolated from *Syzygium campanulatum* Korth, *Evidence-Based Complementary Altern. Med.*, 2014, 470179.
- [33] Tantyani, T.A., and Taufikurohmah, T., 2020, Antibacterial and antifungal activities of silver nanoparticles against *Neisseria gonorrhoeae* and *Candida albicans*, *Intl. J. Res. Granthaalayah*, 8 (6), 179–187.
- [34] Al Aboody, M.S., and Mickymaray, S., 2020, Antifungal efficacy and mechanisms of flavonoids, *Antibiotics*, 9 (2), 45.
- [35] Mierziak, J., Kostyn, K., and Kulma, A., 2014, Flavonoids as important molecules of plant

- interactions with the environment, *Molecules*, 19 (10), 16240–16265.
- [36] Oliveira, V.M., Carraro, E., Auler, M.E., and Khalil, N.M., 2016, Quercetin and rutin as potential agents antifungal against *Cryptococcus* spp., *Braz. J. Biol.*, 76 (4), 1029–1034.

Polyvinyl Alcohol Food Packaging System Comprising Green Synthesized Silver Nanoparticles

Ahmed Elsayed Abdelhamid¹, Eman AboBakr Ali Yousif¹, Manal Mohamed Talaat El-Saidi², and Ahmed Ali El-Sayed^{2*}

¹Polymers & Pigments Department, National Research Centre, 33 El-Behouth St. Dokki, Cairo, Egypt

²Photochemistry Department, Chemical Research Division, National Research Center, Dokki, Giza, 12622, Egypt

* **Corresponding author:**

email: ahmedcheme4@yahoo.com

Received: April 18, 2020

Accepted: September 21, 2020

DOI: 10.22146/ijc.55483

Abstract: Green synthesis of silver nanoparticles (AgNPs) using aqueous *Moringa* extract and their incorporation in polyvinyl alcohol (PVA) as food packaging materials have been performed. The prepared nanoparticles were characterized via Ultraviolet-visible spectra and transmission electron microscope, and the results revealed the formation of silver nanoparticles in a semi-spherical shape with an average size ranged from 2 to 5 nm. The addition of different ratios of the nanoparticles onto the PVA matrix and their crosslinking via citric acid to obtain nanocomposite sheets were performed. The nanocomposite sheets were characterized using FT-IR, UV-Vis, and TGA. In addition, their mechanical properties were evaluated. Water vapor permeability rate and water content were also determined. The composite sheets showed good thermal and optical performance. Antibacterial activities of the prepared nanocomposite sheets were evaluated, and the results exhibited good resistance to bacterial growth.

Keywords: silver nanoparticles; green synthesis; polyvinyl alcohol; *Moringa* extract; food packaging

■ INTRODUCTION

As much of the world has placed concern on improving food safety, active packaging has gained the interest of many researchers. The addition of antioxidants and antibacterial components into packaging materials has proved its potential as an approach to increase the shelf life as well as preserve food nutrition quality [1-2]. Consequently, many attempts have been employed to develop an active packaging system containing bioactive compounds, essential oil, plant extracts, and nanomaterials [3]. The incorporation of nanotechnology helps increase not only the surface area for active components [4] but also the mechanical properties of packaging film [3]. With the development of nanomaterials, metal oxide nanoparticles show promising and far-ranging prospects for the biomedical field, especially for anti-bacteria, anticancer drug/gene delivery, cell imaging, bio-sensing, and so on [5-11]. Nano-silver is one of the predominant nano-metals that is well known for its efficiency as an antimicrobial agent and can be used in many applications

including packaging. There are many techniques for preparing metal nanoparticles to include chemical reduction, physical and biological methods [12-13]. On the whole, the green synthesis of metal nanoparticle preparation has been adapted as a good alternative to those that include microwave assessment or electrochemical reduction. Not only environmental awareness is the driving force for using biosynthesis of metal oxide, but also the low cost and efficiency of this technique. Biosynthesis of metal nanoparticles was implied by many researchers using microorganisms and plant leave [14], seed extract [15], or roots [13]. One of the considerable plants is *Moringa Oleifera*. It is a well-known plant grown not only in Asia but also in some other countries in Africa [16]. The rich content of natural compounds in its flowers, seeds, and leaf has made it an important ingredient in common and modern medicinal treatment. *Moringa* extract has extensively used in different application as anti-microbial, mosquito repellent, and food packaging [17-18].

There are many natural biodegradable polymers as chitosan and cellulose derivative have been employed for food packaging to preserve food safety as well as the environment vitality [19-20]. However, the low water resistance and sensitivity to the variation of pH lead to increasing interest in using synthetic biodegradable polymers. Polyvinyl alcohol (PVA) has characteristic chemical resistance combined with hydrophilic properties made it a promising candidate in food packaging [2,21-22]. Polyvinyl alcohol-based food packaging sheet was prepared using citric acid as crosslinking in the presence of grapefruit seed extract as an antimicrobial agent [23]. These polymeric sheets showed good water stability with weight loss of about 19% after 72 h immersion in water and good transparency with enhanced mechanical and antimicrobial performance. Novel biodegradable polyvinyl alcohol/starch/glycerol/halloysite nanotube nanocomposite films were prepared by solution casting technique [24]. The obtained films were characterized by excellent water resistance and good transparency to be potentially applied in food packaging, especially targeting lipophilic and acidic foodstuffs.

Although the utilization of Moringa extract for AgNPs synthesis has been reported previously, many researchers are still investigating the behavior of the Moringa extract/AgNPs combination. However, there are limited reports that introduce AgNPs in a final product form. In this work, a biodegradable composite sheet was prepared by combining biosynthesized silver nanoparticles (AgNPs with unique particle size) with PVA to produce active packaging. Biosynthesis of Ag nanoparticles using an aqueous *Moringa Oleifera* (MO) leaves extract, which was grown in Egypt, was carried out. After that, the AgNPs/MO suspension was added to the PVA solution with different amounts in the presence of citric acid as a crosslinking. The antimicrobial as well as the physical and mechanical properties of the prepared sheets were investigated.

■ EXPERIMENTAL SECTION

Materials

Polyvinyl alcohol (PVA) (M.Wt:78000) was purchased from Aldrich. *Moringa Oleifera* leaves were delivered from the Egyptian Scientific Society of Moringa

(ESSM), National Research Centre, Dokki, Cairo, Egypt, washed to remove any adhered contamination, dried, and ground. Silver nitrate (AgNO_3), citric acid, and sulfuric acid were delivered from Aldrich.

Procedure

Synthesis of Moringa leaves extract and in-situ nanoparticles production

Dry Moringa leaves (20 g) have been ground using a mortar. The resulted powder was suspended in distilled water (100 mL), heated at 60 °C under stirring for 1 h. The formed extract was then filtered. The Moringa extract (filtrate, 10 mL) was diluted with (90 mL) of deionized water in another conical flask. Silver nitrate (AgNO_3 , 0.17 g, 0.1 mmol) was added to this extract, with continuous stirring at 60 °C for 1 h, in which the in-situ silver formation takes place. The change to the brownish color of the resulting solution is an indication of the formation of silver nanoparticles, the nanoparticles formation was also confirmed and characterized by UV-Vis Spectrophotometer and TEM [25].

Preparation of PVA-AgNPs nanocomposite sheets

The PVA/AgNPs/MO nanocomposite sheets were prepared by adding different volumes (2.5 and 10 mL) of AgNPs/MO suspensions to 25 mL of PVA containing 1 g polymer content that dissolved in distilled water at 90 °C under stirring. After the addition of the nanoparticles, they were stirred for a while and sonicated by a water bath sonicator for 30 min. The citric acid (0.125 g) was added to the polymer solution as a crosslinking agent with the addition of a few drops of sulfuric acid as a catalyst for the esterification process. The mixture was stirred for about 2 h at 70 °C; after that, it was poured into a petri- dish and then left to be dried in an oven at 50 °C for 2 days to obtain PVA-Ag (2.5) and PVA-Ag (10). Blank un-crosslinked PVA (that prepared without citric acid) and crosslinked (CPVA) were also prepared for comparison.

Characterization of nanoparticles and nanocomposite films

Ultraviolet-visible spectroscopy (UV-Vis). AgNPs formation by Moringa leaves extract was monitored using a Jenway UV/Vis spectrophotometer (Jenway

UV/Visible-2605 spectrophotometer, England). The transparency of PVA sheets was evaluated using UV-Vis spectra in the visible range between 400–700 nm.

Transmission electron microscope (TEM). Evaluation of the size and shape of AgNPs was performed using High-Resolution Transmission Electron Microscopy (HR-TEM) JEOL (JEM-2100 TEM). A drop of colloidal solution was placed on a copper grid and was left in the air at room temperature to evaporate the solvent.

FTIR spectroscopy. The functional groups of the nanocomposite PVA films were confirmed using Fourier Transform Infrared (FTIR) (Shimadzu 8400, Japan) spectrophotometer in the spectral range between 400 and 4000 cm^{-1} .

Thermal gravimetric analysis (TGA). Thermal analysis of the prepared samples was achieved using a Shimadzu Instrument. The measurements were carried out with a heating rate of 10 $^{\circ}\text{C}/\text{min}$ within the range of 0 to 400 $^{\circ}\text{C}$ in a nitrogen atmosphere.

Mechanical properties

The mechanical performance (tensile strength and elongation at break) for PVA nanocomposite films containing different ratios of nanoparticles was tested using Zwick/Roell Z010, type Xforce P, S/N: 760608, Germany. The film samples were cut into a dumbbell shape, and the measurements were tested at a crosshead speed of 2 mm/min at 25 $^{\circ}\text{C}$.

Water content

For water content determination, the films ($1.5 \times 1.5 \text{ cm}^2$) were cut and soaked in distilled water for about 24 h, then weighed (W_s) and dried in the oven at 80 $^{\circ}\text{C}$ until a constant weight (W_d) was achieved. The average data of three replicate measurements were used to calculate the water content by applying the following equation:

$$\text{Water content} = \frac{W_s - W_d}{W_s} \times 100 \quad (1)$$

Water vapor permeation rate

For investigating water vapor permeability, a certain volume of distilled water was introduced into vials; then, the vials were mounted tightly with nano-composite film samples with the aid of certain tape and weighted. The vials weight was measured at an interval time, and the

water vapor permeability rate was calculated using the following equation:

$$\text{WVPR} = \frac{k}{A} \quad (2)$$

where k is rate constant can be estimated from the slope of the regression line of the plot of weight differences versus time, and A is the surface area of the sheet [26].

Antibacterial assay

The antibacterial performance of blank PVA and composite sheets against *Escherichia coli* (*E. coli*) as Gram-negative and *Staphylococcus aureus* (*S. aureus*) as Gram-positive bacterial strains, respectively, were examined as reported previously [27]. Agar diffusion plate test was used to explore the antibacterial action; the bacteria strains were cultivated on agar comprises nutrient and incubated for 24 h at 37 $^{\circ}\text{C}$. A hundred μL of diluted bacterial suspension was spread onto the Petri dish, and the test sample disks were fixed on the surface of the agar. These samples were incubated at 37 $^{\circ}\text{C}$ for a day. After incubation, the inhibition zone area was evaluated [28].

RESULTS AND DISCUSSION

Moringa Leaves Extract and in-situ Nanoparticles Preparation

The phytochemical examination of Moringa extract confirms the presence of a variety of unique compounds. This plant category is rich in phenolic compounds that include glucosinolates, a simple sugar, isothiocyanates, and rhamnose [29-30]. It has been found that Moringa extract has appropriate reducing and stabilizing potency during the preparation of AgNPs. The reduction of Ag^+ cation into Ag^0 has been carried out by the glucosinolates and sugar to form and stabilize AgNPs; meanwhile, the glucosinolates have been oxidized to gluconic acid [31]. The reduction of silver cation can also be made by some organic compounds that have reductive groups such as $-\text{OH}$, $-\text{SH}$, $-\text{NH}$, etc. Fig. 1 shows some examples of the organic compounds selected phytochemicals from Moringa as reported in the literature [32]. The preparation of AgNPs from Ag^+ using MO leaves s extract has been followed by the color change of the reaction.

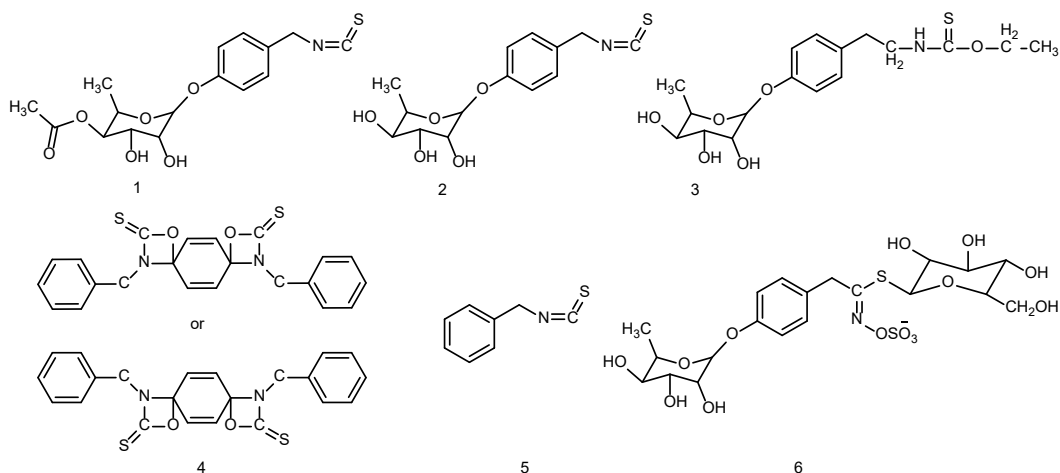


Fig 1. Common compounds of MO extract

Ultraviolet-Visible Spectroscopy (UV-Vis)

The change of color of the Moringa extract to brown one was the first confirmation of the biosynthesis of Ag nanoparticles. Fig. 2 represents another confirmation of AgNPs/MO preparation via the appearance of the characteristic peak in the range of 300–480 nm [25], whereas the peak that appeared at 340 nm may be attributed to the resultant nanoparticles extract suspension. The UV spectra were displayed as combined peaks in the region between 300 and 400 nm that may be due to the high optical density of the solution [33]. Moringa extract is rich with flavonoids and phenolic compounds and thereby helped in preventing aggregation by electrostatic stabilization; also, certain bio-organics presented in the Moringa extract may have brought about electro-steric stabilization [24].

Transmission Electron Microscopy (TEM)

The TEM image of the prepared nanoparticles is shown in Fig. 3. A semi-spherical shape of AgNPs/MO with a unique particle size was successfully obtained. It also reveals a homogenous size of AgNPs/MO with a mean average size of 3.1 ± 0.02 nm width. The histogram chart showed that the size of AgNPs/MO lies in the range between 2 and 5 nm. It was reported that increasing the concentration of MO extract leads to a reduction of particle size [24]. However, in this work, this extraordinary particle size may be attributed to the MO extract richness of phenols, flavonoids, and bioactive compounds. Even the TEM image gives homogenous particle size with no obvious aggregations, the AgNPs/MO suspension may contain some aggregate, and this was assessed by the presence of surface plasmon

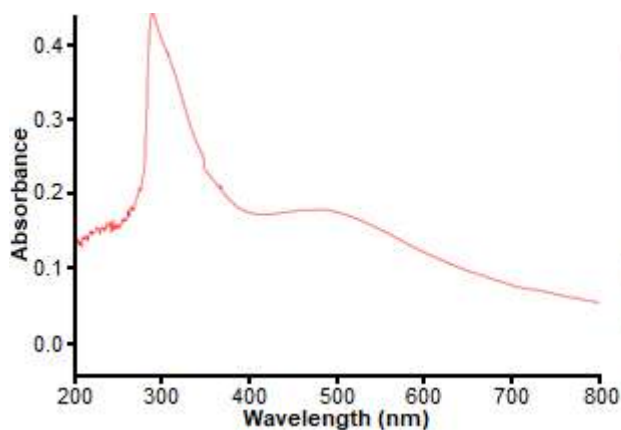


Fig 2. (a) UV-spectra of biosynthesized AgNPs and (b) digital photo for Moringa extract and Moringa/AgNPs

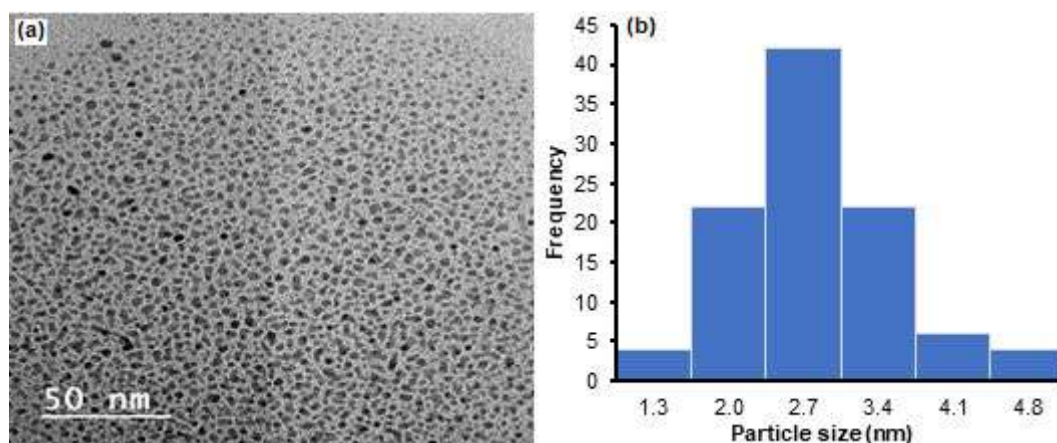


Fig 3. TEM images (a) and histogram (b) of biosynthesized AgNPs Moringa leaves extract

resonance in UV-vis in the region of 455–800 nm [24].

IR Analysis

Fig. 4 shows the change of the chemical structure upon the modification of PVA. The broad band in the range of 3429 cm^{-1} represents the richness of OH groups in pure PVA chains, and the peaks of CH_2 and CH were clearly seen at 2900 and 2854 cm^{-1} , respectively [34-35]. The absorption at 1070 cm^{-1} is related to the C–O stretching vibration of primary alcohol [36]. The absorption at 1720 cm^{-1} is corresponding to the stretching of the carbonyl group of citrate ester. After the addition of

AgNPs/MO, a new peak was observed at 548 cm^{-1} which attributed to silver nanoparticles, and the peak at 1070 cm^{-1} was greatly reduced, which may be involving the OH groups in the reduction or stabilizing silver nanoparticles. There are a small shift of the CH_2 peak from 2900 to 2926 cm^{-1} and the broadening of the OH band around 3429 cm^{-1} which may be due to the formation of hydrogen bonding between OH of PVA and the active compound in MO extract. All these results indicate the successful incorporation of AGNPs/Mo within the PVA polymer matrix.

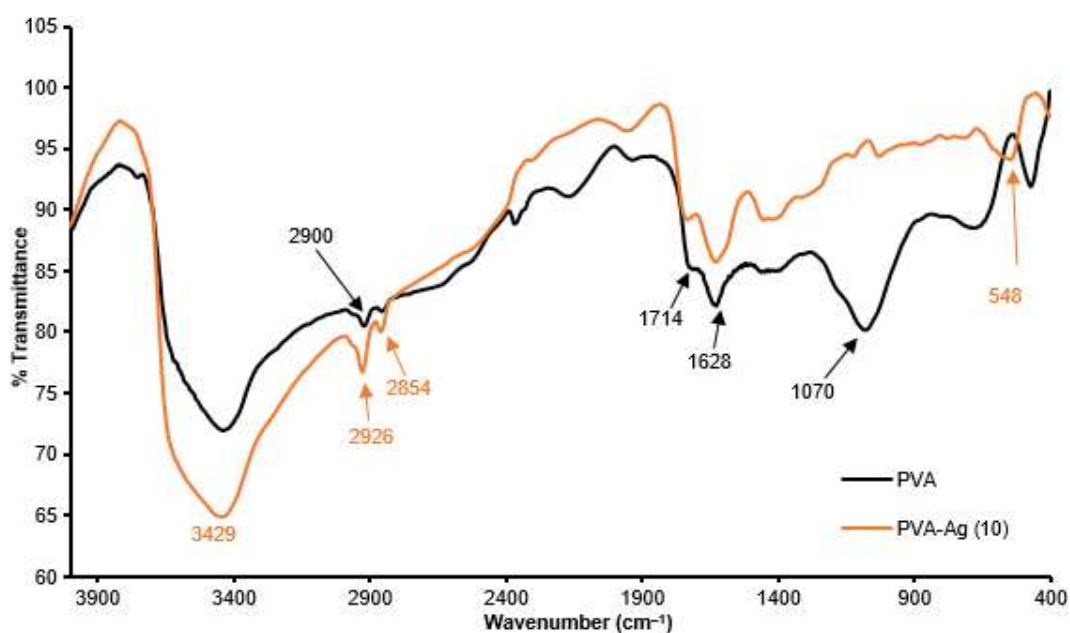


Fig 4. FTIR spectra of (a) PVA (b) PVA-Ag (10)

Ultraviolet-Visible Absorption Spectroscopy (UV-Vis)

The optical properties of PVA composite films were evaluated using UV-Visible spectroscopy. One of the important characteristics of food packaging applications is film transparency in terms of light transmittance (T%) [37]. Fig. 5 shows that pure PVA has a transparency of about 88%, which reflects its high crystallinity, whereas the transmittance of crosslinked PVA film was slightly decreased when compared to control PVA. On the contrary, the addition of AgNPs/MO noticeably has changed the transparency of the PVA films; there is about a 20% fall in the transparency of PVA-Ag (10). These results may be induced by the incident light loss from the light transmission, scattering, absorption, reflection, and refraction of the light when striking an interface while such a loss was increased especially at interfacial areas [38]. Nevertheless, AgNPs/MO incorporation conserved the transparency of PVA to some extent.

Thermal Gravimetric Analysis (TGA)

It is seen from Fig. 6 that PVA has a 7% weight loss at a range from 85 to 160 °C related to the desorbed water, another peak starts at 180 to 280 °C with weight loss of about 10% and the major weight loss of about 60% at temperature maxima around 350 °C. The former peak can

be assigned to the side chain of PVA, while the later peak can be related to a decomposition of the main chain of PVA [25]. After the incorporation of AgNPs/MO, the curves showed a relatively good thermal stability compared with the unmodified sheet with keeping the same behavior of the degradation. There is no great difference between the thermal behavior for PVA-Ag (2.5 and 10). The weight loss peak around 85 to 160 °C was about 5.6% related to the adsorbed water for PVA-Ag (10). For the second and third peaks, the weight loss reached 9 and 58.5% related to side chain and main chain degradation, respectively, of the composite film. These results indicate the good thermal stability of the composite film compared with the blank PVA film.

Mechanical Properties

As previously reported, the mechanical properties likely to be altered as metal nanoparticles are embedded in polymeric films [38]. Fig. 7 displayed that pure PVA has a tensile strength of 55 MPa and elongation at the break of about 222%. For composite sheets, there is no drastic change of the elongation at break when compared to the crosslinked films, whereas the tensile strength was decreased to 46 for both PVA-Ag (2.5 and 10). It was interesting to find out that the concentration of nanoparticle suspension has no great effect on mechanical

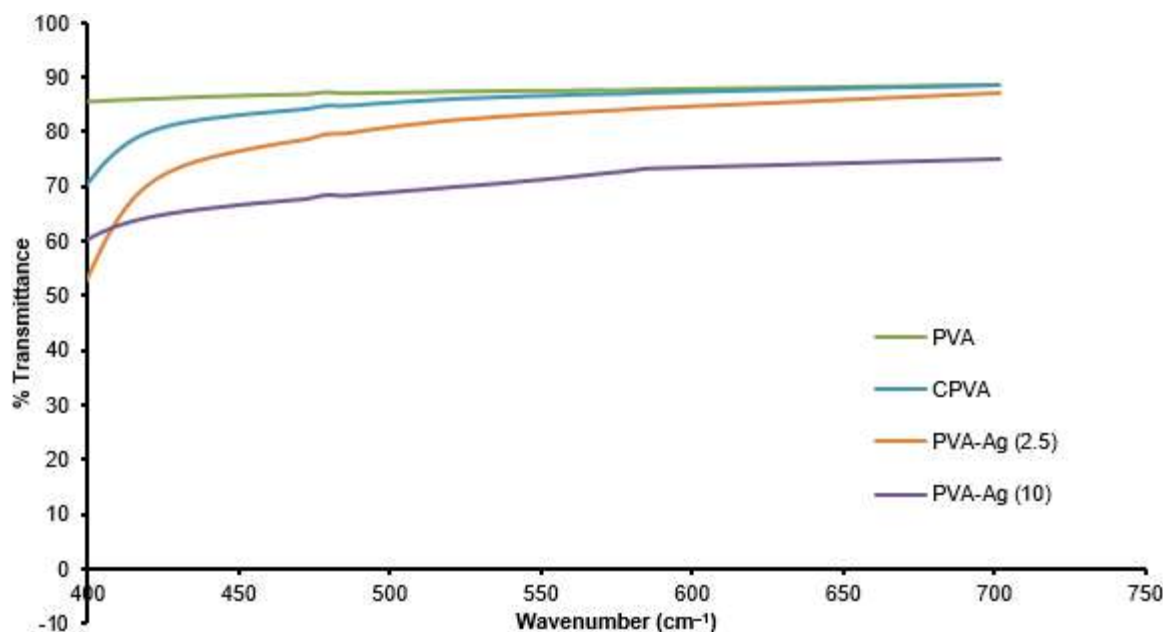


Fig 5. Optical properties of PVA composite films

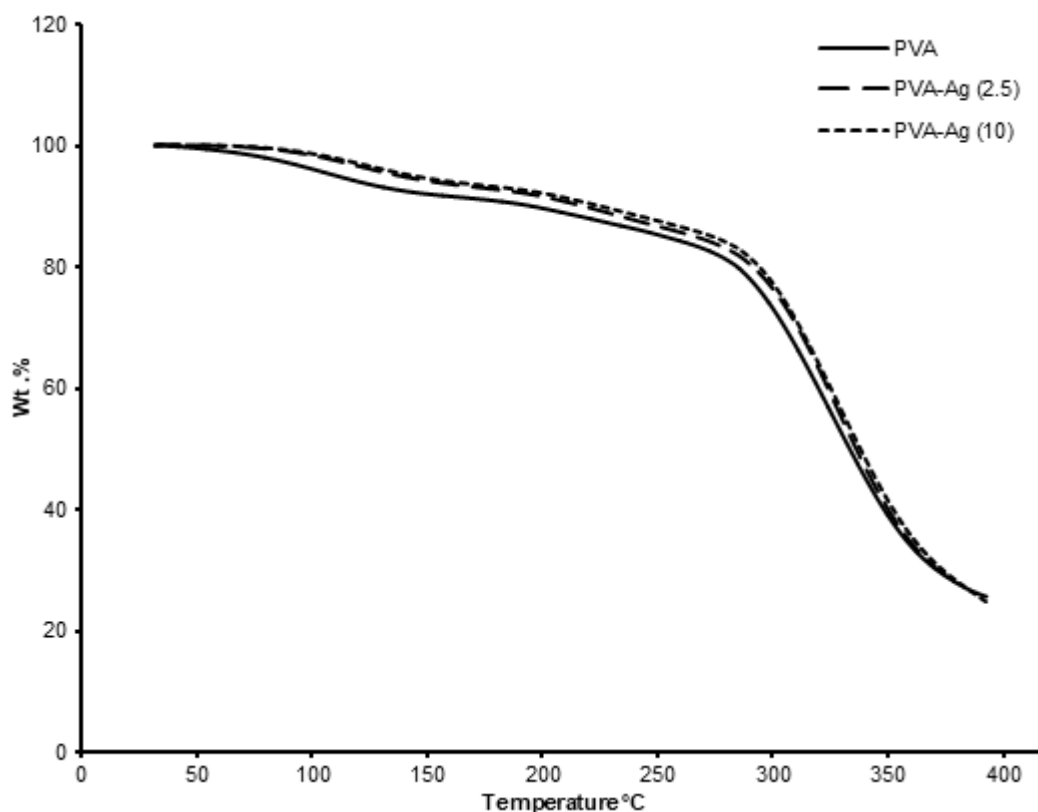


Fig 6. TGA of the prepared PVA sheets; PVA, PVA-Ag (2.5), and PVA-Ag (10)

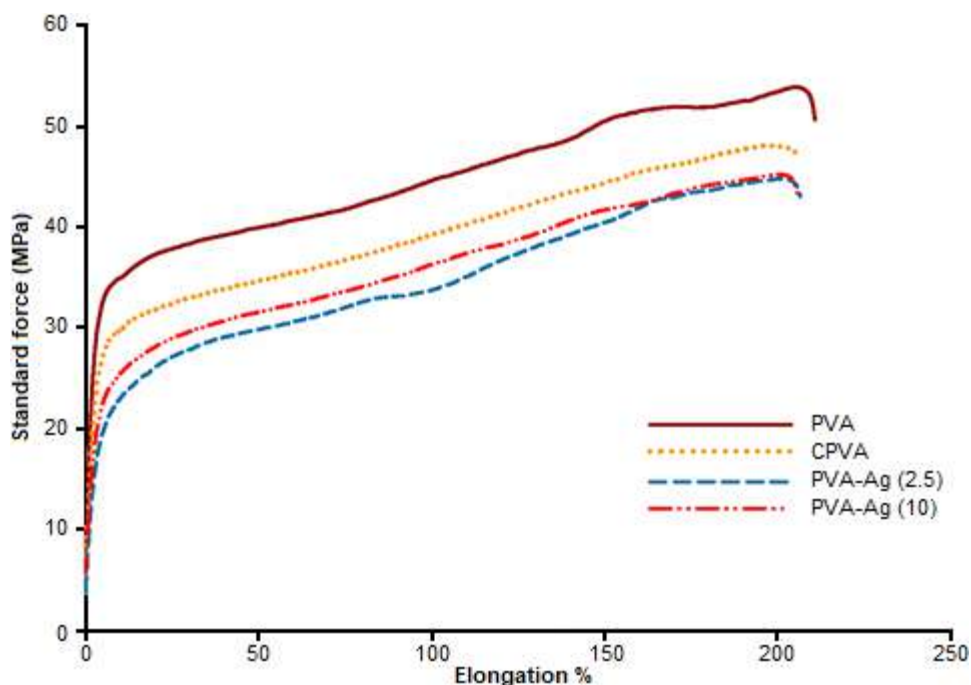


Fig 7. Tensile properties of (a)PVA, (b) CPVA, (c) CPVA-Ag (2.5) and (d) CPVA-Ag (10)

performance. This can be attributed to the reduction of PVA chain interaction due to the presence of AgNPs/MO

between the chains. However, the presence of the phenolic and reactive organic compounds in Moringa

extract can form hydrogen bonding between them and OH of PVA chains, so the decline in mechanical behavior is not so large. Also, the change in the crystallinity of PVA by incorporation of AgNPs/MO leads to a slight stiffness in the films.

Water Content

As most biopolymers have a high sensitivity to water, the study of the water content is an essential aspect, particularly concerning food packaging applications. However, it depends on the type of food and packaging materials. The stability of the packaging system still characterizes the capability of the packaging film to increase the food shelf life. Table 1 shows that the incorporation of AgNPs has no drastic change in the PVA ability to water retention, and there is no drastic change between PVA-Ag (2.5) and PVA-Ag (10).

Water Vapor Permeation

The film's ability to hinder the moisture from penetrating through is considered to be one of the most important characteristic features in food packaging materials as it is favorable to decrease the moisture transfer either from food or from the environment through the packaging films [2]. As shown from the data of Table 1, it is clear that the water vapor permeability rate (WVPR) had significantly decreased by adding AgNPs/MO, while there is no observed difference between the two ratios. These results indicate the improvement of the film to retard the vapor permeation and give an efficient property in food packaging applications.

Antibacterial Activity

The antibacterial properties of the composite films of PVA with AgNP/MO were assessed and demonstrated in Table 2. As shown in the table, all films showed antibacterial performance towards both Gram-positive and Gram-negative bacteria. The antibacterial of blank PVA film may be due to the presence of a trace of sulfuric acid during the preparation step that may unreacted and still present within the film. The antibacterial performance for the silver incorporated film (PVA Ag (10)) showed enhanced performance towards *E. coli* and

Table 1. Water content of nanocomposite PVA films and water vapor permeability rate

Sample	Water content %	WVPR (mg.mm/m ² hkPa)
PVA	-	-
CPVA	82.50397	1337.58
PVA-Ag (2.5)	81.65903	1261.01
PVA-Ag (10)	81.88466	1261.14

Table 2. Inhibition zone (mm) of PVA with and without AgNPs/MO

Film type	<i>E. coli</i>	<i>S. aureus</i>
PVA	12.4 ± 0.15	12.2 ± 0.18
PVA-Ag (10)	15.2 ± 0.20	14.8 ± 0.22

S. aureus and recorded the inhibition zone of 15.2 and 14.8 mm, respectively. The silver nanoparticle is well known for bactericidal action due to their enhanced reactivity resultant from their high surface/volume ratio and can enter the bacteria cell wall causing morphological alterations to the cell wall of bacteria and may result in a significant increase in its permeability and affect proper transport through the plasma membrane [39]. Silver nanoparticles have also been reported to release silver ions inside the bacterial cells and reacted with phosphorus and sulfur compounds producing their bactericidal activity [40].

CONCLUSION

The simple preparation of efficient and green nanocomposite films for active packaging was carried out. First, AgNPs were prepared with a distinguished particle size of 2–5 nm using local MO leaves extract as a reductive agent. Then, AgNPs were blended with a PVA solution and crosslinked with citric acid to form nanocomposite films. It was found upon thermal and mechanical testing that there is a clear enhancement in thermal stability with maintaining the flexibility of PVA. Further enhancement was recorded upon the addition of AgNPs/MO in the water content and water vapor permeability rate. The antimicrobial study showed a significant impact on the growth inhibition of Gram-negative *E. coli* and Gram-positive *S. aureus*.

■ REFERENCES

- [1] Mathew, S., Snigdha, S., Mathew, J., and Radhakrishnan, E.K., 2019, Biodegradable and active nanocomposite pouches reinforced with silver nanoparticles for improved packaging of chicken sausages, *Food Packag. Shelf Life*, 19, 155–166.
- [2] Sarwar, M.S., Niazi, M.B.K., Jahan, Z., Ahmad, T., and Hussain, A., 2018, Preparation and characterization of PVA/nanocellulose/Ag nanocomposite films for antimicrobial food packaging, *Carbohydr. Polym.*, 184, 453–464.
- [3] Garcia, C.V., Shin, G.H., and Kim, J.T., 2018, Metal oxide-based nanocomposites in food packaging: Applications, migration, and regulations, *Trends Food Sci. Technol.*, 82, 21–31.
- [4] Ragab, T.I.M., Nada, A.A., Ali, E.A., Shalaby, A.S.G., Soliman, A.A.F., Emam, M., and El Raey, M.A., 2019, Soft hydrogel based on modified chitosan containing *P. granatum* peel extract and its nano-forms: Multiparticulate study on chronic wounds treatment, *Int. J. Biol. Macromol.*, 135, 407–421.
- [5] El-Ghaffar, M.A.A., Elawady, M.M., Rabie, A.M., and Abdelhamid, A.E., 2020, Enhancing the RO performance of cellulose acetate membrane using chitosan nanoparticles, *J. Polym. Res.*, 27 (11), 337.
- [6] Kołodziejczak-Radzimska, A., and Jesionowski, T., 2014, Zinc oxide-from synthesis to application: A review, *Materials*, 7 (4), 2833–2881.
- [7] Newman, M.D., Stotland, M., and Ellis, J.I., 2009, The safety of nanosized particles in titanium dioxide-and zinc oxide-based sunscreens, *J. Am. Acad. Dermatol.*, 61 (4), 685–692.
- [8] Moodley, J.S., Krishna, S.B.N., Pillay, K., Sershen, and Govender, P., 2018, Green synthesis of silver nanoparticles from *Moringa oleifera* leaf extracts and its antimicrobial potential, *Adv. Nat. Sci.: Nanosci. Nanotechnol.*, 9 (1), 015011.
- [9] El-Shahat, M., Abdelhamid, A.E., and Abdelhameed, R.M., 2020, Capture of iodide from wastewater by effective adsorptive membrane synthesized from MIL-125-NH₂ and cross-linked chitosan, *Carbohydr. Polym.*, 231, 115742.
- [10] Abdelhamid, A.E., and Khalil, A.M., 2019, Polymeric membranes based on cellulose acetate loaded with candle soot nanoparticles for water desalination, *J. Macromol. Sci. Part A Pure Appl. Chem.*, 56 (2), 153–161.
- [11] Elhalawany, N., Wassel, A.R., Abdelhamid, A.E., Elfadl, A.A., and Nouh, S., 2020, Novel hyper branched polyaniline nanocomposites for gamma radiation dosimetry, *J. Mater. Sci. - Mater. Electron.*, 31 (8), 5914–5925.
- [12] Elhalawany, N., El-Naggar, M.E., Elsayed, A., Wassel, A.R., El-Aref, A.T., and Abd Elghaffar, M.A., 2020, Polyaniline/zinc/aluminum nanocomposites for multifunctional smart cotton fabrics, *Mater. Chem. Phys.*, 249, 123210.
- [13] Thakkar, K.N., Mhatre, S.S., and Parikh, R.Y., 2010, Biological synthesis of metallic nanoparticles, *Nanomed. Nanotechnol. Biol. Med.*, 6 (2), 257–262.
- [14] Ahmad, N., Sharma, S., Alam, M.K., Singh, V.N., Shamsi, S.F., Mehta, B.R., and Fatma, A., 2010, Rapid synthesis of silver nanoparticles using dried medicinal plant of basil, *Colloids Surf., B*, 81 (1), 81–86.
- [15] Yallappa, S., Manjanna, J., Peethambar, S.K., Rajeshwara, A.N., and Satyanarayan, N.D., 2013, Green synthesis of silver nanoparticles using *Acacia farnesiana* (Sweet Acacia) seed extract under microwave irradiation and their biological assessment, *J. Cluster Sci.*, 24 (4), 1081–1092.
- [16] Siddhuraju, P., and Becker, K., 2003, Antioxidant properties of various solvent extracts of total phenolic constituents from three different agroclimatic origins of drumstick tree (*Moringa oleifera* Lam.) leaves, *J. Agric. Food Chem.*, 51 (8), 2144–2155.
- [17] Ju, A., Baek, S.K., Kim, S., and Song, K.B., 2019, Development of an antioxidative packaging film based on khorasan wheat starch containing moringa leaf extract, *Food Science Biotechnol.*, 28 (4), 1057–1063.
- [18] El-Sayed, A.A., Amr, A., Kamel, O.M.H.M., El-Saidi, M.M.T., and Abdelhamid, A.E., 2020,

- Eco-friendly fabric modification based on AgNPs@Moringa for mosquito repellent applications, *Cellulose*, 27 (14), 8429–8442.
- [19] Ali, E.A., Eweis, M., Elkholy, S., Ismail, M.N., and Elsabee, M., 2018, The antimicrobial behavior of polyelectrolyte chitosan-styrene maleic anhydride nano composites, *Macromol. Res.*, 26 (5), 418–425.
- [20] Al-Moghazy, M., Mahmoud, M., and Nada, A.A., 2020, Fabrication of cellulose-based adhesive composite as an active packaging material to extend the shelf life of cheese, *Int. J. Biol. Macromol.*, 160, 264–275.
- [21] Tanase, E.E., Popa, E.M., Rapa, M., Popa, O., and Popa, I.V., 2016, Biodegradation study of some food packaging biopolymers based on PVA, *Bull. Univ. Agric. Sci. Vet. Med. Cluj-Napoca*, 73 (1), 11948.
- [22] Liu, B., Xu, H., Zhao, H., Liu, W., Zhao, L., and Li, Y., 2017, Preparation and characterization of intelligent starch/PVA films for simultaneous colorimetric indication and antimicrobial activity for food packaging applications, *Carbohydr. Polym.*, 157, 842–849.
- [23] Musetti, A., Paderni, K., Fabbri, P., Pulvirenti, A., Al-Moghazy, M., and Fava, P., 2014, Poly(vinyl alcohol)-based film potentially suitable for antimicrobial packaging applications, *J. Food Sci.*, 79 (4), E557–E582.
- [24] Bindhu, M.R., Umadevi, M., Esmail, G.A., Al-Dhabi, N.A., and Arasu, M.V., 2020, Green synthesis and characterization of silver nanoparticles from *Moringa oleifera* flower and assessment of antimicrobial and sensing properties, *J. Photochem. Photobiol., B*, 205, 111836.
- [25] Prasad, T.N.V.K.V., and Elumalai, E.K., 2011, Biofabrication of Ag nanoparticles using *Moringa oleifera* leaf extract and their antimicrobial activity, *Asian Pac. J. Trop. Biomed.*, 1 (6), 439–442.
- [26] Abdullah, Z.W., Dong, Y., Han, N., and Liu, S., 2019, Water and gas barrier properties of polyvinyl alcohol (PVA)/starch (ST)/glycerol (GL)/halloysite nanotube (HNT) bionanocomposite films: Experimental characterisation and modelling approach, *Composites, Part B*, 174, 107033.
- [27] Marrez, D.A., Abdelhamid, A.E., and Darwesh, O.M., 2019, Eco-friendly cellulose acetate green synthesized silver nano-composite as antibacterial packaging system for food safety, *Food Packag. Shelf Life*, 20, 100302.
- [28] Zidan, T.A., Abdelhamid, A.E., and Zaki, E.G., 2020, N-Aminorhodanine modified chitosan hydrogel for antibacterial and copper ions removal from aqueous solutions, *Int. J. Biol. Macromol.*, 158, 32–42.
- [29] Bennett, R.N., Mellon, F.A., Foidl, N., Pratt, J.H., Dupont, M.S., and Perkins, L., 2003, Profiling glucosinolates and phenolics in vegetative and reproductive tissues of the multi-purpose trees *Moringa oleifera* L. (Horseradish tree) and *Moringa stenopetala* L., *J. Agric. Food Chem.*, 51 (12), 3546–3553.
- [30] Fahey, J.W., Zalcmann, A.T., and Talalay, P., 2001, The chemical diversity and distribution of glucosinolates and isothiocyanates among plants, *Phytochemistry*, 56 (1), 5–51.
- [31] El-Bisi, M.K., El-Rafie, H.M., El-Rafie, M.H., and Hebeish, A., 2013, Honey bee for eco-friendly green synthesis of silver nanoparticles and application to cotton textile, *Egypt. J. Chem.*, 56 (3), 187–198.
- [32] Pinoni, S.A., and López Mañanes, A.A., 2009, Na⁺ ATPase activities in chela muscle of the euryhaline crab *Neohelice granulata*: Differential response to environmental salinity, *J. Exp. Mar. Biol. Ecol.*, 372 (1-2), 91–97.
- [33] Sathyavathi, R., Krishna, M.B.M., and Rao, D.N., 2011, Biosynthesis of silver nanoparticles using *Moringa oleifera* leaf extract and its application to optical limiting, *J. Nanosci. Nanotechnol.*, 11 (3), 2031–2035.
- [34] Shakir, M.A., Yhaya, M.F., and Ahmad, M.I., 2017, The effect of crosslinking fibers with polyvinyl alcohol using citric acid the effect of crosslinking fibers with polyvinyl alcohol using citric acid, *Imp. J. Interdiscip. Res.*, 3 (4), 758–764.
- [35] Moghazy, R.M., Labena, A., Husien, S., Mansor, E.S., and Abdelhamid, A.E., 2020, Neoteric approach for efficient eco-friendly dye removal and

- recovery using algal-polymer biosorbent sheets: Characterization, factorial design, equilibrium and kinetics, *Int. J. Biol. Macromol.*, 157, 494–509.
- [36] Mansor, E.S., Labena, A., Moghazy, R.M., and Abdelhamid, A.E., 2020, Advanced eco-friendly and adsorptive membranes based on *Sargassum dentifolium* for heavy metals removal, recovery, and reuse, *J. Water Process Eng.*, 37, 101424.
- [37] Abdullah, Z.W., and Dong, Y., 2019, Biodegradable and water resistant poly(vinyl) alcohol (PVA)/starch (ST)/glycerol (GL)/halloysite nanotube (HNT) nanocomposite films for sustainable food packaging, *Front. Mater.*, 6, 58.
- [38] Cai, J., Chen, J., Zhang, Q., Lei, M., He, J., Xiao, A., Ma, C., Li, S., and Xiong, H., 2016, Well-aligned cellulose nanofiber-reinforced polyvinyl alcohol composite film: Mechanical and optical properties, *Carbohydr. Polym.*, 140, 238–245.
- [39] Morones, J.R., Elechiguerra, J.L., Camacho, A., Holt, K., Kouri, J.B., Ramírez, J.T., and Yacaman, M., 2005, The bactericidal effect of silver nanoparticles, *Nanotechnology*, 16 (10), 2346–2353.
- [40] Cardozo, V.F., Oliveira, A.G., Nishio, E.K., Perugini, M.R.E., Andrade, C.G.T.J., Silveira, W.D., Durán, N., Andrade, G., Kobayashi, R.K.T., and Nakazato, G., 2013, Antibacterial activity of extracellular compounds produced by a *Pseudomonas* strain against methicillin-resistant *Staphylococcus aureus* (MRSA) strains, *Ann. Clin. Microbiol. Antimicrob.*, 12 (1), 12.

Hydrocracking of Coconut Oil on the NiO/Silica-Rich Zeolite Synthesized Using a Quaternary Ammonium Surfactant

Sriatun^{1,2*}, Heru Susanto³, Widayat³, and Adi Darmawan²

¹Chemical Engineering Doctoral Programme, Faculty of Engineering, Diponegoro University, Jl. Prof. Soedharto SH, Tembalang, Semarang 50275, Indonesia

²Department of Chemistry, Faculty of Science and Mathematics, Diponegoro University, Jl. Prof. Soedharto SH, Tembalang, Semarang 50275, Indonesia

³Department of Chemical Engineering, Faculty of Engineering, Diponegoro University, Jl. Prof. Soedharto SH, Tembalang, Semarang 50275, Indonesia

* **Corresponding author:**

tel: +62-85100127747

email: sriatun@live.undip.ac.id

Received: April 18, 2020

Accepted: August 7, 2020

DOI: 10.22146/ijc.55522

Abstract: NiO/silica-rich zeolite catalysts were used for coconut oil hydrocracking. The catalyst consists of a mixture of Na_2SiO_3 , $\text{Al}(\text{OH})_3$, NaOH , and quaternary ammonium surfactants. The surfactant was varied of types like as tetrapropylammonium bromide (TPAB) and cetyltrimethylammonium bromide (CTAB). The acidity of the silica-rich sodalite zeolites enhances with the increase in nickel oxide added through a wet impregnation. The hydrocracking process was carried out by a semi-batch method. Liquid products were analyzed using GC-MS. The results showed that the addition of surfactants increased the catalyst surface area and acidity. Meanwhile, the presence of nickel oxide increases the acidity of the catalyst. The hydrocracking results showed an increase in gas products when the surface area was high, i.e., 23.781% in silica-rich sodalite zeolite without template (Z), 32.68% in silica-rich sodalite zeolite with tetrapropylammonium (ZTPA), and 39.673% in silica-rich sodalite zeolite with cetyltrimethylammonium (ZCTA). The presence of NiO increased the liquid product and the selectivity of the bioavtur fraction ($\text{C}_{10}\text{-C}_{15}$), where the highest percentage of liquid product was 60.07% at NiO/ZTPA.

Keywords: hydrocracking; coconut oil; NiO; silica-rich zeolite; sodalite; quaternary ammonium surfactant

■ INTRODUCTION

The most common zeolite in the zeolite mineral group is the sodalite mineral (SOD). The chemical composition of sodalite is $\text{Na}_6(\text{Si}_6\text{Al}_6\text{O}_{24})\cdot\text{H}_2\text{O}$. A sodalite is a host material (host molecule) that is important in forming simple crystal structures of various synthetic zeolites. Sodalite zeolite has a cubic crystal structure. The structure formed by the β -cage framework consists of eight six-member rings in which alternates between the SiO_4 and AlO_4 tetrahedral, and the α -cage consists of six four-membered rings [1]. As the Si concentration in the reactant mixture or the Si/Al ratio increases, the size, and shape of the crystals change, in which the octahedral and

dodecahedral framework in the zeolite's internal structure become dominant [2].

The study of the synthesis of sodalite zeolites has been carried out by Dey et al. [3], who synthesized silica-rich sodalite by adding a trioxane template. The results indicated that trioxane has a strong structural directing or templating effect on the SOD structure. At Si/Al ratios lower than 20, another product was obtained, whereas, at very low temperatures or short synthesis times, the resulting product was still amorphous. Another study has reported zeolite-Y synthesis that successfully used surfactants as templates with the hydrothermal method for 72 h [4]. In another study, CTAB as a structural directive in zeolite synthesis has also been used at

various Si/Al ratios with a hydrothermal temperature of 100 °C for three days. The results indicated that the Si/Al ratio influences the size and shape of zeolite granules/crystals. The use of a CTAB surfactant as a directing agent improves the crystallinity of zeolites and influences the size and homogeneity of zeolite particles [5]. Neutral surfactants such as PEG and cationic surfactants such as CTAB have an important role in the formation of zeolite crystals [6]. Other studies have been reported for LTA type silica-rich zeolite with Si/Al ratio = 17 using tetramethylammonium and 1,2-dimethyl-3-(4-methyl benzyl) imidazolium as templates [7]. Large amounts of Si in the framework cause more durable hydrophobic properties, higher acidity, and greater surface area [8]. These properties satisfy the conditions for this material to be used in reactions that require high temperatures, such as the hydrocracking process. Also, principles of “like dissolves like” can be fulfilled when hydrophobic materials as catalysts interact with nonpolar/hydrophobic feeds and coconut oil. Previous studies concluded that the Si/Al ratio and the use of templates were very influential on the zeolite characters [9-11].

The use of zeolite from bagasse ash as a catalyst in biodiesel production from used cooking oil through the transesterification reaction has also been carried out. Transesterification results showed that at a ratio of methanol: oil of 1:3 for 60 min, 13.83% of Methyl Ester (MES) products were produced, consisting of methyl caprylate, methyl caprate, methyl laurate, methyl myristate, methyl palmitate, methyl linoleate, and methyl stearate. In the methanol: oil ratio of 6:1, the biodiesel obtained was 85.51%, with methyl caprate as the main component [12]. NiO and CoO-supported halloysite nanotubes have also been used as catalysts for hydrocracking of the heavy oil residues. The hydrocracking process was carried out at a temperature of 450 °C with varying H₂ pressures ranging from 1–4 MPa. The results showed an increase in liquid products consisting of gasoline and diesel from 52 to 57% when the pressure rose from 1 to 4 MPa [13]. This information showed that zeolite has excellent performance as a catalyst.

Biofuel can be produced from renewable materials or biomass through several processes such as catalytic cracking, hydrocracking or deoxygenation of vegetable oils containing triglycerides, Fischer-Tropsch process in the synthesis of bio-origin fuels [14-16], from virgin coconut oil waste [17], and marine biofuel from lignocellulose [18]. Castor oil hydroprocessing was promoted by nickel-based bifunctional catalysts to produce bio-jet fuels (bioavtur) [19]. Widiyati et al. [20] had carried out the hydrocracking process using NiMo/Al₂O₃ catalyst on dirty palm oil to produce biokerosene. Besides, the hydrocracking process was carried out using a sulfided NiMo/Al₂O₃ catalyst to produce bio-jet fuel (bioavtur) from natural triglycerides/coconut oil. The operating conditions of the process were at temperature of 280–380 °C, the pressure of 30 bar, liquid hourly space velocity (LHSV) of 1.0–3.0/h, and H₂/feed volume ratio of 600 Nm³/m³ [21]. Meanwhile, Al-Muttaqii et al. [22] and Widayat et al. [23] have produced biokerosene and biofuel from coconut oil using a Ni-Fe/HZSM-5 and Zn/HZSM-5 catalyst through a hydrocracking process.

Coconut oil is a renewable material and can be used as a raw material for biofuel production. Coconut plants are easy to grow and suitable for the Indonesian climate. Therefore, their availability can be maintained. Coconut oil is easily found on the market at a relatively low price. According to Boateng et al. [24], the largest components of coconut oil are lauric acid (49%) and myristic acid (18%). The most important reason for using coconut oil for hydrocracking is as coconut oil contains a high compound of C₁₀–C₁₆, thus providing an opportunity to be converted to hydrocarbons with the same amount of carbon or cracked into hydrocarbons with smaller amounts of carbon.

There has been no report on the use of templates to synthesize silica-rich sodalite. The use of sodalite, a simple structure of the zeolite, has not been reported as a catalyst in the hydrocracking reaction of coconut oil. As the presence of a template of quaternary ammonium surfactant increases surface area and uniformity [25], this research studies the effect of quaternary ammonium surfactant templates on the structure of silica-rich

sodalite zeolites. The choice of cetyltrimethylammonium and tetrapropylammonium bromide surfactants is expected to provide a significant pore size difference. The research also studies the effect of adding NiO in silica-rich zeolites. Ni or NiO metal dispersion to sodalite-rich zeolite silica is expected to increase the acidity and surface area of the material so that the active catalytic site also rises. All materials were tested for their catalytic ability to convert coconut oil into biofuels through a hydrocracking reaction. Catalysts with many active sites are expected to improve hydrocracking products and selectivity.

■ EXPERIMENTAL SECTION

Materials

All chemicals used in this study are analytical grades. The chemicals from Merck were sodium hydroxide (NaOH) 98%, sodium silicate (Na_2SiO_3 , 27% SiO_2), cetyltrimethylammonium bromide (CTAB) 98%, nickel(II) nitrate hexahydrate ($\text{Ni}(\text{NO}_3)_2 \cdot 6\text{H}_2\text{O}$) 99%, hydrofluoric acid (HF) 48%, ammonia (NH_4OH) 25%, hydrochloric acid (HCl) 37%. Meanwhile, the chemicals from Sigma Aldrich were aluminum hydroxide ($\text{Al}(\text{OH})_3$, 50–57% Al_2O_3), and tetrapropylammonium bromide (TPAB) 98%. The hydrocracking process used coconut oil which was purchased from a supermarket in Semarang, Indonesia.

Instrumentation

The crystallinity of synthesized catalysts was characterized using an X-ray diffractometer (XRD) (Bruker D2 Phaser 2nd Gen) with Cu K α radiation, the wavelength of 1.54060 Å, and under the setting of 30 kV and 10 mA. Determination of the surface and pore parameter of the synthesized catalysts was performed using a Gas Sorption Analyzer (GSA) (Quantachrome NovaWin) with sample weight: 0.1129 g, outgas time: 3.0 h, analysis gas: nitrogen, analysis time: 133.3 min, Cell ID: 4, outgas temp: 300 °C, bath temp: 77.3 °K. The surface area was determined by a multi-point Brunauer-Emmett-Teller (BET). The estimation of total pore volume and the distribution of pore size was conducted by the desorption isotherms of the Barret-Joyner-Halenda (BJH) method. The functional groups of the synthesized catalysts after

adsorbing ammonia gas were determined using a Fourier-transform infrared (FTIR) Spectrometer (PerkinElmer Spectrum Version 10.03.06) with the KBr method. Meanwhile, the composition of the liquid product from hydrocracking was identified using GCMS (QP2010S SHIMADZU with column type: Rtx 5 MS, ID: 0.25 mm, carrier gas: Helium, Ionizing: EI 70 Ev, Column temperature: 40 °C, Injection temperature: 310 °C, Injection mode: split, Column flow: 0.57 mL/min).

Procedure

Synthesis of catalyst

An amount of 5.6 g of NaOH was dissolved in 20.7 mL of H_2O and heated until all of the NaOH dissolved. It was subsequently added with 0.45 g of $\text{Al}(\text{OH})_3$ until fully dissolved to give a sodium aluminate solution. The solution was reacted with 16.33 mL of Na_2SiO_3 solution and stirred at room temperature until the mixture thickened. The mixture was transferred into a Teflon container for the hydrothermal process and heated at 200 °C for 24 h in an autoclave. The product was then washed with distilled water until it reached pH ± 7 , and after that, it was dried in an oven at 100 °C for 2 h. This product code was Z.

ZTPA was produced using a TPAB surfactant template, in which 3.328 g of TPAB was dissolved in 25 mL of H_2O , then added to sodium aluminate and stirred until homogeneous. The mixture was added with a 16.33 mL of Na_2SiO_3 solution. The hydrothermal process was carried out at 200 °C for 24 h in an autoclave. The resulting product was washed until a neutral pH obtained (± 7), and after that, it was dried. The solid product was calcined at 550 °C for 3 h to remove the template. The same procedure was applied to synthesize ZCTA using a 4.554 g of CTAB surfactant. Both products were characterized by XRD and GSA techniques.

The NiO/silica-rich zeolite catalysts were prepared by incipient wetness impregnation. Several silica-rich zeolites were impregnated with aqueous solution of nickel(II) nitrate hexahydrate ($\text{Ni}(\text{NO}_3)_2 \cdot 6\text{H}_2\text{O}$) to contain 3% (weight) of nickel. The mixture was stirred at 30 °C for 24 h and evaporated at 90 °C until the paste was formed. Then the paste was dried at 110 °C and

calcined at 550 °C for 3 h. This process aimed to form NiO from Ni²⁺ ions. The impregnation products were NiO/Z, NiO/ZTPA, and NiO/ZCTA, each of which refers to a catalyst without a template, tetrapropylammonium-templated catalyst and the cetyltrimethylammonium-templated catalyst, respectively. Afterward, the catalysts obtained were characterized using GSA.

The catalyst's total acidity was determined using the gravimetric method with ammonia gas as an adsorbed base. The empty porcelain crucible was heated in an oven at 110 °C for 1 h, then cooled and weighed (W_1). A sample of 0.1 g was put into a porcelain crucible and then heated at 110 °C for 1 h and weighed (W_2). Samples in heated porcelain were put into a desiccator and then vacuumed. Next, ammonia gas was introduced to the desiccator until the gas saturated the desiccator. After completion, the desiccator was opened and allowed to run for about 30 min to remove residual ammonia that was not adsorbed. Next, the porcelain crucible containing the sample and absorbing ammonia was weighed (W_3). Calculation of total acidity using Eq. (1).

$$\text{Acidity} = \frac{(W_3 - W_2)}{(W_2 - W_1)M} \quad (1)$$

where, W_1 = weight of empty porcelain crucible after heating (g); W_2 = weight of porcelain crucible + sample after heating (g); W_3 = weight of porcelain crucible + sample after ammonia adsorption (g); M = molecular weight of NH₃ (g/mol).

Analysis using FTIR was conducted to verify the ammonia adsorbed on the material catalyst.

Catalytic activity test

The hydrocracking process was carried out in a semi-batch reactor, in which the catalyst and feed were put into one reactor but not mixed. The reactor was a stainless-steel column. A total of 10 g coconut oil feed was put into the column reactor, then 0.2 g of catalyst was placed in a container and put in the same column reactor. The catalyst/feed ratio was 2% (weight). The reactor column was inserted into a furnace made of stainless-steel coated ceramic and heated to 475 °C at a rate of 10 °C/min with a reaction time of three hours. During the reaction, hydrogen gas flowed to the reactor at a rate of 10 mL/min. The product was streamed through a stainless-steel pipe

connected to a silicone hose and passed through a glass condenser. The liquid products were collected in an Erlenmeyer flask, then weighed (as the mass of the liquid product). Coke mass was the catalyst's weight after the hydrocracking sample subtracted the weight of the initial catalyst. The residual mass was the weight of residual feed in the reactor that was not converted. Gas mass was the weight of the initial feed subtracted by the weight (residue + coke + liquid). The determination of the catalytic activity of the catalyst follows Eq. (2) to Eq. (5).

$$\% \text{Liquid conversion} = \frac{\text{mass of the liquid}}{\text{mass of feed}} \times 100\% \quad (2)$$

$$\% \text{Coke conversion} = \frac{\text{mass of coke}}{\text{mass of feed}} \times 100\% \quad (3)$$

$$\% \text{Gas conversion} = \frac{\text{mass of the gas}}{\text{mass of feed}} \times 100\% \quad (4)$$

$$\% \text{Total conversion} = \frac{\text{mass of (liquid + gas + coke)}}{\text{mass of feed}} \times 100\% \quad (5)$$

Furthermore, the determination of liquid composition was conducted using Gas Chromatography-Mass Spectrometer (GC-MS). The percentage of the C₄-C₉ fraction was obtained by adding up the total area of the C₄-C₉ component in the chromatogram, then divided by the total chromatogram area of each sample. Likewise, the calculation of the percentage of the C₁₀-C₁₅ fraction (bioavtur) was determined in the same procedure by changing C₄-C₉ to C₁₀-C₁₅. The percentage fraction was calculated using Eq. (6) and Eq. (7). The fraction peak area in the chromatogram was applied to calculate selectivity using Eq. (8).

$$\% \text{C}_4 - \text{C}_9 \text{ fraction} = \frac{\% \text{GC area of C}_4 - \text{C}_9 \text{ fraction}}{\% \text{total GC area}} \times 100\% \quad (6)$$

$$\% \text{C}_{10} - \text{C}_{15} \text{ fraction} = \frac{\% \text{GC area of C}_{10} - \text{C}_{15} \text{ fraction}}{\% \text{total GC area}} \times 100\% \quad (7)$$

$$\% \text{selectivity} = \frac{\% \text{GC area bioavtur fraction}}{\% \text{total GC area}} \times \% \text{conversion of liquid} \quad (8)$$

RESULTS AND DISCUSSION

Characteristics of Silica-Rich Sodalite Zeolite Catalysts

Fig. 1 shows the FTIR spectra of the catalysts. According to Mofrad et al. [26], the typical absorption of sodalite is at the peak of 436, 467, 669, 711, 736, 867, and 988 cm⁻¹. In this study, all catalysts showed absorption

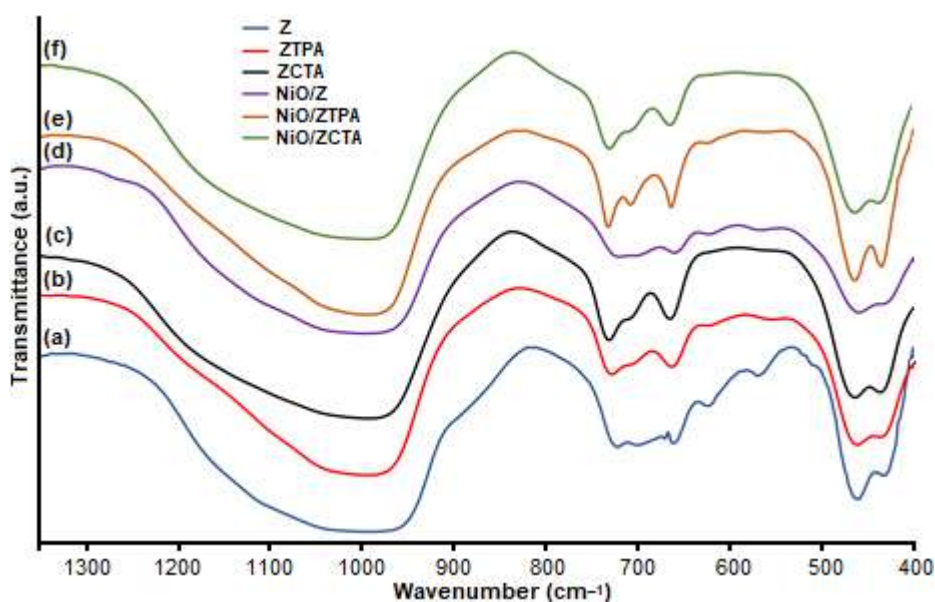


Fig 1. FTIR spectra of the silica-rich sodalite zeolite catalysts (a) without template (Z), (b) with CTAB (Z-CTA) and (c) with TPAB (Z-TPA) (d) NiO/Z (e) NiO/ZTPA (f) NiO/ZCTA

bands in the sodalite zeolite fingerprint area, which are $429\text{--}434\text{ cm}^{-1}$ as S4R bending vibrations, $459\text{--}467\text{ cm}^{-1}$ as O–T–O bending vibration, $660\text{--}664\text{ cm}^{-1}$ as T–O symmetrical stretching vibrations, 697, 722, and $978\text{--}992\text{ cm}^{-1}$ as T–O–T asymmetric stretching vibrations [27–28].

Asymmetrical T–O–T stretching vibration absorption was shifted at a higher wavenumber on the ZTPA and ZCTA catalyst when it was compared to Z. The same thing happened with NiO/ZTPA and NiO/ZCTA catalysts compared to NiO/Z. The wavenumber shift occurred from 978 cm^{-1} on Z to 983 cm^{-1} on ZTPA and 988 cm^{-1} on ZCTA. Whereas after impregnation with NiO, the wavenumber shift occurred from 991 cm^{-1} for NiO/Z to 996 cm^{-1} and 997 cm^{-1} for NiO/ZTPA and NiO/ZCTA, respectively. The shift of the absorption of the wave number in the higher direction indicates the vibration of Si–O–Al or Si–O–Si towards the lower energy. This is presumably because of adding TPA and CTA templates when forming a silica-rich sodalite framework causing longer bond distances. Besides, the asymmetric stretching vibration absorption band of T–O–T in the area experienced an increase in absorption intensity and downsizing of ZTPA, ZCTA, NiO/ZTPA, and NiO/ZCTA catalysts. According to Eterigho-Ikelegbe et al. [29], high intensity absorption in the fingerprint area of the main

framework (not a wide peak) is preferred because it shows the catalyst has a more crystalline structure.

The XRD patterns of silica-rich zeolites are shown in Fig. 2. The characteristic peaks of the structures were determined based on the XRD standard patterns, which were taken from ICDD (International Center of Diffraction Database) or RUFF ID. The XRD patterns of the samples in Fig. 2 are relatively similar to the XRD standard pattern of sodalite zeolite based on RRUFF ID R040141 or ICDD.

Fig. 2 and Table 1 show that the XRD peaks of silica-rich sodalite zeolites from this study are like the previous results reported by Manique et al. [30], who synthesized sodalite through hydrothermal methods. In addition, the prominent data 2θ peak in the sample also complies with JCPDS 75-0709 and RRUFF ID R040141. These results indicate that all synthesis processes successfully produced sodalite. This material is called silica-rich sodalite zeolite because of its high Si content in its structure. These results also show that the addition of template treatment does not give a significant difference on the crystal structure of the resulting sodalites.

When aluminate and silicate interact under alkaline conditions, the Si–O–Si or Si–O–Al zeolite framework is formed, depending on the ratio of silicate

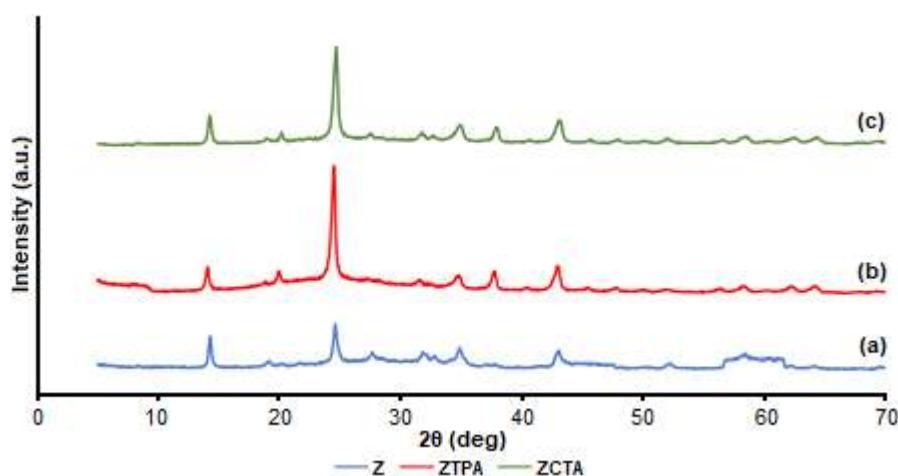


Fig 2. The powder XRD patterns of silica-rich sodalite zeolite (a) without template (Z), (b) with CTAB (Z-CTA) and (c) with TPAB (Z-TPA)

Table 1. Comparison of 2θ ($^{\circ}$) between silica-rich sodalite zeolite and sodalite reference RRUFF ID No. R040141 and JCPDS No. 75-0709

Sodalite Reference 2θ ($^{\circ}$) on		Sample 2θ ($^{\circ}$)		
RRUFF ID R040141	JCPDS 75-0709	Z	ZTPA	ZCTA
14.16	14.1	14.31	14.26	14.11
24.66	24.5	24.65	24.71	24.54
31.99	31.8	31.87	31.79	31.62
35.13	35.0	34.89	34.94	34.79
	37.8	37.20	37.93	37.76
43.39	43.2	43.02	43.15	43.02

and aluminate [31]. The higher the Si/Al ratio, the more Si–O–Si will be formed, resulting in silica-rich sodalite zeolites. The hydrophobicity of silica-rich zeolite is a favorable character for interactions with organic compounds [8]. Hydrophobicity (zeolite-water interactions) in zeolites is primarily influenced by the chemical composition of zeolites, especially the Si/Al ratio. Zeolites with a high Si/Al ratio tend to have more hydrophobic character [32-33]. Bolis et al. [34] proposed that water molecules interact with the Al site of the zeolite framework. The few Si–OH species also influence hydrophobicity because Si–OH species can absorb water by forming stable bonds. Zeolites with the same framework type, their hydrophobicity increases with decreasing aluminum content, so zeolites with a higher Si/Al ratio will be more hydrophobic. This character is suitable for interacting with the raw material for coconut oil, which is also hydrophobic. The efficiency of the interaction of

organic substances, in this case, coconut oil by high silica zeolites, depends on the interaction of organic substances with zeolites. And this is influenced by the structure, surface hydrophobicity, and adsorption sites of high silica zeolites and the character of organic materials [8].

Fig. 2 also shows that the use of templates slightly increases crystallinity. These results are in line with research by [25], who reported that the use of different templates produced different sodalite crystallinity. The use of different templates, CTAB and TPAB, from quaternary ammonium surfactants, is an important factor in the formation of different silicate species from dimers to 4-rings (4R) and the final sodalite zeolite structure [35] in basic conditions. A study conducted by Pavlova et al. [35] showed that the activation barrier of dimerization increased with TPA^+ .

CTAB and TPAB are surface-active agents that work to reduce the surface tension of the liquid. Active

properties are obtained from the dual nature of the molecules. TPAB and CTAB surfactants were selected as pore-forming templates. Both have differences in the head and tail, although the part of heads has the same type of quaternary ammonium, but different tail shapes give different results. Several studies report the role of surfactant-templating that produces different pores in the zeolite [36], and pore size depending on the type of surfactants [37]. The effects of using templates and NiO loading on silica-rich sodalite zeolite pores and surfaces are given in Fig. 3 and Table 2.

Fig. 3(a) presents the adsorption isotherm patterns for samples Z, ZTPA, and ZCTA, which are classified as type IV according to the IUPAC adsorption isotherm classification [38]. Type IV isotherms signify mesoporous material. All three samples show a similar pattern of adsorption isotherms, where there was small amount of nitrogen molecular adsorption at the relative pressure $P/P_0 = 0-0.7$. An increase in the volume of adsorbed nitrogen was observed at $P/P_0 > 0.7$. An increased volume of adsorbed nitrogen molecules indicates mesoporous filling, where the surface of the solid is covered by nitrogen molecules to form a single layer. The slope shows that the first multilayer has formed. The presence of pores on the surface of solid limits the number of layers on the adsorbate, resulting in capillary condensation. This capillary condensation causes hysteresis. The sample follows an H3 type hysteresis loop where the adsorption properties are not limited to high P/P_0 . H3 type loops are observed because the aggregate of particles such as plates

giving rise to pore-shaped slits [39] produces a narrow distribution of pore bodies with a wide neck size distribution [40]. ZTPA provides high absorption of nitrogen gas, which indicates that the pore volume in ZTPA is higher. These results indicate that the use of TPA has successfully enlarged pores, compared to zeolite without a template. However, an anomaly occurred in ZCTA samples, which showed small adsorption. It is estimated that the low nitrogen gas absorbed was caused by imperfect calcination, where many unburned CTA templates were still in the pore. This, in turn, caused pore closure.

On the other hand, Fig. 3(b) shows that the three samples give a similar form of adsorption isotherm with almost the same volume of nitrogen gas. This indicates that the NiO impregnation process in Z, ZTPA, and ZCTA samples produced almost the same pore and surface characteristics. The increase in the volume of nitrogen gas absorbed by NiO/ZCTA is due to the continued calcination process after the impregnation of Ni^{2+} , which burns the remains of the template. In samples of NiO/Z, NiO/ZTPA, and NiO/ZCTA, type H3 loop hysteresis occurs at a relative pressure of $P/P_0 = 0.7-1$. Hysteresis occurs as, at the same relative pressure P/P_0 , the number of desorption of nitrogen adsorbed on the solid is lower than the number of adsorbed nitrogen molecules. This shows that the amount of adsorbate (N_2) remaining in the pore during desorption is high, indicating the number of mesoporous structures in the sample.

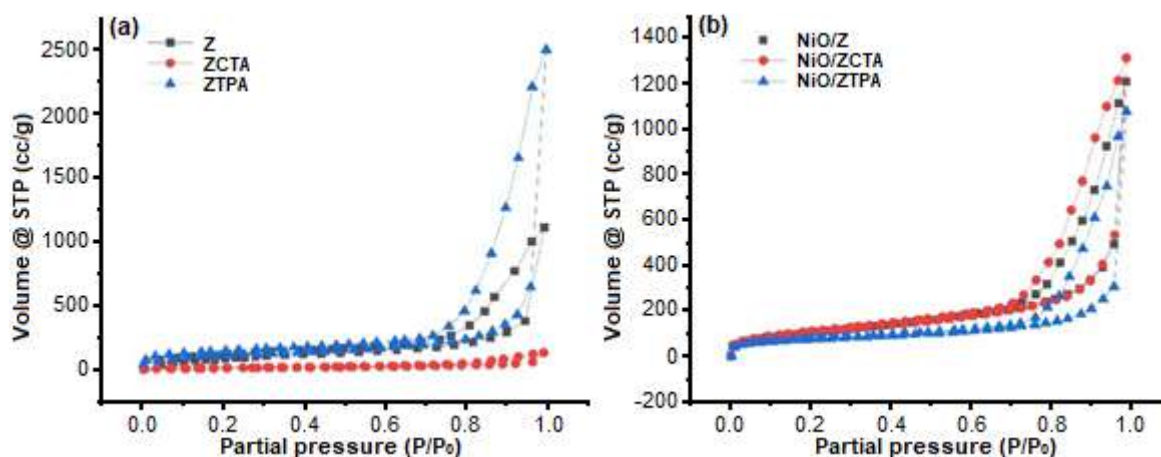


Fig 3. Isotherm adsorption of silica-rich sodalite zeolite (a) effects of template (b) effects of NiO loading

The critical micelle concentration (CMC) of CTAB is 9.2×10^{-4} M at 25 °C [41], whereas CMC of TPAB is 10^{-3} M and the solubility of TPAB at 20 °C > 1000 g/L in H₂O [42]. The addition of surfactant in sodium aluminate solution caused a decrease in the solution's surface tension. After reaching a certain concentration, the surface tension will be constant even though the surfactant concentration increases [43]. There is a difference in the length of the alkyl chain (tail), so the size of micelles will be different. Therefore, sodalite zeolites have different pore sizes. The length of the alkyl chain on CTAB is longer than TPAB; the longest CTAB chain contains 16 carbon, while TPAB only contains three carbon. Goyal et al. [44] reported that CTA⁺ micelle diameters range from 130 to 210 Å. In contrast, according to Thapa et al. [45], TPA⁺ micelle diameter about 13 Å. The larger CTA⁺ micelle diameter from TPA⁺ becomes the rationale for why the volume and surface area of ZCTA is higher than ZTPA, as shown in Fig. 4.

Fig. 4 presents the surface area, pore size, and total pore volume of synthesized silica-rich sodalite zeolites and NiO impregnated zeolites. The data shows that after impregnation by NiO, the surface area and pore volume of zeolite are significantly reduced, except Z, whose

surface area and pore volume increase. Increased surface area and pore volume of Z may be caused by NiO placement on Z, which is more evenly distributed and does not form aggregates so that it does not clog pores. Therefore, the presence of NiO particles present on the surface of Z increases the surface area. On the other hand, the decrease in surface area on NiO/ZTPA and NiO/ZCTA is easily understood as a result of surface closure by NiO. The presence of carbon from incomplete combustion residues might accelerate pore aggregation. It may also be caused by the dispersion of NiO particles into the zeolite sodalite pores non-uniformly. This results in mouth obstruction of the porous channels and the outer surface of zeolites. For all silica-rich sodalite zeolite, the pore radius is almost the same and does not significantly change after NiO's impregnation. This indicates that the thickness of the NiO layer is much lower than the pore radius. All these results indicate that NiO particles were successfully impregnated on the surface and pore of silica-rich sodalite [24].

Metal loading increases the Brønsted and Lewis acid sites [46] as total acidity, as given in Table 2. It is hoped that more acid sites interact with the feed. Adsorption of ammonia base occurs through interactions with protons,

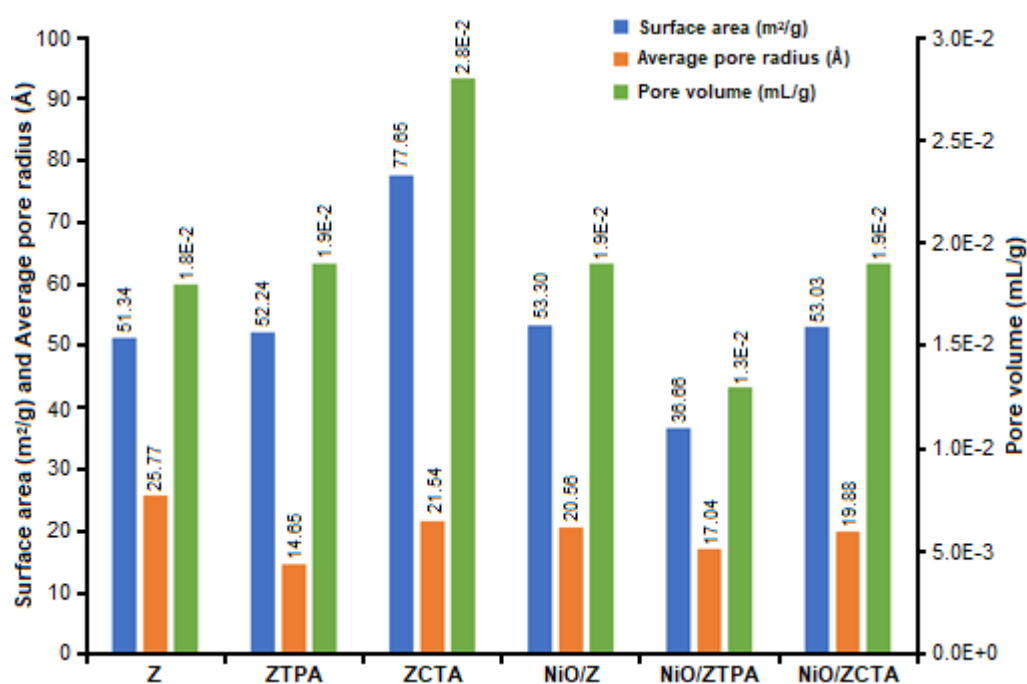


Fig 4. Surface area, pore diameter, and volume of synthesized silica-rich sodalite zeolites

Table 2. Total acidity of the catalyst

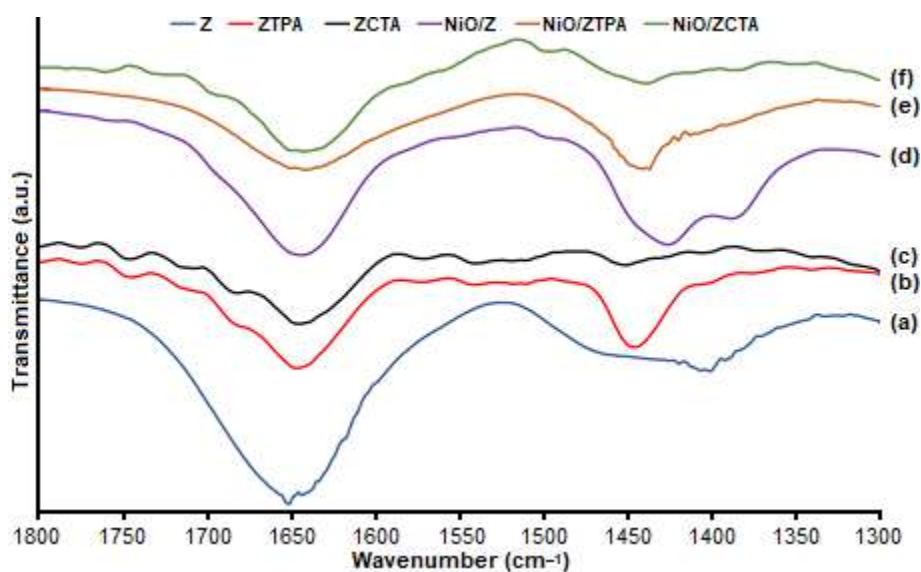
Catalyst Code	Acidity (mmol/g)
Silica-rich sodalite zeolite without template (Z)	7.9
Silica-rich sodalite zeolite - TPAB (ZTPA)	8.2
Silica-rich sodalite zeolite - CTAB (ZCTA)	11.4
NiO/Z	11.2
NiO/ZTPA	11.5
NiO/ZCTA	17.2

which are Brønsted acid sites or by receiving electron pairs from nitrogen atoms in ammonia where the catalyst acts as Lewis acid. In this data, it is known that an increase in acidity occurs when the preparation of a silica-rich zeolite catalyst support was carried out using a surfactant as a template. Total acidity increased by 3.79 and 44.30% in ZTPA and ZCTA, respectively.

The higher acidity value in ZCTA may be due to the greater surface area, as presented in Fig. 4 so that acidic sites are available on the surface. The addition of NiO significantly increases acidity. Ni metals from NiO are spread on the surface and in the pores. Moreover, silica-rich sodalite zeolite have empty orbitals that can accept electron pairs from the ammonia base [47]. NiO/Z acidity increased by 41.77% from Z, NiO/ZTPA increased by 40.24% from ZTPA, and NiO/ZCTA increased by 50.87% from ZCTA. Meanwhile, when compared to the catalyst without a template (Z), NiO/ZTPA acidity increased by 45.56%, and NiO/ZCTA increased by 117.7%. There is a

correlation between total acidity and surface area and pore volume, wherewith increasing surface area and pore volume in Z, ZCTA, and ZTPA, acidity increases. This indicates that NiO is evenly distributed in line with surface area and pore volume.

Amorphous aluminosilicates formed at the beginning of zeolite preparations have many Lewis acid sites and several Brønsted acid sites. This is because Brønsted acid sites develop more on the surface of zeolites when well-defined crystals are formed [48]. The FTIR spectra in Fig. 5 show some firm absorption peaks at a wavenumber of 1635–1640 cm^{-1} on almost all catalysts, which are characteristic for ammonia bonding with Lewis acid sites [49]. It can be noted that there is not much difference at the peak of 1636 cm^{-1} , which indicates that the interaction of ammonia with Lewis acid sites is weak and does not depend on the zeolite structure and the amount of NiO added. In comparison, peaks at 1430–1450 cm^{-1} show ammonia interactions with

**Fig 5.** FTIR spectra of the catalysts after acidity test

Brønsted acid sites [50]. Unfortunately, in this area, absorption presents a very irregular form and overlaps with several other sub-bands. According to Barzetti [50], peaks in this area originate from ammonia decomposition into NH and NH_2^- . The effect of the addition of surfactants and NiO on Brønsted acid sites is difficult to explain. It can only be concluded that all catalysts have active Lewis and Brønsted acid sites.

Hydrocracking of Coconut Oil

Fig. 6 shows the effect of the addition of surfactants and NiO on the total conversion and composition of the coconut oil hydrocracking results after the hydrocracking process at 475 °C for 180 min, hydrogen flow rate of 10 mL/min, catalyst concentration of 2% to the feed.

The role of the templates TPA and CTA created catalyst porosity because, in hydrocracking, the porosity network was susceptible to the diffusion of unrestricted reactants and the resulting product. Besides, based on the data in Table 2, the presence of a template could increase the acidity. This case accorded with the report of Emdadi et al. [51]. The acidity and porosity of catalysts were significant; the acid sites of catalysts could effectively consume intermediates to form aiming products. Meanwhile, the porosities and cavities of catalysts could mediate the molecular sizes and structures of products [52].

Fig. 6 shows that the use of CTAB and TPAB templates in the formation of ZTPA and ZCTA silica-rich sodalite zeolite pores influences the increase in gas fraction yield. This is due to the specific pore size and shape as in the data in Fig. 4 where ZTPA and ZCTA have

smaller pore sizes than Z, so that the catalyst is more selective than before to produce short-chain gas or hydrocarbon fractions. On the other hand, impregnation with NiO on NiO/Z, NiO/ZTPA, and NiO/ZCTA catalysts significantly rises liquid products. This is in accordance with Vichaphund et al. [53] report that the addition of metals is expected to modify the acidic properties and texture of the supporting material to promote cracking activity in terms of removing oxygenated compounds and increasing the number of hydrocarbons. It can be said that the role of nickel oxide as an active site is crucial. Fig. 6 also presents a catalytic activity for converting triglycerides into products consisting of liquid, gas, and coke. However, there is no significant difference in residue and coke due to the addition of surfactant and NiO treatment.

A total conversion is only slightly affected by the size and shape of the pores caused using templates and the loading of nickel oxide. Total conversions ranged from 70–86%, which did not show a significant difference. So, it can be concluded that the combination of the acidity of the catalyst and the accessibility of acid sites is an essential factor in the catalyst activity [54] towards the conversion of triglycerides in coconut oil.

Fig. 7(a) shows the catalyst effect on the composition of liquid product components from the hydrocracking process. The compounds presented in the liquid products are grouped into n-paraffin, consisting of biogasoline ($\text{C}_4\text{--}\text{C}_9$) and bioavtur hydrocarbon range ($\text{C}_{10}\text{--}\text{C}_{15}$). Both fractions are n-paraffin compounds that

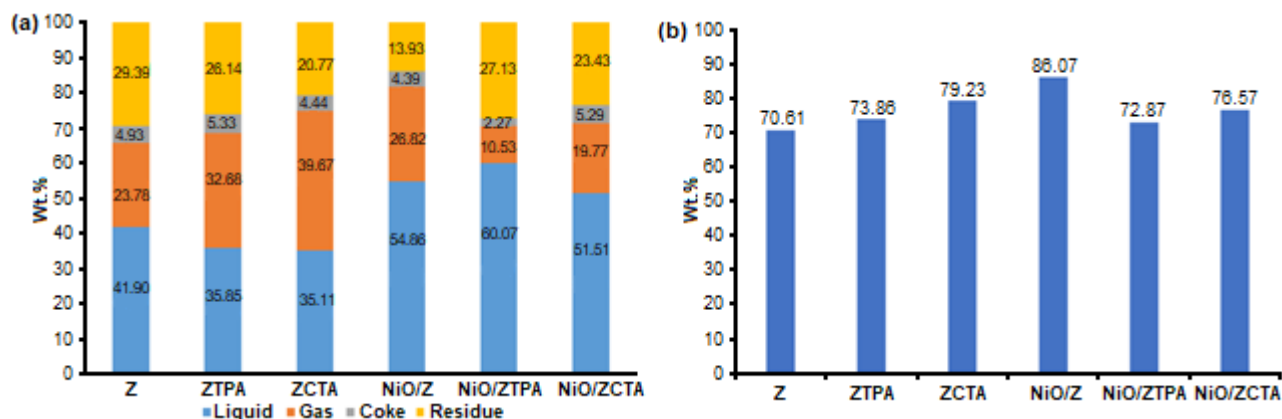


Fig 6. The effect of templates and NiO on (a) type of hydrocracking products and (b) total conversion

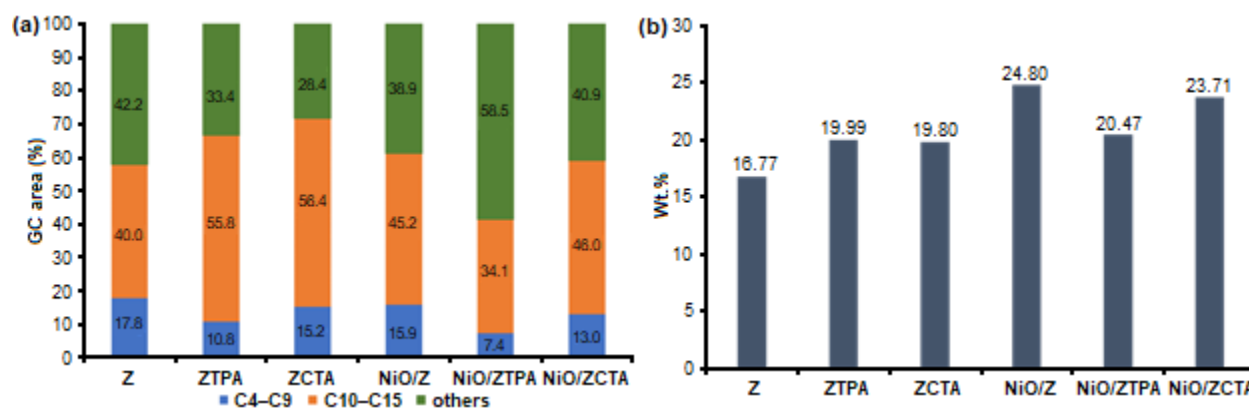


Fig 7. Effect of catalysts on (a) the composition of liquid products (b) The percentage of bioavtur fraction (C_{10} - C_{15}) selectivity

are produced in the hydrocracking reaction at temperature of 475 °C. According to Li et al. [55], paraffin is formed through decarboxylation and decarbonylation reactions. Fig. 7(a) also shows that the hydrocracking process also produces other products such as alkenes, carboxylic acids, ethers, alcohols, etc. with a percentage of 30–40% except for NiO/ZTPA which is 58.54%. The percentage of bioavtur fuel fraction increased in the ZTPA and ZCTA catalysts. This data shows the TPA and CTA templates are significant in increasing the bioavtur fraction.

The role of templates in enhancing bioavtur products is by increasing the ability of the feeds (triglycerides) to diffuse into the pores and active sites of the catalyst. Based on Fig. 4, catalysts with TPA and CTA templates have more pores than without templates. Pores and cavities produce more active sites. Therefore, more triglycerides were able to diffuse and interact with active sites and in cavities of a specific size and shape, thus producing short and long-chain hydrocarbon products. The C_4 - C_9 short-chain hydrocarbon fraction was produced in smaller quantities than C_{10} - C_{15} , probably due to the lighter fraction being faster. At the same time, the presence of many pores allows the reaction to be retained in the cavity to produce a longer carbon chain.

Fig. 7(a) shows the ability of the catalyst to produce bioavtur fractions after impregnation with NiO seems to decrease, except Z, which is impregnated into NiO/Z. The surface area of NiO/Z is relatively higher than NiO/ZTPA and NiO/ZCTA. Therefore, it has a higher ability to

produce bioavtur. The increase in product selectivity obtained from catalysts containing NiO can be observed in Fig. 7(b). It appears that the addition of NiO does not provide more selective results on biogasoline and bioavtur products.

The high yield in the liquid products in Fig. 6 and selectivity performed by catalysts in Fig. 7 are due to their pore size and shape of the catalysts and the easiness of NiO loading. The fact indicated the incorporation of nickel oxide into Z, ZTPA, and ZCTA catalysts depict a bifunctional character consisting of acid and metal sites in agreement with Xu et al. [56]. The acidity properties of zeolites indicated their catalytic potential for various hydrocarbon reactions.

CONCLUSION

The CTAB surfactant as a template was able to increase the surface area of the catalyst from 51.338 m²/g in silica-rich zeolites without surfactants (Z) to 77.653 m²/g on the CTAB template (ZCTA). However, it did not occur in the TPAB template (ZTPA). The use of templates slightly increased the acidity of the catalysts from 7.9 mmol/g to 8.2 mmol/g on ZTPA and 11.4 mmol/g on ZCTA. The addition of NiO on catalysts also improved the acidity property. The highest acidity was 17.2 mmol/g in the NiO/ZCTA sample.

NiO/silica-rich sodalite zeolites in the hydrocracking process resulted in gas products when the surface area was greater, namely 23.781, 32.68, and 39.673% for Z, ZTPA, and ZCTA, respectively. The

presence of NiO increased liquid products and selectivity of bioavtur fraction (C₁₀-C₁₅), where the highest percentage of liquid obtained was 60.07% from NiO/ZTPA.

■ ACKNOWLEDGMENTS

The authors would like gratefully to acknowledge to the Directorate General of Research and Development, the Ministry of Research, Technology, and Higher Education of Indonesia, for financial support in the 2019 fiscal year with the grant number 101-27/UN7.P4.3/PP/2019. The authors would like to extend the gratitude to our research team, i.e., R. Kurniasari and R. Kurniawati, for the support during the experiments.

■ REFERENCES

- [1] Esaifan, M., Warr, L.N., Grathoff, G., Meyer, T., Schafmeister, M.T., Kruth, A., and Tetrich, H., 2019, Synthesis of hydroxy-sodalite/canocrinite zeolites from calcite-bearing kaolin for the removal of heavy metal ions in aqueous media, *Minerals*, 9, 484.
- [2] Buhl, J.C., 2016, Enhanced methods of crystallization: The crossover synthesis from gel to melt flow - A case study on sodalites, *Microporous Mesoporous Mater.*, 236, 13-20.
- [3] Dey, K.P., Ghosh, S., and Naskar, M.K., 2013, Organic template-free synthesis of ZSM-5 zeolite particles using rice husk ash as silica source, *Ceram. Int.*, 39 (2), 2153-2157.
- [4] Sriatun, S., Taslimah, T., Cahyo, E.N., and Saputro, F.D., 2017, Sintesis dan karakterisasi zeolit Y, *JKSA*, 20 (1), 19-24.
- [5] Sriatun, S., Taslimah, T., and Suyati, L., 2018, Synthesis of zeolite from sugarcane bagasse ash using cetyltrimethylammonium bromide as structure directing agent, *Indones. J. Chem.*, 18 (1), 159-165.
- [6] Wang, L., Lei, H., Bu, Q., Ren, S., Wei, Y., Zhu, L., Zhang, X., Liu, Y., Yadavalli, G., Lee, J., Chen, S., and Tang, J., 2014, Aromatic hydrocarbons production from ex situ catalysis of pyrolysis vapor over Zinc modified ZSM-5 in a packed-bed catalysis coupled with microwave pyrolysis reactor, *Fuel*, 129, 78-85.
- [7] Jo, D., Ryu, T., Park, G.T., Kim, P.S., Kim, C.H., Nam, I.S., and Hong, S.B., 2016, Synthesis of high-silica LTA and UFI zeolites and NH₃-SCR performance of their copper-exchanged form, *ACS Catal.*, 6 (4), 2443-2447.
- [8] Jiang, N., Shang, R., Heijman, S.G.J., and Rietveld, L.C., 2018, High-silica zeolites for adsorption of organic micro-pollutants in water treatment: A review, *Water Res.*, 144, 145-161.
- [9] Gao, Y., Zheng, B., Wu, G., Ma, F., and Liu, C., 2016, Effect of the Si/Al ratio on the performance of hierarchical ZSM-5 zeolites for methanol aromatization, *RSC Adv.*, 6 (87), 83581-83588.
- [10] Smirniotis, P.G., and Zhang, W., 1996, Effect of the Si/Al ratio and of the zeolite structure on the performance of dealuminated zeolites for the reforming of hydrocarbon mixtures, *Ind. Eng. Chem. Res.*, 35 (9), 3055-3066.
- [11] Shvets, O.V., Kasian, N., Zukal, A., Pinkas, J., and Čejka, J., 2010, The role of template structure and synergism between inorganic and organic structure directing agents in the synthesis of UTL zeolite, *Chem. Mater.*, 22 (11), 3482-3495.
- [12] Sriatun, S., Taslimah, T., and Suyati, 2015, Pemanfaatan katalis silika alumina dari bagasse pada pembuatan biodiesel dari minyak goreng sisa pakai, *Jurnal Teknologi Industri Pertanian*, 25 (1), 35-42.
- [13] Abbasov, V.M., Ibrahimov, H.C., Mukhtarova, G.S., and Abdullayev, E., 2016, Acid treated halloysite clay nanotubes as catalyst supports for fuel production by catalytic hydrocracking of heavy crude oil, *Fuel*, 184, 555-558.
- [14] Romero, M.J.A., Pizzi, A., Toscano, G., Busca, G., Bosio, B., and Arato, E., 2016, Deoxygenation of waste cooking oil and non-edible oil for the production of liquid hydrocarbon biofuels, *Waste Manage.*, 47, 62-68.
- [15] Vonortas, A., Kubička, D., and Papayannakos, N., 2014, Catalytic co-hydroprocessing of gasoil-palm oil/AVO mixtures over a NiMo/ γ -Al₂O₃ catalyst, *Fuel*, 116, 49-55.

- [16] Hanaoka, T., Miyazawa, T., Shimura, K., and Hirata, S., 2015, Jet fuel synthesis in hydrocracking of Fischer–Tropsch product over Pt-loaded zeolite catalysts prepared using microemulsions, *Fuel Process. Technol.*, 129, 139–146.
- [17] Yotsomnuk, P., and Skolpap, W., 2017, Biofuel production from waste virgin coconut oil by hydrocracking over HZSM-5 zeolite, *Int. J. Adv. Sci. Eng. Technol.*, 5 (2), 54–57.
- [18] Tanzer, S.E., Posada, J., Geraedts, S., and Ramírez, A., 2019, Lignocellulosic marine biofuel: Technoeconomic and environmental assessment for production in Brazil and Sweden, *J. Cleaner Prod.*, 239, 117845.
- [19] Liu, S., Zhu, Q., Guan, Q., He, L., and Li, W., 2015, Bio-aviation fuel production from hydroprocessing castor oil promoted by the nickel-based bifunctional catalysts, *Bioresour. Technol.*, 183, 93–100.
- [20] Widiyati, A., Guspiani, G.A., Riady, J., Andreanto, R., Chaiunnisa, S.D., and Widayat, W., 2018, Preparation and characterization of NiMo/Al₂O₃ catalyst for hydrocracking processing, *E3S Web Conf.*, 31, 03011.
- [21] Eller, Z., Varga, Z., and Hancsók, J., 2016, Advanced production process of jet fuel components from technical grade coconut oil with special hydrocracking, *Fuel*, 182, 713–720.
- [22] Al-Muttaqii, M., Kurniawansyah, F., Prajitno, D.H., and Roesyadi, A., 2019, Bio-kerosene and bio-gasoil from coconut oils via hydrocracking process over Ni-Fe/HZSM-5 catalyst, *Bull. Chem. React. Eng. Catal.*, 14 (2), 309–319.
- [23] Widayat, W., Saputro, S.A., Ginting, E.M., Annisa, A.N., and Satriadi, H., 2017, Biofuel production by catalytic cracking method using Zn/HZSM-5 catalyst, *ARPN J. Eng. Appl. Sci.*, 12 (22), 6347–6351.
- [24] Boateng, L., Ansong, R., Owusu, W., and Steiner-Asiedu, M., 2016, Coconut oil and palm oil's role in nutrition, health and national development: A review, *Ghana Med. J.*, 50 (3), 189–196.
- [25] Lapari, S.S., Ramli, Z., and Triwahyono, S., 2015, Effect of different templates on the synthesis of mesoporous sodalite, *J. Chem.*, 2015, 272613.
- [26] Mofrad, A.M., Schellenberg, P.S., Peixoto, C., Hunt, H.K., and Hammond, K.D., 2020, Calculated infrared and Raman signatures of Ag⁺, Cd²⁺, Pb²⁺, Hg²⁺, Ca²⁺, Mg²⁺, and K⁺ sodalites, *Microporous Mesoporous Mater.*, 296, 109983.
- [27] Song, Q., Shen, J., Yang, Y., Wang, J., Yang, Y., Sun, J., Jiang, B., and Liao, Z., 2020, Effect of temperature on the synthesis of sodalite by crystal transition process, *Microporous Mesoporous Mater.*, 292, 109755.
- [28] Sari, M.E.F., Suprpto, S., and Prasetyoko, D., 2018, Direct synthesis of sodalite from kaolin: The influence of alkalinity, *Indones. J. Chem.*, 18 (4), 607–613.
- [29] Eterigho-Ikelegbe, O., Bada, S., Daramola, M.O., and Falcon, R., 2020, Synthesis of high purity hydroxy sodalite nanoparticles via pore-plugging hydrothermal method for inorganic membrane development: Effect of synthesis variables on crystallinity, crystal size and morphology, *Mater. Today: Proc.*, In Press, Corrected Proof.
- [30] Manique, M.C., Lacerda, L.V., Alves, A.K., and Bergmann, C.P., 2017, Biodiesel production using coal fly ash-derived sodalite as a heterogeneous catalyst, *Fuel*, 190, 268–273.
- [31] Lutz, W., 2014, Zeolite Y: Synthesis, modification, and properties—A case revisited, *Adv. Mater. Sci. Eng.*, 2014, 724248.
- [32] Güvenç, E., and Ahunbay, M.G., 2012, Adsorption of methyl tertiary butyl ether and trichloroethylene in MFI-type zeolites, *J. Phys. Chem. C*, 116 (41), 21836–21843.
- [33] Grieco, S.A., and Ramarao, B.V., 2013, Removal of TCEP from aqueous solutions by adsorption with zeolites, *Colloids Surf., A*, 434, 329–338.
- [34] Bolis, V., Busco, C., and Ugliengo, P., 2006, Thermodynamic study of water adsorption in high-silica zeolites, *J. Phys. Chem. B*, 110 (30), 14849–14859.
- [35] Pavlova, A., Trinh, T.T., van Santen, R.A., and Meijer, E.J., 2013, Clarifying the role of sodium in the silica oligomerization reaction, *Phys. Chem. Chem. Phys.*, 15 (4), 1123–1129.

- [36] Al-Ani, A., Haslam, J.J.C., Mordvinova, N.E., Lebedev, O.I., Vicente, A., Fernandez, C., and Zholobenko, V., 2019, Synthesis of nanostructured catalysts by surfactant-templating of large-pore zeolites, *Nanoscale Adv.*, 1 (5), 2029–2039.
- [37] Cho, K., Na, K., Kim, J., Terasaki, O., and Ryoo, R., 2012, Zeolite synthesis using hierarchical structure-directing surfactants: Retaining porous structure of initial synthesis gel and precursors, *Chem. Mater.*, 24 (14), 2733–2738.
- [38] Sotomayor, F.J., Cychosz, K.A., and Thommes, M., 2018, Characterization of micro/mesoporous materials by physisorption: concepts and case studies, *Acc. Mater. Surf. Res.*, 3 (2), 34–50.
- [39] Yurdakal, S., Garlisi, C., Özcan, L., Bellardita, M., and Palmisano, G., 2019, “(Photo)catalyst characterization techniques: Adsorption isotherms and BET, SEM, FTIR, UV-Vis, photoluminescence, and electrochemical characterizations” in *Heterogeneous Photocatalysis: Relationships with Heterogeneous Catalysis and Perspectives*, Eds. Marci, G., and Palmisano, L., Elsevier, 87–152.
- [40] Cychosz, K.A., and Thommes, M., 2018, Progress in the physisorption characterization of nanoporous gas storage materials, *Engineering*, 4 (4), 559–566.
- [41] Goronja, J.M., Janošević-Ležaić, A., Dimitrijević, B.M., Malenović, A., Stanisavljev, D., and Pejić, N., 2016, Determination of critical micelle concentration of cetyltrimethyl-ammonium bromide: Different procedures for analysis of experimental data, *Hem. Ind.*, 70 (4), 485–492.
- [42] Steigman, J., Cohen, I., and Spingola, F., 1965, Micelle formation by a long-chain cation surfactant in aqueous solutions of the lower quaternary ammonium bromides, *J. Colloid Sci.*, 20 (7), 732–741.
- [43] Vitagliano, V., D'Errico, G., Ortona, O., and Paduano, L., 2001, “Isothermal diffusion and intradiffusion in surfactant solutions” in: *Handbook of Surfaces and Interfaces of Materials: Biomolecules, Biointerfaces, and Applications*, Eds. Nalwa, H.S., Academic Press, Burlington, US, 545–611.
- [44] Goyal, P.S., Dasannacharya, B.A., Kelkar, V.K., Manohar, C., Srinivasa Rao, K., and Valaulikar, B.S., 1991, Shapes and sizes of micelles in CTAB solutions, *Physica B*, 174 (1-4), 196–199.
- [45] Thapa, U., Dey, J., Kumar, S., Hassan, P.A., Aswal, V.K., and Ismail, K., 2013, Tetraalkylammonium ion induced micelle-to-vesicle transition in aqueous sodium dioctylsulfosuccinate solutions, *Soft Matter*, 9 (47), 11225–11232.
- [46] Trisunaryanti, W., Triyono, T., Armunanto, R., Hastuti, L.P., Ristiana, D.D., and Ginting, R.V., 2018, Hydrocracking of α -cellulose using Co, Ni, and Pd supported on mordenite catalysts, *Indones. J. Chem.*, 18 (1), 166–172.
- [47] Efiyanti, L., and Trisunaryanti, W., 2014, Hidrorengkah katalitik minyak kulit biji jambu mete (CNSL) menjadi fraksi bensin dan diesel, *JPHH*, 32 (1), 71–81.
- [48] Khan, G.M., Arafat, S.M.Y., Reza, M.N., Razzaque, S.M., and Alam, M., 2010, Linde Type-A zeolite synthesis and effect of crystallization on its surface acidity, *Indian J. Chem. Technol.*, 17, 303–308.
- [49] Al Sofy, S.A.A., 2018, Fourier transformation infrared spectroscopic studies of acidity of NaH-13 X zeolites, *Al-Nahrain J. Eng. Sci.*, 21 (3), 428–435.
- [50] Barzetti, T., Selli, E., Moscotti, D., and Forni, L., 1996, Pyridine and ammonia as probes for FTIR analysis of solid acid catalysts, *J. Chem. Soc., Faraday Trans.*, 92 (8), 1401–1407.
- [51] Emdadi, L., Oh, S.C., Wu, Y., Oliaee, S.N., Diao, Y., Zhu, G., and Liu, D., 2016, The role of external acidity of meso-/microporous zeolites in determining selectivity for acid-catalyzed reactions of benzyl alcohol, *J. Catal.*, 335, 165–174.
- [52] Jiao, W., Su, J., Zhou, H., Liu, S., Liu, C., Zhang, L., Wang, Y., and Yang, W., 2020, Dual template synthesis of SAPO-18/34 zeolite intergrowths and their performances in direct conversion of syngas to olefins, *Microporous Mesoporous Mater.*, 306, 110444.
- [53] Vichaphund, S., Aht-ong, D., Sricharoenchaikul, V., and Atong, D., 2015, Production of aromatic compounds from catalytic fast pyrolysis of *Jatropha* residues using metal/HZSM-5 prepared by ion-exchange and impregnation methods, *Renewable Energy*, 79, 28–37.

- [54] Socci, J., Saraeian, A., Stefanidis, S.D., Banks, S.W., Shanks, B.H., and Bridgwater, T., 2019, The role of catalyst acidity and shape selectivity on products from the catalytic fast pyrolysis of beech wood, *J. Anal. Appl. Pyrolysis*, In Press, Corrected Proof.
- [55] Li, T., Cheng, J., Huang, R., Yang, W., Zhou, J., and Cen, K., 2016, Hydrocracking of palm oil to jet biofuel over different zeolites, *Int. J. Hydrogen Energy*, 41 (47), 21883–21887.
- [56] Xu, W., Chen, B., Jiang, X., Xu, F., Chen, X., Chen, L., Wu, J., Fu, M., and Ye, D., 2020, Effect of calcium addition in plasma catalysis for toluene removal by Ni/ZSM-5: Acidity/basicity, catalytic activity and reaction mechanism, *J. Hazard. Mater.*, 387, 122004.

Microwave-Assisted Preparation of Zinc-Doped β -Tricalcium Phosphate for Orthopedic Applications

Ali Taha Saleh^{1*} and Dheyaa Alameri²

¹Department of Chemistry, College of Science, University of Misan, Misan, Iraq

²Department of Physics, College of Science, University of Misan, Misan, Iraq

* Corresponding author:

email: ali_6222@yahoo.com.sg

Received: May 8, 2020

Accepted: May 30, 2020

DOI: 10.22146/ijc.55931

Abstract: A novel two-step methodology delivering zinc into the structure of β -tricalcium phosphate (β -TCP) has been investigated. Incorporating wet precipitation of calcium-deficient apatite [$\text{Ca}_{9-x}\text{Zn}_x(\text{HPO}_4)(\text{PO}_4)_5(\text{OH})$] ($x = 0.00$ – 1.00 mol) using a microwave-assisted process followed by two-hour calcination at 1000 °C has been conducted to generate a ratio of 1.48 of Zn doped β -TCP. The products were characterized by X-ray diffraction (XRD), Fourier-transform infrared (FTIR) spectrometer, and field emission scanning electron microscope (FESEM). Our results confirmed that the product was crystalline Zn^{2+} -doped β -tricalcium phosphate. The incorporation of Zn^{2+} into the β -TCP lattice resulted in a shifting of diffraction peaks to higher 2θ values, which were attributed to the substitution of larger-sized Ca^{2+} ions with smaller-sized Zn^{2+} ions. A reduction in the intensity of the XRD peaks was also observed due to the reduction in the degree of crystallinity of the samples. Lattice parameters along the a and c -axis showed a gradual decrease in length with an increase in the amount of Zn^{2+} doping. This decrease was attributed to the replacement of Ca^{2+} ion by the smaller-sized Zn^{2+} ions. The microstructure of the powders consisted of microscale aggregates fused together. EDX analysis of all samples showed that the Zn^{2+} doping had successfully taken place and the amount of Zn^{2+} present in the samples was in good agreement with the theoretical values.

Keywords: microwave-assisted; β -tricalcium phosphate; zinc; characterization

■ INTRODUCTION

Given the wide range of applications for bioceramics, there has been substantial and sustained interest in researching calcium phosphate (CaP)-based ceramics for use in medical applications, such as in orthopedic and dental use, over many years [1-3]. Similar in composition to bones, CaP-based ceramics are generally accepted as bone substitutes and to augment existing bone [4-6]. The medical applications are mainly focused on two CaP ceramics/CaPs, namely tricalcium phosphate/ $\text{Ca}_3(\text{PO}_4)_2$ (TCP), and hydroxyapatite $\text{Ca}_{10}(\text{PO}_4)_6(\text{OH})_2$ (HA), that possess key properties of resorption and surface induction of bone formation, respectively. Furthermore, ceramics based on HA, with superior osteoconductivity and excellent bone replacement abilities, are proven not to induce immune

responses that lead to toxicity and inflammation in response to their presence in the body [7-8].

CaPs are one of the most common and widely used bioceramic materials used to promote regeneration of bone as a result of its biocompatibility, osteoconductivity, osseointegration, and its similar profile to human bone and teeth [9-10]. There are two crystallographic forms of TCP, that is β -TCP and α -TCP [11-13]. Heating of the beta form of TCP above 1100 °C produces the alpha crystalline phase [14-15].

While both α and β TCP are chemically similar, their structures and physical properties, such as solubility, are different [16-17]. Consequently, a different performance would be obtained from its use in a biomedical situation, such as for use in dicalcium phosphate (DCP) cements [16,18-19]. Furthermore, the use of α -TCP is limited as it is resorbed quicker than new

bone [20]. In addition, a DFT assessment has demonstrated that β -TCP has more stability than α -TCP [17].

Manufacturing conditions for β -TCP offer a variety of methods that are conducted at lower temperatures than required for α -TCP. For example, β -TCP is formed by the thermal composition of Calcium-Deficient Hydroxy Apatitic CDHAp at temperatures over 800 °C [5]. Furthermore, at a temperature of as low as 50 °C, deposition in the organic medium will produce β -TCP [21-22]. β -TCP can also be produced directly from the calcining of the bone.

The excellent properties of β -TCP allow it to be used for many biomedical solutions, including bone cement [22], bioceramics, and dental applications [23]. The bone apatite is non-stoichiometric and comprises of multiple elements (Mg, Mn, Zn, and Na), compounds (HPO_4^{2-} and CO_3^{2-}) [5], and metal oxides (MgO and ZnO) [6-7]. These compounds are generally associated with multiple functions of bone apatite, including biological, mechanical, and physiochemical roles [24]. Vital for bone metabolism, zinc (Zn) is a key element that is necessary for bone growth and regeneration, and also osteoclast resorption [8,10-12]. However, the balance of Zn and other elements is vital, as increased levels of zinc and similar elements may induce unwanted consequences [9]. In this study, we describe a novel microwave-based method for doping ions that maintain a 1.48 ratio of Ca/P for producing Zn doped β -TCP. As far as we can ascertain, this is the first report of the insertion of zinc ions and its effect towards the β -TCP lattice. This study represents the first account of the influence of Zn ion substitution on the main parameters of the lattice structure. Specifically, we describe the extent of crystallization and the size of crystals in β -TCP. We propose that β -TCP is an appropriate transporter to moderate the release of zinc for biomedical use.

■ EXPERIMENTAL SECTION

Materials

Reagent grade chemicals and materials were acquired from Qrec (New Zealand), including calcium nitrate ($\text{Ca}(\text{NO}_3)_2 \cdot 4\text{H}_2\text{O}$), diammonium hydrogen

phosphate ($(\text{NH}_4)_2\text{HPO}_4$), ammonium hydroxide (NH_4OH), and zinc nitrate $\text{Zn}(\text{NO}_3)_2$.

Instrumentation

Physical characteristics, such as phase purity, lattice structure, and extent of crystallinity, were determined by X-ray diffractometry (Bruker D8 Advance XRD). The structural morphology and specific element composition were determined by field emission scanning electron microscopy (FESEM) (Zeiss-LEO 1530) in combination with (EDX) (Oxford instrument, Swift ED 3000). Lastly, the synthesis of functional phosphate groups was confirmed by the standard KBr pellet method using Fourier-transformed infrared spectrometry (FTIR) (Nicolet iS50).

Procedure

The phase purity, lattice specification, and level of crystallinity of the prepared samples were determined by analysis of five individual areas to obtain the average composition of elements via X-ray diffractometry. The XRD outcomes for the Zn doped β -TCP samples are shown in Fig. 1. The diffractogram shows the 2θ range between 20°–80° with 1-sec steps of 0.02° conducted at room temperature. All of the peaks detected from the synthesized β -TCP align with the β -TCP phase (JCPDS 09-0169), indicating that the crystalline phases are composed, in the majority, of β -TCP phases.

Crystallinity, denoted by X_c , is a measure of the proportion of crystalline β -TCP phase in the test volume of powdered sample, and is calculated as follows:

$$X_c = 1 - V_{300/0210} / I_{0210}$$

where I_{0210} is the intensity (0 2 1 0) reflection of the β -TCP structure, and $V_{300/0210}$ is the intensity of the hollow between the (3 0 0) and (0 2 1 0) reflections.

Unit cell software (program UnitCell-method of TJB Holland & SAT Redfern 1995) was used to define the lattice parameters.

As previously described [6], a microwave-assisted wet precipitation method was used to synthesize both β -TCP and Zn doped β -TCP with samples produced in molar ratios of Ca/P and (Ca + Zn)/P of 1.48, as seen in Table 1. In brief, a typical reaction to produce β -TCP

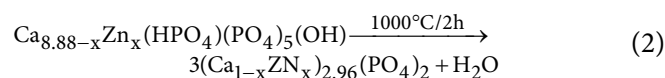
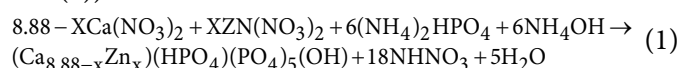
Table 1. Molar quantities of reactants used for the synthesis of β -TCP and Zn- β -TCP

Sample ID	Ca(NO ₃) ₂ ·4H ₂ O(mol)	(NH ₄) ₂ HPO ₄ (mol)	Zn(NO ₃) ₂ (mol)	Zn (wt.%)
β -TCP	8.88	6	0.00	-
1Zn- β -TCP	8.63	6	0.25	2.3
2Zn- β -TCP	8.38	6	0.50	6.4
3Zn- β -TCP	8.13	6	0.75	7.1
4Zn- β -TCP	7.88	6	1.00	8.6

required the dissolution of calcium nitrate (Ca(NO₃)₂·4H₂O) in 100 mL of double-distilled water, to which diammonium hydrogen phosphate (NH₄)₂HPO₄) was dropwise added with stirring. The resulting solution was adjusted to pH 7 with ammonium hydroxide (NH₄OH), prior to refluxing in a microwave (SHARP, model R-218LS) for 5 min at 800 W. The suspension was filtered before drying for 17 h at a temperature of 80 °C then calcined at 1000 °C for 2 h. Similarly, four concentrations of Zn-doped β -Ca₃(PO₄)₂ samples were prepared by the addition of a certain amount of zinc nitrate Zn(NO₃)₂ into the Ca(NO₃)₂·4H₂O solution. Details of the molar quantities of reactants series are shown in Table 1. In short, this method was the same, with only two exceptions. The successful incorporation of Zn ions required an initial Ca + Zn/P ratio of 1.48 to produce calcium-deficient apatite containing Zn²⁺ ion (Ca_{8.88-x}Zn_x)(HPO₄)(PO₄)₅(OH), Zn doped β -TCP (as described in Eq. (1) and (2)), and the pH was adjusted to 7.4 by the dropping (NH₄OH) solution.

■ RESULTS AND DISCUSSION

In this study, the synthesis of β -TCP through a microwave-assisted wet precipitation method involved the preparation of calcium-deficient apatite structure [Ca_{8.88}(HPO₄)(PO₄)₅(OH)] by exposing the reaction mixture with a Ca/P molar ratio of 1.48 to 800 W microwave radiations for 5 min. Calcination of this calcium deficient structure at 1000 °C for 2 h furnished the β -TCP. Zn doped β -TCP samples were prepared in the same manner except for the initial Ca + Zn/P ratio that was adjusted to 1.48 to ensure the successful incorporation of the Zn²⁺ ions into the structure (Eq. (1) and (2)).



where $x = [0.00-1.00]$

XRD analysis showed that the inclusion of Zn in the β -TCP lattice shifted the diffraction peaks to higher 2θ values and simultaneously caused a reduction in the intensity of the XRD peaks. These changes are likely a direct result of ionic radius difference, where the larger Ca²⁺ ions (0.99 Å) were replaced by smaller Zn²⁺ ions (0.74 Å), as shown in Fig. 1. The largest β -TCP phase peak corresponding to the (0 2 1 0) plane was observed at $2\theta = 31.392^\circ$. The diffractions of the (0 2 1 0) plane for samples 1 to 4 of the Zn- β -TCP were observed at $2\theta = 31.441, 31.690, 31.939, \text{ and } 32.188$, respectively, which is considered to be a consequence of the decreasing levels of crystallinity of these samples [17].

The formation of a solid solution of β -Ca₃(PO₄)₂ and Zn²⁺ ions can be confirmed since the XRD patterns did not exhibit any additional peaks. Applying the Debye-Scherrer equation generated an estimated crystallite size of 36 nm for β -TCP. As the level of Zn²⁺ doping increased, the a and c axes of the lattice structure decreased in length, which is attributed to the replacement of the Ca²⁺ ion by the smaller-size Zn²⁺ ion, as seen in Table 2 [25]. The decreases in the (4Zn- β -TCP) sample were 10.4375 to 10.4276 Å and 37.3645 to 37.2035 Å, for the a and c axes, respectively. The unit cell volume was also reduced from 3526.3572 to 3512.6672 Å as a consequence of the smaller size of Zn²⁺ in the structure [6,20] (Table 2).

The FTIR spectra, recorded at a wavenumber range of 400–4000 cm⁻¹ in transmission mode with 32 scans and 4 cm⁻¹ resolutions, of Zn²⁺ doped β -TCP calcined at 1000 °C is shown in Fig. 2. The bands observed at 548 and 610 cm⁻¹ correspond to the bending mode (ν_4) of the

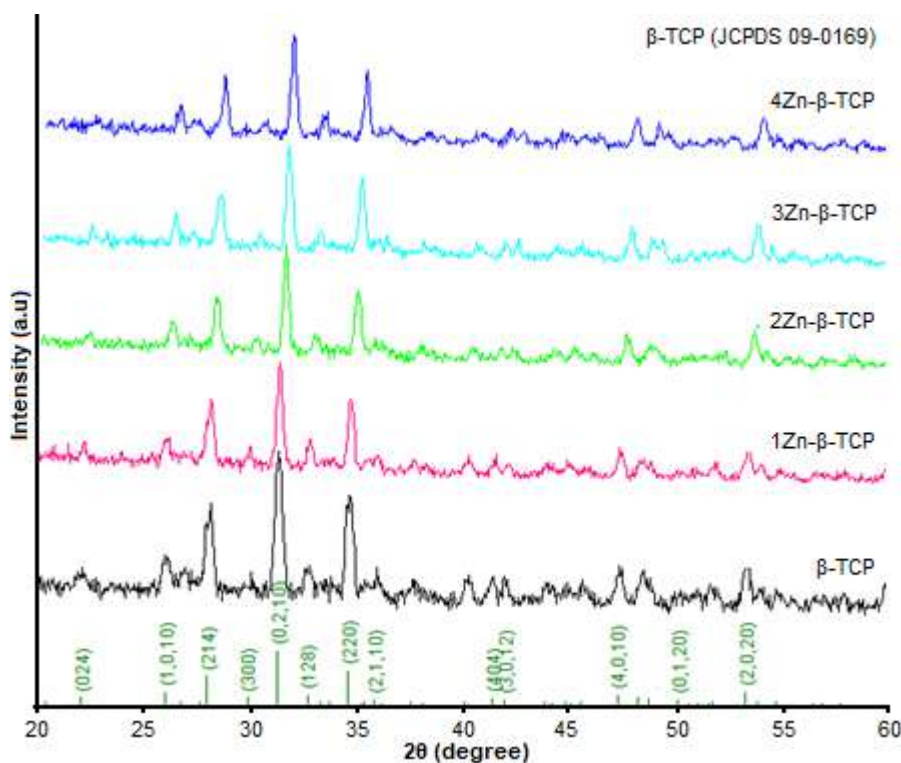


Fig 1. XRD pattern of a β -TCP and Zn- β -TCP

Table 2. Lattice parameters of β -TCP substituted with different amounts of Zn^{2+} ions and the degree of crystallinity

Samples	Chemical formula	Lattice parameter			Degree of crystallinity
		a-Axis (Å)	c-Axis (Å)	Cell Vol. (Å) ³	(% X _c)
β -TCP	Ca _{8.88} (PO ₄) ₆	10.4381	37.3943	3531.2669	85
1Zn- β TCP	Ca _{8.63} Zn _{0.25} (PO ₄) ₆	10.4375	37.3645	3526.3572	75
2Zn- β TCP	Ca _{8.38} Zn _{0.5} (PO ₄) ₆	10.4337	37.2474	3521.3914	79
3Zn- β TCP	Ca _{8.13} Zn _{0.75} (PO ₄) ₆	10.4309	37.2217	3518.4521	64
4Zn- β TCP	Ca _{7.88} Zn ₁ (PO ₄) ₆	10.4276	37.2035	3512.6672	59

O–P–O bonds, while the bands observed at 934, 1030, and 1124 cm^{-1} were attributable to the stretching modes (ν_3 and ν_1) of P–O. In addition, the bands at 1640 and 3445 cm^{-1} are a consequence of adsorbed water in the sample. The phosphate (PO_4^{3-}) band widened and shifted from 965 cm^{-1} to 940 cm^{-1} and 1123 cm^{-1} to 1157 cm^{-1} in response to the doping of Zn^{2+} ion into β -TCP. This finding is likely a result of the lower level of crystallinity, as observed in the XRD analysis (Fig. 1) [26]. We can ascertain that the samples were hydroxyapatite-free, given the lack of peak formation at 630 cm^{-1} and 3570 cm^{-1} [6].

The morphology and structure at the level of the elements were investigated by field emission scanning electron microscopy (FESEM) in combination with Energy

Dispersive X-Ray (EDX). Fig. 3 presents the FESEM micrographs of the pure β -TCP powders and Zn- β -TCP calcined at 1000 °C. Fig. 3(a) shows that the samples present as compact, irregular masses, with microporous surface structures (Fig. 3). Furthermore, the micrographs demonstrate a creation between particulates, a decrease in size, and an increase in Zn^{2+} content. Actual levels of Zn^{2+} doping, shown to have successfully obtained via EDX analysis, correlated with the calculated theoretical values (Table 3). Furthermore, the combined data from EDX and the changes to peak height, width, and shifting observed by XRD (Fig. 1) confirms that the substitution by Zn^{2+} ions occurred within the crystal structure and not only as surface absorption on β -TCP.

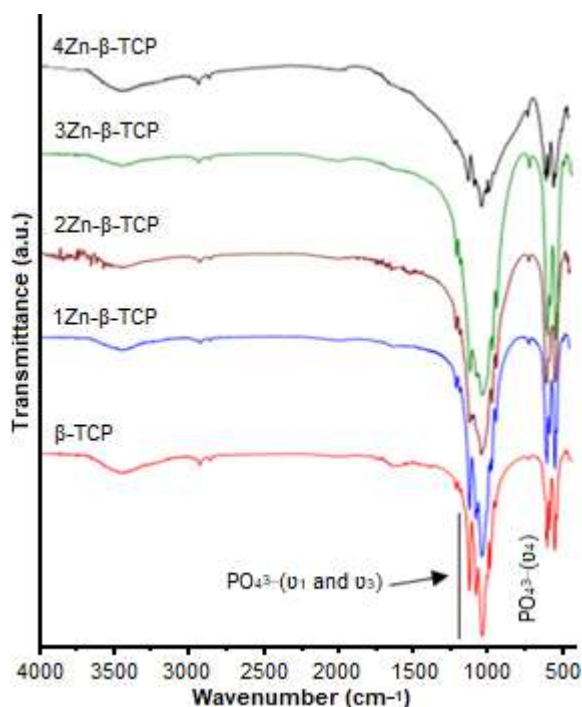


Fig 2. FTIR spectrum of β -TCP and Zn- β -TCP

Table 3. Chemical composition of β -TCP and Zn- β -TCP series by EDX

Samples	Theoretical ratios	Measured ratios
	Zn/Ca + Zn = X_{Zn}	Zn/Ca + Zn = X_{Zn}
β -TCP	0.000	0.000
1Zn- β -TCP	0.025	0.022
2Zn- β -TCP	0.050	0.049
3Zn- β -TCP	0.075	0.073
4Zn- β -TCP	0.100	0.097

CONCLUSION

Zinc is an essential trace element, which has been shown to promote bone formation both in vitro and in vivo, and β -TCP is an effective carrier of zinc. We successfully produced phases of Zn-doped β -TCP powders, using a microwave irradiation methodology. The integration of the zinc ions within the crystal structure was confirmed by EDX. The zinc ions decreased the crystallinity of the product as confirmed by XRD and FTIR spectroscopy. The overall cell volume decreased as a result of the substitution of the calcium ion by the smaller ionic radius of the zinc ion. The lattice parameter on a and c axes was also demonstrated to be smaller in the zinc-doped product. The changes in the morphology confirmed by FESEM showed a substantial change from densely packed nanoflakes to micron-sized microporous granules, which became smaller as zinc content in the doped β -TCP increased. We propose that the prepared powders will be widely useful and applicable to a range of biomedical applications.

REFERENCES

- [1] Zhou, H., Agarwal, A.K., Goel, V.K., and Bhaduri, S.B., 2013, Microwave-assisted preparation of magnesium phosphate cement (MPC) for orthopedic applications: A novel solution to the exothermicity problem, *Mater. Sci. Eng., C*, 33 (7), 4288–4294.

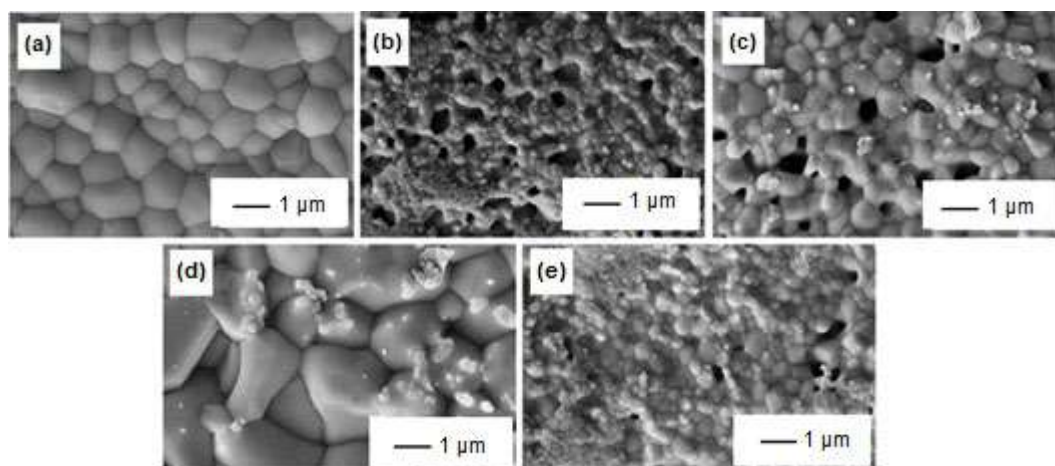


Fig 3. FESEM images showing the morphology of (a) β -TCP, (b) 1Zn- β -TCP, (c) 2Zn- β -TCP, (d) 3Zn- β -TCP, and (e) 4Zn- β -TCP calcination at 1000 °C

- [2] Taha, A., Akram, M., Jawad, Z., Alshemary, A.Z., and Hussain, R., 2017, Strontium doped injectable bone cement for potential drug delivery applications, *Mater. Sci. Eng., C*, 80, 93–101.
- [3] Gozalian, A., Behnamghader, A., Daliri, M., and Moshkforoush, A., 2011, Synthesis and thermal behavior of Mg-doped calcium phosphate nanopowders via the sol gel method, *Sci. Iran.*, 18 (6), 1614–1622.
- [4] Torres, P.M.C., Gouveia, S., Olhero, S., Kaushal, A., and Ferreira, J.M.F., 2015, Injectability of calcium phosphate pastes: Effects of particle size and state of aggregation of β -tricalcium phosphate powders, *Acta Biomater.*, 21, 204–216.
- [5] Zhang, J., Liu, W., Schnitzler, V., Tancret, F., and Bouler, J.M., 2014, Calcium phosphate cements for bone substitution: Chemistry, handling, and mechanical properties, *Acta Biomater.*, 10 (3), 1035–1049.
- [6] Saleh, A.T., Ling, L.S., and Hussain, R., 2016, Injectable magnesium-doped brushite cement for controlled drug release application, *J. Mater. Sci.*, 51 (16), 7427–7439.
- [7] Zhao, J., Zhao, J., Chen, J.H., Wang, X.H., Han, Z., and Li, Y., 2014, Rietveld refinement of hydroxyapatite, tricalcium phosphate and biphasic materials prepared by solution combustion method, *Ceram. Int.*, 40 (2) 3379–3388.
- [8] Xu, H.H.K., Carey, L.E., Simon, C.G., Takagi, S., and Chow, L.C., 2007, Premixed calcium phosphate cements: Synthesis, physical properties, and cell cytotoxicity, *Dent. Mater.*, 23 (4), 433–441.
- [9] Forouzandeh, A., Hesaraki, S., and Zamanian, A., 2014, The releasing behavior and in vitro osteoinductive evaluations of dexamethasone-loaded porous calcium phosphate cements, *Ceram. Int.*, 40 (1, Part A), 1081–1091.
- [10] Ribeiro, G.B.M., Trommer, R.M., dos Santos, L.A., and Bergmann, C.P., 2011, Novel method to produce β -TCP scaffolds, *Mater. Lett.*, 65 (2), 275–277.
- [11] Ma, H., Feng, C., Chang, J., and Wu, C., 2018, 3D-printed bioceramic scaffolds: From bone tissue engineering to tumor therapy, *Acta Biomater.*, 79, 37–59.
- [12] Han, B., Ma, P.W., Zhang, L.L., Yin, Y.J., Yao, K.D., Zhang, F.J., Zhang, Y.D., Li, X.L., and Nie, W., 2009, β -TCP/MCPM-based premixed calcium phosphate cements, *Acta Biomater.*, 5 (8), 3165–3177.
- [13] Pina, S., Torres, P.M.C., and Ferreira, J.M.F., 2010, Injectability of brushite-forming Mg-substituted and Sr-substituted α -TCP bone cements, *J. Mater. Sci. - Mater. Med.*, 21 (2), 431–438.
- [14] Yashima, M., Sakai, A., Kamiyama, T., and Hoshikawa, A., 2003, Crystal structure analysis of β -tricalcium phosphate $\text{Ca}_3(\text{PO}_4)_2$ by neutron powder diffraction, *J. Solid State Chem.*, 175 (2), 272–277.
- [15] Carrodegua, R.G., and De Aza, S., 2011, α -Tricalcium phosphate: Synthesis, properties, and biomedical applications, *Acta Biomater.*, 7 (10), 3536–3546.
- [16] Cacciotti, I., and Bianco, A., 2011, High thermally stable Mg-substituted tricalcium phosphate via precipitation, *Ceram. Int.*, 37 (1), 127–137.
- [17] Kannan, S., Goetz-Neunhoeffler, F., Neubauer, J., Pina, S., Torres, P.M.C., and Ferreira, J.M.F., 2010, Synthesis and structural characterization of strontium- and magnesium-co-substituted β -tricalcium phosphate, *Acta Biomater.*, 6 (2), 571–576.
- [18] Tamimi, F., Sheikh, Z., and Barralet, J., 2012, Dicalcium phosphate cements: Brushite and monetite, *Acta Biomater.*, 8 (2), 474–487.
- [19] Razali, N.N., and Sopyan, I., 2018, Incorporation of poly(vinyl alcohol) for the improved properties of hydrothermal derived calcium phosphate cements, *Indones. J. Chem.*, 18 (2), 354–361.
- [20] Alshemary, A.Z., Goh, Y.F., Shakir, I., and Hussain, R., 2015, Synthesis, characterization and optical properties of chromium doped β -Tricalcium phosphate, *Ceram. Int.*, 41 (1, Part B), 1663–1669.
- [21] Zhang, S., Zhang, X., Cai, Q., Wang, B., Deng, X., and Yang, X., 2010, Microfibrous β -TCP/collagen scaffolds mimic woven bone in structure and composition, *Biomed. Mater.*, 5 (6), 065005.

- [22] Tao, J., Pan, H., Zhai, H., Wang, J., Li, L., Wu, J., Jiang, W., Xu, X., and Tang, R., 2009, Controls of tricalcium phosphate single-crystal formation from its amorphous precursor by interfacial energy, *Cryst. Growth Des.*, 9 (7), 3154–3160.
- [23] Shayegan, A., Petein, M., and Vanden Abbeele, A., 2009, The use of beta-tricalcium phosphate, white MTA, white Portland cement and calcium hydroxide for direct pulp capping of primary pig teeth, *Dent. Traumatol.*, 25 (4), 413–419.
- [24] Gbureck, U., Barralet, J.E., Spatz, K., Grover, L.M., and Thull, R., 2004, Ionic modification of calcium phosphate cement viscosity. Part I: Hypodermic injection and strength improvement of apatite cement, *Biomaterials*, 25 (11), 2187–2195.
- [25] Torres, P.M.C., Abrantes, J.C.C., Kaushal, A., Pina, S., Döbelin, N., Bohner, M., and Ferreira, J.M.F., 2016, Influence of Mg-doping, calcium pyrophosphate impurities and cooling rate on the allotropic $\alpha \leftrightarrow \beta$ -tricalcium phosphate phase transformations, *J. Eur. Ceram. Soc.*, 36 (3), 817–827.
- [26] Dong, L., He, G., and Deng, C., 2016, Effects of strontium substitution on the phase transformation and crystal structure of calcium phosphate derived by chemical precipitation, *Ceram. Int.*, 42 (10), 11918–11923.

Stability, Hydrogen Bond Occupancy Analysis and Binding Free Energy Calculation from Flavonol Docked in DAPK1 Active Site Using Molecular Dynamic Simulation Approaches

Adi Tiara Zikri^{1,2}, Harno Dwi Pranowo^{1,2*}, and Winarto Haryadi²

¹Austrian-Indonesian Centre (AIC) for Computational Chemistry, Faculty of Mathematics and Natural Sciences, Universitas Gadjah Mada, Sekip Utara, Yogyakarta 55281, Indonesia

²Department of Chemistry, Faculty of Mathematics and Natural Sciences, Universitas Gadjah Mada, Sekip Utara, Yogyakarta 55281, Indonesia

* Corresponding author:

email: harnodp@ugm.ac.id

Received: May 13, 2020

Accepted: July 22, 2020

DOI: 10.22146/ijc.56087

Abstract: Stability and hydrogen bond occupancy analysis of flavonol derivative docked in DAPK1 have been carried out using molecular dynamics simulation approach. Six flavonol derivatives were docked in DAPK1 as protein target, then continued with molecular dynamics simulation. NVT and NPT ensembles were used to equilibrate the system, followed by 20 ns sampling time for each system. Structural stability and hydrogen bond occupancy analyses were carried out at the NVT ensemble, while free binding energy analysis was done at NPT ensemble. From all compounds used in this work, compound B (5,7-dihydroxy-2-(4-hydroxyphenyl)-6-methoxy-4H-chromen-4-one) has a similar interaction with reference ligands (quercetin, kaempferol, and fisetin), and the most stable complex system has the maximum RMSD around 2 Å. Compound C complex has -48.06 kJ/mol binding free energy score, and it was slightly different from quercetin, kaempferol, and fisetin complexes. Even though complex C has similar binding free energy with the reference compound, complex B shows more stable interactions due to their hydrogen bond and occupancy.

Keywords: flavonol; hydrogen bond occupancy; molecular dynamics simulation

■ INTRODUCTION

Flavonoids are one of the natural polyphenol produced from plant secondary metabolites. In human diet, they are most concentrated in fruits, vegetables, wines, tea, and cocoa. Flavonoids have substantial pharmacological properties such as antioxidant, anti-inflammatory, antiproliferative, photoprotective, depigmentation, and anti-aging, which are very useful for skin treatment [1-4]. Flavonoids are benzo- γ -pyrone derivative consisting of phenolic and pyran rings (Fig. 1).

There is some classification of flavonoids such as flavanols, flavone, flavonol, flavanone, isoflavone, and anthocyanidin. In this work, we use six flavonoids derivative from flavanol class with functional group shown in Table. 1.

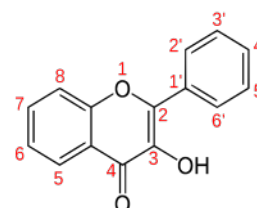
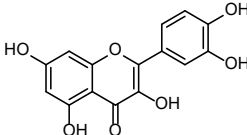
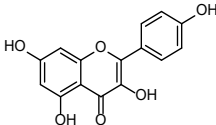
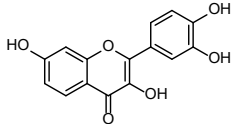
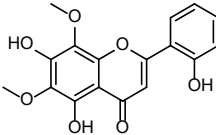
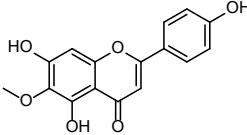
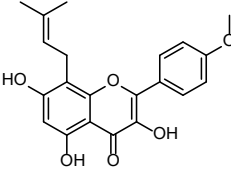


Fig 1. Flavonol analogue

Quercetin (3,3',4',5,7-pentahydroxyflavone), kaempferol (3,4',5,7-tetrahydroxyflavone), and fisetin (3,3',4',7-tetrahydroxyflavone) are flavonol derivative in a number of fruits and vegetables such as strawberry, apple, persimmon, grape, onion, and cucumber. Some studies have shown that fisetin has a beneficial effect against numerous diseases [5-8]. The hydroxy group in fisetin can be used as a radical scavenging agent. Quercetin

Table 1. Reference compounds and test compounds [4]

Compound	IUPAC name	Structure	Similarity score to quercetin
Quercetin	3,3',4',5,7-pentahydroxy-2-phenylchromen-4-one		1.000
Kaempferol	3,4',5,7-tetrahydroxy-2-phenylchromen-4-one		0.946
Fisetin	3,3',4',7-tetrahydroxy-2-phenylchromen-4-one		0.959
A	5,7-dihydroxy-2-(2-hydroxyphenyl)-6,8-dimethoxy-4H-chromen-4-one		0.785
B	5,7-dihydroxy-2-(4-hydroxyphenyl)-6-methoxy-4H-chromen-4-one		0.804
C	3,5,7-trihydroxy-2-(4-methoxyphenyl)-8-(3-methylbut-2-en-1-yl)-4H-chromen-4-one		0.768

has 5 hydroxy groups, which is more than fisetin and kaempferol. In some works [9-13], it is assumed that the hydroxy group has a positive correlation with radical scavenging agent activity. However, yet no accurate data to prove this hypothesis.

DAPK1 (Death-Associated Protein Kinase) is one of Ca^{2+} /calmodulin-dependent protein kinase that includes 160 kDA serine/threonine protein kinase [14]. In the earlier study, DAPK1 was identified as a mediator of γ -interferon-induced cell death, tumor suppressor, and autophagy activation [15-17]. The structure-binding affinity of DAPK1 and flavonol at the atomic-level could be explained using crystallographic analysis [16]. In the previous work [18], they investigated flavonoids activity in DAPK1 protein [19], but the dynamical properties of flavonol and its stability with water solvent to predict their

interaction have not been done yet.

Molecular docking is a computational chemistry method to observe the active site of a protein and its interaction with ligand [20-22]. Their interactions usually involve hydrogen bonds between the ligand and amino acid from protein [23-25]. In this work, flavonol derivatives are ligand, and DAPK1 is the target protein. Subsequently, molecular dynamics simulation is performed to investigate stability, hydrogen bond occupancy, and binding free energy of ligand and protein in an aqueous system.

■ COMPUTATIONAL METHODS

Molecular Docking

Death-associated protein kinase 1 (DAPK1) was obtained from RCSB protein databank with code: 5AUW.

The structure was prepared for re-docking using UCSF Chimera 1.12 [26]. Quercetin in DAPK1 was redocked using PLANTS 1.2 [27], followed by fisetin and kaempferol docking. Compound A, B, and C were obtained from drugbank.ca with a similarity structure score above 0.7 from quercetin structure [28]. Ten conformations were formed by this docking method. The conformation that has similar conformation with quercetin was used to analyze their interaction. The interaction of flavonoid compound and amino acid were shown in Table 2. The length of interaction was in the range of 1.6–2.4 Å. This distance indicated a hydrogen bond interaction was formed. Hydrogen bond analysis was generated using VMD [29].

Simulation Protocol

Structure and dynamics of flavonoid, protein, and water were studied using molecular dynamics (MD) simulation. A cubic simulation box [30] was built with a volume of 589.89 nm³. In this box, 1 flavonoid compound and 1 DAPK1 were immersed in 18,183 water molecules by employing SPC water model. GROMOS 54A7 force field [31-32] was used in this simulation method. Steepest descent algorithm was performed to obtain minimization energy followed by equilibration in NVT and NPT ensemble for 250 ps (125,000 steps) and 500 ps (250,000 steps) with a time step of 2 fs. A periodic boundary condition to all three-dimensional space was applied. To integrate the equation of motion, a leapfrog integrator was employed. The temperature was kept at 300.15 K using a V-rescale Berendsen thermostat [33]. The pressure was kept constant at 1 bar by employing Parrinello-Rahman pressure coupling. Particle Mesh Ewald (PME) [34], and it was used to correct the long electrostatic interaction as well. MD production data of simulation was generated in 20 ns (10,000,000 steps) for each simulation system. Binding Free energy was calculated using the Free Energy Perturbation (FEP) method for solvated complex [35-36].

RESULTS AND DISCUSSION

Molecular Docking Interaction

In this work, DAPK1 was downloaded from the protein data bank. Quercetin was already available inside

the DAPK1 active site. Redocking was performed to determine the ligand coordinate inside DAPK1. This coordinate was then used to perform molecular docking of reference and test compounds.

Fig. 2 shows the overlapping of all flavonol compounds in the DAPK1 active site. Quercetin and

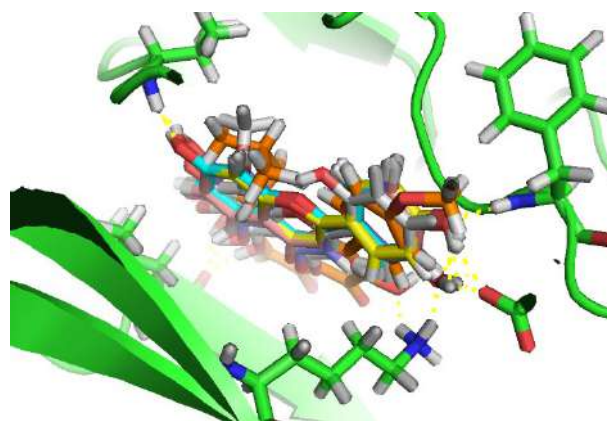


Fig 2. Visualization of flavonol inside DAPK 1 active site

Table 2. Residue interaction between flavonol and DAPK1

Compound	Residue interaction	Distance (Å)
Quercetin	VAL 95	2.1
	VAL 95	1.6
	PHE 159	2.1
	GLU 63	1.8
	GLU 63	1.6
	LYS 41	2.0
Kaempferol	VAL 95	2.1
	VAL 95	1.7
	PHE 159	2.1
	GLU 63	1.9
Fisetin	VAL 95	2.1
	VAL 95	1.7
	PHE 159	2.2
	GLU 63	1.7
	GLU 63	1.8
	LYS 41	1.9
A	VAL 95	2.1
	LEU 18	2.0
B	VAL 95	1.7
	VAL 95	2.1
	PHE 159	2.2
	GLU 63	1.7
	LEU 18	2.3
C	ASP 158	2.4
	LYS 41	2.0
	LEU 18	1.9

fisetin have 6 interactions with distance 1.6 to 2.4 Å (see Table 2).

The amino acids that interact with quercetin and fisetin are LYS 41, GLU 63, PHE 159, and VAL 95, where GLU63 takes a role as the amino acid with the closest interaction with quercetin and fisetin. Meanwhile, there are 4 interactions in kaempferol, which the interaction to LYS 41 and one interaction with GLU 63 is unidentified. Compound A, B, and C give significant difference interaction in molecular docking. New interactions are observed after docking process. LEU 18 forms an interaction to compound A, B, and C. Interaction with ASP 158 is only formed in compound C. Most of the interactions are unidentified because of the position of the hydroxy functional group. The more occurred interactions between flavonol will enhance the strength of flavonol binding. From the molecular docking data, compound B has nearly similar interaction to the DAPK1 active site with quercetin, kaempferol, and fisetin. The similar interaction between flavonol and DAPK1 indicates that the conformation structure of flavonol is not much different.

Molecular Dynamics Simulation

The stability of flavonol complexes with DAPK1 shown in Fig. 3. RMSDs of each system are combined to see the difference from that.

Kaempferol complex has the highest RMSD of all systems when the simulation time exceeds 15 ns. After 15 ns, RMSD values reach 3.8 Å, and this RMSD score

increased as the simulation run got longer. It indicates that the kaempferol complex has less stability during the simulation. For the fisetin complex, the RMSD value is relatively lower than other complexes, which assumed that the complex might be stable. However, some atoms in the fisetin complex that have high RMSF values make RMSD distance be fluctuating. The fisetin complex becomes less stable at simulation time 12 and 18 ns with RMSD value of 2.5 Å. The quercetin complex has constant RMSD with an average value of 3 Å. The highest RMSD value of 3.5 Å was found at 6 and 16 ns. From the new compound complexes, compound B complex has the lowest RMSD with an average value of 2.3 Å. The RMSD of compound B complex reaches its maximum value of 3.2 Å at 7, 12, 15, and 17 ns. Although the backbone distance of the compound B complex is getting higher, it immediately becomes lower at once. It indicates that compound B complex forms a stable complex with protein. This trend takes effect in hydrogen occupancy, where the more occupancy of complex, the more stable the complex is. For other complex, compound A is the least stable compare to those three compounds with an average RMSD value of 2.7 Å, followed by compound C complex with an average RMSD value of 2.5 Å.

Hydrogen bond occupancy of quercetin, fisetin, and kaempferol during simulation

Hydrogen bond occupancy is analyzed using VMD package and is depicted in Fig 4. Fisetin has 15 hydrogen

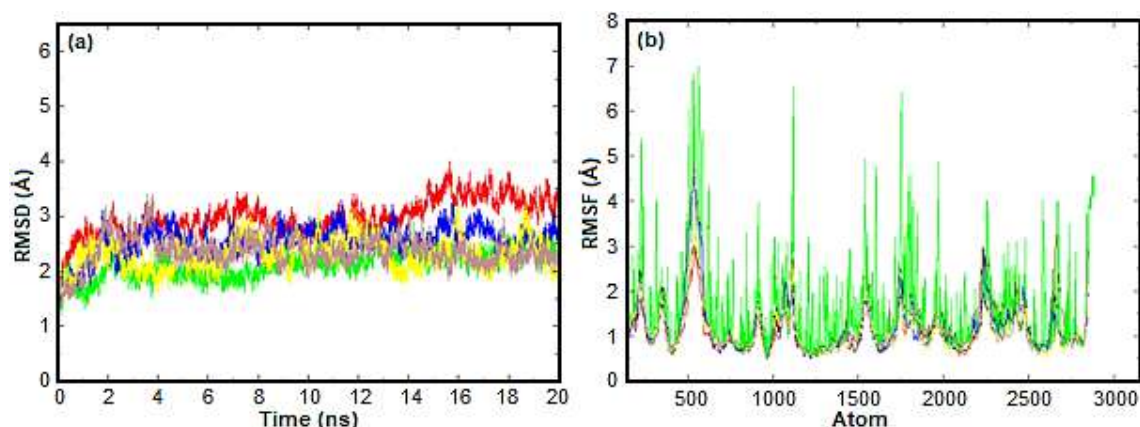


Fig 3. (a) RMSD and (b) RMSF of quercetin (black), kaempferol (red), fisetin (green), compound A (blue), compound B (yellow), compound C (brown) with DAPK1

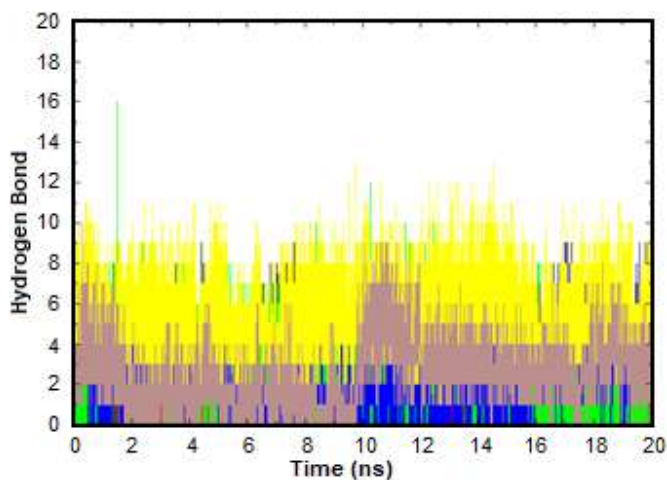


Fig 4. Hydrogen bond of quercetin (black), kaempferol (red), fisetin (green), compound A (blue), compound B (yellow), compound C (brown) with DAPK1 amino acid

bonds in a very short time at the beginning of simulation time, and compound B has the largest total hydrogen bond among test compounds. Compound A and compound C only have 8 hydrogen bonds. Table 3 lists the three most stable hydrogen bonds of each complex.

For reference compound, quercetin has 57 total hydrogen bonds with the highest occupancy of 26.04%, where quercetin forms the hydrogen bond with GLY 98.

Then 15.47% occupancy where quercetin plays a role as a donor to LEU 92 and 14.62% with LEU 144. Kaempferol has 39 total hydrogen bonds with the highest occupancy of 29.91%, where kaempferol and GLY 97 form hydrogen bonds. Then 19.15% occupancy where kaempferol plays a role as a donor to GLU 99 and 15.49% with ILE 76. Fisetin has 48 total hydrogen bonds with the highest occupancy of 24.61%, where fisetin has the role of a donor and GLY as an acceptor of hydrogen bond formation 19. Then 21.07% occupancy where fisetin plays a role as a donor to ASP 158 and 20.90% with GLU 140. For the test compound, compound A has 39 total hydrogen bonds with the highest occupancy of 49.69%, where compound A and GLU 99 have a high probability of forming hydrogen bonds. Then 29.71% occupancy where compound A plays a role as a donor to MET 143 and 26.87% where compound A form hydrogen bonds with ASP 158. Compound B has 30 total hydrogen bonds with the highest occupancy of 212.74%, where compound B has a high probability with GLU 63 to form hydrogen bonds. Then 132.71% occupancy where compound B plays a role as a donor to GLU 93, and 59.66% with compound B interact with PHE 159 and form hydrogen bonds. Compound C has 37 total hydrogen bond with the

Table 3. Hydrogen bond occupancy

Compound	Donor	Acceptor	Occupancy (%)
Quercetin	QUE 275-Side	GLY 98-Main	26.60
	QUE 275-Side	LEU 92-Side	15.47
	QUE 275-Side	LEU 144-Main	14.62
Kaempferol	GLY 97-Main	KAEM 275-Side	29.91
	KAEM 275-Side	GLU 99-Side	19.15
	KAEM 275-Side	ILE 76-Side	15.49
Fisetin	FISE 275-Side	GLY 19-Main	24.61
	FISE 275-Side	ASP 158-Side	21.07
	FISE 275-Side	GLU 140-Side	20.90
A	Com A 275-Side	GLU 99-Side	49.69
	Com A 275-Side	MET 143-Side	29.71
	ASP 158-Main	Com A 275-Side	26.87
B	Com B 275-Side	GLU 63-Side	212.74
	Com B 275-Side	GLU 93-Main	132.71
	PHE 159-Main	Com B 275-Side	59.66
C	Com C 275-Side	GLU 99-Side	135.91
	ASP 158-Main	Com C 275-Side	33.71
	GLU 99-Main	Com C 275-Side	19.57

Table 4. Free energies of hydrated ligands, protein – ligand complexes and binding energies of flavonol complexes

Compound	ΔG Complex (kJ/mol)	ΔG Ligand (kJ/mol)	ΔG Binding (kJ/mol)
Quercetin	-85.69	-46.39	-39.3
Kaempferol	-90.98	-45.06	-45.92
Fisetin	-110.36	-63.7	-46.66
Compound A	-87.01	-78.87	-8.14
Compound B	-78.48	-49.51	-28.97
Compound C	-92.39	-44.33	-48.06

highest occupancy 135.91% where compound A form hydrogen bond with GLU 99. Then 33.71% occupancy where compound C play a role as acceptor from ASP 158 and 19.57% where compound C form hydrogen bond with GLU 99. Hydrogen bond occupancy with a score of more than 100% indicates that more than one atom pair interacts to form hydrogen bonds. For reference compounds, fisetin has more hydrogen bond and hydrogen bond occupancy than test compounds. Meanwhile, compound B has less total hydrogen bond but has the highest hydrogen bond occupancy. This total hydrogen bond and hydrogen bond occupancy determine the stability of each system. The number and occupancy of hydrogen bonds are the keys to the interaction stabilization of protein – ligand complex.

Free binding energy

In the molecular dynamic simulation, free energy calculation takes a major role in determining the binding energy of ligand inside protein [24]. In this work, the free energy perturbation (FEP) method was used to calculate binding energy. In this approach, the dummy ligand is involved in changing partial charge in ligand into Lennard-Jones potential [30]. Lambda factor is used for smoothing the transition from dummy to the real ligand in the protein – ligand complex. In this work, the lambda value is ranging from 0 to 10. Binding Free energies score are presented in Table 4.

Compound C complex has the most negative binding free energy of -48.06 kJ/mol. This energy has slightly different from the reference compound, and it means that the interaction in compound C complex is the most stable interaction during simulation followed by protein - compound B complex. Although compound B complex has more hydrogen occupancy than compound

C complex as explained above, the compound C complex has more stable interaction than compound B. Compound A complex has the most positive binding energy, indicating that the interaction between compound C in DAPK1 active site is the weakest.

CONCLUSION

In this work, stability, hydrogen occupancy, and binding free energy of several protein – flavonol complexes had been investigated through molecular dynamics simulation. For 20 ns of production time, complex compound B has the most stable structure during simulation with RMSD value of 2.5 Å and the highest hydrogen bonds with 212.74% occupancy against GLU 63. Even though the binding energy of compound B is higher than compound C, compound B has an upper head against other test compounds in terms of stability and hydrogen bond occupancy.

REFERENCES

- [1] Heim, K.E., Tagliaferro, A.R., and Bobilya, D.J., 2002, Flavonoid antioxidant: Chemistry, metabolism and structure activity relationship, *J. Nutr. Biochem.*, 13 (10), 572–584.
- [2] Bucar, F., Wube, A., and Schmid, M., 2013, Natural product isolation – How to get from biological material to pure compounds, *Nat. Prod. Rep.*, 30 (4), 525–545.
- [3] Rha, C.S., Jeoung, H.W., Park, S., Lee, S., Jung, Y.S., and Kim, D.O., 2019, Antioxidative, anti-inflammatory, and anticancer effects of purified flavonol glycosides and aglycones in green tea, *Antioxidants*, 8 (8), 278.
- [4] Yokoyama, T., Kosaka, Y., and Mizuguchi, M., 2015, Structural insight into the interactions

- between death-associated protein kinase 1 and natural flavonoids, *J. Med. Chem.*, 58 (18), 7400–7408.
- [5] Chen, L.Z., Yao, L., Jiao, M.M., Shi, J.B., Tan, Y., Ruan, B.F., Hua, X., and Liu, 2019, Novel resveratrol-based flavonol derivatives: Synthesis and anti-inflammatory activity *in vitro* and *in vivo*, *Eur. J. Med. Chem.*, 175, 114–128.
- [6] Bai, J., Zhao, S., Fan, X., Chen, Y., Zou, X., Hu, M., Wang, B., Jin, J., Wang, X., Hu, J., Zhang, D., and Li, Y., 2019, Inhibitory effects of flavonoids on P-glycoprotein *in vitro* and *in vivo*: Food/herb-drug interactions and structure–activity relationships, *Toxicol. Appl. Pharmacol.*, 369, 49–59.
- [7] Serafini, M., Peluso, I., and Raguzzini, A., 2010, Flavonoids as anti-inflammatory agents, *Proc. Nutr. Soc.*, 69 (3), 273–278.
- [8] Bakoyiannis, I., Daskaloupoulou, A., Pergialiotis, V., and Perrea, D., 2019, Phytochemicals and cognitive health: Are flavonoids doing the trick?, *Biomed. Pharmacother.*, 109, 1488–1497.
- [9] Hatahet, T., Morille, M., Hommos, A., Devoisselle, J.M., Müller, R.H., and Bégu, S., 2016, Quercetin topical application, from conventional dosage forms to nanodosage forms, *Eur. J. Pharm. Biopharm.*, 108, 41–53.
- [10] Hatahet, T., Morille, M., Hommos, A., Dorandeu, C., Müller, R.H., and Bégu, S., 2016, Dermal quercetin smartCrystals®: Formulation development, antioxidant activity and cellular safety, *Eur. J. Pharm. Biopharm.*, 102, 51–63.
- [11] Rho, H.S., Ghimeray, A.K., Yoo, D.S., Ahn, S.M., Kwon, S.S., Lee, K.H., Cho, D.H., and Cho, J.Y., 2011, Kaempferol and kaempferol rhamnosides with depigmenting and anti-inflammatory properties, *Molecules*, 16 (4), 3338–3344.
- [12] Nagula, R.L., and Wairkar, S., 2019, Recent advances in topical delivery of flavonoids: A review, *J. Controlled Release*, 296, 190–201.
- [13] Fan, M., Ding, H., Zhang, G., Hu, X., and Gong, D., 2019, Relationships of dietary flavonoid structure with its tyrosinase inhibitory activity and affinity, *LWT Food Sci. Technol.*, 107, 25–34.
- [14] Tu, W., Xu, X., Pheng, L., Zhong, S., Zhang, W., Soudarapandian, M.M., Belal, C., Wang, M., Jia, N., Zhang, W., Lew, F., Chan, S.L., Chen, Y., and Lu, Y., 2010, DAPK1 interaction with NMDA receptor NR2B subunits mediates brain damage in stroke, *Cell*, 140 (2), 222–234.
- [15] Chen, Z., Picaud, S., Filippakopoulos, P., D’Angiolella, V., and Bullock, A.N., 2019, Structural basis for recruitment of DAPK1 to the KLHL20 E3 ligase, *Structure*, 27 (9), 1395–1404.e4.
- [16] Xu, L.Z., Li, B.Q., and Jia, J.P., 2019, DAPK1: A novel pathology and treatment target for Alzheimer’s disease, *Mol. Neurobiol.*, 56 (4), 2838–2844.
- [17] Park, G.B., Jeong, J.Y., and Kim, D., 2019, Gliotoxin enhances autophagic cell death via the DAPK1-TAp63 signaling pathway in paclitaxel-resistant ovarian cancer cells, *Mar. Drugs*, 17 (7), 412.
- [18] Wei, R., Zhang, L., Hu, W., Wu, J., and Zhang, W., 2019, Long non-coding RNA AK038897 aggravates cerebral ischemia/reperfusion injury *via* acting as a ceRNA for miR-26a-5p to target DAPK1, *Exp. Neurol.*, 314, 100–110.
- [19] Singh, P., and Talwar, P., 2017, Exploring putative inhibitors of Death Associated Protein Kinase 1 (DAPK1) via targeting Gly-Glu-Leu (GEL) and Pro-Glu-Asn (PEN) substrate recognition motifs, *J. Mol. Graphics Modell.*, 77, 153–167.
- [20] Shoichet, B.K., Kuntz, I.D., and Bodian, D.L., 1992, Molecular docking using shape descriptor, *J. Comput. Chem.*, 13 (3), 380–397.
- [21] Pinzi, L., and Rastelli, G., 2019, Molecular docking: Shifting paradigms in drug discovery, *Int. J. Mol. Sci.*, 20 (18), 4331.
- [22] Torres, P.H.M., Sodero, A.C.R., Jofily, P., and Silva Jr., F.P., 2019, Key topics in molecular docking for drug design, *Int. J. Mol. Sci.*, 20 (18), 4574.
- [23] Li, J., Fu, A., and Zhang, L., 2019, An overview of scoring functions used for protein–ligand interactions in molecular docking, *Interdiscip. Sci.*, 11 (2), 320–328.
- [24] Turkan, F., Cetin, A., Taslimi, P., Karaman, M., and Gulçin, I., 2019, Synthesis, biological evaluation and

- molecular docking of novel pyrazole derivatives as potent carbonic anhydrase and acetylcholinesterase inhibitors, *Bioorg. Chem.*, 86, 420–427.
- [25] Saikia, S., and Bordoloi, M., 2019, Molecular docking: Challenges, advances and its use in drug discovery perspective, *Curr. Drug Targets*, 20 (5), 501–521.
- [26] Pettersen, E.F., Goddard, T.D., Huang, C.C., Couch, G.S., Greenblatt, D.M., Meng, E.C., and Ferrin, T.E., 2004, UCSF Chimera-A visualization system for exploratory research and analysis, *J. Comput. Chem.*, 25 (13), 1605–1612.
- [27] Korb, O., Stützel, T., and Exner, T.E., 2006, PLANTS: Application of ant colony optimization to structure-based drug design, *Lect. Notes Comput. Sci.*, 4150, 247–258.
- [28] Hodgkin, E.E., and Richards, W.G., 1987, Molecular similarity based on electrostatic potential and electric field, *Int. J. Quantum Chem.*, 32 (S14), 105–110.
- [29] Humphrey, W., Dalke, A., and Schulten, K., 1996, VMD-Visual molecular dynamics, *J. Mol. Graphics*, 14 (1), 33–38.
- [30] de Leeuw, S.W., Perram, J.W., and Smith, E.R., 1980, Simulation of electrostatic systems in periodic boundary conditions. I. Lattice sums and dielectric constants, *Proc. R. Soc. London, Ser. A*, 373 (1752), 27–56.
- [31] Silva, T.F.D., Vila-Viçosa, D., Reis, P.B.P.S., Victor, B.L., Diem, M., Oostenbrink, C., and Machuqueiro, M., 2018, The impact of using single atomistic long-range cutoff schemes with the GROMOS 54A7 force field, *J. Chem. Theory Comput.*, 14 (11), 5823–5833.
- [32] Berendsen, H.J.C., van der Spoel, D., and van Drunen, R., 1995, GROMACS: A message-passing parallel molecular dynamics implementation, *Comput. Phys. Commun.*, 91 (1-3), 43–56.
- [33] van Gunsteren, W.F., and Berendsen, H.J.C., 1977, Algorithms for macromolecular dynamics and constraint dynamics, *Mol. Phys.*, 34 (5), 1311–1327.
- [34] Darden, T., York, D., and Pedersen, L., 1993, Particle mesh Ewald: An $N \cdot \log(N)$ method for Ewald sums in large systems, *J. Chem. Phys.*, 98 (12), 10089.
- [35] Bash, P.A., Singh, U.C., Langridge, R., and Kollman, P.A., 1987, Free energy calculation by computer simulation, *Science*, 236 (4801), 564–568.
- [36] Brandsal, B.O., Österberg, F., Almlöf, M., Feierberg, I., Luzhkov, V.B., and Åqvist, J., 2003, Free energy calculations and ligand binding, *Adv. Protein Chem.*, 66, 123–158.

Synthesis, Characterization and Antibacterial Properties of Nickel(II) Complex with 4-Aminoantipyrine Ligand

Yusica Amalia Rasyda¹, Mudhita Kusuma Widowati¹, Soerya Dewi Marliyana², and Sentot Budi Rahardjo^{2*}

¹Postgraduate Program, Department of Chemistry, Faculty of Mathematics and Natural Sciences, Sebelas Maret University, Jl. Ir. Sutami 36A, Surakarta 57126, Central Java, Indonesia

²Department of Chemistry, Faculty of Mathematics and Natural Sciences, Sebelas Maret University, Jl. Ir. Sutami 36A, Surakarta 57126, Central Java, Indonesia

* **Corresponding author:**

tel: +62-81228255050
email: sentotbr@staff.uns.ac.id

Received: June 2, 2020
Accepted: October 4, 2020

DOI: 10.22146/ijc.56552

Abstract: The novel nickel(II) complex has been successfully synthesized through the reaction of $\text{Ni}(\text{NO}_3)_2 \cdot 6\text{H}_2\text{O}$ with 4-aminoantipyrine (AAP) ligand in a 1:3 mole ratio of Ni(II) to AAP. The complex was characterized using UV-Vis, Atomic Absorption Spectroscopy (AAS), Infrared spectrophotometry (IR), Thermogravimetry/Differential Scanning Calorimetry (TG/DSC), conductivity, and magnetic susceptibility. The complex formula was $[\text{Ni}(\text{AAP})_3](\text{NO}_3)_2 \cdot 5\text{H}_2\text{O}$. AAP was a bidentate ligand that coordinated through the primary amine nitrogen and the carbonyl oxygen to the nickel ion. The electronic spectra of the complex displayed two peaks at 646 nm and 385 nm in accordance with the ${}^3\text{A}_{2g}(\text{F}) \rightarrow {}^3\text{T}_{1g}(\text{F})$ and ${}^3\text{A}_{2g}(\text{F}) \rightarrow {}^3\text{T}_{1g}(\text{P})$ transitions, respectively. This complex gave a paramagnetic property with the effective magnetic moment (μ_{eff}) of 2.96 BM and the shape of an octahedron. The antibacterial test of this complex showed higher activity than the metal and its free ligand.

Keywords: nickel(II); 4-aminoantipyrine; complex; antibacterial activity

■ INTRODUCTION

Antipyrine is a derivative of pyrazolone, a well-known compound used for analgesic and antipyretic drugs. The compound has several biologically active moieties in its structure, such as O, N, and methyl groups [1-3]. Aside from biological activities, antipyrine can form stable coordination bonds with central metal ions through carbonyl groups, such as the diketone complex containing transition metals, showing antibacterial activity [4]. Other transition metal complexes from antipyrine derivatives are also reported to be useful antimicrobial agents [4]. One antipyrine derivative, in particular, the 4-aminoantipyrine (AAP) has gained significant attention from medicinal chemists due to the various pharmacological activities such as antimicrobial, anti-inflammatory, analgesic, and antiviral [5-8]. The cyclic structure of AAP contains two nitrogen atoms, the carbonyl, and amine groups (shown in Fig. 1), impart an

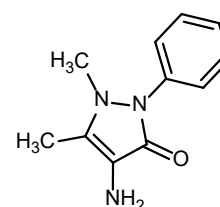


Fig 1. Structure of 4-aminoantipyrine (AAP)

enormous influence on its biological activity. Meanwhile, the carbonyl and amine groups in AAP act as donor ligands to form various coordination assemblies [9] and chelate structures. The organic-metal chelate formation imparts major changes in the ligand's biological properties and metal ions [10], thus making the study on AAP complexes fascinating. Biologically, the active central ion of complexes with stable and non-toxic is very noteworthy, in which nickel is one of the transition metals exhibiting such features, alongside antibacterial activity [11].

In this present work, the new nickel complex with AAP ligand was synthesized and characterized by various spectroscopic techniques. Further, the antibacterial activity of nickel(II), AAP, and the complex was studied using the diffusion method described by Kirby Bauer [12].

■ EXPERIMENTAL SECTION

Materials

All chemical substances and solvents used in the synthesis were of analytical grade and applied without purification. All chemicals such as $\text{Ni}(\text{NO}_3)_2 \cdot 6\text{H}_2\text{O}$, 4-aminoantipyrine, methanol, dimethyl sulfoxide (DMSO), nitric acid, $\text{CuSO}_4 \cdot 5\text{H}_2\text{O}$, $\text{FeSO}_4 \cdot 7\text{H}_2\text{O}$, $\text{CuCl}_2 \cdot 2\text{H}_2\text{O}$, $\text{CoCl}_2 \cdot 6\text{H}_2\text{O}$, $\text{CrCl}_3 \cdot 6\text{H}_2\text{O}$, and $\text{FeCl}_3 \cdot 6\text{H}_2\text{O}$ were procured from E. Merck.

Instrumentation

The electronic spectra of $\text{Ni}(\text{NO}_3)_2 \cdot 6\text{H}_2\text{O}$ and the complex in the methanol solution were analyzed on a UV-Vis Double Beam Lambda 25 Perkin Elmer spectrophotometer. The metal percentage in the complex sample was identified by the Atomic Absorption Spectrometer (AAS) Shimadzu AA-6650. The samples' IR spectra of KBr pellets were recorded on the Prestige-21 Shimadzu spectrophotometer for frequencies ranging from 400 to 4000 cm^{-1} . Thermal analysis (TG/DSC) was performed on a Diamond STA Linseis PT-1600 with a heating rate of 80 $^\circ\text{C}/\text{min}$. Molar conductivity was measured on a Jenway CE 4071 conductivity meter at 29 $^\circ\text{C}$, while the effective magnetic moment (μ_{eff}) was read on the Auto Sherwood Scientific 10169 Magnetic Susceptibility Balance at 26 $^\circ\text{C}$. The diameter of the inhibition zone of the antibacterial activity test was measured using an electronic digital caliper OEM 25363 with a precision of ± 0.025 mm.

Procedure

Synthesis of Ni(II)-4-aminoantipyrine

The complex was prepared by constantly stirring a 10 mL of the methanolic solution of AAP (0.610 g, 3 mmol) followed by the dropwise addition of $\text{Ni}(\text{NO}_3)_2 \cdot 6\text{H}_2\text{O}$ (0.291 g, 1 mmol) into 7 mL methanol. Thereafter, the admixture was refluxed for 3 h, and the resulting solution was evaporated into half of the initial volume. A final dark

green precipitate was obtained after three weeks. The solid was recrystallized with methanol, filtered, and dried under a vacuum desiccator (yield: 0.285 g, 32.29%). UV-Vis spectroscopy (in methanol, λ_{max} nm): 385, 729. Atomic Absorption spectroscopy (in HNO_3 , %): calc., for Ni: 6.65, found: Ni, 6.63. Selected FTIR (KBr, cm^{-1}): 3397 $\nu(\text{O-H})_{\text{H}_2\text{O}}$, 3198; 3108 $\nu(\text{N-H})$, 1616 $\nu(\text{C=O})$, 1384 cm^{-1} $\nu(\text{N-O})_{\text{NO}_3}$, 1353 $\nu(\text{C-N})$, 507 $\nu(\text{Ni-O})$, 431 $\nu(\text{Ni-N})$. Molar conductivity (in water, $\text{S cm}^2 \text{mol}^{-1}$): 234. μ_{eff} (BM): 2.93.

Antibacterial activity test

The antibacterial activities of the nickel salt, AAP, and the nickel complex were evaluated against *Escherichia coli* ATCC 25922 (Gram-negative) and *Staphylococcus aureus* ATCC 25923 (Gram-positive) using the agar disc diffusion method (Kirby-Bauer). Both bacterial suspensions in NaCl solution were inoculated on the surface of the Mueller Hinton agar media. Varying concentrations of the tested samples were prepared in DMSO at 62.5, 125, 250, 500, and 1000 ($\mu\text{g}/\text{mL}$). Each sample (10 μL) was transferred onto a 6 mm blank paper disc before transferring onto the agar media. For each assay, chloramphenicol and DMSO were used as the positive and negative control, respectively. The inhibition zones were observed by measuring the clear zone around the paper discs after incubation at 37 $^\circ\text{C}$ for 24 h, and the results were statistically analyzed with the Duncan Multiple Range Test (DMRT).

■ RESULTS AND DISCUSSION

The Ni(II) complex was synthesized in a 1:3 mole ratio of metal-ligand in methanol. AAP ligand was coordinated to nickel ion to form a 0.285 g dark green solid. The obtained complex was stable in air, non-hygroscopic, and completely soluble in water, methanol, ethanol, DMSO, and DMF.

Formation of The Complex

Ni(II)-AAP complex formation can be indicated by the shift of UV-Vis maximum wavelength of Ni(II) solution in methanol towards the lower wavelength, which can be seen in Fig. 2. Maximum wavelength of

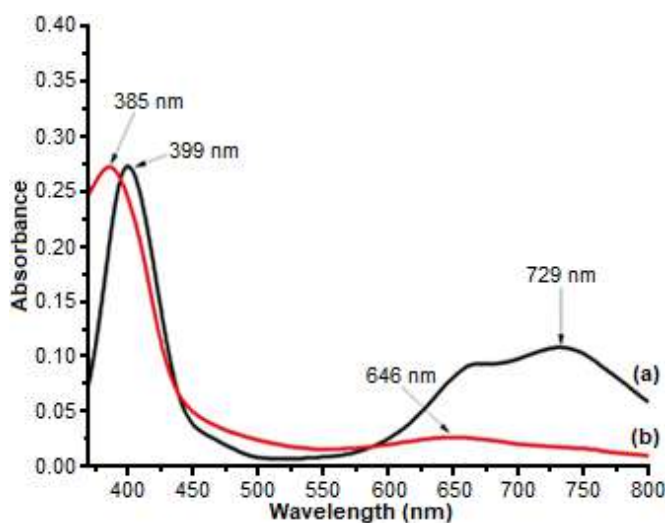


Fig 2. The electronic spectra of (a) $\text{Ni}(\text{NO}_3)_2 \cdot 6\text{H}_2\text{O}$ (0.0439 M) and (b) $\text{Ni}(\text{II})\text{-AAP}$ complex (0.0058 M) in methanol

$\text{Ni}(\text{NO}_3)_2 \cdot 6\text{H}_2\text{O}$ shifted from 729 and 399 nm to 646 and 385 nm, respectively in the complex. The shift showed that the AAP has stronger ligand field energy than H_2O , as expected from the chelate effects. Moreover, AAP can substitute the coordinated position of water molecules to nickel ion solution in methanol. Hence, the proposed formula of the complex is $\text{Ni}(\text{AAP})_n(\text{NO}_3)_2(\text{H}_2\text{O})_x$, in which the “n” and “x” values were based on metal content (AAS), conductance, and TG/DSC.

Nickel Ion Analysis by Atomic Absorption Spectroscopy (AAS)

The nickel content in the complex was found to be 6.63%, the result was compared to calculations of nickel contents of the various possible complex formula [13], as shown in Table 1. Thus, it can be estimated that the empirical formula of the nickel complex is $\text{Ni}(\text{AAP})_3(\text{NO}_3)_2(\text{H}_2\text{O})_n$ ($n = 4, 5, 6$).

Thermal Analysis by TG/DSC

TG/DSC analysis is necessary to determine the possibility of the attachment of water molecules to the central metal ion, either as lattice water or coordinated ligands. The TG and DSC curves in the thermogram of the complex (Fig. 3) shows the occurrence of endothermic reaction at 85.4 °C (DSC) in the temperature range 52.9–119.3 °C, with a one-step 11.04% weight loss (TG) that was equivalent to the release of five water molecules. It was reported that the degradation stage at 30–130 °C involves the release of water molecules as crystalline water, which are not coordinated [14], whereas the coordinated water molecules will be degraded at 150–200 °C [15]. Hence, the nickel complex has five water molecules as hydrates or lattice water, and it can be approximated that the formula of this complex is $\text{Ni}(\text{AAP})_3(\text{NO}_3)_2 \cdot 5\text{H}_2\text{O}$. The reduction of mass continued up to 560 °C, as expected for the decomposition of organic compounds. The complex was seen to achieve stability at temperatures

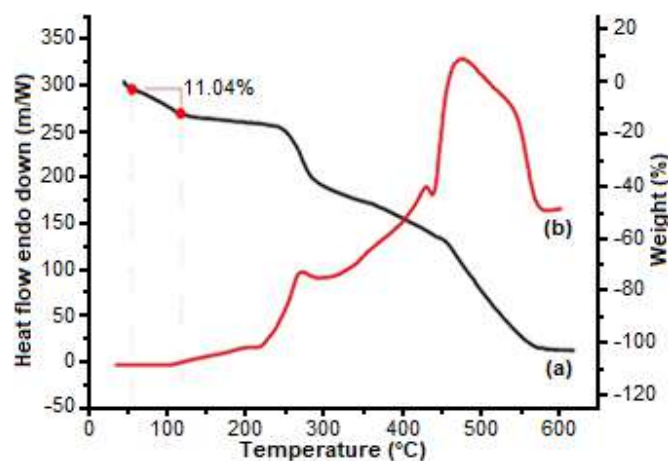


Fig 3. Thermograms of (a) TG and (b) DSC of the $\text{Ni}(\text{II})\text{-AAP}$ complex

Table 1. Nickel content in the complex and the plausible complex formula

No	Empirical Formula	Mr	Nickel content theoretically (%)	AAS Result (%)
1	$\text{Ni}(\text{AAP})_3(\text{NO}_3)_2(\text{H}_2\text{O})_4$	864.48	6.79	
2	$\text{Ni}(\text{AAP})_3(\text{NO}_3)_2(\text{H}_2\text{O})_5$	882.50	6.65	6.63
3	$\text{Ni}(\text{AAP})_3(\text{NO}_3)_2(\text{H}_2\text{O})_6$	900.51	6.51	

higher than 550 °C due to the production of NiO residue (8.53%). The amount of nickel oxide residue was found to be in accordance with the nickel content found in the complex from the AAS analysis results.

Infrared Spectra Analysis

Infrared spectra of the free ligand and Ni(II)-complex (Fig. 4) were recorded to determine the functional groups of ligand that were bound to the metal ion, and their prominent infrared spectra are shown in Table 2. The complex's infrared spectrum exhibited new broadband at 3397 cm⁻¹, which is ascribed to the $\nu(\text{O-H})$ group of lattice water [16]. Also, a new band of the nitrate group as counterions appeared at 1384 cm⁻¹ [17]. Bands corresponding to the $\nu(\text{N-H})$ at 3198 cm⁻¹; 3108 cm⁻¹ and $\nu(\text{C=O})$ at 1616 have shifted to lower wavenumbers compared to its free ligand. This result is the consequence of the shortening of bonds of N-H and C-O. This showed

that the nitrogen of amino groups and oxygen of carbonyl group in the AAP ligand was coordinated to the central ion [18-19]. This coordination was strengthened by the existence of bands at 507 cm⁻¹ and 431 cm⁻¹ which represented the Ni-O and Ni-N, respectively [20].

Electrical Conductivity Analysis

The complex electrical conductivity measurement is applied to determine the position of nitrate ions, which can act as ligands or counterions, by comparing to the electrical conductivity of the standard solutions of known metal salts shown in Table 3. The result showed that the complex solution in water was an electrolyte with a molar conductance of 234 S cm² mol⁻¹. The value is also in the range of the standard solutions with a cation-anion charge ratio of 2:1. It signified that the nitrate ions acted as uncoordinated counterions. Thus,

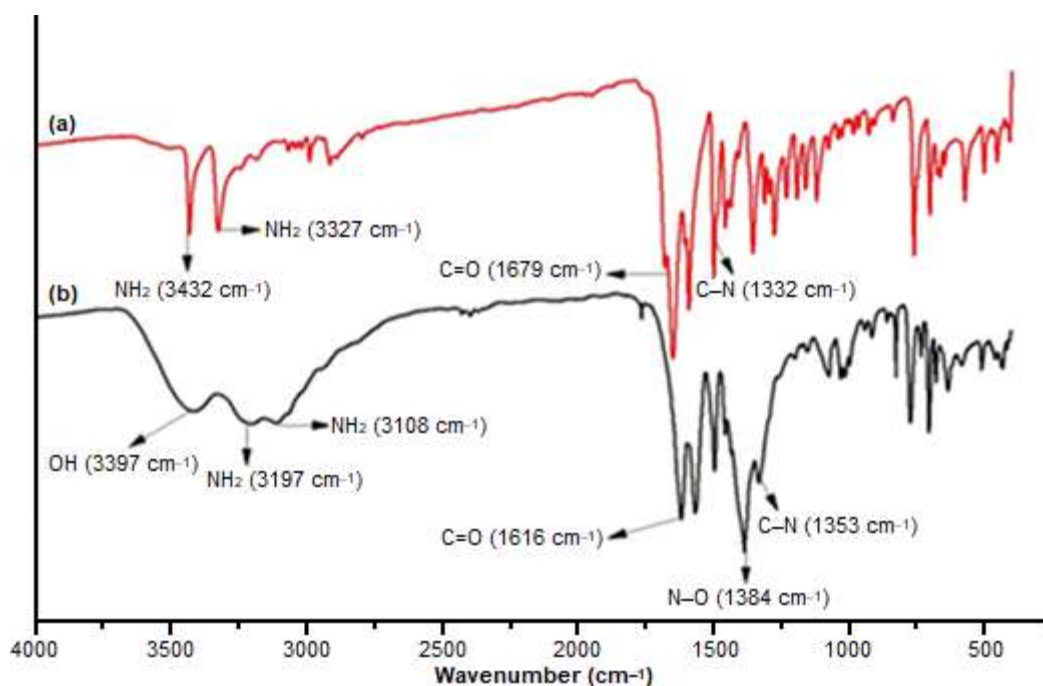


Fig 4. FTIR spectra of the (a) AAP and (b) Ni(II)-AAP complexes

Table 2. Infrared spectra absorption data of the AAP and its nickel complexes

No	Compound	IR absorption (cm ⁻¹)					
		$\nu(\text{O-H})$	$\nu(\text{N-H})$	$\nu(\text{C=O})$	$\nu(\text{N-O})$	$\nu(\text{Ni-O})$	$\nu(\text{Ni-N})$
1	AAP	-	3432 _{sym} 3327 _{asym}	1679	-	-	-
2	Ni(II)-AAP	3397	3198	1616	1384	507	431

Table 3. Electrical conductivity of metal salts standard and nickel(II) complex in water

No	Solution	Λ_m (S cm ² mol ⁻¹)	Cation:anion charge
1	Water	4	-
2	CuSO ₄ ·5H ₂ O	185	1:1
3	FeSO ₄ ·6H ₂ O	196	1:1
4	Co(NO ₃) ₂ ·6H ₂ O	235	2:1
5	Ni(NO ₃) ₂ ·6H ₂ O	248	2:1
6	CrCl ₃ ·6H ₂ O	363	3:1
7	Ni(II)-AAP	234	2:1

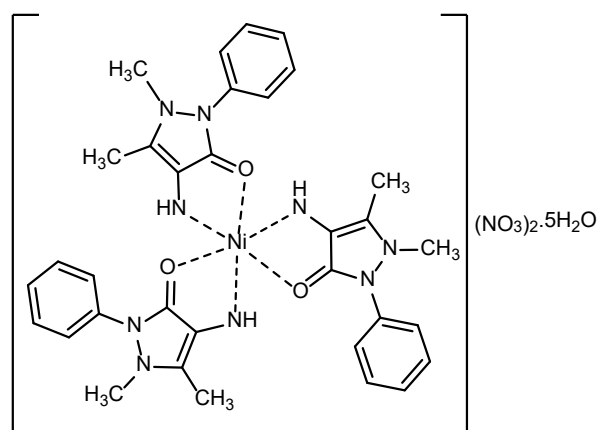
the complex could dissociate into [Ni(AAP)₃]²⁺ and two NO₃⁻ ions in solution, and it reinforced the prediction of complex formula into [Ni(AAP)₃](NO₃)₂·5H₂O, namely trisaminoantipyrinenickel(II) nitrate pentahydrate.

Electronic Spectra

Two spectral peaks that appeared at 646 nm (15468 cm⁻¹) and 385 (25940 cm⁻¹) (Fig. 2) were in accord with the transitions of ³A_{2g}(F) → ³T_{1g}(F) and ³A_{2g}(F) → ³T_{1g}(P), respectively, which was indicative of an octahedral geometry [21]. Additionally, the molar absorptivity range of the complex electronic spectrum in the range of 1–100 L mol⁻¹ cm⁻¹ (4.4 and 45.8 L mol⁻¹ cm⁻¹) was characteristic of an octahedral Ni(II) complex [22]. Thus, it was evident that the complex formed an octahedral environment among the Ni(II) central ion.

Magnetic Study

Measurement of the magnetic moment showed the nickel magnetic property of the nickel complex, which effective magnetic moment (μ_{eff}) value was 2.93 BM. It indicated that the paramagnetic nickel complex has two unpaired electrons [23]. Meanwhile, the μ_{eff} value slightly differed compared to the spin only moment of 2.83 BM due to the donation of orbitals in the metal ion. Other contributing influences include corrections by temperature and diamagnetic factors. The magnetic moments of octahedral complexes in the range of 2.9 to 3.4 BM [23–25] were also supported by the Ni(II)-AAP complex being a six coordinated octahedral structure [26]. This value was in agreement with the electronic spectrum of the Ni(II)-AAP complex. Based on the characterization data, a complex structure with facial isomers was proposed (Fig. 5). The complex is the most

**Fig 5.** Suggested structure of the [Ni(AAP)₃](NO₃)₂·5H₂O

preferred because it has three O–M–N bonding configurations with opposite electronic characteristics when interacting with the same metal d orbital. Therefore, such coordination avoided the reduction in electron delocalization and also contributed to a stronger M–ligand bond [27].

Antibacterial Activity

The antibacterial activity assays of the complex, metal salt, and the free ligand were carried out against *S. aureus* (Gram-positive bacterial) and *E. coli* (Gram-negative bacterial) using the agar diffusion method. The inhibition of bacterial growth is demonstrated by the formation of a clear zone around the paper disc, and results of the inhibition zone are collected in Table 4. The was shown that all compounds could inhibit the growth of both types of bacteria. The diameter of AAP and Ni(NO₃)₂·6H₂O inhibition zones against *E. coli* bacteria was smaller than that of *S. aureus*. This was due to differences in their membrane composition, in which

Table 4. Antibacterial result of AAP, nickel salt, and its complex

No	Compounds	Concentration ($\mu\text{g mL}^{-1}$)	The diameter of Inhibition zone (mm)	
			<i>E. coli</i> (G-)	<i>S. aureus</i> (G+)
1	AAP	62.5	6.21	6.85
		125	6.25	7.01
		250	6.63	7.12
		500	6.73	7.18
		1000	6.93	7.21
2	$\text{Ni}(\text{NO}_3)_2 \cdot 6\text{H}_2\text{O}$	62.5	6.71	7.19
		125	6.95	7.38
		250	7.14	7.57
		500	7.23	7.77
		1000	7.36	8.00
3	$[\text{Ni}(\text{AAP})_3](\text{NO}_3)_2 \cdot 5\text{H}_2\text{O}$	62.5	8.59	8.13
		125	8.70	8.22
		250	8.78	8.33
		500	8.89	8.88
		1000	8.96	8.95
4	DMSO	0	0	0
5	Chloramphenicol	30	27.12	28.74

E. coli has a more complex cell membrane structure [28-29]. However, this was not the case for the complex, which has a smaller inhibition zone difference between both bacteria. Their antibacterial activity was found to increase with increasing concentration [4], but the complex exhibited a higher inhibitory activity than the metal and free ligand, as shown in the following order: nickel complex > nickel salt > AAP.

Duncan Multiple Range Test (DMRT) was performed on the inhibitory diameters of all compounds against both bacteria at varying concentrations of 62.5; 125; 250; 500 and 1000 $\mu\text{g/mL}$. Each compound showed significance values of $p < 0.05$, in which the mean results were significantly different from each other for the inhibition of bacterial growth by the nickel complex, nickel salt, and AAP ligand. In addition, it also showed a significant increase in the antibacterial activity when Ni(II) and AAP were complexed into $[\text{Ni}(\text{AAP})_3](\text{NO}_3)_2 \cdot 5\text{H}_2\text{O}$.

The nickel complex exhibited the highest antibacterial activity due to complexation with AAP. Results of the inhibitory tests showed that the metal and ligand worked in synergy after complexing. AAP is a bidentate ligand chelated with the metal ion and deactivated various enzyme cells which roles are

important in bacterial metabolism [30]. The chelation effect can be described by Tweedy's chelation theory that explains the chelate can reduce nickel polarity [31]. This, consequently, increases the lipophilic character of the metal ion, which facilitates the penetration of the complex through the lipid membrane [32]. Thus, the complex can disrupt the synthesis or other biological processes in bacteria, for instance, deactivating enzymes and also breaking down bacterial cells [33] and ultimately inhibit bacterial growth.

■ CONCLUSION

In this work, the nickel(II) complex, $[\text{Ni}(\text{AAP})_3](\text{NO}_3)_2 \cdot 5\text{H}_2\text{O}$, namely trisaminoantipyrine nickel(II) nitrate pentahydrate, was synthesized and characterized. The ligand to metal ion binding mode was confirmed by IR studies, also supported by TG/DSC and electrical conductivity studies. AAP was coordinated to nickel ion through carbonyl oxygen and amino nitrogen. The octahedral geometry of the Ni(II)-AAP complex was corroborated by electronic spectra and magnetic studies, in which the complex was paramagnetic and displayed electrolyte property. The complex exhibited the highest inhibitory zones due to the chelating effect.

The coordination of AAP with nickel(II) seems to be promising to increase the antibacterial activity.

■ ACKNOWLEDGMENTS

The authors would like to acknowledge the Sebelas Maret University for financial support through the Hibah Penelitian Fundamental PNBPUNS.

■ AUTHOR CONTRIBUTIONS

YAR, MKW, SDM, and SBR conceived and planned the experiment. YAR and MKW contributed to sample preparation and conducted the experiment. YAR, SDM, and SBR contributed to the interpretation of the results. YAR and SBR took the lead in writing the manuscript. All authors agreed to the final version of this manuscript.

■ REFERENCES

- [1] Poormohammadi, E.B., Behzad, M., Abbasi, Z., and Astaneh, S.D.A., 2020, Copper complexes of pyrazolone-based Schiff base ligands: Synthesis, crystal structures and antibacterial properties, *J. Mol. Struct.*, 1205, 127603.
- [2] Selvi, E.T., and Mahalakshmi, S., 2017, Synthesis and characterisation of a new heterocyclic Schiff base ligand derived from 4-aminoantipyrine, *Int. J. Adv. Res. Dev.*, 2 (2), 51–56.
- [3] Singh, G., Satija, P., Singh, B., Sinha, S., Sehgal, R., and Sahoo, S.C., 2020, Design, crystal structures and sustainable synthesis of family of antipyrine derivatives: Abolish to bacterial and parasitic infection, *J. Mol. Struct.*, 1199, 127010.
- [4] Masruri, M., Amini, R.W., and Rahman, M.F., 2016, Potassium permanganate-catalyzed alpha-pinene oxidation: Formation of coordination compound with zinc(II) and copper(II), and growth inhibition activity on *Staphylococcus aureus* and *Escherichia coli*, *Indones. J. Chem.*, 16 (1), 59–64.
- [5] Sageer, A.G., Saheeb, A.A., and Mekky, A.H., 2020, Microwave synthesis, characterization of some novel curcumin compound and its metal complexes with antimicrobial, antioxidant studies, *Int. J. Pharm. Res.*, 12 (1), 1092–1103.
- [6] Teran, R., Guevara, R., Mora, J., Dobronski, L., Barreiro-Costa, O., Beske, T., Pérez-Barrera, J., Araya-Maturana, R., Rojas-Silva, P., Poveda, A., and Heredia-Moya, J., 2019, Characterization of antimicrobial, antioxidant, and leishmanicidal activities of Schiff base derivatives of 4-aminoantipyrine, *Molecules*, 24 (15), 2696.
- [7] Kumar, K.V., Sunand, K., Ashwini, K., Kumar, P.S., Vishnu, S., and Samala, A., 2017, Synthesis characterization and antibacterial studies of 4-aminoantipyrine Schiff's bases, *Int. J. Appl. Pharm. Sci. Res.*, 2 (1), 8–14.
- [8] Mohammed, L.A., Mehdi, R.T., and Ali, A.A.M., 2018, Synthesis and biological screening of the gold complex as anticancer and some transition metal complexes with new heterocyclic ligand derived from 4-aminoantipyrine, *Nano Biomed. Eng.*, 10 (3), 199–212.
- [9] Singh, M.K., Roy, S., Hansda, A., Kumar, S., Kumar, M., Kumar, V., Peter, S.C., and John, R.P., 2017, Synthesis, characterization and antibacterial activity evaluation of trinuclear Ni(II) complexes with N-substituted salicylhydrazide ligands, *Polyhedron*, 126, 100–110.
- [10] Jayalakshmi, R., Priya, D.D., Jayakkumar, V., and Rajavel, R., 2017, Synthesis and characterization of 4-aminoantipyrine based Schiff base complexes: antimicrobial, cytotoxicity and DNA cleavage studies, *Int. J. Eng. Res. Technol.*, 6 (8), 1–9.
- [11] Soltani, S., Akhbari, K., and White, J., 2020, Synthesis, crystal structure and antibacterial activity of a homonuclear nickel(II) metal-organic nanosupramolecular architecture, *Polyhedron*, 176, 114301.
- [12] Sarker, D., Hossen, M.F., Kudrat-E-Zahan, M., Haque, M.M., Zamir, R., and Asraf, M.A., 2020, Synthesis, characterization, thermal analysis and antibacterial activity of Cu(II) and Ni(II) complexes with thiosemicarbazone derived from thiophene-2-aldehyde, *J. Mater. Sci. Res. Rev.*, 5 (2), 15–25.
- [13] Syaima, H., Rahardjo, S.B., and Zein, I.M., 2018, Synthesis and characterization of diranitidinecopper(II) sulfatedehydrate, *IOP Conf. Ser.: Mater. Sci. Eng.*, 349 (1), 012025.

- [14] Wang, X., Gao, C.Q., Gao, Z.Y., Wu, B.L., and Niu, Y.Y., 2018, Synthesis, crystallographic and spectral studies of homochiral cobalt(II) and nickel(II) complexes of a new terpyridylaminoacid ligand, *J. Mol. Struct.*, 1157, 395–363.
- [15] Anupama, B., Sunita, M., Shiva Leela, D., Ushaiah, B., and Gyana Kumari, C., 2014, Synthesis, spectral characterization, DNA binding studies and antimicrobial activity of Co(II), Ni(II), Zn(II), Fe(III) and VO(IV) complexes with 4-aminoantipyrine Schiff base of ortho-vanillin, *J. Fluoresc.*, 24 (4), 1067–1076.
- [16] Sinthuja, S.A., Shaji, Y.C., and Rose, G.L., 2018, Synthesis, characterization and evaluation of biological properties of transition metal chelates with Schiff base ligands derived from glutaraldehyde with L-leucine, *Int. J. Sci. Res. Sci. Technol.*, 4 (2), 587–593.
- [17] Tyagi, M., Chandra, S., Tyagi, P., Akhtar, J., Kandan, A., and Singh, B., 2017, Synthesis, characterization and anti-fungal evaluation of Ni(II) and Cu(II) complexes with a derivative of 4-aminoantipyrine, *J. Taibah Univ. Sci.*, 11 (1), 110–120.
- [18] de Souza, Í.P., Machado, B.P., de Carvalho, A.B., Binatti, I., Krambrock, K., Molphy, Z., Kellett, A., Pereira-Maia, E.C., and Silva-Caldeira, P.P., 2019, Exploring the DNA binding, oxidative cleavage, and cytotoxic properties of new ternary copper(II) compounds containing 4-aminoantipyrine and N, N-heterocyclic co-ligands, *J. Mol. Struct.*, 1178, 18–28.
- [19] Venugopal, N., Krishnamurthy, G., Bhojyanaik, H.S., and Krishna, P.M., 2019, Synthesis, spectral characterization and biological studies of Cu(II), Co(II) and Ni(II) complexes of azo dye ligand containing 4-aminoantipyrine moiety, *J. Mol. Struct.*, 1183, 37–51.
- [20] Fathima, S.S.A., Paulpandiyan, R., and Nagarajan, E.R., 2019, Expatriating biological excellence of aminoantipyrine derived novel metal complexes: Combined DNA interaction, antimicrobial, free radical scavenging studies and molecular docking simulations, *J. Mol. Struct.*, 1178, 179–191.
- [21] Rahardjo, S.B., and Aditya, H.P., 2017, Synthesis and characterization of tetrakis(2-amino-3-methylpyridine)di(aqua)nickel(II), *IOP Conf. Ser.: Mater. Sci. Eng.*, 172, 012048.
- [22] Cotton, F.A., Wilkinson, G., Murillo, C.A., and Bochmann, M., 1999, *Advanced Inorganic Chemistry*, John Wiley & Sons Inc., New York.
- [23] Kumari, P., Lobana, T.S., Butcher, R.J., Castineiras, A., and Zeller, M., 2018, The effect of substituents at C²/N¹ atoms of salicylaldehyde and 2-hydroxyacetophenone based thiosemicarbazones on the nature of nickel(II) complexes with 1,10-phenanthroline and terpyridine as co-ligands, *Inorg. Chim. Acta*, 482, 268–274.
- [24] Sharma, S., Sachar, R., Bajju, G.D., and Sharma, V., 2018, Synthesis and characterization of some adducts of o-hexyl dithiocarbonates of nickel (II) with heterocyclic amines, *Chem. Sci. Trans.*, 7 (4), 610–617.
- [25] Baul, T.S.B., Nongsiej, K., Ka-Ot, A.L., Joshi, S.R., Rocha, B.G.M., and da Silva, M.F.C.G., 2020, Synthesis, crystal structures, magnetic properties and antimicrobial screening of octahedral nickel(II) complexes with substituted quinolin-8-olates and pyridine ligands, *J. Mol. Struct.*, 1200, 127106.
- [26] Rasyda, Y.A., Rahardjo, S.B., and Nurdiyah, F., 2019, Synthesis and characterization complex nickel(II) with diphenylamine, *IOP Conf. Ser.: Mater. Sci. Eng.*, 578, 012008.
- [27] Lima, C.F.R.A.C., Taveira, R.J.S., Costa, J.C.S., Fernandes, A.M., Melo, A., Silva, A.M.S., and Santos, L.M.N.B.F., 2016, Understanding M–ligand bonding and *mer-/fac*-isomerism in tris(8-hydroxyquinolate) metallic complexes, *Phys. Chem. Chem. Phys.*, 18 (24), 16555–16565.
- [28] Susanthy, D., Santosa, S.J., and Kunarti, E.S., 2020, Antibacterial activity of silver nanoparticles capped by *p*-aminobenzoic acid on *Escherichia coli* and *Staphylococcus aureus*, *Indones. J. Chem.*, 20 (1), 182–189.
- [29] Pratama, A., Sebayang, F., and Nasution, R.B., 2018, Antibacterial properties of biofilm Schiff base derived from dialdehyde cellulose and chitosan, *Indones. J. Chem.*, 19 (2), 405–412.

- [30] Shebl, M., 2016, Mononuclear, homo- and hetero-binuclear complexes of 1-(5-(1-(2-aminophenylimino)ethyl)-2,4-dihydroxyphenyl)ethanone: Synthesis, magnetic, spectral, antimicrobial, antioxidant, and antitumor, *J. Coord. Chem.*, 69 (2), 199–214.
- [31] Nithya, P., Rajamanikandan, R., Simpson, J., Ilanchelian, M., and Govindarajan, S., 2018, Solvent assisted synthesis, structural characterization and biological evaluation of cobalt(II) and nickel(II) complexes of Schiff bases generated from benzyl carbazate and cyclic ketones studies, *Polyhedron*, 145, 200–217.
- [32] Malik, S., Das, S., and Jain, B., 2010, First-row transition metal complexes of omeprazole as anti-ulcerative drugs, *Indones. J. Chem.*, 10 (3), 382–389.
- [33] Doan, V.D., Cuong, N.V., Le, P.H.A., Anh, T.T.L., Viet, P.T., and Huong, N.T.L., 2020, Orange peel essential oil nanoemulsions supported by nanosilver for antibacterial application, *Indones. J. Chem.*, 20 (2), 430–439.

Formulation and Characterization of a Kinetically Stable Topical Nanoemulsion Containing the Whitening Agent Kojic Acid

Gan Yi Yun¹, Nur Azzanizawaty Yahya^{1,2}, Roswanira Abdul Wahab^{1,2*}, and Mariani Abdul Hamid³

¹Department of Chemistry, Faculty of Science, Universiti Teknologi Malaysia, 81310 UTM Skudai, Johor, Malaysia

²Enzyme Technology and Green Synthesis Group, Faculty of Science, Universiti Teknologi Malaysia, 81310 UTM Skudai, Johor, Malaysia

³School of Chemical and Energy Engineering, Faculty of Engineering, Universiti Teknologi Malaysia, 81310 Skudai, Johor, Malaysia

* **Corresponding author:**

email: roswanira@kimia.fs.utm.my

Received: June 3, 2020

Accepted: July 6, 2020

DOI: 10.22146/ijc.56587

Abstract: The research was carried out to synthesize a stable kojic acid (KA) encapsulated nanoemulsion as a whitening agent for topical skin usage. In this study, the oil-in-water (O/W) KA nanoemulsion was formulated using integrated low and high energy methods that combined ultrasonic and hot temperature inversion methods. Several different combinations of parameters were screened, viz. xanthan gum amount (1.0 to 2.0 g), kojic acid (KA) amount (0.5 to 1.5 g), and surfactant-to-water ratio (1:10.75 to 1:4.875), to prepare a stable KA nanoemulsion. The identified best parameters to design the O/W KA nanoemulsion were then subjected to different stability tests: storage and pH stability (freeze-thaw and centrifugal tests). Results revealed that the Trial 6 formulation, with the highest ratio of Tween 80 to water (1:4.875 v/v), yielded the best polydispersity index at 0.255 ± 0.006 with an average particle size of 90.57 ± 1.401 nm. The formulation retained the recommended pH range (pH 4.95–5.18) for topical skin applications within six-week storage under room condition. The nanoemulsions were also kinetically stable as proven by the absence of phase separation after the centrifugation, freeze-thaw cycle, and storage temperature (2 and 25 °C) tests, except at the 37 °C three-week extended storage. The results collectively showed that the formulated O/W KA nanoemulsion is suitable for topical application on human skin.

Keywords: oil-in-water nanoemulsion; kojic acid; topical skin application; skin whitening; ultrasonic and hot temperature inversion methods

■ INTRODUCTION

Melanogenesis is a complex physiological process controlled by both tyrosinase and tyrosinase-related protein-1 and -2 (TRP-1 and TRP-20) found in melanocytes, responsible for producing the melanin pigment. This natural pigment has an important role in protecting the human skin from injury due to sunlight while affording color to the skin and hair. However, melanin's over-production leads to aesthetic problems such as hyperpigmentation, wrinkling, melasma, and other dermatological disorders [1-2].

To inhibit skin pigmentation, 5-hydroxy-2-hydroxymethyl-4H-pyran-4-one, commonly known as

kojic acid (KA), is gaining popularity as an agent that inhibits melanin synthesis [3]. KA imparts its skin whitening effect by blocking ultraviolet radiation, suppressing hyperpigmentation, and preventing melanin formation by its tyrosinase inhibitory activity [1,4-5]. KA is also a widely used active ingredient in an array of cosmetics, medicines, foods, and agriculture and chemical industries due to its antibacterial, antimicrobial, antileukemic, and antifungal properties [6]. For KA to exhibit their depigmentation effect, a sufficient amount of this whitening agent should remain close to melanocytes for a stipulated duration. Such cells are typically located between the epidermis and dermis. One of the challenges for using KA as a hydrophilic

active whitening agent is its poor penetration into the skin, and consequently, transportation to the target location. This is due to difficulties in KA to pass through the skin barrier that protects against ultraviolet light, pathogenic bacteria, and pollution. A hydrophobic active agent, on the other hand, is better adsorbed on the stratum corneum but is unable to penetrate deep into the skin due to the presence of water in the skin epidermis [1,7].

Hence, surfactants and alcohols can be employed simultaneously to overcome such issues and enhance the transportation of KA through the human skin. In this research, sorbitan monooleate (Tween 80) was used as the surfactant to expedite the KA nanoemulsion formulation. Tween 80 also kinetically stabilizes the nanoemulsion for extended storage by minimizing the interfacial tension. The KA should also be encapsulated to improve the depigmentation effect by increasing the system's physicochemical stability, aside from preventing the general accumulation of whitening agents within the system [1,8]. This enhances the delivery of the active ingredient as diffusion issues through the stratum corneum barrier can be overcome, in turn, facilitating a higher presence of the active ingredient at the targeting area [9]. Encapsulated nanoparticles have a high surface area to volume ratio to effectively allow a controllable delivery of the active ingredient to targeted cells [10-11] and facilitate the transportation of hydrophilic molecules such as KA in the skin [12]. Besides that, the polymeric nanoparticles in the nanoemulsion system further stabilize the drug/active ingredients and boost the delivery of poorly soluble or poorly absorbed substances, alongside other chemicals, heat- and photo-labile components [13]. The nanoemulsions' small droplet size boosts the penetration of active ingredients, i.e., KA through the skin. This enhances their intended efficacies to reduce hyperpigmentation, wrinkling, melasma and other dermatological disorders, as well as promote a faster turnover cycle, and inhibition of melanosome transfer [14-15]. As far as we know, different forms of esterified kojic acid, viz. kojic dipalmitate and kojic monooleate were investigated as active ingredients in water/oil/water

multiple emulsions and nanoemulsion, respectively [16-17].

Cosmetic products with an active whitening agent such as KA are currently the topical skin whitening action choice. Hence, it makes sense that the potential of nanotechnology-based systems (DDS) to carry out encapsulation of the active whitening ingredient in nanoemulsion is investigated. To develop a kinetically stable topical oil-in-water (O/W) nanoemulsion using KA as the active ingredient, this study aimed to identify the best composition of xanthan gum amount, kojic acid (KA) amount, surfactant:water ratio in the formulation. Hence, this is the first-ever report that prepares a simplified, single surfactant (Tween 80) O/W KA nanoemulsion for topical delivery through an integrated ultrasonication and hot temperature technique. The turbulent micro-implosions from repeated acoustic bombardment during ultrasonication are highly effective in breaking up primary droplets of dispersed oil into droplets of sub-micron size.

In contrast, the hot temperature technique can flexibly tune the mixing temperature to achieve the nanodroplet quality in the O/W KA nanoemulsion [18]. The prepared O/W KA nanoemulsion was tested for stability in particle size and polydispersity index (PDI). In addition, tests were also carried out to determine the stability of the KA nanoemulsions in terms of storage and freeze-thaw stability and the system's pH stability for 6 weeks.

■ EXPERIMENTAL SECTION

Materials

Xanthan gum from *Xanthomonas campestris* and kojic acid (KA) were purchased from Personal Formula Resources (Malaysia), while Tween 80 (polyoxyethylene sorbitan monooleate HLB = 15.0) were purchased from Scharlau (Barcelona, Spain). Grape seed oil was procured from Aceies Borges Pont (Spain), and fragrance oil and phenoxyethanol (as preservative) were purchased from Luzi Fragrance Compounds (Johor, Malaysia), and Thor Specialty (US), respectively. All other chemicals were obtained from the General Chemistry Laboratory of

Faculty of Science, Universiti Teknologi Malaysia, Malaysia.

Instrumentation

A 20 kHz ultrasonic generator (130 W, KH5200DB type, Kunshan ultrasonic instrument Co., Ltd., Jiangsu, China) was used to produce the coarse emulsion. Hettich-EBA20 (Germany) was used to create a centrifugal force (10,000 rpm, 10 min) for the O/W stability test. The KA nanoemulsion's pH stability was measured at 25 °C using the Delta 320 pH meter (Melter-Toledo, Schwerzenbach, Switzerland) after a 6-week incubation. Particle size and polydispersity index (PDI) were monitored using the Zetasizer Nano ZSP, Malvern Instrument, Malvern (UK).

Procedure

Preparation and screening of formulation parameters for preparing KA nanoemulsion

In this research, an integrated ultrasonication and hot-temperature method were used to prepare the O/W KA nanoemulsion. Firstly, grapeseed oil and Tween 80 (surfactant) were combined in a beaker to form the oil phase. In another beaker, the aqueous phase was prepared by mixing KA, xanthan gum, and deionized water under moderate stirring (100 rpm) for 5 min. Both liquid phases were transferred to an oil bath and heated to 80 °C. Upon reaching the temperature, the liquids were removed from

the heat. The oil phase was added dropwise into the aqueous phase under constant magnetic stirring at 600 rpm for 10 min, followed by the occasional manual stirring. Next, the coarse KA emulsion was transferred to an ice bath and ultrasonicated for 5 min to emulsify the mixture. Other components, for instance, fragrance and phenoxyethanol, were added dropwise during the ultrasonication process. For screening purposes, the above steps were repeated for another 6 sets to test for the varying amounts of xanthan gum, KA, surfactant to water ratio (Table 1). Lastly, the prepared KA nanoemulsions were transferred into screw-capped vials until further use.

Particle size and PDI analysis

It is important to note that PDI indicates homogeneity and stability, wherein the target range should be lower than 0.5 for a nanoemulsion. This value shows similar and narrow size distribution in the KA formulation, representing a more stable and uniformed nanoemulsion system [19]. For all cases, nanoparticles carrying encapsulated KA should be of sizes less than 100 nm to enable efficacious delivery of KA through the skin. In this study, all readings were taken at 25 °C as temperature change can influence the stability of nanoemulsion, drug loading, and drug release [20].

Table 1. The different formulation parameters

	Trial 1		Trial 2		Trial 3		Trial 4		Trial 5		Trial 6		Trial 7	
	%	Amount	%	Amount	%	Amount	%	Amount	%	Amount	%	Amount	%	Amount
Oil Phase														
Grapeseed Oil	6	3 mL	6	3 mL	6	3 mL	6	3 mL	6	3 mL	6	3 mL	3 mL	6
Tween 80	12	6 mL	12	6 mL	12	6 mL	12	6 mL	12	6 mL	16	8 mL	6 mL	16
Aqueous Phase														
H ₂ O	82	41 mL	82	41 mL	82	41 mL	82	41 mL	82	41 mL	78	39 mL	86	43 mL
Kojic Acid	-	0.5 g	-	1.0 g	-	1.5 g	-	1.0 g	-	1.0 g	-	1.0 g	-	1.0 g
Xanthan Gum	-	1.5 g	-	1.5 g	-	1.5 g	-	1.0 g	-	2.0 g	-	1.5 g	-	1.5 g
Additives														
Phenoxyethanol	-	500 µL	-	500 µL	-	500 µL	-	500 µL	-	500 µL	-	500 µL	-	500 µL
Perfume	-	20 µL	-	20 µL	-	20 µL	-	20 µL	-	20 µL	-	20 µL	-	20 µL
Total	100	50 mL	100	50 mL	100	50 mL	100	50 mL	100	50 mL	100	50 mL	100	50 mL

Trial 1: Kojic Acid amount (lowest), Trial 2: Kojic Acid amount (moderate), Xanthan gum, amount (moderate), Surfactant to water ratio (moderate), Trial 3: Kojic Acid amount (highest), Trial 4: Xanthan gum amount (lowest), Trial 5: Xanthan gum amount (highest), Trial 6: Surfactant to water ratio (highest), Trial 7: Surfactant to water ratio (lowest)

Stability test

In this study, stability tests on the formulated KA nanoemulsion were done to provide reasonable assurance that the product remains at an acceptable level of fitness or quality over different conditions. This study's stability tests were simulated under conditions that are likely to destabilize the KA nanoemulsion over time. The tests of the KA nanoemulsions included accelerated storage stability under centrifugal force, freeze-thaw cycles, as well as under conditions of high heat and cold. To enable comparison, each sample's initial conditions, such as appearance, color, fragrance, pH, and viscosity, were recorded before each test [21-22].

For the storage stability test, triplicates of the KA nanoemulsion were subjected to variable temperatures (2, 25, 37 °C). This second test specifically observes the stability of the KA nanoemulsion under an accelerated destabilizing condition, i.e., centrifugal force (10,000 rpm, 10 min). It is worth indicating here that a correctly formulated KA nanoemulsion is stable under the previous tests and capable of resisting phase separation that transforms the system back into its individual components [21].

Next, the freeze-thaw stability test was conducted by subjecting each sample to a triply repeated cycle of freezing and thawing. Each condition was maintained for 24 h before the condition was changed. The physical appearance of an adequately stable KA nanoemulsion post-evaluation test should be similar to the pre-evaluated one and without any phase separation [21]. The pH stability of the KA nanoemulsion was then measured at 25 °C after a 6-week incubation.

■ RESULTS AND DISCUSSION

The rationale of the Preparation of Encapsulated Kojic Acid (KA) Nanoemulsion

Literature has shown that the optimum pH range for topical nanoemulsions should closely resemble the pH of the surface of healthy human skin, which typically ranges between pH 4.0–6.0 [23-24]. However, a condition for better hydration is pH < 5.0 compared to skin with pH > 5.0. Conversely, a higher pH on the skin surface tends to intensify itching and skin dryness [22-23]. Thus,

a slightly acidic skin surface protects against a myriad of invading microorganisms and offers better resistance against SLS-induced irritant dermatitis [25]. For these reasons, the formulated KA nanoemulsion was kept within the recommended pH range for healthy skin.

In this research, ultrasonic and hot temperature methods were used to prepare a stable oil-in-water (O/W) nanoemulsion containing encapsulated KA. It is important to indicate here that the preparation of KA nanoemulsions required two separate phases involving the oil phase and aqueous phase. The components of the oil phase used in this study comprised grapeseed oil and Tween 80. The study used grapeseed seed oil as the oil phase due to its high antioxidant content and anti-aging properties [26]. Moreover, grapeseed oil contains antioxidants, which include vitamin E and oligomeric proanthocyanidins. These components help reduce wrinkles by repairing collagen damaged by free radicals, moisturizing the skin, and enhancing skin elasticity [22]. The bulk physicochemical characteristics of the oil phase, for example, viscosity, are also important factors when preparing stable nanoemulsions. They can limit the type of homogenization method(s) preparing a nanoemulsion from a given oil phase. To be specific, the higher viscosity of grapeseed oil is crucial during the ultrasonication (high-energy method) is useful for the disruption of oil droplets into sub-micron size [18]. This enables the nanoemulsion to have a longer shelf-life as the creaming rate is decreased [27].

Another factor of concern when preparing the O/W KA nanoemulsion is the suitability of Tween 80 for the KA encapsulation process to yield nanoparticle sizes of below 100 nm [20]. In this study, the non-ionic Tween 80 was chosen due to its low irritation and low toxicity, high surface activity even at a low concentration, and suitable for nanoemulsions prepared via both high-energy and low-energy methods [27-30]. Whereas the Hydrophilic Lipid Balance (HLB) value of 15 of Tween 80 stabilizes the O/W KA nanoemulsions by increasing the affinity between the interacting molecules and lowers the interfacial tension between the water and KA in the oil phase. It also changes the interfacial layer's optimum curvature and increases the repulsive

interactions (steric or electrostatic) between droplets [31]. Thus, the nanoemulsion system has higher stability, formulating flexibility, and wider compatibility [32]. Thus, the use of Tween 80 is popular in the cosmetic, pharmaceutical, and food industries.

Meanwhile, xanthan gum, KA, and distilled water formed the aqueous phase components since the innocuous, non-irritating, and non-sensitizing properties [33] of xanthan gum can stabilize the O/W nanoemulsion. The system also contributes to the electrostatic and steric effects that repel similarly charged emulsion droplets. The condition sustains the bulky stabilizing layer barrier that maintains the kinetic stability of O/W emulsions [34]. The high molecular weight and high viscosity of Tween 80 also promote a low shear rate that effectively decreases nanoparticle aggregation and enhances nanoemulsion stability [14]. Meanwhile, KA was chosen as the study's whitening agent due to its ability to inhibit tyrosinase activity and exhibit anti-oxidizing, anti-proliferative, anti-inflammatory, alongside radioprotective tendencies [6].

Characterization of Encapsulated KA Nanoemulsion

Determination of particle size and polydispersity index (PDI)

In this study, all prepared KA nanoemulsions were found to satisfy the required nanosize and data for particle sizes and PDIs for all formulations (Fig. 1). It is important to note that all the KA nanoemulsions were characterized within 24 h after preparation to ensure consistency of

measurements. Rapid characterization is required because the structural organization of the KA nanoemulsion, alongside its composition and physicochemical properties, can fluctuate over time and space when there is a mix of the organic and aqueous phases [35]. Results revealed that KA nanoemulsions showed the presence of KA droplets with diameters ranging between 10–100 nm [20], as well as a well-distributed nanoparticle showing an average PDI of less than 0.5 [19]. The findings conveyed that the O/W KA nanoemulsions were well-formulated and appeared uniform in terms of size distribution. The narrow size distribution is seen in this study (PDI = 0.5) effectively illustrated the successful preparation of a stable and uniformed nanoemulsion system [19], where Trial 6 formulation showed the highest ratio of Tween 80 to water (1:4.875 v/v). The best PDI was 0.255 ± 0.006 with an average size of 90.57 ± 1.401 nm.

It is important to mention here that currently, cosmeceutical products formulated with smaller droplet sizes are trending among consumers, as the system supports a better permeation of the bioactive ingredient, i.e., KA through the stratum corneum. The minute size of KA particles seen in this study was the likelihood of the unsaturated non-polar tails of Tween 80 that facilitated an ideal packing of the surfactant molecules. This state essentially allowed the ultrafine droplets to form at the oil-water boundary freely [35]. Another study reported that an optimal ratio of the effective cross-sectional areas of the Tween 80 hydrophobic tail

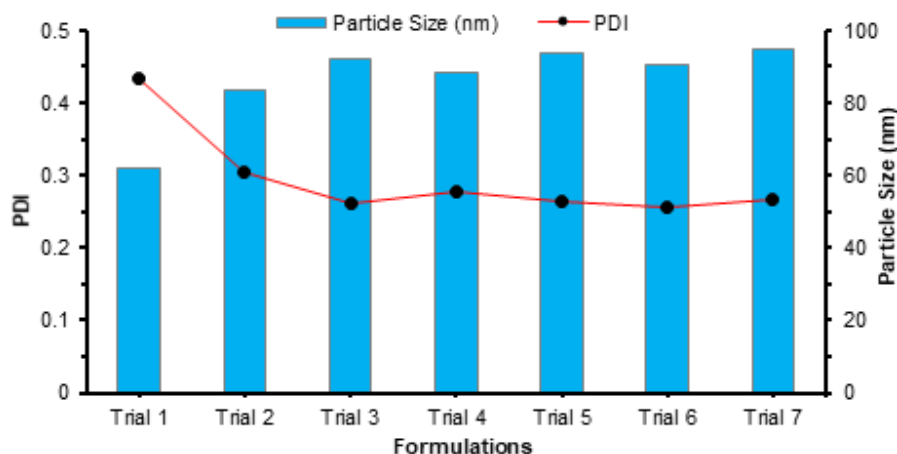


Fig 1. Graph of particle sizes and PDI for all seven trials

part and its hydrophilic head part can synergistically and exclusively influence the surfactant's molecular geometry.

Based on the desirable small droplet size (90.57 ± 1.401 nm) and the satisfactory PDI (0.255 ± 0.006) of the KA nanoemulsion, it was clear that the formulation in Trial 6 resulted in an optimal ratio of Tween 80 to water. The formulation allowed the adoption of an optimum curvature of surfactants surrounding the KA particles during spontaneous emulsification. This phenomenon occurs due to the kinked nature of the unsaturated non-polar tails of Tween 80, which have been irrefutably shown to promote a more 'curved' packing of the surfactant molecules over the oil-water interface [14]. As a matter of fact, several studies have achieved smaller droplet sizes when using non-polar chains of non-ionic unsaturated surfactants with more double bonds as the emulsifier in spontaneously formed nanoemulsions [36-37]. At smaller particle sizes, the effect of Brownian motion is dominant over gravitational force, thus giving better emulsion stability [14]. The graph of particle size and PDI for all the trials are also shown in Fig. 1.

Thermodynamic stability test

In this investigation, the thermodynamic stability tests' phases consist of three components: centrifugation study, freeze-thaw cycle, and storage stability. As can be seen, all seven KA formulations were stable, and no phase separations were observed after centrifugation. This particular test allows the user to anticipate the destabilization of the prepared nanoemulsions through the creaming or coalescence of the dispersed phase. This test is also useful for predicting the prepared KA nanoemulsions' shelf life under storage normal conditions [38]. This study believed that differences in density of the oil and aqueous phase could have played a role in stabilizing the KA nanoemulsion. The findings also communicated normally distributed components in the nanoemulsion system [39].

The freeze-thaw cycle test was done in three replicates for temperatures -10 °C (in the freezer), followed at room temperature (± 25 °C) at 24 h intervals. The test was triplicated, and the results are tabulated in Table 2. The noteworthy absence of phase separation in all tested samples affirmed the stability of the

nanoemulsion system. The O/W KA nanoemulsion stability was assisted by the bulky hydrophilic head groups of the incorporated Tween 80 that acted as a stearic barrier at the oil/water interface. This molecular arrangement prohibited the destabilization of the oil phase KA droplets by coalescence. It also averted collisions between the droplets, as similarly reported by other studies [40-41]. The additional presence of xanthan gum in the aqueous phase further precluded the movement of dispersed KA droplets and further stabilized the O/W nanoemulsion. Sriprabom et al. [34]

Table 2. Thermostability test results on phase separation for Trial 1–7

Trials		1	2	3	4	5	6	7
Centrifugation	Week 1	×	×	×	×	×	×	×
	Week 2	×	×	×	×	×	×	×
	Week 3	×	×	×	×	×	×	×
	Week 4	×	×	×	×	×	×	×
	Week 5	×	×	×	×	×	×	×
	Week 6	×	×	×	×	×	×	×
Freeze-Thaw Cycle Test	Week 1	×	×	×	×	×	×	×
	Week 2	×	×	×	×	×	×	×
	Week 3	×	×	×	×	×	×	×
	Week 4	×	×	×	×	×	×	×
	Week 5	×	×	×	×	×	×	×
	Week 6	×	×	×	×	×	×	×
2 °C	Week 1	×	×	×	×	×	×	×
	Week 2	×	×	×	×	×	×	×
	Week 3	×	×	×	×	×	×	×
	Week 4	×	×	×	×	×	×	×
	Week 5	×	×	×	×	×	×	×
	Week 6	×	×	×	×	×	×	×
Storage Stability 25 °C	Week 1	×	×	×	×	×	×	×
	Week 2	×	×	×	×	×	×	×
	Week 3	×	×	×	×	×	×	×
	Week 4	×	×	×	×	×	×	×
	Week 5	×	×	×	×	×	×	×
	Week 6	×	×	×	×	×	×	×
37 °C	Week 1	×	×	×	×	×	×	×
	Week 2	×	×	×	×	×	×	×
	Week 3	×	×	×	×	×	×	×
	Week 4	√	√	√	√	√	√	√
	Week 5	√	√	√	√	√	√	√
	Week 6	√	√	√	√	√	√	√

× = No phase separation occurs; √ = Phase separation occurs

also reported a comparable outcome when they incorporated xanthan gum in the aqueous phase of whey protein stabilized O/W emulsions. The reason behind this is the presence of shear-thinning high molecular weight polymers that encourages the formation of a high viscosity nanoemulsion at low shear rates, thereby decreasing the likelihood of a destabilized continuous phase [14].

Results for the storage stability, on the one hand, showed that all formulated emulsions placed under different temperatures (2, 25, 37 °C), remained stable and phase separation was not observed in the first three weeks. The tested KA nanoemulsions for the stability tests are shown in Fig. 2(a-e). Again, the study's observation supported the stability of the KA nanoemulsions under varying storage conditions and extended storage duration. All KA nanoemulsions samples subjected to extended storage at the lowest temperature (2 °C) appeared whiter in color due to the gelation process [31].

On the other hand, all KA formulations were notably more yellowish when stored at the highest tested temperature (37 °C) after three weeks. This outcome was caused by an increase in the growth rate of KA droplets in the system due to coalescence. This was somewhat expected as the issue typically affects O/W nanoemulsions stored at higher temperatures [31], particularly when a thermal sensitive non-ionic surfactant is used in the formulation [19]. The study believed that the thermal sensitive nature of Tween 80 was to blame for the more rapid destabilization of the O/W KA nanoemulsion stored at 37 °C. Hence, the formulations produced here were not suitable for storage at temperatures exceeding 30 °C (Table 2).

pH Stability over an Extended Storage Period

It is important to highlight here, the optimum pH range for a topical application of a nanoemulsion should be close to the pH of natural healthy human skin (pH 4.0–6.0) [20] to maintain good hydration and protect against invading microorganisms [23]. In this research, the pH of formulated O/W nanoemulsions was determined weekly for six weeks, and they were found to range between pH 4.66 to 5.55. All formulations generally showed a decreasing

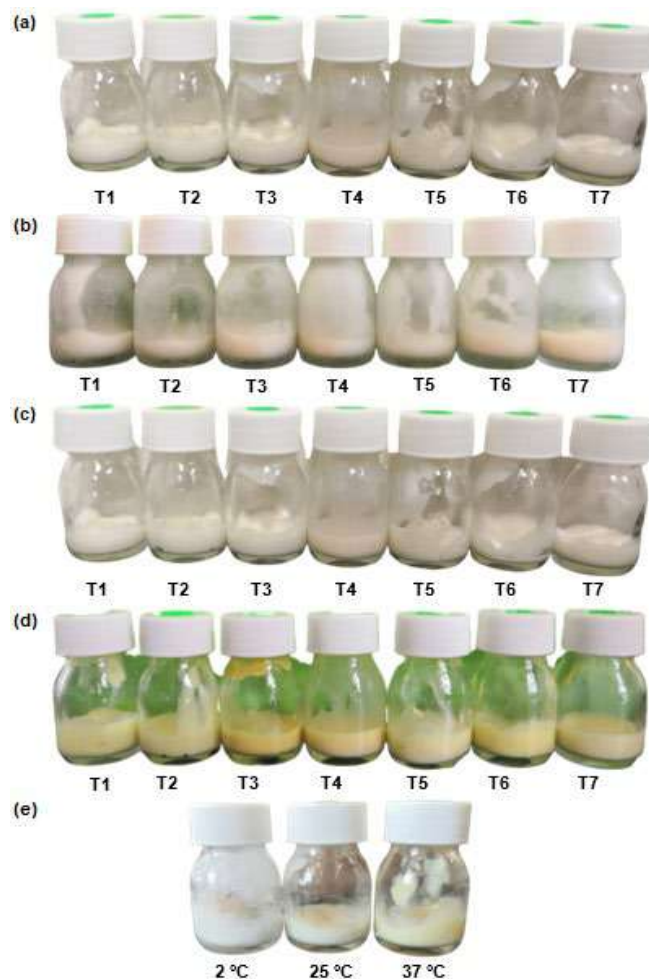


Fig 2. The appearance of Formulations 1–7 after the (a) freeze-thaw cycle test, (b) extended storage at 2 °C after 6 weeks, (c) storage at 25 °C after 6 weeks and (d) storage at 37 °C after 6 weeks (e) Formulations of Trial 6 (best formulation) stored under different temperatures (2, 25, 37 °C) after 6 weeks

trend in terms of pH value from week 1 to week 6. This can be attributed to the presence of free fatty acids liberated by the degradation of the oil phase components or the hydrolysis process caused by the temperature factor [14].

The outcome of this study corroborated the likelihood that the O/W KA nanoemulsions had undergone oxidation under the high storage temperature. Literature has shown that high temperatures tend to promote the release of a higher concentration of free hydrogen ions, which lowers a system's pH. In the case of

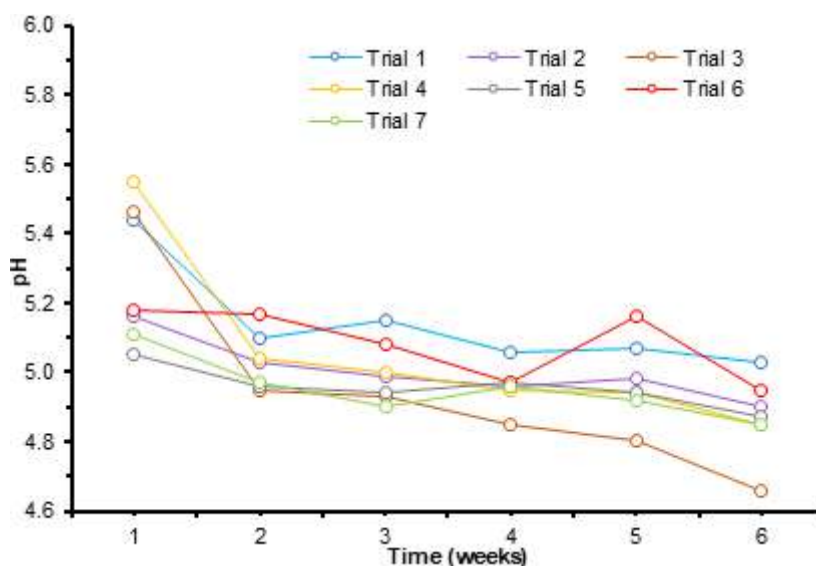


Fig 3. Graph of pH values for Trial 1–7 over 6 weeks

this study, the destabilizing factor of a reduced pH in the KA nanoemulsion has to be the surplus of hydrogen ions. These ions counteracted the negatively charged ions and undesirably reduced the zeta potential. This accelerated flocculation within the O/W system [42]. However, all KA formulations' pH values observably remained within the ideal range of the skin pH (between 4–6), thus indicating their stability [14]. In conclusion, the results demonstrated that the formulated KA nanoemulsions are within the suggested pH range and suitable for topical applications on human skin. The trend of pH value over six weeks observed in this study is illustrated in Fig. 3.

CONCLUSION

In this study, the nanoemulsion containing KA screening was done successfully to prepare by a combined treatment of ultrasonication and hot-temperature methods. The study discovered that the Trial 6 formulation with the highest ratio of Tween 80 to water (1:4.875 v/v) yielded the best PDI at 0.255 ± 0.006 , which corresponded to an average particle size of 90.57 ± 1.401 nm. Trial 6 formulated KA nanoemulsion showed good storage capability under low temperature (2 °C) and room temperature (25 °C), as supported by the absence of phase separation. However, three weeks into storage at 37 °C, the KA nanoemulsion turned slightly yellowish, which signified the onset of phase separation. Thus, a review of

parameters to prepare the nanoemulsion must be done to improve the storage stability at this temperature. The absence of phase separation after three consecutive freeze-thaw cycles and centrifugal tests affirmed the kinetically stable KA nanoemulsions, as their pH remained within the recommended pH range of pH 4.95 to 5.18 for 6 weeks storage. The results collectively thus, supported the continued suitability of the KA emulsion for topical human skin applications.

ACKNOWLEDGMENTS

This work was supported by the Fundamental Research Grant Scheme (QJ130000.2526.17H48) from the Ministry of Higher Education.

REFERENCES

- [1] Ha, J.H., Jeong, Y.J., Kim, A.Y., Hong, I.K., Lee, N.H., and Park, S.N., 2018, Preparation and Physicochemical properties of a cysteine derivative-Loaded deformable liposomes in hydrogel for enhancing whitening effects, *Eur. J. Lipid Sci. Technol.*, 120 (9), 1800125.
- [2] Zhou, J., Ren, T., Li, Y., Cheng, A., Xie, W., Xu, L., Peng, L., Lin, J., Lian, L., Diao, Y., Jin, X., and Yang, L., 2017, Oleoylethanolamide inhibits α -melanocyte stimulating hormone-stimulated melanogenesis via ERK, Akt and CREB signaling

- pathways in B16 melanoma cells, *Oncotarget*, 8 (34), 56868–56879.
- [3] Seino, H., Arai, Y., Nagao, N., Ozawa, N., and Hamada, K., 2016, Efficient percutaneous delivery of the antimelanogenic agent glabridin using cationic amphiphilic chitosan micelles, *PLoS One*, 11 (10), e0164061.
- [4] Hseu, Y.C., Cheng, K.C., Lin, Y.C., Chen, C.Y., Chou, H.Y., Ma, D.L., Leung, C.H., Wen, Z.H., and Wang, H.M.D., 2015, Synergistic effects of linderanolide B combined with arbutin, PTU or kojic acid on tyrosinase inhibition, *Curr. Pharm. Biotechnol.*, 16 (12), 1120–1126.
- [5] Wang, X.R., Cheng, H.M., Gao, X.W., Zhou, W., Li, S.J., Cao, X.L., and Yan, D., 2019, Intercalation assembly of kojic acid into Zn-Ti layered double hydroxide with antibacterial and whitening performances, *Chin. Chem. Lett.*, 30 (4), 919–923.
- [6] Saeedi, M., Eslamifar, M., and Khezri, K., 2019, Kojic acid applications in cosmetic and pharmaceutical preparations, *Biomed. Pharmacother.*, 110, 582–593.
- [7] Parvez, S., Kang, M., Chung, H.S., Cho, C., Hong, M.C., Shin, M.K., and Bae, H., 2006, Survey and mechanism of skin depigmenting and lightening agents, *Phytother. Res.*, 20 (11), 921–934.
- [8] Ephrem, E., Elaissari, H., and Greige-Gerges, H., 2017, Improvement of skin whitening agents efficiency through encapsulation: Current state of knowledge, *Int. J. Pharm.*, 526 (1-2), 50–68.
- [9] Zhu, L.F., Zheng, Y., Fan, J., Yao, Y., Ahmad, Z., and Chang, M.W., 2019, A novel core-shell nanofiber drug delivery system intended for the synergistic treatment of melanoma, *Eur. J. Pharm. Sci.*, 137, 105002.
- [10] Calixto, G.M.F., de Annunzio, S.R., Victorelli, F.D., Frade, M.L., Ferreira, P.S., Chorilli, M., and Fontana, C.R., 2019, Chitosan-based drug delivery systems for optimization of photodynamic therapy: A review, *AAPS PharmSciTech*, 20 (7), 253.
- [11] Mondal, S., Hoang, G., Manivasagan, P., Kim, H., and Oh, J., 2019, Nanostructured hollow hydroxyapatite fabrication by carbon templating for enhanced drug delivery and biomedical applications, *Ceram. Int.*, 45 (14), 17081–17093.
- [12] Anirudhan, T., and Nair, S.S., 2019, Development of voltage gated transdermal drug delivery platform to impose synergistic enhancement in skin permeation using electroporation and gold nanoparticle, *Mater. Sci. Eng., C*, 102, 437–446.
- [13] Bangun, H., Tandiono, S., and Arianto, A., 2018, Preparation and evaluation of chitosan-tripolyphosphate nanoparticles suspension as an antibacterial agent, *J. Appl. Pharm. Sci.*, 8 (12), 147–156.
- [14] Ribeiro, R.C.A., Barreto, S.M.A., Ostrosky, E.A., da Rocha-Filho, P.A., Verissimo, L.M., and Ferrari, M., 2015, Production and characterization of cosmetic nanoemulsions containing *Opuntia ficus-indica* (L.) mill extract as moisturizing agent, *Molecules*, 20 (2), 2492–2509.
- [15] Sung, H.J., Khan, M.F., and Kim, Y.H., 2019, Recombinant lignin peroxidase-catalyzed decolorization of melanin using in-situ generated H₂O₂ for application in whitening cosmetics, *Int. J. Biol. Macromol.*, 136, 20–26.
- [16] Roselan, M.A., Ashari, S.E., Faujan, N.H., Mohd Faudzi, S.M., and Mohamad, R., 2020, An Improved nanoemulsion formulation containing kojic monooleate: Optimization, characterization and in vitro studies, *Molecules*, 25 (11), 2616.
- [17] Gonçalves, M.L., Marcussi, D.G., Calixto, G.M.F., Corrêa, M.A., and Chorilli, M., 2015, Structural characterization and in vitro antioxidant activity of kojic dipalmitate loaded W/O/W multiple emulsions intended for skin disorders, *Biomed Res. Int.*, 2015, 304591.
- [18] Che Marzuki, N.H., Wahab, R.A., and Abdul Hamid, M., 2019, An overview of nanoemulsion: Concepts of development and cosmeceutical applications, *Biotechnol. Biotechnol. Equip.*, 33 (1), 779–797.
- [19] Mohd Narawi, M., Chiu, H.I., Yong, Y.K., Mohamad Zain, N.N., Ramachandran, M.R., Tham, C.L., Samsurrijal, S.F., and Lim, V., 2020,

- Biocompatible nutmeg oil-loaded nanoemulsion as phyto-repellent, *Front. Pharmacol.*, 11, 214.
- [20] Aboofazeli, R., 2010, Nanometric-scaled emulsions (nanoemulsions), *Iran. J. Pharm. Res.*, 9 (4), 325–326.
- [21] Ali, M.S., Alam, M.S., Alam, N., and Siddiqui, M.R., 2014, Preparation, characterization and stability study of dutasteride loaded nanoemulsion for treatment of benign prostatic hypertrophy, *Iran. J. Pharm. Res.*, 13 (4), 1125–1140.
- [22] Sumaiyah, and Leisyah, B.M., 2019, The effect of antioxidant of grapeseed oil as skin anti-aging in nanoemulsion and emulsion preparations, *Rasayan J. Chem.*, 12 (13), 1185–1194.
- [23] Ali, S.M., and Yosipovitch, G., 2013, Skin pH: From basic science to basic skin care, *Acta Derm. Venereol.*, 93 (3), 261–267.
- [24] Panther, D.J., and Jacob, S.E., 2015, The importance of acidification in atopic eczema: an underexplored avenue for treatment, *J. Clin. Med.*, 4 (5), 970–978.
- [25] Lambers, H., Piessens, S., Bloem, A., Pronk, H., and Finkel, P., 2006, Natural skin surface pH is on average below 5, which is beneficial for its resident flora, *Int. J. Cosmet. Sci.*, 28 (5), 359–370.
- [26] Garavaglia, J., Markoski, M.M., Oliveira, A., and Marcadenti, A., 2016, Grape seed oil compounds: Biological and chemical actions for health, *Nutr. Metab. Insights*, 9, 59–64.
- [27] McClements, D.J., and Rao, J., 2011, Food-grade nanoemulsions: Formulation, fabrication, properties, performance, biological fate, and potential toxicity, *Crit. Rev. Food Sci. Nutr.*, 51 (4), 285–330.
- [28] Pulce, C., and Descotes, J., 1996, “Household products” in *Human Toxicology*, 1st Ed., Eds. Descotes, J., Elsevier Science B.V., Amsterdam, 683–702.
- [29] Sharma, N., Mohanakrishnan, D., Sharma, U.K., Kumar, R., Richa, Sinha, A.K., and Sahal, D., 2014, Design, economical synthesis and antiplasmodial evaluation of vanillin derived allylated chalcones and their marked synergism with artemisinin against chloroquine resistant strains of *Plasmodium falciparum*, *Eur. J. Med. Chem.*, 79, 350–368.
- [30] Manning, M.C., Liu, J., Li, T., and Holcomb, R.E., 2018, Rational design of liquid formulations of proteins, *Adv. Protein Chem. Struct. Biol.*, 112, 1–59.
- [31] Rao, J., and McClements, D.J., 2010, Stabilization of phase inversion temperature nanoemulsions by surfactant displacement, *J. Agric. Food Chem.*, 58 (11), 7059–7066.
- [32] Anuar, N., Mohd Adnan, A.F., Saat, N., Aziz, N., and Mat Taha, R., 2013, Optimization of extraction parameters by using response surface methodology, purification, and identification of anthocyanin pigments in *Melastoma malabathricum* fruit, *Sci. World J.*, 2013, 810547.
- [33] Kumar, A., Rao, K.M., and Han, S.S., 2018, Application of xanthan gum as polysaccharide in tissue engineering: A review, *Carbohydr. Polym.*, 180, 128–144.
- [34] Sriprabhom, J., Luangpituksa, P., Wongkongkatep, J., Pongtharangkul, T., and Suphantharika, M., 2019, Influence of pH and ionic strength on the physical and rheological properties and stability of whey protein stabilized O/W emulsions containing xanthan gum, *J. Food Eng.*, 242, 141–152.
- [35] Saberi, A.H., Fang, Y., and McClements, D.J., 2013, Fabrication of vitamin E-enriched nanoemulsions: Factors affecting particle size using spontaneous emulsification, *J. Colloid Interface Sci.*, 391, 95–102.
- [36] Nejadmansouri, M., Hosseini, S.M.H., Niakosari, M., Yousefi, G.H., and Golmakani, M.T., 2017, Changes in the surface tension and viscosity of fish oil nanoemulsions developed by sonication during storage, *Iran. Food Sci. Technol. Res. J.*, 13 (6) 105–116.
- [37] Wang, L., Dong, J. Chen, J. Eastoe, J., and Li, X., 2009, Design and optimization of a new self-nanoemulsifying drug delivery system, *J. Colloid. Interface. Sci.*, 330 (2), 443–448.
- [38] Mat Hadzir, N., Basri, M., Abdul Rahman, M.B., Salleh, A.B., Raja Abdul Rahman, R.N., and Basri, H., 2013, Phase behaviour and formation of fatty acid esters nanoemulsions containing piroxicam, *AAPS PharmSciTech*, 14 (1), 456–463.
- [39] El-Din, M.R.N., El-Hamouly, S.H., Mohamed,

- H.M., Mishrif, M.R., and Ragab, A.M., 2014, Investigating factors affecting water-in-diesel fuel nanoemulsions, *J. Surfactants Deterg.*, 17 (4), 819–831.
- [40] Chang, Y., McLandsborough, L., and McClements, D.J., 2015, Fabrication, stability and efficacy of dual-component antimicrobial nanoemulsions: Essential oil (thyme oil) and cationic surfactant (lauric arginate), *Food Chem.*, 172, 298–304.
- [41] Samson, S., Basri, M., Fard Masoumi, H.R., Abedi Karjiban, R., and Abdul Malek, E., 2016, Design and development of a nanoemulsion system containing copper peptide by D-optimal mixture design and evaluation of its physicochemical properties, *RSC Adv.*, 6 (22), 17845–17856.
- [42] Suminar, M.M., and Jufri, M., 2017, Physical stability and antioxidant activity assay of a nanoemulsion gel formulation containing tocotrienol, *Int. J. Appl. Pharm.*, 9, 140–143.

Development of a Simple Fe(II) Ion Colorimetric Sensor from the Immobilization of 1,10-Phenanthroline In Alginate/Pectin Film

Nindya Tri Muliawati, Dwi Siswanta*, and Nurul Hidayat Aprilita

Department of Chemistry, Faculty of Mathematics and Natural Sciences, Universitas Gadjah Mada, Sekip Utara, 55281 Yogyakarta, Indonesia

* **Corresponding author:**

tel: +62-8157951198

email: dsiswanta@ugm.ac.id

Received: June 9, 2020

Accepted: October 6, 2020

DOI: 10.22146/ijc.56759

Abstract: An optical analytical sensor was proposed based on the complexation reactions of 1,10-phenanthroline derivative in aqueous solutions. This study aims to synthesize a metal ion sensor for detecting Fe(II) ion from the immobilization of 1,10-phenanthroline compound in alginate/pectin film. This was carried out by characterizing the films using the Fourier-transform infrared spectrometry (FT-IR) and scanning electron microscope (SEM). The determination of the optimal condition for Fe(II) ion detection and validation of the parameters was conducted by measuring the absorbance of the films using a UV-Vis spectrophotometer. After the addition of Fe(II) ion, the color of the alginate/pectin-phenanthroline film changed from transparent yellow to orange-red, showing its potential as a visual colorimetric sensor for iron(II) ion. It was found that the optimum condition for Fe(II) ion sensing was at 513 nm after 2 min of detection at pH 2. The alginate/pectin-phenanthroline film had good linearity, precision, selectivity, and accuracy with a detection limit as low as 0.446 mg L⁻¹, which was remarkable.

Keywords: alginate/pectin film; colorimetric sensor; Fe(II) ion detection; 1,10-phenanthroline

■ INTRODUCTION

Iron (Fe) is one of the most essential heavy metals in the industrial field due to its low cost, sturdiness, and ease of mass production, which has made it an ideal choice for transportation, mining, and construction. However, the disposal of iron waste from various industrial activities, such as mining sports, hydrometallurgy, foundries, and smelters [1] into the aquatic environment, causes some adverse effects not only to the environment but also to human health. In the form of Fe(II) and Fe(III) ions, they are indispensable as the micronutrient for living organisms; however, they cause problems for ecosystems and human health at higher concentrations. According to the WHO regulation, the limit for Fe(II) and Fe(III) ions should be less than 0.3 mg L⁻¹ in municipal drinking water [2]. When their amounts exceed this limit, they generate an unpleasant taste and odor in drinking water, causing tissue damage in humans and also blockage of pipes or transmission lines in the processing industry due to the formation of iron hydroxide precipitations [3].

Several analytical methods have been established for the determination of Fe ions concentration in environmental samples, such as atomic absorption spectrometry (AAS) [4], UV-Visible spectrophotometry [5], inductively coupled plasma-optical emission spectrometry (ICP-OES), and inductively coupled plasma-mass spectrometry (ICP-MS) [6]. However, these methods still have several limitations, such as complicated protocols, time and cost consumption, and requiring a specific technique. Therefore, a simple method for the determination of Fe ions is highly required. The colorimetric sensor becomes an extremely enticing method since it is easy to read using a low-cost portable instrument and even naked-eye observation [7].

Colorimetric methods are carried out using specific chemicals which are immobilized in a suitable matrix, where they selectively bind the analytes and produce characteristic color change [8]. The optical sensors for the analysis of Fe(II) ions have been previously developed using PVC-based membranes as a

matrix for immobilizing 2,6-bis(carboxamide methyl ester) as the chromogenic reagent [9]. However, these methods required complicated reagent synthesis processes. Similarly, a simple optical sensor was developed using the polypropylene-based paper strip with the immobilized 1,10-phenanthroline reagent [3]. However, this method uses a synthetic polymer-based matrix, which is less environmentally friendly.

In this study, a new film sensor for Fe(II) ion determination using a functionalized, environmentally friendly membrane was developed. This comprises of pectin, a polysaccharide composed of D-galacturonic acid monomers forming a long chain through 1,4-glycoside bonds, and commonly found on the plant cell walls [10]. And alginate, a hydrophilic polysaccharide composed of bonds (1,4) between β -D-mannuronate (M) and α -L-guluronate (G) copolymers, and commonly found in seaweed [11]. Both biomaterials are capable of forming strong gels in the presence of divalent cations, such as Ca^{2+} ion. The combination of these polymers provides unique properties that are strong, water-resistant, and are widely used in several fields as a carrier matrix [12]. Then, the 1,10-phenanthroline reagent is immobilized on the alginate/pectin film to obtain the functionalized optical membrane that provides a rapid, sensitive, and simple alternative method for determining Fe(II) in the aqueous sample.

■ EXPERIMENTAL SECTION

Materials

Sodium alginate was obtained from Sigma Aldrich. Mannuronic to the guluronic acid ratio (M/G) of alginate was 1.56. High methoxyl content pectin was procured from Bintang Utama Sentosa Inc. (Bekasi, Indonesia). Ethanol (99.9%) and 1,10-phenanthroline (99.9%) were purchased from Merck. Stock solution (100 mg L^{-1}) of Fe(II) ion 100 mL was prepared from the solid $(\text{NH}_4)_2\text{Fe}(\text{SO}_4)_2 \cdot 6\text{H}_2\text{O}$ (Merck) 0.07 g, which was dissolved in distilled water by adding 0.50 g of hydroxylamine hydrochloride 99.9% (Merck) and 5 mL of H_2SO_4 (Merck) 2 M. Standard solution 1000 mg L^{-1} of Cu^{2+} , Zn^{2+} , Co^{2+} , Fe^{3+} , Pb^{2+} , Ni^{2+} , Ca^{2+} , and Mg^{2+} (Merck) were used for the interference study and prepared using distilled water

from CV. Progo Mulyo (Yogyakarta, Indonesia). All chemical used were analytical reagent grade without further purification process.

Instrumentation

The color absorbance of sensor films was determined using a UV-Vis Spectrophotometer (Shimadzu UV-1800). The prepared membrane was characterized by a Fourier Transform-Infrared Spectrophotometer (Shimadzu IR Prestige 21), while the morphology of surface membranes was analyzed using a Scanning Electron Microscope (JOEL type JSM-6701F).

Procedure

Synthesis of alginate/pectin film immobilized 1,10-phenanthroline

The alginate/pectin-phenanthroline film was made by mixing 0.05 g alginate and 0.20 g pectin in 10 mL of distilled water. The homogeneous solution was then poured into a petri dish (60 mm) and dried at $55 \text{ }^\circ\text{C}$ for 16 h. The alginate/pectin film was immersed for 24 h in a solution of 2% (w/v) CaCl_2 to allow the crosslinking reaction. The crosslinking alginate/pectin film was then immersed in 5 mL 1,10-phenanthroline for 24 h. After that, the obtained film was dried at room temperature and was used for further characterization. The thickness of the alginate/pectin-phenanthroline film was $0.029 \pm 0.005 \text{ mm}$, with an average weight of 0.1258 g. For all the experiments, the film was cut into $1 \times 1 \text{ cm}^2$ size and used.

Optimization of the measurement parameters

Colorimetric detection of Fe(II) ions using alginate/pectin-phenanthroline film was carried out by immersing the film in 2 mL of Fe(II) solution for 2 min. Various concentration ($2\text{--}10 \text{ mg L}^{-1}$) of Fe(II) ion was adjusted at pH 1–6 using 0.1 M HCl and 0.1 M NaOH solutions. The maximum absorption wavelength of the alginate/pectin film was measured by scanning the absorbance of the film at 450–600 nm using a UV-Visible spectrophotometer. The λ_{max} was used to obtain the amount of phenanthroline to be added during the synthesis of the alginate/pectin film by varying the concentration of 1,10-phenanthroline (0.1–0.3% w/v). The interference study of alginate/pectin-phenanthroline film was investigated by performing the detection of

Fe(II) ion in the presence of other metal ions (Cu^{2+} , Zn^{2+} , Co^{2+} , Fe^{3+} , Pb^{2+} , Ni^{2+} , Ca^{2+} , and Mg^{2+}) under optimum condition.

Film alginate/pectin sensing ability

The different concentrations (0, 2.0, 4.0, 6.0, 8.0, and 10.0 mg L^{-1}) of Fe(II) solutions were tested using a film sensor in triplicate to obtain the calibration curve. The detection limit is calculated using the $3s/S$ criterion, where 's' is the standard deviation of the absorbance of 10 blank alginate/pectin film, and 'S' is the slope of the linear calibration curve [3]. The accuracy of the film sensor is determined based on the % recoveries of Fe(II) concentration added into the tap water sample. The tap water sample from the Laboratory of Analytical Chemistry, Faculty of Mathematics and Natural Sciences, Universitas Gadjah Mada, Yogyakarta, Indonesia, was used as a real water sample. The tap water was collected in a 1.5 L plastic bottle and was added with 50 mL of H_2SO_4 2 M and 5.0 g hydroxylamine hydrochloride. The sample was filtrated using Whatman filter paper 42. Fe(II) solution 100 mg L^{-1} (0.20, 0.50, and 1.00 mL) was spiked into the tap water sample in a 10 mL volumetric flask. All of the tap water samples were examined using the alginate/pectin film. The absorbance of the film was measured using a UV-Visible spectrophotometer under optimum condition. The % recoveries are calculated by comparing the concentration of Fe(II) obtained from the measurement with the concentration of Fe(II) added in the sample.

RESULTS AND DISCUSSION

FTIR Characterization of Alginate/Pectin-Phenanthroline Film

The FTIR spectra of alginate/pectin-phenanthroline film and the initial reagents were shown in Fig. 1. The spectrum of sodium alginate (see Fig. 1(a)) had a broad peak at 3320 cm^{-1} due to the stretching of O-H bond, while the sharp peaks between $1584\text{--}1413 \text{ cm}^{-1}$ were attributed to the asymmetric and symmetrical vibration of COO^- respectively [13]. The FTIR spectrum of pectin (see Fig. 1(b)) had two bands that were associated with the stretching vibration of the carbonyl group ($\text{C}=\text{O}$) in the $1800\text{--}1500 \text{ cm}^{-1}$ region. The band at 1731 cm^{-1} was

assigned to the methyl ester group ($-\text{COOCH}_3$), while the one observed at 1634 cm^{-1} originated from the asymmetric vibration of the carbonyl group in the carboxylate ion ($-\text{COO}^-$). The bands around 1065 cm^{-1} were associated with the stretching of the C-O-C bond [14].

The characteristic peaks of 1,10-phenanthroline commonly occur at $1620\text{--}1400 \text{ cm}^{-1}$, which were attributed to the stretching of $\text{C}=\text{C}$ and $\text{C}=\text{N}$ in the aromatic ring of phenanthroline [15] (see Fig. 1(c)). Meanwhile, a broad water band in the region of 3400 cm^{-1} was usually present on the FTIR spectrum of phenanthroline due to the highly hygroscopic nature of phenanthroline [16].

The crosslinking process with Ca^{2+} ions caused an obvious shift of $-\text{COO}^-$ asymmetric and symmetric stretching to higher wavenumbers in the alginate/pectin-phenanthroline spectrum (Fig. 1(d)). This indicated the formation of an ionic bond between $-\text{COO}^-$ from alginate and pectin and Ca^{2+} in order to form an "egg-box structure" [12]. The non-crosslinked alginate/pectin film containing the negatively charged carboxyl interacted with the positively charged proteins through electrostatic interaction [17]. Therefore, the protonated 1,10-phenanthroline, which was the positively

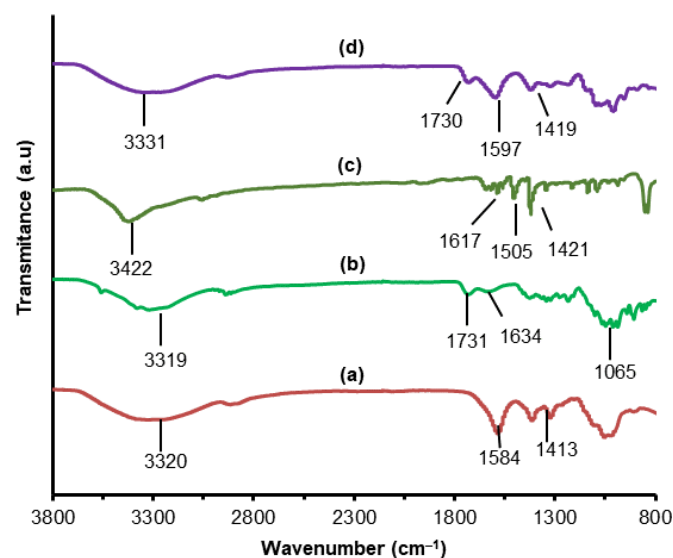


Fig 1. FTIR spectra of (a) sodium alginate, (b) pectin, (c) 1,10-phenanthroline, and (d) alginate/pectin-phenanthroline films

charged group, interacted with the alginate/pectin film through electrostatic interaction. Fig. 2 showed the proposed immobilization process of 1,10-phenanthroline in alginate/pectin film. There was no significant shifting on the methyl ester, indicating that this functional group did not involve in the interactions of alginate/pectin film with Ca^{2+} cation. The shifted peak from 3320 to 3331 cm^{-1} exhibited an overlap between the stretching of OH groups in the alginate/pectin polymers and the 1,10-phenanthroline spectrum.

The nature of alginate and pectin were known to be very hydrophilic since they consisted of many $-\text{OH}$ and $-\text{COOH}$ groups. The presence of divalent cations, such as Ca^{2+} , replaced the Na^+ ions in the sodium alginate and caused the polymer chains of alginate/pectin to cross-link [18]. This process increased the mechanical strength of alginate/pectin film, reducing its dissolution in water; however, it still has the ability to swelling. The film must be able to undergo the swelling process so that the Fe(II) ion presented in the solution may diffuse into the matrix in order to interact with the 1,10-phenanthroline reagent that is bound to the film matrix. In addition, films formed only from alginate are very soft, brittle, easily dissolve in water but visually more transparent than alginate/pectin

films. In contrast, films made only from pectin are rigid but have yellow in color. The mixture of alginate and pectin then produces a stronger, more stable, and transparent film. The transparency of the alginate/pectin film must be preserved because the absorbance of the film will be measured using a UV-Vis spectrophotometer.

SEM Characterization of Alginate/Pectin-Phenanthroline Film

The morphology of alginate/pectin-phenanthroline films before (Fig. 3(a)) and after sensing (Fig. 3(b)) Fe(II) ion was analyzed using the SEM instrument. The irregular surface shape and some pores were observed on the alginate/pectin-phenanthroline films before Fe(II) sensing (see Fig. 3(a)). This was due to the crosslinking process that did not occur in all polymer chains [17]. After the addition of Fe(II) ion, the film morphology slightly changed in the formation of 1,10-phenanthroline- Fe(II) complexes causing the surface to be more dense and compact (see Fig. 3(b)) [19]. In addition, some agglomerates were observed, indicating the distribution of 1,10-phenanthroline- Fe(II) complexes.

Table 1 shows the results of the SEM-EDS analysis

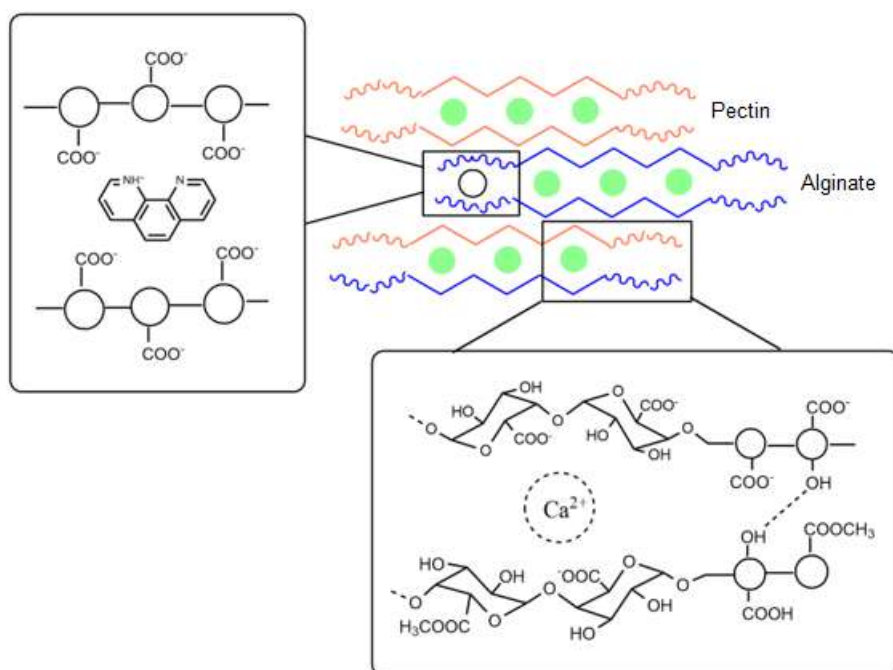


Fig 2. Proposed interaction between alginate/pectin matrix and 1,10-phenanthroline

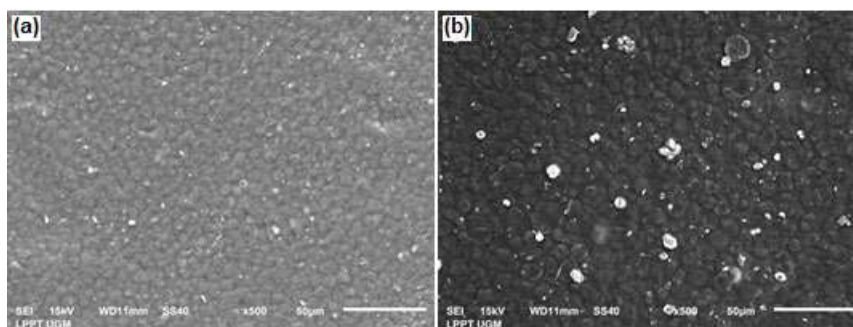


Fig 3. SEM image of alginate/pectin-phenanthroline films (a) before and (b) after sensing with Fe(II) ion

Table 1. Results of EDS analysis of alginate/pectin-phenanthroline films

Before sensing			After sensing		
Element	% Mass	% Atom	Element	% Mass	% Atom
C	34.88	42.64	C	34.78	42.70
O	60.73	55.74	O	60.15	55.44
Ca	4.16	1.53	Ca	5.04	1.85
Cl	0.23	0.10	Fe	0.02	0.01

of alginate/pectin-phenanthroline films before and after the sensing process. The presence of Fe(II) ions can be proven through the data from the EDS (Energy Dispersive X-ray Spectroscopy) analysis. The presence of Fe can be seen in the alginate/pectin-phenanthroline film after the sensing process, even though the amount (% mass) is relatively small (0.02%). The amount of Fe element in the film is very small compared to the amount of C and O elements, which are the key elements of the alginate/pectin film. Other elements such as Ca and Cl contained in the alginate/pectin-phenanthroline film are derived from CaCl_2 , which acts as a crosslinking agent.

Optimization of the Condition for Fe(II) Ions Detection Using Alginate/Pectin-Phenanthroline Film

The principle of the colorimetric method was based on the formation of a complex between the chromogenic reagent and the analyte. In this study, 1,10-phenanthroline was used as the chromogenic reagent and immobilized in alginate/pectin films, while the analyte was Fe(II) ions. Therefore, when the alginate/pectin-phenanthroline film was contacted with Fe(II) ions, the orange-red color of the complexes formed was observed. Although the formation of phenanthroline-Fe(II) complexes was observed by naked-eye (qualitative

analysis), the UV-Vis spectrophotometer analysis was performed by quantitative measurement. The maximum absorption wavelength of the phenanthroline-Fe(II) complex formed at 513 nm (see Fig. 4) was not significantly different from the previous study found at 510–515 nm [3,20].

It was well known that the nature of the chromogenic reagent and the metal ions depended on the pH of the aqueous system. Therefore, the 1,10-phenanthroline and Fe(II) ions formed a soluble and stable complex in the pH range 2–9 [20–21]. However, at

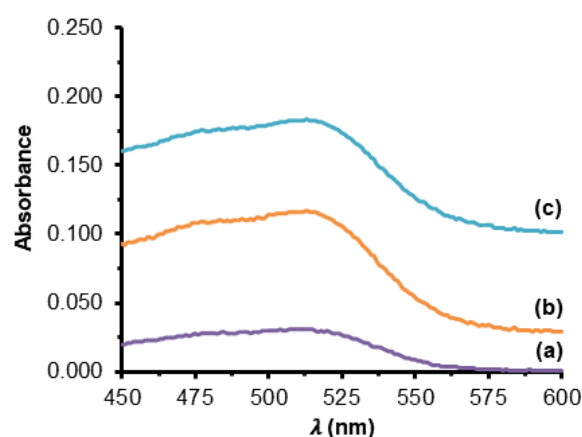


Fig 4. UV-Vis spectra of alginate/pectin-phenanthroline film after the addition of Fe(II) ion at the concentrations of (a) 2, (b) 5, and (c) 10 mg L^{-1}

pH above 4, Fe(II) ion reacted with OH^- to form $\text{Fe}(\text{OH})^+$ and the insoluble $\text{Fe}(\text{OH})_2$, which blocked the active site of the film, resulting in the decrease of absorbance. Fig. 5 showed that the highest absorbance was achieved at pH 2. At pH 3 and 4, the amount of protonated 1,10-phenanthroline is less than at pH 2. The unprotonated form of 1,10-phenanthroline tends to leach into the solution and react with free Fe(II) ions forming $[\text{Fe}(\text{II})(\text{phen})_3]^{2+}$ in the solution. This phenomenon causes a decrease in the absorbance of the alginate/pectin film. However, at a very strong acidic solution (pH = 1), the amount of H^+ in the solution is huge compared to the amount of Fe(II) ions, thus lowering the affinity of the 1,10-phenanthroline present in the film to react with Fe(II) ions.

The optimum concentration (in wt/v) of 1,10-phenanthroline was determined by varying the solution in the alginate/pectin films. Meanwhile, the films' capacity depended on the number of carboxyl groups (anions) that interacted with phenanthroline. Fig. 6 showed that the highest absorbance of the films was found in 0.2% 1,10-phenanthroline. This indicated that there were still negative charges in the alginate/pectin film, which have not bound for the optimal formation of complexes between Fe(II) ion and phenanthroline. This absorbance reached a plateau at a concentration of 0.2–0.3% since all the negative charges of alginate/pectin have been bound to 1,10-phenanthroline. The effect of the sensing method was also studied by the varying contact time between 0 to 2 min. The result showed that 2 min was sufficient to give a measurable absorbance of the color changes in alginate/pectin-phenanthroline films (see Fig. 7). This indicated that the films were suitable as a rapid optical sensor agent for Fe(II) detection.

Interference Study of Fe(II) Ions Detection in the Presence of Other Metal Ions

The main purpose of preparing the alginate/pectin-phenanthroline film as the optical sensor was to detect Fe(II) ions in environmental samples, especially on surface water. Therefore, some of the interference of metal ions that were present in the water samples became very important to be considered. This was due to the other metal ions that also reacted with 1,10-phenanthroline, lowering its ability

to bind Fe(II) ions. This study was carried out using three different concentrations (5, 10, and 20 mg L^{-1}) of

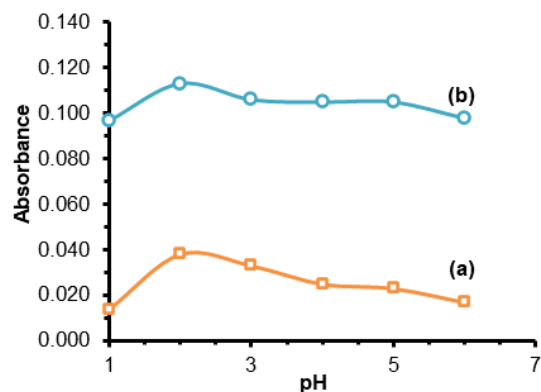


Fig 5. The effect of pH solution on the absorbance of alginate/pectin-phenanthroline films when the Fe(II) concentrations were (a) 2 and (b) 8 mg L^{-1}

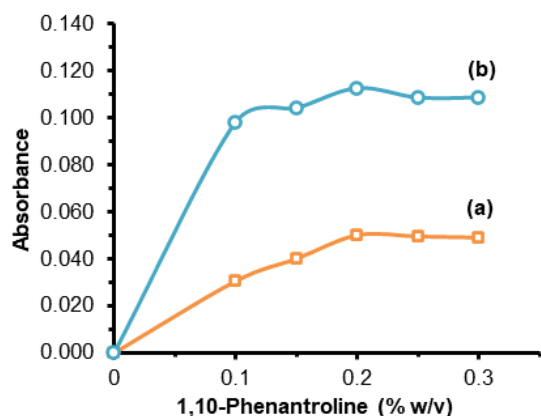


Fig 6. The influence of 1,10-phenanthroline concentration on the absorbance of alginate/pectin-phenanthroline films, when the used Fe(II) concentration was (a) 2 and (b) 8 mg L^{-1}

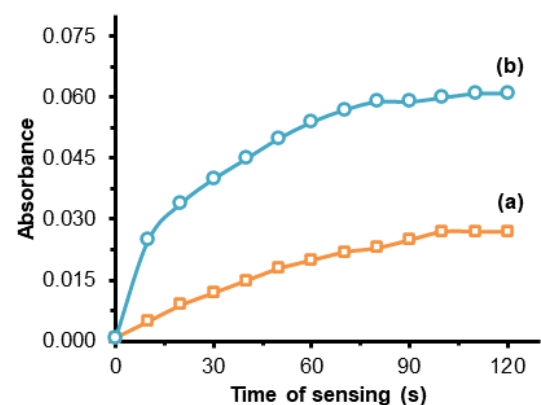


Fig 7. Optimization time of sensing when the used Fe(II) concentration was (a) 2 and (b) 4 mg L^{-1}

interference ions, such as Pb(II), Ni(II), Fe(III), Cu(II), Zn(II), Co(II), Mg(II), and Ca(II), in 25 mL solution while Fe(II) was fixed at 5 mg L⁻¹. As shown in Fig. 8, the addition of various interference metal ions except for Fe(III) ion. It did not significantly influence the Fe(II) ions detection using alginate/pectin-phenanthroline film. Even though some metal ions existed at 4 times higher concentration than Fe(II) ions, the absorbance value of the films tends to be constant, demonstrating a good selectivity for Fe(II) detection. However, Fe(III) ions influence the Fe(II) detection due to their similar cationic

size and physicochemical properties. To overcome this problem, the Fe(III) ions were reduced first using hydroxylamine hydrochloride at pH 2 solution. Therefore, the total Fe ions concentration at the environmental samples was measured.

Calibration Curve and Sensitivity of Alginate/Pectin-Phenanthroline Film for Fe(II) Quantification

Using the optimum condition for Fe(II) detection (i.e., 2 min contact time at pH 2 solution with 0.2% wt/v of 1,10-phenanthroline), a linear calibration curve with

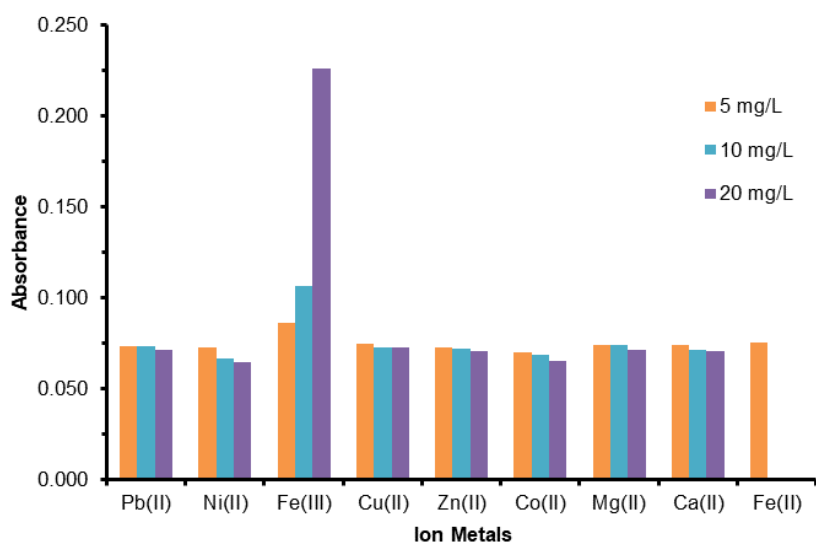


Fig 8. The colorimetric response of alginate/pectin-phenanthroline films in various concentrations of interference metal solution (5, 10, and 20 mg L⁻¹). The concentration of Fe(II) ion was fixed at 5 mg L⁻¹ in all solutions

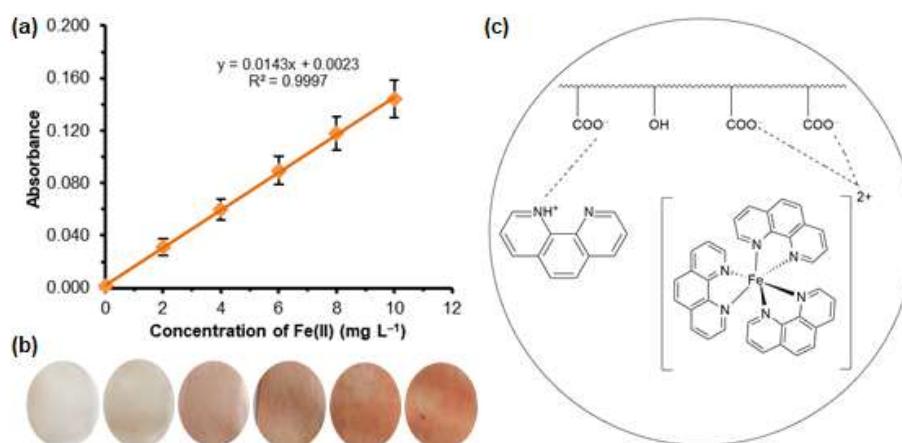


Fig 9. (a) Calibration curve of alginate/pectin-phenanthroline films at various Fe(II) concentrations, (b) the corresponding color of the alginate/pectin-phenanthroline films. From left to right, the concentration of Fe(II) solution was 0, 2, 4, 6, 8, and 10 mg L⁻¹, respectively, and (c) proposed interaction between alginate/pectin matrix and [Fe(II)(phen)₃]²⁺

high R^2 (0.997) in the range concentration of Fe(II) 0–10 mg L⁻¹ was obtained (Fig. 9(a)). The corresponding color of the alginate/pectin-phenanthroline films and proposed interaction between alginate/pectin matrix and [Fe(II)(phen)₃]²⁺ are shown in Fig. 9(b) and (c), respectively. The limit of detection for Fe(II) ions (0.446 mg L⁻¹) was remarkable. The precision of the quantification method was evaluated by testing the repeatability of the sensor films. The colorimetric response of the films was measured with 3 repetition tests in 3 different batches. Based on the statistical method, the relative standard deviation (RSD) of the different batches were range from 0.70–3.13%, indicating good precision of the proposed method.

Detection of Fe(II) Ions in the Tap Water Sample Using Alginate/Pectin-Phenanthroline Film

The applicability of the film sensor was performed by determining the Fe(II) concentration in the tap water sample. Tap water samples were analyzed using atomic absorption spectrometry, resulting in concentrations of Ca, Fe, Mg, K, and Na ions of 7.0, 0.04, 4.9, 9.5, 63.1 ppm, respectively. The sample was spiked with Fe(II) standard solution at 2, 5, and 10 mg L⁻¹, then measured using a UV-Vis spectrophotometer in optimum condition. Table 2 showed that the films sensor had good % recoveries between 102.10–110.72%, indicating a good accuracy for Fe(II) detection. The range of % recoveries value obtained was in accordance with that of the sample category in ppm

units, between 80–110% [22]. This showed that the presence of other disruptive matrices or other interferent metal ions in the tap water sample did not affect the detection of Fe(II) ions using alginate/pectin-phenanthroline films. However, there was a possibility that Fe(III) ions were contained in the tap water sample and might affect the detection of Fe(II). To overcome this problem, the tap water sample needed to be treated with hydroxylamine hydrochloride, causing the total Fe ions in the tap water sample to be in the form of Fe(II) ions for its detection to be optimal.

In addition, we have also compared the performance of the present sensor film with the other sensors available in the literature (Table 3). It can be seen that the detection of Fe(II) using alginate/pectin-phenanthroline film is promising to be an alternative method of Fe(II) in the water sample. Alginate/pectin film could be easily degraded in the environment. It makes this research has more advantage than other sensors. In addition, the complicated stages of reagent

Table 2. Determination of Fe(II) ion concentration in tap water sample using alginate/pectin-phenanthroline film in the optimum condition

Fe(II) added (mg L ⁻¹)	Fe(II) (mg L ⁻¹)	% recovery
0	0.469	-
2	2.683	110.72
5	5.667	103.96
10	10.678	102.10

Table 3. Comparison of performance of different Fe sensors with the presence sensor

Analyte	Method	Medium	LOD (mg L ⁻¹)	Ref.
Fe(II)	Potentiometric determination	Solid probe (2, 6-bis (carboxamide methyl ester) pyridine derivative as neutral ionophore in plasticized PVC membrane)	0.224	[9]
Fe(II)	UV-Vis absorption of Fe-2-(2-pyridyl) imidazole complex	Solid probe (2-(2-pyridyl)imidazole functionalize poly(vinylbenzyl chloride) (PVBC) nanofibers made into membrane)	2.0	[23]
Fe(III)	Naked eye observation	Solid Probe (Curcumin loaded in Zein membrane)	0.40	[24]
Fe(II & III)	UV-Vis absorption of Fe-1,10-phenanthroline complex	Solid probe (1,10-phenanthroline entrapped in poly(acrylamide) membrane)	0.02	[3]
Fe(II)	UV-Vis absorption of Fe-1,10-phenanthroline complex	Solid probe (1,10-phenanthroline entrapped in alginate/pectin film)	0.446	Present work

syntheses did not require for this study. The 1,10-phenanthroline reagents can be obtained easily and react very selectively with Fe(II) ion compared to other metal ions.

■ CONCLUSION

The alginate/pectin-phenanthroline film optical sensors were successfully prepared by immobilizing 1,10-phenanthroline in alginate/pectin films. The optimum condition for Fe(II) detection was obtained at pH 2 for 2 min contact time and 0.2% of 1,10-phenanthroline concentration. The alginate/pectin-phenanthroline provided high accuracy, precision, and selectivity for Fe(II) in the aquatic environmental samples, with a detection limit of 0.446 mg L⁻¹. Therefore, the alginate/pectin-phenanthroline film optical sensor was found as a simple, fast, accurate, and alternative method for Fe(II) ions detection in the environmental samples for routine daily analysis.

■ ACKNOWLEDGMENTS

The authors are grateful to the Directorate of Research of Universitas Gadjah Mada for funding this study through the RTA (Final Project Research) Scheme.

■ REFERENCES

- [1] Chakrabarty, S., Tonu, N.T., and Saha, N.K., 2018, Removal of iron(II) ion from aqueous solution using waste tea leaves, *Int. J. Eng. Sci.*, 6 (12), 62–67.
- [2] World Health Organization, 1996, *Guidelines for Drinking Water*, Geneva.
- [3] Kumar, S.A., Thakur, N., Parab, H.J., Pandey, S.P., Shinde, R.N., Pandey, A.K., Kumar, S.D., and Reddy, A.V.R., 2014, A visual strip sensor for determination of iron, *Anal. Chim. Acta*, 851, 87–94.
- [4] Pavlovska, G., Stafilov, T., and Čundeva, K., 2015, Determination of iron in drinking water after its flotation concentration by two new dithiocarbamate collectors, *J. Environ. Sci. Health. Part A Environ.*, 50 (13), 1386–1392.
- [5] Adebayo, B.K., Ayejuyo, S., Okoro, H.K., and Ximba, B.J., 2011, Spectrophotometric determination of iron(III) in tap water using 8-hydroxyquinoline as a chromogenic reagent, *Afr. J. Biotechnol.*, 10 (71), 16051–16057.
- [6] Poirier, L., Nelson, J., Leong, D., Berhane, L., Hajdu, P., and Lopez-Linares, F., 2016, Application of ICP-MS and ICP-OES on the determination of nickel, vanadium, iron, and calcium in petroleum crude oils via direct dilution, *Energy Fuels*, 30 (5), 3783–3790.
- [7] Lou, T., Chen, L., Chen, Z., Wang, Y., Chen, L., and Li, J., 2011, Colorimetric detection of trace copper ions based on catalytic leaching of silver-coated gold nanoparticles, *ACS Appl. Mater. Interfaces*, 3 (11), 4215–4220.
- [8] Murthy, Y.L.N., Govindh, B., Diwakar, B.S., Nagalakshmi, K., and Singh, R., 2011, A simple inexpensive detection method of nickel in water using optical sensor, *Int. J. ChemTech. Res.*, 3 (3), 1285–1291.
- [9] Abounassif, M.A., Al-Omar, M.A., Amr, A.G.E., and Mostafa, G.A.E., 2011, PVC membrane sensor for potentiometric determination of iron(II) in some pharmaceutical formulations based on a new neutral ionophore, *Drug Test. Anal.*, 3 (6), 373–379.
- [10] Galus, S., and Lenart, A., 2013, Development and characterization of composite edible films based on sodium alginate and pectin, *J. Food Eng.*, 115 (4), 459–465.
- [11] Bierhalz, A.C.K., da Silva, M.A., and Kieckbusch, T.G., 2012, Natamycin release from alginate/pectin films for food packaging applications, *J. Food Eng.*, 110 (1), 18–25.
- [12] Rezvani, M., Ahmad, N., Mohd Amin, M.C.I., and Ng, S., 2017, Optimization, characterization, and *in vitro* assessment of alginate-pectin ionic cross-linked hydrogel film for wound dressing applications, *Int. J. Biol. Macromol.*, 97, 131–140.
- [13] Hua, S., Ma, H., Li, X., Yang, H., and Wang, A., 2010, pH-sensitive sodium alginate/poly(vinyl alcohol) hydrogel beads prepared by combined Ca²⁺ crosslinking and freeze-thawing cycles for controlled release of diclofenac sodium, *Int. J. Biol. Macromol.*, 46 (5), 517–523.
- [14] Coimbra, P., Ferreira, P., de Sousa, H.C., Batista, P., Rodrigues, M.A., Correia, I.J., and Gil, M.H., 2011,

- Preparation and chemical and biological characterization of a pectin/chitosan polyelectrolyte complex scaffold for possible bone tissue engineering applications, *Int. J. Biol. Macromol.*, 48 (1), 112–118.
- [15] Fayad, N.K., Al-Noor, T.H., Mahmood, A.A., and Malih, I.K., 2013, Synthesis, characterization, and antibacterial studies of Mn(II), Fe(II), Co(II), Ni(II), Cu(II) and Cd(II) mixed-ligand complexes containing amino acid (L-valine) and (1,10-phenanthroline), *Chem. Mater. Res.*, 3 (5), 66–74.
- [16] Smith, R.C., 1961, Infrared Spectra of Substituted 1,10-Phenanthrolines, *Dissertation*, Department of Chemistry Iowa University, Iowa, USA.
- [17] Aguilar, K.C., Tello, F., Bierhalz, A.C.K., Romo, M.G.G., Flores, H.E.M., and Grosso, C.R.F., 2015, Protein adsorption onto alginate-pectin microparticles and films produced by ionic gelation, *J. Food Eng.*, 154, 17–24.
- [18] Awasthi, R., Kulkarni, G.T., Ramana, M.V., Pinto, T.J.A., Kikuchi, I.S., Ghisleni, D.D.M., Braga, M.S., and Dua, K., 2017, Dual crosslinked pectin–alginate network as sustained release hydrophilic matrix for repaglinide, *Int. J. Biol. Macromol.*, 97, 721–732.
- [19] Siracusa, V., Romani, S., Gigli, M., Mannozi, C., Cecchini, J.P., Tylewicz, U., and Lotti, N., 2018, Characterization of active edible films based on citral essential oil, alginate and pectin, *Materials*, 11 (10), 1980.
- [20] Wang, L., Zhang, Y., Park, Y., Chen, L., and Jung, Y.M., 2017, Quantitative determination of iron ions based on a resonance, *Anal. Sci.*, 33 (1), 23–27.
- [21] Adhikamsetty, R.K., Gollapalli, N.R., and Jonnalagadda, S.B., 2008, Complexation kinetics of Fe²⁺ with 1,10-phenanthroline forming ferriin in acidic solutions, *Int. J. Chem. Kinet.*, 40 (8), 515–523.
- [22] Harris, D.C., 2010, *Quantitative Chemical Analysis*, W.H. Freeman and Company, New York, USA.
- [23] Ondigo, D.A., Tshentu, Z.R., and Torto, N., 2013, Electrospun nanofiber based colorimetric probe for rapid detection of Fe²⁺ in water, *Anal. Chim. Acta*, 804, 228–234.
- [24] Saithongdee, A., Praphairaksit, N., and Imyim, A., 2014, Electrospun curcumin-loaded zein membrane for iron(III) ions sensing, *Sens. Actuators, B*, 202, 935–940.

High Reusability of NiAl LDH/Biochar Composite in the Removal Methylene Blue from Aqueous Solution

Aldes Lesbani^{1,2*}, Neza Rahayu Palapa¹, Rabellia Juladika Sayeri², Tarmizi Taher³, and Nurlisa Hidayati⁴

¹Graduate School of Mathematics and Natural Sciences, Faculty of Mathematics and Natural Sciences, Universitas Sriwijaya, Jl. Palembang Prabumulih Km. 32, Ogan Ilir 30662, Indonesia

²Research Center of Inorganic Materials and Coordination Complexes, Faculty of Mathematics and Natural Sciences, Universitas Sriwijaya, Jl. Palembang Prabumulih Km. 32, Ogan Ilir 30662, Indonesia

³Department of Environmental Engineering, Institut Teknologi Sumatera, Jl. Terusan Ryacudu, Way Hui, Kecamatan Jati Agung, Lampung Selatan 35365, Indonesia

⁴Department of Chemistry, Faculty of Mathematics and Natural Sciences, Universitas Sriwijaya, Jl. Palembang Prabumulih Km. 32, Ogan Ilir 30662, Indonesia

* Corresponding author:

email: aldeslesbani@pps.unsri.ac.id

Received: June 16, 2020

Accepted: January 4, 2021

DOI: 10.22146/ijc.56955

Abstract: Ni/Al layered double hydroxide was used as a starting material for composite formation with biochar as a matrix. The materials were characterized using X-ray, FTIR, nitrogen adsorption-desorption, thermal, and morphology analyses. The NiAl LDH/Biochar material is then used as an adsorbent of methylene blue from an aqueous solution. The factor that was influencing adsorption such as pH, time, methylene blue concentration, and temperature adsorption was studied systematically. The regeneration of adsorbent was performed to know the stability of NiAl LDH/Biochar under several cycle adsorption processes. The results showed that NiAl LDH/Biochar has a specific diffraction peak at 11.63° and 22.30°. NiAl LDH/Biochar has more than ten-fold surface area properties (438,942 m²/g) than biochar (50.936 m²/g), and Ni/Al layered double hydroxide (92.682 m²/g). The methylene blue adsorption on NiAl LDH/Biochar follows a pseudo-second-order kinetic adsorption model and classify as physical adsorption. The high reusability properties were found for NiAl LDH/Biochar, which was largely different from biochar and Ni/Al layered double hydroxide.

Keywords: Ni/Al; layered double hydroxide; biochar; composite; methylene blue; adsorption; reusability

■ INTRODUCTION

The presence of hazardous dyes in industrial activities is a severe problem for humans and the ecology system [1]. These dyes are toxic, carcinogenic, and mutagenic, thus cause human and environmental health. The dyes are produced from industrial activities such as cosmetics, painting, textile, leather, food, and also drug industries [2-4]. The dyes are challenging to degrade since they are stable structures under oxidation and light [5]. One of the toxic dyes is methylene blue, a methylthionium chloride compound and classifies as a

cationic dye [6]. The structure of methylene blue is shown in Fig. 1. Thus, the removal of methylene blue from wastewater is crucial. Some methods are available to remove methylene blue from an aqueous solution, such as purification, membrane separation, and adsorption [7-9].

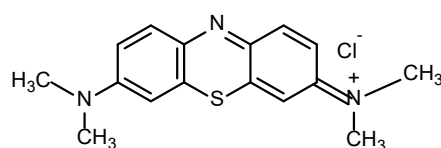


Fig 1. Chemical structure of methylene blue

Among these methods, adsorption is an appropriate method to remove methylene blue from the aqueous solution. This method was easy to do, simple way, low-cost operation, and fast process [10]. On the other hand, the effectivity of adsorbent in the adsorption process is one factor in getting high adsorption capacity and stability of the material. Numerous adsorbents have been applied to remove methylene blue from an aqueous solution, such as zeolite, bentonite, carbon nanotube, biomass, activated carbon, chitosan, and also layered double hydroxide [11-13].

Layered double hydroxide (LDH) is an inorganic material that has the general formula $[M^{2+}_{1-x}M^{3+}_x(OH)_2] + xA_x^{-n}mH_2O$, where M^{2+} is a divalent metal ion, M^{3+} is a trivalent metal ion, A_x^{-n} is an anion with n valent state, and water of crystallization [14-15]. LDH consists of an anion on the interlayer distance, which can be exchangeable to other anions to get unique properties of LDH. The common anion in LDH is nitrate, sulfate, hydroxide, chloride, and carbonate [16-18]. The total charge of LDH is positively due to neutralizing negative charge from anion on interlayer space. LDH has well-known as an adsorbent of dyes due to its high adsorption capacity and high surface area properties.

On the other hand, the use of LDH several times the regeneration process is ineffective due to sprayed and exfoliated LDH structure [19]. Thus modification of LDH for reuse adsorbent aim should be conducted, such as the formation of the composite using matrix/support materials which can reduce the particle size of LDH to be facile for reuse adsorbent. One of the promising materials as a matrix for LDH is biochar. Biochar is an organic compound from the pyrolysis of biomass under high temperature [20]. The use of biochar for many applications is reported, such as water treatment, soil improvement materials, and also pharmaceutical applications [21-22]. The composite of LDH-biochar as an adsorbent of many organic and inorganic pollutants has been reported in many publications.

MgAl and Mg/Fe-biochar were prepared as adsorbents of phosphate [23]. Phosphate was also successfully removed from an aqueous solution using Mg/Al LDH-biochar [24]. Biochar from date palm was

used as a matrix for the composite of MgAl LDH-biochar. This biochar has an adsorption capacity of 302.75 mg/g at 100 mg/L in 180 min adsorption time [25]. LDH Mg/Al-biochar has been prepared to form a composite as an adsorbent of methylene blue. This adsorbent can achieve adsorption capacity until 406.47 mg/g [9]. Lins et al. [26] introducing liquid phase co-precipitation of Mg-Al LDH on a biochar matrix for enhanced phosphate adsorption. Wang et al. [27] reporting high arsenic adsorption onto Ni-Fe LDH-biochar composite. Despite different biochars used, these studies, in general, suggest that selective adsorption of anionic pollutants depends on the type of LDHs used, and the adsorption mechanisms are linked to interlayer spacing and electrical properties of LDHs. All these studies showed that LDH is commonly used to prepare composite using biochar as a matrix.

This study aims to use LDH based nickel-aluminum as a starting material to form a composite with biochar as an adsorbent of methylene blue. Formation of Ni/Al LDH/biochar was prepared by mixing the co-precipitation method. The materials were characterized using X-ray, FTIR, BET, thermal, and photo SEM-EDX analyses. The adsorption was studied through the effect of pH medium, adsorption time, initial concentration of methylene blue, and temperature adsorption. The performance of the adsorbent was investigated through reusability adsorbent several times. Prior to these processes, desorption is conducted to know the suitable solvent to desorb methylene blue on the solid adsorbent.

■ EXPERIMENTAL SECTION

Chemicals and Instrumentation

Chemicals used in this research were nickel(II) nitrate, aluminum(III) nitrate, sodium hydroxide, and methylene blue. These chemical reagents were used directly from Merck and Sigma-Aldrich without further purification. Biochar based on Indonesian rice husk was obtained from Bukata Organic, Java Island. Water was obtained from Research Center of Inorganic Materials and Complexes FMIPA Universitas Sriwijaya using Purite® water ion exchange purification system.

Characterization of the material was performed using X-ray Rigaku Miniflex-6000. The material was analyzed in the range 5–80° with scan speed 1°/min. FTIR spectrum was obtained from FTIR Shimadzu Prestige-21. Materials were mixed with KBr to form a pellet and were scanned at wavenumber 400–4000 cm⁻¹. Nitrogen adsorption-desorption analysis was conducted using ASAP Micrometric at 77 K. Sample was degassed under liquid nitrogen several times prior to analysis. The thermal stability of the material was measured using TG-DTA Shimadzu under atmospheric nitrogen. The temperature analysis was at room temperature to 800 °C. Material photos were obtained using SEM-EDX Quanta-650 Oxford Instrument. The concentration of methylene blue was analyzed using UV-Visible spectrophotometer BIO-Base BK-UV 1800 PC at wavelength 664 nm.

Procedure

Synthesis of Ni/Al LDH

Synthesis of Ni/Al LDH was conducted using the co-precipitation method at pH 10 [28]. Nickel(II) nitrate and aluminum(III) nitrate with equal volume and concentration ratio (3:1) were mixed and stirred at room temperature. Sodium carbonate (0.3 M) was added with equal volume slowly and sodium hydroxide to achieve pH 10. The reaction mixture was kept at 80 °C for 18 h. The solid material was obtained and washed with water, and dried at 110 °C.

Synthesis of composite Ni/Al LDH-biochar

Synthesis of NiAl LDH/Biochar was conducted by mixing the co-precipitation method. The solution of nickel(II) nitrate 0.3 M and aluminum(III) nitrate 0.1 M with equal volume was mixed for 60 min. Biochar (3 g) was added to the reaction mixture following by the addition of sodium hydroxide (2 M). The pH mixture was adjusted to 10 by adding sodium hydroxide. The reaction was kept for 72 h with constant stirring. The solid material was obtained and washed several times with water, and dried at 110 °C for several days.

Adsorption process

Adsorption was studied by variation of pH solution, adsorption time, initial concentration, and adsorption temperature using 0.1 g of NiAl LDH/Biochar and

starting materials as control. The adsorption was conducted using a batch small reactor system equipped with shaking apparatus control. The variation pH solution was 2–10. Adsorption time was conducted at 5–200 min. Adsorption temperature was carried out at 30, 40, 50, and 60 °C using an initial concentration of methylene blue from 5–20 mg/L for NiAl LDH as adsorbent, 5–40 mg/L for biochar, and 5–60 mg/L for NiAl LDH/Biochar. All filtrate of methylene blue was analyzed using UV-Visible at wavelength 664 nm.

Desorption and regeneration

Desorption of methylene blue after the adsorption process was conducted using several solvents such as ethanol, acetone, diethyl ether, water, hydrochloric acid, and sodium hydroxide. The solvent has been classified as organic and inorganic solvents. The filtrate from the desorption process was measured using UV-Vis at 664 nm.

Prior regeneration process, the adsorbent was desorbed using maximum desorption solvent followed by washed using water several times, dried at 110 °C overnight, and ready to use. The cycle of adsorption was conducted three times the cycle for adsorption of methylene blue using a similar adsorbent.

RESULTS AND DISCUSSION

The results of XRD pattern of NiAl LDH/Biochar, biochar, and Ni/Al LDH were shown in Fig. 2. Fig. 2(a) showed Ni/Al LDH has peak at 11.63° (003); 23.00° (006); 35.16° (012); 39.56° (015); 47.4° (018) and 61.59° (110). The formation of a well-layered structure of Ni/Al was identified at 11.63 (003) and 61.59 (110) [29]. These results are appropriate with Tao et al. (2019) where the crystallinity of Ni/Al LDH was high [30]. Fig. 2(b) shows the diffraction of biochar. Biochar is an organic compound; thus, the diffraction peak is broad due to the high organic content on the material. The diffraction peak at 22.30° (002) for biochar was characteristic of organic content, especially carbon [31-32]. Fig. 2(c) shows the NiAl LDH/Biochar based Ni/Al LDH and biochar. The diffraction peak of NiAl LDH/Biochar is a little broad, with several peaks were identified at 11.63° and 22.30°. These two peaks are Ni/Al LDH and biochar

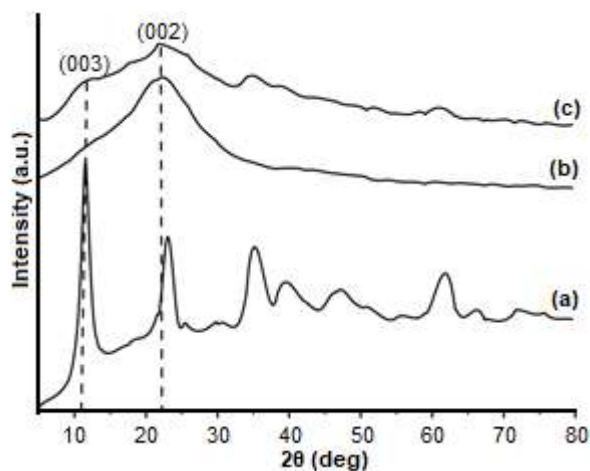


Fig 2. X-ray diffraction of Ni/Al LDH (a), biochar (b), and NiAl LDH/Biochar (c)

characterized; thus, NiAl LDH/Biochar consists of LDH and biochar.

FTIR spectrum of materials was presented in Fig. 3. Fig. 3(a) shows the IR spectrum of Ni/Al LDH. The peak vibration was appeared at 3664 cm^{-1} (ν O–H stretching), 1630 cm^{-1} (ν O–H bending), 1381 cm^{-1} (ν N–O nitrate), 748 cm^{-1} (ν Al–O, trivalent metal), and 563 cm^{-1} (ν Ni–O, divalent metal) [24]. Fig. 3(b) shows the FTIR spectrum of biochar. There are several peaks identified at wavenumber 3448 cm^{-1} , 2924 cm^{-1} , 2854 cm^{-1} , 2368 cm^{-1} , 2337 cm^{-1} , 1620 cm^{-1} , and 1130 cm^{-1} . All these vibrations were identified in the fingerprint area and consist of an organic vibration component [33]. Fig. 3(c) shows the FTIR spectrum of NiAl LDH/Biochar. The peaks are found at 3441 cm^{-1} , 2931 cm^{-1} , 2368 cm^{-1} , 2283 cm^{-1} , 1627 cm^{-1} , 1381 cm^{-1} , 1049 cm^{-1} , and 578 cm^{-1} . All these vibrations contain vibrations of Ni/Al LDH and biochar. Thus, NiAl LDH/Biochar in this research is based on two components.

The nitrogen adsorption-desorption analysis data of Ni/Al LDH, biochar, and NiAl LDH/Biochar was shown in Fig. 4. The isotherm in Fig. 4 shows a hysteresis loop

where the adsorption curve has a different type from the desorption step. The NiAl LDH/Biochar has a type II isotherm model, and the material has a mesoporous class with contains a larger pore than the microporous type [34]. The isotherm data in Fig. 4 was then used to obtain surface area, pore-volume, and pore diameter, as shown in Table 1.

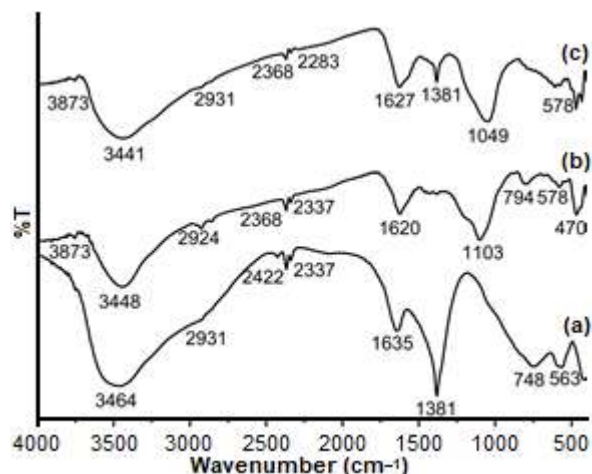


Fig 3. FTIR spectrum of Ni/Al LDH (a), biochar (b), and NiAl LDH/Biochar (c)

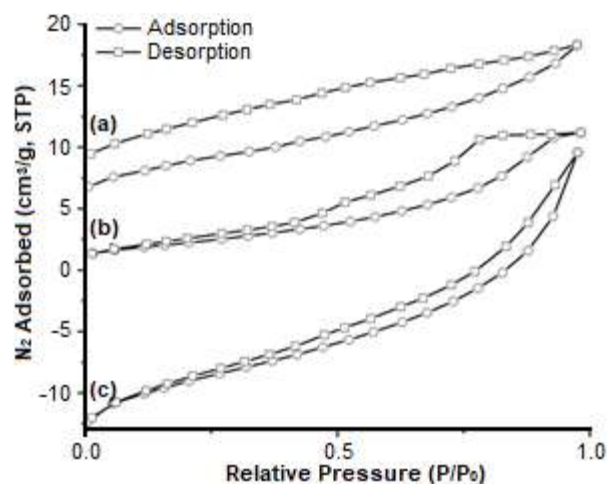


Fig 4. Nitrogen adsorption-desorption profile of Ni/Al LDH (a), biochar (b), and NiAl LDH/Biochar (c)

Table 1. BET surface area analysis

Materials	Surface area (m^2/g)	Pore volume (cm^3/g)	Pore diameter (nm)
Ni/Al LDH	92.683	0.001	13.206
Biochar	50.936	0.002	12.088
NiAl LDH/Biochar	438.942	0.002	12.301

Table 1 shows NiAl LDH/Biochar has large surface area properties than Ni/Al LDH and biochar. The NiAl LDH/Biochar has a surface area of 438.942 m²/g and almost ten-fold higher than starting materials. These phenomena are probably due to the biochar as matrix-assisted to reduce the size and agglomeration of LDH [23].

The TG-DTA pattern of the material was presented in Fig. 5. Ni/Al LDH has two endothermic peaks at 90 °C and 310 °C, which is assigned as water loss and nitrate on interlayer LDH decomposition. On the other hand, the DTA profile of biochar contains not only an endothermic peak but also an exothermic peak. The endothermic peak was found at 95 °C due to the loss of water of

crystallization [11]. The exothermic peak was found at 500 °C because of the oxidation of organic compounds on biochar [35]. The TG-DTA pattern of NiAl LDH/Biochar was shown in Fig. 5(c) and contained one endothermic peak at 95 °C and two exothermic peaks at 430 °C and 500 °C. The exothermic peaks are the LDH decomposition peak, and the endothermic peak is the oxidation of organic biochar.

The surface material photos were presented in Fig. 6. The layer structure of Ni/Al was seen in Fig. 6(a) with the agglomeration process. The biochar, as seen in Fig. 6(b) has an irregular pore. The NiAl LDH/Biochar shown in Fig. 6(c) has small particle distribution than

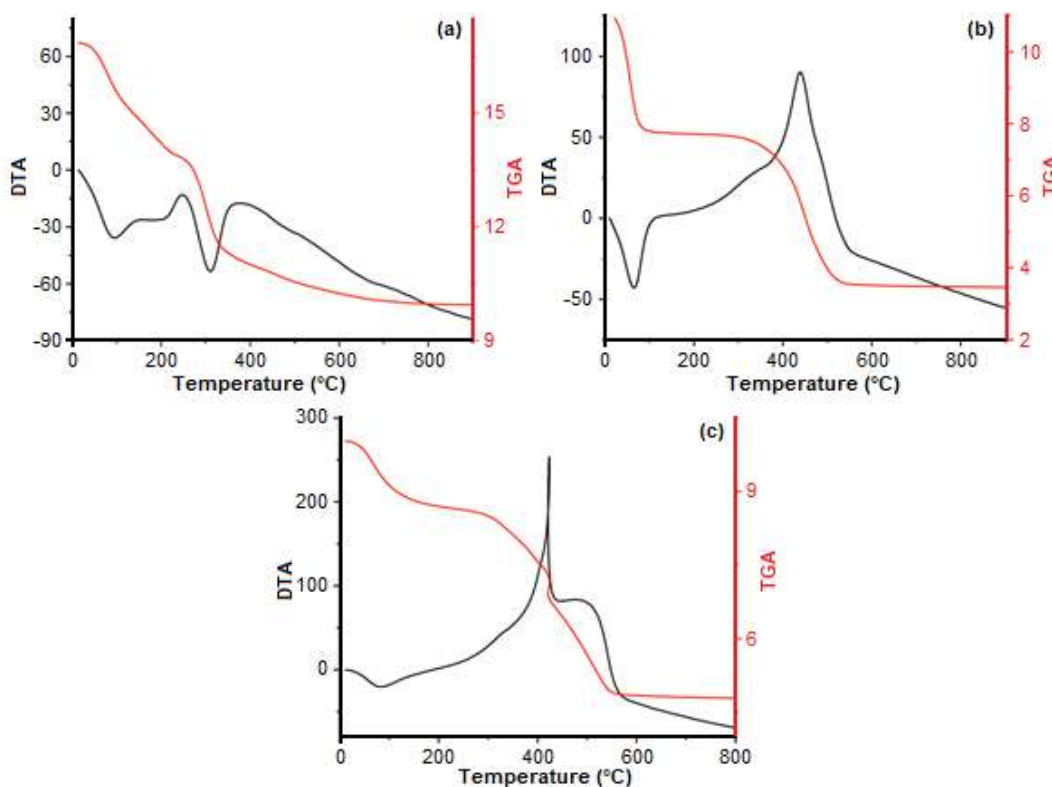


Fig 5. TG-DTA profile of Ni/Al LDH (a), biochar (b), and NiAl LDH/Biochar (c)

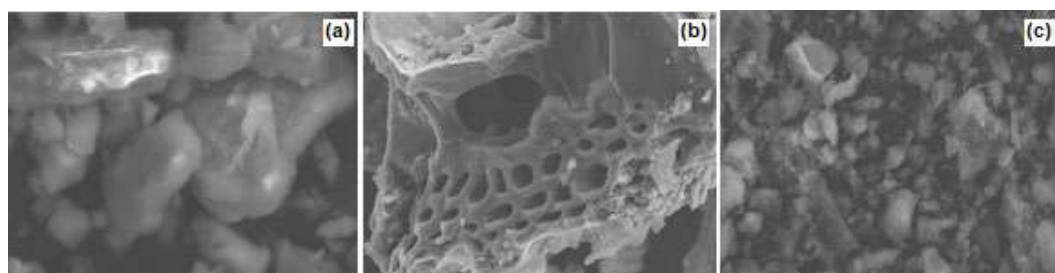


Fig 6. Surface photo of materials

Ni/Al LDH with minor agglomeration. These photos in Fig. 6(c) are related to a high surface area of NiAl LDH/Biochar in this research.

The composition of materials analysis using EDX was shown in Table 2. The main composition of LDH was nickel, aluminum, oxygen, and nitrogen. Nitrogen is higher because nitrate ion was located on the interlayer space of LDH. Biochar has high carbon content (58.3%). The NiAl LDH/Biochar contains all elements of starting materials except carbon because carbon is associated with oxygen in the agglomeration process, and the percentage of oxygen will be higher than starting materials.

The effect of the pH medium of methylene blue adsorption on Ni/Al LDH, biochar, and NiAl LDH/Biochar is shown in Fig. 7. The optimum pH for NiAl LDH/Biochar, biochar, and Ni/Al LDH was 4, 4, and 3. All adsorbents have methylene blue adsorption at acid medium. The solution of methylene blue has a pH range of 3.0–4.3, the optimum pH adsorption using NiAl LDH/Biochar, biochar, and Ni/Al LDH is inside the natural range of methylene blue, for further adsorption was conducted at this optimum pH.

Fig. 8 shows the effect of adsorption time and fitting with kinetic pseudo-first-order (PF-O) and pseudo-second-order (PS-O). The amount of methylene blue adsorbed on NiAl LDH/Biochar, biochar, and Ni/Al LDH was gradually increased by increasing adsorption time until optimum. The amount of methylene blue stable on the adsorbent. The optimum adsorption time for NiAl LDH/Biochar, biochar, and Ni/Al LDH is started from 150 min, as shown in the black circle symbol. These data then were applied to obtain PF-O and PS-O using the equation as following [36]:

PF-O:

$$\log(q_e - q_t) = \log q_e - \left(\frac{k_1}{2.303} \right) t \quad (1)$$

where: q_e is adsorption capacity at the equilibrium (mg g^{-1}); q_t is adsorption capacity at t min (mg g^{-1}); t is adsorption time (min), and k_1 is kinetic adsorption rate at PF-O (min^{-1}).

PS-O:

$$\frac{t}{q_t} = \frac{1}{k_2 q_e^2} + \frac{1}{q_e} t \quad (2)$$

where q_e is adsorption capacity at the equilibrium (mg g^{-1}); q_t is adsorption capacity at t min (mg g^{-1}); t is adsorption time (min), and k_2 is adsorption rate at PS-O ($\text{g mg}^{-1} \text{min}^{-1}$). The PF-O and PS-O results are shown in Table 3.

The data in Table 3 showed that the R^2 value for NiAl LDH/Biochar and biochar is closed to one for PS-O. On the other hand, Ni/Al LDH has R^2 closed to one

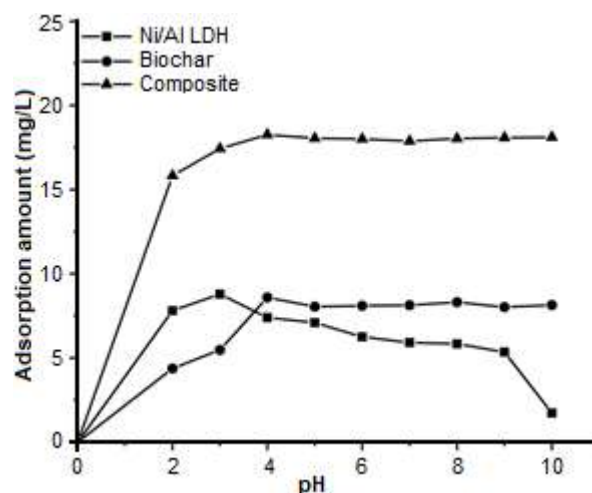


Fig 7. The pH adsorption effect of methylene blue on Ni/Al LDH, biochar, and NiAl LDH/Biochar

Table 2. Analysis composition of materials by EDX

Ni/Al LDH		Biochar		NiAl LDH/Biochar	
Element	(%)	Element	(%)	Element	(%)
Ni	88.3	C	58.3	Ni	14.6
Al	1.3	O	27.3	Al	3.3
O	1.4	Si	11.0	N	1.3
N	9.1	Al	3.3	O	55.6
				Si	25.2

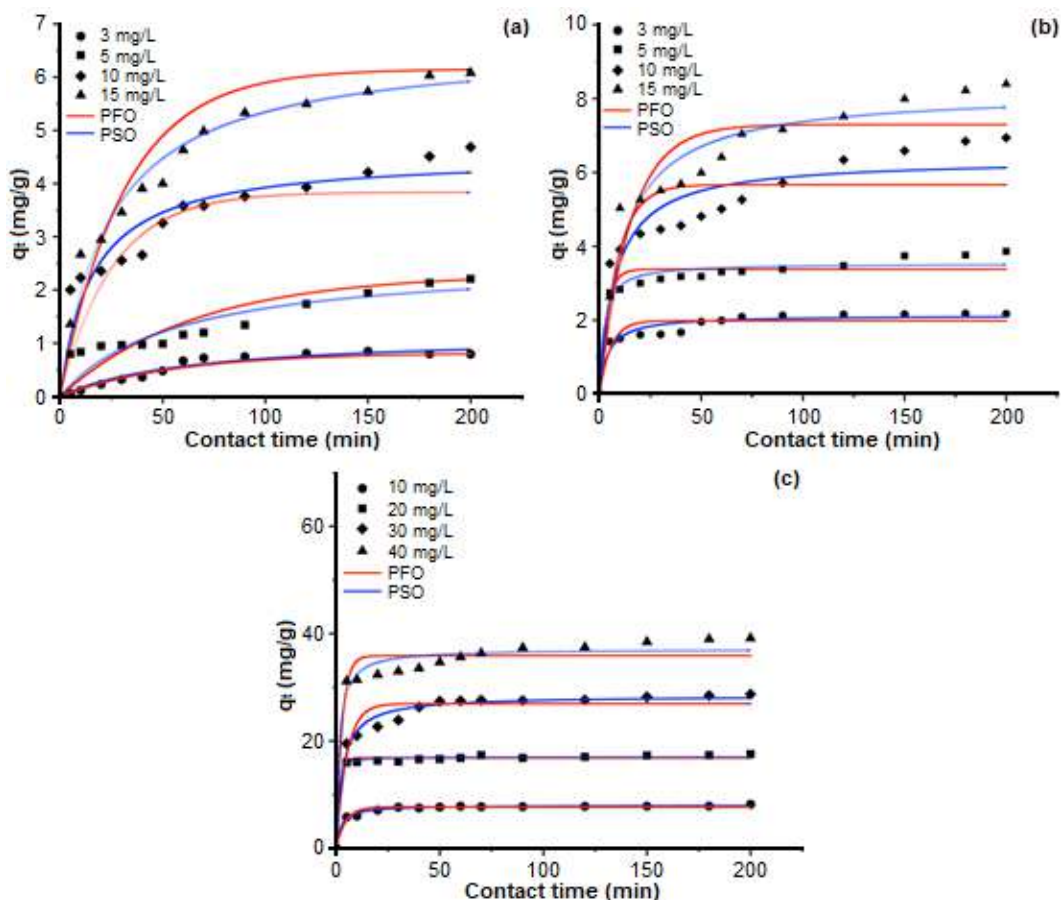


Fig 8. Kinetic adsorption of methylene blue on Ni/Al LDH (a), biochar (b), and NiAl LDH/Biochar (c)

Table 3. Kinetic parameter of pseudo first-order and second-order

Kinetic Models	Parameter	3 mg/L	5 mg/L	10 mg/L	15 mg/L
Ni/Al LDH					
<i>Pseudo first order</i>	q_e exp (mg/g)	0.396	1.183	2.343	3.258
	q_e calc (mg/g)	1.924	1.073	1.603	2.922
	k_1 (min^{-1})	0.033	0.012	0.014	0.022
	R^2	0.921	0.921	0.955	0.939
<i>Pseudo second order</i>	q_e exp (mg/g)	0.396	1.183	2.343	3.258
	q_e calc (mg/g)	0.620	10.417	7.299	4.484
	k_2 (g/mg min)	0.020	0.004	0.004	0.014
	R^2	0.900	0.964	0.920	0.917
Biochar					
<i>Pseudo first Order</i>	q_e exp (mg/g)	1.085	1.932	3.469	4.198
	q_e calc (mg/g)	1.554	1.312	2.582	2.843
	k_1 (min^{-1})	0.035	0.015	0.020	0.018
	R^2	0.961	0.857	0.929	0.961
<i>Pseudo second order</i>	q_e exp (mg/g)	1.085	1.932	3.469	4.198
	q_e calc (mg/g)	1.133	1.951	7.633	2.222
	k_2 (g/mg min)	0.114	0.062	0.006	0.104
	R^2	0.997	0.995	0.971	0.942

Table 3. Kinetic parameter of pseudo first-order and second-order (*Continued*)

Kinetic Models	Parameter	3 mg/L	5 mg/L	10 mg/L	15 mg/L
NiAl LDH/Biochar					
<i>Pseudo first order</i>	q_e exp (mg/g)	4.103	8.787	14.368	19.586
	q_e calc (mg/g)	1.402	2.345	4.249	5.532
	k_1 (min ⁻¹)	0.025	0.032	0.020	0.020
	R ²	0.581	0.587	0.823	0.944
<i>Pseudo second order</i>	q_e exp (mg/g)	4.103	8.787	14.368	19.586
	q_e calc (mg/g)	4.061	8.787	14.577	19.920
	k_2 (g/mg min)	0.083	0.057	0.015	0.009
	R ²	0.999	0.999	0.999	0.999

for PF-O. The main reason is probably due to the inorganic-organic adsorbent character for NiAl LDH/Biochar, biochar, and Ni/Al LDH. Furthermore, the value of k_2 for NiAl LDH/Biochar and biochar was decreased with increasing concentration of methylene blue. These phenomena are also similar for k_1 of Ni/Al LDH. The reason is that the mobility of the concentrated sample is lower than the aqueous sample. The value of k_2 is getting low for both the dyes, which indicates that the adsorption process is rapid. It means that two molecules can be adsorbed in a single site, or a single molecule can interact with two adsorption sites. Furthermore, this finding also supports that the adsorption rate depends on active sites proposing a chemisorption process.

The effect of initial concentration and temperature adsorption of methylene blue on NiAl LDH/Biochar, biochar, and Ni/Al LDH was presented in Fig. 9. The amount of methylene blue adsorbed on materials was sharply increased by increasing the initial concentration of methylene blue and temperature. The adsorption patterns for Ni/Al LDH and biochar were similar to the form two stages adsorption step. Still, NiAl LDH/Biochar has a straight adsorption pattern toward initial concentration and temperature. The isotherm Langmuir and Freundlich, as shown in Table 4 was obtained from data in Fig. 8 using the equation as following [37]:

Langmuir:

$$\frac{C}{m} = \frac{1}{bK_L} + \frac{C}{b} \quad (3)$$

where C is a saturated concentration of adsorbate; m is the amount of adsorbate; b is the maximum adsorption

capacity (mg g⁻¹), and K_L is the Langmuir constant (L mg⁻¹).

Freundlich:

$$\log q_e = \log K_F + 1/n \log C_e \quad (4)$$

where q_e is adsorption capacity at equilibrium (mg g⁻¹); C_e is the adsorbate concentration at equilibrium (mg L⁻¹), and K_F is Freundlich constant. Table 4 showed the maximum adsorption capacity of Langmuir by NiAl LDH/Biochar was 61.728 mg/g, which is relatively higher than some previously reported in Table 5. Table 5 was shown the comparison of the adsorption capacity of methylene blue using several adsorbents.

The data in Table 4 showed that the adsorption of methylene blue on NiAl LDH/Biochar, biochar, and Ni/Al LDH almost follows the Langmuir isotherm adsorption model rather than the Freundlich model. The R² for Langmuir isotherm is nearly close to one than Freundlich isotherm. The Q_m for NiAl LDH/Biochar is higher than biochar and Ni/Al LDH. As expected of increasing surface area properties, this higher Q_m is a logical result.

The thermodynamic data, as shown in Table 6, was also calculated from data in Fig. 9 using the equation as follow:

$$\ln K_L = \frac{\Delta S}{R} - \frac{\Delta H}{RT} \quad (5)$$

$$\Delta G^\circ = -RT \ln K_L \quad (6)$$

where T is the temperature (K), R is the gas constant (8.314 J mol⁻¹ K⁻¹), and K_L is the Langmuir constant from Table 4.

For all methylene blue conditions, the ΔG of

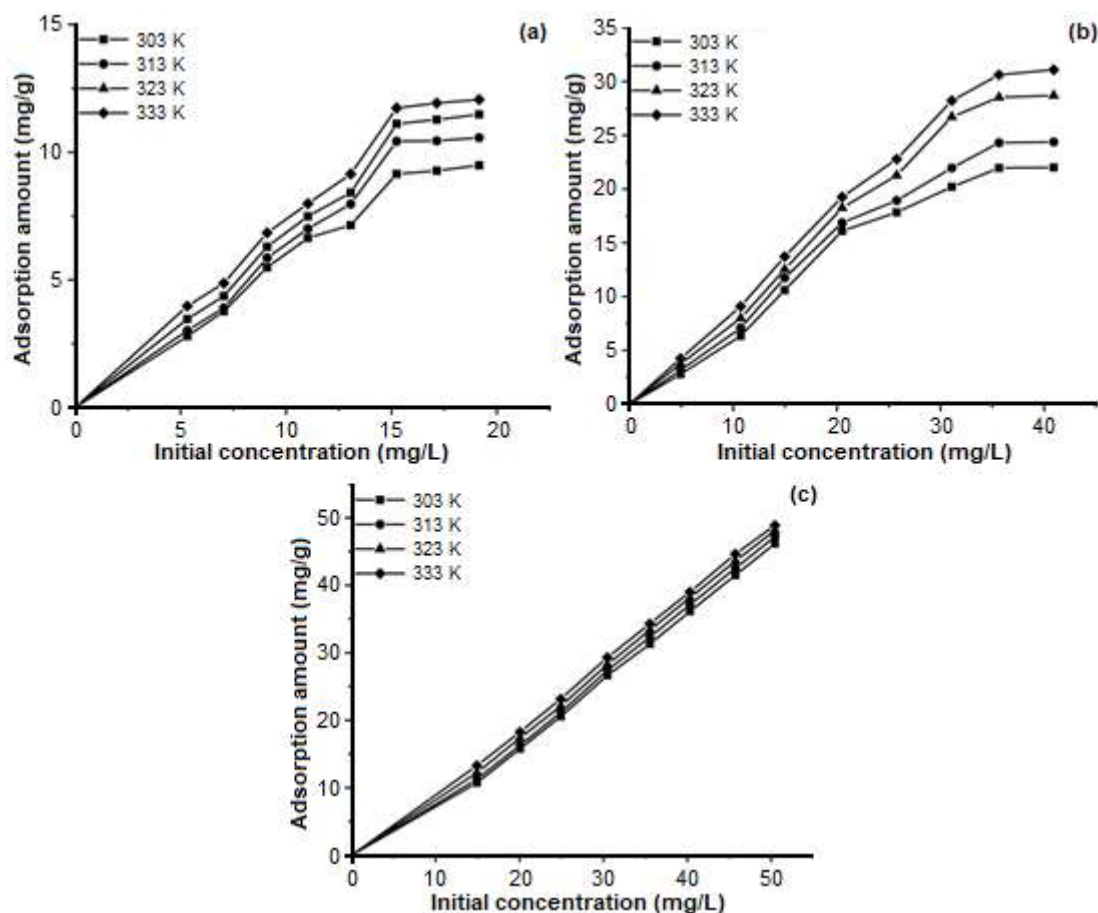


Fig 9. The effect of initial concentration and temperature adsorption on Ni/Al LDH (a), biochar (b), and NiAl LDH/Biochar (c)

Table 4. The isotherm adsorption of methylene blue

Adsorbent	Isotherm					
	Langmuir			Freundlich		
	Q_m	K_L	R^2	n	K_F	R^2
NiAl LDH	22.989	0.173	0.919	1.477	3.603	0.953
Biochar	36.101	0.622	0.990	4.296	1.336	0.993
NiAl LDH/Biochar	61.728	0.354	0.945	0.621	1.423	0.987

adsorption has a negative value means adsorption of methylene blue on NiAl LDH/Biochar, biochar, and Ni/Al LDH have spontaneously occurred in a batch small reactor system. The ΔH value is less than 80 kJ/mol and in the range 15.502–43.402 kJ/mol for all adsorbents. This value belongs to chemi-physical adsorption [51]. The value of ΔS is irregular for increasing methylene blue concentration means growing randomness for adsorption of methylene blue on the adsorbent.

Desorption of methylene blue on NiAl LDH/Biochar and starting materials were conducted using several reagents such as ethanol, acetone, diethyl ether, sodium hydroxide solution, hydrochloric acid solution, and water. The results are shown in Figure 10. NiAl LDH/Biochar and biochar were efficiently desorbed using acetone and Ni/Al LDH using hydrochloric acid. The involvement of acid-base reaction in the desorption using Ni/Al LDH was dominated,

Table 5. Comparison of the adsorption capacity of methylene blue

Adsorbent	Adsorption capacity (mg/g)	References
Wheat shells	21.50	[38]
Activated biochar-TA	53.28	[39]
MW-SiO ₂	186.1	[40]
MgAl LDO	49.53	[41]
Cockle Shells-Treated Banana Pith	85.47	[42]
MgAl LDH	49	[43]
Alginate Beads Powder	48.2	[44]
Activated Carbon	11.40	[45]
Fe/SCD-LDH	83.40	[46]
Orange Peels	18.60	[10]
Rice husk	40.58	[47]
Catton Waste	24.00	[48]
Ca/Al LDH-biochar	32.535	[49]
LDH-bacteria aggregates	5.23	[50]
NiAl/Biochar	61.728	This study

Table 6. The thermodynamic parameter adsorption of methylene blue

Initial Concentration	T (K)	Q _e (mg/g)	ΔH (kJ/mol)	ΔS (J/mol K)	ΔG (kJ/mol)
NiAl LDH	303	9.489	40.951	0.145	-0.489
	313	10.570			-1.094
	323	11.479			-1.700
	333	12.061			-2.306
Biochar	303	16.097	43.402	0.153	-2.945
	313	16.873			-4.394
	323	18.255			-5.843
	333	19.269			-7.292
NiAl LDH/Biochar	303	15.661			-2.883
	313	16.533			-4.410
	323	17.878			-5.938
	333	18.924			-7.465

but like dissolve like principle [52] is found in the desorption of methylene blue on NiAl LDH/Biochar and biochar.

The regeneration of adsorbent was studied after desorption using suitable reagents as described in Fig. 10 following by washing by water several times and dried at 110 °C. It was performed until three-cycle adsorption of methylene blue using the same adsorbent from fresh materials. The results of the regeneration process are shown in Fig. 11. The reusability of Ni/Al LDH and biochar was sharply decreased for second and third cycle adsorption. At the same time, the NiAl LDH/Biochar is

almost stable until the three-cycle adsorption process. The structure of Ni/Al LDH is easily exfoliated during the second and third reuse cycles. Biochar is also unstable toward reuse adsorbent due to the stability of organic materials toward washing and drying. On the other hand, NiAl LDH/Biochar has almost stable reuse adsorbent until the third cycle adsorption process due to small particle formation during NiAl LDH/Biochar synthesis as presented in SEM photos. Thus NiAl LDH/Biochar in this research is a promising adsorbent for high reusability adsorption of methylene blue.

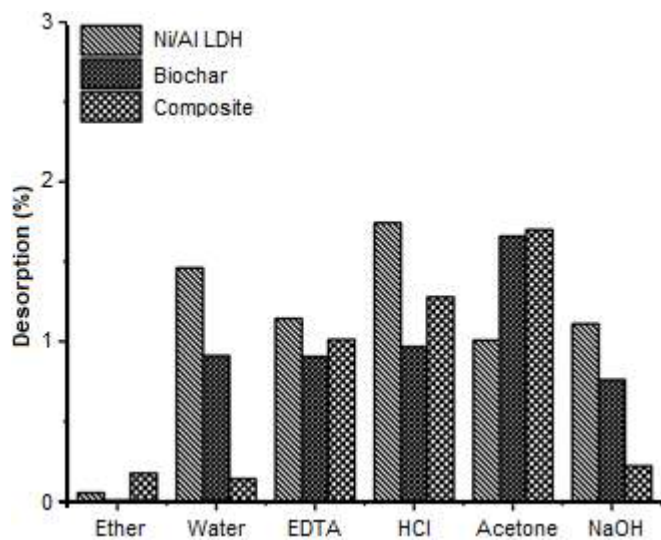


Fig 10. Desorption of methylene blue

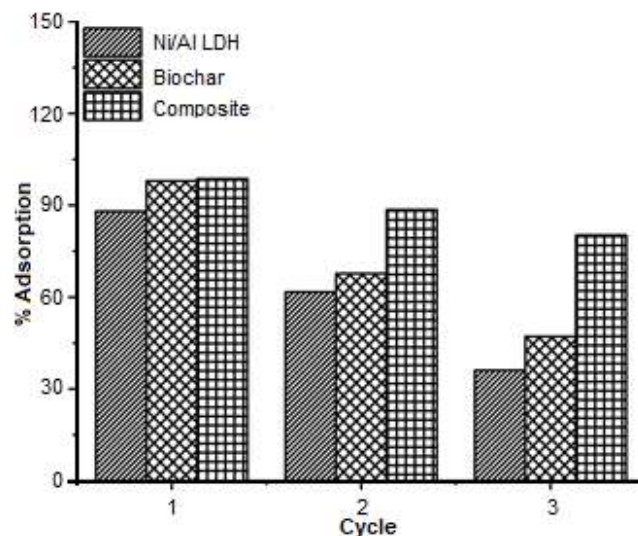


Fig 11. Cycling process of adsorbent

CONCLUSION

Ni/Al LDH-biochar Ni/Al LDH/Biochar has diffraction at 11.63° and 22.30° . Ni/Al LDH/Biochar has the vibration of both biochar and LDH at wavenumber 3441 cm^{-1} , 2931 cm^{-1} , 2368 cm^{-1} , 2283 cm^{-1} , 1627 cm^{-1} , 1381 cm^{-1} , 1049 cm^{-1} , and 578 cm^{-1} . Ni/Al LDH/Biochar has more than ten-fold surface area properties ($438.942\text{ m}^2/\text{g}$) than biochar ($50.936\text{ m}^2/\text{g}$), and Ni/Al layered double hydroxide ($92.682\text{ m}^2/\text{g}$). Thermal analysis showed that Ni/Al LDH/Biochar has one endothermic peak and two exothermic peaks related to both starting materials. Ni/Al LDH/Biochar has a small agglomeration and a more regular form than starting materials. Adsorption of methylene blue on Ni/Al LDH/Biochar follows the pseudo-second-order kinetic adsorption model and is classified as chemi-physical adsorption. Ni/Al LDH/Biochar has high reusability properties and can be used as a potential adsorbent to remove methylene blue from an aqueous solution.

ACKNOWLEDGMENTS

Authors thank Universitas Sriwijaya for this research's financial support by Hibah Profesi 2020–2021 No. 0687/UN9/SK.BUK.KP/2020 and thank Research Center of Inorganic Materials and Complexes FMIPA Universitas Sriwijaya for analysis instrumentation measurement.

AUTHOR CONTRIBUTIONS

NRP and RJS conducted the experiment, collecting and assembling the data; AL wrote the manuscript and concept of the research; TT and NH analysis, and interpreted the data. All authors agreed to the final version of this manuscript.

REFERENCES

- [1] Hu, H., Wageh, S., Al-Ghamdi, A.A., Yang, S., Tian, Z., Cheng, B., and Ho, W., 2020, NiFe-LDH nanosheet/carbon fiber nanocomposite with enhanced anionic dye adsorption performance, *Appl. Surf. Sci.*, 511, 145570.
- [2] Yaseen, M., Singh, M., and Ram, D., 2014, Growth, yield and economics of vetiver (*Vetiveria zizanioides* L. Nash) under intercropping system, *Ind. Crops Prod.*, 61, 417–421.
- [3] Tezcan Un, U., and Ates, F., 2019, Low-cost adsorbent prepared from poplar sawdust for removal of disperse orange 30 dye from aqueous solutions, *Int. J. Environ. Sci. Technol.*, 16 (2), 899–908.
- [4] Palapa, N.R., Juleanti, N., Taher, T., and Lesbani, A., 2020, Unique adsorption properties of malachite green on interlayer space of Cu-Al and Cu-Al-SiW₁₂O₄₀ layered double hydroxides, *Bull. Chem. React. Eng. Catal.*, 15 (3), 653–661.

- [5] Yan, H., Li, H., Yang, H., Li, A., and Cheng, R., 2013, Removal of various cationic dyes from aqueous solutions using a kind of fully biodegradable magnetic composite microsphere, *Chem. Eng. J.*, 223, 402–411.
- [6] Long, Y., Wang, Y., Zhang, D., Ju, P., and Sun, Y., 2016, Facile synthesis of BiOI in hierarchical nanostructure preparation and its photocatalytic application to organic dye removal and biocidal effect of bacteria, *J. Colloid Interface Sci.*, 481, 47–56.
- [7] Soleimani, K., Tehrani, A.D., and Adeli, M., 2018, Bioconjugated graphene oxide hydrogel as an effective adsorbent for cationic dyes removal, *Ecotoxicol. Environ. Saf.*, 147, 34–42.
- [8] Logita, H.H., Tadesse, A., and Kebede, T., 2015, Synthesis, characterization and photocatalytic activity of $\text{MnO}_2/\text{Al}_2\text{O}_3/\text{Fe}_2\text{O}_3$ nanocomposite for degradation of malachite green, *Afr. J. Pure Appl. Chem.*, 9 (11), 211–222.
- [9] Meili, L., Lins, P.V., Zanta, C.L.P.S., Soletti, J.I., Ribeiro, L.M.O., Dornelas, C.B., Silva, T.L., and Vieira, M.G.A., 2019, MgAl-LDH/Biochar composites for methylene blue removal by adsorption, *Appl. Clay Sci.*, 168, 11–20.
- [10] Annadurai, G., Juang, R.S., and Lee, D.J., 2002, Use of cellulose-based wastes for adsorption of dyes from aqueous solutions, *J. Hazard. Mater.*, 92 (3), 263–274.
- [11] Elmoubarki, R., Mahjoubi, F.Z., Elhalil, A., Tounsadi, H., Abdennouri, M., Sadiq, M., Qourzal, S., Zouhri, A., and Barka, N., 2017, Ni/Fe and Mg/Fe layered double hydroxides and their calcined derivatives: Preparation, characterization and application on textile dyes removal, *J. Mater. Res. Technol.*, 6 (3), 271–283.
- [12] Özdemir, M., Durmuş, Ö., Şahin, Ö., and Saka, C., 2016, Removal of methylene blue, methyl violet, rhodamine B, alizarin red, and bromocresol green dyes from aqueous solutions on activated cotton stalks, *Desalin. Water Treat.*, 57 (38), 18038–18048.
- [13] Zhang, P., O'Connor, D., Wang, Y., Jiang, L., Xia, T., Wang, L., Tsang, D.C.W., Ok, Y.S., and Hou, D., 2020, A green biochar/iron oxide composite for methylene blue removal, *J. Hazard. Mater.*, 384, 121286.
- [14] Kubo, D., Tadanaga, K., Hayashi, A., and Tatsumisago, M., 2012, Hydroxide ion conduction in Ni-Al layered double hydroxide, *J. Electroanal. Chem.*, 671, 102–105.
- [15] Oktriandi, M., Palapa, N.R., Mohadi, R., and Lesbani, A., 2020, Effective removal of iron(II) from aqueous solution by adsorption using Zn/Cr layered double hydroxides intercalated with Keggin ion, *J. Ecol. Eng.*, 21 (5), 63–71.
- [16] Liao, X.J., and Chen, G.S., 2016, A hybrid hydrogel based on clay nanoplatelets and host-guest inclusion complexes, *Chin. Chem. Lett.*, 27 (4), 583–587.
- [17] González, M.A., Pavlovic, I., and Barriga, C., 2015, Cu(II), Pb(II) and Cd(II) sorption on different layered double hydroxides. A kinetic and thermodynamic study and competing factors, *Chem. Eng. J.*, 269, 221–228.
- [18] Guo, Y., Zhu, Z., Qiu, Y., and Zhao, J., 2013, Synthesis of mesoporous Cu/Mg/Fe layered double hydroxide and its adsorption performance for arsenate in aqueous solutions, *J. Environ. Sci.*, 25 (5), 944–953.
- [19] Kovanda, F., Jindová, E., Lang, K., Kubát, P., and Sedláková, Z., 2010, Preparation of layered double hydroxides intercalated with organic anions and their application in LDH/poly(butyl methacrylate) nanocomposites, *Appl. Clay Sci.*, 48 (1-2), 260–270.
- [20] Liu, Z., and Zhang, F.S., 2009, Removal of lead from water using biochars prepared from hydrothermal liquefaction of biomass, *J. Hazard. Mater.*, 167 (1-3), 933–939.
- [21] Tan, X., Liu, Y., Zeng, G., Wang, X., Hu, X., Gu, Y., and Yang, Z., 2015, Application of biochar for the removal of pollutants from aqueous solutions, *Chemosphere*, 125, 70–85.
- [22] Ahmad, R., and Mondal, P.K., 2010, Application of modified water nut carbon as a sorbent in Congo red and Malachite green dye contaminated wastewater remediation, *Sep. Sci. Technol.*, 45 (3), 394–403.
- [23] Wan, S., Wang, S., Li, Y., and Gao, B., 2017, Functionalizing biochar with Mg–Al and Mg–Fe layered double hydroxides for removal of

- phosphate from aqueous solutions, *J. Ind. Eng. Chem.*, 47, 246–253.
- [24] Zhang, M., Gao, B., Yao, Y., and Inyang, M., 2013, Phosphate removal ability of biochar/MgAl-LDH ultra-fine composites prepared by liquid-phase deposition, *Chemosphere*, 92 (8), 1042–1047.
- [25] Zubair, M., Manzar, M.S., Mu'azu, N.D., Anil, I., Blaisi, N.I., and Al-Harathi, M.A., 2020, Functionalized MgAl-layered hydroxide intercalated date-palm biochar for enhanced uptake of cationic dye: Kinetics, isotherm and thermodynamic studies, *Appl. Clay Sci.*, 190, 105587.
- [26] Lins, P.V.S., Henrique, D.C., Ide, A.H., da Silva Duarte, J.L., Dotto, G.L., Yazidi, A., Sellaoui, L., Erto, A., Zanta, C.L.P.S., and Meili, L., 2020, Adsorption of a non-steroidal anti-inflammatory drug onto MgAl/LDH-activated carbon composite – Experimental investigation and statistical physics modeling, *Colloids Surf., A*, 586, 124217.
- [27] Wang, S., Gao, B., Li, Y., Zimmerman, A.R., and Cao, X., 2016, Sorption of arsenic onto Ni/Fe layered double hydroxide (LDH)-biochar composites, *RSC Adv.*, 6 (22), 17792–17799.
- [28] Palapa, N.R., Mohadi, R., and Lesbani, A., 2018, Adsorption of direct yellow dye from aqueous solution by Ni/Al and Zn/Al layered double hydroxides, *AIP Conf. Proc.*, 2026, 020018.
- [29] Bai, Z., Hu, C., Liu, H., and Qu, J., 2019, Selective adsorption of fluoride from drinking water using NiAl-layered metal oxide film electrode, *J. Colloid Interface Sci.*, 539, 146–151.
- [30] Tao, X., Han, Y., Sun, C., Huang, L., and Xu, D., 2019, Plasma modification of NiAlCe-LDH as improved photocatalyst for organic dye wastewater degradation, *Appl. Clay Sci.*, 172, 75–79.
- [31] Xiao, F., Cheng, J., Cao, W., Yang, C., Chen, J., and Luo, Z., 2019, Removal of heavy metals from aqueous solution using chitosan-combined magnetic biochars, *J. Colloid Interface Sci.*, 540, 579–584.
- [32] Xia, Y., Yang, T., Zhu, N., Li, D., Chen, Z., Lang, Q., Liu, Z., and Jiao, W., 2019, Enhanced adsorption of Pb(II) onto modified hydrochar: Modeling and mechanism analysis, *Bioresour. Technol.*, 288, 121593.
- [33] Wang, T., Li, C., Wang, C., and Wang, H., 2018, Biochar/MnAl-LDH composites for Cu(II) removal from aqueous solution, *Colloids Surf., A*, 538, 443–450.
- [34] Shaji, A., and Zachariah, A.K., 2017, “Surface area analysis of nanomaterials, in *Micro and Nano Technologies, Thermal and Rheological Measurement Techniques for Nanomaterials Characterization*, Volume 3, Eds. Thomas, S., Thomas, R., Zachariah, A.K., and Mishra, R.K., Elsevier Inc., 197–231.
- [35] Beakou, B.H., El Hassani, K., Houssaini, M.A., Belbahloul, M., Oukani, E., and Anouar, A., 2017, A novel biochar from *Manihot esculenta* Crantz waste: Application for the removal of malachite green from wastewater and optimization of the adsorption process, *Water Sci. Technol.*, 76 (6), 1447–1456.
- [36] Iftekhhar, S., Ramasamy, D.L., Srivastava, V., Asif, M.B., and Sillanpää, M., 2018, Understanding the factors affecting the adsorption of Lanthanum using different adsorbents: A critical review, *Chemosphere*, 204, 413–430.
- [37] Kushwaha, A.K., Gupta, N., and Chattopadhyaya, M.C., 2014, Removal of cationic methylene blue and malachite green dyes from aqueous solution by waste materials of *Daucus carota*, *J. Saudi Chem. Soc.*, 18 (3), 200–207.
- [38] Bulut, E., Özacar, M., and Şengil, İ.A., 2008, Adsorption of malachite green onto bentonite: Equilibrium and kinetic studies and process design, *Microporous Mesoporous Mater.*, 115 (3), 234–246.
- [39] Wang, Y., Zhang, Y., Li, S., Zhong, W., and Wei, W., 2018, Enhanced methylene blue adsorption onto activated reed-derived biochar by tannic acid, *J. Mol. Liq.*, 268, 658–666.
- [40] Peres, E.C., Slaviero, J.C., Cunha, A.M., Hosseini-Bandegharai, A., and Dotto, G.L., 2018, Microwave synthesis of silica nanoparticles and its application for methylene blue adsorption, *J. Environ. Chem. Eng.*, 6 (1), 649–659.

- [41] Qiao, Y., Li, Q., Chi, H., Li, M., Lv, Y., Feng, S., Zhu, R., and Li, K., 2018, Methyl blue adsorption properties and bacteriostatic activities of Mg-Al layer oxides via a facile preparation method, *Appl. Clay Sci.*, 163, 119–128.
- [42] Hasan, R., Ying, W.J., Cheng, C.C., Jaafar, N.F., Jusoh, R., Jalil, A.A., and Setiabudi, H.D., 2020, Methylene blue adsorption onto cockle shells-treated banana pith: Optimization, isotherm, kinetic, and thermodynamic studies, *Indones. J. Chem.*, 20 (2), 368–378.
- [43] Aguiar, J.E., Bezerra, B.T.C., Braga, B.M., Lima, D.S., Nogueira, R.E.F.Q., de Lucena, S.M.P., and da Silva, I.J., 2013, Adsorption of anionic and cationic dyes from aqueous solution on non-calcined Mg-Al layered double hydroxide: Experimental and theoretical study, *Sep. Sci. Technol.*, 48 (15), 2307–2316.
- [44] Purnaningtyas, M.A.K., Sudiono, S., and Siswanta, D., 2020, Synthesis of activated carbon/chitosan/alginate beads powder as an adsorbent for methylene blue and methyl violet 2B dyes, *Indones. J. Chem.*, 20 (5), 1119–1130.
- [45] Rao, V.V.B., and Rao, S.R.M., 2006, Adsorption studies on treatment of textile dyeing industrial effluent by fly ash, *Chem. Eng. J.*, 116 (1), 77–84.
- [46] Hu, W., Wu, X., Jiao, F., Yang, W., and Zhou, Y., 2016, Preparation and characterization of magnetic Fe₃O₄@sulfonated β -cyclodextrin intercalated layered double hydroxides for methylene blue removal, *Desalin. Water Treat.*, 57 (53), 25830–25841.
- [47] Vadivelan, V., and Kumar, K.V., 2005, Equilibrium, kinetics, mechanism, and process design for the sorption of methylene blue onto rice husk, *J. Colloid Interface Sci.*, 286 (1), 90–100.
- [48] Yavuz, E., Bayramoğlu, G., Arica, M.Y., and Senkal, B.F., 2011, Preparation of poly (acrylic acid) containing core-shell type resin for removal of basic dyes, *J. Chem. Technol. Biotechnol.*, 86 (5), 699–705.
- [49] Lesbani, A., Asri, F., Palapa, N.R., Taher, T., and Rachmat, A., 2020, Efficient removal of methylene blue by adsorption using composite based Ca/Al layered double hydroxide-biochar, *Global NEST J.*, 22 (2), 250–257.
- [50] Liu, J., Li, X., Luo, J., Duan, C., Hu, H., and Qian, G., 2014, Enhanced decolourisation of methylene blue by LDH-bacteria aggregates with bioregeneration, *Chem. Eng. J.*, 242, 187–194.
- [51] Taher, T., Mohadi, R., Rohendi, D., and Lesbani, A., 2017, Kinetic and thermodynamic adsorption studies of Congo red on bentonite, *AIP Conf. Proc.*, 1823, 020028.
- [52] Mahmoodi, N.M., Hayati, B., Arami, M., and Lan, C., 2011, Adsorption of textile dyes on Pine Cone from colored wastewater: Kinetic, equilibrium and thermodynamic studies, *Desalination*, 268 (1-3), 117–125.

Total Mercury (THg) Concentration in Indian Scad (*Decapterus russelli*) and Torpedo Scad (*Megalaspis cordyla*) from Southern Waters of Binuangeun, Banten

Suratno^{1*}, Zahriza Purnadayanti², Hilda Novianty¹, and Selvia Oktaviyani³

¹Research Division for Natural Product Technology, Indonesian Institute of Sciences, Jl. Jogja-Wonosari Km 31.5, Gading, Yogyakarta 55861, Indonesia

²Department of Fisheries and Marine Science, Brawijaya University, Jl. Veteran, Ketawanggede, Malang 65145, Indonesia

³Research Center for Oceanography, Indonesian Institute of Sciences, Pasir Putih I, Ancol Timur, Jakarta 14430, Indonesia

* **Corresponding author:**

tel: +62-274-392570

email: nanosan80@gmail.com

Received: June 17, 2020

Accepted: July 24, 2020

DOI: 10.22146/ijc.56967

Abstract: The high level of fish consumption was the main factor in the vulnerability of Hg exposure to the human body. The preliminary information of the total mercury (THg) concentration of Indian scad (*Decapterus russelli*) and Torpedo scad (*Megalaspis cordyla*) from Binuangeun fish auction in Lebak, Banten, Indonesia, was presented in this research. The objective of this research was to understand the distribution of THg in each organ of *D. russelli* (muscle, gut tissues, gonad, and eggs) and *M. cordyla* (muscle, liver, and gut contents). The results showed that THg in all samples were below the National Regulation limit from the National Agency of Drug and Food in mg/kg ww. THg gonad from *D. russelli* was showed highly significant ($P < 0.01$) lower compare THg in muscle, gut tissues, and eggs. Pearson's correlation from THg in each organ of *D. russelli* compare to total weight and total length showed that concentration of THg in gonad highly significantly ($p < 0.01$) correlated with total body weight ($r^2 = 0.97$) and total length ($r^2 = 0.96$). *M. cordyla* was showed no correlation of THg in muscle compare to total length and total weight. The present study showed that *D. russelli* could accumulate higher mercury compare to *M. cordyla* and need caution while consuming this fish.

Keywords: *Decapterus russelli*; *Megalaspis cordyla*; total mercury concentration

■ INTRODUCTION

Fishes are an essential source of protein, providing essential fatty acids, such as docosahexaenoic acid and eicosapentaenoic acid, which aid in reducing cholesterol levels and incidence of heart disease [1]. Although fish is beneficial to human health, human exposure to Hg can occur primarily through the consumption of fish and is a public health concern worldwide [2]. Human activities such as all activity related industries have significantly increased the input of heavy metals into the aquatic organism and may be further transferred to the trophic level [3].

Mahaffey states that in addition to fish consumption [4], it is suitable for humans, but fishes might also expose

the human body to mercury (Hg). About 95% of methyl mercury (MeHg) from fish consumed will be absorbed in the human bloodstream within 4 to 14 h [5]. Maycock and Benford [6] explained that organic mercury (MeHg/EtHg) could easily pass through the plasma membrane compared with inorganic mercury. In the case of pregnant women, MeHg can directly transfer to the fetus through the placenta. The high level of fish consumption produced by fisheries was a factor in the vulnerability of Hg exposure to the human body. The threshold concentration of Hg in fish permitted by the National Agency of Drug and Food Control from the Indonesian Government [7] and JECFA [8] was 0.5 mg/kg wet weight and 1.0 mg/kg wet weight for predatory fish such as tuna, sharks and marlin.

One of the fisheries food products that are very popular in Indonesia was “pindang” (steamed fish), which used *Decapterus russeli* or *Decapterus kuroides* as the main ingredient of the product. In the production, generally, the organs have not been removed from the body of fishes. Besides, people commonly consumed the scad fish group, such as *Megalaspis cordyla*, as a source of protein for daily needs and then processed to be fried, grilled, or smoked fish. So far, information about total mercury (THg) concentration in fish consumed in Indonesian waters is still limited, especially from the Southern Java Sea. Therefore, to fill the information gap, this study has the aim to measure the total concentration of Hg (THg) in organs of *D. russelli* and *M. cordyla* from the Southern Waters of Binuangeun, Banten, Indonesia. Measurements were specified in the gut tissue, gonads, eggs, and muscle/meat of *D. russelli*, while for *M. cordyla*, the extraction of total mercury was in its muscle, liver, and gut content. The result was expected to be a piece of essential information to determine the potential of risk human consumption of these seafood products.

■ EXPERIMENTAL SECTION

Materials

Fish samples were obtained from the Binuangeun Fish Auction (latitude: -6.838101° , longitude: 105.883637°) in Lebak, Banten, in September 2019. Fifteen individuals of *D. russelli* and thirty individuals of *M. cordyla* were rinsed using clean water to remove dirt and directly placed in a zip-lock plastic bag and freeze until further analysis. In this study, the samples analyzed were meat, gonad, liver, eggs, digestive content, and digestive tract in the fish sample. The samples were taken to Biogeochemistry Laboratory at Research Center for Oceanography, Indonesian Institute of Sciences (RCO-LIPI). All reagents used were of analytical-reagent grade. The solutions prepared using ultra-pure water (Milli-Q). Mercury Standard solution 1.000 mg/L (Merck) and L-Cysteine from Nacalai Tesque Inc. Japan.

Instrumentation

Morphometric measurement was performed by a digital caliper and Sartorius BP 210 S analytical balance.

Heraeus Oven Instrument was used to dry the samples and percentage of moisture content, mortar, pestle, spatula, petri dish, and Mercury Analyzer NIC MA-3000.

Procedure

Preparation samples

Measurement of total length (TL) have done using a digital caliper, while the measurement of total weight (TW) of fishes used a digital scale with the accuracy of two digits behind the comma (0.01 g). Each fish was separated from meat (muscle after the head of the fishes or near first dorsal fin), eggs, gonad, and digestive tract for *D. russelli* and muscle, liver, and digestive contents for *M. cordyla*. The fish samples were then dried at 60°C for 24 h to obtain samples with a homogenous matrix [9].

Furthermore, the samples were mashed using a mortar to form a homogenous powder and stored in a desiccator until mercury analysis was performed. Measurement of moisture content has done by drying the sample at 105°C for 24 h [10]. Water content was needed to convert the THg concentration from dry weight to wet weight.

Mercury analysis

The THg concentration was analyzed using the mercury analyzer (NIC-3000), Nippon Instrument Corporation, Japan at RCO-LIPI, in Jakarta. The main principle of mercury analyzer was thermal decomposition, amalgamation, and atomic absorption, according to USEPA 7473 [11]. Three replicates of dried organs from each sample were weighed less than 20 mg and directly inserted in the sample boat, and analyzed with a mercury analyzer for THg. Three replicates of Certified Reference Materials (DORM-4) have been used to check the recovery of the methods. The Hg concentration in the sample was displayed in μg mercury per kg of the sample's dry weight. The use of DORM4 as a control of the Hg measurement method showed 98.73% of the recovery.

Data analysis

Data analysis was performed by converting the THg concentration from dry weight to wet weight and changing its concentration unit from $\mu\text{g}/\text{kg}$ dry weight ($\mu\text{g}/\text{kg}$ dw) to mg/kg wet weight (mg/kg ww). All

graphical plots based on the R program and statistical analysis expressed a p-value of less than 0.05, indicating a statistically significant difference.

RESULTS AND DISCUSSION

During the study, a total of 15 individuals of Indian Scad (*D. russelli*) and 30 individuals of Torpedo Scad (*M. cordyla*) were collected from Binuangeun Fish Auction, Banten. The total length of the Indian Scad ranged from 25.0–30.5 cm and 16.2–21.7 cm for Torpedo Scad. The total weight ranged from 124.74–235.57 g and 48.58–86.68 g for Indian Scad and Torpedo Scad, respectively (Table 1). All specimens of Indian Scad were mature or adult fish. According to Pralampita and Chodriyah [12], *D. russelli* achieve adults for males in a total length of 21.2 cm and females at 18.97 cm. Meanwhile, it different for Torpedo Scad, which had a total length lower than the size at maturity, which indicates that all species were immature or maturing fish. Based on Rahmayani [13], females *M. cordyla* mature in total length 28.0–28.4 cm and male at total length 32.1–32.6 cm.

Samples of *D. russelli* were separated into four parts

of organs and labeled as meat/muscle, digestive tract/gut tissues, gonad, and eggs. Mercury concentration in muscle ranged from 0.120 to 0.431 mg/kg ww, gut tissues from 0.036 to 0.253 mg/kg ww, gonad ranged from 0.025 to 0.107 mg/kg ww, and eggs ranged from 0.068 to 0.227 mg/kg ww. The THg concentration in *D. russelli* muscle ($p < 0.05$) and gonad ($p < 0.01$) were showed statistically significant differences compared with other organs (gonad and eggs).

Samples of *M. cordyla* were divided into three parts of organs and labeled as muscle, liver, and gut contents. Mercury concentration in muscle ranged from 0.042 to 0.090 mg/kg ww, liver ranged from 0.012 to 0.051 mg/kg ww, and gut contents ranged from 0.007 to 0.054 mg/kg ww. The THg concentration in *M. cordyla* muscle shows a higher concentration ($p < 0.01$) compared to gut content ($p < 0.01$) and showed statistically significant differences compared to other organs (Fig. 1).

The THg concentration of *D. russelli* in gonad have shown a correlation with total length (TL) and total weight (TW) with statistically significant level $p < 0.01$, and THg concentration in the digestive tract (gut) shows statistically

Table 1. Morphometric of samples *D. russelli* and *M. cordyla* from Binuangeun Fish Auction in Banten

Local name/Common name	N	Scientific name	Total Weight (g)	Total length (cm)	Main food/Feeding habit/TL [*])
Layang/Indian Scad	15	<i>Decapterus russelli</i>	124.74–235.57 (166.50 ± 28.79)	25.00–30.50 (26.97 ± 1.56)	Small fishes, zooplankton, zoobenthos/carnivorous/3.7 [*])
Selar Tetengkek/Torpedo Scad	30	<i>Megalaspis cordyla</i>	48.58–86.68 (70.92±10.60)	16.20–21.70 (20.08 ± 1.27)	Small fishes and crustacean, zooplankton, zoobenthos, detritus/carnivorous/4.4 [*])

^{*}) based on Froese and Pauly (2019) [14], Tropic level (TL) based [2], mean ± SD from Total Weight (TW) and Total Length (TL)

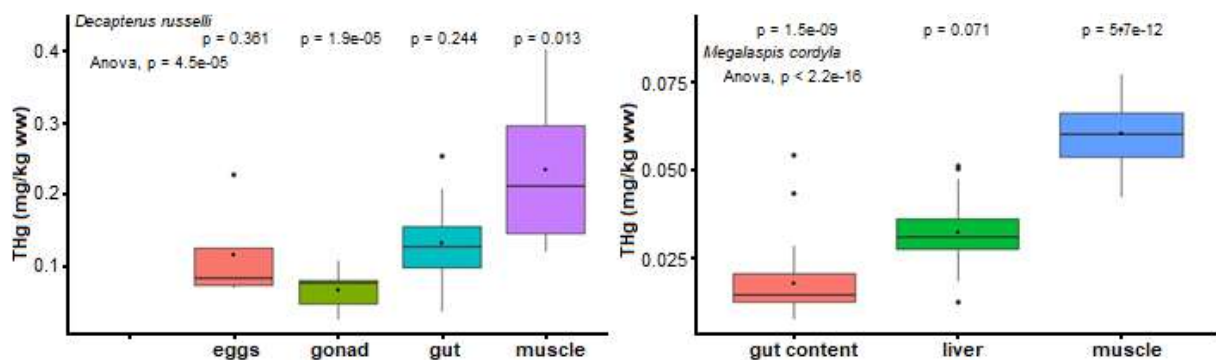


Fig 1. THg concentration (mg/kg ww) on *D. russelli* and *M. cordyla* organs. ● in the center of boxplot graphs indicate mean of THg in each organ

correlation with a total weight (TW) with significant level $p < 0.05$ (Fig. 2). Based on Fig. 2, THg concentration in the muscle of *D. russelli* from Binuangun does not correlate with TL and TW.

Fig. 3 describes the mean of THg concentration in muscle, the average concentration of *D. russelli* was 0.21 mg/kg ww and *M. cordyla* 0.07 mg/kg ww and a highly statistically significant level $p < 0.001$. Based on this average, the concentration of THg in the muscle of *D. russelli* and *M. cordyla* were below the limit of the guidelines from the National Agency of Drug and Food Control, Indonesia (NADFC) [7] and JECFA/WHO [8]

with the maximum value of 0.5 mg/kg ww THg; thus, was permitted for fish and fisheries products. According to Monperrus et al. [15], there is active transport of mercury within different organs, and the muscle is transferred in the last. Bridges and Zalups [16] and Mela et al. [17] explained that dietary mercury would be conveyed through a portal system after uptake in the intestine to the liver organ. Meanwhile, the concentration on fish's gonad and egg is related to maternally transfer of Hg that may impact survival, behavior, and development milestones of the embry-larval stages of fish [18].

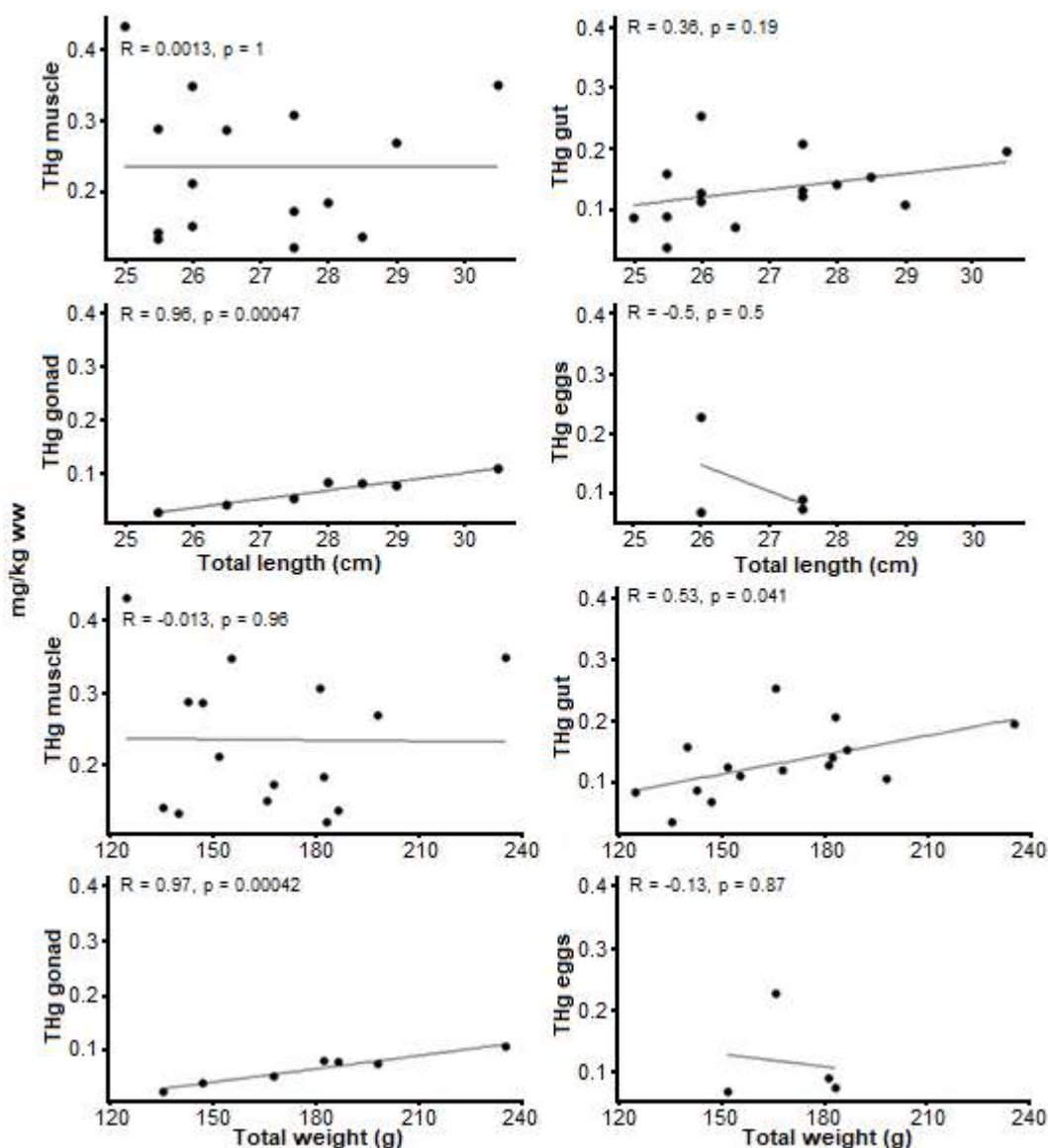


Fig 2. Relationship between total weight (TW) and total length (TL) vs THg (mg/kg ww) in *D. russelli* organs

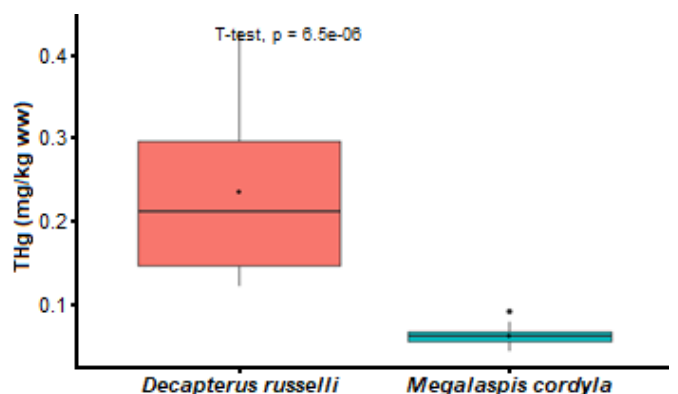


Fig 3. THg concentration (mg/kg ww) on *D. russelli* and *M. cordyla* from Binuangeun, Banten. • indicates the mean of THg

The data from this study is reverse with previous studies [19-20] where the mercury concentration in fish with higher trophic levels (*M. cordyla*) were significantly lower than in fish with lower trophic levels (*D. russelli*) [2] (Fig. 3). The factor that relevant for mercury has found to be the bioaccumulation process based on its bioavailability and speciation of mercury ion, rate uptake [21] physiological and behavior of feeding habit differences between fish species [22], the biological activity of fishes, wetland runoff/source of pollution [23], habitat and season [24] and also their specific prey [25]. Both species were pelagic species found in inshore waters in-depth, not exceeding 100 m [26-27]. However, Pauly et al. [28]

reported that *D. russelli* was also found in up to 275 m depth.

The origin of fish and migration patterns was also relevant factors for mercury to bioaccumulate in fish tissues [29]. The main factors were showed in this study probably a combination of specific prey (*M. cordyla* gut contents were *Stelephorus* sp. while *D. russelli* did not indicate specific prey in their gut tissues) and ages (*M. cordyla* was juvenile compare to *D. russelli* that already in adult size) of the samples were responsible for the differences of THg in this study compared to previous results (Table 2). Besides, Agah et al. [30] and Astani et al. [31] stated that trace concentration of mercury compounds in the fish body related to their concentration in the environment and fish condition, for instance, their size, age, sex, reproductive condition, diet, and trophic level.

Fig. 4 described that THg has a positive relationship, with the size (TW and TL) of all samples were indicating that THg will increase over time during the growth of fishes; bigger and longer fishes usually indicate a higher concentration of Hg [4,29,33-34]. The results have indicated a positive correlation between THg concentration and total weight ($R^2: 0.77, p < 0.01$) and total length ($R^2: 0.78, p < 0.01$) of fish samples from Binuangeun, Banten. The THg concentration in *D. russelli*

Table 2. Previous research publication of THg in *D. russelli* and *M. cordyla* outside Binuangeun area

Species and Σ samples (N)	Location	THg concentration	Reference
<i>M. cordyla</i> (3)	West Peninsular Malaysia	Muscle (0.207 ± 0.089 mg/kg ww)	[20]
<i>D. russelli</i> (1)	West Peninsular Malaysia	0.073 mg/kg ww	[20]
<i>D. russelli</i> (10)	Peninsular Malaysia	0.078-0.304 (0.195) mg/kg dw	[19]
<i>M. cordyla</i> (20)	Peninsular Malaysia	0.202-0.913 (0.319) mg/kg dw	[19]
<i>M. cordyla</i>	Palu Bay, Indonesia	Gills (0.033 mg/kg ww)	[32]
		Muscle (0.028 mg/kg ww)	
		Liver (0.073 mg/kg ww)	
<i>M. cordyla</i> (30)	Binuangeun, Banten	Muscle (0.060 ± 0.011 mg/kg ww)	This study
		Liver (0.032 ± 0.008 mg/kg ww)	
		Gut contents (0.017 ± 0.010 mg/kg ww)	
<i>D. russelli</i> (15)	Binuangen, Banten	Muscle (0.235 ± 0.097 mg/kg ww)	This study
		Gut tissues (0.132 ± 0.056 mg/kg ww)	
		Gonad (0.066 ± 0.028 mg/kg ww)	
		Eggs (0.115 ± 0.075 mg/kg ww)	

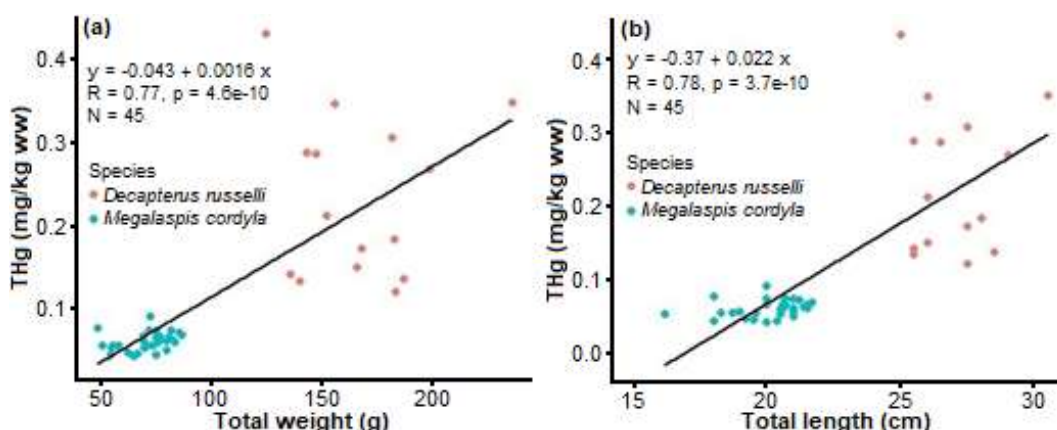


Fig 4. (a) Relationship between THg concentrations (mg/kg ww) on total weight (TW), (b) Relationship between THg vs. total length (TL) of fish samples from Binuangeun, Banten

and *M. cordyla* will contribute toward baseline data on THg in marine fish that are commonly caught and consumed in the Binuangeun area or West Java Sea near the Sunda Strait waters. This study shows lower THg concentration compared to the National Guideline from NADFC, but it would impact human health if the fishes consumed in excessive amounts.

■ CONCLUSION

This study measured total mercury (THg) in two species of small pelagic fishes from Binuangeun Fish Auction in Banten. The average THg concentration in the muscle (edible portion) of *D. russelli* was 0.21 mg/kg ww and *M. cordyla* 0.07 mg/kg ww. In general, THg concentration in all samples (muscle) was below permissible national and international mercury consumption guidelines (0.5 mg/kg ww for fish and fishery products). This study's results showed that THg in predator fish (*M. cordyla*) is lower than in *D. russelli* with low trophic levels. Further research is needed, which the specimens were analyzed has a large size range in order to assess the life cycle regarding total mercury concentration.

■ ACKNOWLEDGMENTS

Authors thanks to *Riset Prioritas* COREMAP CTI-LIPI No: B-5849/IPK.2/KP.06/VI/2019 Research Centre for Oceanography, LIPI year fiscal 2019 for funding and this publication was part of research on title Data Collection and Biological Aspects of Sharks and Rays that listed on Appendix CITES and Endangered Species. The

authors would like to thank Mr Johan Picasouw (Rest in Peace) for assistance in the preparation sample from the location and laboratory.

■ AUTHOR CONTRIBUTIONS

S as the main contributor to the concept idea, data analysis, and drafted the manuscript, ZP, HN, and SO executed sample and drafted the manuscript.

■ REFERENCES

- [1] Lim, T.O., Ding, L.M., Suleiman, A.B., Fatimah, S., Siti, S., Tahir, A., and Maimunah, A.H., 2000, Distribution of body weight, height and body mass index in a national sample of Malaysian adults, *Med. J. Malays.*, 55 (1), 108–128.
- [2] Stergiou, K.I., and Karpouzi, V.S., 2002, Feeding habits and trophic levels of Mediterranean fish, *Rev. Fish Biol. Fish.*, 11 (3), 217–254.
- [3] Reinfelder, J.R., Fisher, N.S., Luoma, S.N., Nichols, J.W., and Wang, W.X., 1998, Trace element trophic transfer in aquatic organisms: A critique of the kinetic model approach, *Sci. Total Environ.*, 219 (2-3), 117–135.
- [4] Mahaffey, K.R., 2004, Fish and shellfish as dietary sources of methylmercury and the ω -3 fatty acids, eicosahexanoic acid, and docosahexaenoic acid: Risks and benefits, *Environ. Res.*, 95 (3), 414–428.
- [5] Kershaw, T.G., Clarkson, T.W., and Dhahir, P.H., 1980, The relationship between blood levels and a

- dose of methylmercury in man, *Arch. Environ. Health*, 35 (1), 28–36.
- [6] Maycock, B., and Benford, D., 2007, Risk assessment of dietary exposure to methylmercury in fish in the UK, *Hum. Exp. Toxicol.*, 26 (3), 185–190.
- [7] BPOM, 2018, *Batas Maksimum cemaran logam berat dalam pangan olahan*, Badan Pengawas Obat dan Makanan Republik Indonesia No. 5, Jakarta, 1–15.
- [8] Codex Alimentarius, 2016, *General standard for contaminants and toxin in food and feed*, CODEX STAND 193-1995, 1–65.
- [9] SNI, 2016, *Cara uji Kimia – Bagian 6: Penentuan kadar logam berat merkuri (Hg) pada produk perikanan*, SNI-01-2354.6, Badan Standardisasi Nasional-BSN, Jakarta, 1–15.
- [10] SNI, 2006, *Cara uji Kimia – Bagian 2: Penentuan kadar air pada produk perikanan*, SNI-01-2354.2, Badan Standardisasi Nasional-BSN, Jakarta, 1–12.
- [11] USEPA, 1998, *Method 7473: Mercury in solids and solution by thermal decomposition, amalgamation, and atomic absorption spectrophotometry*, <https://www.epa.gov/sites/production/files/2015-07/documents/epa-7473.pdf>.
- [12] Pralampita, W.A., and Chodriyah, U., 2010, Aspek biologi reproduksi ikan laying (*Decapterus russelli*) dan ikan banyar (*Rastrelinger kanagurta*) yang didaratkan di Rembang, Jawa Tengah, *Bawal Widya Riset Perikanan Tangkap*, 3 (1), 17–23.
- [13] Rahmayani, 2016, Biologi Reproduksi Ikan Tetengkek *Megalaspis cordyla* (Linnaeus, 1758) di Perairan Selat Sunda, *Undergraduate Thesis*, Institut Pertanian Bogor, Indonesia.
- [14] Froese, R., and Pauly, D., 2019, FishBase, *World Wide Web electronic publication*, www.fishbase.org.
- [15] Monperrus, M., Pécheyran, C., and Bolliet, V., 2020, Imaging differential mercury species bioaccumulation in glass eels using isotopic tracers and laser ablation inductively coupled plasma mass spectrometry, *Appl. Sci.*, 10 (7), 2463.
- [16] Bridges, C.C., and Zalups, R.K., 2010, Transport of inorganic mercury and methylmercury in target tissues and organs, *J. Toxicol. Environ. Health Part B*, 13 (5), 385–410.
- [17] Mela, M., Neto, F.F., Yamamoto, F.Y., Almeida, R., Grötzner, S.R., Ventura, D.F., and de Oliveira Ribeiro, C.A., 2013, Mercury distribution in target organs and biochemical responses after sub-chronic and trophic exposure to Neotropical fish *Hoplias malabaricus*, *Fish Physiol. Biochem.*, 40 (1), 245–256.
- [18] Bridges, K.N., Soulen, B.K., Overturf, C.L., and Roberts, A.P., 2016, Embryotoxicity of maternally transferred methylmercury to fathead minnows (*Pimephales promelas*), *Environ. Toxicol. Chem.*, 35 (6), 1436–1441.
- [19] Ahmad, N.I., Mohd Noh, M.F., Wan Mahiyuddin, W.R., Jaafar, H., Ishak, I., Wan Azmi, W.N.F., Veloo, Y., and Hairi, M.H., 2015, Mercury levels of marine fish commonly consumed in Peninsular Malaysia, *Environ. Sci. Pollut. Res.*, 22 (5), 3672–3686.
- [20] Anual, Z.F., Maher, W., Krikowa, F., Hakim, L., Ahmad, N.I., and Foster, S., 2018, Mercury and risk assessment from consumption of crustaceans, cephalopods, and fish from West Peninsular Malaysia, *Microchem. J.*, 140, 214–221.
- [21] Burger, J., Gaines, K.F., Boring, C.S., Stephens, W.L., Snodgrass, J., and Gochfeld, M., 2001, Mercury and selenium in fish from the Savannah River: Species, trophic level, and locational differences, *Environ. Res.*, 87 (2), 108–118.
- [22] Al-Majed, N.B., and Preston, M.R., 2000, Factors influencing the total mercury and methyl mercury in the hair of the fishermen of Kuwait, *Environ. Pollut.*, 109 (2), 239–250.
- [23] Kinghorn, A., Solomon, P., and Chan, H.M., 2007, Temporal and spatial trends of mercury in fish collected in the English–Wabigoon river system in Ontario, Canada, *Sci. Total Environ.*, 372 (2-3), 615–623.
- [24] Saei-Dehkordi, S.S., Fallah, A.A., and Nematollahi, A., 2010, Arsenic and mercury in commercially valuable fish species from the Persian Gulf: Influence of season and habitat, *Food Chem. Toxicol.*, 48 (10), 2945–2950.

- [25] Eagle-Smith, C.A., Suchanek, T.H., Colwell, A.E., and Anderson, N.L., 2008, Mercury trophic transfer in a eutrophic lake: The importance of habitat-specific foraging, *Ecol. Appl.*, 18 (Sp8), A196–A212.
- [26] Smith-Vaniz, W.F., 1999, “Carangidae. Jacks and scads (also trevallies, queenfishes, runners, amberjacks, pilotfishes, pampanos, etc)” in *FAO Species Identification Guide for Fishery Purposes, the Living Marine Resources of the Western Central Pacific*, Vol. 4. Bony Fishes Part 2 (Mugilidae to Carangidae), Eds. Carpenter, K.E., and Niem, V.H., Food and Agriculture Organization of the United Nations, Rome, 2659–2756.
- [27] Al Sakaff, H., and Esseen, M., 1999, Occurrence and distribution of fish species off Yemen (Gulf of Aden and Arabian Sea), *Naga*, 22 (1), 43–47.
- [28] Pauly, D., Cabanban, A., and Torres, Jr., F.S.B., 1996, “Fishery biology of 40 trawl-caught teleost of western Indonesia” in *Baseline Studies of Biodiversity: The Fish Resource of Western Indonesia*, Eds. Pauly, D., and Martusubroto, P., ICLARM, Manila, Philippines, 135–216.
- [29] Gochfeld, M., Burger, J., Jeitner, C., Donio, M., and Taryn, P., 2012, Seasonal, locational and size variations in mercury and selenium levels in striped bass (*Morone saxatilis*) from New Jersey, *Environ. Res.*, 112, 8–19.
- [30] Agah, H., Leermakers, M., Elskens, M., Fatemi, S.M.R., and Baeyens, W., 2007, Total mercury and methyl mercury concentrations in fish from the Persian Gulf and the Caspian Sea, *Water Air Soil Pollut.*, 181 (1), 95–105.
- [31] Astani, E., Vahedpour, M., and Babaei, H., 2016, Organic and total mercury concentration in fish muscle and thermodynamic study of organic mercury extraction in fish protein, *Ecopersia*, 4 (3), 1517–1526.
- [32] Paundanan, M., Riani, E., and Anwar, S., 2015, Kontaminasi logam berat merkuri (Hg) dan timbal (Pb) pada air, sedimen dan ikan selar tetengkek (*Megalaspis cordyla* L) di teluk Palu, Sulawesi Tengah, *JPSL*, 5 (1), 161–168.
- [33] Seixas, T.G., Moreira, I., Malm, O., and Kehrig, H.A., 2013, Ecological and biological determinants of methylmercury accumulation in tropical coastal fish, *Environ. Sci. Pollut. Res.*, 20 (2), 1142–1150.
- [34] Horvat, M., Degenek, N., Lipej, L., Tratnik, J.S., and Faganeli, J., 2014, Trophic transfer and accumulation of mercury in ray species in coastal waters affected by historic mercury mining (Gulf of Trieste, northern Adriatic Sea), *Environ. Sci. Pollut. Res.*, 21 (6), 4163–4176.

Supplementary Data

This supplementary data is a part of paper entitled "Synthesis and Characterization of 2,3-Diaminomaleonitrile Derivatives by One Pot Schiff Base Reaction and Their Application in Dye Synthesized Solar Cells".

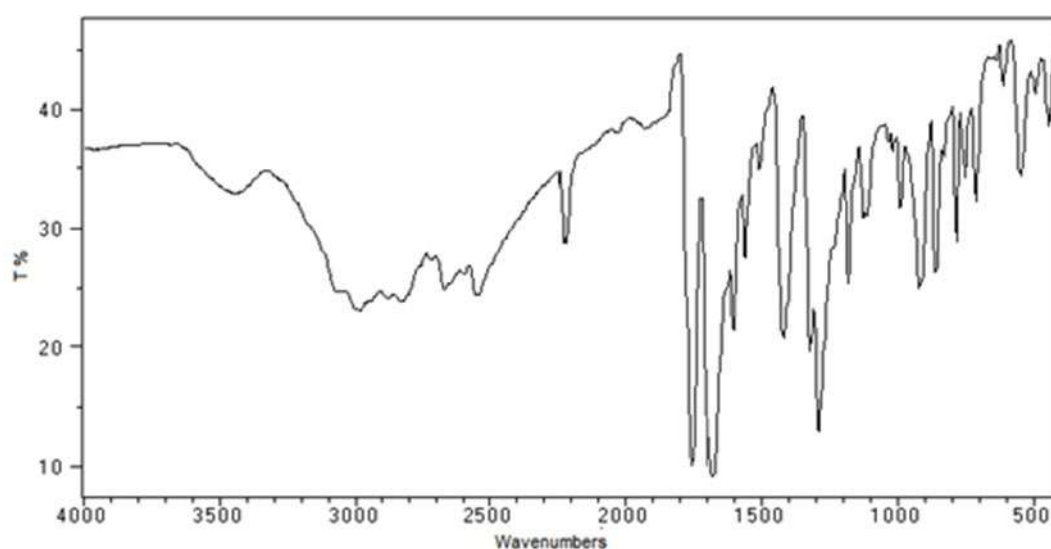


Fig S1. (a) FT-IR spectrum of 4-((E)-(((E)-2-((E)-benzylideneamino)-1,2-dicyanovinyl)imino)methyl) benzoic acid (SA1)

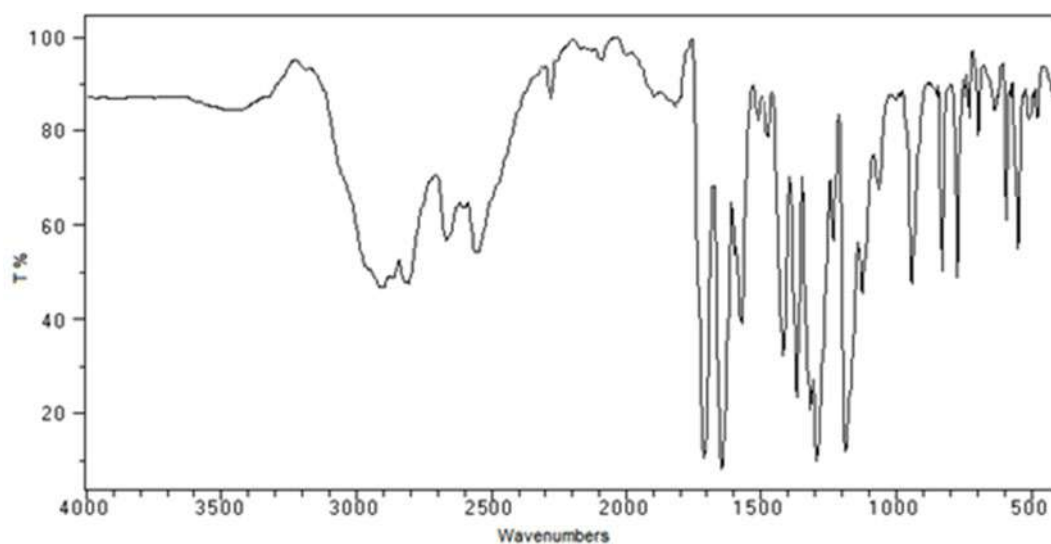


Fig S1. (b) FT-IR spectrum of 4-((E)-(((E)-1,2-dicyano-2-((E)-(4-(dimethylamino)benzylidene)amino)vinyl)imino)methyl) benzoic acid (SA2)

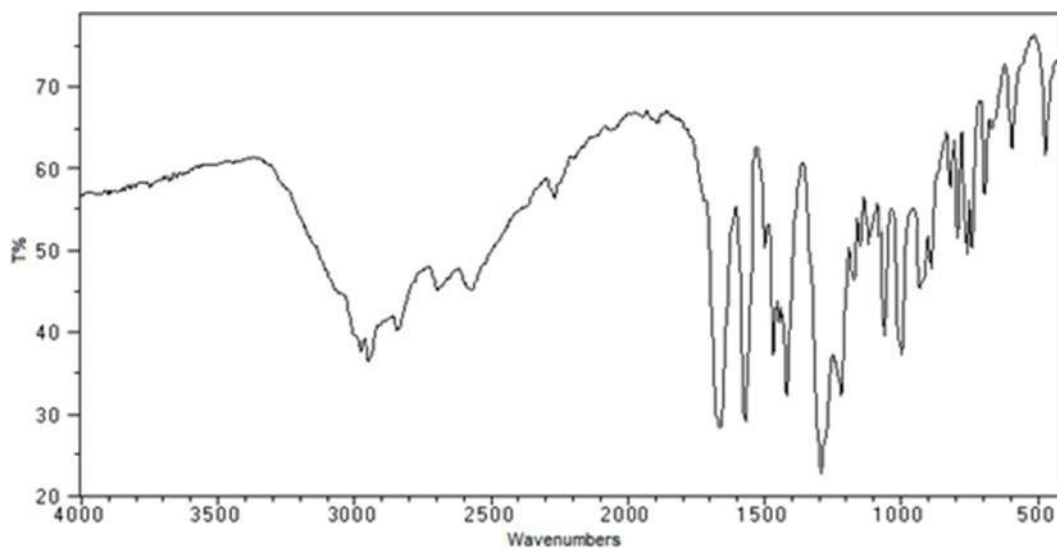


Fig S1. (c) FT-IR spectrum of 4-((E)-(((E)-1,2-dicyano-2-((E)-(3,5-dimethoxybenzylidene)amino)vinyl)imino)methyl) benzoic acid (SA3)

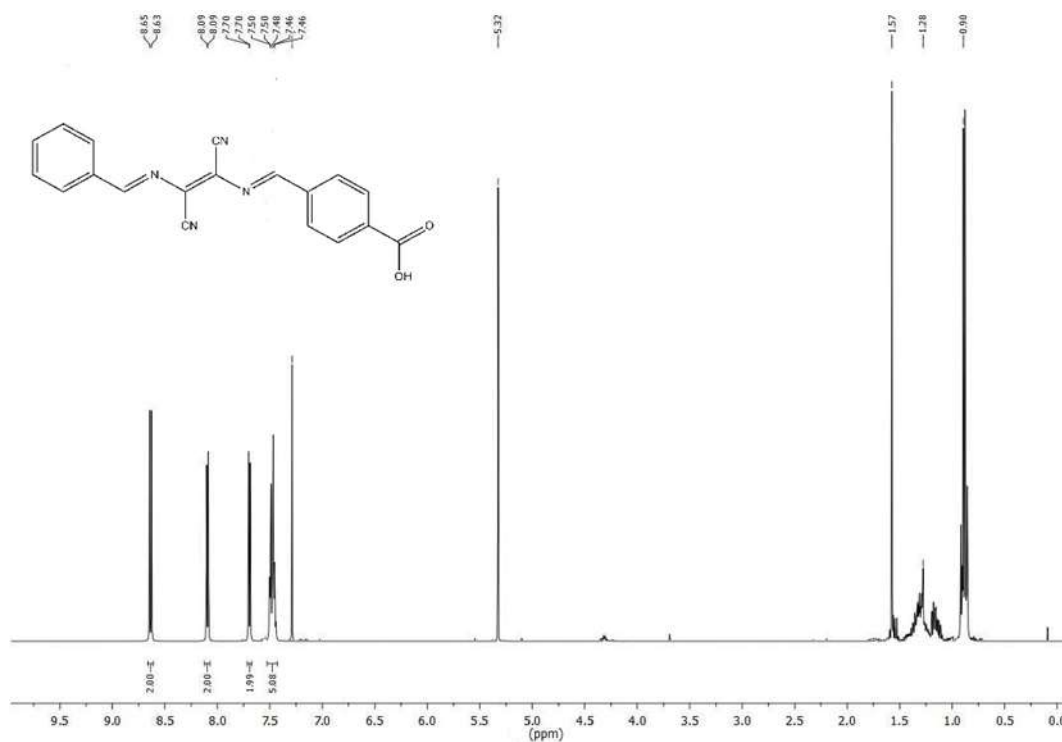


Fig S2. (a) ¹H-NMR spectrum of 4-((E)-(((E)-2-((E)-benzylideneamino)-1,2-dicyanovinyl)imino)methyl) benzoic acid (SA1)

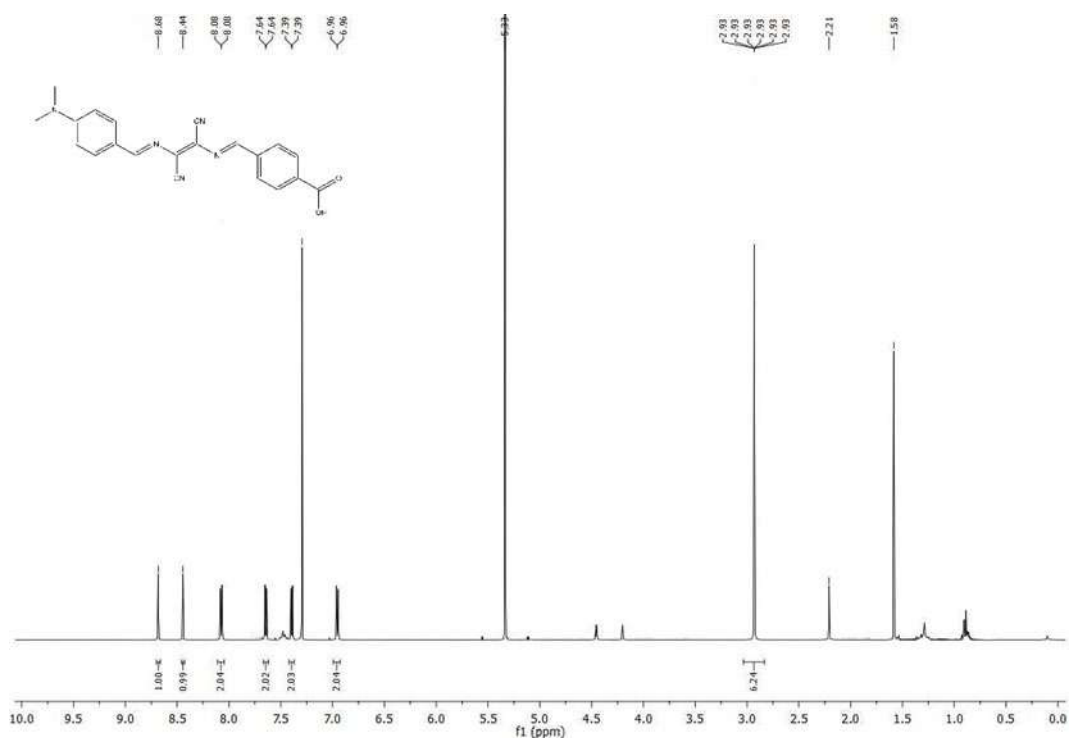


Fig S2. (b) ¹H-NMR spectrum of 4-((E)-(((E)-1,2-dicyano-2-((E)-(4-(dimethylamino)benzylidene)amino)vinyl)imino)methyl) benzoic acid (SA2)

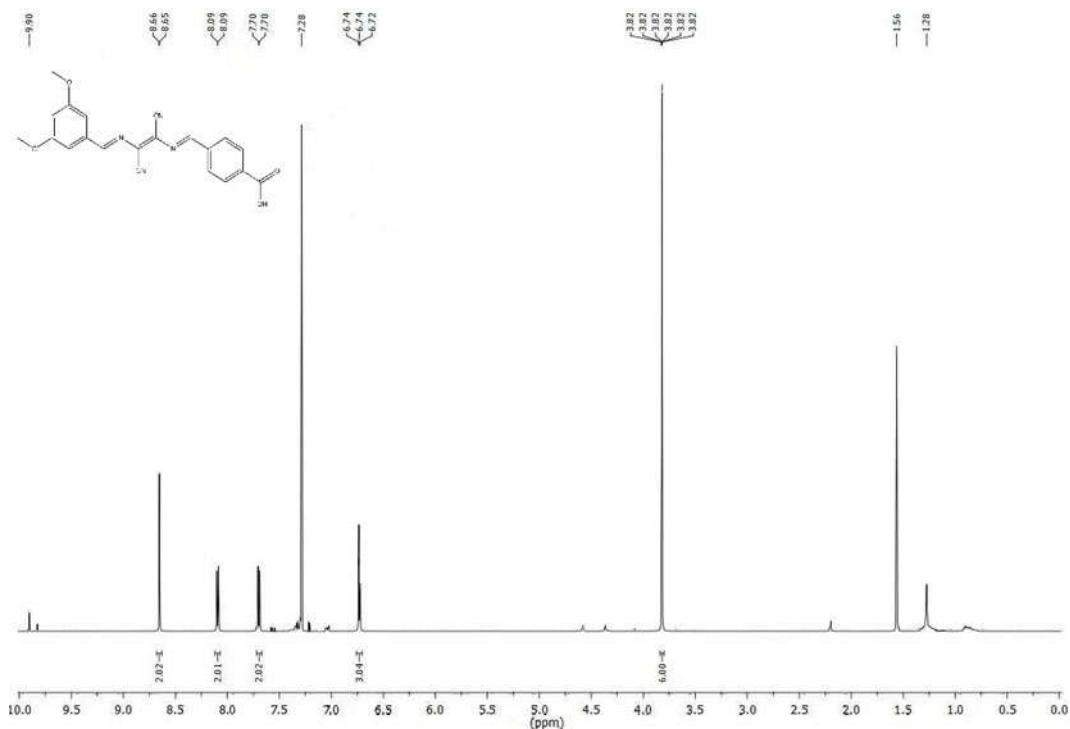


Fig S2. (c) ¹H-NMR spectrum of 4-((E)-(((E)-1,2-dicyano-2-((E)-(3,5-dimethoxybenzylidene) amino) vinyl)imino) methyl) benzoic acid (SA3)

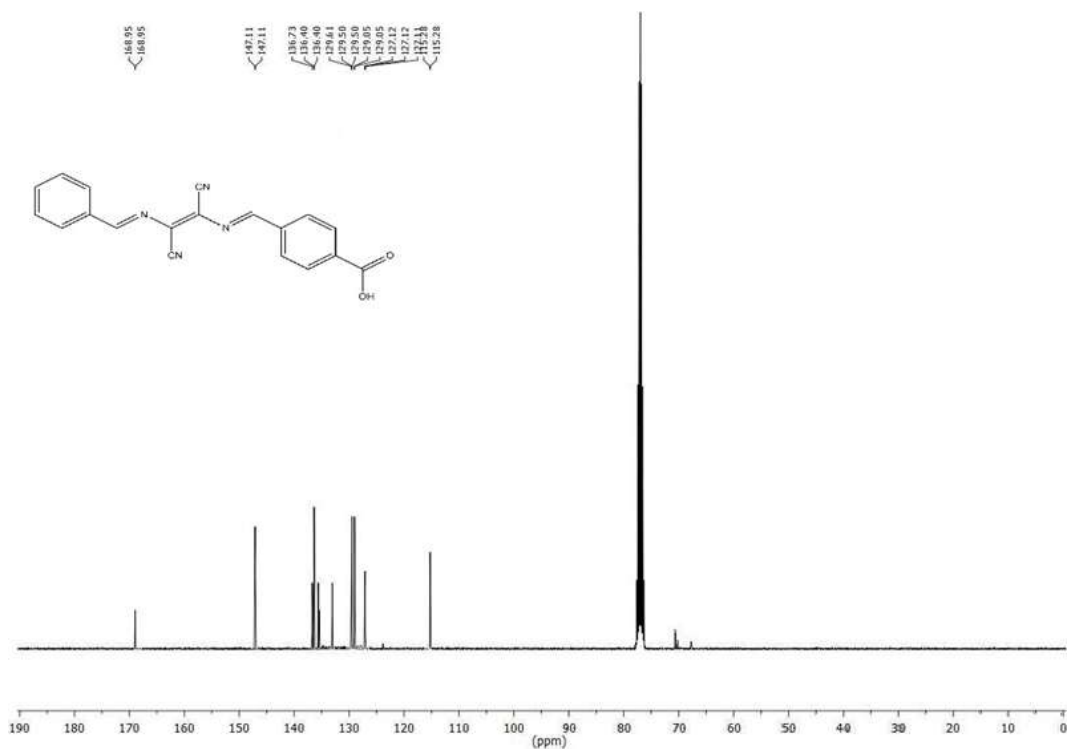


Fig S3. (a) ^{13}C -NMR spectrum of 4-((E)-(((E)-2-((E)-benzylideneamino)-1,2-dicyanovinyl)imino)methyl) benzoic acid (SA1)

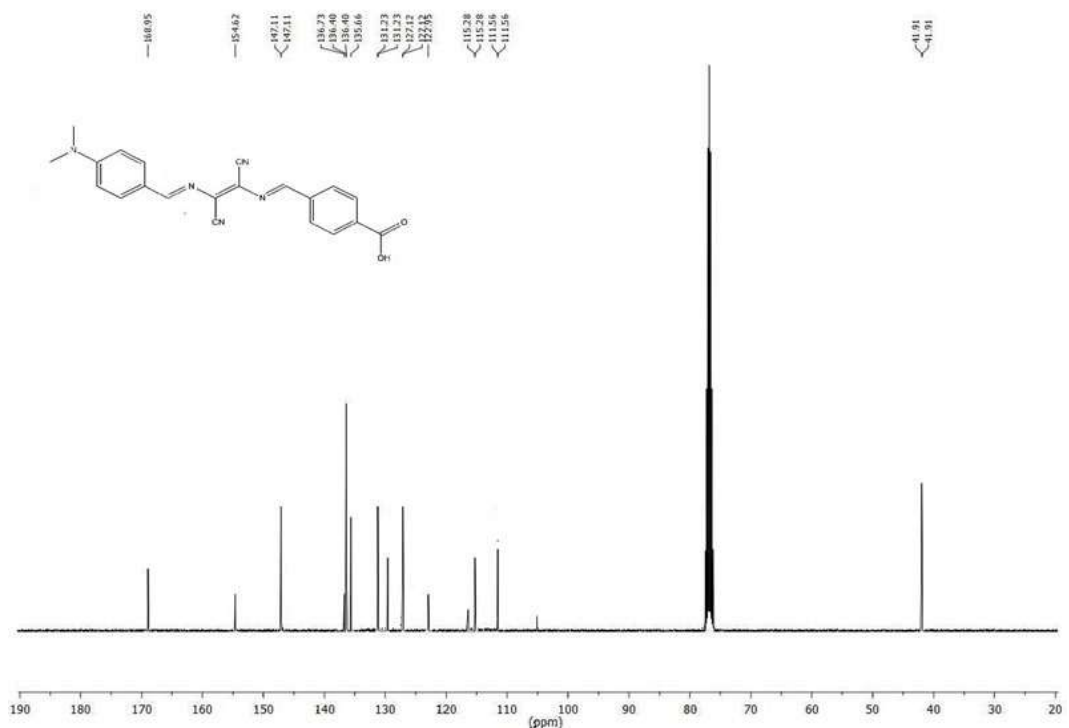


Fig S3. (b) ^{13}C -NMR spectrum of 4-((E)-(((E)-1,2-dicyano-2-((E)-(4-(dimethylamino)benzylidene)amino)vinyl)imino)methyl) benzoic acid (SA2)

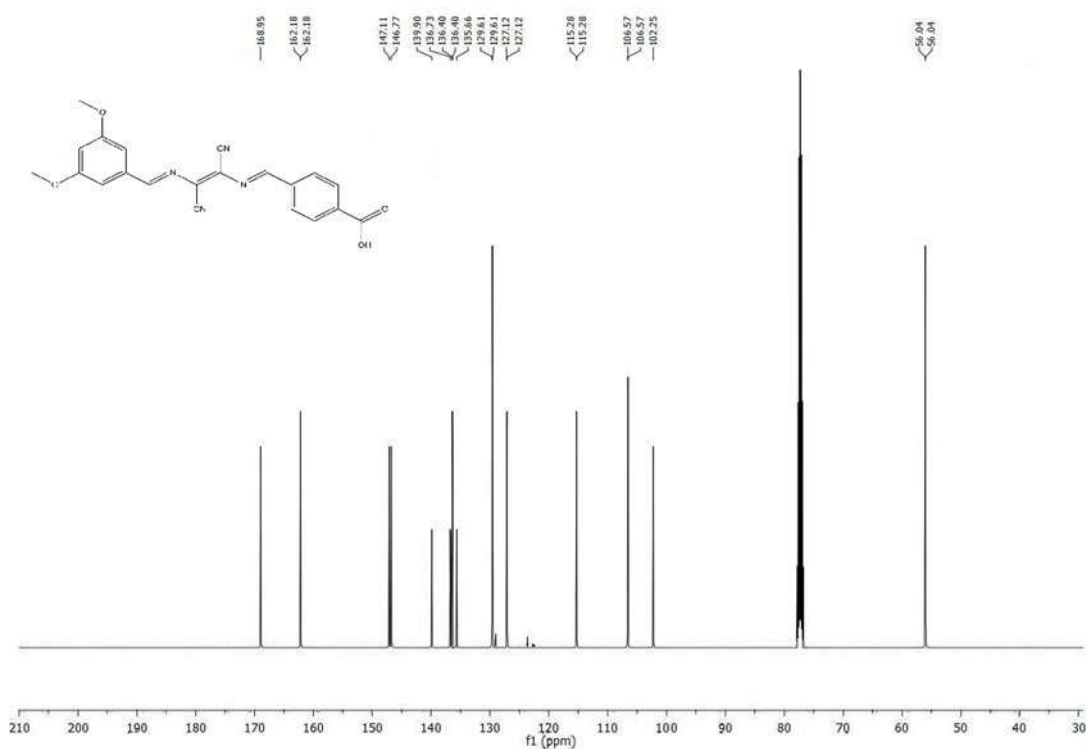


Fig S3. (c) ^{13}C -NMR spectrum of 4-((E)-(((E)-1,2-dicyano-2-((E)-(3,5-dimethoxybenzylidene)amino)vinyl)imino)methyl)benzoic acid (SA3)

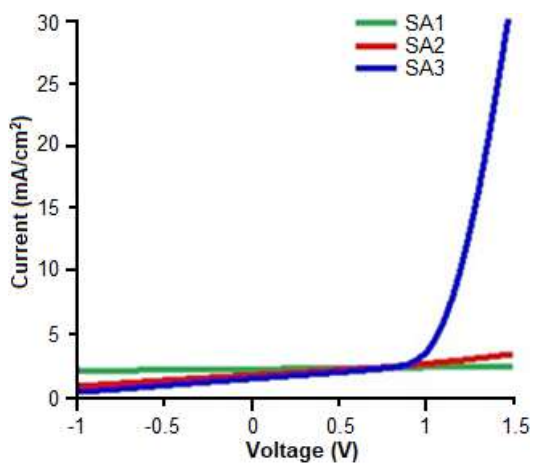


Fig S4. I-V curve for SA1, SA2 and SA3

Synthesis and Characterization of 2,3-Diaminomaleonitrile Derivatives by One-Pot Schiff Base Reaction and Their Application in Dye Synthesized Solar Cells

Saifaldeen Muwafag Abdalhadi^{1*}, Asmaa Yahya Al-Baitai², and Hazim Abdulrazzaq Al-Zubaidi³

¹Department of Remote Sensing, College of Remote Sensing and Geophysics, Al-Karkh University of Science, Baghdad, Iraq

²Department of Chemistry, College of Science, Al-Nahrain University, Baghdad, Iraq

³Department of Biomedical Science, College of Science, Al-Karkh University of Science, Baghdad, Iraq

* **Corresponding author:**

tel: +964-7702777191

email: dr.saifaldeen80@gmail.com

Received: July 3, 2020

Accepted: October 5, 2020

DOI: 10.22146/ijc.57535

Abstract: In a one-pot reaction, three new 2,3-diaminomaleonitrile (DAMN) derivative dyes were prepared by simple Schiff base reaction. The compounds were designed as a sensitizer in dye synthesizes solar cells (DSSCs). Many conditions have been used to provide the methodology to get the best yield. The prepared dyes were characterized by melting point, elemental microanalysis, mass spectroscopy, FT-IR, ¹H-NMR, and UV-Vis spectroscopy. A computational study was carried out to support our results. The DSSC data was shown the best performance for SA3 dye with 0.38% efficiency at AM 1.5 then SA2 with 0.22% and the last dye is SA1 with 0.09%, compared to control cell (N719) 5.4%.

Keywords: one-pot reaction; 2,3-diaminomaleonitrile; Schiff base; DSSCs

■ INTRODUCTION

Photovoltaic technology is one of the most important techniques which involved generating clean energy from free sunlight [1-3]. During the last two decades, dye-sensitized solar cells (DSSCs) arguably offer a promising photovoltaic technology due to their cheap and simple fabrication process and methods [4-8]. DSSCs have other specific advantages represented by the possible flexibility, chemical versatility, colorful appearances, and a vast synthetic way to different organic and organometallic molecular structures [9-13]. DSSCs consists of different parts: (1) Transparent conductive glass sheet electrode which is coated with fluorine-doped tin oxide (FTO) or indium tin oxide (ITO); (2) Semiconductor layer coated on the FTO glass sheet such as TiO₂ or ZnO₂ which is used as a working electrode; (3) Organic or organometallic dye which is design as a donor, π -bridge and acceptor to improve the transferring the excited electron from the donor to acceptor part; (4) Electrolyte solution which carries the electron from counter electrode to the dye and usually used an iodide/triiodide as a redox electrolyte in DSSC; (5) A counter electrode which is used to close the circuit of the

solar cells from glass sheet coated with a metal such as Platinum [1-2].

In 1991, O'Regan and co-workers developed the first effective DSSCs, with a power conversion efficiency (PCE) of 7% under the illumination of AM 1.5 [14]. Ten years later, Nazeeruddin and co-workers employed nano-powder (TiO₂) as a semiconductor electrode, and the efficiency of DSSCs was reported to be 11.4% [15]. A wide range of organic dyes with the donor and acceptor system has been designed for DSSCs [16-18].

The free-metal organic dyes have many advantages over organometallic dyes such as cost efficiency, high extinction coefficient, and environmentally friendly [19-21]. The best organic dyes in DSSC are based on the chromophore as a donor part such as dimethylaniline [22-24] and coumarins derivatives [25-27]. Also, π bridge played significant roles in dyes design. For instance, Michele C. and co-workers reported the synthesis of two porphyrin dyes with two different π bridge spacers. The two dyes (PorF and PorT) contain the furan and thiophene group, respectively as a π conjugation linker between the same donor and acceptor parts. A significant difference in the efficiencies (η) has been noticed, which based furan dye ($\eta = 4.5\%$)

being more efficient than thiophene dye ($\eta = 3.6\%$) [28]. Gao and co-workers published their work used four different dyes with the elongation of a π -conjugated bridge by using 3,4-ethylenedioxythiophene (EDOT) as a π bridge spacer. Unexpectedly, the longest π -bridge dye showed the lowest efficiency [29].

2,3-Diaminomaleonitrile (DAMN) has been used to prepare a wide range of organic compounds due to the significant applications of DAMN derivatives to synthesis symmetrical and unsymmetrical dyes with different physical and chemical properties [30-34]. There are few studies available about the DAMN derivative as a dye in DSSCs. This paper describes the synthesis of three unsymmetrical push-pull systems by using the Schiff base reaction in a one-pot process. The three dyes are based in DAMN as a π conjugation linker, benzene derivative as a donor part, and benzoic acid as an acceptor part, and these dyes are used as dyes in DSSCs. Different types of conditions were used in these reactions to get the best yield for the final compound. Finally, the advantages of the one-pot reaction protocol were represented by a significant reduction in synthesis time and purification cost [35-37].

■ EXPERIMENTAL SECTION

Materials

All starting materials and solvents were purchased from Alfa Aesar, TCI, and Sigma-Aldrich and used as received without any purification. All reactions were run under a nitrogen atmosphere. Silica gel of column chromatography was used from Merck (40–63 μm 60 Å).

Instrumentation

$^1\text{H-NMR}$ and $^{13}\text{C-NMR}$ spectra were recorded with a Bruker Avance-DPX-250/400 spectrometer operating 400/100 MHz respectively, using tetramethylsilane (TMS) as an internal standard and DMSO-d_6 or CDCl_3 as the solvent. UV-Vis absorption spectra were recorded on a Shimadzu UV-3600 UV-Vis-NIR spectrometer. Mass spectra were obtained on a Bruker MicroTOF QII. Elemental analyses (C, H, and N) were tested on a Perkin Elmer 240 C analyzer. Computational studies were performed using Gaussian 09 software. The molecular

structure was initially optimized by semi-empirical (AM1) and then reoptimized by Density Functional Theory (DFT).

Procedure

Preparation of dyes

The three Schiff base dyes were synthesized by the same procedure, Fig. 1, 1.0 mmol of one of the aldehyde derivatives ((0.11 g, 1.0 mmol) benzaldehyde (1), (0.15 g, 1.0 mmol) 4-(dimethyl-amino)benzaldehyde (2), (0.17g, 1.0 mmol) 3,5-dimethoxybenzaldehyde (3)) and (0.16 g, 1.5 mmol) of DAMN (4) were introduced to 2-neck round-bottom flask under a nitrogen atmosphere. Absolute ethanol (50 mL) was added to the mixture with two drops of glacial acetic acid as a catalyst. The mixture was allowed to stir for 5 h at 80 °C. After this time 0.3 g, 2.0 mmol of 4-formylbenzoic acid (5) was dissolved in 10 mL of absolute ethanol and added *via* a syringe to the mixture, and left to stir at 80 °C for 15 h. The mixture was allowed to cool at room temperature and the crude product was left to precipitate overnight in the mother solution. Then, the precipitate was filtered and washed with cold methanol. The crude product was purified by column chromatography (SiO_2 , $\text{DCM}:\text{acetone}$; 9:1) to give a compound as a powder.

Preparation and testing DSSCs

ITO conductive glass sheets were cleaned by using a detergent solution in an ultrasonic bath for 10 min, then rinsed with distilled water and ethanol. TiO_2 was prepared by adding 15 mL of ethanol to the 3.0 g of TiO_2 nanopowder (10–25 nm, US Research Nanomaterial, Inc, USA) and then added 2.5 mL of Triton X-100. The mixture was stirred using a small magnetic bar for 45 min to form TiO_2 paste. The TiO_2 paste was dropped to the top of the ITO glass sheet by using an eye pipette and then deposited by doctor blade technique to form a TiO_2 thin layer (0.5 cm^2 area). The glass sheet with the TiO_2 layer was heated at 70 °C for 30 min then sintered at 400 °C for 45 min. After cooling, the deposit TiO_2 was immersed in the dye solution (10^{-3} M) for 5 h. The counter electrode was made by sketching a pencil (graphite pencil) on the surface of another conductive glass (ITO). The TiO_2 thin layer with dye and counter

electrode were assembled to form a DSSC by sandwiching with a redox electrolyte solution (I^-/I_3^-).

For DSSCs testing, a solar simulator with a xenon light source (450 W, Osram XBO 450) and filter (Schott 113) was used to test fabricated solar cells. The power of the solar simulator was controlled to the standard test of the DSSCs AM 1.5 by using Si photodiode as a reference and color-matched filter (KG-3, Schott) which was used to reduce the mismatch in the wavelength (350–750 nm) between AM 1.5 and simulated light to less than 5%. The setting time between voltage and current density of the *J-V* characterization of the solar cells was fixed with a digital source meter (Keithley model 2400) to 80 ms.

■ RESULTS AND DISCUSSION

Synthesis of Dyes

Dye characterization

4-((E)-(((E)-2-((E)-benzylideneamino)-1,2-dicyanovinyl)imino)methyl) benzoic acid (SA1). Yield 36%; mp. 211–213 °C; FT-IR, cm^{-1} (rel. intensity), 3411 (w), 2245 (s), 1788 (s), 1682(s), 1575 (m), 1433, 1082 (m), 863 (w), 776 (w). 1H -NMR ($CDCl_3$, 400 MHz): δ 8.65 (s, 1H, CH), 8.63 (s, 1H, CH), 8.09 (d, $J = 9.1$ Hz, 2H, Ar-H), 7.70 (d, $J = 9.1$ Hz, 2H, Ar-H), 7.60–7.39 (m, 5H, Ar-H). ^{13}C -NMR ($CDCl_3$, 100 MHz): δ 168.95, 147.11, 136.73, 136.40, 135.66, 135.49, 133.06, 129.61, 129.60, 129.50, 129.05, 127.12, 115.28. Anal. Calcd. For $C_{19}H_{12}N_4O_2$: C, 69.51; H, 3.68; N, 17.06. Found: C, 69.53; H, 3.64; N, 17.10. EI-MS: m/z 328.

4-((E)-(((E)-1,2-dicyano-2-((E)-4-(dimethylamino)benzylidene)amino)vinyl)imino)methyl) benzoic acid (SA2). Yield 45%; mp. 231–233 °C; FT-IR, cm^{-1} (rel. intensity), 3432 (w), 2854 (m), 2259 (s), 1716 (s), 1641 (m), 1544 (m), 1419 (s), 1290 (m), 1091 (m), 860 (w), 769 (w). 1H -NMR ($CDCl_3$, 400 MHz): δ 8.68 (s, 1H, CH), 8.44 (s, 1H, CH), 8.06 (d, $J = 9.1$ Hz, 2H, Ar-H), 7.64 (d, $J = 9.1$ Hz, 2H, Ar-H), 7.39 (d, $J = 8.4$ Hz, 2H, Ar-H), 6.96 (d, $J = 8.4$ Hz, 2H, Ar-H), 2.93 (s, 6H, CH). ^{13}C -NMR ($CDCl_3$, 100 MHz): δ 168.94, 154.62, 147.11, 136.73, 136.40, 135.66, 131.23, 129.61, 127.12, 122.95, 115.28, 111.56, 41.91. Anal. Calcd. For $C_{23}H_{23}N_5O_2$: C, 68.81; H, 5.77; N, 17.44. Found: C, 68.86; H, 5.75; N, 17.42. EI-MS: m/z 371.

4-((E)-(((E)-1,2-dicyano-2-((E)-3,5-dimethoxybenzylidene)amino)vinyl)imino)methyl) benzoic acid (SA3). Yield 44%; mp. 254°256 °C; FT-IR, cm^{-1} (rel. intensity), 3008 (s), 2241 (s), 1691 (s), 1665 (s), 1583 (m), 1411 (s), 1186 (s), 1051 (m), 872 (w), 782 (w). 1H -NMR ($CDCl_3$, 400 MHz): δ 8.66 (s, 1H, CH), 8.65 (s, 1H, CH), 8.09 (d, $J = 9.0$ Hz, 2H, Ar-H), 7.70 (d, $J = 9.0$ Hz, 2H, Ar-H), 6.78–6.67 (m, 3H, H-Ar), 3.82 (s, 6H, CH). ^{13}C -NMR ($CDCl_3$, 100 MHz): δ 168.95, 162.18, 147.11, 146.77, 139.90, 136.73, 136.40, 135.66, 129.61, 127.12, 115.28, 106.57, 102.25, 56.04. Anal. Calcd. For $C_{21}H_{16}N_4O_4$: C, 64.94; H, 4.15; N, 14.43. Found: C, 65.02; H, 4.12; N, 14.39. EI-MS: m/z 388.

The general one-pot dyes reaction scheme is given in Fig. 1. Schiff base reaction process was used to prepare three dyes for DSSC devices by using different aromatic compounds. The aldehyde derivatives (1, 2, and 3 in Fig. 1) were used as a donor part, DAMN as a π -bridge, and benzoic acid as an acceptor part. Different conditions were used to obtain maximum yields for these reactions, and Table 1 shows the summary of these reactions with different conditions. In these conditions were used a different equivalents addition of starting materials with different types of solvent to get the best yield. In all conditions, the donor was added firstly to react with the DAMN compound for 5 h and after that, the acceptor was added to the mixture to react with the resulted compound (got from the reaction of donor and DAMN) for 15 h. Seven conditions were used to prepare SA1 compound and the best condition (number 5) was applied to the donor 2 and 3 to prepare compound SA2 and SA3 respectively. The same equivalents of the donor, π -bridge, and acceptor were used in condition number 1 and the yield was 18%. In condition number 2, the yield of reaction decreases (15%) because the equivalent of the donor was more than the equivalent of acceptor and that led to the effect of the substitution of acceptor in the DAMN compound. The same reason affected the percentage yield in condition number 3. The yields of reactions increased in conditions 4 and 5 and because the equivalent of the donor decreased, and the equivalents of acceptor and DAMN increased.

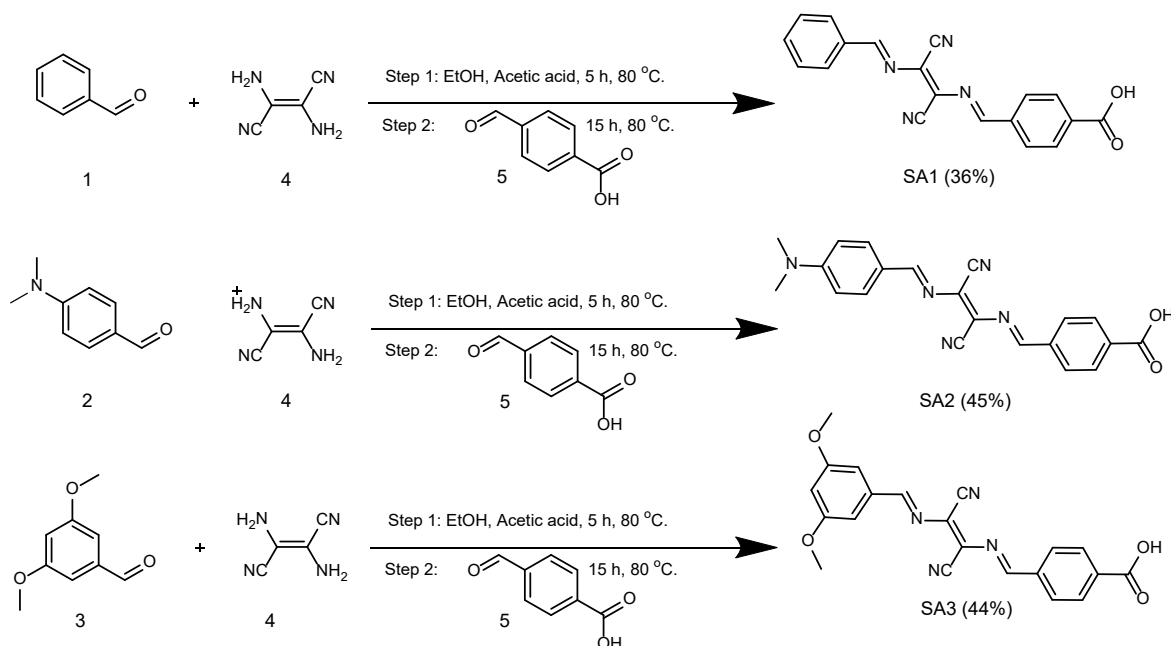


Fig 1. The synthesis scheme of SA1, SA2, and SA3 dyes

Table 1. The conditions of one-pot reaction in different equivalent (eq), solvent, and time

Conditions	Donor (eq)	DAMN] (eq)	Acceptor (eq)	Solvent	Time (h)	Yield (%)
1	1.0 (1)	1.0	1.0	EtOH	20	18
2	1.5 (1)	1.0	1.0	EtOH	20	15
3	1.5 (1)	1.0	1.5	EtOH	20	15
4	1.0 (1)	1.5	1.5	EtOH	20	30
5	1.0 (1)	1.5	2.0	EtOH	20	36
6	1.0 (1)	1.5	2.0	DMF	20	28
7	1.0 (1)	1.5	2.0	THF	20	18
8	1.0 (2)	1.5	2.0	EtOH	20	45
9	1.0 (3)	1.5	2.0	EtOH	20	44

The solvent of the best condition (number 5) was changed by using DMF in condition number 6 and THF in condition number 7 but the yields were decreased to 28% and 18% respectively and that is could be due to the solubility effect of the starting materials.

The best yields in these conditions were given around 36%, 45%, and 44% as a product for compounds SA1, SA2, and SA3 respectively. The best yield was achieved by reacting 1 mole of donor with 1.5 mol of DAMN for 5 h then added 2 mol of acceptor to the continuous reaction to get the final product. In general, the low yield of the resulted compounds could be due to the side products of the reaction (Fig. 2) which was come from disubstitutions of DAMN with a donor (compound

7) and disubstitutions of DAMN with acceptor (compound 8) and the yield of the side products was around ~55% for both.

FT-IR Spectroscopy

The FTIR spectra of three dyes indicate a strong broad band for carboxylic acid at $\sim 3400\text{ cm}^{-1}$ for OH stretching and a strong sharp band at $\sim 1700\text{ cm}^{-1}$ for C=O stretching. One strong band was observed in the three dyes within $\sim 2250\text{ cm}^{-1}$ due to the nitrile group of DAMN. A medium two bands were absorbed in ~ 1630 and $\sim 1410\text{ cm}^{-1}$ for C=N stretching and C-N stretching respectively for Schiff base reaction. Many weak to medium bands were observed between 990 and 650 cm^{-1}

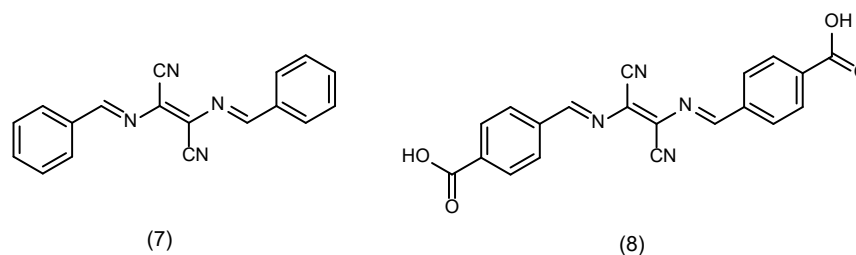


Fig 2. The chemical structure of two side product compounds for the first reaction

due to in-plane and out-of-plane of C–H vibration for benzene ring. A medium intensity band was observed at 1291 cm^{-1} due to C–N stretching (N–CH₃) for SA2 compound and a strong band was observed at 1186 cm^{-1} due to stretching of O–ether bond for SA3 compound.

Proton NMR Spectroscopy

The proton NMR (CDCl₃) of the first dye (SA1) shows two singlet peaks at δ 8.65 and 8.63 for two protons of two imines groups, which resulted from the Schiff base reaction. Two doublets peak were investigated at δ 8.02 and 7.70, also multiples peak from δ 7.60 to 7.39 for C–H proton of two benzene rings. The second dye (SA2) indicates singlet peaks at δ 8.68 and 8.44 for two C–H groups. Four doublet peaks as δ 8.06, 7.64, 7.39, and 6.96 due to 8 protons in two benzene rings. Singlet peak shows at δ 2.93 for 6 protons of the dimethylamine group. The last dye (SA3) shows two singlet peaks at δ 8.66 and 8.65 for two C–H groups and two doublet peaks for four protons appear at δ 8.09 and 7.70 with multiples peak between 6.78 and 6.67 for two benzene rings. One singlet peak was investigated at δ 3.82 for 6 protons of two ether groups (See supplementary information data).

UV-Vis Spectroscopy

The UV-Vis spectroscopy of three dyes (Fig. 3) was carried out in acetonitrile as a solvent. The three dyes SA1, SA2, and SA3 show a strong absorption band in the visible region with λ_{max} at 398, 440, and 442 nm respectively as well as good molar absorptivity ranging from 1.61×10^4 to $1.76 \times 10^4\text{ M}^{-1}\text{ cm}^{-1}$ and this is possibly due to π - π^* transition within conjugated between benzene rings in a day. The absorption band showed the redshift direction on going from SA1 to SA2 and SA3. Finally, the optical the

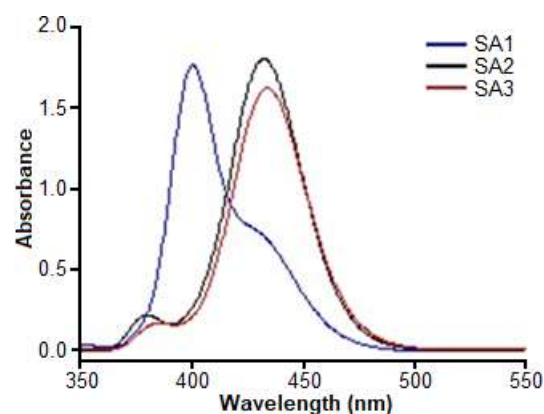


Fig 3. Absorption spectra of the three dyes SA1, SA2, and SA3 ($1 \times 10^{-4}\text{ M}$)

band gap (E_{opt}) of the dyes SA1, SA2, and SA3 were 2.88, 2.53, and 2.50 eV respectively.

Theoretical Calculation

The geometry and electronic properties of the three dyes were investigated theoretically by using density functional theory (DFT) performed by using Gaussian 09 software. All dyes calculations were tested under vacuum by using Lee–Yang–Parr's gradient corrected correlation (B3LYP) functional and 6-311G (d, p) basis set [38-39].

The molecular orbital and geometry for three dyes showed in Fig. 4. For compound SA1 and SA2, the HOMO orbital is delocalized throughout the benzene ring and dimethylaniline, respectively as well as on the DAMN part. The LUMO for the same dyes is delocalized over the DAMN and benzoic acid (acceptor part). This mixing in electron distribution between donor and acceptor part negatively affects the charge separation in the dye and that led to the effect of dye efficiency in the solar cell. On the other hand, the HOMO orbital

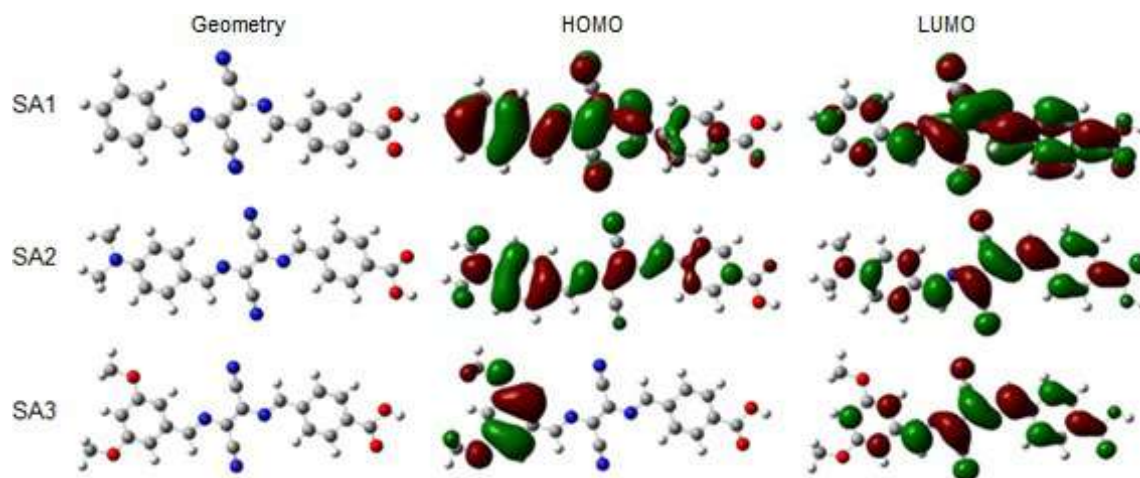


Fig 4. The geometry and frontier molecular orbital of three dyes (SA1, SA2, and SA3) calculated by DFT

in dye SA3 is delocalized over dimethoxybenzene and the LUMO is delocalized throughout the DAMN and benzoic acid which made charge separation in the dye. The optimization geometry of the three dyes was shown a planer shape with the substitution in dimethylamine for compound SA2 and dimethoxy in compound SA3 laying out-of-plane to avoid dye aggregation which improved the solubility. The computed energy gap for the SA1, SA2, and SA3 were 2.56, 2.50, and 2.51 eV respectively and these results are similar to the E_{opt} results.

Device Testing

The three sensitizers were tested as a dye in DSSCs by using iodide/triiodide as electrolyte solution between two electrodes and the devices were tested at AM 1.5 (100 mW cm^{-2}). Power conversion efficiency (PCE) of dyes was measured by open-circuit voltage (V_{oc}), short circuit current (J_{sc}), and fill factor (FF) and all the results are shown in Table 2. There is a big difference in I-V curve data between SA3 and other dyes (see supplementary information). The J_{sc} value of compound SA3 is 1.21 mA/cm^2 and for SA1 and SA2 are 0.15, 0.77 respectively, indicating that the charge mobility of SA3

dye is more efficient than other dyes [40]. The I-V curve data show that the best efficiency was recorded with SA3 dye (0.38%) then with SA2 (0.22%) and finally with SA1 (0.09%). The low efficiency of the three dyes was may be due to the mixing of electron distribution donor and acceptor in DAMN part and that affected the charge separation between two parts.

CONCLUSION

In conclusion, three novel dyes containing a DAMN as a π -bridge spacer were synthesized in a one-pot reaction. The design of the dyes has given us to investigate the ability of the DAMN compound as a π -conjugated spacer on DSSCs performance. The reaction conditions were optimized to get the highest yield. All dyes were characterized by different techniques such as FT-IR, $^1\text{H-NMR}$, elemental microanalysis, mass spectroscopy, and UV-Vis. The computational studies of these dyes showed a mixing in electron distribution between donor and acceptor in π -bridge part (DAMN) which affected the efficiency of dyes in DSSC devices and the three dyes were indicated a poor efficiency in DSSC.

Table 2. I-V data for SA1, SA2, and SA3 dyes with N719 as a control

Dyes	J_{sc} (mA/cm^2)	V_{oc} (V)	FF	PCE (%)	PCE avg. (%)
SA1	0.15	0.82	35.6	0.09	0.07
SA2	0.77	0.82	36.1	0.22	0.19
SA3	1.21	0.91	37.9	0.38	0.34
N719	10.2	0.76	64.2	5.40	5.38

■ ACKNOWLEDGMENTS

This work was supported by Al-Karkh University of science and Al-Nahrain University, Baghdad, Iraq.

■ REFERENCES

- [1] Singh, G.K., 2013, Solar power generation by PV (photovoltaic) technology: A review, *Energy*, 53, 1–13.
- [2] Gong, J., Sumathy, K., Qiao, Q., and Zhou, Z., 2017, Review on dye-sensitized solar cells (DSSCs): Advanced techniques and research trends, *Renewable Sustainable Energy Rev.*, 68, 234–246.
- [3] Malinowski, M., Leon, J.I., and Abu-Rub, H., 2017, Solar photovoltaic and thermal energy systems: Current technology and future trends, *Proc. IEEE*, 105 (11), 2132–2146.
- [4] Abdalhadi, S.M., Connell, A., Zhang, X., Wiles, A.A., Davies, M.L., Holliman, P.J., and Cooke, G., 2016, Convenient synthesis of EDOT-based dyes by CH-activation and their application as dyes in dye-sensitized solar cells, *J. Mater. Chem. A*, 4 (40), 15655–15661.
- [5] Shalini, S., Balasundaraprabhu, R., Kumar, T.S., Prabavathy, N., Senthilarasu, S., and Prasanna, S., 2016, Status and outlook of sensitizers/dyes used in dye sensitized solar cells (DSSC): A review, *Int. J. Energy Res.*, 40 (10), 1303–1320.
- [6] Prabavathy, N., Shalini, S., Balasundaraprabhu, R., Velauthapillai, D., Prasanna, S., and Muthukumarasamy, N., 2017, Enhancement in the photostability of natural dyes for dye-sensitized solar cell (DSSC) applications: A review, *Int. J. Energy Res.*, 41 (10), 1372–1396.
- [7] Sugathan, V., John, E., and Sudhakar, K., 2015, Recent improvements in dye sensitized solar cells: A review, *Renewable Sustainable Energy Rev.*, 52, 54–64.
- [8] Ahmad, M.S., Pandey, A.K., and Abd Rahim, N., 2017, Advancements in the development of TiO₂ photoanodes and its fabrication methods for dye sensitized solar cell (DSSC) applications. A review, *Renewable Sustainable Energy Rev.*, 77, 89–108.
- [9] Mozaffari, S., Nateghi, M.R., and Zarandi, M.B., 2017, An overview of the challenges in the commercialization of dye sensitized solar cells, *Renewable Sustainable Energy Rev.*, 71, 675–86.
- [10] Urbani, M., Grätzel, M., Nazeeruddin, M.K., and Torres, T., 2014, Meso-substituted porphyrins for dye-sensitized solar cells, *Chem. Rev.*, 114 (24), 12330–12396.
- [11] Obotowo, I.N., Obot, I.B., and Ekpe, U.J., 2016, Organic sensitizers for dye-sensitized solar cell (DSSC): Properties from computation, progress and future perspectives, *J. Mol. Struct.*, 1122, 80–87.
- [12] Carella, A., Borbone, F., and Centore, R., 2018, Research progress on photosensitizers for DSSC, *Front. Chem.*, 6, 113–127.
- [13] Ludin, N.A., Al-Alwani Mahmoud, A.M., Mohamad, A.B., Kadhum, A.A.H., Sopian, K., and Abdul Karim, N.S., 2014, Review on the development of natural dye photosensitizer for dye-sensitized solar cells, *Renewable Sustainable Energy Rev.*, 31, 386–396.
- [14] O'Regan, B., and Grätzel, M., 1991, A low-cost, high-efficiency solar cell based on dye-sensitized colloidal TiO₂ films, *Nature*, 353 (6346), 737–740.
- [15] Nazeeruddin, M.K., Péchy, P., Renouard, T., Zakeeruddin, S.M., Humphry-Baker, R., Comte, P., Liska, P., Cevey, L., Costa, E., Shklover, V., Spiccia, L., Deacon, G.B., Bignozzi, C.A., and Grätzel, M., 2001, Engineering of efficient panchromatic sensitizers for nanocrystalline TiO₂-based solar cells, *J. Am. Chem. Soc.*, 123 (8), 1613–1624.
- [16] Kim, B.G., Zhen, C.G., Jeong, E.J., Kieffer, J., and Kim, J., 2012, Organic dye design tools for efficient photocurrent generation in dye-sensitized solar cells: Exciton binding energy and electron acceptors, *Adv. Funct. Mater.*, 22 (8), 1606–1612.
- [17] Choi, H., Baik, C., Kang, S.O., Ko, J., Kang, M.S., Nazeeruddin, M.K., and Grätzel, M., 2008, Highly efficient and thermally stable organic sensitizers for solvent-free dye-sensitized solar cells, *Angew. Chem. Int. Ed.*, 47 (2), 327–330.
- [18] Lin, R.Y.Y., Wu, F.L., Li, C.T., Chen, P.Y., Ho, K.C., and Lin, J.T., 2015, High-performance aqueous/organic dye-sensitized solar cells based on

- sensitizers containing triethylene oxide methyl ether, *ChemSusChem*, 8 (15), 2503–2513.
- [19] Hara, K., Sato, T., Katoh, R., Furube, A., Ohga, Y., Shinpo, A., Suga, S., Sayama, K., Sugihara, H., and Arakawa, H., 2003, Molecular design of coumarin dyes for efficient dye-sensitized solar cells, *J. Phys. Chem. B*, 107 (2), 597–606.
- [20] Jiao, Y., Zhang, F., Grätzel, M., and Meng, S., 2013, Structure-property relations in all-organic dye-sensitized solar cells, *Adv. Funct. Mater.*, 23 (4), 424–429.
- [21] Mishra, A., Fischer, M.K.R., and Bäuerle, P., 2009, Metal-free organic dyes for dye-sensitized solar cells: From structure: Property relationships to design rules, *Angew. Chem. Int. Ed.*, 48 (14), 2474–2499.
- [22] El-Meligy, A.B., Koga, N., Iuchi, S., Yoshida, K., Hirao, K., Mangood, A.H., and El-Nahas, A.M., 2018, DFT/TD-DFT calculations of the electronic and optical properties of bis-*N,N*-dimethylaniline-based dyes for use in dye-sensitized solar cells, *J. Photochem. Photobiol., A*, 367, 332–346.
- [23] Naik, P., Su, R., Babu, D.D., El-Shafei, A., and Adhikari, A.V., 2017, Structurally simple D-A-type organic sensitizers for dye-sensitized solar cells: Effect of anchoring moieties on the cell performance, *J. Iran. Chem. Soc.*, 14 (11), 2457–2466.
- [24] Hara, K., Sato, T., Katoh, R., Furube, A., Yoshihara, T., Murai, M., Kurashige, M., Ito, S., Shinpo, A., Suga, S., and Arakawa, H., 2005, Novel conjugated organic dyes for efficient dye-sensitized solar cells, *Adv. Funct. Mater.*, 15 (2), 246–252.
- [25] Sánchez-de-Armas, R., San Miguel, M.Á., Oviedo, J., and Sanz, J.F., 2012, Coumarin derivatives for dye sensitized solar cells: A TD-DFT study, *Phys. Chem. Chem. Phys.*, 14 (1), 225–233.
- [26] Wang, Z.S., Cui, Y., Hara, K., Dan-oh, Y., Kasada, C., and Shinpo, A., 2007, A high-light-harvesting-efficiency coumarin dye for stable dye-sensitized solar cells, *Adv. Mater.*, 19 (8), 1138–1141.
- [27] Wang, Z.S., Cui, Y., Dan-oh, Y., Kasada, C., Shinpo, A., and Hara, K., 2007, Thiophene-functionalized coumarin dye for efficient dye-sensitized solar cells: Electron lifetime improved by coadsorption of deoxycholic acid, *J. Phys. Chem. C*, 111 (19), 7224–7230.
- [28] Cariello, M., Abdalhadi, S.M., Yadav, P., Decoppet, J.D., Zakeeruddin, S.M., Grätzel, M., Hagfeldt, A., and Cooke, G., 2018, An investigation of the roles furan versus thiophene π -bridges play in donor- π -acceptor porphyrin based DSSCs, *Dalton Trans.*, 47 (18), 6549–6556.
- [29] Gao, P., Tsao, H.N., Yi, C., Grätzel, M., and Nazeeruddin, M.K., 2014, Extended π -bridge in organic dye-sensitized solar cells: The longer, the better?, *Adv. Energy Mater.*, 4 (7), 1301485.
- [30] Tsuzuki, K., and Tada, M., 1986, The syntheses of pteridin-2-one derivatives from diaminomaleonitrile (DAMN), *J. Heterocycl. Chem.*, 23 (5), 1299–1301.
- [31] Zhou, H., Wang, J., Chen, Y., Xi, W., Zheng, Z., Xu, D., Cao, Y., Liu, G., Zu, W., Wu, J., and Tian, Y., 2013, New diaminomaleonitrile derivatives containing aza-crown ether: Selective, sensitive and colorimetric chemosensors for Cu(II), *Dyes Pigm.*, 98 (1), 1–10.
- [32] Anitha, C., Sheela, C.D., Tharmaraj, P., and Shanmugakala, R., 2013, Studies on synthesis and spectral characterization of some transition metal complexes of azo-azomethine derivative of diaminomaleonitrile, *Int. J. Inorg. Chem.*, 2013, 436275.
- [33] Aruna, A., Rani, B., Swami, S., Agarwala, A., Behera, D., and Shrivastava, R., 2019, Recent progress in development of 2,3-diaminomaleonitrile (DAMN) based chemosensors for sensing of ionic and reactive oxygen species, *RSC Adv.*, 9 (52), 30599–30614.
- [34] Li, Z., Liu, C., Wang, J., Wang, S., Xiao, L., and Jing, X., 2019, A selective diaminomaleonitrile-based dual channel emissive probe for Al³⁺ and its application in living cell imaging, *Spectrochim. Acta, Part A*, 212, 349–355.
- [35] Fuse, S., Sugiyama, S., Maitani, M.M., Wada, Y., Ogomi, Y., Hayase, S., Katoh, R., Kaiho, T., and Takahashi, T., 2014, Elucidating the structure-property relationships of donor- π -acceptor dyes

- for dye-sensitized solar cells (DSSCs) through rapid library synthesis by a one-pot procedure, *Chem. Eur. J.*, 20 (34), 10685–10694.
- [36] Matsumura, K., Yoshizaki, S., Maitani, M.M., Wada, Y., Ogomi, Y., Hayase, S., Kaiho, T., Fuse, S., Tanaka, H., and Takahashi, T., 2015, Rapid synthesis of thiophene-based, organic dyes for dye-sensitized solar cells (DSSCs) by a one-pot, four-component coupling approach, *Chem. Eur. J.*, 21 (27), 9742–9747.
- [37] Irie, S., Fuse, S., Maitani, M.M., Wada, Y., Ogomi, Y., Hayase, S., Kaiho, T., Masui, H., Tanaka, H., and Takahashi, T., 2016, Rapid synthesis of D-A'- π -A dyes through a one-pot three-component Suzuki–Miyaura coupling and an evaluation of their photovoltaic properties for use in dye-sensitized solar cells, *Chem. Eur. J.*, 22 (7), 2507–2514.
- [38] Lee, C., Yang, W., and Parr, R.G., 1988, Development of the Colle-Salvetti correlation-energy formula into a functional of the electron density, *Phys. Rev. B: Condens. Matter*, 37 (2), 785–789.
- [39] Becke, A.D., 1993, Density-functional thermochemistry. III. The role of exact exchange, *J. Chem. Phys.*, 98 (7), 5648–5652.
- [40] Qu, S., Wang, B., Guo, F., Li, J., Wu, W., Kong, C., Long, Y., and Hua, J., 2012, New diketo-pyrrolopyrrole (DPP) sensitizer containing a furan moiety for efficient and stable dye-sensitized solar cells, *Dyes Pigm.*, 92 (3), 1384–1393.

Synthesis, Molecular Docking, and Evaluation of Some New Curcumin Analogs as Antimalarial Agents

Endang Astuti^{1*}, Tri Joko Raharjo¹, Putra Makmur Boangmanalu¹, Ilham Satria Raditya Putra¹, Stephanus Satria Wira Waskitha¹, and Junita Solin²

¹Department of Chemistry, Faculty of Mathematics and Natural Sciences, Universitas Gadjah Mada, Sekip Utara, Yogyakarta 55281, Indonesia

²Department of Agronomy, Faculty of Agriculture, Universitas Gadjah Mada, Jl. Flora, Yogyakarta 55821, Indonesia

* **Corresponding author:**

tel: +62-8112809898

email: endangastuti@ugm.ac.id

Received: July 7, 2020

Accepted: November 18, 2020

DOI: 10.22146/ijc.57646

Abstract: This research involves the synthesis, antimalarial evaluation, and molecular docking of several curcumin analogs. A total of six curcumin analog compounds were synthesized using aldol condensation using hydrochloric acid and sodium hydroxide catalysts. The synthesized compounds were elucidated using FTIR, ¹H-NMR, ¹³C-NMR, and LC-MS/MS. Subsequently, all curcumin analogs were tested as an antimalarial agent against *Plasmodium falciparum* 3D7 strain, and their mechanism of action was evaluated through a molecular docking study. Six curcumin analogs, i.e. 2,6-bis(2-hydroxybenzylidene)cyclohexanone; 2,6-bis(2-hydroxybenzylidene)cyclopentanone; 1,5-bis(2-hydroxyphenyl)penta-1,4-diene-3-one; 2,6-bis(3-hydroxybenzylidene)cyclohexanone; 2,6-bis(3-hydroxybenzylidene)cyclopentanone; and 1,5-bis(3-hydroxyphenyl)penta-1,4-diene-3-one have been successfully synthesized. In addition, 2,6-bis(2-hydroxybenzylidene)cyclopentanone demonstrated the lowest IC₅₀ value and binding affinity of 0.04 μM and -7.6 kcal/mol, respectively. Based on molecular docking studies, this compound also showed the most potent antimalarial activity targeted at PfATP6.

Keywords: curcumin analogs; antiplasmodium; aldol condensation; molecular docking

■ INTRODUCTION

Malaria is a life-threatening disease caused by the plasmodium parasitic class and is transmitted through the bite of a female *Anopheles* mosquito. This infection spreads rapidly among people in the tropical region. Based on the World Health Organization (WHO) report in 2018, malaria has been identified as the leading cause of death worldwide (405,000 people). This prognosis has instigated the recommendation of antimalarial drugs for over 20 years, and resistance to the *Plasmodium* strain has recently been reported [1].

The incidence of antimalarial drug resistance is principally attributed to gene mutation and inappropriate or wrong dosage. This potentially provokes the mutation of transporter protein *Plasmodium falciparum* (*P. falciparum*). Studies have shown a consequent effect on the entry pathway of artemisinin in the vacuole of

parasitic cells [2-3]. These mutation conditions tend to influence the role of glycoprotein-p and further increases the drug export rate [4]. Therefore, identifying alternatives to the targeted protein is a plausible approach toward addressing antimalarial drug resistance.

Furthermore, curcumin is a polyphenol compound isolated from the rhizome of *Curcuma longa*, which has a tautomeric form, termed keto and enol. Curcumin generally has the properties shown in Table 1. Ji and Shen (2009) conducted *in vitro* evaluation on the antiplasmodial activity of curcumin, and the results showed IC₅₀ value within the range of 15–18 μM [5]. Also, the interaction with PfATP6 protein was further assessed through molecular docking. In addition, previous studies have shown the capacity for cyclopiazonic acid (CPA) to inhibit the calcium pump in PfATP6 protein due to the intrinsic molecular docking interaction residues on Gln⁵⁶, Leu⁶¹, Val⁶¹, and Asn¹⁰¹ [6].

The experimental study showed an IC_{50} value of 1.15 and 2.45 μ M for the keto and enol forms, respectively. However, other reports have highlighted the poor bioavailability of curcumin in clinical applications [7-8].

The variation of α,β -diketone group to mono-carbonyl, as shown in Fig. 1, potentially improves curcumin stability and bioavailability [9]. This phenomenon is attributed to the transfer of oxygen electron pairs in the carbonyl group to generate a conjugation structure of unsaturated carbonyls under alkaline conditions ($pH > 6.5$) [10]. Therefore, it is necessary to identify the novel curcumin analogs with a tendency to enhance bioavailability. In addition, both benzyl substituents have similar activating hydroxyl units, symmetrically aligned with the analog curcumin structure. These subsequently require two steps to achieve the aldol condensation mechanism, followed by dehydration after the enolate is formed. The current research is aimed at successfully synthesizing six curcumin analogs using an aldol condensation reaction. Therefore, all synthesized compound was investigated for antimalarial activity against *P. falciparum* 3D7 strain and docked against PfATP6 to evaluate the intrinsic mechanism of action.

Table 1. Chemical and physical properties of curcumin

Chemical and physical properties	Curcumin
Molecular formula	$C_{21}H_{20}O_6$
Molecular weight	368.35 g/mol
Melting point	183 °C
Color	Yellow
Solubility in water	Low
Reaction under base	Bright color
Reaction under acid	Bright yellow color

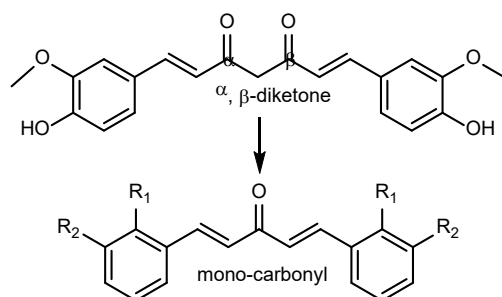


Fig 1. Simplification of the α,β -diketone of curcumin to mono-carbonyl chemical structure

■ EXPERIMENTAL SECTION

Materials

The reagents, including 2-hydroxybenzaldehyde, 3-hydroxybenzaldehyde, cyclohexanone, cyclopentanone, acetone, ethanol, tetrahydrofuran, and sodium hydroxide, were purchased from Merck in pro analysis specification. In addition, hydrochloric acid was purchased from Mallinckrodt, while the materials used in the antimalarial evaluation include RPMI-1640, serum-blood, RBC (Red Blood Cell), curcumin, dimethyl sulfoxide (DMSO), and three-dimensional structure of PfATP6 (PDB ID: 2OA0).

Instrumentation

Structure elucidation of curcumin analogs was carried out using FTIR spectrophotometer (with KBr pellet method), 1H -NMR (JEOL 500 MHz), ^{13}C -NMR (JEOL 125 MHz) spectrometers. The deuterated solvents, i.e., CD_3OD and $DMSO-d_6$, were used for NMR measurement. Liquid Chromatography-Mass Spectrometry (LC-MS/MS) analysis was conducted using Water Xevo Q-Tof.

Procedure

Synthesis of 2,6-bis(2-hydroxybenzylidene)cyclohexanone (A)

The synthesis process was performed using a modified Pana et al. (2014) method [11]. This involved dissolving 2-hydroxybenzaldehyde (4.2 mL, 0.04 mol) in 5 mL of ethanol and mixing with cyclohexanone (2.1 mL, 0.02 mol) before excess sodium hydroxide was added. Furthermore, the solution was then stirred for 24 h to attain a reddish precipitate, which was further diluted with distilled water and neutralized with hydrochloric acid. The yellow solid was then filtered and recrystallized with methanol/ethanol (1:2 v/v), and a yield of 61% was obtained. This product possess the following characteristics 1H -NMR ($DMSO-d_6$) δ (ppm): 1.71–1.62 (m, 2H), 2.81 (t, $J = 6$ Hz, 4H), 6.84 (t, $J = 8$ Hz, 2H), 6.90 (d, $J = 8$ Hz, 2H), 7.20 (t, $J = 8$ Hz, 2H), 7.32 (d, $J = 8$ Hz, 2H), 7.81 (s, 2H), 9.93 (s, 2H). ^{13}C -NMR ($DMSO-d_6$) δ (ppm): 23.4 (CH_2), 28.6 (CH_2), 116.0 (CH), 119.1 (CH), 122.9 (CH), 130.5 (CH), 130.7 (CH), 132.1 (CH=C),

135.7 (C=CH), 157.1 (C-OH), 189.5 (C=O). LC-MS/MS: $[M+H]^+ = 307$.

Synthesis of 2,6-bis(2-hydroxybenzylidene)cyclopentanone (B)

The synthesis of 2,6-bis(2-hydroxybenzylidene)cyclopentanone involved similar procedures observed with analog A. This involved the mixture and stirring of 2-hydroxybenzaldehyde (2.1 mL, 0.04 mol), 5 mL ethanol, cyclopentanone (1.77 mL, 0.02 mol), and excess sodium hydroxide for 24 h. Therefore, the precipitate generated was diluted with distilled water and neutralized with hydrochloric acid before filtering and recrystallizing with methanol/ethanol (1:2 v/v). The orange solid yield was 88%, and characterized by the following properties: $^1\text{H-NMR}$ (DMSO- d_6) δ (ppm): 2.07 (s, 4H), 6.88 (t, $J = 8$ Hz, 2H), 6.97 (t, $J = 8$ Hz, 2H), 7.23 (m, 2H), 7.53 (dd, $J = 8$ and 2 Hz, 2H), 7.80 (s, 2H), 10.21 (s, 2H). $^{13}\text{C-NMR}$ (DMSO- d_6) δ (ppm): 26.6 (CH_2), 116.2 (CH), 119.6 (CH), 122.9 (CH), 127.4 (CH), 130.1 (CH), 131.4 (CH=C), 136.9 (C-CH), 158.1 (C-OH), 195.8 (C=O). LC-MS/MS: $[M+H]^+ = 293$.

Synthesis of 1,5-bis(2-hydroxyphenyl)penta-1,4-diene-3-one (C)

In addition, 1,5-bis(2-hydroxybenzylidene)penta-1,4-diene-3-one was synthesized using similar procedure. This involved mixing and stirring 2-hydroxybenzaldehyde (2.1 mL, 0.04 mol), ethanol (5 mL), acetone (1.48 mL, 0.02 mol), and excess sodium hydroxide for 24 h. The precipitate was then diluted with distilled water and neutralized with hydrochloric acid before filtering and recrystallizing with methanol/ethanol (1:2 v/v). The yellow solid yield was 58%, and was characterized by the following properties: $^1\text{H-NMR}$ (CD_3OD) δ (ppm): 4.46 (s, 2H), 6.88 (d, $J = 8$ Hz, 2H), 6.88 (t, $J = 8$ Hz, 2H), 7.24 (t, $J = 8$ Hz, 2H), 7.30 (d, $J = 8$ Hz, 2H), 7.62 (dd, $J = 8$ and 2 Hz, 2H), 8.09 (d, $J = 16$ Hz, 2H). $^{13}\text{C-NMR}$ (CD_3OD) δ (ppm): 117.1 (CH), 120.9 (CH), 123.1 (CH=CH), 126.2 (CH), 130.0 (CH), 133.0 (CH), 140.8 (CH=CH), 158.7 (C-OH), 192.7 (C=O). LC-MS/MS: $[M+H]^+ = 267$.

Synthesis of 2,6-bis(3-hydroxybenzylidene)cyclohexanone (D)

The synthesis of 2,6-bis(3-hydroxybenzylidene)cyclo

hexanone was performed using the method reported by Persittamaia (2018) [12]. This involved mixing 3-hydroxybenzaldehyde (1 g, 8.2 mmol) and cyclohexanone (0.4 mL, 4.1 mmol) in 0.5 mL tetrahydrofuran, followed by the dropwise introduction of 1 mL hydrochloric acid. The reaction was then stirred at 20–50 °C for several hours to yield 79% Sorrel solid with the following properties: $^1\text{H-NMR}$ (DMSO- d_6) δ (ppm): 1.66–1.71 (m, 2H), 2.84–2.86 (m, 4H), 6.82 (d, $J = 7.5$, 2H), 6.91 (s, 2H), 6.94 (d, $J = 7.5$ Hz, 2H), 7.25 (t, $J = 8$ Hz, 2H), 7.54 (s, 2H), 9.62 (s, 2H). $^{13}\text{C-NMR}$ (DMSO- d_6) δ (ppm): 22.5 (CH_2), 28.0 (CH_2), 116.1 (CH), 116.9 (CH), 121.2 (CH), 121.4 (CH), 129.6 (CH), 136.4 (CH=C), 136.7 (C=CH), 157.4 (C-OH), 189.0 (C=O). LC-MS/MS: $[M+H]^+ = 307$.

Synthesis of 2,6-bis(3-hydroxybenzylidene)cyclopentanone (E)

The synthesis of 2,6-bis(3-hydroxybenzylidene)cyclopentanone involved a similar procedure as analog D. This required mixing 3-hydroxybenzaldehyde (1 g, 8.2 mmol) and cyclopentanone (0.36 mL, 4.1 mmol) in 0.5 mL tetrahydrofuran, followed by the dropwise introduction of 1 mL hydrochloric acid. Therefore, 54% yield of a light-yellow solid was produced, featuring the following characteristics: $^1\text{H-NMR}$ (DMSO- d_6) δ (ppm): 3.01 (s, 4H), 6.84 (d, $J = 8$ Hz, 2H), 7.07 (s, 2H), 7.10 (d, $J = 7.5$ Hz, 2H), 7.26 (t, $J = 8$ Hz, 2H), 7.34 (s, 2H), 9.66 (s, 2H). $^{13}\text{C-NMR}$ (DMSO- d_6) δ (ppm): 26.1 (CH_2), 116.4 (CH), 116.8 (CH), 122.1 (CH), 130.1 (CH), 132.7 (CH), 136.5 (C=CH), 137.7 (CH=C), 157.5 (C-OH), 195.4 (C=O). LC-MS/MS: $[M+H]^+ = 293$.

1,5-bis(3-hydroxyphenyl)penta-1,4-diene-3-one (F)

In addition, 1,5-bis(3-hydroxybenzylidene)penta-1,4-diene-3-one was synthesized using a similar procedure as analog D. This involved mixing 3-hydroxybenzaldehyde (1 g, 8.2 mmol) and acetone (0.3 mL, 4.1 mmol) in 0.5 mL tetrahydrofuran, followed by the dropwise introduction of 1 mL hydrochloric acid. Therefore, 65% yield of a brown solid was produced, with the following characteristic features: $^1\text{H-NMR}$ (DMSO- d_6) δ (ppm): 6.85 (d, $J = 8$ Hz, 2H), 7.14 (s, 2H), 7.22 (d, $J = 8$ Hz, 2H), 7.36 (d, $J = 7$ Hz, 2H), 7.41 (t, $J = 8$ Hz, 2H), 9.63 (s, 2H), 9.93 (d, $J = 7$ Hz, 2H). $^{13}\text{C-NMR}$ (DMSO- d_6) δ (ppm): 114.7 (CH), 117.9 (CH), 119.8

(CH), 125.6 (CH=CH), 130.1 (CH), 136.1 (CH), 143.1 (CH=CH), 157.8 (C–OH), 188.7 (C=O). LC-MS/MS: $[M+H]^+ = 267$.

Antiplasmodium activity

These products were assayed for antiplasmodium activity, based on Trager and Jansen (1976) [13] against *P. falciparum* 3D7 culture. The *in vitro* micro-technique method used was developed by Basco (2007) [14]. This required the preparation of 96-well assay plates, followed by the distribution of 5400 μ L RPMI, 1200 μ L serum-blood, 104.62 μ L RBC, and 15.38 μ L parasites. In addition, the curcumin analogs were then prepared with the following concentrations 100.00; 50.00; 25.00; 12.50; and 6.25 μ g/mL, and poured into the 96-well at three repetitions. Subsequently, the *P. falciparum* parasite culture obtained at a 7.6% schizont stage was synchronized and divided into each well of the pre-treated 96-well microtiter plate. Therefore, the entire unit was placed in a 5% CO₂ incubator at 37 °C for 72 h, using a candle jar method. The number of schizonts counted by microscopy comprised at least 1000 normal red blood cells, while the inhibition percentage was determined as follows:

$$\text{Inhibition(\%)} = \frac{A-B}{A} \times 100\% \quad (1)$$

where A and B denote the parasitemia percentage of the negative control and the sample, respectively. Subsequently, statistical analysis was performed using

SPSS version 7 software, with significance tested at 0.05 level to calculate the IC₅₀ value.

Molecular docking

The three-dimensional structure of curcumin analogs was optimized using Gaussian® 09W, with the semiempirical AM1 method [15]. In addition, the enzyme crystal arrangement of the PfATP6 receptor was downloaded from Protein Data Bank (PDB ID: 2OA0), while the ligand and receptor were prepared using Discovery Studio Visualizer and Autodock Tools [16]. The molecular docking process was performed using Autodock Vina by setting the exhaustiveness value to 160, although polar hydrogen atoms were added to the receptor before this step. Furthermore, redocking was then carried out against native ligands to validate the molecular docking procedure and the RMSD value at < 2.000 Å [17].

RESULTS AND DISCUSSION

Synthesis of Curcumin Analogs

The pharmacophore modification of curcumin involves the replacement of α,β -diketone with mono-carbonyl. This process featured the use of hydroxy group alongside electron-donating to generate some novel compounds, including the mono-carbonyl analogs [10], as presented in Fig. 2. In addition, the reaction was controlled by TLC, and all compounds were characterized

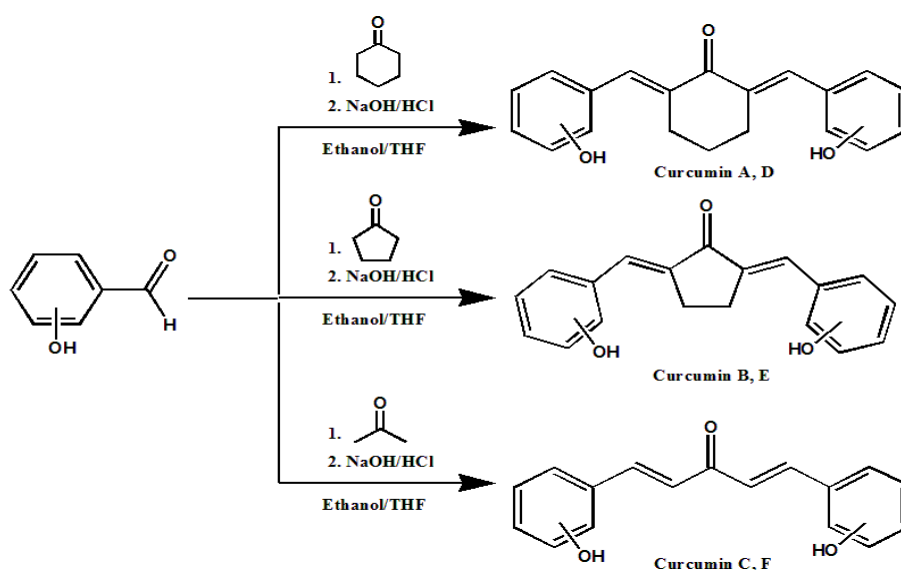


Fig 2. Scheme of synthesis of curcumin analog A-F

using FTIR, $^1\text{H-NMR}$, $^{13}\text{C-NMR}$, and LC-MS/MS spectrometers.

The results show a distinctive yellow color in each of the synthesized analogs, except for curcumin B (orange), D (Sorrel), and F (brownish). These discrepancies were possibly influenced by the stability and level of acidity while the compound is in the solid phase. Therefore, colors appearing more orange indicate higher alkalinity, while brown denotes acidity [11]. Fig. 3 shows the FTIR spectra from six synthesized curcumin analogs, which exhibit peaks of 3330 , 1574 , 1545 , and 1651 cm^{-1} , representing the OH, $\text{C}=\text{C}_{\text{aliphatic}}$, $\text{C}=\text{C}_{\text{aromatic}}$, and $\text{C}=\text{O}$ stretching vibration frequencies, respectively. In addition, the $\text{C}=\text{O}$ stretching frequency typically appeared at 1715 cm^{-1} although the conjugation with $\text{C}=\text{C}$ double bond and the decline in two double-bonds characters instigate the reduction in values [11]. The mono-carbonyl and cyclic-groups of curcumin analog A, B, D, and E are possibly distinguished by the peaks present in regions 2931 and 2928 cm^{-1} for the C-H stretching vibration frequencies. Also, another prominent successful feature

was observed based on the peak correspondence to ortho-disubstituted (curcumin analog A, B, and C). This is one strong band in close proximity to 750 cm^{-1} , which is easily distinguished from meta-disubstituted (curcumin analog D, E, and F), and therefore indicates the presence of three medium bands between $690\text{--}880\text{ cm}^{-1}$.

The synthesized compounds were then analyzed using LC-MS/MS to obtain a more accurate quantitative and qualitative analysis. In addition, most of the products demonstrated a single peak on the LC chromatogram, indicating the high purity of the synthesized compound. The mass spectrometers also displayed the protonated peak mass of the molecular ion ($[\text{M}+\text{H}]^+$) at 307 (A and D), 293 (B and E), and 267 (C and F).

Furthermore, the structures were confirmed based on hydrogen splitting position on the $^1\text{H-NMR}$ spectra in α,β -unsaturated hydrogenated at the δ $7.0\text{--}7.5$ ppm region, which is more downfield than the usual range of δ $4.5\text{--}6.5$ ppm [15]. This theoretically occurs due to electron delocalization in the α,β -unsaturated system. Meanwhile, the proton attached to a hydroxyl group also

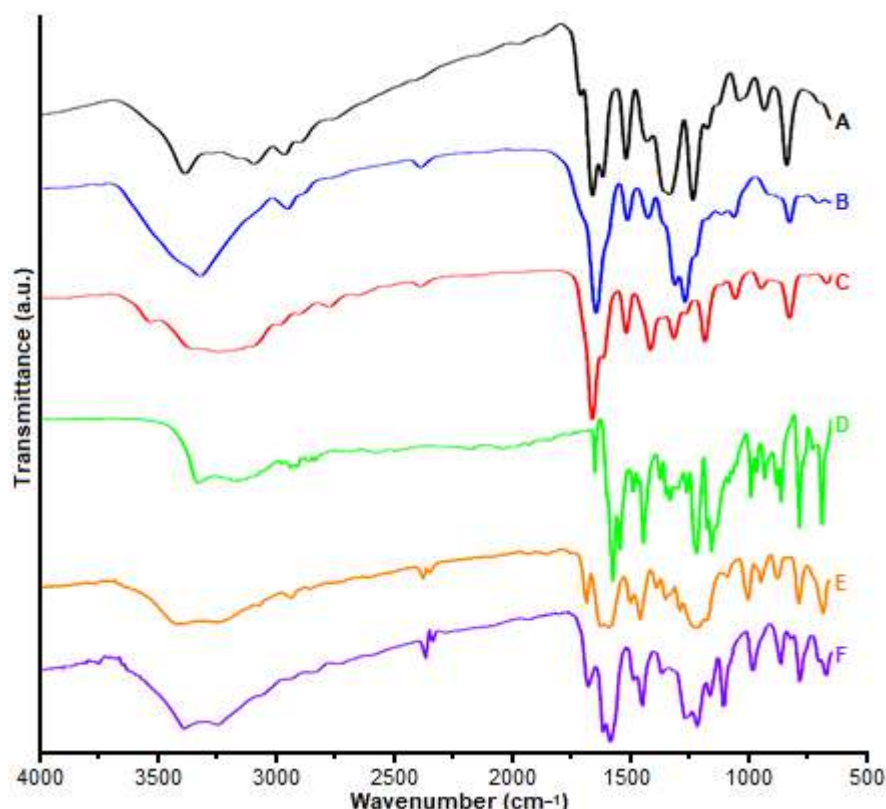


Fig 3. FTIR spectra of curcumin analogs A-F

displays a peak at the deshielding region δ 9–10 ppm because of the oxygen lone pair attraction. The position 2-hydroxy of curcumin analog A, B, and C possessed no splitting hydrogen, while 3-hydroxy has one between the hydroxyl and benzyl substituents with D (δ 6.91 ppm), E (δ 7.07 ppm), and F (δ 7.14 ppm). In addition, the number of carbons observed with the ^{13}C -NMR spectra also corresponds to the curcumin analogs, comprising eleven peaks for A and D, ten for B and E, and nine for curcumin C and F. These consist of CH_2 aliphatic at δ 22–28 ppm and CH aromatic δ 114–136 ppm. Moreover, splitting C–OH for all products at the δ 157–158 ppm range was more deshielded than the CH aromatics, due to the pair in electron atom O. The C=CH or CH=C in cyclohexane and cyclopentane groups were observed at range δ 131–136 ppm, while CH=CH for penta-1,4-dien-3-one group was at δ 120–125 ppm (near C=O) and 140–143 ppm (near benzene). Finally, the signal for C=O was marked at range δ 188–195 ppm.

Antiplasmodium Activity

Antiplasmodium assay was performed on cultured *P. falciparum* cells obtained at the blood-stage to determine the IC_{50} values. This treatment demonstrates the effect on schizont development in RBC and in medium RPMI-1640. In addition, the IC_{50} values of each curcumin analog (A-F) were divided into four categories, including promising ($\text{IC}_{50} < 1 \mu\text{M}$), active (IC_{50} 1–20 μM), moderate (IC_{50} 20–100 μM), and inactive ($\text{IC}_{50} > 100 \mu\text{M}$) [18]. The results tabulated in Table 2 showed the most potent activity against parasitic cells in compound B and C ($\text{IC}_{50} < 1 \mu\text{M}$). Moreover, curcumin analog A and D were classified as moderate, while E and F demonstrated higher IC_{50} . These products are considered active in

interfering with cell inhibition and are comparable to curcumin, which is characterized by the ability to reduce parasitemia percentage by about 85–95%.

Molecular Docking

The results of molecular docking are related to binding affinity and interaction between ligand on the active site of the calcium ATPase receptor, as shown in Table 3. The RMSD value of redocking was 0.801 Å, indicating a positive method validity with excellent resolution [17]. Furthermore, all products possessed a higher binding affinity than the CPA inhibitor, alongside good stability and adequate interaction with the active site. Table 3 showed the mediating role of Leu⁶¹, Val⁶², Glu³⁰⁹, Asn¹⁰¹, Ala¹⁰², and Leu³¹¹ amino acid residues during the bonding of CPA inhibitor with the active site [6]. Fig. 4 demonstrates the interaction between curcumin analog and any of the vital amino acids, as well as the potential to inhibit calcium ATPase in the absence of CPA inhibitors. This effect corresponds with one of the mechanisms to break the life cycle of parasites and the conforming IC_{50} value [3,6].

Dohutia et al. (2017) reported the correlation between percentage inhibition of schizont and binding affinity using an *in silico* method. The presence of hydroxyl groups on the benzene ring potentially increases the interaction between the compounds produced and the active site by lowering the binding affinity with hydrogen bonding [19]. In addition, curcumin analog A is characterized by two hydrogen bonds (Gln⁵⁶, Asn¹⁰¹) and six van der Waals interactions (Leu⁹⁸, Pro³¹², Gln²⁵, Lys²⁴, Pro³⁰⁸, Leu⁶¹), and further yields -8.3 kcal/mol, while B has no hydrogen bond and seven van der Waals interaction (Leu⁹⁸, Asn¹⁰¹, Ile³⁰⁷, Leu⁶¹,

Table 2. The IC_{50} value of compound assayed

No.	Compound	IC_{50} value (μM)
1	2,6-bis(2-hydroxybenzylidene)cyclohexanone (A)	11.53
2	2,6-bis(2-hydroxybenzylidene)cyclopentanone (B)	0.04
3	1,5-bis(2-hydroxyphenyl)penta-1,4-dien-3-one (C)	0.63
4	2,6-bis(3-hydroxybenzylidene)cyclohexanone (D)	16.93
5	2,6-bis(3-hydroxybenzylidene)cyclopentanone (E)	31.88
6	1,5-bis(3-hydroxyphenyl)penta-1,4-dien-3-one (F)	39.04
7	Curcumin	2.39

Table 3. Interaction and binding affinity of CPA and curcumin analogs against *PfATP6*

Compound	Binding affinity (kcal/mol)	Interaction
CPA* (standard ligand)	-10.0	H-Bond: Gln ⁵⁶ Alkyl/ π -alkyl: Pro ³¹² , Ile ³⁰⁷ , Val ⁶² , Leu ⁶⁵ , Leu ²⁵³ , Leu ³¹¹ π - σ : Leu ⁶¹ van der Waals: Ala ¹⁰² , Asn ¹⁰¹ , Leu ⁹⁸ , Glu ³⁰⁹ , Pro ³⁰⁸ , Phe ²⁵⁶
A	-8.3	H-Bond: Gln ⁵⁶ , Asn ¹⁰¹ Alkyl/ π -alkyl: Leu ³¹¹ , Leu ²⁵ , Pro ³¹² , Ile ³¹⁵ π - σ : Val ⁶² van der Waals: Leu ⁹⁸ , Pro ³¹² , Gln ²⁵ , Lys ²⁴ , Pro ³⁰⁸ , Leu ⁶¹
B	-7.6	Alkyl/ π -alkyl: Leu ²⁵³ , Pro ³¹² , Leu ³¹¹ , Leu ⁶⁵ , Val ⁶² van der Waals: Leu ⁹⁸ , Asn ¹⁰¹ , Ile ³⁰⁷ , Leu ⁶¹ , Pro ³⁰⁸ , Ile ³¹⁵ , Gln ²⁵⁰ Carbon H. bonding: Glu ³⁰⁹
C	-8.5	H-Bond: Lys ²⁵² π -stacked: Phe ⁸³⁴ π -alkyl: Val ⁷⁶⁹ , Ile ⁸²⁹ , Leu ⁸²⁸ van der Waals: Leu ²⁵³ , Glu ²⁵⁵ , Phe ²⁵⁶ , Tyr ⁸³⁷ , Met ⁸³⁸ , Ile ⁷⁶⁵ , Ile ⁷⁶¹
D	-8.4	H-Bond: Thr ³¹⁶ , Val ¹⁰⁴ Alkyl/ π -alkyl: Val ⁶² , Pro ³¹² , Ile ³¹⁵ , Leu ³¹¹ , Pro ³⁰⁸ π - σ : Leu ⁶¹ van der Waals: Gly ¹⁰ , Glu ¹⁰ , Asp ²⁵ , Leu ²⁵³ , Gly ²⁵ , Phe ²⁵⁶ , Ile ³⁰⁷ , Asn ¹⁰¹ , Gln ⁵⁶
E	-7.8	H-Bond: Asp ²⁵⁴ , Asn ¹⁰¹ , Glu ³⁰⁹ π -alkyl: Val ⁶² , Leu ⁶⁵ , Ile ³⁰⁷ π - σ : Leu ²⁵³ van der Waals: Leu ⁹⁸ , Pro ³¹² , Gln ²⁵ , Lys ²⁴ , Pro ³⁰⁸ , Leu ⁶¹
F	-8.1	H-Bond: Lys ²⁵² π -alkyl: Val ⁷⁶⁹ , Ile ⁸²⁸ π - σ : Leu ⁸²⁸ π -stacked: Phe ⁸³⁴ van der Waals: Met ⁸³ , Tyr ⁸³⁷ , Ile ⁷⁶⁵ , Ile ⁷⁶¹ , Leu ²⁵ , Phe ²⁵⁶

Pro³⁰⁸, Ile³¹⁵, Gln²⁵⁰), with a higher binding affinity value of -7.6 kcal/mol. Moreover, C possesses one hydrogen bond (Lys²⁵²) and seven van der Waals interactions (Leu²⁵³, Glu²⁵⁵, Phe²⁵⁶, Tyr⁸³⁷, Met⁸³⁸, Ile⁷⁶⁵, Ile⁷⁶¹) alongside the best affinity of -8.5 kcal/mol, while D has two hydrogen bond (Thr³¹⁶, Val¹⁰⁴) and nine van der Waals interaction (Gly¹⁰, Glu¹⁰, Asp²⁵, Leu²⁵³, Gly²⁵, Phe²⁵⁶, Ile³⁰⁷, Asn¹⁰¹, Gln⁵⁶), at -8.4 kcal/mol. The curcumin analog E features three hydrogen bond (Asp²⁵⁴, Asn¹⁰¹, Glu³⁰⁹) and six van der Waals interaction (Leu⁹⁸, Pro³¹², Gln²⁵, Lys²⁴, Pro³⁰⁸, Leu⁶¹), while F possesses 1 possible hydrogen bond and six van der Waals interaction, accompanied by a binding affinity of -7.8 kcal/mol and -8.1 kcal/mol,

respectively. These properties indicate the possibility of determining binding affinity based on the ratio between a possible number of hydrogen bonds and van der Waals interaction [20]. Also, the similarity between the associations of synthesized compounds and the standard ligand are significant factors in the inhibitory properties. In addition, the hydrophobic relations with amino acid residues are also enhanced by the aromatic ring present in the transmembrane of *PfATP6*, which will stabilize the transmembrane helices [21]. This is evidenced by the interface of π -stacked with Phe⁸³⁴ and π - σ bonds with Leu⁶¹, Val⁶², Leu²⁵³, and Leu⁸²⁸ residue observed in most target compound.

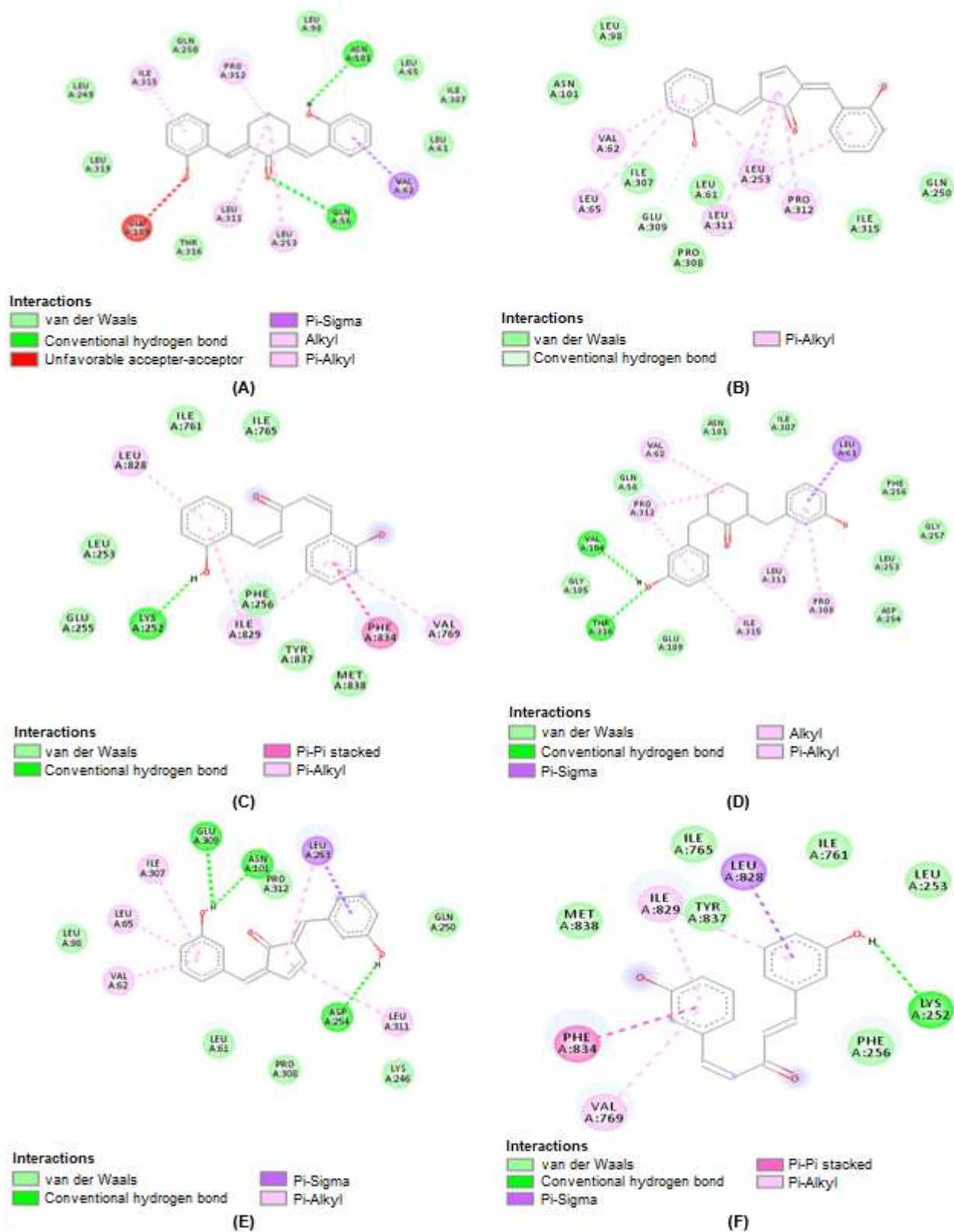


Fig 4. Visualization of molecular docking curcumin analog A-F toward the active site of *Pf*ATP6 protein

■ CONCLUSION

Based on the results and discussion, curcumin analogs of 2,6-bis(2-hydroxybenzylidene)cyclohexanone, 2,6-bis(2-hydroxybenzylidene)cyclopentanone, 1,5-bis(2-hydroxyphenyl)penta-1,4-diene-3-one, 2,6-bis(3-hydroxybenzylidene)cyclohexanone, 2,6-bis(3-hydroxybenzylidene)cyclopentanone, and 1,5-bis(hidroxyphenyl)penta-1,4-diene-3-one were successfully synthesized. The antimalarial activity of the yielded compounds was evaluated against *P. falciparum* 3D7 strain, and the effects demonstrated were good. In addition, the molecular docking result showed potential inhibitory characteristics in all curcumin analogs against PfATP6.

■ ACKNOWLEDGMENTS

This work was financially funded by a research grant of Faculty Mathematics and Natural Sciences, Universitas Gadjah Mada.

■ AUTHOR CONTRIBUTIONS

Endang Astuti, Tri Joko Raharjo, Putra Makmur Boangmanalu, Ilham Satria Raditya Putra conducted the experiment, Stephanus Satria Wira Waskitha performed the computation, Putra Makmur Boangmanalu, Ilham Satria Raditya Putra, Stephanus Satria Wira Waskitha wrote and revised the manuscript, Junita Solin and Tri Joko Raharjo translated and revised the manuscript. All authors agreed to the final version of this manuscript.

■ REFERENCES

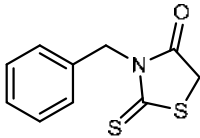
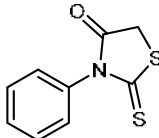
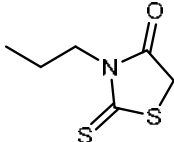
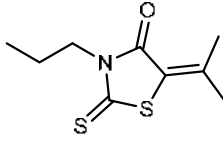
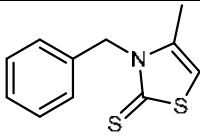
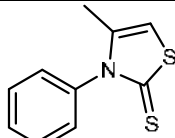
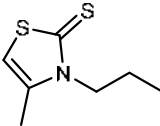
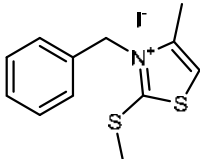
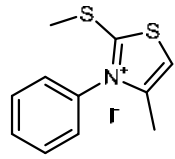
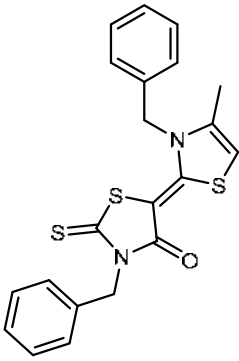
- [1] Ministry of Health Republic of Indonesia, 2015, *Indonesia Health Profile*, Ministry of Health RI, Jakarta, Indonesia.
- [2] Arnou, B., Montingny, C., Morth, J.P., Nissen, P., Jaxel, C., Møller, J.V., and le Maire, M., 2011, The *Plasmodium falciparum* Ca²⁺ ATPase PfATP6 Insensitive to artemisinin, but a potential drug target, *Biochem. Soc. Trans.*, 39 (3), 823–831.
- [3] Soni, R., Sharma, D., Rai, P., Sharma, B., and Bhatt, T.K., 2017, Signalling strategies of malaria parasite for its survival, proliferation, and infection during erythrocytic stage, *Front. Immunol.*, 8, 349.
- [4] Brochet, M., and Billker, O., 2016, Calcium signalling in malaria parasites, *Mol. Microbiol.*, 100 (3), 397–408.
- [5] Ji, H.F., and Shen, L., 2009, Interactions of curcumin with the PfATP6 model and the implications for its antimalarial mechanism, *Bioorg. Med. Chem. Lett.*, 19 (9), 2453–2455.
- [6] Moncoq, K., Trieber, C.A., and Young, H.S., 2007, The Molecular Basis for Cyclopiazonic Acid inhibition of the Sarcoplasmic Reticulum Calcium Pump, *J. Biol. Chem.*, 282 (13), 9784–9757.
- [7] Coma-Cros, E.M., Biosca, A., Lantero, E., Manca, M.L., Caddeo, C., Gutiérrez, L., Ramírez, M., Borgheti-Cardoso, L.N., Manconi, M., and Fernández-Busquets, X., 2018, Antimalarial activity of orally administered curcumin incorporated in Eudragit®-containing liposomes, *Int. J. Mol. Sci.*, 19 (5), 1361.
- [8] Kim, Y.J., Lee, H.J., and Shin, Y., 2013, Optimization and validation of high-performance liquid chromatography method for individual curcuminoids in tumeric by heat-refluxed extraction, *J. Agric. Food Chem.*, 61 (46), 10911–10918.
- [9] Manohar, S., Khan, S.I., Kandi, S.K., Raj, K., Sun, G., Yang, X., Molina, A.D.C., Ni, N., Wang, B., and Rawat, D.S., 2013, Synthesis antimalarial activity and cytotoxic potential of new monocarbonyl analogues of curcumin, *Bioorg. Med. Chem. Lett.*, 23 (1), 112–116.
- [10] Kumavat, S.D., Chaudhari, Y.S., Borole, P., Mishra, P., Shenghani, K., and Duvvuri, P., 2013, Degradation studies of curcumin, *IJPRR*, 3 (2), 50–55.
- [11] Pana, A.M., Badea, V., Bănică, R., Bora, A., Dudas, Z., Cseh, L., and Costisor, O., 2014, Network reaction of 2,6-bis(2-hydroxybenzylidene)cyclohexanone by external stimuli, *J. Photochem. Photobiol.*, A, 283, 22–28.
- [12] Persittamaia, I., 2018, Sintesis dan Uji Aktivitas Antibakteri Senyawa Analog Kurkumin 2,6-bis-(3'-hidroksibenziliden)-sikloheksanon, *Undergraduate*

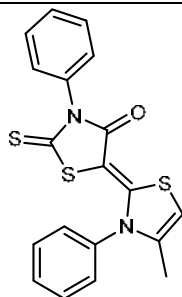
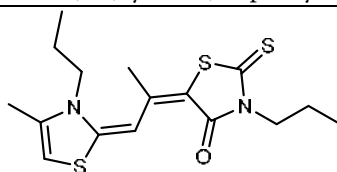
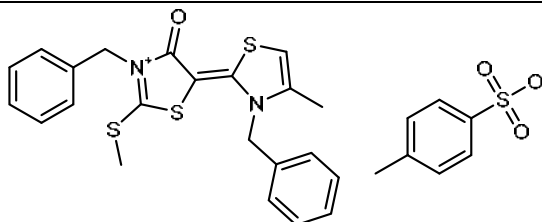
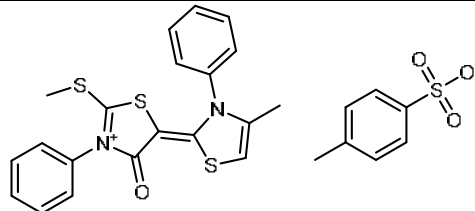
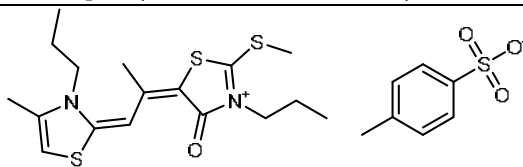
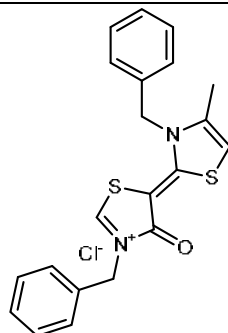
- Thesis, Faculty of Pharmacy, Universitas Gadjah Mada, Yogyakarta.
- [13] Thomas, J.A., Collins, C.R., Das, S., Hackett, F., Graindorge, A., Bell, D., Deu, E., and Blackman, M.J., 2016, Development and application of a simple plaque assay for the human malaria parasite *Plasmodium falciparum*, *PLoS One*, 11 (6), e0157873.
- [14] Basco, L.K., 2007, *Field Application of in vitro Assays for the Sensitivity of Human Malaria Parasites to Antimalarial Drugs*, World Health Organization, France.
- [15] Pranowo, H.D., and Hetadi, A.K.R., 2011, *Pengantar Kimia Komputasi*, Lubuk Agung, Bandung, Indonesia.
- [16] Forli, S., Huey, R., Pique, M.E., Sanner, M.F., Goodsell, D.S., and Olson, A.J., 2016, Computational protein–ligand docking and virtual drug screening with the AutoDock suite, *Nat. Protoc.*, 11 (5), 905–919.
- [17] Mena-Ulecia, K., Tiznado, W., and Caballero, J., 2015, Study of the differential activity of thrombin inhibitors using docking, QSAR, molecular dynamics, and MM-GBSA, *PLOS One*, 10 (11), e0142774.
- [18] Kamaraj, C., Kaushik, N.K., Mohanakrishnan, D., Elango, G., Bagavan, A., Zahir, A.A., Rahuman, A.A., and Sahal, D., 2012, Antiplasmodial potential of medicinal plant extracts from Malaiyur and Javadhu hills of South India, *Parasitol. Res.*, 111 (2), 703–715.
- [19] Dohutia, C., Chetia, D., Gogoi, K., Bhattacharyya, D.R., and Sarma, K., 2017, Molecular docking, synthesis, and *in vitro* antimalarial evaluation of certain novel curcumin analogues, *Braz. J. Pharm. Sci.*, 53 (4), e00084.
- [20] Chen, D., Oezguen, N., Urvil, P., Ferguson, C., Dann, S.M., and Savidge, T.C., 2016, Regulation of protein-ligand binding affinity by hydrogen bond pairing, *Sci. Adv.*, 2 (3), e1501240.
- [21] Makwana, K.M., and Mahalakshmi, R., 2015, Implications of aromatic-aromatic interactions: From protein structures to peptide models, *Protein Sci.*, 24 (12), 1920–1933.

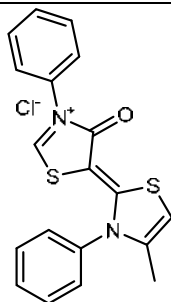
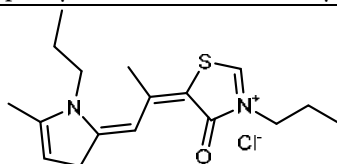
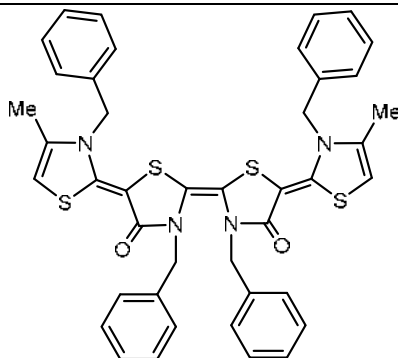
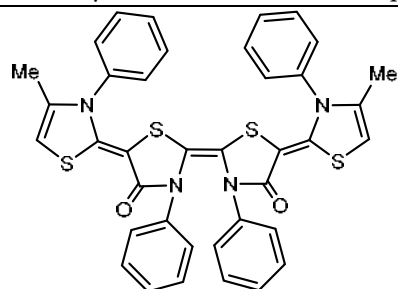
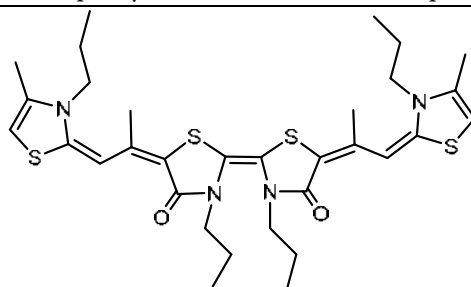
Supplementary Information (SI)

This supplementary data is a part of paper entitled “Study of the Electrochemical Behavior of Merocyanine and Merocarbocyanine Salts and Their Transformation into Π -Electron Donor Molecules, Namely Tetrathiatetraazafulvalenes”.

STRUCTURES OF SYNTHESIZED MOLECULES

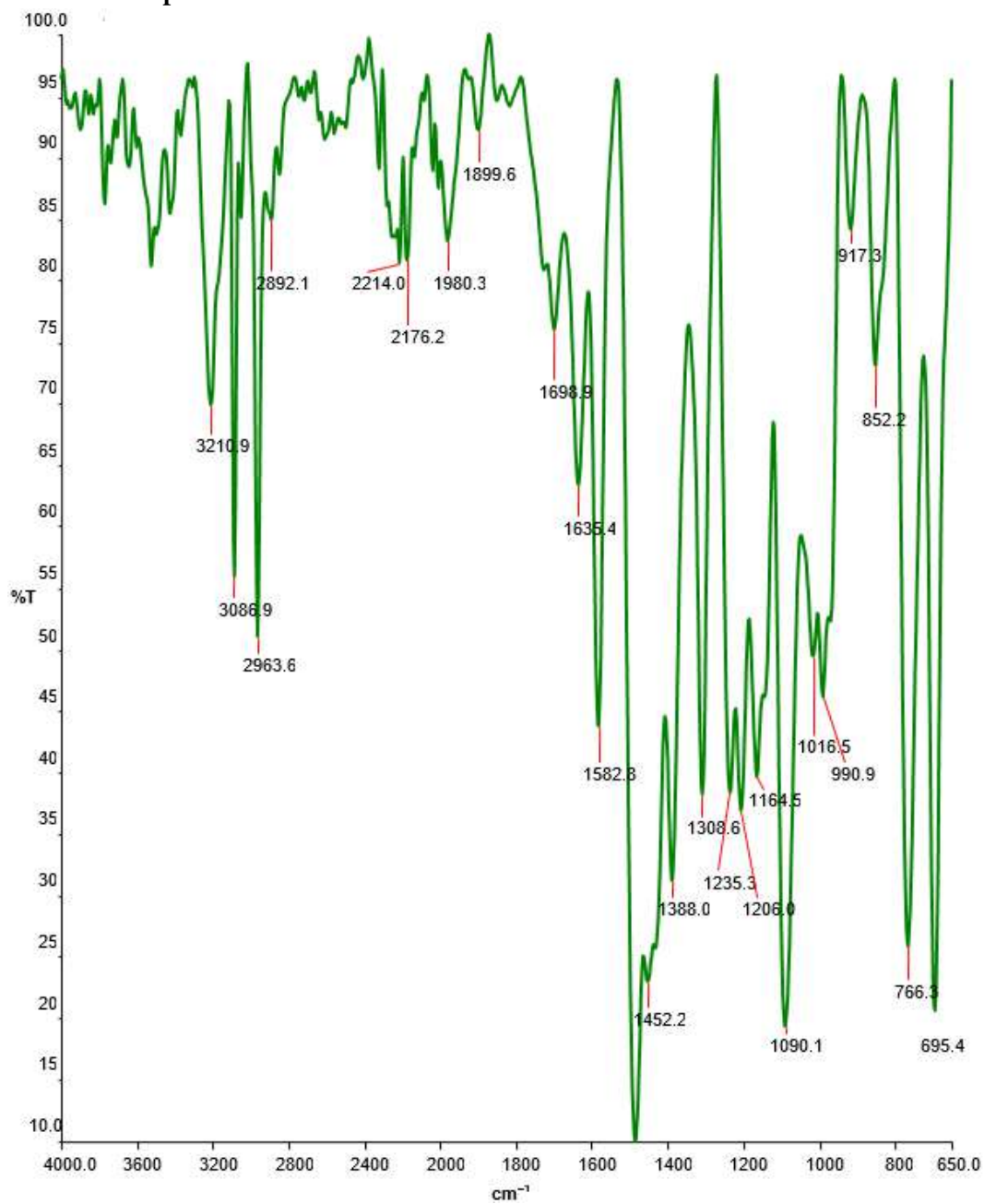
	
3-Benzyl-2-thioxo-1,3-thiazolidin-4-one (1a)	3-Phenyl-2-thioxo-1,3-thiazolidin-4-one (1b)
	
3-propyl-2-thioxo-1,3-thiazolidin-4-one (1c)	5-(Propan-2-ylidene)-3-propyl-2-thioxo-1,3-thiazolidin-4-one (3c)
	
3-Benzyl-4-methyl-1,3-thiazole-2(3H)-thione (2a)	4-Methyl-3-phenyl-1,3-thiazole-2(3H)-thione (2b)
	
4-Methyl-3-propyl-1,3-thiazole-2(3H)-thione (2c)	
	
3-Benzyl-4-methyl-2-(methylsulfanyl)-1,3-thiazol-3-ium iodide (3a)	4-Methyl-2-(methylsulfanyl)-3-phenyl-1,3-thiazol-3-ium iodide (3b)
	
(5E)-3-benzyl-5-(3-benzyl-4-methyl-1,3-thiazol-2(3H)-ylidene)-2-thioxo-1,3-thiazolidin-4-one (4a)	

(5E)-5-(4-methyl-3-phenyl-1,3-thiazol-2(3H)-ylidene)-3-phenyl-2-thioxo-1,3-thiazolidin-4-one (**4b**)(E)-5-((E)-1-(4-methyl-3-propylthiazol-2(3H)-ylidene)propan-2-ylidene)-3-propyl-2-thioxothiazolidin-4-one (**4c**)(E)-3,3'-dibenzyl-4-methyl-2'-(methylthio)-4'-oxo-3H,4'H-[2,5'-bithiazolylydene]-3'-ium-4-methylbenzenesulfonate (**5a**)(E)-4-methyl-2'-(methylthio)-4'-oxo-3,3'-diphenyl-3H,4'H-[2,5'-bithiazolylydene]-3'-ium-4-methylbenzenesulfonate (**5b**)(E)-5-((E)-1-(4-methyl-3-propylthiazol-2(3H)-ylidene)propan-2-ylidene)-2-(methylthio)-4-oxo-3-propyl-4,5-dihydrothiazol-3-ium 4-methylbenzenesulfonate (**5c**)(E)-3,3'-dibenzyl-4-methyl-4'-oxo-3H,4'H-[2,5'-bithiazolylydene]-3'-ium chloride (**6a**)

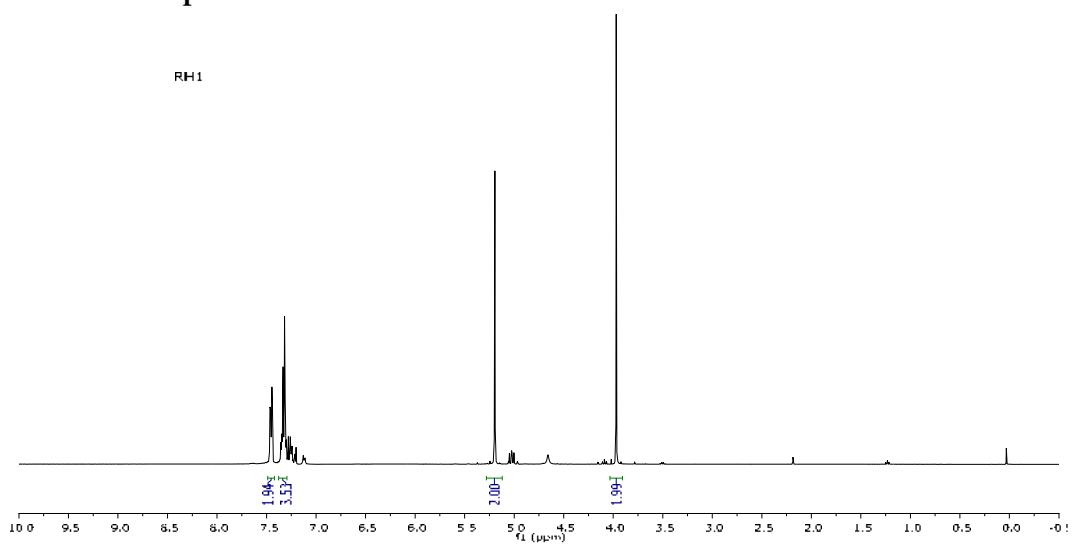
(E)-4-methyl-4'-oxo-3,3'-diphenyl-3H,4'H-[2,5'-bithiazolyli-dene]-3'-ium chloride (**6b**)(E)-5-((Z)-1-(5-methyl-1-propyl-1,3-dihydro-2H-pyrrol-2-ylidene)propan-2-ylidene)-4-oxo-3-propyl-4,5-dihydrothiazol-3-ium chloride (**6c**)(2E,2'Z,2'''E)-3,3',3'',3'''-tetrabenzyl-4,4'''-dimethyl-3H,3'''H-[2,5':2',2'':5'',2'''-quaterthiazole]-4',4''(3'H,3'''H)-dione (**7a**)(2E,2'Z,2'''E)-4,4'''-dimethyl-3,3',3'',3'''-tetraphenyl-3H,3'''H-[2,5':2',2'':5'',2'''-quaterthiazole]-4',4''(3'H,3'''H)-dione (**7b**)(2Z,5E,5'E)-5,5'-bis((E)-1-(4-methyl-3-propylthiazol-2(3H)-ylidene)propan-2-ylidene)-3,3'-dipropyl-3H,3'H-[2,2'-bithiazolyli-dene]-4,4'(5H,5'H)-dione (**8c**)

SPECTROSCOPIC DATA

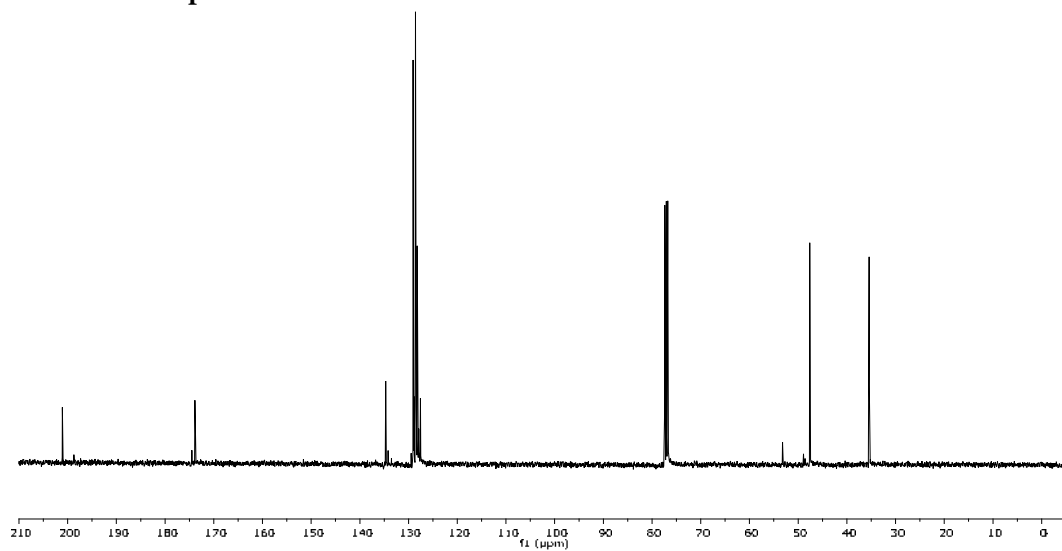
Infrared Spectrum of Compound 1a



¹H-NMR Spectrum of Compound 1a



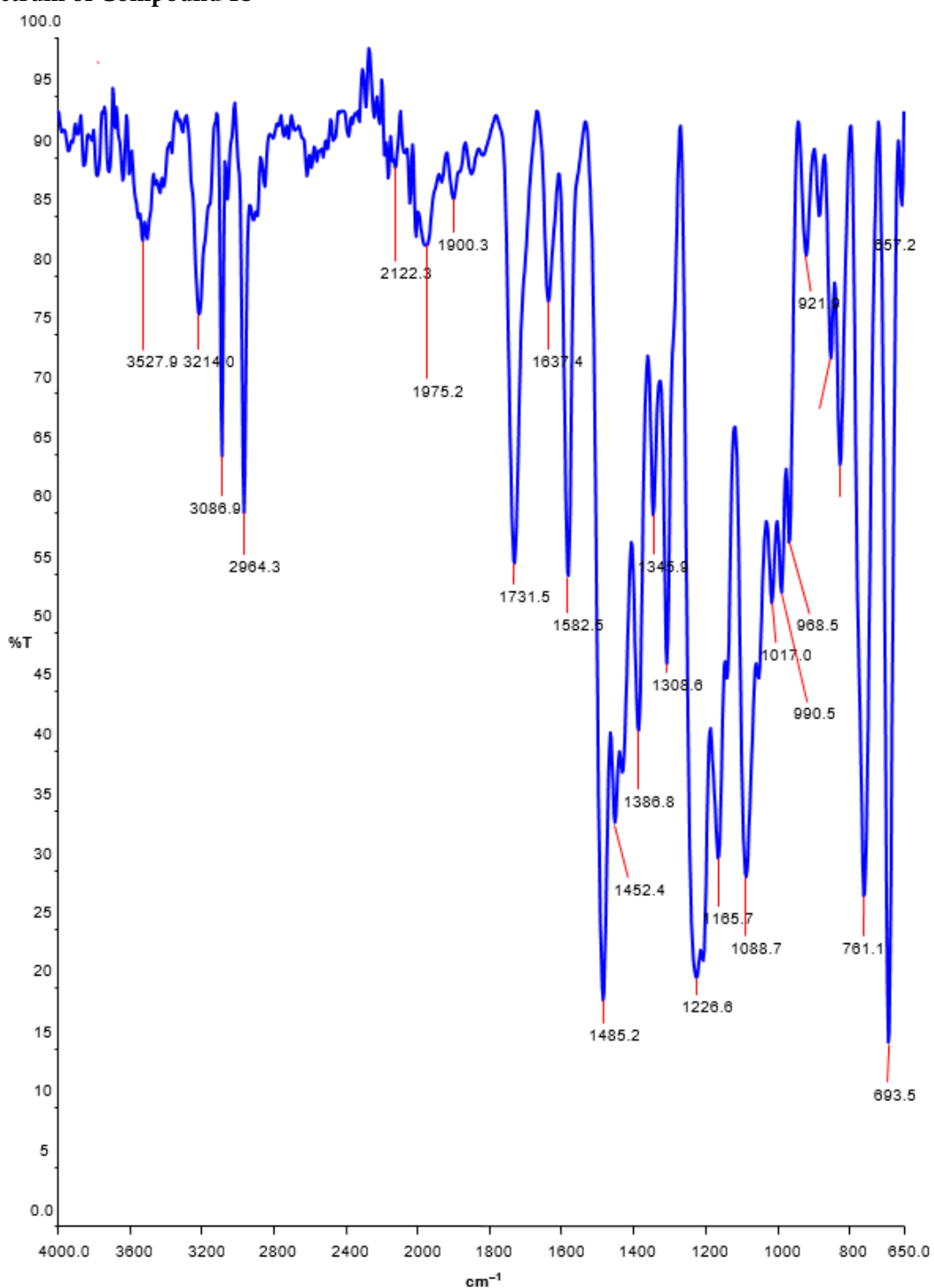
¹³C-NMR Spectrum of Compound 1a

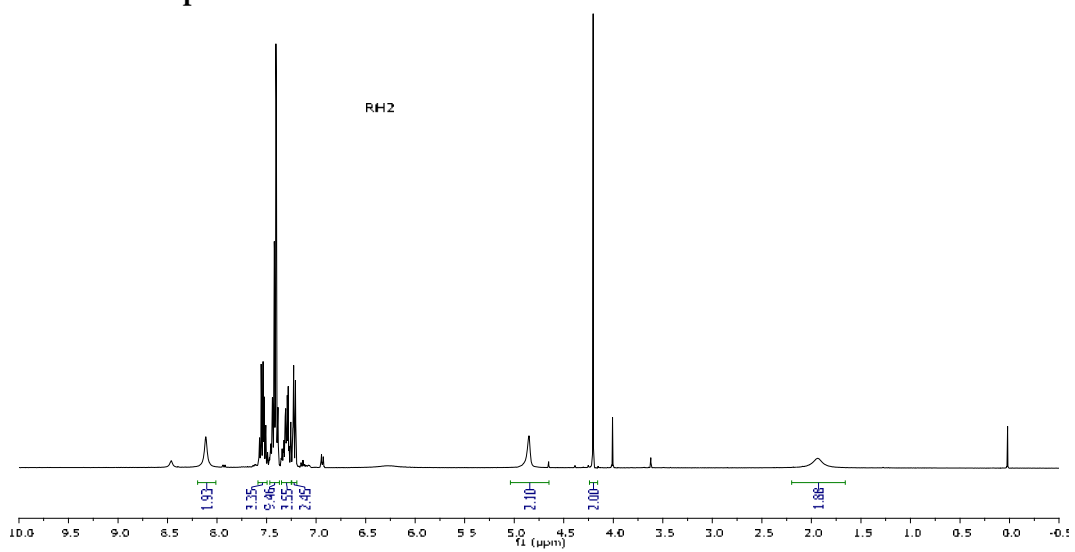


Mass Spectrum of Compound 1a

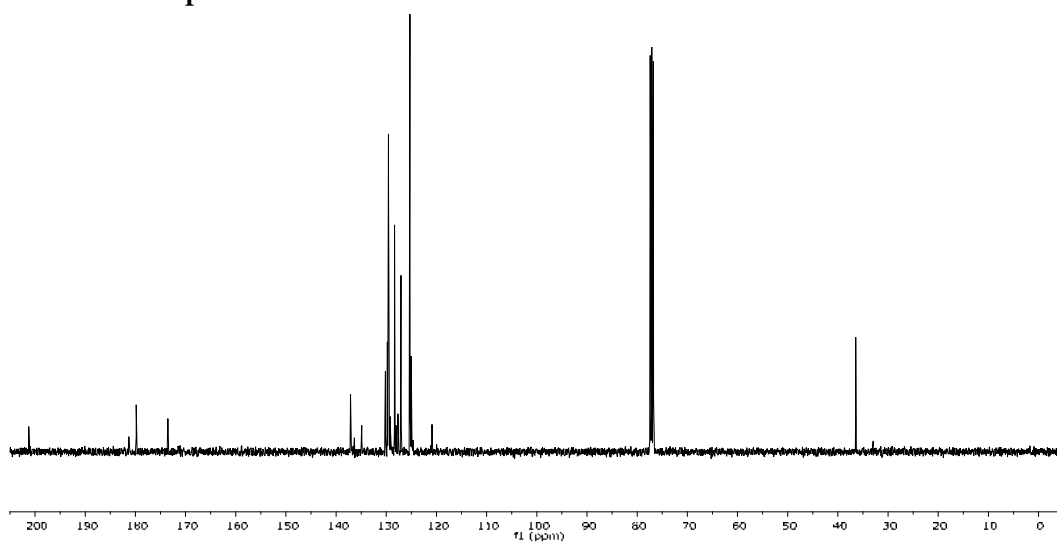


Infrared Spectrum of Compound 1b

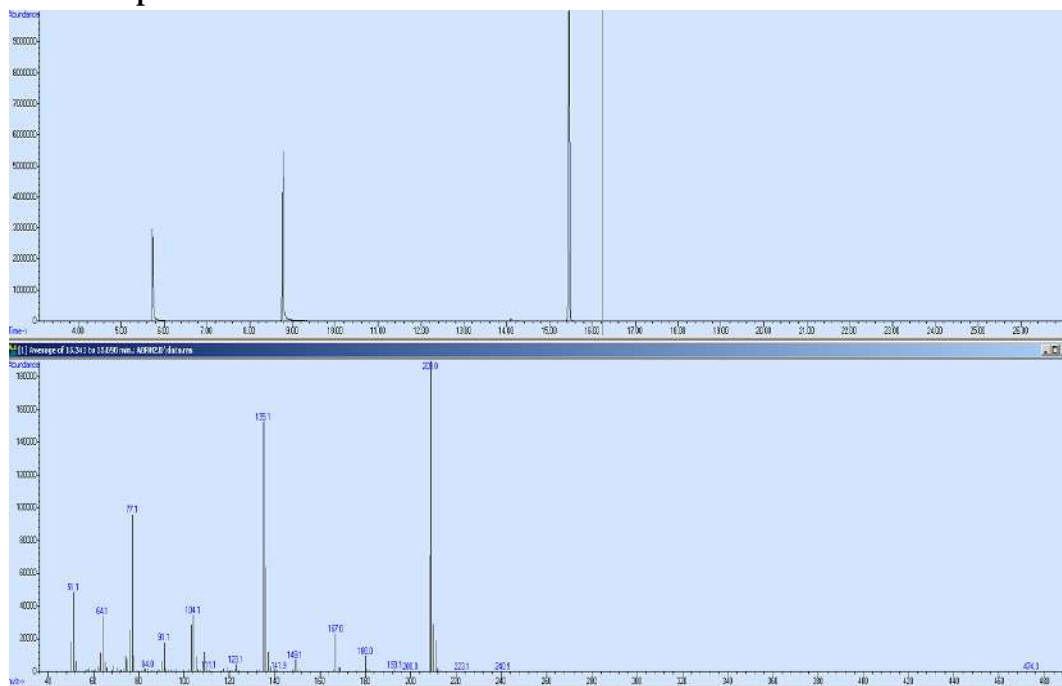


¹H-NMR Spectrum of Compound 1b**¹³C-NMR Spectrum of Compound 1b**

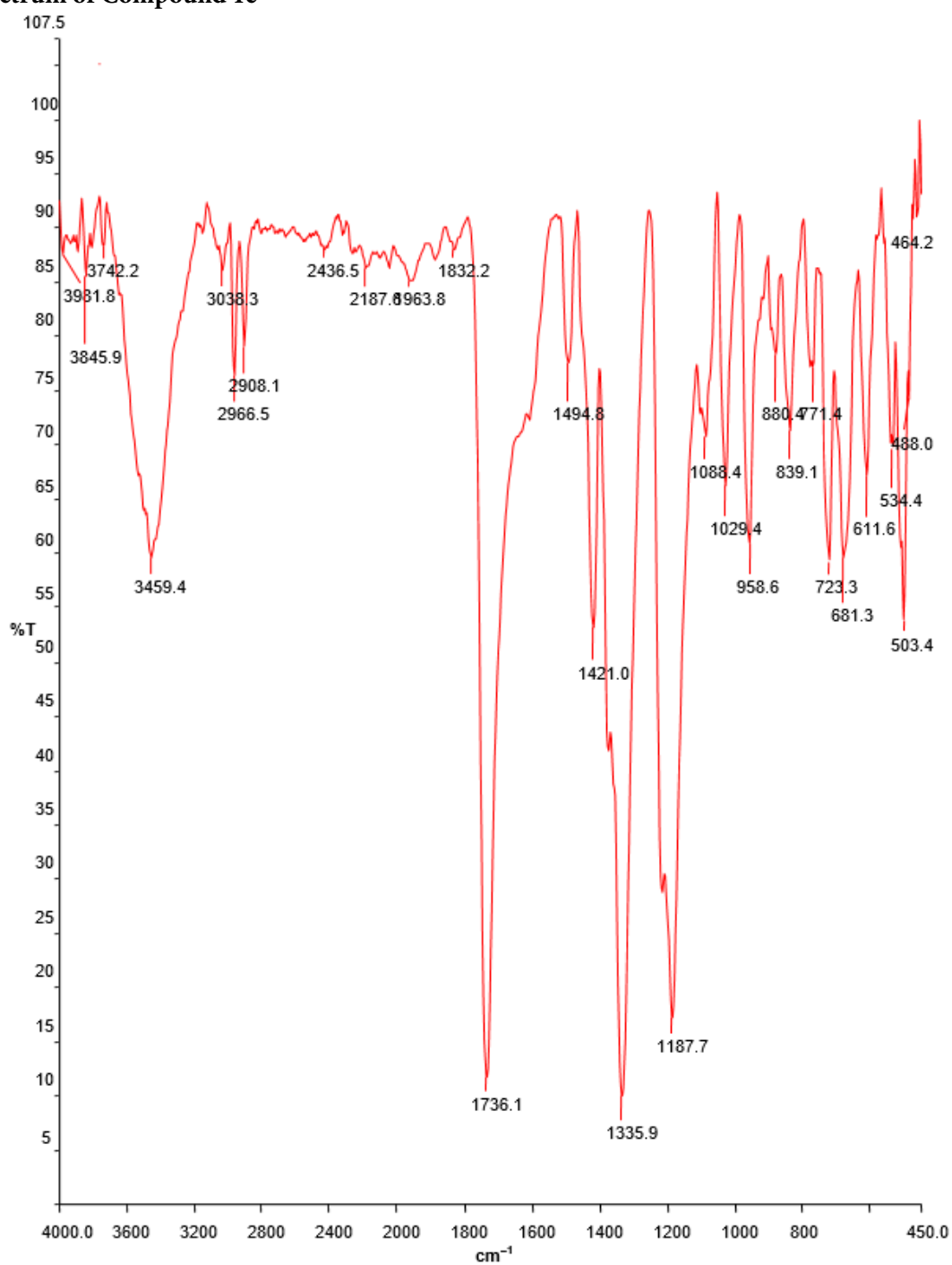
RH2



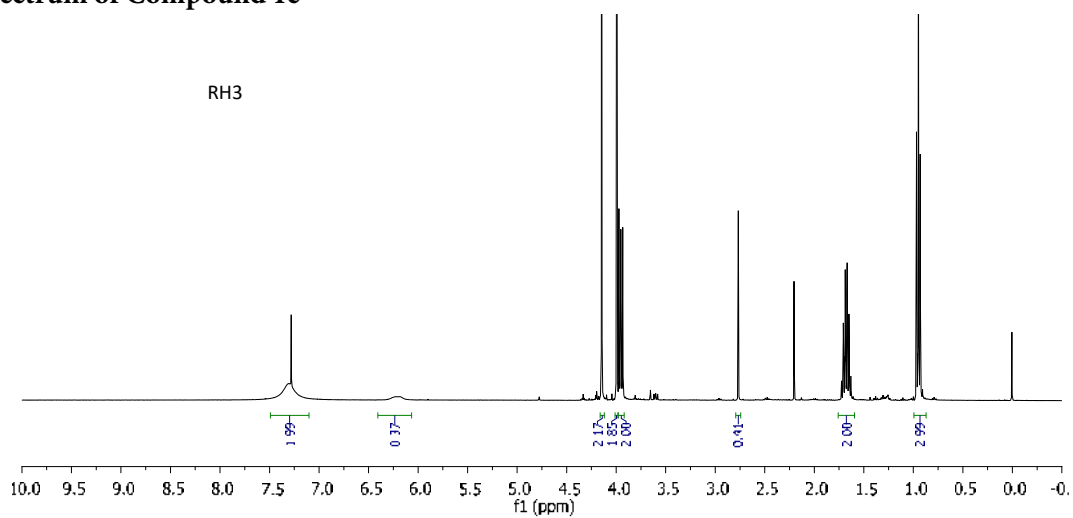
Mass Spectrum of Compound 1b



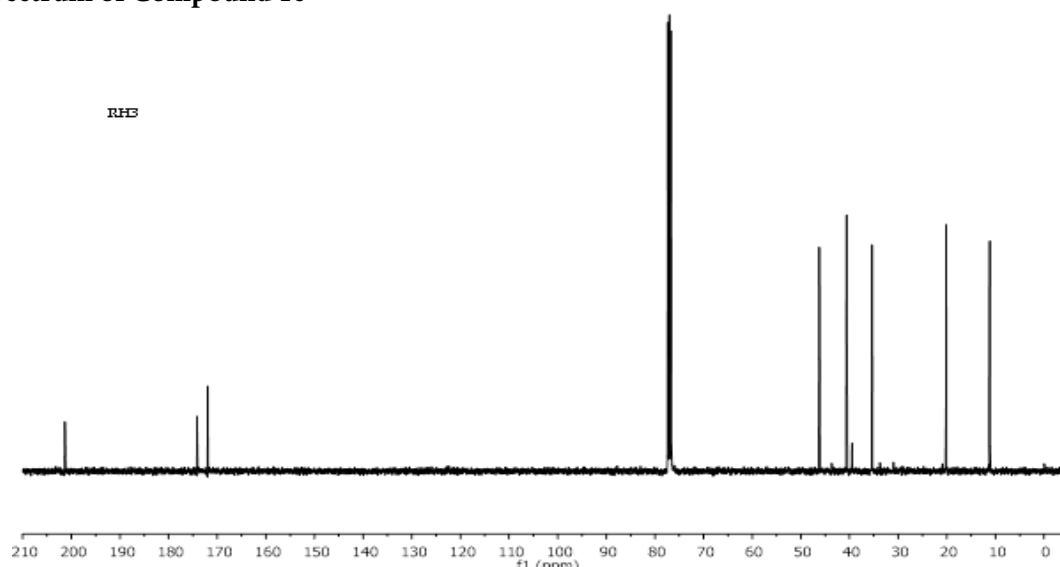
Infrared Spectrum of Compound 1c



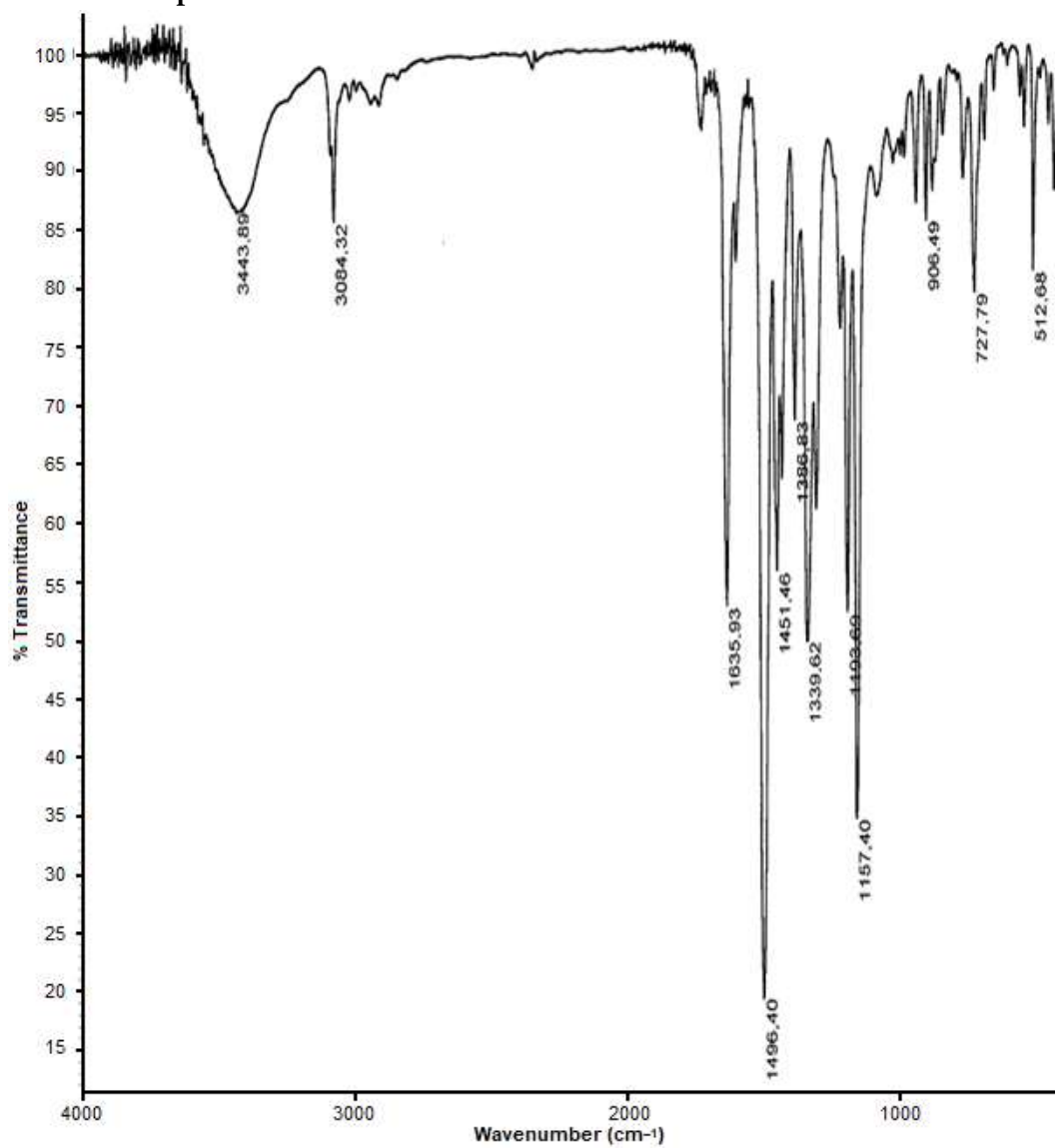
¹H-NMR Spectrum of Compound 1c



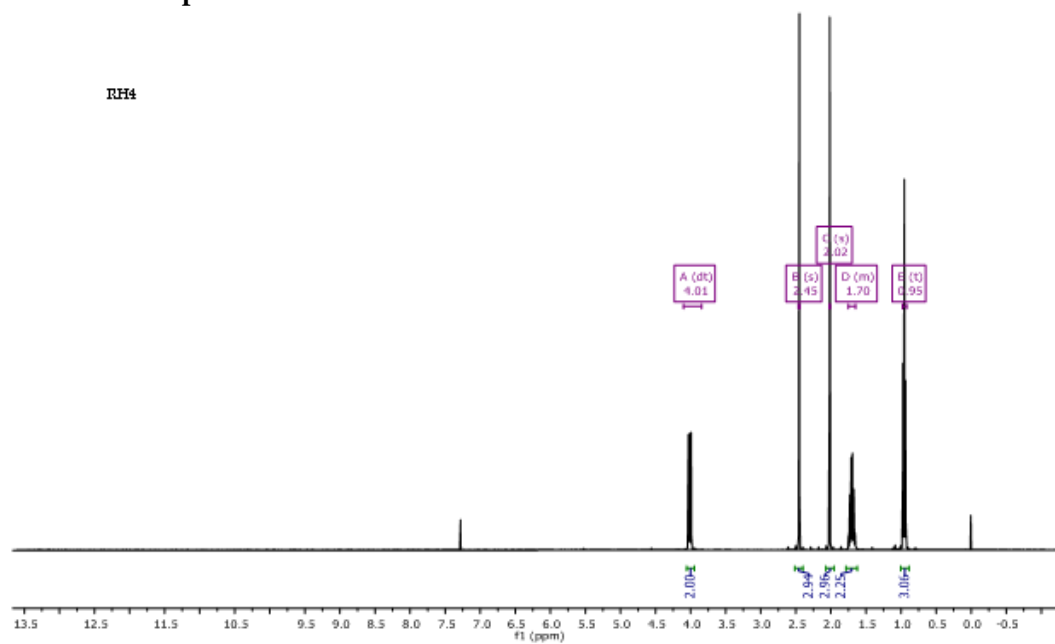
¹³C-NMR Spectrum of Compound 1c



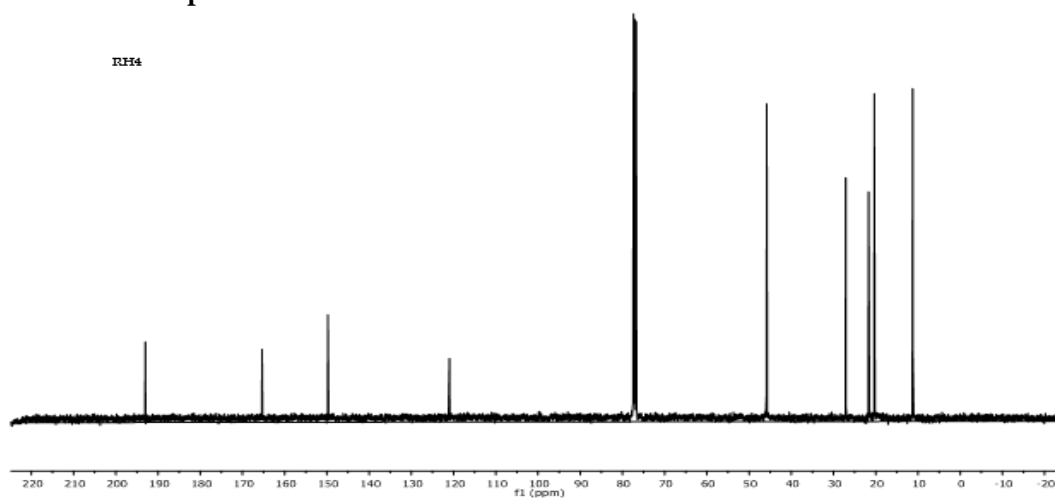
Infrared Spectrum of Compound 3c



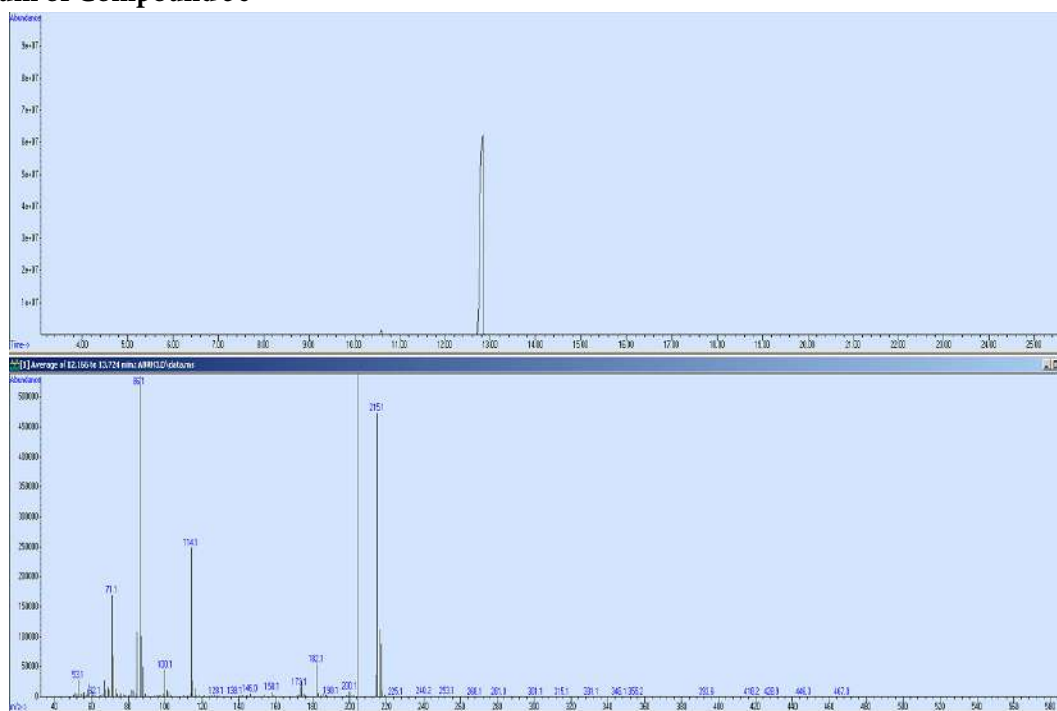
¹H-NMR Spectrum of Compound 3c



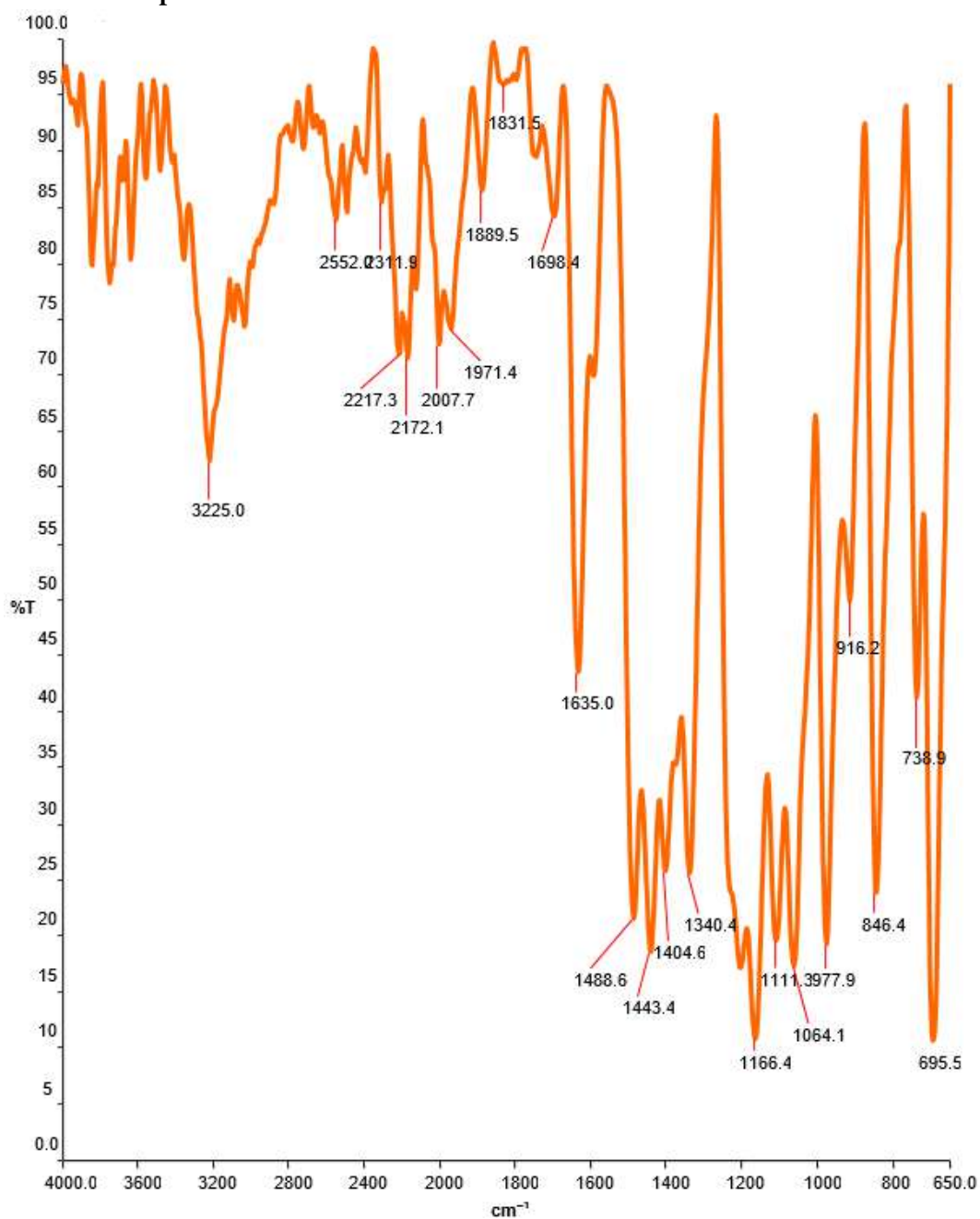
¹³C-NMR Spectrum of Compound 3c

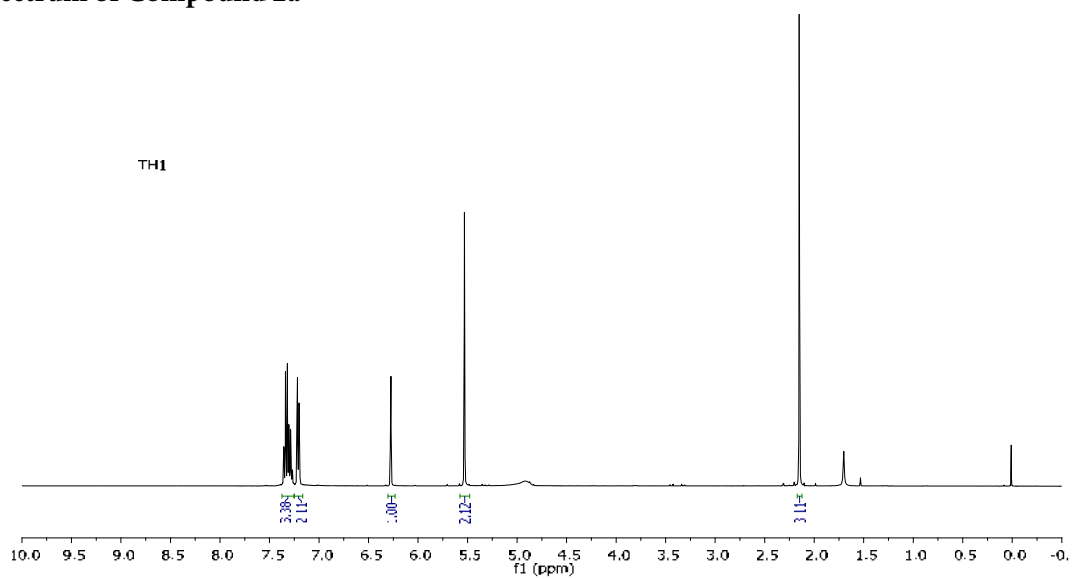
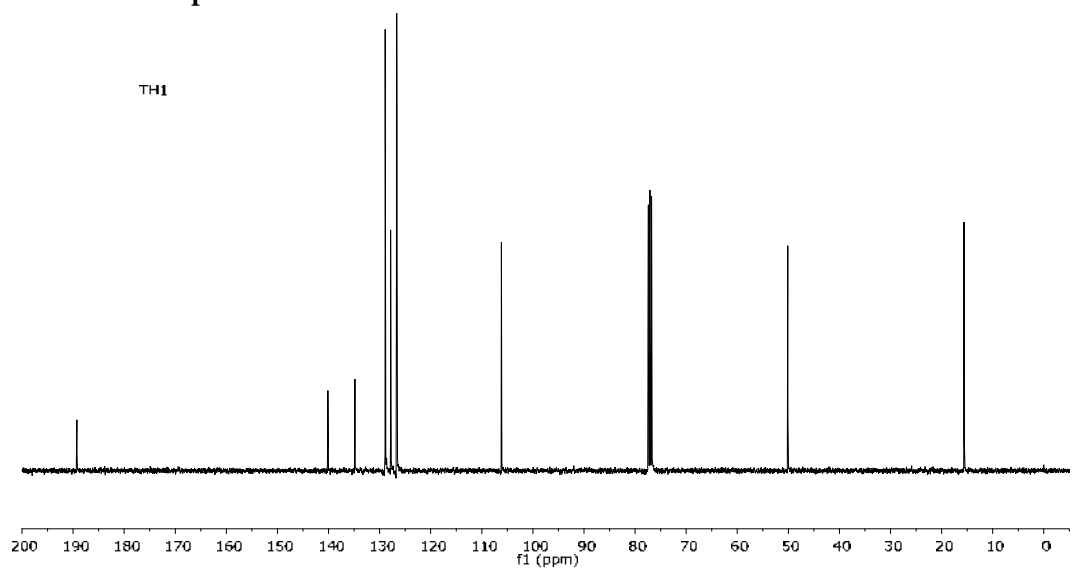


Mass Spectrum of Compound 3c

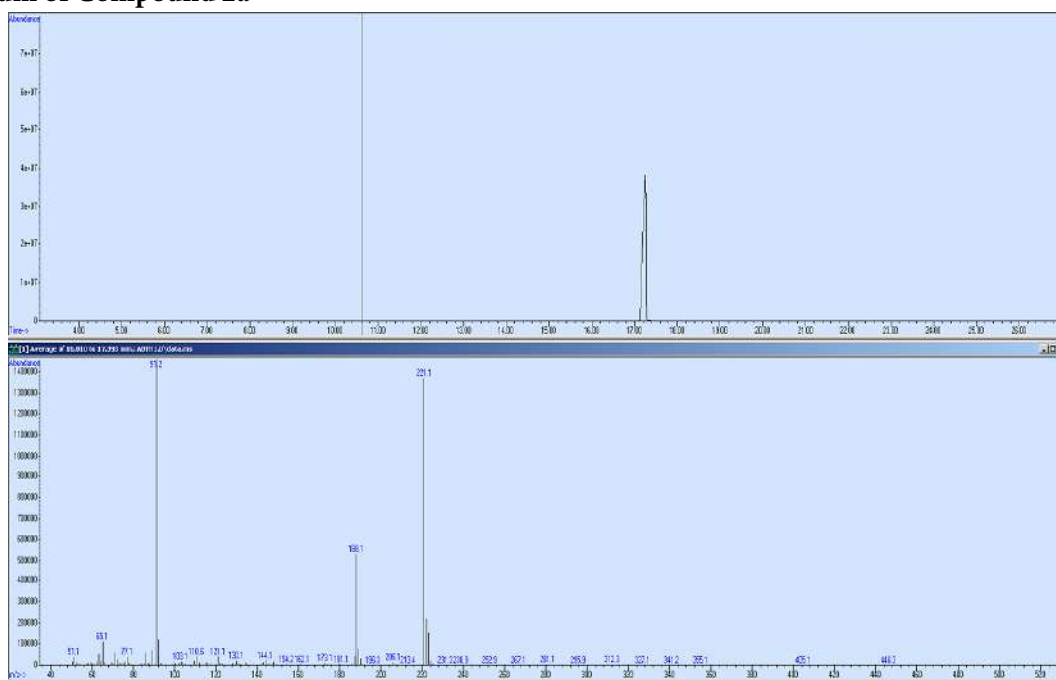


Infrared Spectrum of Compound 2a

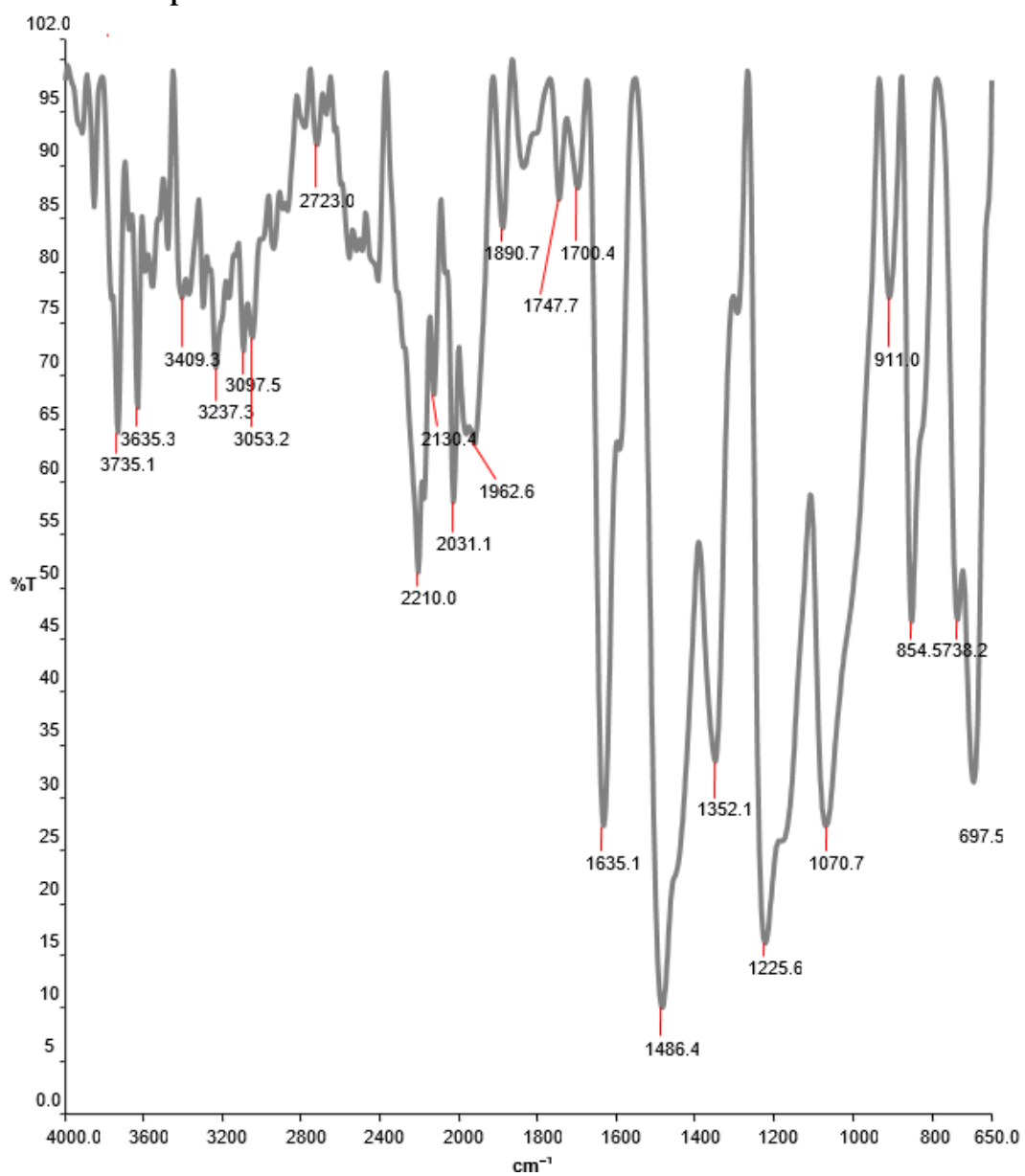


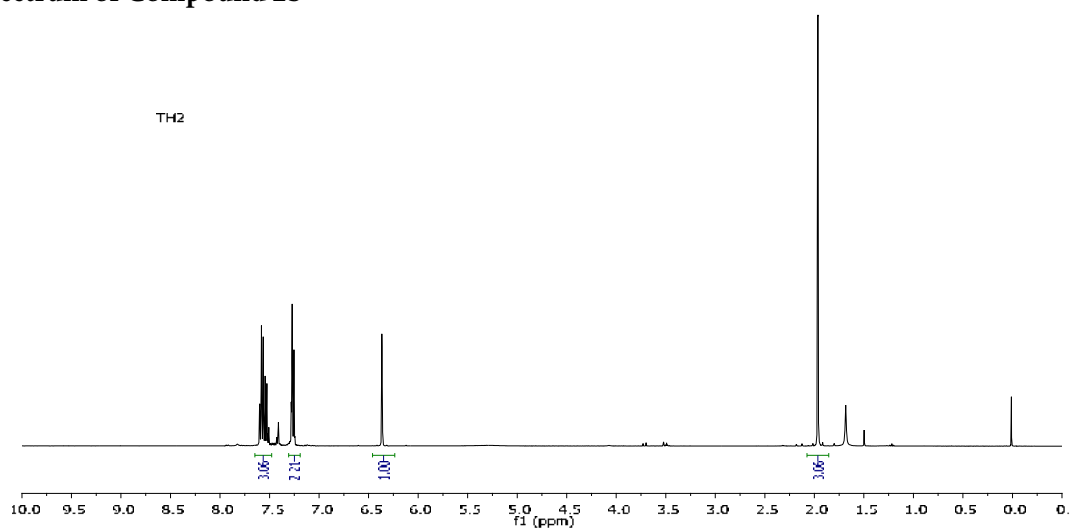
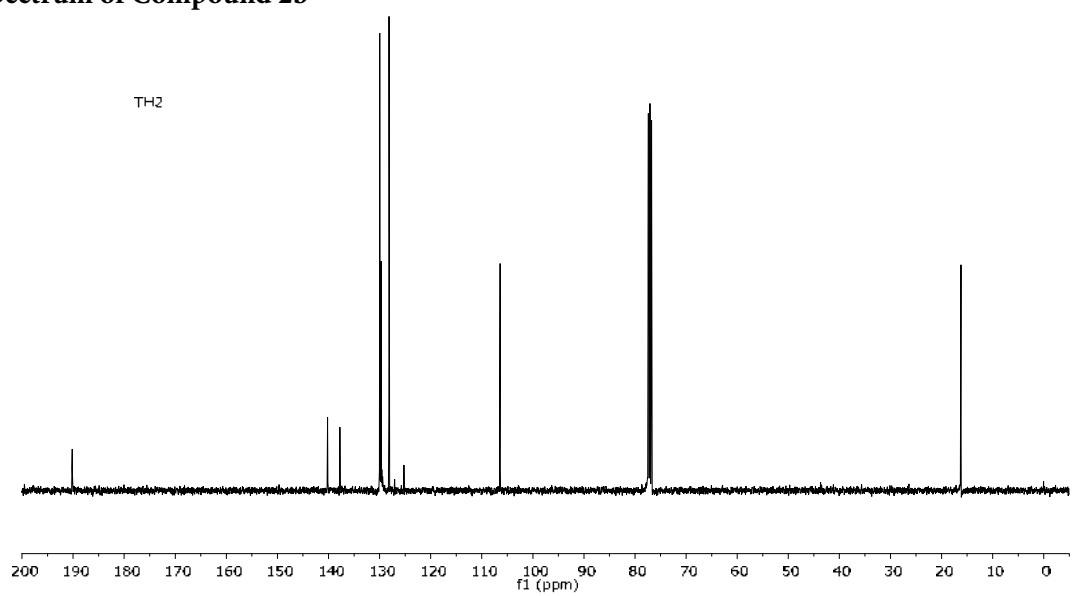
¹H-NMR Spectrum of Compound 2a**¹³C-NMR Spectrum of Compound 2a**

Mass Spectrum of Compound 2a

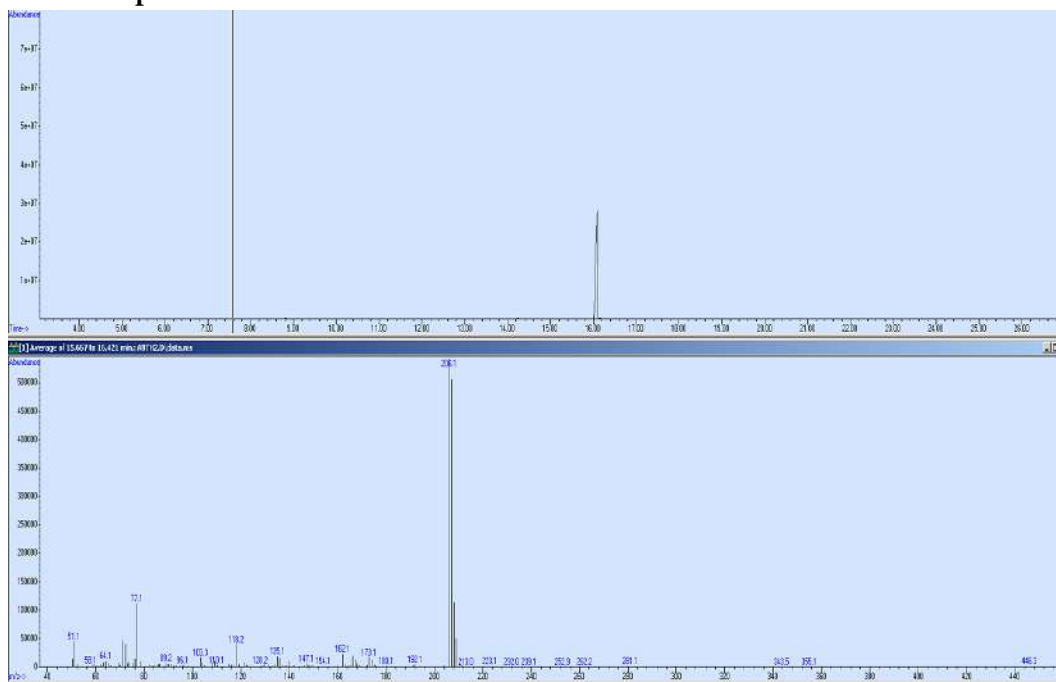


Infrared Spectrum of Compound 2b

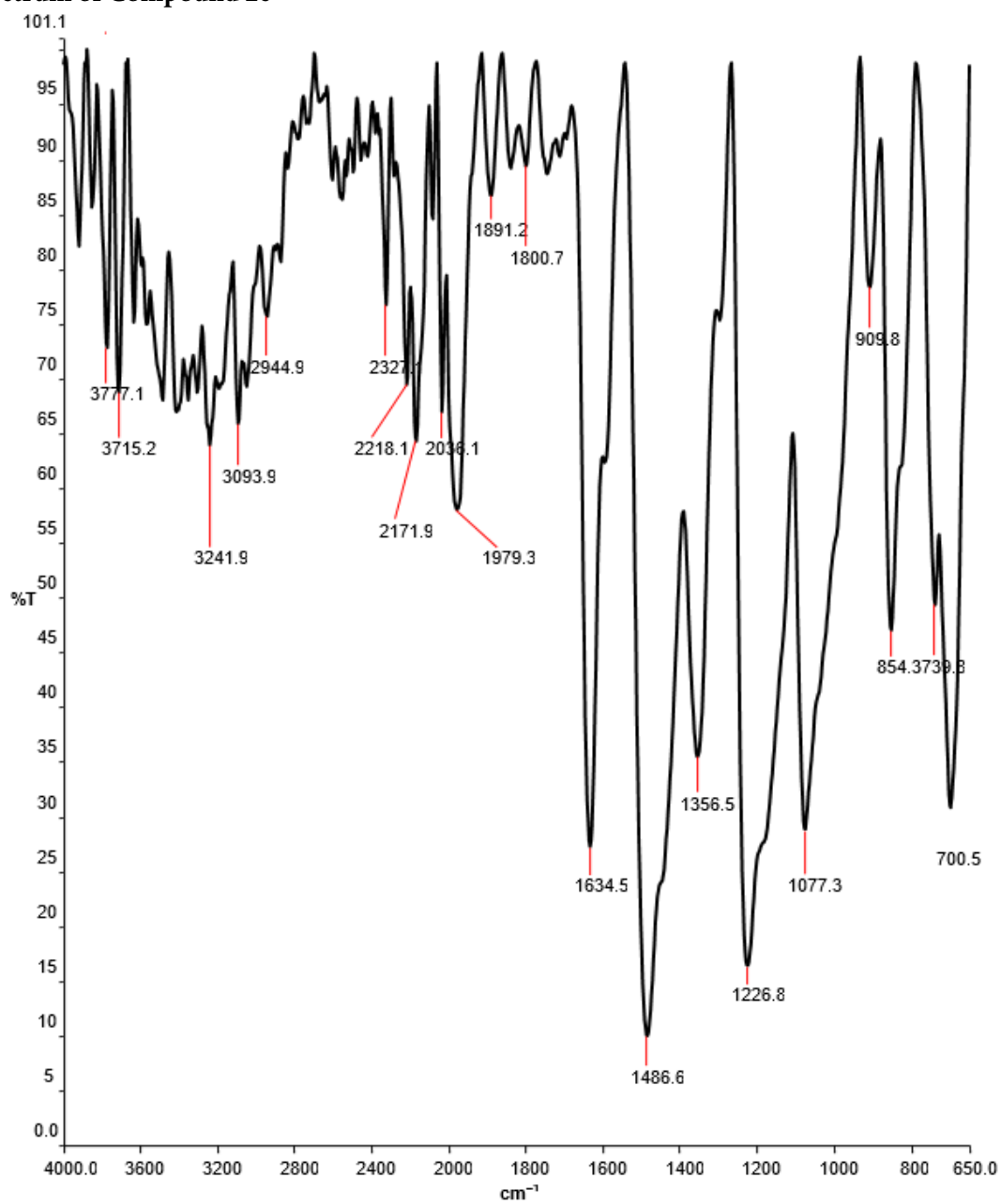


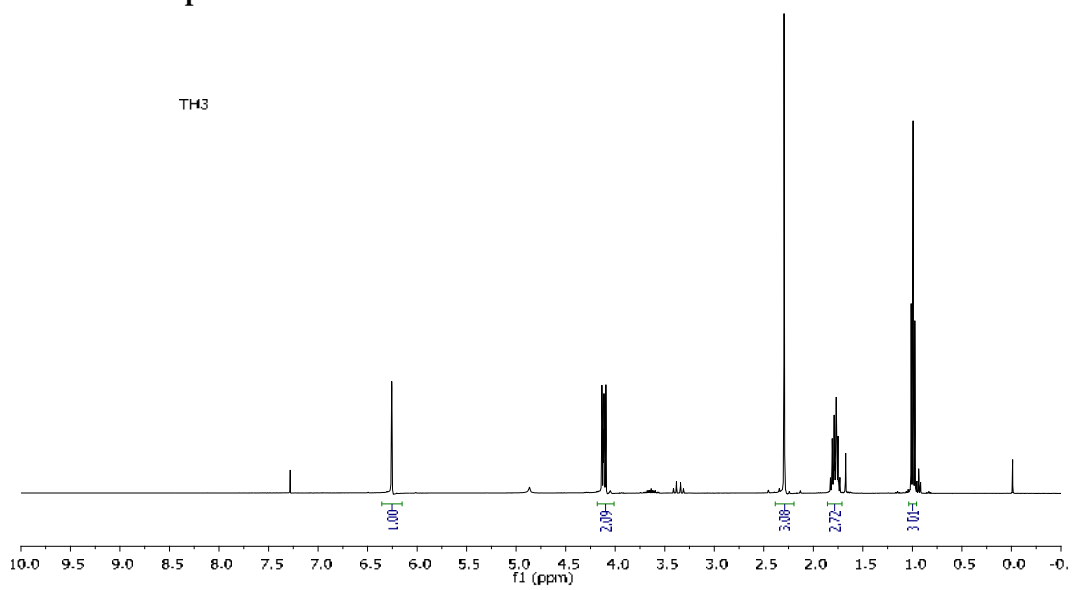
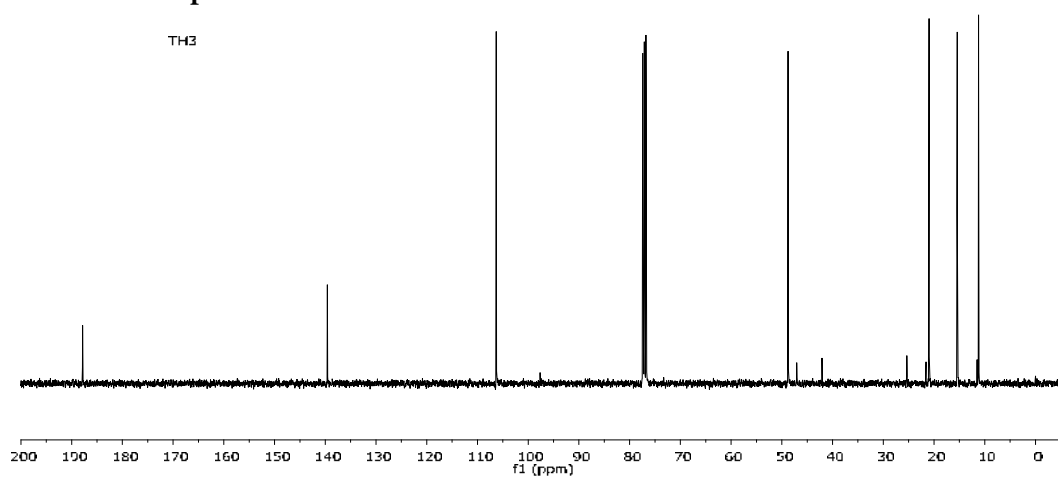
¹H-NMR Spectrum of Compound 2b**¹³C-NMR Spectrum of Compound 2b**

Mass Spectrum of Compound 2b

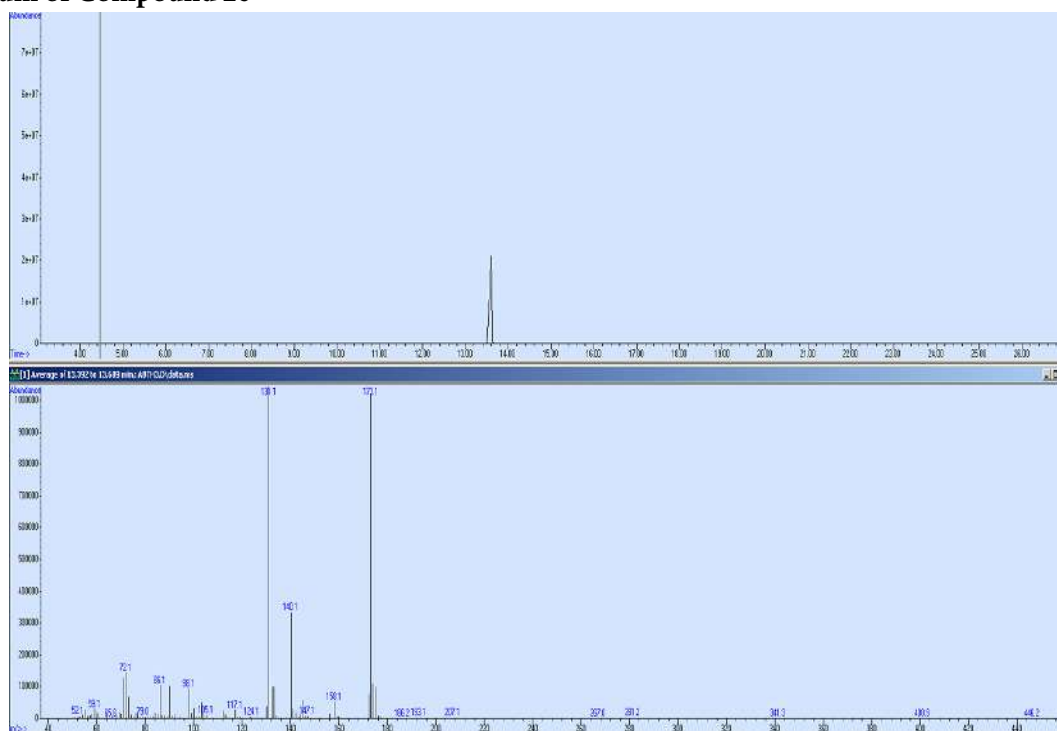


Infrared Spectrum of Compound 2c

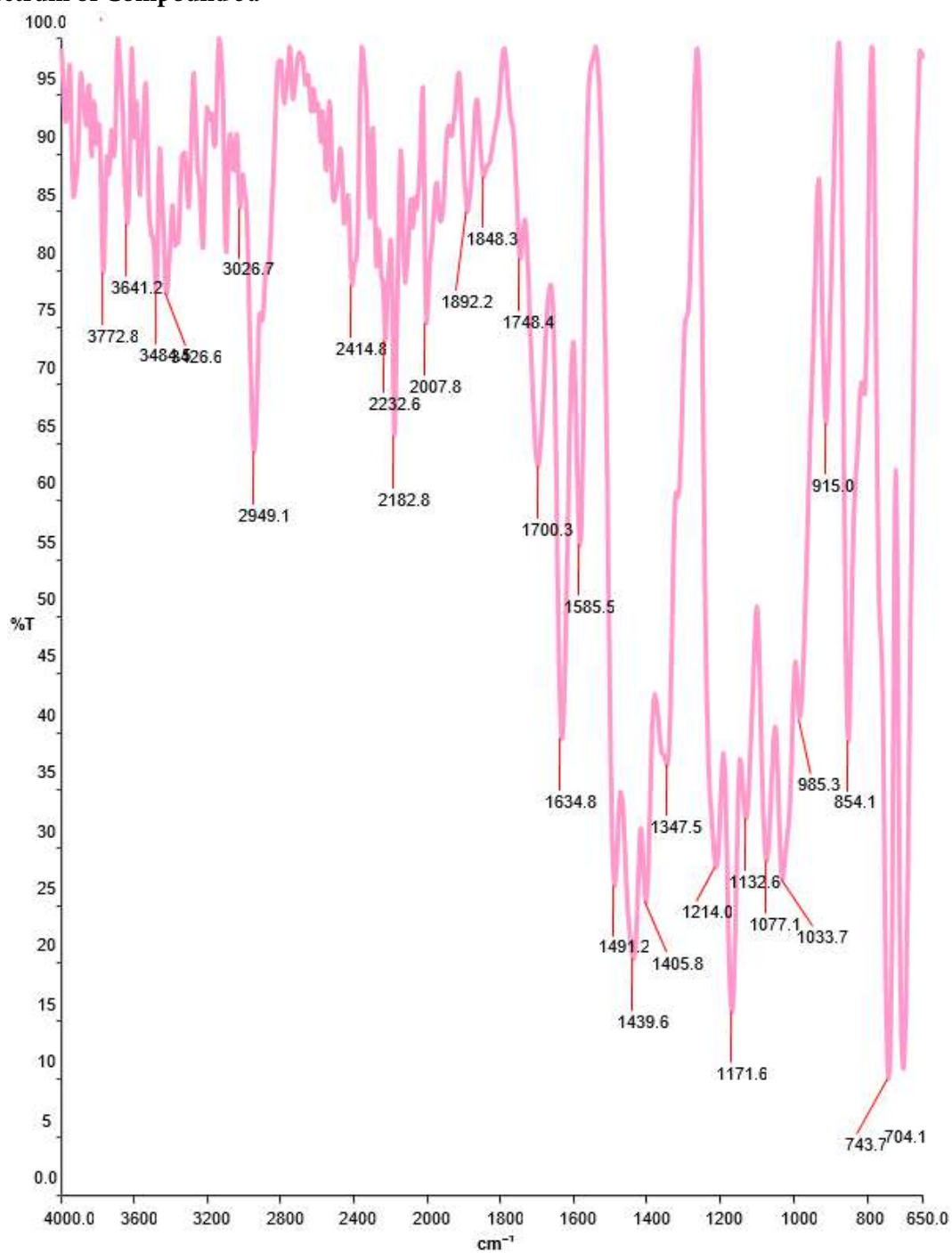


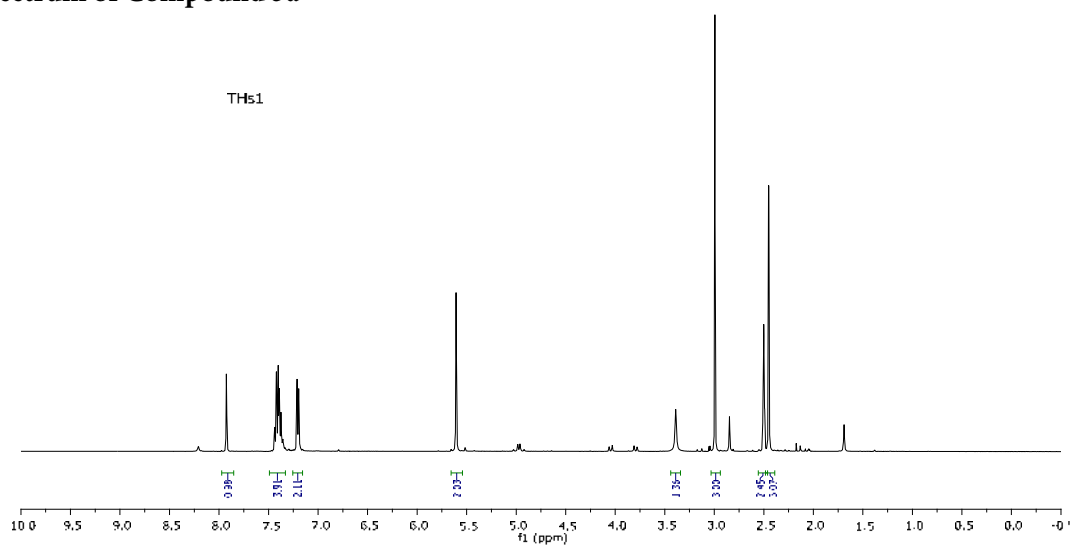
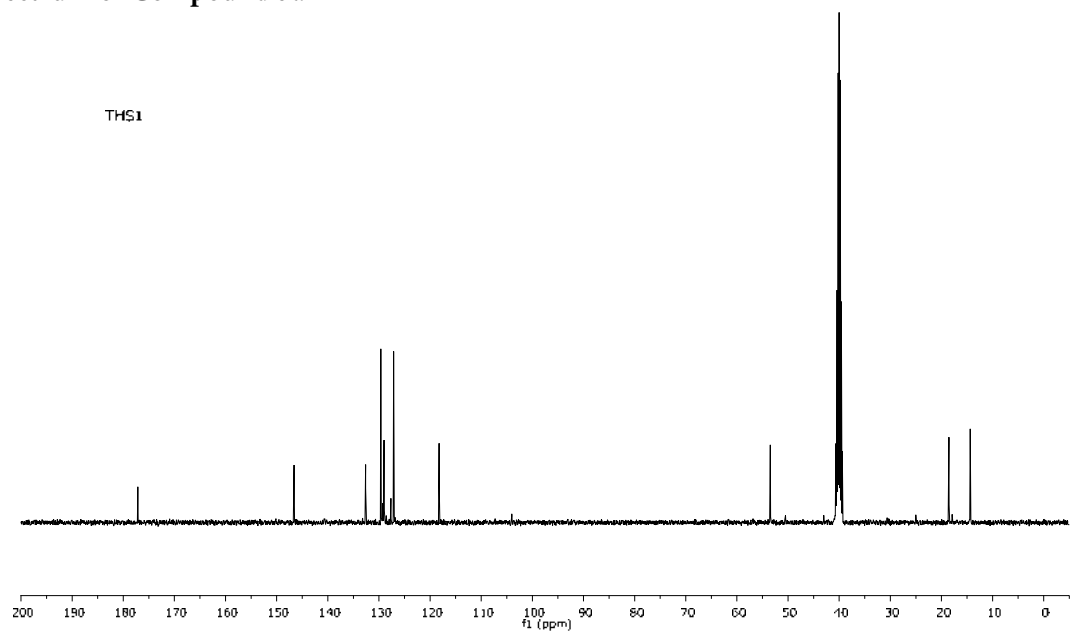
¹H-NMR Spectrum of Compound 2c**¹³C-NMR Spectrum of Compound 2c**

Mass Spectrum of Compound 2c

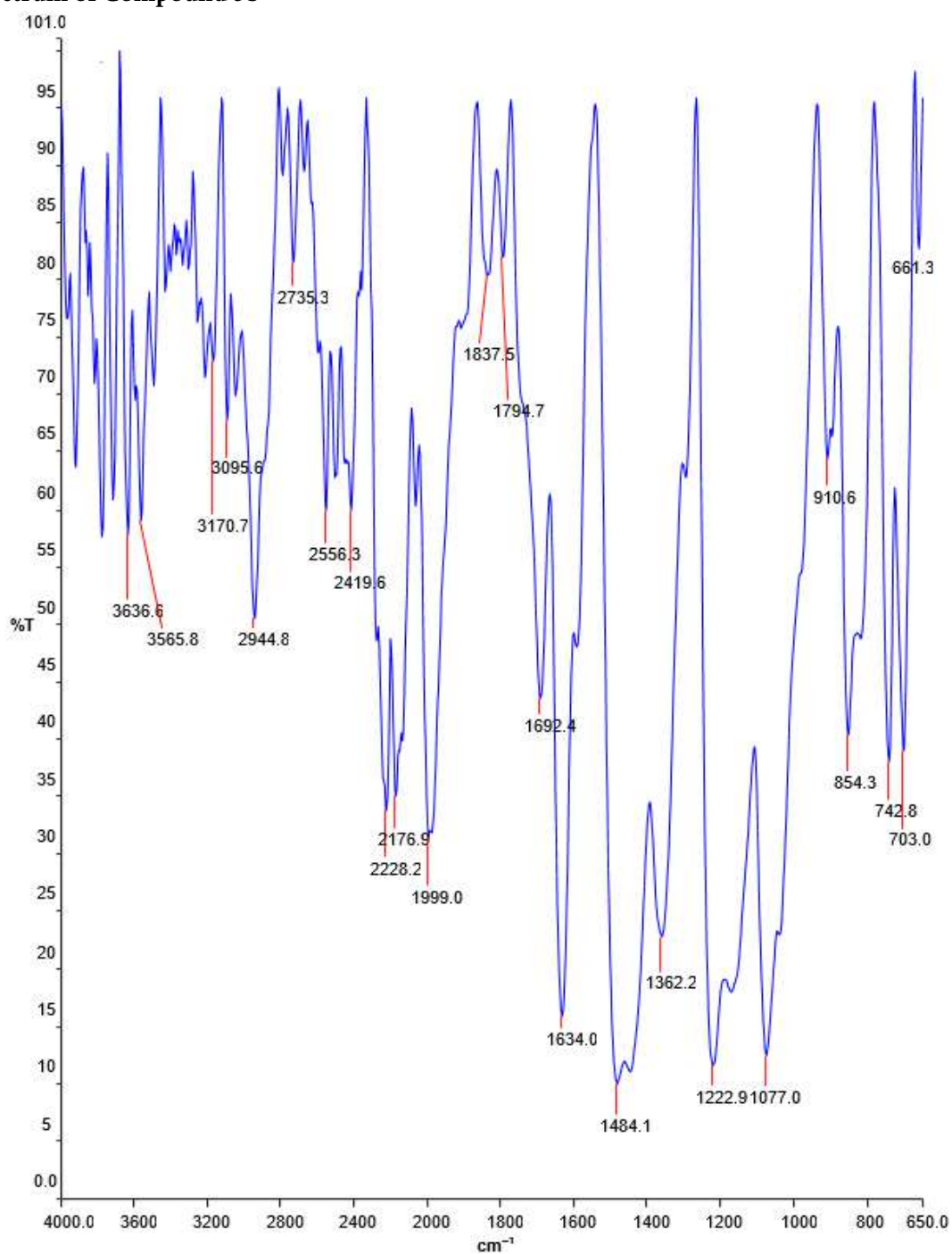


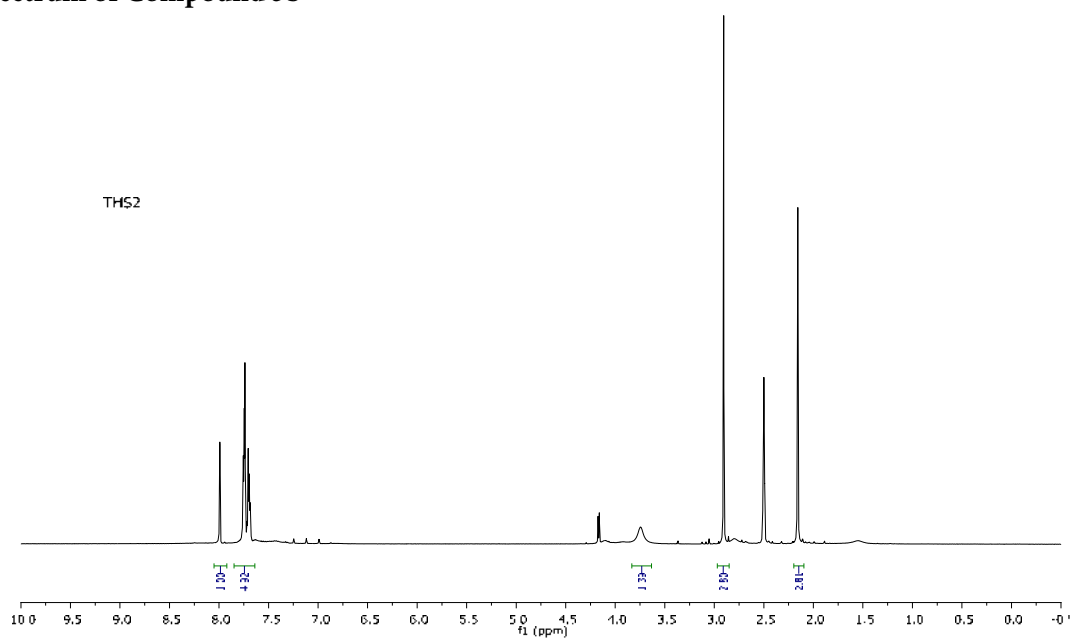
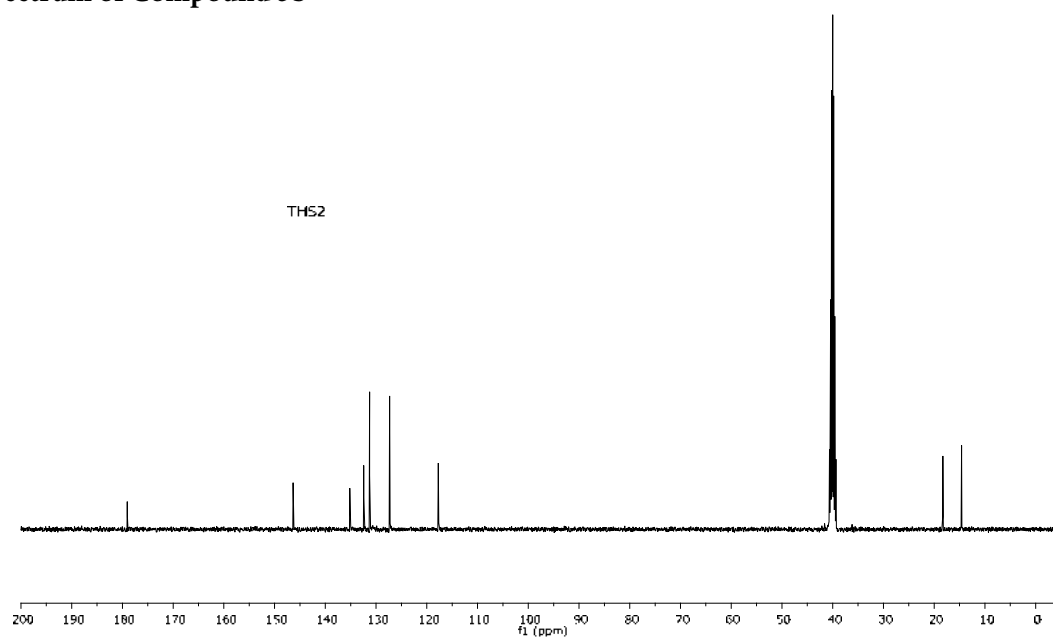
Infrared Spectrum of Compound 3a



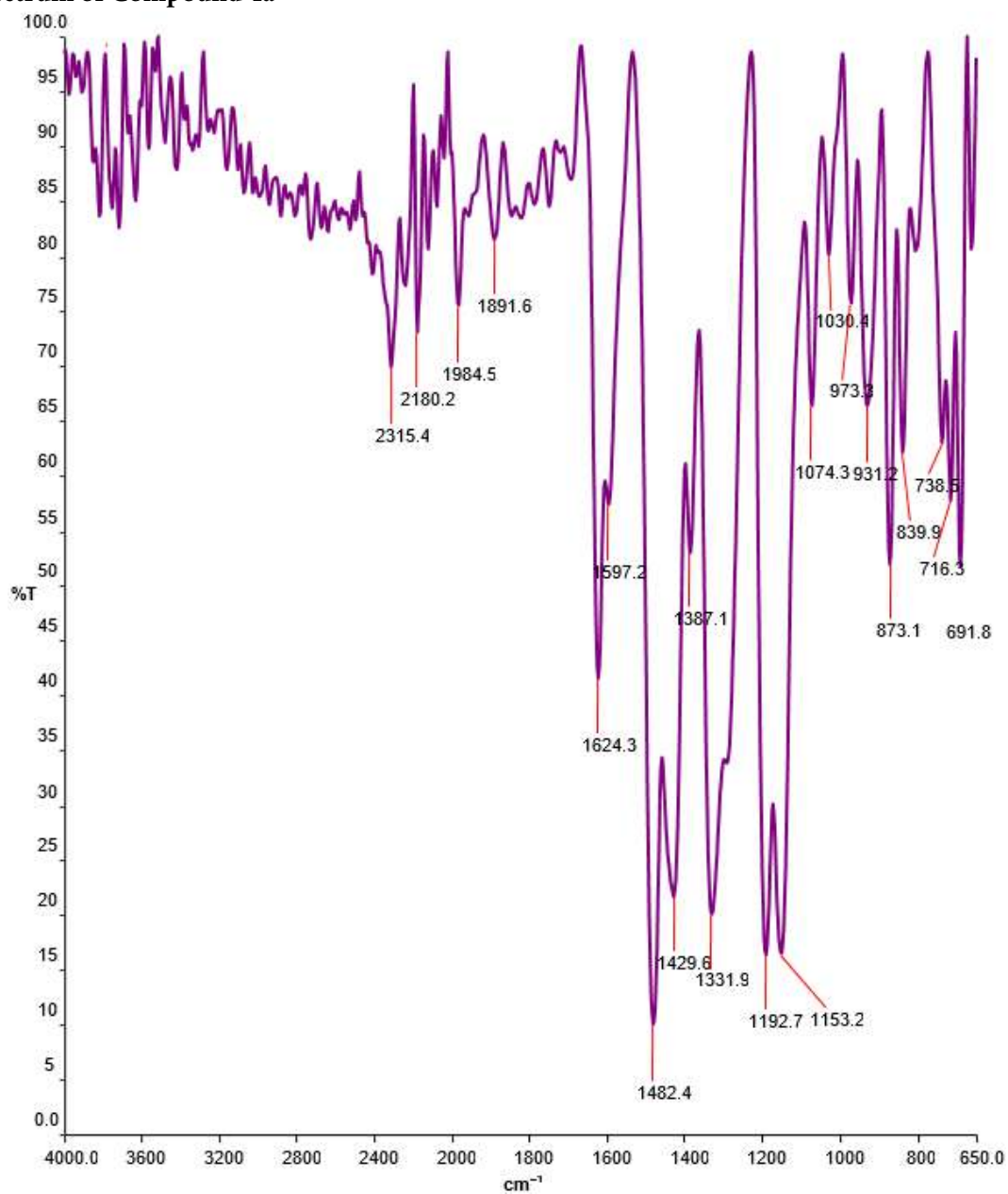
¹H-NMR Spectrum of Compound 3a**¹³C-NMR Spectrum of Compound 3a**

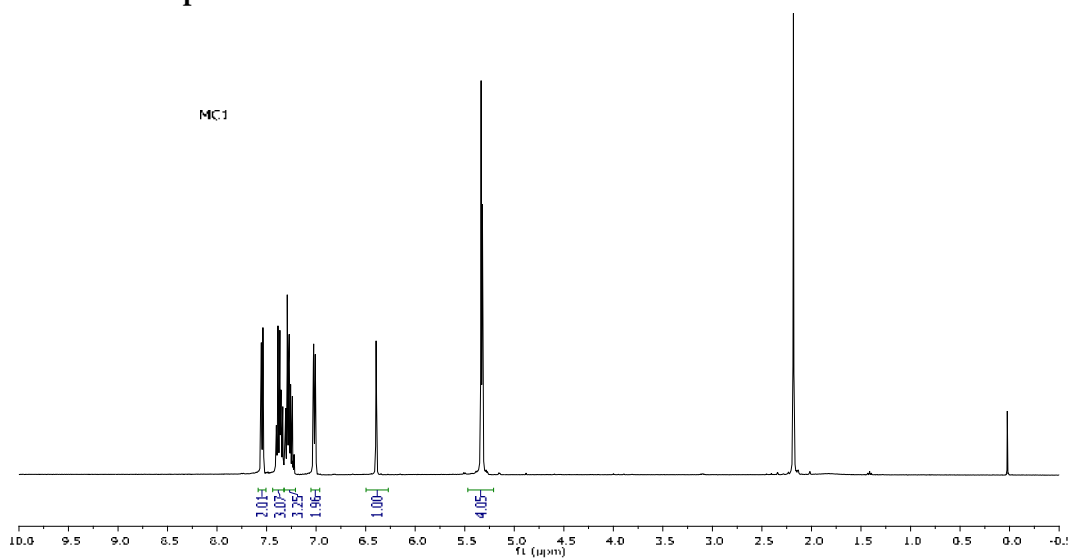
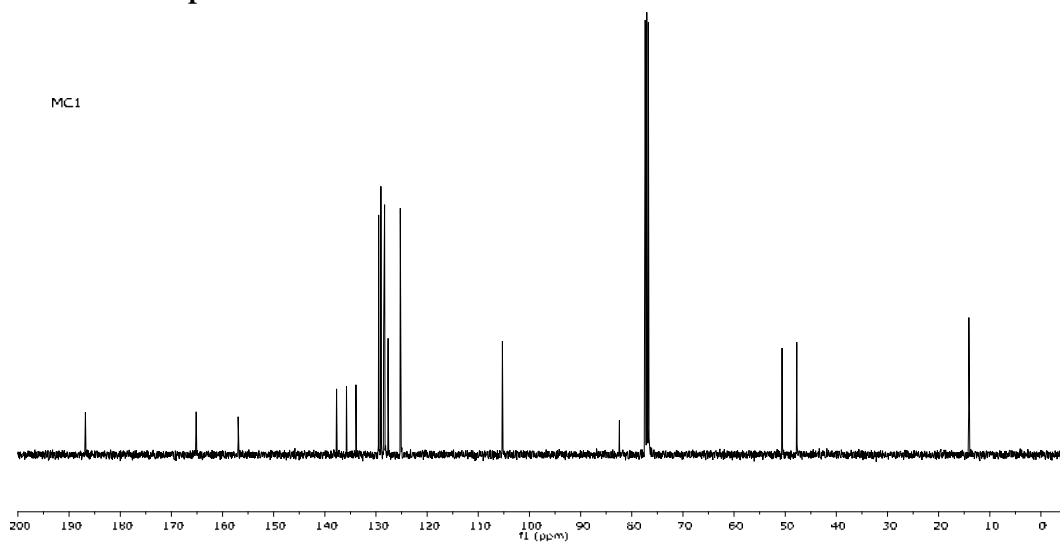
Infrared Spectrum of Compound 3b



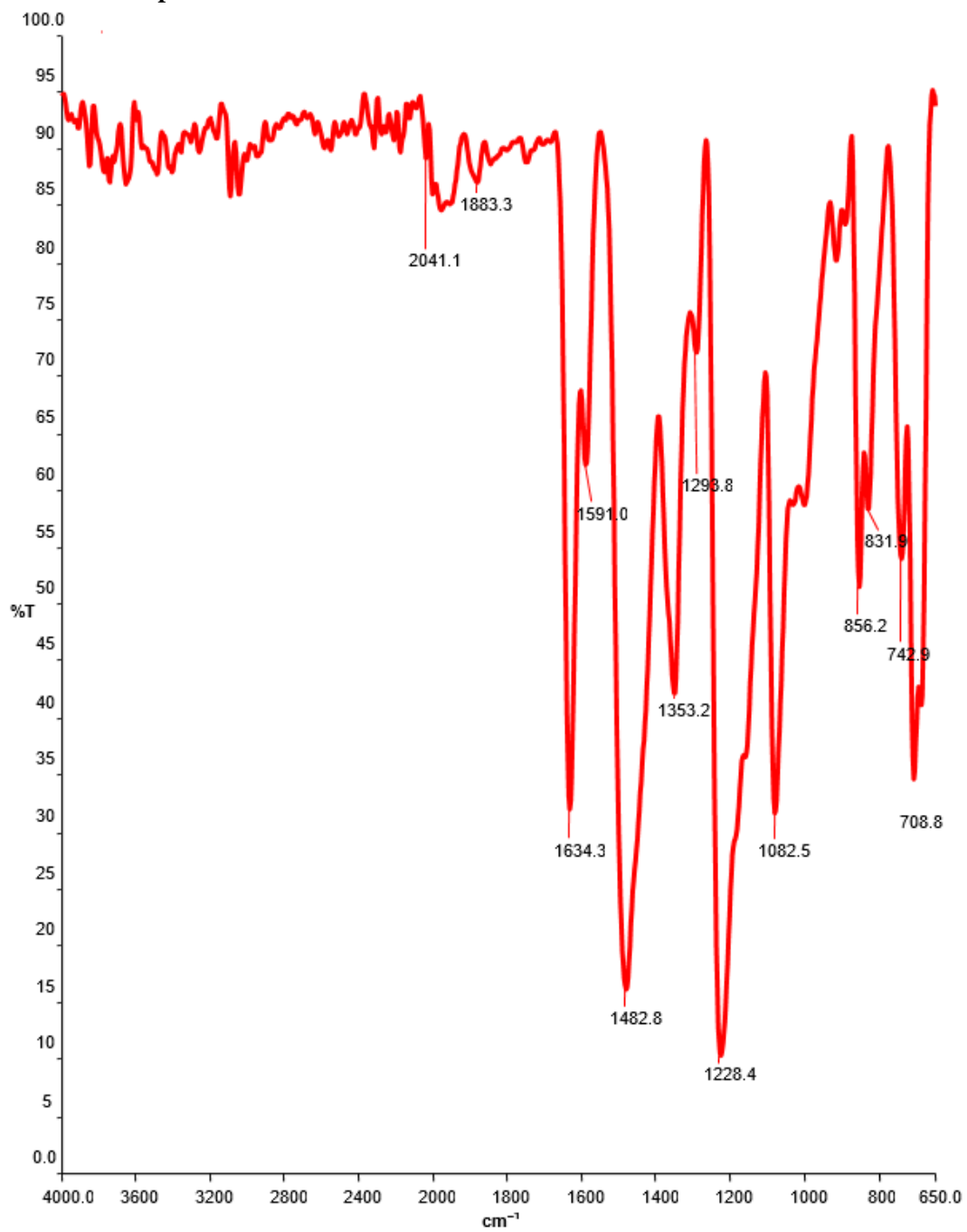
¹H-NMR Spectrum of Compound 3b**¹³C-NMR Spectrum of Compound 3b**

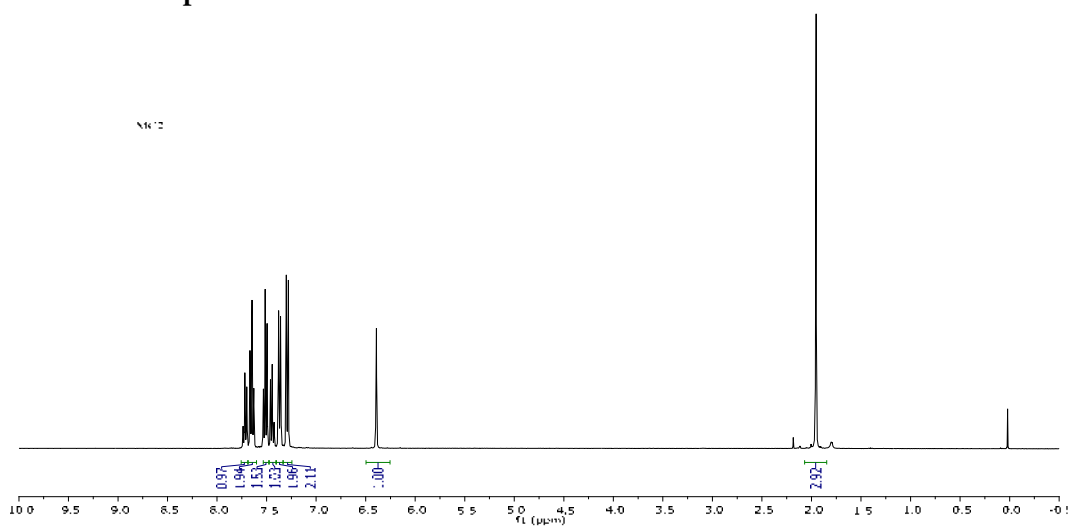
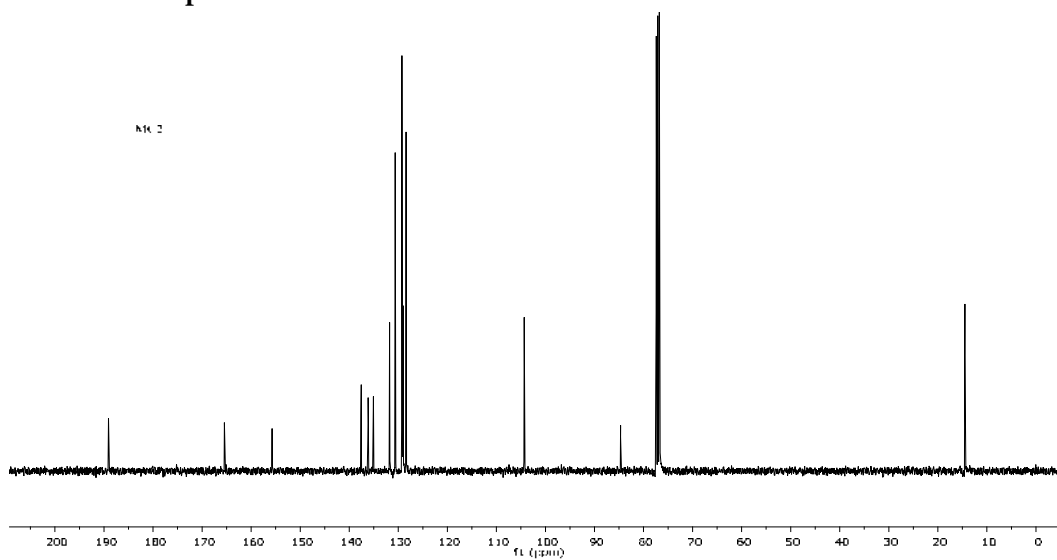
Infrared Spectrum of Compound 4a



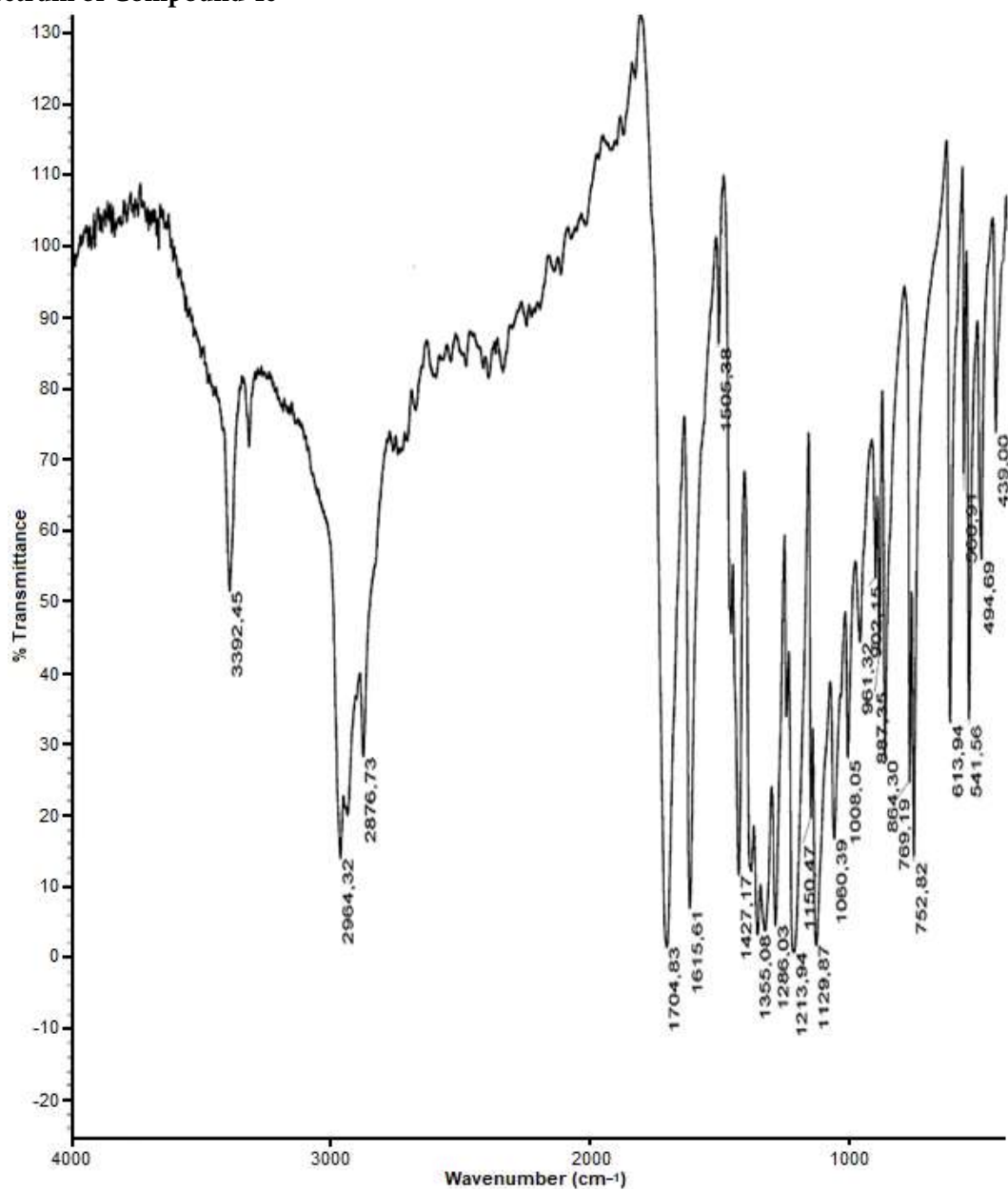
¹H-NMR Spectrum of Compound 4a**¹³C-NMR Spectrum of Compound 4a**

Infrared Spectrum of Compound 4b

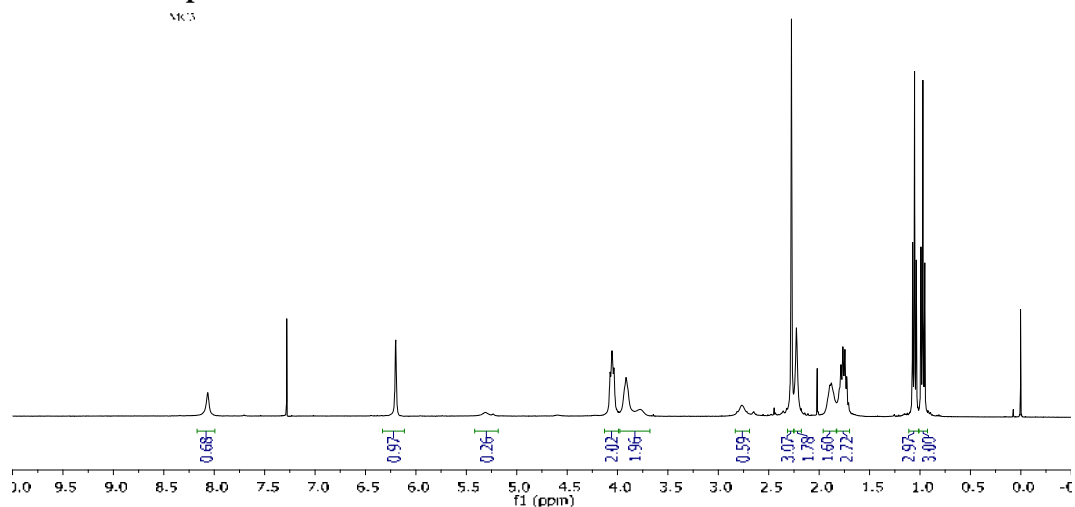


¹H-NMR Spectrum of Compound 4b**¹³C-NMR Spectrum of Compound 4b**

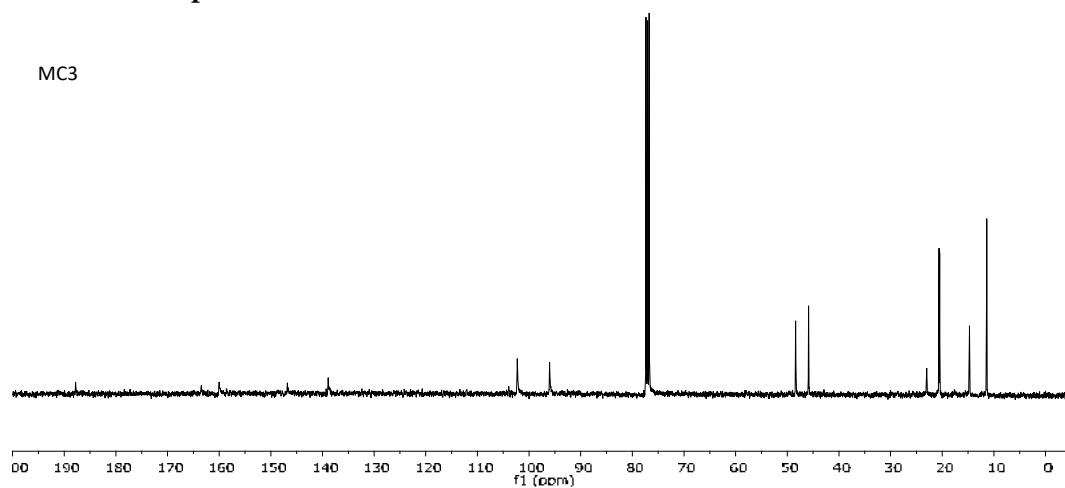
Infrared Spectrum of Compound 4c



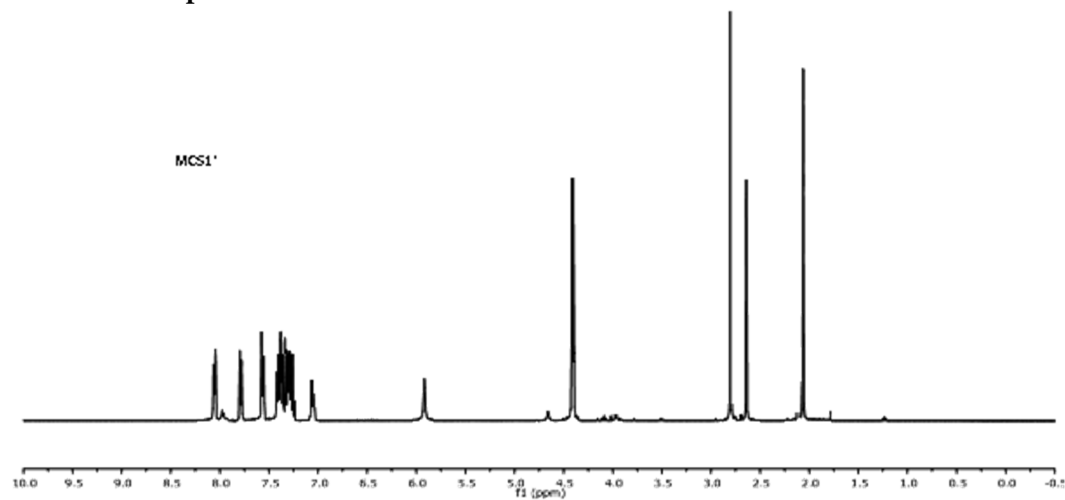
¹H-NMR Spectrum of Compound 4c

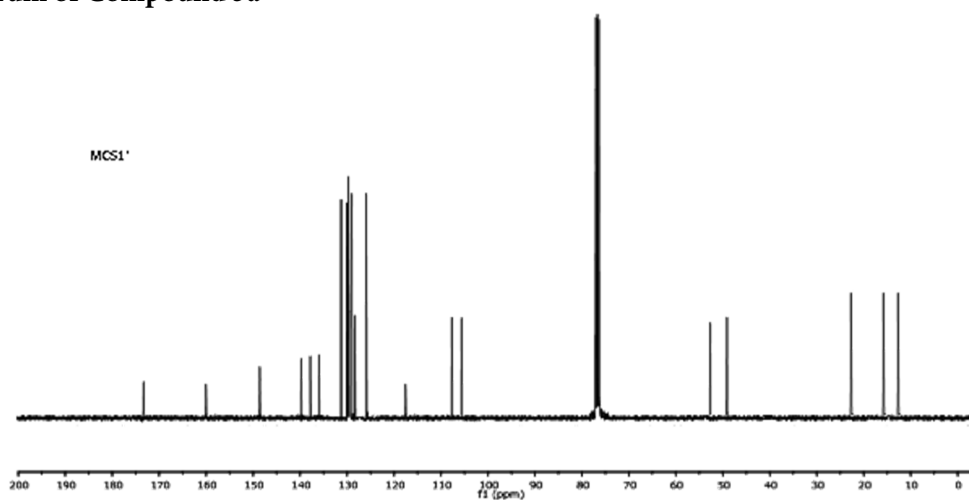
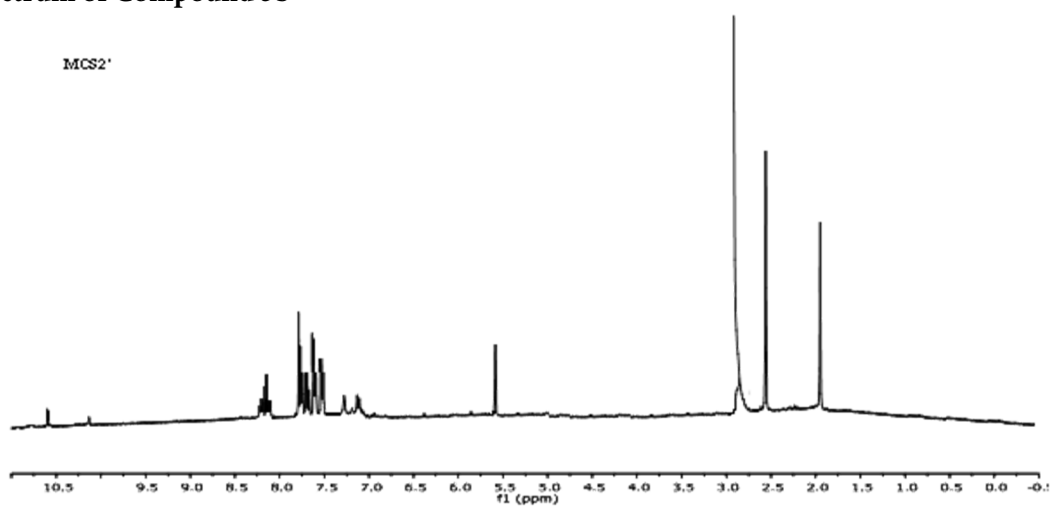
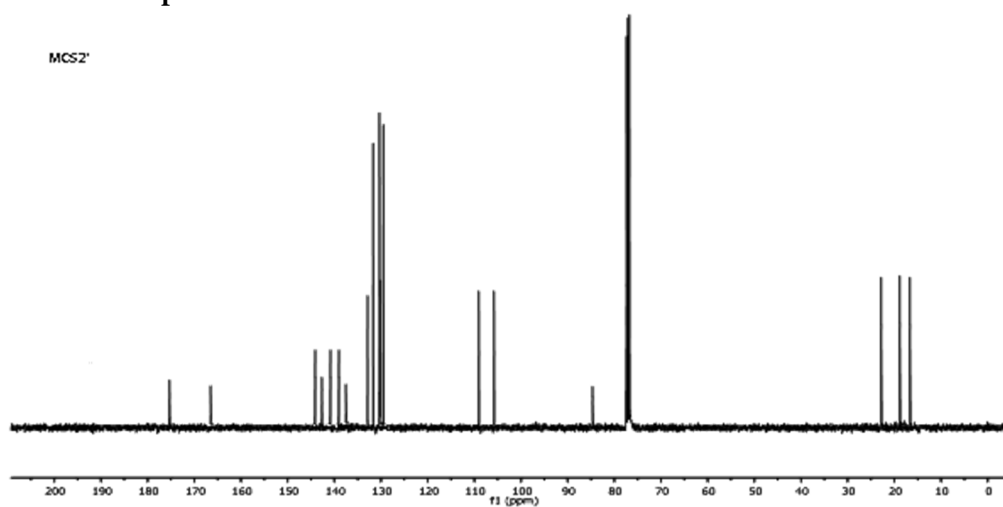


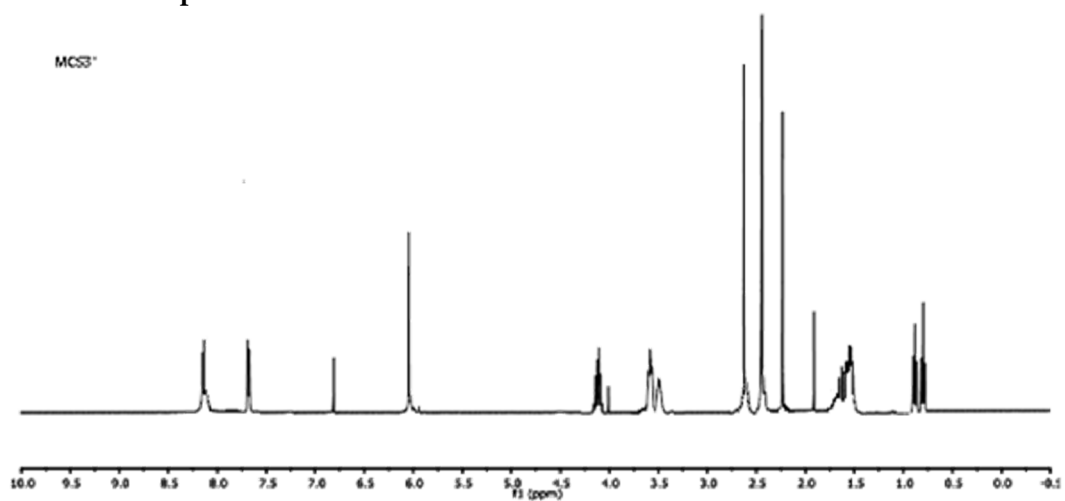
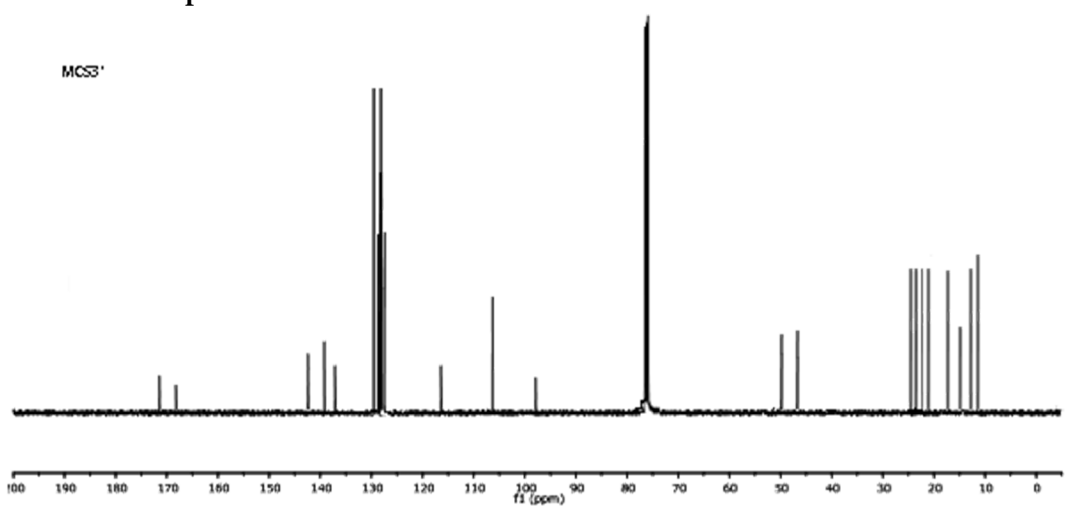
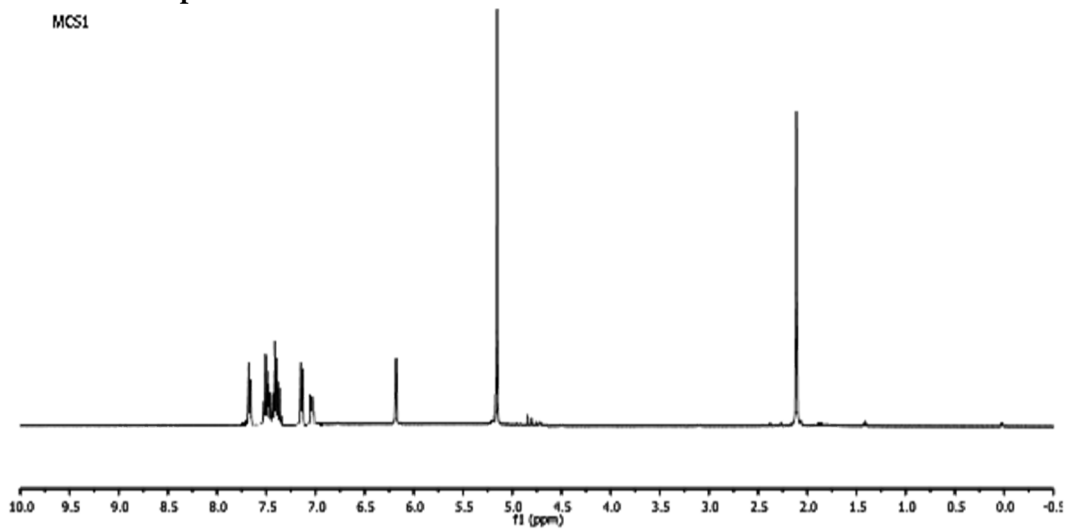
¹³C-NMR Spectrum of Compound 4c

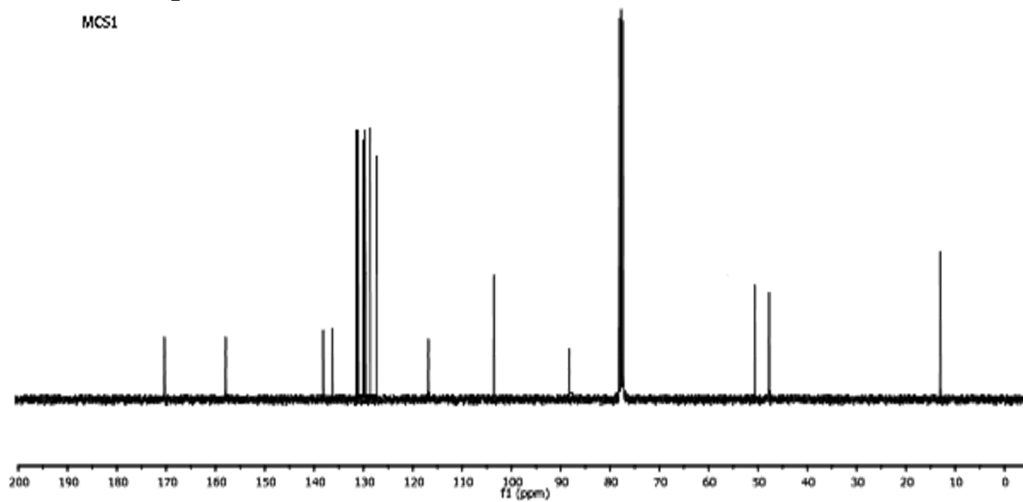
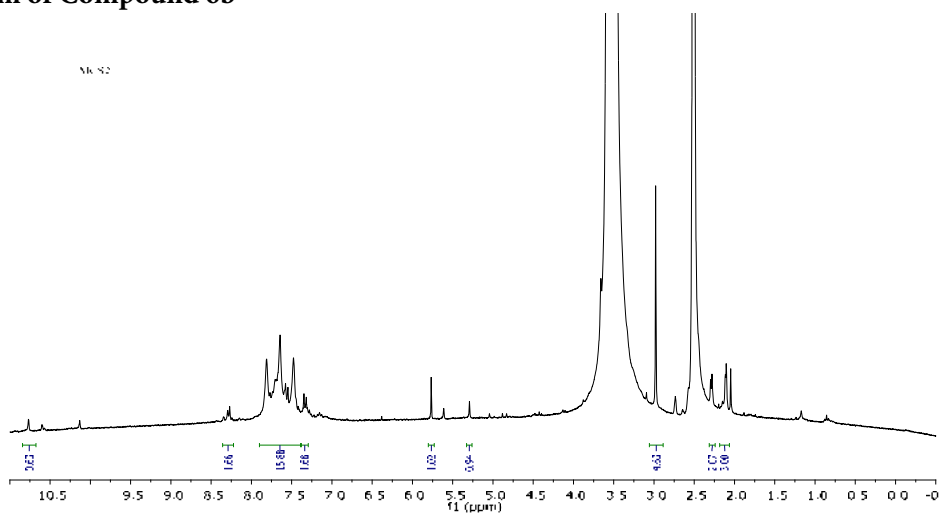
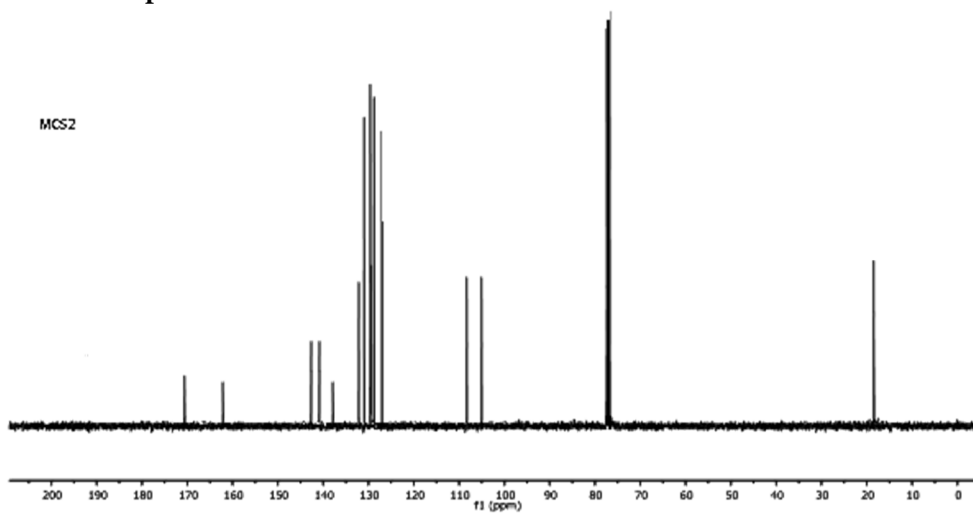


¹H-NMR Spectrum of Compound 5a

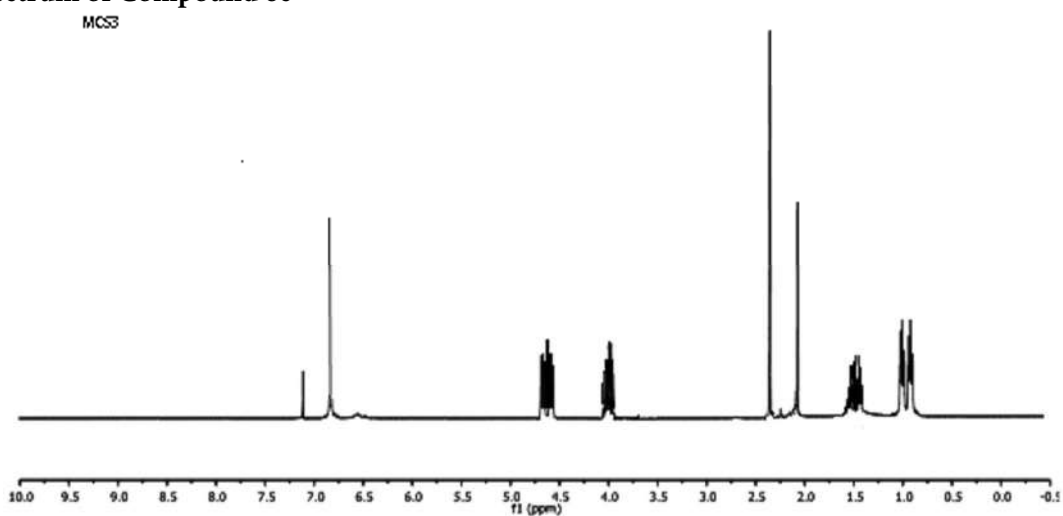


¹³C-NMR Spectrum of Compound 5a¹H-NMR Spectrum of Compound 5b¹³C-NMR Spectrum of Compound 5b

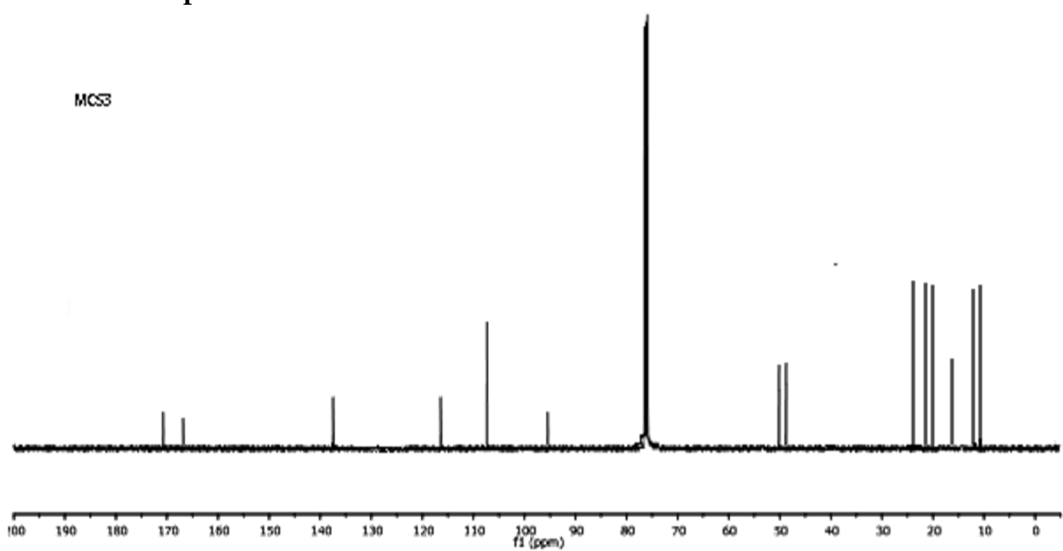
¹H-NMR Spectrum of Compound 5c**¹³C-NMR Spectrum of Compound 5c****¹H-NMR Spectrum of Compound 6a**

¹³C-NMR Spectrum of Compound 6a**¹H-NMR Spectrum of Compound 6b****¹³C-NMR Spectrum of Compound 6b**

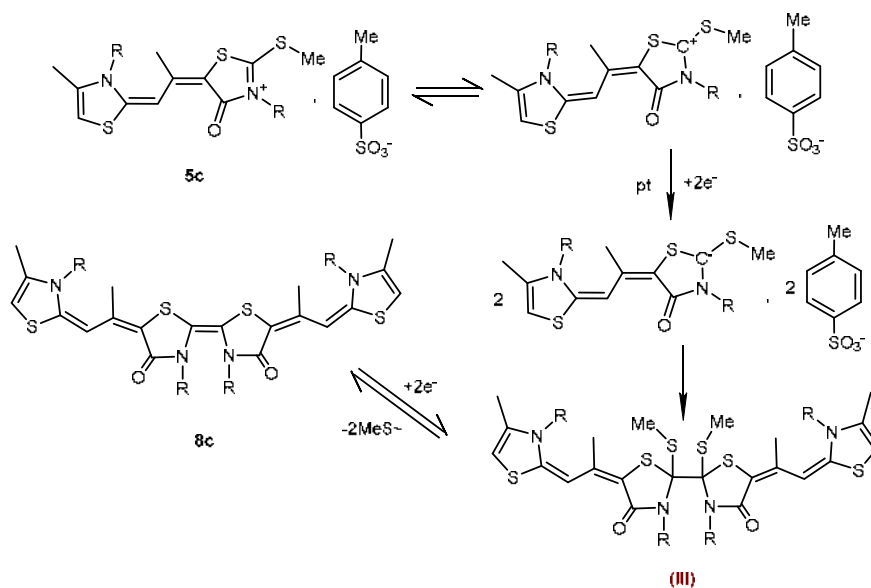
¹H-NMR Spectrum of Compound 6c



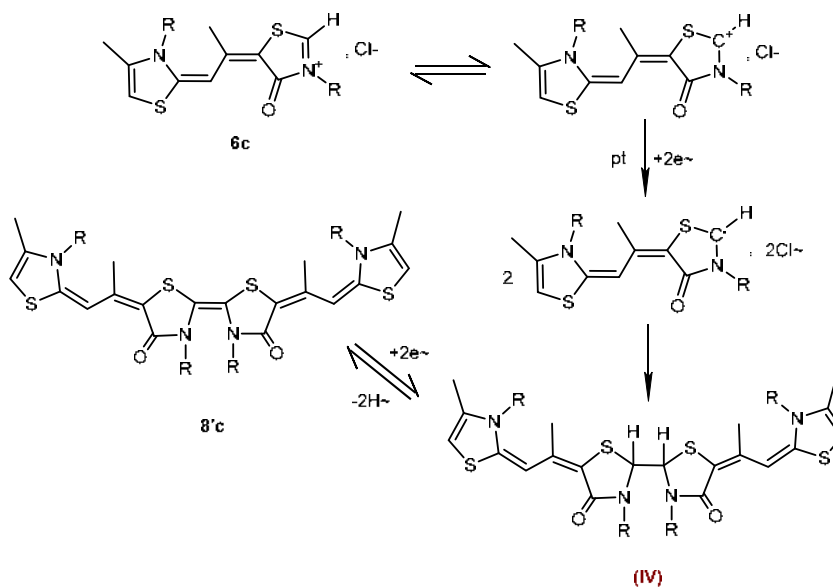
¹³C-NMR Spectrum of Compound 6c



Formation of tetrathiatetraazafulvalènes 8c and 8'c

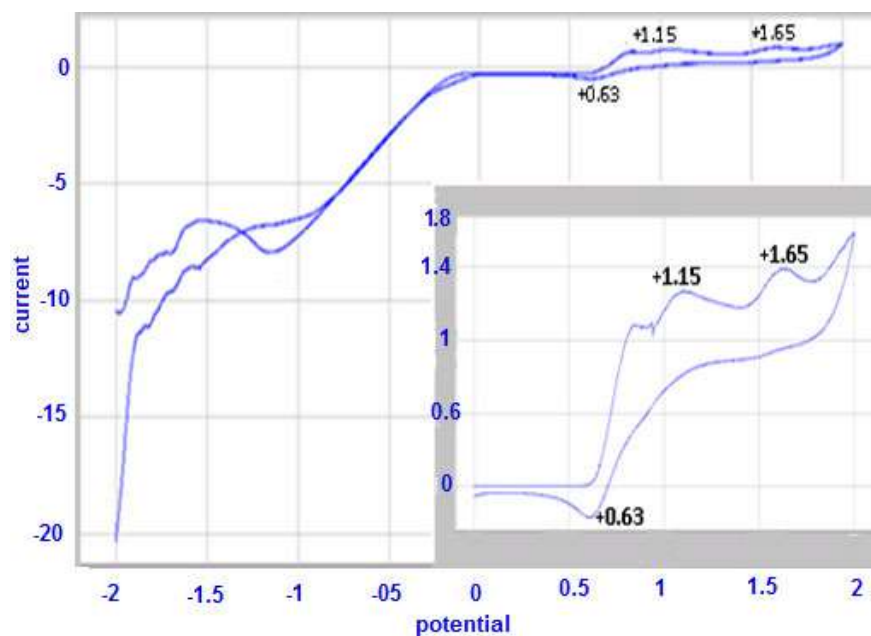


Scheme 5. The strategy of electrochemical transformation of alkylidenthiazolidenium sulfonate salt (5c) into TTTAF (8c)

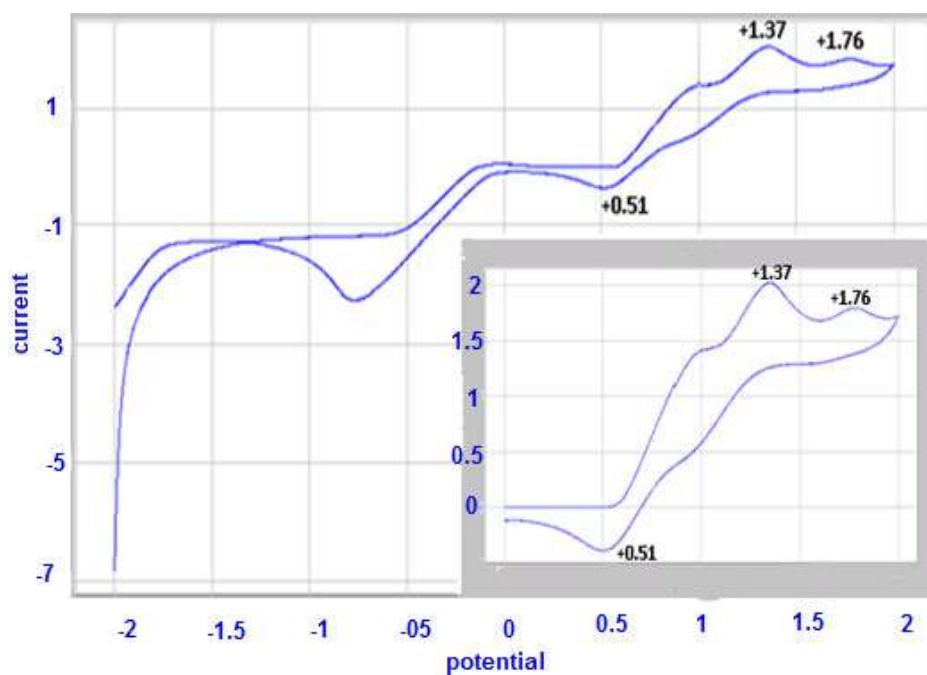


Scheme 6. The strategy of electrochemical transformation of alkylidenthiazolidenium chloride salt (6c) into TTTAF (8'c)

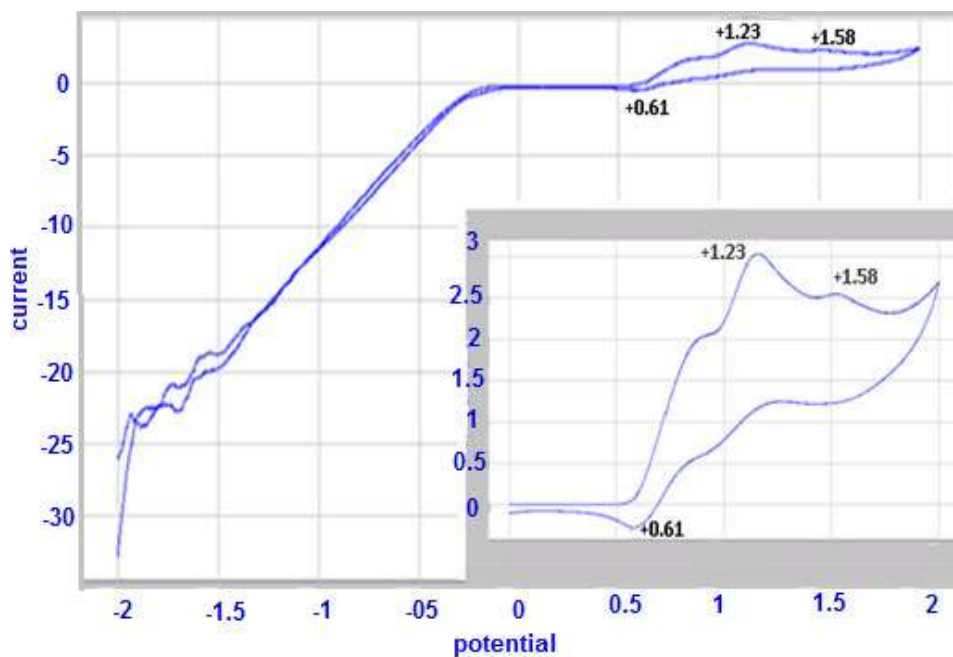
The Voltammograms obtained from the Voltalab 40 PGZ 301 potentiostat
Range: -2000/2000 and 0/2000



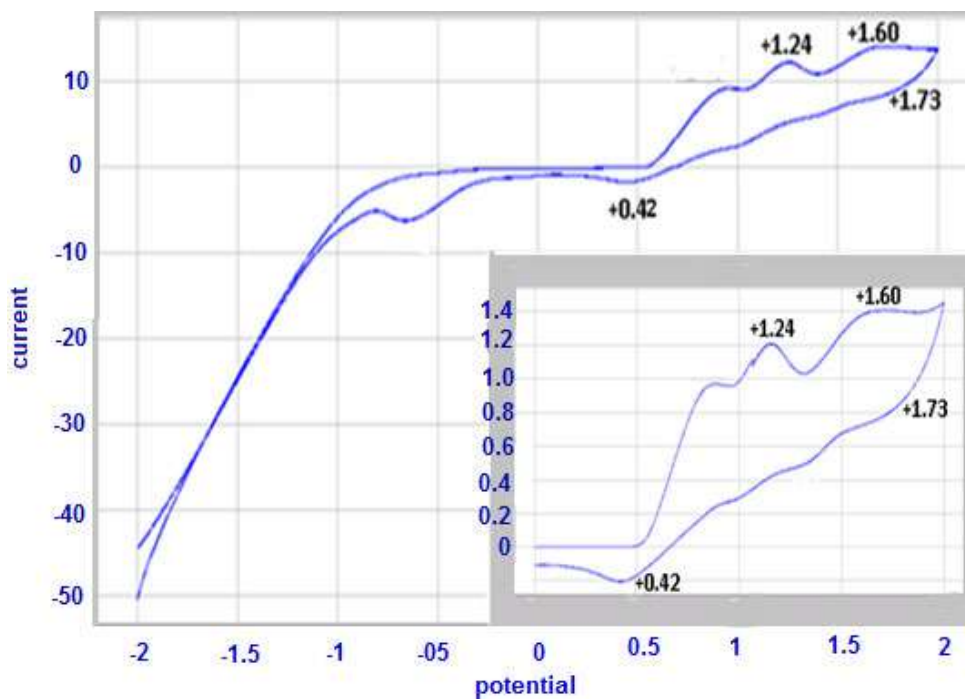
Voltammogram of compound 4a (CH_3CN , NBu_4Br 0.1 M, HClO_4 , PT, Ag/AgCl , 0.1 V/s)



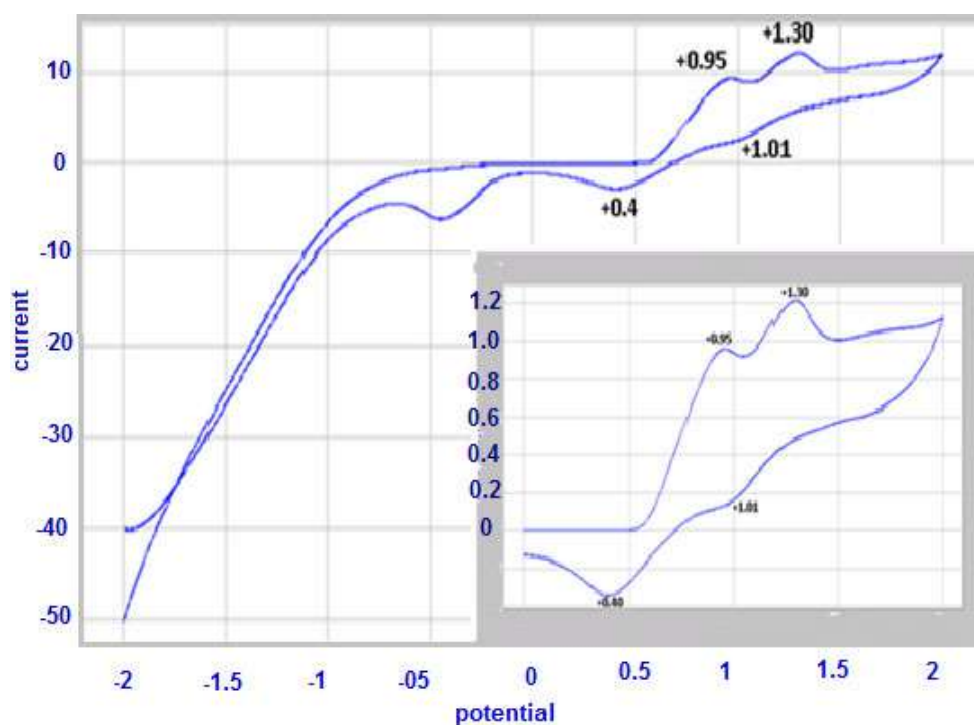
Voltammogram of compound 4b (CH_3CN , NBu_4Br 0.1 M, HClO_4 , PT, Ag/AgCl , 0.1 V/s)



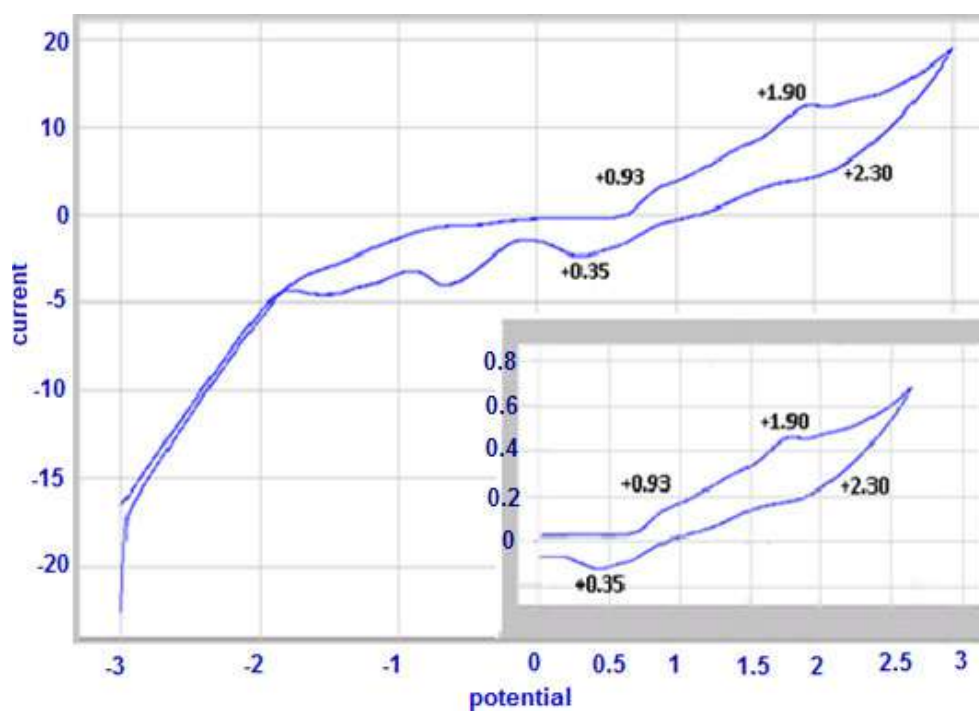
Voltammogram of compound 4c (CH_3CN , NBu_4Br 0.1 M, HClO_4 , PT, Ag/AgCl, 0.1 V/s)



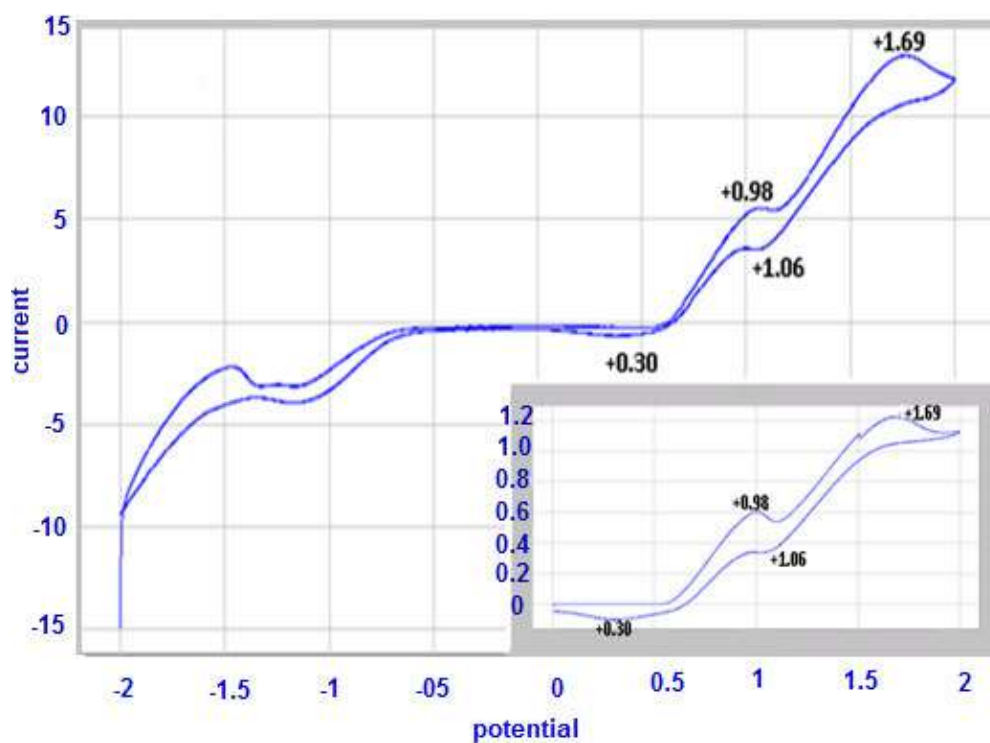
Voltammogram of compound 5a (CH_3CN , NBu_4Br 0.1 M, HClO_4 , PT, Ag/AgCl, 0.1 V/s)



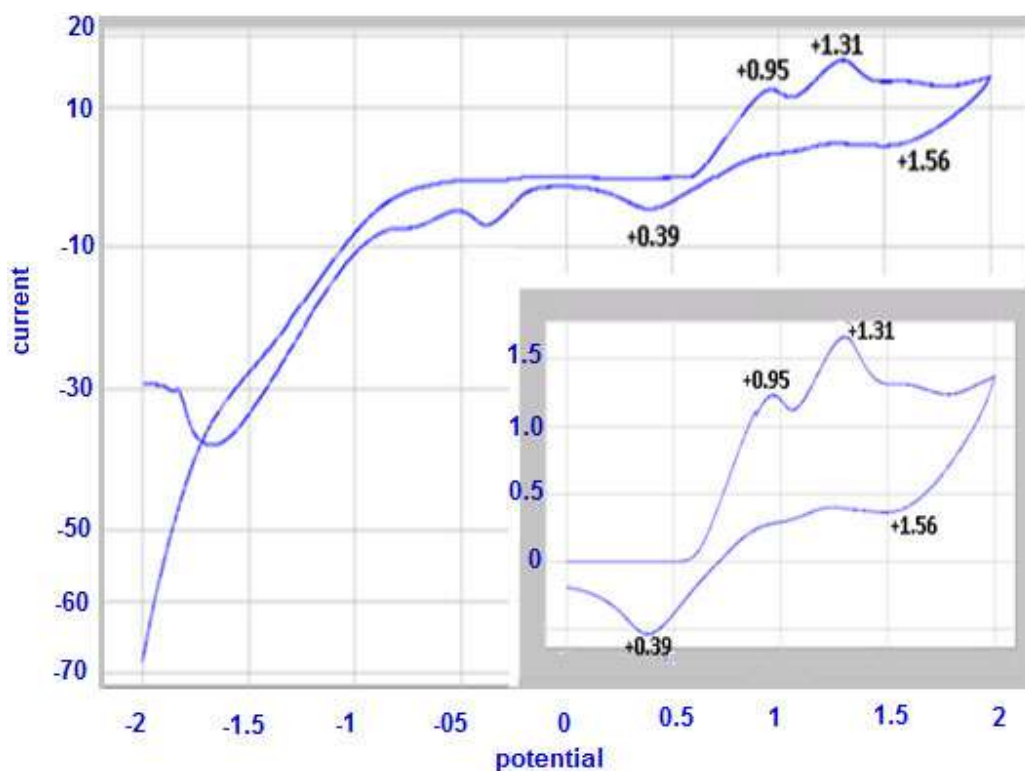
Voltammogram of compound 5b (CH_3CN , NBu_4Br 0.1 M, HClO_4 , PT, Ag/AgCl, 0.1 V/s)



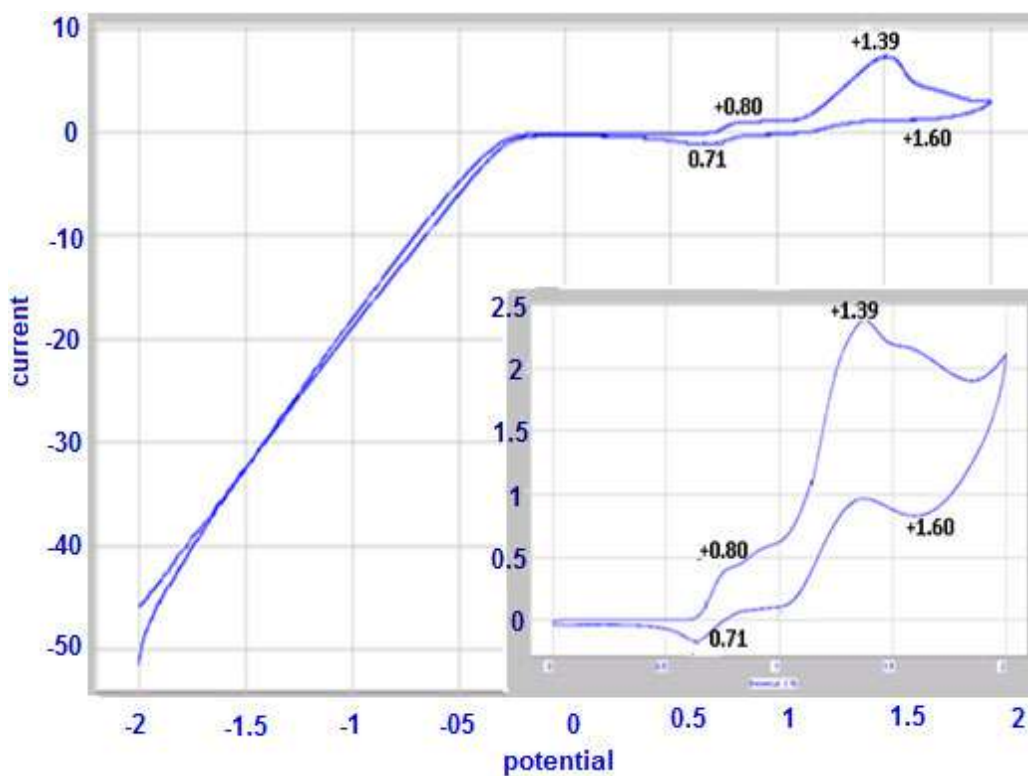
Voltammogram of compound 6a (CH_3CN , NBu_4Br 0.1M, HClO_4 , PT, Ag/AgCl, 0.1V/s)



Voltammogram of compound 6b (CH_3CN , NBu_4Br 0.1 M, HClO_4 , PT, Ag/AgCl, 0.1 V/s)



Voltammogram of compound 5c (CH_3CN , NBu_4Br 0.1 M, HClO_4 , PT, Ag/AgCl, 0.1 V/s)



Voltammogram of compound 6c (CH_3CN , NBu_4Br 0.1 M, HClO_4 , PT, Ag/AgCl, 0.1 V/s)

Study of the Electrochemical Behavior of Merocyanine and Merocarbocyanine Salts and Their Transformation into π -Electron Donor Molecules, Namely Tetrathiatetraazafulvalenes

Manel Khiat^{1*}, Fatima-Zohra Zradni¹, Souad Kasmi-Mir², and Alejandro Baeza³

¹Laboratory of Organic Synthesis, Physico-Chemistry, Biomolecules and Environment (LSPBE), Department of Chemical Engineering, Faculty of Chemistry, University of Sciences and Technology of Oran "Mohamed Boudiaf" - USTOMB, El Mnaouar, BP 1505, Bir El Djir 31000 Oran, Algeria

²Faculty of Science, Department of Chemistry, Saad Dahlab University Blida 1, 9000 Blida, Algeria

³Institute of Organic Synthesis (ISO), Faculty of Sciences, University of Alicante Carretera of San Vicente del Raspeig, s/n, 03690 Alicante, Spain

* **Corresponding author:**

tel: +213-662135178

email: t_khiatmanel@yahoo.fr

Received: July 26, 2020

Accepted: December 28, 2020

DOI: 10.22146/ijc.58132

Abstract: An electrochemical study using the cyclic voltammetry method was carried out on some previously prepared merocyanines salts, namely thiazolideniumsulfonate salts **5a-b**, and thiazolidenium chloride salts **6a-b**, and merocarbocyanines salts, namely alkylidenthiazolidenium sulfonate salt **5c**, and alkylidenthiazolidenium chloride salt **6c**. These salts are transformed by dimerization in situ in a voltammetric cell into tetrathiatetraazafulvalenes (TTAFs) **7a-b**, **7'a-b**, **8c**, and **8'c** supposed to be π -electron donor molecules due to the existing conjugation in their structure. The structure of all new chemically synthesized molecules was confirmed by IR, ¹H-NMR, ¹³C-NMR, and MS. The transformation of salts into TTAF was confirmed by a reversible voltammogram curve and the variation of observed potentials.

Keywords: rhodanines; thiazolium salts; merocyanines; tetrathiafulvalenes; dithiadiazafulvalenes; cyclic voltammetry

■ INTRODUCTION

For many years, organic materials have been considered as insulators. However, the discovery of perylene bromide in 1954 as a semi-conductor profoundly upset this vision by showing that organic materials could possess electrical conduction properties [1]. In a few decades, the development and study of organic conductors and superconductors have occupied a considerable position in the molecular sciences [2].

One of the first breakthroughs in the field of organic electrical conductors came with the discovering of the TTF (Fig. 1), endowed with a π -electron donor character [3], and TCNQ (Fig. 1) (structure b), endowed with a π -electron acceptor character [4]. The association of both motifs leads to the formation of the crystalline charge transfer complex TTF-TCNQ, which was the first organic compound with extraordinary electrical properties [5].

After this pioneering work, the synthesis of many other charge-transfer complexes by modifications made on the TTF structure has been developed. For example, the substitution of sulfur by other chalcogens such as tellurium and selenium, as in the case of tetramethyltetraselenafulvalene (TMTSeF), is called radical ionic salts of Bechgaard [6].

In addition, these TTF derivatives have been the object of many studies because of their various applications such as Self-Assembled Monolayer (SAM) systems functionalized with TTF [7-10], fructose biosensors (TTF co-immobilized on SAM) [11], metal ion sensors (complexation of crown ethers to TTF-SAM) [12-18], complexes of C60-tetrathiafulvalene [19-24], supramolecular switches [25], natural photosynthesis structures (TTF containing catenanes) [26], their use in enzymatic reactions [27-28], radical reactions [29-30],

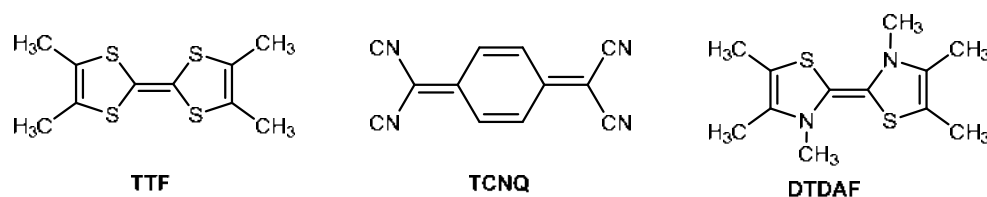


Fig 1. Structure of tetrathiafulvalene (TTF), tetracyanoquinodimethane (TCNQ) and dithiadiazafulvalene (DTDAF)

redox polymers [31-32], dendritic macromolecules incorporating TTF [33-34]. Therefore, it is not surprising that considerable efforts are being made to synthesize and study new electron-donating organic molecules, allowing synergy between physical properties, such as electrical conductivity or superconductivity and magnetic effects, optical properties or spin transition [35]. Indeed a nitrogenous derivative of the TTF has been synthesized by substituting the sulfur atoms with nitrogen ones, namely the dithiadiazafulvalenes (DTDAFs) (Fig. 1) [36].

The idea behind this work is to obtain electroactive species, analogs to TTFs, and DTDAFs, namely tetrathiatetraazafulvalenes (TTTAFs) **7a-b**, **7'a-b**, **8c**, and **8'c**, by dimerization of merocyanine salts *in situ* in an electrochemical cell. Indeed, the electrochemical studies using the cyclic Voltammetry method have been performed on thiazolidenium sulfonate salts **5a-b**, thiazolidenium chloride salts **6a-b**, alkylidenthiazolidenium sulfonate salt **5c**, and alkylidenthiazolidenium chloride salt **6c** as precursor candidates to demonstrate their redox behavior, their cathodic coupling, and consequently their transformation into TTTAFs.

■ EXPERIMENTAL SECTION

Materials

The chemicals and reagents used for the synthesis were purchased at 99% purity from commercial sources (Biochem Chemopharma and Sigma-Aldrich companies in France).

Instrumentation

The conversion of the reactions and purity of the synthesized compounds was verified by thin-layer chromatography (TLC) on silica gel G. The melting points were determined on a Buchi apparatus (melting

point B-545). Infrared spectroscopy (IR) was recorded using KBr pellets, in a Fourier transform spectrophotometer JASCO FT/IR between 400 and 4000 cm^{-1} , NMR spectra were recorded on Bruker Avance 400 spectrometer (400 MHz for ^1H and 101 MHz for ^{13}C), using CDCl_3 , DMSO- d_6 as a solvent. The values of the chemical shifts are expressed in scale delta part per million (δ ppm) compared to tetramethylsilane (TMS) used as an internal standard. Mass spectra were obtained on the GCMS\QP mass spectrometer at 70 eV. The cyclic voltammetry was carried out with Voltalab 40 PGZ 301 potentiostat. The counter electrode was a platinum (Pt) wire, and the reference electrode an Ag/AgCl electrode. The working electrode was a platinum disk ($A = 1 \text{ mm}^2$).

Procedure

General procedure for the synthesis of thioxothiazolidinones (1a-b) and alkylidenthioxothiazolidinone (1c)

Under magnetic stirring at 0 °C, in a 250 mL round-bottom flask, 0.1 mol of primary amine (RNH_2) and 0.18 mol (20 mL) of concentrated ammonium hydroxide (NH_4OH) were mixed for 15 min. Then 0.1 mol (7 mL) of carbon disulfide (CS_2) was added dropwise to the mixture. After stirring for 2 h, the dithiocarbamate salt (DTC) formed was filtered and then washed several times with diethyl ether or recovered using a separating funnel if it is a liquid. The DTC prepared was dissolved in 150 mL of water, and 0.11 mol (10.6 g) of chloroacetic acid were added in two portions, under magnetic stirring for 2 h at 0 °C. The reaction mixture is then heated in a bath between 60–70 °C for 3 h. After cooling down to room temperature, the precipitate was separated by decantation to give thioxothiazolidinones (**1a-b**) as crystals and (**1c**) as a liquid. A water/acetone mixture was added to the

compound **1c** with stirring and was heated at 60 °C. After cooling down to room temperature, the mixture is left standing for 48 h to obtain the alkylideneethioxothiazolidinone (**3c**) in the form of orange crystals.

3-Benzyl-2-thioxo-1,3-thiazolidin-4-one (1a). Beige crystals; Yield: 68%; M.p.: 74 °C; R_f : 0.80 (ethyl acetate/methanol 6:4). IR (KBr, ν cm^{-1}): 3086.9 (C–H aromatic), 2963.6 (C–H aliphatic), 1698.9 (C=O), 1582.8, 1452.2 (C=C aromatic), 1164.5 (C=S). $^1\text{H-NMR}$ (400 MHz, CDCl_3) δ 7.52–7.41 (m, 1H), 7.38–7.26 (m, 2H), 5.20 (s, 1H), 3.97 (s, 1H). $^{13}\text{C-NMR}$ (101 MHz, CDCl_3) δ 201.08 (–C=S), 173.87 (–C=O), 134.69 (C, Ar), 129.06 (CH, Ar), 128.91 (CH, Ar), 128.58 (CH, Ar), 128.41 (CH, Ar), 128.21 (CH, Ar), 127.56 (CH, Ar), 47.61 (H₂C–N), 35.42 (–S–CH₂). Mass spectrum, m/z: 223.1.

3-Phenyl-2-thioxo-1,3-thiazolidin-4-one (1b). Clear Yellow Crystals; Yield: 59%; M.p.: 115 °C; R_f : 0.35 (ethyl acetate/ methanol 6:4). IR (KBr, ν cm^{-1}): 3086.9 (C–H aromatic), 2964.3 (C–H aliphatic), 1731.5 (C=O), 1582.5–1452.4 (C=C aromatic), 1165.7 (C=S). $^1\text{H-NMR}$ (400 MHz, CDCl_3) δ 8.11 (s, 1H), 7.77–7.52 (m, 1H), 7.51–7.34 (m, 4H), 7.34–7.11 (m, 3H), 4.85 (s, 1H), 4.20 (s, 1H). $^{13}\text{C-NMR}$ (101 MHz, CDCl_3) δ 201.26 (–C=S), 173.52 (–C=O), 137.12 (C, Ar), 130.18 (CH, Ar), 129.79 (CH, Ar), 129.65 (CH, Ar), 129.57 (CH, Ar), 128.36 (CH, Ar), 127.68 (CH, Ar), 36.45 (–S–CH₂). Mass spectrum, m/z: 209.0.

3-Propyl-2-thioxothiazolidin-4-one (1c). Brown oily liquid; Yield: 62%; R_f : 0.78 (ethyl acetate/methanol 6:4). IR (KBr, ν cm^{-1}): 2966.5 (C–H aliphatic), 1736.1 (C=O), 1187.7 (C=S), 1088.4 (C–N). $^1\text{H-NMR}$ (400 MHz, CDCl_3) δ 4.37 (s, 1H), 3.79 (d, 1H), 1.58 (m, 1H), 0.86 (t, 1H). $^{13}\text{C-NMR}$ (101 MHz, CDCl_3) δ 198.32 (–C=S), 169.81 (–C=O), 46.27 (N–CH₂), 36.75 (–S–C–), 21.54 (H₂C–C–), 11.28 (CH₃). Mass spectrum, m/z: 215.1.

5-(Propan-2-ylidene)-3-propyl-2-thioxo-1,3-thiazolidin-4-one (3c). Orange crystals; Yield: 59%; M.p.: 33 °C; R_f : 0.81 (ethyl acetate/methanol 6:4). IR (KBr, ν cm^{-1}): 3084.32 (C–H aliphatic), 1783.15 (C=O), 1635.93 (C=C), 1157.40 (C=S). $^1\text{H-NMR}$ (400 MHz, CDCl_3) δ 4.01 (d, 2H), 2.45 (s, 3H), 2.02 (s, 3H), 1.75–1.65 (m, 2H), 0.95 (t, 3H). $^{13}\text{C-NMR}$ (101 MHz, CDCl_3) δ 192.99 (–C=S),

165.37 (–C=O), 149.76 (–C=C–S–), 120.99 (=C–S–), 45.84 (N–CH₂), 21.70 (H₂C–CH₂–), 20.35 (H₃C–C=C), 11.26 (CH₃). Mass spectrum, m/z: 215.1.

General procedure for the synthesis of thiazolinethiones (2a-c)

In a 250 mL round-bottom flask, 0.18 mol of concentrated ammonium hydroxide was mixed with 0.1 mol of a primary amine (RNH₂) under magnetic stirring at 0 °C. After 15 min, 0.1 mol of carbon disulfide was added dropwise to the mixture, and the stirring was maintained for 2 h. The dithiocarbamate salt formed was filtered and then washed several times with diethyl ether or recovered using a separating funnel if it is a liquid. The DTC prepared was dissolved in 200 mL of water. Chloroacetone (0.15 mol) was added in two portions. The pH must be acidic (2 to 3). The reaction mixture was then heated in a water bath at 60–70 °C for 2 h. The precipitate was separated by filtration and recrystallized from ethanol.

3-Benzyl-4-methyl-1,3-thiazole-2(3H)-thione (2a). Beige crystals; Yield: 83.55%; M.p.: 91 °C; R_f : 0.76 (Dichloromethane/Methanol 6:4). IR (KBr, ν cm^{-1}): 3075.1 (C–H aromatic), 2956.6 (C–H aliphatic), 1635.0 (C=C aliphatic), 1488.6–1404.6 (C=C aromatic), 1166.4 (C=S). $^1\text{H-NMR}$ (400 MHz, CDCl_3) δ 7.39–7.26 (m, 3H), 7.24–7.16 (m, 2H), 6.28 (d, 1H), 5.53 (s, 2H), 2.15 (d, 3H). $^{13}\text{C-NMR}$ (101 MHz, CDCl_3) δ 189.26 (–C=S), 140.13 (N–C=C), 134.84 (C, Ar), 128.91 (CH, Ar), 127.85 (CH, Ar), 126.64 (CH, Ar), 106.17 (S–HC=C), 50.11 (H₂C–N), 15.60 (CH₃). Mass spectrum, m/z: 221.1.

4-Methyl-3-phenyl-1,3-thiazole-2(3H)-thione (2b). Beige crystals; Yield: 61.55%; M.p.: 124 °C; R_f : 0.82 (Dichloromethane/Methanol 6:4). IR (KBr, ν cm^{-1}): 3097.5 (C–H aromatic), 2957.2 (C–H aliphatic), 1635.1 (C=C aliphatic), 1486.4 (C=C aromatic), 1225.6 (C=S). $^1\text{H-NMR}$ (400 MHz, CDCl_3) δ 7.65–7.48 (m, 1H), 7.29–7.19 (m, 1H), 6.36 (q, 1H), 1.96 (d, 1H). $^{13}\text{C-NMR}$ (101 MHz, CDCl_3) δ 190.17 (–C=S), 140.19 (N–C=C), 137.79 (C, Ar), 129.97 (CH, Ar), 129.70 (CH, Ar), 128.16 (CH, Ar), 106.42 (S–HC=C), 16.19 (CH₃). Mass spectrum, m/z: 206.1.

4-Methyl-3-propyl-1,3-thiazole-2(3H)-thione (2c). Beige crystals; Yield: 76.52%; M.p.: 83 °C; R_f : 0.65

(Dichloromethane/Methanol 6:4). IR (KBr, ν cm^{-1}): 3093.9 (C–H aromatic), 2944.9 (C–H aliphatic), 1634.5 (C=C aliphatic), 1226.8 (C=S). $^1\text{H-NMR}$ (400 MHz, CDCl_3) δ 6.26 (d, 1H), 4.16–4.06 (m, 1H), 2.29 (d, 1H), 1.86–1.71 (m, 1H), 0.99 (t, 1H). $^{13}\text{C-NMR}$ (101 MHz, CDCl_3) δ 187.85 (–C=S), 139.59 (N–C=C), 106.31 (S–HC=C), 48.77 ($\text{H}_2\text{C-N}$), 20.98 (CH_2), 15.43 (CH_3), 11.21 (CH_3). Mass spectrum, m/z : 173.1.

General procedure for the synthesis of thiazolium salts (3a-b)

In a flask containing 100 mL of acetone, 5 mmol of thiazolinethione already prepared was mixed with 15 mmol of methyl iodide (MeI). The mixture was stirred at room temperature for 24 h. The salt obtained was filtered and then washed with acetone.

3-Benzyl-4-methyl-2-(methylsulfanyl)-1,3-thiazol-3-ium-iodide (3a). White crystals; Yield: 60.58%; M.p.: 139 °C; R_f : 0.71. IR (KBr, ν cm^{-1}): 3026.7 (C–H aromatic), 2949.1 (C–H aliphatic), 1634.8 (C=C aliphatic), 1491.2–1405.8 (C=C aromatic), 1077 (C–S). $^1\text{H-NMR}$ (400 MHz, DMSO) δ 7.93 (s, 1H), 7.45–7.33 (m, 9H), 7.27–7.09 (m, 5H), 5.61 (s, 5H), 2.99 (s, 7H), 2.53–2.50 (m, 4H), 2.45 (d, 7H). $^{13}\text{C-NMR}$ (101 MHz, DMSO) δ 177.16 (–C=S), 146.61 (N–C=C), 132.61 (C, Ar), 129.63 (CH, Ar), 129.00 (CH, Ar), 127.13 (CH, Ar), 118.24 (S–HC=C), 53.49 ($\text{H}_2\text{C-N}$), 18.54 (–S– CH_3), 14.36 (CH_3).

4-Methyl-2-(methylsulfanyl)-3-phenyl-1,3-thiazol-3-ium-iodide (3b). Beige crystals; Yield: 53.64%; M.p.: 132 °C; R_f : 0.78. IR (KBr, ν cm^{-1}): 3095.6 (C–H aromatic), 2944.8 (C–H aliphatic), 1634.0 (C=C aliphatic), 1484.1 (C=C aromatic), 1077 (C–S). $^1\text{H-NMR}$ (400 MHz, DMSO) δ 7.99 (d, 1H), 7.82–7.63 (m, 5H), 3.74 (s, 1H), 2.91 (s, 3H), 2.16 (d, 3H). $^{13}\text{C-NMR}$ (101 MHz, DMSO) δ 179.02 (–C=S), 146.36 (N–C=C), 135.19 (C, Ar), 132.43 (CH, Ar), 131.28 (CH, Ar), 127.35 (CH, Ar), 117.73 (S–HC=C), 18.30 (–S– CH_3), 14.60 (CH_3).

General procedure for the synthesis of merocyanines (4a-b) and merocarbocyanines (4c)

1st Method: In a flask containing 20 mL of acetone and under magnetic stirring, 10 mmol of thiazolium salt (3a-b) was mixed with 10 mmol of rhodanine (1a-b) or arylidenerhodanine (3c) already prepared, and 2 mL of triethylamine was added to the mixture. After stirring for

24 h at room temperature or 1 h at reflux, the precipitate was separated by filtration and recrystallized from a mixture of Ethanol/ DMF.

2nd Method: In a flask containing 20 mL of acetonitrile and under magnetic stirring, 10 mmol of thiazolinethione (2a-c) was mixed with 15 mmol of dimethyl sulfate. After heating for 1 h and cooling back to room temperature, 10 mmol of rhodanine (1a-b) or arylidenerhodanine (3c) and 2 mL of triethylamine were added. Immediate formation of a solid was noticed. The reaction is left for 1 h at reflux until the release of CH_3SH . The resulting solid was filtered and recrystallized from a mixture (Ethanol/DMF).

(5E)-3-Benzyl-5-(3-benzyl-4-methyl-1,3-thiazol-2(3H)-ylidene)-2-thioxo-1,3-thiazolidin-4-one (4a). Yellow crystals; Yield: 84.21%; M.p.: 191 °C; R_f : 0.30 (ethyl acetate/methanol 6:4). IR (KBr, ν cm^{-1}): 3078.2 (C–H aromatic), 2958.4 (C–H aliphatic), 1891.6 (C=O), 1624.3 (C=C aliphatic), 1597.2–1429.6 (C=C aromatic), 1192.7 (C=S). $^1\text{H-NMR}$ (400 MHz, CDCl_3) δ 7.59–7.50 (m, 1H), 7.42–7.33 (m, 1H), 7.32–7.18 (m, 1H), 7.02 (d, 1H), 6.39 (d, 1H), 5.33 (d, 1H). $^{13}\text{C-NMR}$ (101 MHz, CDCl_3) δ 186.80 (–C=S), 165.16 (–C=O), 156.94 (–S–C=C), 137.72 (C, Ar), 135.77 (C, Ar), 133.91 (CH, Ar), 129.49 (CH, Ar), 129.03 (CH, Ar), 128.51 (CH, Ar), 128.34 (CH, Ar), 127.63 (CH, Ar), 125.25 (N–C=C), 105.29 (S–HC=C), 82.40 (–C=C–S–), 50.62 (N– CH_2 –C=C), 47.74 (N– CH_2 –C=C), 14.10 (CH_3).

(5E)-5-(4-Methyl-3-phenyl-1,3-thiazol-2(3H)-ylidene)-3-phenyl-2-thioxo-1,3-thiazolidin-4-one (4b). Yellow crystals; Yield: 81.53%; M.p.: 235 °C; R_f : 0.27 (ethyl acetate/methanol 6:4). IR (KBr, ν cm^{-1}): 3078.2 (C–H aromatic), 2959.6 (C–H aliphatic), 1883.3 (C=O), 1634.3 (C=C aliphatic), 1591.0–1482.8 (C=C aromatic), 1228.4 (C=S). $^1\text{H-NMR}$ (400 MHz, CDCl_3) δ 7.77–7.68 (m, 1H), 7.65 (t, 2H), 7.55–7.48 (m, 2H), 7.47–7.42 (m, 1H), 7.39–7.35 (m, 2H), 7.31–7.26 (m, 2H), 6.39 (d, 1H), 1.95 (d, 3H). $^{13}\text{C-NMR}$ (101 MHz, CDCl_3) δ 189.07 (–C=S), 165.45 (–C=O), 155.74 (–S–C=C), 137.56 (N–C=C), 136.14 (C, Ar), 135.07 (C, Ar), 131.79 (CH, Ar), 130.62 (CH, Ar), 129.28 (CH, Ar), 129.26 (CH, Ar), 129.04 (CH, Ar), 128.43 (CH, Ar), 104.34 (–S–C=C), 84.68 (–S–C=C), 14.49 (CH_3).

(E)-5-((E)-1-(4-Methyl-3-propylthiazol-2(3H)-ylidene)propan-2-ylidene)-3-propyl-2-thioxothiazolidin-4-one (4c). Purple crystals; Yield: 87.32%; M.p.: 149 °C; R_f : 0.64 (ethyl acetate/methanol 6:4). IR (KBr, ν cm^{-1}): 2964.32 (C-H aliphatic), 2876.73 (C-H aliphatic), 1704.83 (C=O), 1615.61 (C=C aliphatic), 1150.47 (C=S). $^1\text{H-NMR}$ (400 MHz, CDCl_3) δ 8.06 (s, 1H), 7.28 (s, 1H), 6.20 (s, 1H), 5.27 (d, 1H), 4.49–3.68 (m, 5H), 3.29–1.59 (m, 14H), 1.38–0.75 (m, 8H), 0.37–0.17 (m, 1H). $^{13}\text{C-NMR}$ (101 MHz, CDCl_3) δ 187.79 (–C=S), 163.45 (–C=O), 160.01 (C=C–C), 146.80 (N=C=C), 138.90 (N=C=C), 102.28 (S=C=), 96.03 (=C–H), 48.39 (N– CH_2), 45.88 (N– CH_2), 23.02 (CH_2), 20.62 (CH_2), 20.48(CH_3), 14.74(CH_3), 11.42 (CH_3), 11.3(CH_3).

Note: when the merocyanines (**4a-b**) and merocarbocyanines (**4c**) were injected into the mass spectroscopy apparatus, they decompose because of their instability.

General procedure for the synthesis of thiazolidenium sulfonate salts (5a-b) and alkylidenthiazolidenium sulfonate salt (5c)

A mixture of 5 mmol of thiazolydenethioxothiazolidinones or alkylidenthiazolydene-thioxothiazolidinone, 15 mmoles of methylparatoluenesulphonate (MPTS), and 5 mL of DMF is stirred at 110–120 °C for 4 h. After this time, the reaction mixture is cooled down to 40 °C, and then 50 mL of acetone were added. When the reaction is complete, the mixture is left to reach room temperature and then refrigerated overnight. The corresponding salt obtained is filtered and dried under a vacuum.

(E)-3,3'-Dibenzyl-4-methyl-2'-(methylthio)-4'-oxo-3H,4'H-[2,5'-bithiazolylidene]-3'-ium-4-methylbenzene sulfonate (5a). Brown crystals; Yield: 78.96%; M.p.: 239 °C. $^1\text{H-NMR}$ (400 MHz, DMSO) δ 8.12–7.96 (m, 2H), 7.75–7.69 (m, 2H), 7.64–7.60 (m, 1H), 7.51–7.42 (m, 1H), 7.38–7.33 (m, 2H), 7.29–7.26 (m, 3H), 7.24 (m, 1H), 7.20–7.18 (m, 2H), 5.98 (d, 1H), 4.49 (d, 2H), 3.52 (d, 2H), 2.73 (s, 3H), 2.61 (d, 3H), 2.14 (d, 3H). $^{13}\text{C-NMR}$ (101 MHz, DMSO) δ 174.21 (–C=O), 160.14 (C=N), 149.27 (C, Ar–S=O), 140.02 (C, Ar), 138.73 (C, Ar), 136.94 (C, Ar), 131.58 (CH, Ar), 131.20 (CH, Ar), 130.98 (CH, Ar), 130.64 (CH, Ar), 129.86 (CH, Ar), 128.52 (CH, Ar), 126.09 (CH, Ar), 117.20 (N=C=C), 108.87 (S=C=C),

105.78 (S=C=C), 52.73 (N– CH_2 –C=C), 49.63 (N– CH_2 –C=C), 22.06 (CH_3), 15.37 (CH_3), 14.25 (CH_3).

(E)-4-Methyl-2'-(methylthio)-4'-oxo-3,3'-diphenyl-3H,4'H-[2,5'-bithiazolylidene]-3'-ium-4-methylbenzenesulfonate (5b). Brown crystals; Yield: 71.24%; M.p.: 256 °C. $^1\text{H-NMR}$ (400 MHz, DMSO) δ 10.65–10.58 (m, 2H), 8.29–8.17 (m, 2H), 7.96 (m, 2H), 7.58 (m, 2H), 7.89–7.78 (m, 1H), 7.46–7.42 (m, 2H), 7.37–7.30 (m, 1H), 7.26–7.22 (m, 2H), 5.64 (d, 1H), 2.68 (s, 3H), 2.54 (d, 3H), 1.98 (d, 3H). $^{13}\text{C-NMR}$ (101 MHz, DMSO) δ 175.13 (–C=O), 165.85 (N=C), 144.15 (C, Ar), 143.57 (C–S=O), 141.96 (C, Ar), 140.09 (C, Ar), 139.65 (N=C=C), 133.24 (CH, Ar), 132.11 (CH, Ar), 131.02 (CH, Ar), 130.64 (CH, Ar), 129.98 (CH, Ar), 109.45 (S=C=C), 106.13 (S=C=C), 23.13 (CH_3), 19.20 (CH_3), 17.09 (CH_3).

(E)-5-((E)-1-(4-Methyl-3-propylthiazol-2(3H)-ylidene)propan-2-ylidene)-2-(methylthio)-4-oxo-3-propyl-4,5-dihydrothiazol-3-ium-4-methylbenzenesulfonate (5c). Brown crystals; Yield: 84.53%; M.p.: 198 °C. $^1\text{H-NMR}$ (400 MHz, DMSO) δ 8.23–8.14 (m, 2H), 7.80–7.72 (m, 2H), 6.98 (d, 1H), 6.23 (s, 1H), 4.28 and 3.56 (2 \times m, 2 \times 2H), 2.71 (s, 3H), 2.58 (d, 3H), 2.41 (d, 3H), 2.20 (d, 3H), 1.57–1.43 (m, 4H), 1.11–0.80 (2 \times m, 2 \times 3H). $^{13}\text{C-NMR}$ (101 MHz, DMSO) δ 171.02 (–C=O), 168.25 (C=C–C), 142.97 (C–S=O), 140.28 (C, Ar), 138.97 (N=C=C), 130.64 (CH, Ar), 128.94 (CH, Ar), 116.17 (N=C=C), 105.82 (S=C=C), 97.58 (–C=C), 50.18 (N– CH_2), 46.32 (N– CH_2), 24.09 (CH_2), 22.76 (CH_3), 21.98 (CH_3), 21.02 (CH_2), 16.95 (CH_3), 15.46 (CH_3), 12.41 (CH_3), 11.29 (CH_3).

General procedure for the synthesis of thiazolidenium chloride salts (6a-b) and alkylidenthiazolidenium chloride salt (6c)

At 0 °C, a mixture of 10 mL of acetonitrile (CH_3CN), 2 mmol of merocyanine or merocarbocyanines already prepared, 0.5 mL of 12 N hydrochloric acid (HCl), and 0.8 mL of hydrogen peroxide (H_2O_2) 30% were placed in a flask under stirring. The reaction can be exothermic. Stirring is maintained for 40 min or more until a homogeneous mixture appears, then 0.5 g of Barium chloride BaCl_2 (2 mmol) contained in 5 mL of H_2O was added. The mixture is stirred for 1 to 2 h until BaSO_4 precipitates.

The mixture was filtered to remove BaSO₄, and the thiazolidenium salt was crystallized in methanol (MeOH). **(E)-3,3'-Dibenzyl-4-methyl-4'-oxo-3H,4'H-[2,5'-bithiazolylidene]-3'-ium-chloride (6a)**. Beige crystals; Yield: 68.20%; M.p.: 221 °C. ¹H-NMR (400 MHz, DMSO) δ 7.68–7.63 (m, 1H), 7.54–7.46 (m, 1H), 7.43–7.37 (m, 1H), 7.34–7.30 (m, 2H), 7.28 (m, 1H), 7.21–7.19 (m, 2H), 6.25 (d, 1H), 5.20 (d, 1H), 2.19 (d, 3H). ¹³C-NMR (101 MHz, DMSO) δ 170.11 (–C=O), 158.64 (–N–C=C), 138.86 (C, Ar), 136.57 (C, Ar), 132.74 (CH, Ar), 128.69 (CH, Ar), 128.43 (CH, Ar), 128.26 (CH, Ar), 128.13 (CH, Ar), 127.78 (CH, Ar), 116.85 (N–C=C), 104.16 (S–C=C), 89.44 (–C=C–S–), 51.36 (N–CH₂–C=C), 48.52 (N–CH₂–C=C), 14.07 (CH₃).

(E)-4-Methyl-4'-oxo-3,3'-diphenyl-3H,4'H-[2,5'-bithiazolylidene]-3'-ium (6b). Beige crystals; Yield: 75.92%; M.p.: 240 °C. ¹H-NMR (400 MHz, DMSO) δ 10.79–10.72 (m, 1H), 8.32–8.22 (m, 2H), 7.92–7.80 (m, 1H), 7.52–7.47 (m, 2H), 7.40–7.35 (m, 1H), 7.28–7.26 (m, 2H), 5.86–5.70 (d, 1H), 2.07 (d, 3H). ¹³C-NMR (101 MHz, DMSO) δ 170.36 (–C=O), 162.05 (N–C=C), 143.98 (C, Ar), 141.02 (C, Ar), 138.87 (N–C=C), 132.11 (CH, Ar), 132.11 (CH, Ar), 131.02 (CH, Ar), 130.64 (CH, Ar), 129.98 (CH, Ar), 128.62 (CH, Ar), 108.69 (S–C=C), 105.20 (S–C=C), 18.97 (CH₃).

(E)-5-(Z)-1-(5-Methyl-1-propyl-1,3-dihydro-2H-pyrrol-2-ylidene)propan-2-ylidene-4-oxo-3-propyl-4,5-dihydrothiazol-3-ium-chloride (6c). Beige crystals; Yield: 85.22%; M.p.: 175 °C. ¹H-NMR (400 MHz, DMSO) δ 7.15 (d, 1H), 6.88 (s, 1H), 4.57–4.51 (m, 2H), 3.95–4.07 (m, 2H), 2.45 (d, 1H), 2.24 (d, 1H), 1.60–1.47 (m, 4H), 1.12–0.92 (m, 6H). ¹³C-NMR (101 MHz, DMSO) δ 170.53 (–C=O), 167.46 (C=C–C), 139.22 (N–C=C), 116.05 (N–C=C), 105.21 (S–C=C), 96.38 (–C=C), 50.12 (N–CH₂), 49.73 (N–CH₂), 23.72 (CH₂), 21.15 (CH₃), 20.69 (CH₂), 15.18 (CH₃), 12.05 (CH₃), 10.91 (CH₃).

General procedure for the study of the transformation of merocyanines and merocarbocyanines salts to TTAFs

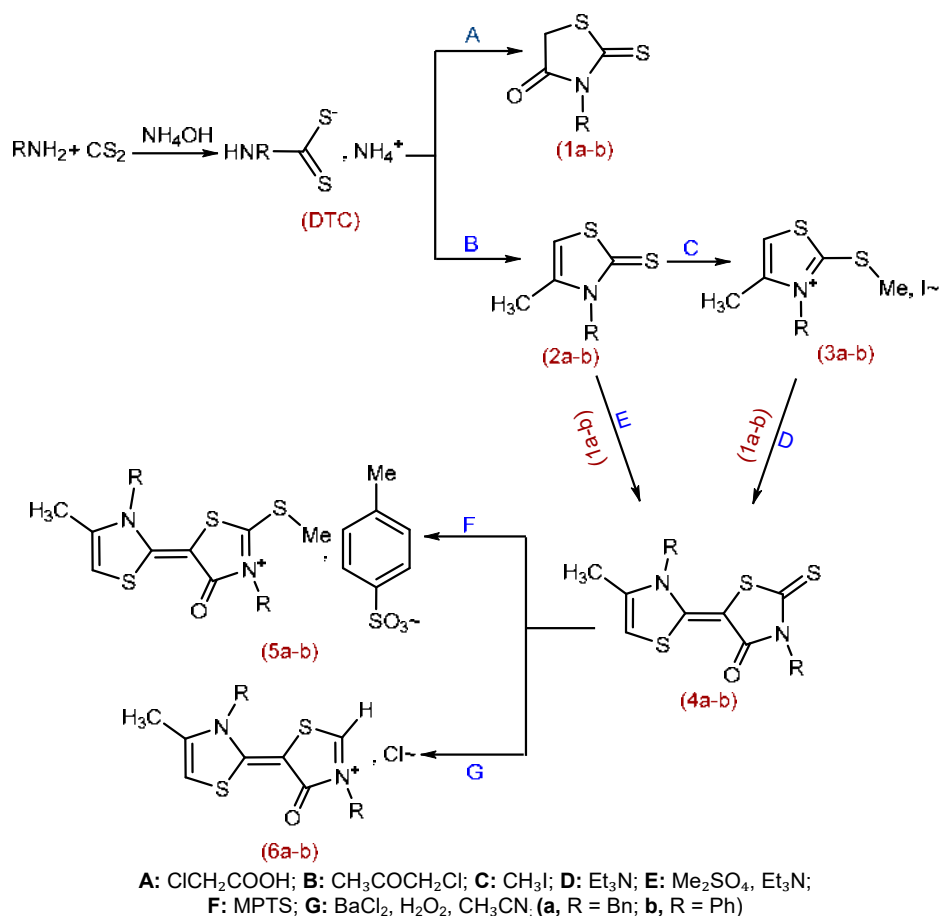
The thiazolidenium sulfonate salts (**7a-c**) (0.05 mol) or thiazolidenium chloride salts (**8a-c**) (0.05 mol) were introduced into the electrolysis cell containing 0.1 M solution of tetra-n-butylammonium bromide TBAB

(NBu₄Br), 5 μL of perchloric acid and, 50 mL of acetonitrile. The environment was degassed by a stream of nitrogen for 5 min and maintained under an inert atmosphere. The reduction of salt is carried out on a platinum electrode. The voltammograms were recorded at ambient temperature with a scanning speed of 100 mV.S⁻¹. The selected scanning range was -2000 to +2000 mV and 0 to 2000 mV.

■ RESULTS AND DISCUSSION

Chemical Synthesis Part

In this study, we described practical approaches for the preparation of thiazolidenium salts obtained from merocyanine derivatives. Firstly, thioxothiazolidinones (**1a-c**), alkylidenethioxothiazolidinone (**3c**), and thiazoline thiones (**2a-c**), as well as the thiazolium salts (**3a-b**), were prepared. The coupling of such compounds results in the formation of thiazolydenethioxothiazolidinones (**4a-b**) and alkylidenthiazolidenethioxothiazolidinone (**4c**), which are subsequently converted to thiazolidenium sulfonate salts (**5a-b**), thiazolidenium chloride salts (**6a-b**), alkylidenthiazolidenium sulfonate salt (**5c**), and alkylidenthiazolidenium chloride salt (**6c**) successively. The synthetic strategies for the preparation of these salts are grouped in Scheme 1 and Scheme 2. Concerning the first scheme, thioxothiazolidinones (**1a-b**) were synthesized by a cyclo condensation of chloroacetic acid with ammonium dithiocarbamate salt (DTC) [37]. DTCs were obtained from the following primary amines: BnNH₂, PhNH₂, and *n*-PrNH₂ that ultimately with CH₃COOH leads to the formation of the corresponding products **1a** (Beige crystals; 68%), and **1b** (Yellow Crystals; 59%) successively. Thiazolinethiones **2a** (Beige crystals; 83.55%) and **2b** (Beige crystals; 61.55%) were obtained by the reaction between chloroacetone and the same preceding dithiocarbamate salts (DTCs). The treatment of thiazolinethiones with iodomethane in the presence of acetone leads to the formation of the thiazolium salt **3a** (White crystals; 60.58%) and **3b** (Beige crystals; 53.64%). Finally, merocyanines **4a** (Yellow crystals; 84.21%) and **4b** (Yellow crystals; 81.53%) were obtained using two methods: (i) The first

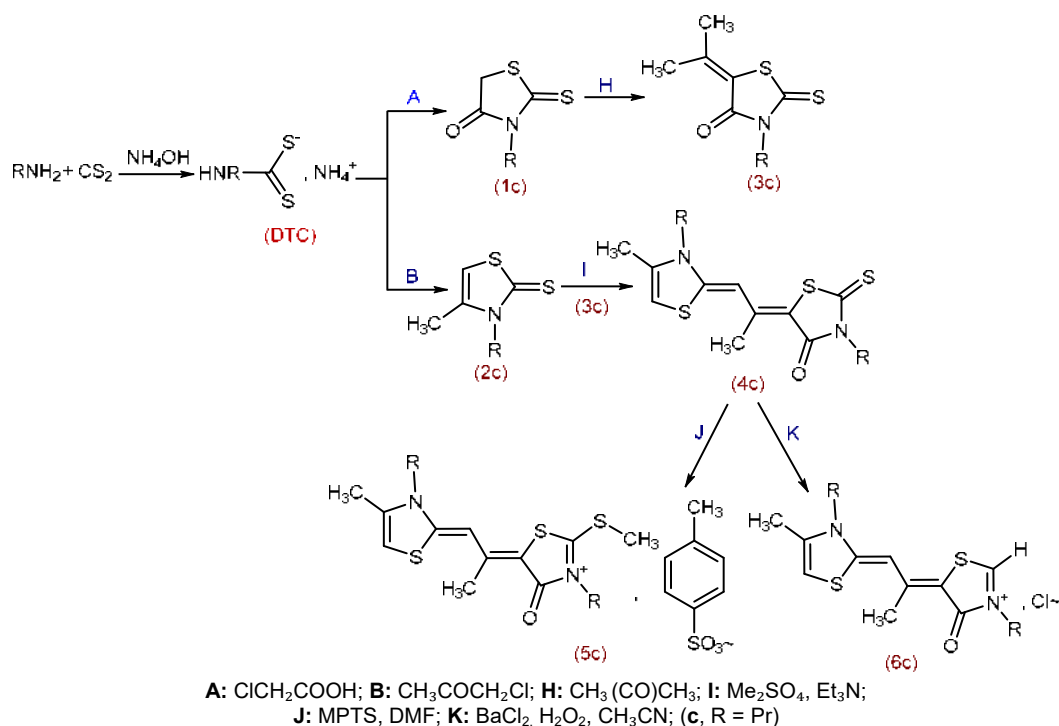


Scheme 1. The synthetic procedure of thiazolidenium sulfonate salts (**5a-b**) and thiazolidenium chloride salts (**6a-b**)

was a coupling between a neutral heterocycle (thioxothiazolidinone **1a-b**) and a cationic heterocycle (thiazolium salts **3a-b**) in the presence of triethylamine. (ii) The second method was an *in situ* reaction between compounds (**2a-b**) and compounds (**1a-b**) in the presence of dimethyl sulfate and triethylamine.

Comparing the two methods, the second one is easier and faster than the first one. The reaction of the prepared merocyanines (**4a-b**) with methyl *p*-toluene sulfonate (MPTS) in the presence of acetone leads to the formation of the thiazolideniumsulfonate salts **5a** (Brown crystals; 78.96%) and **5b** (Brown crystals; 71.24%). The reaction of the same prepared merocyanines (**4a-b**) with barium chloride (BaCl₂) in the presence of acetonitrile and hydrogen peroxide leads to the formation of the thiazolidenium chloride salts **6a** (Beige crystals; 68.20%), and **6b** (Beige crystals; 75.92%). Another strategy was followed for the preparation of alkylidenthiazolidene-

thioxothiazolidinone (merocarbocyanines) **4c** (Purple crystals; 87.32%) and their salts **5c** (Brown crystals; 84.53%), and **6c** (Beige crystals; 85.22%), which is illustrated in Scheme 2. Thioxothiazolidinones **1c** (Brown oily liquid; 62%) was obtained by the same previous method. The reaction between compound **1c** (containing active methylene in position 5) with acetone (containing a carbonyl group) in the presence of ammonium hydroxide used as catalyst, with heating under reflux for 20 h, leads to the formation of alkylidenthiooxo thiazolidinone **3c** (Orange crystals; 59%), according to the Knoevenagel condensation [38]. Thiazolinethione **2c** (Beige crystals; 76.52%) was obtained by the same previous method. The compound **4c** (Purple crystals; 87.32%) was obtained by an *in situ* reaction between a compound **3c** and **2c** in the presence of dimethyl sulfate and triethylamine. The alkylidenthiazolideniumsulfonate salt **5c** (Brown crystals; 84.53%)



Scheme 2. The synthetic procedure of alkylidenthiazolidenium sulfonate salt (5c) and alkylidenthiazolidenium chloride salt (6c)

was obtained by the reaction of compound 4c with MPTS in the presence of DMF and acetone. The treatment of the compound 4c with a mixture of hydrogen peroxide (H_2O_2) and barium chloride (BaCl_2) in the presence of acetonitrile leads to the formation of alkylidenthiazolidenium chloride salt 6c (Beige crystals; 85.22%) with precipitation of BaSO_4 , which was removed by filtration through celite. The method used to generate the chloride salt 6c was inspired from the work of Lorcy and Guérin [39] and Yano et al. [40]. The yields of the synthesized compounds are satisfactory (60–87%), and the data obtained from IR, NMR, MS spectroscopic analyses were in good agreement with the proposed structures of the synthesized molecules.

Electrochemical (Cyclic-Voltammetry) Study Part

By studying the behavior of thiazolidenium sulfonate salts (5a-b), thiazolidenium chloride salts (6a-b), alkylidenthiazolidenium sulfonate salt (5c), and alkylidenthiazolidenium chloride salt (6c) in a voltammetric cell on a platinum electrode; we noticed that they turn into TTTAFs. Because of the conjugation

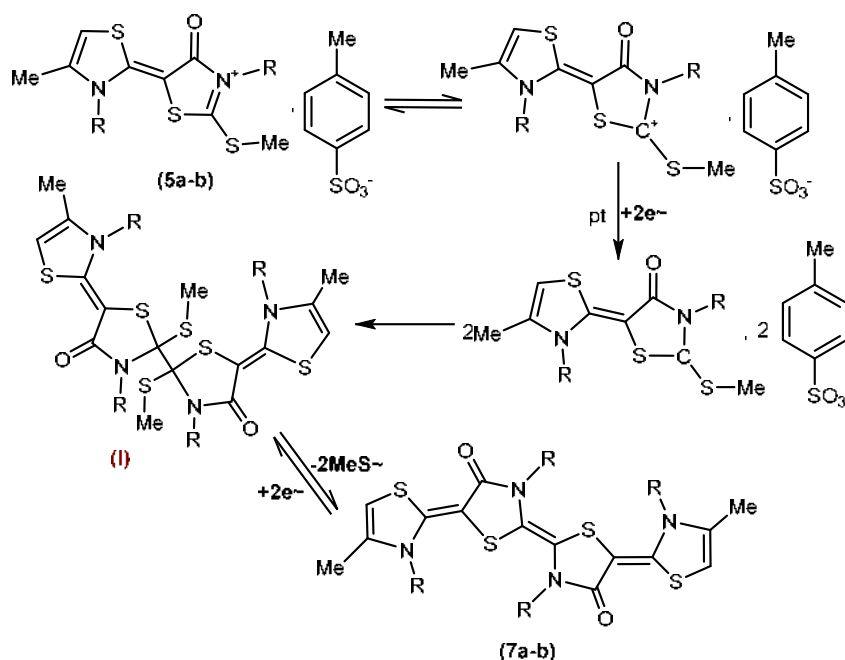
existing in the structure of these salts, there is delocalization of the π -electrons in their molecules, which have the effect of generating a radical. The latter is dimerized into an intermediate (each salt gives an intermediate: I, II, III, IV). The reduction of each intermediate derivative, after elimination of two MeS^- or H^- groups, to the formation of TTTAFs (7a-b, 7'a-b, 8c, and 8'c) successively, according to Scheme 3, 4 (see SI). It should be noted that the presence of acid facilitates the elimination of the thiomethyl group and facilitates the formation of TTTAF.

Interpretation of Voltammograms

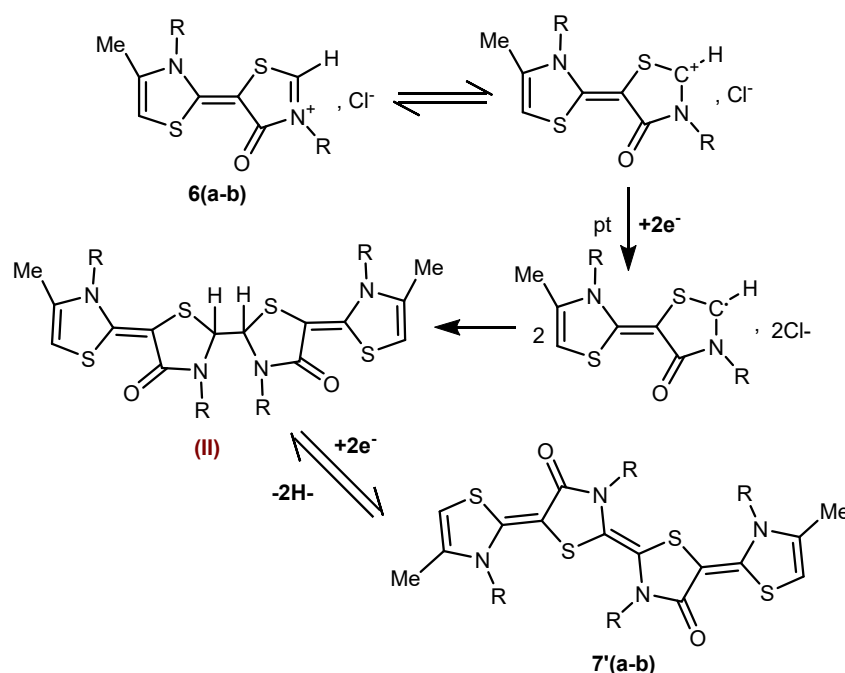
The range of the cyclic scan chosen was (-2000 to +2000 mV) and (0 to +2000 mV) from right to left with a constant speed of 100 mV/s for all voltammograms.

Solvent and support electrolyte voltammograms

From the two scans below, it is noted that there are no oxidation or reduction peaks. Therefore, there has been no electrochemical phenomenon on the solvent or the electrolyte support, despite the appearance of weak "bumps" probably due to traces of oxygen (see Fig. 2).



Scheme 3. The strategy of electrochemical transformation of thiazolidenium sulfonate salts (5a-b) into TTTAFs (7a-b)



Scheme 4. The strategy of electrochemical transformation of thiazolideniumchloride salts (6a-b) into TTTAFs (7'a-b)

Voltammograms of the merocyanines 4a, 4b, and merocarbocyanine 4c (Fig. 3, and SI)

According to the appearance of the voltammograms of the three compounds **4a**, **4b**, **4c**, two peaks of oxidation are observed in each scan at different potentials; (compound **4a**: Ep_{a1} = 1.15; Ep_{a2} = 1.65), (compound **4b**:

Ep_{a1} = 1.15; Ep_{a2} = 1.65), and (compound **4c**: Ep_{a1} = 1.15; Ep_{a2} = 1.6). A single reduction peak for each scan are also observed at different potentials; (compound **4a**: Ep_{c2} = 0.63, compound **4b**: Ep_{c2} = 0.63, and compound **4c**: Ep_{c2} = 0.63).

According to the peaks, the first wave of oxidation

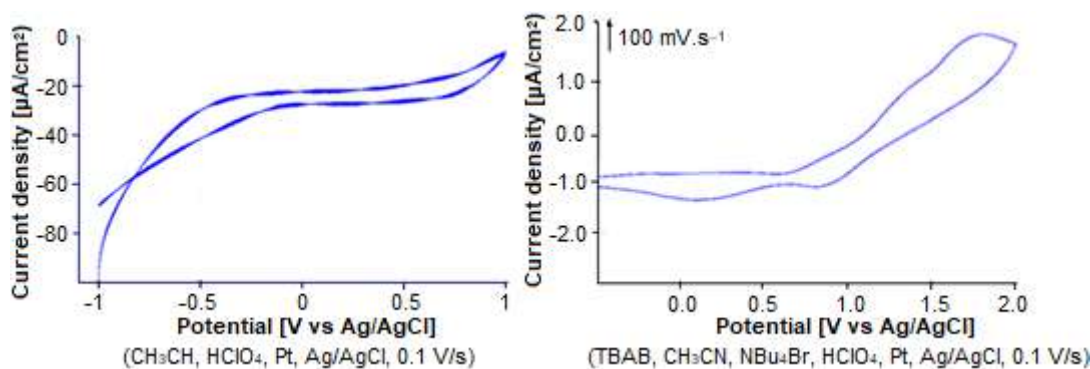


Fig 2. Solvent and support electrolyte voltammograms

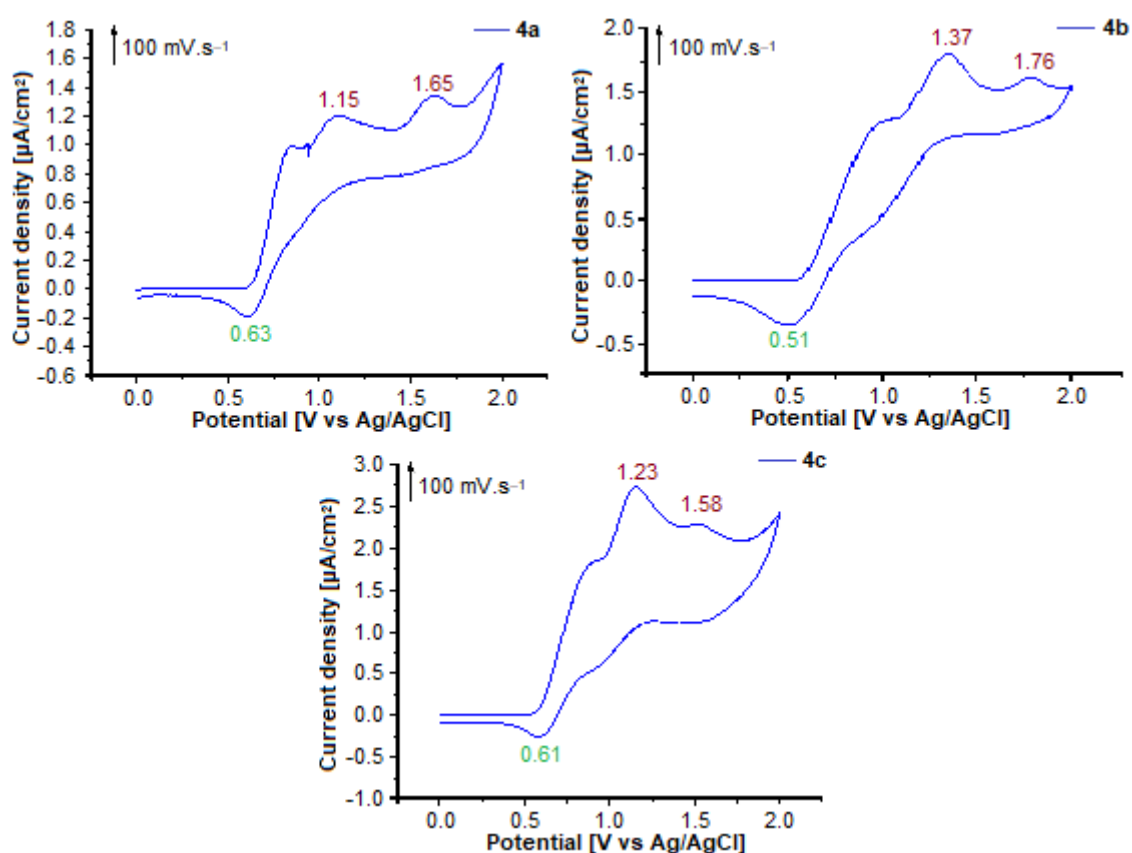


Fig 3. Voltammograms of compounds **4a**, **4b**, **4c** (CH_3CN , NBu_4Br 0.1 M, HClO_4 , pt, Ag/AgCl , 0.1 V/s)

is reversible, but not the second (irreversible). This indicates that there was the oxidation of two electrons and the reduction of only one electron for each compound. Therefore, it is an irreversible anodic oxidation process, and consequently, there is no coupling phenomenon on these precursors.

Note: **4a**, **4b**, and **4c** are the precursors of the thiazolidenium salts: (**4a** precursor of **5a** and **6a**), (**4b** precursor of **5b** and **6b**), (**4c** precursor of **5c** and **6c**).

Merocyanines salts voltammograms

Voltammograms of thiazolidenium sulfonate salts 5a, 5b (Fig. 4, and SI), and thiazolidenium chloride salts 6a, 6b (Fig. 5, and SI). The four voltammograms indicate a well-defined redox process, which corresponds to the reversible oxidations of the four merocyanine salts **5a**, **5b**, **6a**, **6b**. The anodic peaks (oxidation) of each compound are observed at (**5a**: $E_{p1} = 1.24$; $E_{p2} = 1.60$), (**5b**: $E_{p1} = 0.95$; $E_{p2} = 1.30$), (**6a**: $E_{p1} = 0.93$; $E_{p2} = 1.90$),

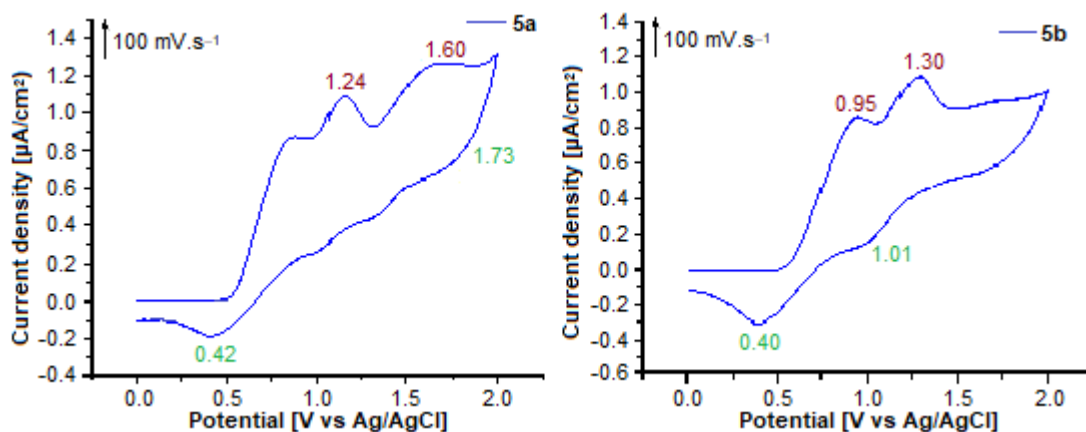


Fig 4. Voltammograms of compounds **5a**, **5b** (CH_3CN , NBu_4Br 0.1 M, HClO_4 , pt, Ag/AgCl , 0.1 V/s)

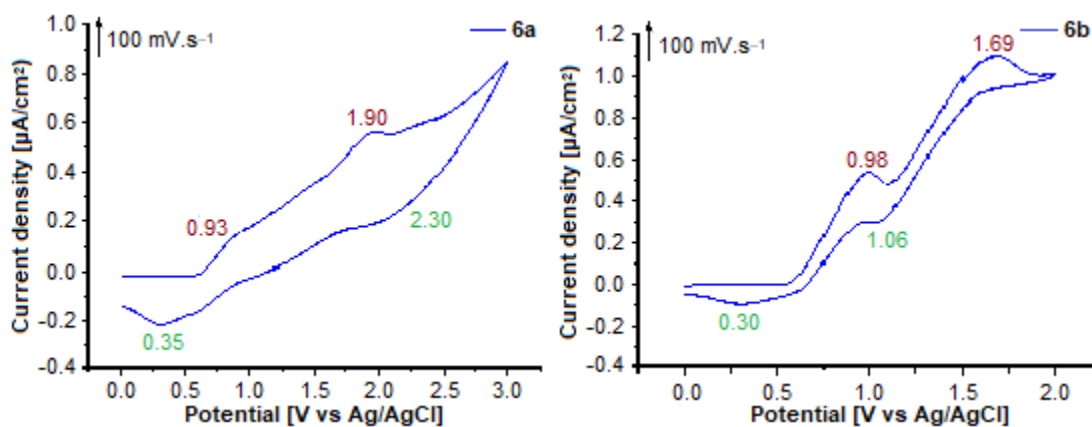


Fig 5. Voltammograms of compounds **6a**, **6b** (CH_3CN , NBu_4Br 0.1 M, HClO_4 , pt, Ag/AgCl , 0.1 V/s)

(**6b**: $E_{p_{a1}} = 0.98$; $E_{p_{a2}} = 1.69$). The cathodic peaks (reduction) of each compound are observed at (**5a**: $E_{p_{c1}} = 1.73$, $E_{p_{c2}} = 0.42$), (**5b**: $E_{p_{c1}} = 1.01$, $E_{p_{c2}} = 0.40$), (**6a**: $E_{p_{c1}} = 2.30$, $E_{p_{c2}} = 0.35$), (**6b**: $E_{p_{c1}} = 1.06$, $E_{p_{c2}} = 0.30$).

According to the scans and peaks, the two waves of oxidation are reversible in each voltammogram. This indicates that there was a transfer of electrons: the oxidation of two electrons and the reduction of two electrons for each compound. The redox of the first two electrons corresponds to the generation of the radical, which is subsequently dimerized to an intermediate, and the redox of the other two electrons corresponds to the transformation of the latter into TTTAFs. Therefore the thiazolidenium sulfonate salts **5a**, **5b** have been transformed into TTTAFs **7a,b** and that the thiazolidenium chloride salts **6a,b** have been transformed

into TTTAFs **7'a,b**.

Merocarbocyanines salts voltammograms **Voltammograms of alkylidenthiazolidenium sulfonate salt 5c and alkylidenthiazolidenium chloride salt 6c (Fig. 6, and SI).**

The scans of the two voltammograms allow us to observe two reversible waves with two anode peaks and two cathodic responses. The two peaks corresponding to the oxidation of the salts are located at (**5c**: $E_{p_{a1}} = 0.95$; $E_{p_{a2}} = 1.31$), (**6c**: $E_{p_{a1}} = 0.80$; $E_{p_{a2}} = 1.39$), and the other two peaks corresponding to the reduction of the salts are located at (**5c**: $E_{p_{c1}} = 1.56$, $E_{p_{c2}} = 0.39$), (**6c**: $E_{p_{c1}} = 1.60$, $E_{p_{c2}} = 0.71$), this indicates that there was a transfer of electrons: oxidation and reduction of two electrons for each compound and therefore the transformation of salts **5c** and **6c** at TTTAF **8c** and **8'c**, respectively.

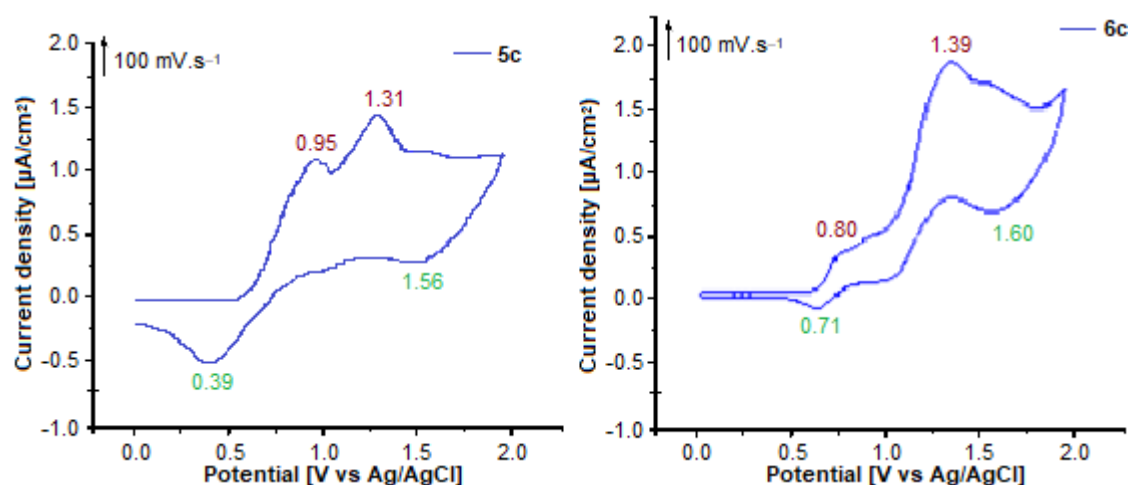


Fig 6. Voltammograms of compounds 5c, 6c (CH₃CN, NBu₄Br 0.1M, HClO₄, pt, Ag/AgCl, 0.1 V/s)

Summary Table of the Different Oxidation-Reduction Potentials of the Thiazolidenium-Sulfonate and Chloride Salts and Their Precursors

We present, in Table 1, 2, 3 a summary of the different oxidation-reduction potentials of each merocyanines and merocarbocyanines salts 5a, 6a, 5b, 6b, 5c, 6c with their precursor's merocyanines and merocarbocyanines 4a, 4b, 4c successively, to compare the results.

Confirmation

The cyclic Voltammetry method allowed us to follow the behavior of merocyanine salts (thiazolideniumsulfonate salts 5a, 5b, and thiazolidenium

chloride salts 6a, 6b, and merocarbocyanine salts thiazolideniumsulfonate salts 5c and thiazolidenium chloride salts 6c at different potentials. By comparing the voltammograms and the different potentials of the salts with their precursors 4a, 4b, 4c taken as references, we observe that for the salts, we have a redox system of 4 π -electrons and consequently their delocalization, which leads to the coupling of these latest; It is, therefore, easy to confirm their transformation to TTTAFs 7a, 7b, 7a', 7b', 8c, 8c' as shown in Scheme 3, 4 (see SI). For the precursor molecules, there was not a redox system, and therefore no coupling.

The confirmation of the presence of TTTAFs was made only by an *in situ* electrochemical detection method

Table 1. Differents oxidation-reduction potentials of the compounds (4a, 5a, 6a)

Potentials of the compound (4a) (volt)			Potentials of the compound (5a) (volt)			Potentials of the compound (6a) (volt)		
Ep _{a1}	Ep _{a2}	ΔE_{Pox}	Ep _{a1}	Ep _{a2}	ΔE_{Pox}	Ep _{a1}	Ep _{a2}	ΔE_{Pox}
+ 1.15	+ 1.65	+ 0.50	+ 1.24	+ 1.60	+ 0.36	+ 0.93	+ 1.92	+ 0.99
Ep _{c1}	Ep _{c2}	ΔE_{Red}	Ep _{c1}	Ep _{c2}	ΔE_{Red}	Ep _{c1}	Ep _{c2}	ΔE_{Red}
0	+ 0.63	+ 0.63	+ 0.42	+ 1.73	+ 1.31	+ 0.35	+ 2.30	+ 1.95

Table 2. Differents oxidation-reduction potentials of the compounds (4b, 5b, 6b)

Potentials of the compound (4b) (volt)			Potentials of the compound (5b) (volt)			Potentials of the compound (6b) (volt)		
Ep _{a1}	Ep _{a2}	ΔE_{Pox}	Ep _{a1}	Ep _{a2}	ΔE_{Pox}	Ep _{a1}	Ep _{a2}	ΔE_{Pox}
+ 1.37	+ 1.76	+ 0.39	+ 0.95	+ 1.30	+ 0.35	+ 0.98	+ 1.69	+ 0.71
Ep _{c1}	Ep _{c2}	ΔE_{Red}	Ep _{c1}	Ep _{c2}	ΔE_{Red}	Ep _{c1}	Ep _{c2}	ΔE_{Red}
0	+ 0.51	+ 0.51	+ 0.4	+ 1.01	+ 0.61	+ 0.30	+ 1.06	+ 0.76

Table 3. Different oxidation-reduction potentials of the compounds (4c, 5c, 6c)

Potentials of the compound (4c) (volt)			Potentials of the compound (5c) (volt)			Potentials of the compound (6c) (volt)		
Ep _{a1}	Ep _{a2}	ΔE _{Pox}	Ep _{a1}	Ep _{a2}	ΔE _{Pox}	Ep _{a1}	Ep _{a2}	ΔE _{Pox}
+ 1.23	+ 1.58	+ 0.35	+ 0.95	+ 1.31	+ 0.36	+ 0.80	+ 1.39	+ 0.59
Ep _{c1}	Ep _{c2}	ΔE _{Red}	Ep _{c1}	Ep _{c2}	ΔE _{Red}	Ep _{c1}	Ep _{c2}	ΔE _{Red}
0	+ 0.61	+ 0.61	+ 0.39	+ 1.56	+ 1.17	+ 0.71	+ 1.60	+ 0.89

under an inert atmosphere and not with usual spectroscopic methods (NMR, MS, UV, etc.) for the reason that the TTTAFs are very unstable species and very reactive to air and therefore their isolation causes their degradation.

According to the literature [40-42], DTDAFs (analogs of TTTAFs), which are also unstable in air and not isolable, have been transformed into DTDAF²⁺ dications more stable and isolable; as a perspective, we can transform the TTTAFs that we could not isolate to TTTAF⁴⁺ tetracations more stable and isolable, to characterize them by spectroscopic methods.

Structure-Property Relationship of TTTAFs

TTTAFs are nitrogen analogs of TTFs (family of electroactive donors) where rings thiol have been replaced by rings thiazole (presence of nitrogen which can undergo oxidation or bind to a metal center), which gives them a very high electro-donor character and which make them very reactive to electron-acceptor compounds and therefore they can be used in assembly reactions to obtain new charge transfer complexes having superconducting properties.

TTTAFs have a π -conjugate system, which gives them a conductive character, and consequently, they have redox properties.

TTTAFs have very high electron donor properties, and therefore are very unstable and reactive in air, to make them react with other molecules such as electron-attracting compounds; we must use an electrochemical detection method *In situ* in a cell, under an inert atmosphere (medium degassed with nitrogen).

CONCLUSION

In summary, in this work, we sought to obtain TTTAFs from salts of merocyanines used as precursor

molecules. After various attempts, by applying electroanalysis (cyclic voltammetry) to these salts and by following their behavior *in situ* in the electrochemical cell, we were able to lead to the intramolecular coupling of these latter and consequently to the formation of TTTAFs, which was confirmed by the displacement of the oxidation-reduction waves and the variation of the observed potentials. From the structure of TTTAFs, which contains electron donor groups (nitrogen and sulfur) and several double bonds, we can consider them as π -electron donor's molecules, which will be tested subsequently against another π -electron acceptor structure.

SUPPORTING INFORMATION (SI)

Copies of the original spectra (IR, ¹H-NMR, ¹³C-NMR, Mass) and data CV of all the molecules reported in the experimental section are included in the Supporting Information.

ACKNOWLEDGMENTS

The authors would like to thank any person who helped in the realization of this work, as well as the team of the laboratory of the Organic Chemistry Department of the University Alicante.

REFERENCES

- [1] Akamatsu, H., Inokuchi, H., and Matsunaga, Y., 1954, Electrical conductivity of the perylene-bromine complex, *Nature*, 173 (4395), 168–169.
- [2] Saito, G., and Yoshida, Y., 2012, Frontiers of organic conductors and superconductors, *Top. Curr. Chem.*, 312, 67–126.
- [3] Martin, N., 2013, Tetrathiafulvalene: The advent of organic metals, *Chem. Commun.*, 49 (63), 7025–7027.

- [4] Filatre-Furcate, A., Higashino, T., Lorcy, D., and Mori, T., 2015, Air-stable n-channel organic field-effect transistors based on a sulfur rich π -electron acceptor, *J. Mater. Chem. C*, 3 (15), 3569–3573.
- [5] Gal-Oz, R., Patil, N., Khalfin, R., Cohen, Y., and Zussman, E., 2013, Conductive PVDF-HFP nanofibers with embedded TTF-TCNQ charge transfer complex, *ACS Appl. Mater. Interfaces*, 5 (13), 6066–6072.
- [6] Prokhorova, T.G., and Yagubskii, E.B., 2017, Organic conductors and superconductors based on bis(ethylenedithio)tetrathiafulvalene radical cation salts with supramolecular tris(oxalato)metallate anions, *Russ. Chem. Rev.*, 86 (2), 164.
- [7] Paxton, W.F., Kleinman, S.L., Basuray, A.N., Stoddart, J.F., and Van Duyne, R.P., 2011, Surface-enhanced Raman spectroelectrochemistry of TTF-modified self-assembled monolayers, *J. Phys. Chem. Lett.*, 2 (10), 1145–1149.
- [8] Pérez-Rentero, S., Eritja, R., Häring, M., Saldías, C., and Díaz, D.D., 2018, Synthesis, characterization, and self-assembly of a tetrathiafulvalene (TTF)-triglycyl derivative, *Appl. Sci.*, 8 (5), 671.
- [9] Nair, M.N., Mattioli, C., Cranney, M., Malval, J.P., Vonau, F., Aubel, D., Bubendorff, J.L., Gourdon, A., and Simon, L., 2015, STM studies of self-assembled tetrathiafulvalene (TTF) derivatives on graphene: Influence of the mode of deposition, *J. Phys. Chem. C*, 119, 9334–9341.
- [10] Tian, J., Ding, Y.D., Zhou, T.Y., Zhang, K.D., Zhao, X., Wang, H., Zhang, D.W., Liu, Yi., and Li, Z.T., 2014, Self-assembly of three-dimensional supramolecular polymers through cooperative tetrathiafulvalene radical cation dimerization, *Chem. Eur. J.*, 20 (2), 575–584.
- [11] Jain, A., Rao, K.V., Mogera, U., Sagade, A.J., and George, S., 2011, Dynamic self-assembly of charge-transfer nanofibers of tetrathiafulvalene derivatives with F₄TCNQ, *Chem. Eur. J.*, 17 (44), 12355–12361.
- [12] Evans, N.H., Rahman, H., Davis, J.J., and Beer, P.D., 2012, Surface-attached sensors for cation and anion recognition, *Anal. Bioanal. Chem.*, 402 (5), 1739–1748.
- [13] Zhao, B.T., Cao, S.N., Guo, H.M., and Qu, G.R., 2013, Metal-ion-promoted intermolecular electron transfer between anthraquinone-based tetrathiafulvalene derivative and *p*-chloranil, *Synth. Met.*, 174, 14–18.
- [14] Shao, M., Dongare, P., Dawe, L.N., Thompson, D.W., and Zhao, Y., 2010, Biscrown-annulated TTFAQ–dianthracene hybrid: Synthesis, structure, and metal ion sensing, *Org. Lett.*, 12 (13), 3050–3053.
- [15] Blanchard, P.Y., Alévêque, O., Boisard, S., Gautier, C., El-Ghayoury, A., Le Derf, F., Breton, T., and Levillain, E., 2011, Intermolecular interactions in self-assembled monolayers of tetrathiafulvalene derivatives, *Phys. Chem. Chem. Phys.*, 13 (6), 2118–2120.
- [16] Yuge, R., Miyazaki, A., Enoki, T., Tamada, K., Nakamura, F., and Hara, M., 2002, Electrochemical properties of self-assembled monolayers composed of TTF derivative, *Mol. Cryst. Liq. Cryst.*, 377 (1), 395–398.
- [17] Gomar-Nadal, E., Ramachandran, G.K., Chen, F., Burgin, T., Rovira, C., Amabilino, D.B., and Lindsay, S.M., 2004, Self-assembled monolayers of tetrathiafulvalene derivatives on Au(111): Organization and electrical properties, *J. Phys. Chem. B*, 108 (22), 7213–7218.
- [18] Yokota, Y., Yuge, R., Miyazaki, A., Enoki, T., and Hara, M., 2003, Property of self-assembled monolayers of long-alkyl-chain-substituted TTF derivative, *Mol. Cryst. Liq. Cryst.*, 407 (1), 121–127.
- [19] Yuge, R., Miyazaki, A., Enoki, T., Ito, E., Nakamura, F., and Hara, M., 2001, Characterization and electronic properties of TTF SAMs on Au(111), *Mol. Cryst. Liq. Cryst. Sci. Technol., Sect. A*, 370 (1), 273–276.
- [20] Suzuki, A., Inoue, K., Yano, K., Oku, T., and Kikuchi, K., 2010, Fabrication and characterization of C₆₀/tetrathiafulvalene solar cells, *J. Phys. Chem. Solids*, 71 (11), 1587–1591.
- [21] Martín, N., Sánchez, L., Herranz, M.Á., Illescas, B., and Guldi, D.M., 2007, Electronic communication in tetrathiafulvalene (TTF)/C₆₀ systems: Toward

- molecular solar energy conversion materials, *Acc. Chem. Res.*, 40 (10), 1015–1024.
- [22] Martin-Gomis, L., Nielsen, K.A., Fernandez-Lázaro, F., Jeppesen, J.O., and Sastre-Santos, A., 2011, Supramolecular (2,5,7-trinitrofluorene)-C₆₀/tetrathiafulvalene-calix[4]pyrrole systems, *Meet. Abstr.*, 01, 1692.
- [23] Konarev, D.V., Shul'ga, Y.M., Roshchupkina, O.S., and Lyubovskaya, R.N., 1997, Synthesis and some properties of charge transfer complexes of C₆₀ with asymmetric donors of tetrathiafulvalene family, *J. Phys. Chem. Solids*, 58 (11), 1869–1872.
- [24] Lai, G., Liu, Y., Zhang, Y., Ruan, J., Li, M., and Shen, Y., 2009, Synthesis and properties of tetrathiafulvalene-fluorescein dyads, *Front. Chem. Eng. China*, 3 (3), 314–317.
- [25] Mas-Torrent, M., Hadley, P., Bromley, S.T., Ribas, X., Tarrés, J., Mas, M., Molins, E., Veciana, J., and Rovira, C., 2004, Correlation between crystal structure and mobility in organic field-effect transistors based on single crystals of tetrathiafulvalene derivatives, *J. Am. Chem. Soc.*, 126 (27), 8546–8553.
- [26] Schröder, H.V., and Schalley, C.A., 2018, Tetrathiafulvalene – A redox-switchable building block to control motion in mechanically interlocked molecules, *Beilstein J. Org. Chem.*, 14, 2163–2185.
- [27] Wang, C., Dyar, S.M., Cao, D.C., Fahrenbach, A.C., Horwitz, N., Colvin, M.T., Carmieli, R., Stern, C.L., Dey, S.K., Wasielewski, M.R., and Stoddart, J.F., 2012, Tetrathiafulvalene hetero radical cation dimerization in a redox-active [2]catenane, *J. Am. Chem. Soc.*, 134 (46), 19136–19145.
- [28] Pauliukaite, R., Malinauskas, A., Zhylyak, G., and Spichiger-Keller, U.E., 2007, Conductive organic complex salt TTF-TCNQ as a mediator for biosensors. An overview, *Electroanalysis*, 19 (24), 2491–2498.
- [29] Cao, Z., Jiang, X., Xie, Q., and Yao, S., 2008, A third-generation hydrogen peroxide biosensor based on horseradish peroxidase immobilized in a tetrathiafulvalene-tetracyanoquinodimethane/multi walled carbon nanotubes film, *Biosens. Bioelectron.*, 24 (2), 222–227.
- [30] Tehfe, M.A., Monot, J., Malacria, M., Fensterbank, L., Fouassier, J.P., Curran, D.P., Lacôte, E., and Lalevée, J., 2012, A water-compatible NHC-borane: Photopolymerizations in water and rate constants for elementary radical reactions, *ACS Macro Lett.*, 1 (1), 92–95.
- [31] Zappe, L., Schönfeld, S., Hörner, G., Zenere, K.A., Leong, C.F., Kepert, C.J., D'Alessandro, D.M., Weber, B., and Neville, S.M., 2020, Spin crossover modulation in a coordination polymer with the redox-active bis-pyridyltetrathiafulvalene (py₂TTF) ligand, *Chem. Commun.*, 56 (72), 10469–10472.
- [32] Wang, H.Y., Cui, L., Xie, J.Z., Leong, C.F., D'Alessandro, D.M., and Zuo, J.L., 2017, Functional coordination polymers based on redox-active tetrathiafulvalene and its derivatives, *Coord. Chem. Rev.*, 345, 342–361.
- [33] Nambu, S., Nakahodo, T., and Fujihara, H., 2014, Synthesis and properties of conducting polymer nanotubes with redox-active tetrathiafulvalene, *Heterocycles*, 88 (2), 1633–1638.
- [34] Nielsen, M.B., Lomholt, C., and Becher, J., 2000, Tetrathiafulvalenes as building blocks in supramolecular chemistry II, *Chem. Soc. Rev.*, 29 (3), 153–164.
- [35] Miyasaka, H., Motokawa, N., Matsunaga, S., Yamashita, M., Sugimoto, K., Mori, T., Toyota, N., and Dunbar, K.R., 2010, Control of charge transfer in a series of Ru^{II}/TCNQ two-dimensional networks by tuning the electron affinity of TCNQ units: A route to synergistic magnetic/conducting materials, *J. Am. Chem. Soc.*, 132 (5), 1532–1544.
- [36] Guérin, D., Carlier, R., Guerro, M., and Lorcy, D., 2003, Crown-ether annelated dithiadiazafulvalenes, *Tetrahedron*, 59 (28), 5273–5278.
- [37] Singh, S.P., Parmar, S.S., Raman, K., and Stenberg, V.I., 1981, Chemistry and biological activity of thiazolidinediones, *Chem. Rev.*, 81 (2), 175–203.
- [38] Mahalle, S.R., Netankar, P.D., Bondge, S.P., and Mane, R.A., 2008, An efficient method for Knoevenagel condensation: a facile synthesis of 5-arylidene 2,4-thiazolidinedione, *Green Chem. Lett. Rev.*, 1 (2), 103–106.

- [39] Guérin, D., 2001, Modulation des propriétés rédox du donneur π dithiadiazafulvalène appliquée à la formation de matériaux moléculaires, *Dissertation*, Institut des Sciences Chimiques de Rennes (ISCR), Université de Rennes 1, Rennes, France.
- [40] Broggi, J., Terme, T., and Vanelle, P., 2014, Organic electron donors as powerful single-electron reducing agents in organic synthesis, *Angew. Chem. Int. Ed.*, 53 (2), 384–413.
- [41] Janikowska, K., and Makowiec, S., 2010, Simple method for the preparation of dialkyl (2,3-dihydro-1,3-thiazol-2-yl)-phosphonates, *Phosphorus, Sulfur Silicon Relat. Elem.*, 186 (1), 12–20.
- [42] Časar, Z., Leban, I., Majcen-le Marechal, A., Piekara-Sady, L., and Lorcy, D., 2009, Charge transfer complexes and cation radical salts of azino-diselenadiazafulvalene, *C.R. Chim.*, 12 (9), 1057–1065.

Spatial Distribution of Heavy Metals in Al-Zarqa, Jordan

Reem Dabaibeh

Department Physics and Applied Sciences, Faculty of Engineering Technology, Al-Balqa' Applied University, Al-Salt, Jordan

* **Corresponding author:**

tel: +962-798903008

email: reem.dabaibeh@bau.edu.jo

Received: July 31, 2020

Accepted: September 21, 2020

DOI: 10.22146/ijc.58304

Abstract: Al-Zarqa is experiencing challenges in industry conversion and extensive urbanization. The environmental quality of soil in the Al-Zarqa region was analyzed by Spatial analysis for the identification of sources and estimation of the concentration of heavy metals, which helped in the assessment of soil quality and heavy metal pollution. The reason for the elevation of heavy metal pollution is increased urbanization, industrialization, traffic, oil refinery emissions, and mixed anthropogenic sources in that region. The main objective of this research was to assess the ecological impact of heavy metal pollutants in the Al-Zarqa region. The concentrations of Cd, Cr, Cu, Mn, Ni, Pb, Zn, and Fe were estimated and compared with the existing literature. The distribution pattern of each metal was identified by spatial distribution analysis. Results revealed that the concentration of Cd, Cr, and Ni was high, while the concentration of Pb, Zn, and Cu was lower than the maximum allowed limits. Factor analysis identified the potential sources of heavy metals in the investigated area, and spatial distribution showed the geographical distribution of the heavy metals over the study area. It was concluded that identification of the potential sources of pollutants along with their geographical variations was more beneficial than only considering the individual point concentrations.

Keywords: heavy metals; soil pollution; Al-Zarqa; genotoxicity

■ INTRODUCTION

Heavy metal pollution is one of the biggest challenges of the present century. Heavy metals cause negative impacts on aquatic and terrestrial organisms. These pollutants are also affecting the economy of the farming community [1]. Since the shortage of freshwater is a great concern in Jordan [2], the heavy metals available in drinking water can be considered as a threat to human health. The oncogenic risk of such metals has been proven in several studies [3]. The environmental occurrence of heavy metals is also causing adversarial effects on human health [4]. Heavy metal poisoning is identified as an important underlying factor for several diseases. These metallic elements have a relatively higher density than water [5].

Metal pollutants are one of the major environmental concerns across the globe [6]. Their presence could pose risks and hazards to humans and their trace levels in the environment are regulated by various laws and various authorities in each country [7]. Industrial, agricultural,

and domestic development have also increased human exposure to heavy metals. Although these metals are naturally occurring elements in soil, major sources of metals in the environment include anthropogenic activities, industrial waste, agricultural practices, pharmaceuticals, and metal based industry operations [8]. Environmental pollution by heavy metals is considered dangerous and is particularly hazardous to human health [9]. Mineral rock weathering is also a well-identified source of metal pollutants in the environment [10].

Many studies have identified that the concentration of hazardous metals in topsoil is persistently increasing. Yaseen and Al-Hawari [11] discussed that there is a momentous increase in the total contents of metals in soils in areas experiencing increased industrialization. The major soil contaminants include Pb, Cd, Zn, and Cu, which are released into the environment through mechanical abrasion [12]. Soil contamination with metal ions is also increased through metal corrosion, soil erosion, and

other natural phenomena. Industrial sources such as oil refineries, petroleum combustion, power-plants, and recycling and waste treatment plants are also important contributors of these metals in the environment [2]. Metals such as cobalt (Co), copper (Cu), chromium (Cr), iron (Fe), manganese (Mn), molybdenum (Mo), nickel (Ni), selenium (Se), and zinc (Zn) are considered as vital nutrients for biochemical activities. Therefore, agricultural practices are also contributing to soil contamination of metals [4].

Heavy metal ions are toxic as they can gather in the human body and affect the central nervous system. Heavy metal poisoning is a serious health issue that causes physiological and neurological health problems [13]. The most hazardous metals to human health include Hg, Pb, Cd, Au, Pt, Ag, Bi, As, Se, V, Cr, and Ti [12]. Metal ions can interact with cell components such as DNA and cause carcinogenesis. Metals are also causing oxidative stress in the human body, which results in the carcinogenicity of these metals [11]. The level of exposure to heavy metals decides the degree of toxicity and their carcinogenic effects. High exposure to these metals may result in multiple organ failure and life-threatening situations [13].

Al-Zarqa has been experiencing rapid and uncontrolled urbanization and industrialization, resulting in the increase of environmental problems in this region. Heavy metals, which pose a potential health risk for human beings, are ubiquitous pollutants in urban dust because of the increase in urban population and intensity of anthropogenic activities [14].

Jordan Petroleum Refinery Company (JPRC), situated in Al-Zarqa, is a primary source of pollution and other environmental problems [15]. Al-Hussein thermal power stations, Russeifa dump, and Es-ssammra wastewater treatment complex are also important sources of pollutants in the environment [16]. The purpose of this study is to assess the key sources of pollutants in Al-Zarqa and compare the metal contamination in this region. The heavy metal contents in the soil were identified, and their concentration was measured.

Naser [10] studied the sources of contamination in soil and found that the metals naturally occur in the soil as a result of rock weathering. Metals occur in trace

quantities in the environment and are often not toxic. Gao and Chen [5] highlighted that urbanization in various areas could disturb and accelerate the natural geochemical cycle of metals and results in their amassing in soil. According to Li et al. [1], anthropogenic sources are also important contributors to metal pollutants in soil. To assess the level of anthropogenic contamination of soil, it is necessary to conduct special monitoring studies. The issue of anthropogenic soil pollution caused by emissions from coal-fired thermal power stations has been studied worldwide, especially in countries where coal mining is an important industry [17]. They further added that metal mine tailings, petrochemicals, fertilizers, pesticides, landfilling with metal compounds, lead-based paints are also important sources of metal deposition in soil.

El-Hasan and Lataifeh [2] studied the impact of essential micronutrients in soil. Their findings revealed that micronutrients, including Co, Cu, Fe, Mn, Mo, Ni, and Zn, are crucial for plants and are frequently used in fertilizers. Several metals, which are essential as nutrients in lower concentrations (i.e. Zn, Cu, Fe, and Mn) can be considered harmful for plant growth if the levels of these elements in soil and atmosphere are increased [18]. The fertilizers used to supply these nutrients to soil frequently contain trace amounts of metals, including Cd and Pb. Some phosphate base fertilizers also contain impurities of F and Hg. The excessive use of these fertilizers also contributes to the accumulation of metals in soil. Yaseen and Al-Hawari [11] also presented similar findings and revealed that more than 10% of the pesticides and fungicides commonly used in agriculture are based on compounds that contain Cu, Hg, Mn, Pb, or Zn. These compounds are also an important source of soil contamination.

Municipal and industrial wastewater is an extensively discussed source of soil contamination. Wang et al. [6] found that industrial waste and effluents are commonly discharged over land. Their findings revealed that more than 20 million hectares of land received wastewater annually around the globe. Meanwhile, Al-Khashman [12] found that in developing countries, around 50% of the irrigation is based on

wastewater supply. The negative impact of heavy metal accumulation in soils includes the decrease of the yield and quality of crops, and also the quality of the atmospheric and aquatic environments. Generally, irrigation with wastewater elevates the total and available heavy metal concentrations in soils [19]. Even if the wastewater contains relatively low amounts of heavy metals, enduring exposure to this kind of wastewater can result in significant amassing of metal pollutants in soil.

Al-Taani et al. [20] studied the impact of urbanization on the heavy metals contamination in soil. The study identified that urbanization affected the ecological functions and increased Zn accumulation in soil. According to Massadeh et al. [21], sewage sludge, livestock manures, vehicle exhaust, industrial emission, and agricultural practices have become major environmental concerns worldwide. The extent of urbanization and increased population can significantly affect the inherent function of soil and facilitate the accumulation of polluted contents, as discussed by Zhang et al. [4].

According to Al-Najjar et al. [15], the natural concentration of trace elements in soil plays a critical role in controlling the effect of human activities on the soil. Heavy metals in urban soils have been widely studied due to their ubiquity, toxicity, and persistence [22]. The amassing of metals in topsoil is contributed through several environmental and human activities. Massadeh et al. [21] studied the urban population index map of different regions, and their findings revealed that in urban areas, the soil is found to be enriched in heavy metals. Soil pollution by heavy metals in industrialized areas is an on-going challenge.

Spatial analysis is frequently used to quantify the quality of soil and to assess the presence of contamination in soil. According to Al-Taani et al. [20], spatial analysis is an important predictive approach to assess the impact of urbanization on soil quality and the presence of heavy metals. The accuracy of heavy metal spatial distribution maps is critical for risk control [23]. The spatial distribution of metal ions helps in the assessment of the concentration of these pollutants in soil. According to Shan et al. [8], the rising values of these metals indicate toxicity and soil pollution. Alloway [24] suggests that heavy metals are

toxic and not easy to decompose naturally. These metals are transferred from soil to the environment through water, plants, and contaminated foods.

Coal mining industries generate large volumes of gangue wastes, from which a considerable amount of toxic HMs could be released during weathering of the waste under the joint effects of water, microorganisms, vegetation, sunlight radiation, and heat. These hazardous substances enter the ecosystem by a variety of pathways where they could be detrimental to crops and animals, and might be taken up by humans through direct contact (ingestion, dermal absorption, and inhalation) or food chains [25].

Abderahman and Abu-Rukah [16] showed that heavy metal toxicity in the soil gradually increased through anthropogenic processes, including waste dumping in landfills, waste incineration, and smokestack emission. They also stated that the US environmental protection agency had identified seven metals as the priority control pollutants known for their hazardous effects on human health. These metals include nickel, zinc, copper, lead, mercury, arsenic, cadmium, and chromium. Al-Khashman [12] identified that contamination of these metal pollutants in the soil is a serious and rapidly growing problem in regions that are experiencing industrial development and urban expansion.

According to Li et al. [13], the level of topsoil contamination can be assessed through their spatial distribution. They defined spatial analysis as a geographical process that involves the topological, geometrical, and geographical properties of soil. It is based on the analysis of the pattern of human behaviors and their spatial expression. Al-Khashman [26] highlighted that spatial analysis is used to identify location-oriented problems. Digital mapping and spatial analysis are commonly used to characterize the soil quality and assess the spatial distribution of metals. Jaradat et al. [27] performed the comparison of non-restructured soil and restructured soil through the spatial distribution of heavy metals. The spatial variability of soil properties includes variations in soil moisture, physical and chemical properties, etc.

Moreover, temporal and spatial variations of heavy metals relate to both natural variability of soils and human activities, thus to be considered as powerful tracers for monitoring the impact of human activity [28]. Their findings revealed that territorial and human factors subsidize the gathering of various pollutants in soil, including heavy metals.

Al-Khashman [26] studied the extent of contamination in topsoil and spatial distribution of metals. Their findings indicated that the concentrations of Pb, Cu, Cr, Zn, and Cd are higher in areas near industries. They identified that the accretion of these metals was higher in areas near cement factories. Al-Khashman [12] studied the heavy-metals concentration in the urban samples of topsoil from Jordan. According to their findings, Zn and Pb had high concentrations, while Cd and Ni had lower concentrations. It was further concluded that large scale industrialization is a major factor for soil degradation and heavy metal pollution.

Al-Khashman [26] studied the extent of pollution in Karak Industrial estate, Jordan. Their findings revealed that the soil in the studied area was polluted with metals, including Fe, Cu, Zn, and Pb. They also found that the concentration of these metals exceeded the limits in topsoil, but their concentration was found to be decreased in lower soil. They concluded that the main sources of these pollutants were the nearby industrial places. El-Hasan and Lataifeh [2] extended the discussion by analyzing the topsoil composition in the Nepal region. They analyzed the amounts of eight trace metals, including Cd, Cr, Cu, Fe, Mn, Pb, V, and Zn. Their findings suggested that Pb and Zn were greater in concentration near the metropolitan regions while Cr, Fe, and V were found in exceeding concentrations in controlled soil.

Banat et al. [29] performed the spatial pattern study of metal pollutants in central Jordan. They identified that Cd, Pb, and Hg were found to be in high concentrations in urban areas. They also identified the major sources of these pollutants to be the cement industry, fertilizers, and vehicle emission. These metals were found in both residual and active phases. Al-Khashman and Shawabkeh [30] studied the distribution analysis of Pb, Zn, Cd, and Cr in Southern Jordan near industrial areas. Their results

highlighted that Pb, Zn, and Cd were in higher concentration in areas near the cement manufacturing plant. The study further stated that anthropogenic activities are the major contributors to the pollutants in urban soil.

Soil, an important environmental medium, is exposed to a number of pollutants including toxic heavy metals by various natural and anthropogenic activities [19]. Extensive urbanization and industrialization lead to the accretion of toxic metals in topsoil. The current study is aimed to assess the sources of contamination and amounts of heavy metals in the Al-Zarqa region of Jordan.

■ EXPERIMENTAL SECTION

Materials

Analytical reagent-grade of acids, bases, nitrate salts of metals, and other chemicals obtained from Merck (Darmstadt, Germany) were used as received. All solutions were prepared in double deionized water (DDW). All plastics and glassware were cleaned by soaking in HNO₃ solution (10% v/v) and then rinsed with DDW before use. The stock standard solutions of analytes (1000 mg L⁻¹) were prepared from analytical grade nitrate salts of the analytes. The working standard solutions were prepared by appropriate dilution of the stock solutions. ATP was purchased from Sigma-Aldrich [31].

Instrumentation

A Shimadzu model AA-680 atomic absorption spectrometer (Japan) with a hollow cathode lamp as a radiation source and a deuterium background corrector at respective wavelengths (using an air-acetylene flame) was used for metal ions determination in standard and sample solutions. All operating parameters were those recommended by the manufacturer. A Metrohm 691 pH/ion meter (Buchs, Switzerland) supplied with a combined glass-calomel electrode was used for the pH adjustments. The size and morphology of GO were observed by TEM using a CM120 microscope (Philips, Netherlands). Raman spectra of GO were prepared using a SENTERRA microscope (BRUKER, Germany). FT-IR spectra were taken on a BRUKER VECTOR 22 Spectrometer. The flow of the sample and eluent

through the column was adjusted using a 10 roller peristaltic pump (Ultrateck Labs Co. Iran) [31].

Procedure

Studied area

Al-Zarqa is situated in the northeast part of Jordan, at the basin of the Zarqa River, Fig. 1. It has a total area of 4586 km²; about 4074 km² of which is within Jordan and 512 km² is within Syria [32]. The city is located northeast of Amman and has a population of more than 640,000 inhabitants. The city is experiencing extensive industrialization and urbanization since the past decades. The Al Zarqa Channelized Stream is considered to be one of the most polluted regions in Jordan due to massive discharge and accumulation of pollutants over the years [33]. The city is situated near the international Amman-Baghdad highway. It is also the main industrial center of Jordan, and more than 50% of the country's industries are situated in this city. Jordan oil refinery plants, leather and garment factories, new agricultural and pharmaceutical factories represent the recent industrial development in

this region. The increased industrial development has facilitated the growth of the city's population. The increased rate of population growth and industries has caused serious environmental problems in this region.

Sampling strategy

About one kilometer was included for acquiring the soil samples from the studied area. Different samples were collected with the help of an auger and were transferred into labeled polyethylene bags. The sample bags were labeled according to the sampling area, date, and weight of the collected samples. The samples were also documented with clear details to avoid any mixing between samples.

Sample processing

The pre-treatment of samples was performed by cleaning all glassware with tap water, detergent, and distilled water. Then the glassware was soaked in 10% HNO₃ (v/v) for one night. Finally, all glassware was cleaned and rinsed with deionized water. The collected samples were spread out to separate the extra materials such as grass, stones, mosses, and roots. All materials sized above 2 cm were separated from the samples using physical procedures. Afterwards, the samples were air-dried at room temperature for two weeks by placing them in a clean area. Later, the dried sections were sieved through 2 mm mesh; the attained sections were then further divided into three labeled polyethylene bags. These samples were stored at 4 °C in a refrigerator until it was time to perform the chemical analysis.

Chemical analysis

pH. The pH of all collected soil samples was measured by making a 1:1 ratio of soil and deionized water mixture (w/v). A potentiometric approach was used to measure the pH following the EPA standard analysis method 9045D [20]. The measured pH values were reported as pH (H₂O) at 25 °C.

Cation exchange capacity (CEC). An excess of sodium acetate solution mixed with soil samples resulted in the exchange of sodium cations with matrix cations. The mixture was then rinsed with isopropyl alcohol. Ammonium acetate solution was later added, which exchanged the adsorbed sodium with ammonium ion. This sample was then embedded in each batch (8 samples). In addition, a blank was embedded within

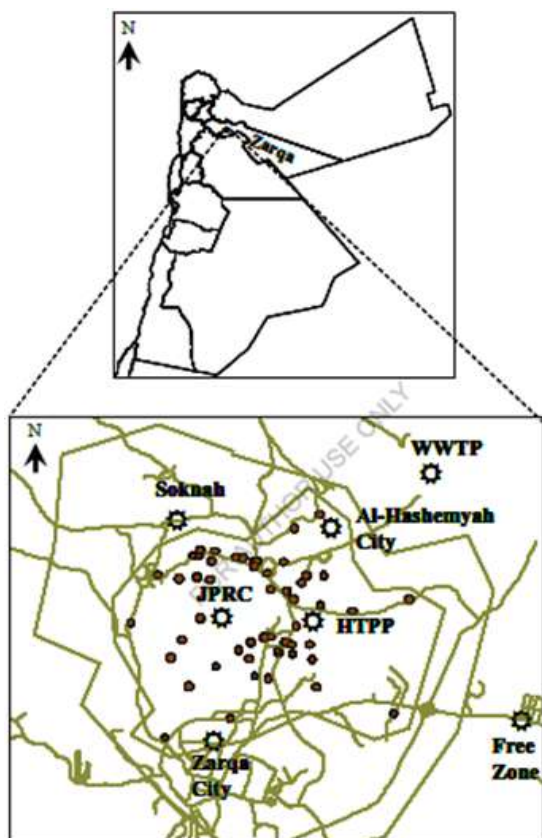


Fig 1. Jordan map shows the Al-Zarqa city

every three successive batches. The concentration of the released Na^+ was determined by atomic emission spectroscopy at 589 nm wavelength. The results were shown in centimoles of positive charge per kilogram of soil (cmol [+]/kg); (cmol Na = {(weight of Na in the sample/ atomic weight of Na) \times 100}).

Total organic carbon (TOC). A 0.15 mm sieve was used to sieve soil samples, and about 0.5 g of soil that passed the sieve was weighed to the nearest of 0.0001 g and placed in a digestion tube (250 mL). Then, 15 mL of the digestion solution (0.066 M $\text{K}_2\text{Cr}_2\text{O}_7$ and 9 M H_2SO_4) was poured into the digestion tube and boiled gently over a hot plate for 45 min. The digested samples were then allowed to cool before adding 50 mL H_2O , 5 mL 85% H_3PO_4 , and four drops of the indicator (*o*-Phenanthroline). Finally, the solution was titrated against ferrous ammonium sulfate with the endpoint color change from green to reddish-brown. The quality of the analysis was monitored by triplicate analysis of a known sample, and then it was embedded with each batch (10 samples). In addition, two unheated blanks and two heated blanks were also analyzed with each batch. Before titration, ferrous ammonium sulfate solution was standardized against $\text{K}_2\text{Cr}_2\text{O}_7$. The TOC of the samples was reported as a percentage of TOC.

Metals. About 0.5 g of each air-dried and sieved samples were taken and placed in a Teflon beaker. Around 15 mL of HNO_3 , 4 mL of HF, and 4 mL of HClO_4 were added to the sample filled beakers, and the attained mixtures were then boiled in a sand bath at 170 ± 20 °C. The boiling was done in closed beakers until the samples were completely dissolved. Then the covers were removed to allow the

solution to evaporate and become dry. Afterwards, 5 mL of HNO_3 was dropped into the samples and evaporated until 2 mL was left. Then the mixture was diluted with deionized water. The obtained mixtures were kept in polyethylene bottles. All samples were again labeled and documented in sample preparation sheets.

Flame atomic absorption spectrometry analysis was performed for all obtained samples, certified reference materials, reagent blanks, and method blanks. An air-acetylene flame was utilized in the spectrometer to attain the details of present metals. The stock solution of 1000 ppm was obtained, and different successive dilutions were prepared to attain the calibration graphs. The graphs were analyzed to identify the linear relationship. Table 1 presents all-instrumental parameters used in this experiment.

Method validation

The accurate analysis of metal contamination requires comparison with blank measurements. The contamination of metals was detected by measuring the sample to blank ratios. Blank samples or acid samples were prepared and treated like samples. The effects of used acids and reagents were calculated. The sample to blank ratios of all metals except Cd were estimated to be larger than 10, while the sample to blank ratio of Cd was measured around 9. These findings suggest that blank subtraction has no significant impact on the observed concentrations of metals. The limits of detection of the measured metals were also calculated, and the results indicate that measured elements were higher than the LOD, Table 2.

The limits of detection (LOD) of the identified metals in the samples were measured as the concentration

Table 1. The instrumental parameters used in this study

Element	λ (nm)	Air flow (L/min)	Acetylene flow (L/min)	Slit width (nm)	Lamp current (mA)
Pb	217.0	3.5	1.5	1.0	10.0
Cr	357.9	4.0	2.5	0.2	7.0
Cd	228.8	3.5	1.5	0.5	4.0
Zn	213.9	3.5	1.5	1.0	5.0
Cu	324.8	3.5	1.5	0.5	4.0
Ni	232.0	3.5	1.5	0.2	4.0
Mn	279.5	3.5	1.5	0.2	5.0
Fe	386.0	3.5	1.5	0.2	5.0

Table 2. Sample to blank ratio and detection limits of elements

Elements	Average concentration (mg/L)	Average blank concentration (mg/L)	Sample to blank ratio	LOD (mg/L)
Cu	1.113	0.015	74	0.013
Ni	4.140	0.119	35	0.053
Zn	2.582	0.180	20	0.004
Mn	3.437	0.029	119	0.011
Pb	2.501	0.040	63	0.031
Cd ^a	0.037	0.0048	9	0.008
Cr	0.883	0.043	21	0.040
Fe	396	0.27	1467	1.25

^a: Blank levels were below the detection limits. Therefore, half of the detection limit was used to calculate the sample to blank ratio

that produces three times the SD at a particular wavelength. The LOD was calculated for each sample with the help of a blank sample. The calculated values were much higher than the Limits of detection. A periodic examination of Standard Reference Materials (SRM) was performed to assure the accuracy of the results. The SRM was collected from the National Institute of Standards and Technology. The results of the SRM were found to be fairly close to the certified values. Table 3 represents the list of SRMs used in this study, and Table 4 shows the accuracy and precision based on three standard reference materials for FAAS analysis.

Method of heavy metal pollution assessment

This study utilized extensive field research, and it is derivative in nature. The collected soil samples were examined for the presence of metals. Geostatistical methods were used for the mapping of metal concentrations. The correlation analysis was used for

principal components analysis of the collected soil samples.

RESULTS AND DISCUSSION

Chemical Characteristics of Soil

The descriptive analyses of the chemical properties of the topsoil samples collected from Al-Zarqa city are presented in Table 5. The studied chemical properties include pH, total organic carbon (%TOC), and cation exchange capacity (CEC). A conventional pH scale 1–14 was used to measure the pH of soil at 25 °C. The % TOC indicates the total organic carbon per gram of soil. CEC indicates the centimoles of the sodium cation per kilogram

Table 3. Standard reference materials used in the study

SRM code	Material
SRM-1646aS	Estuarine sediments
SRM-1633b	Trace elements in coal fly ash
SRM-2702	Inorganics in marine sediments

Table 4. Accuracy and precision based on three standard reference materials for FAAS analysis

Elements	SRM-1646a		SRM-1633b		SRM-2702	
	Found ± SD	Certified ±SD	Found ± SD	Certified ± SD	Found ± SD	Certified ± SD
Cu	10.53 ± 2.01	10.01 ±0.34	107.0 ± 3.34	112.8 ± 2.6	102.2 ± 3.77	
Cr	45.2 ± 3.5	40.9 ± 1.9	352 ± 54	352 ± 22	202	198.2 ± 4.7
Ni	24.4 ± 2.3	23	146.1 ± 12.9	102.6 ± 1.8	78.3 ± 4.8	75.4 ± 1.5
Pb	12.9 ± 4.6	11.7 ± 1.2	73.7 ± 9.4	68.2 ± 1.1	135.6 ± 16.7	132.8 ± 1.1
Cd	0.18 ± 0.18	0.15 ± 0.01	2.43 ± 0.29	0.784 ± 0.01	0.99 ± 0.22	0.82 ± 0.01
Zn	55.0 ± 2.9	48.9 ± 1.6	214.0 ± 2.7	210	479.2 ± 1.4	485.3 ± 4.2
Mn	236.0 ± 10.9	234.5 ± 2.8	133.9 ± 1.5	131.8 ± 1.7	1685 ± 64	1757 ± 58
^a Fe	2.15 ± 0.19	2.00 ± 0.04	7.70 ± 0.53	7.78 ± 0.23	7.81 ± 0.28	7.91 ± 0.24

Note: all concentrations are in µg/g except for Fe in (w/w) percent

of soil (cmol [Na⁺]/kg), as presented in Table 5.

The results indicate that the pH of all studied samples was between 7.0–8.2, with an average of 7.7. These findings suggest that the soil was neutral to slightly alkaline in nature. pH is an important chemical property that plays a decisive role in the determination of the behavior of different chemical components of soil samples such as metals. Acidic pH is more favorable for the mobility of metal ions, while alkaline pH usually limits the bioavailability of metal ions [6].

The %TOC values ranged between 0.2–3.6%, while the average of %TOC for all soil samples was 0.8%. These findings revealed that the distribution patterns of the organic matter in the studied area were irregular. This indicates the variable distributions of the vegetation in the studied region. Abderahman and Abu-Rukah [12] suggested that the extent of organic matter significantly affects the absorption of the heavy metals in soil due to the cation exchange characteristic of organic matter. Therefore, the varied distribution of organic matter also resulted in the varied distribution of heavy-metals throughout the investigated area.

The CEC ranged from 14.46 to 42.9 cmol [Na⁺]/kg with an average of 28.5 cmol [Na⁺]/kg. It is also evident that the pH and amount of organic matter have a direct effect on CEC values of soil, and an increase in these values can also increase the CEC values [17].

Measured Concentrations of Metals

The concentrations of seven metals, Cd, Cr, Cu, Ni, Mn, Zn, and Pb, were measured in mg/kg of the dry weight. The concentration of Fe was measured in w/w or mass to mass ratio of the dry soil. The results revealed that

the measured concentrations of all metals were significantly higher than their detection limits. The values of the metals concentrations, their mean, standard deviations (SD), minimum and maximum concentration are presented in Table 6. It is evident that the concentrations of the metals in topsoil are log-normally distributed rather than normally distributed.

There are several factors that can influence the concentration of metals in soil. The important factors which can alter the concentration of heavy metals in soils include pH, the ion-exchange capacity of the organic matter, wind directions, nature, and composition of the soil [21]. The distribution and mobility of metal ions are also varied according to the mentioned soil properties. The findings of the current study indicate that there was a lack of correlation between the pH, CEC, and % TOC of the soil samples and the concentrations of the heavy metals. The results of this study show strong agreement with Khashman and Shawabkeh [19].

Comparison with the Literature

The studied literature and the findings of the present study were matched to analyze the extent of the soil contamination by the studied metals. This comparison increased the understanding of the extent of soil pollution by metals in the investigated area. The metals that include Pb, Cd, Cr, Zn, Al, Fe, and Mn, are mostly discussed in the literature as heavy metal pollutants

Table 5. Chemical characteristics of soil

	Average	SD	Median	Min	Max
% TOC	0.8	0.6	0.6	0.2	3.6
CEC	28.5	6.6	27.8	14.6	42.9

Table 6. The concentration of metals in the studied area

Metals	Unit	Mean	SD	Median	G. Mean	Min	Max
Cd	mg/kg	6.6	5.2	4.8	5.5	2.3	27.1
Cr	mg/kg	88.2	29.4	84.0	83.8	41.6	183.1
Cu	mg/kg	21.7	8.8	19.10	20.8	9.2	57.1
Mn	mg/kg	492.2	164.3	502	459.0	79.2	932.4
Ni	mg/kg	113.1	128.5	62.2	81.7	41.9	600.5
Pb	mg/kg	58.9	30.6	64.0	47.8	5.7	166.7
Zn	mg/kg	122.0	71.2	109.9	105.9	27.8	356.2
Fe	% (w/w)	1.8	1.0	1.6	1.6	0.2	4.8

in soil [17,21]. The literature also indicated that these metals are the more frequently occurring metal pollutants in urban soil [22-23]. The comparison of the metal concentrations in soil in the present study and the reported metal concentrations in literature are presented in Table 7.

The result indicates that Cd concentrations in the studied areas ranged from 2.3 to 27.1 mg/kg, with a mean concentration of 6.6 (mg/kg). This suggests that the mean concentration of Cd in the current study is around 30 times higher than that was found in the proximity of an oil refinery in Spain. This concentration is also higher than what had been found in the Ankara region [18,23]. The obtained Cd concentration in the current research validates the previously measured concentrations of Cd in this region which was 7.0 mg/kg [25].

The Cr concentration ranged from 41.6 to 183.1 mg/kg, with a mean concentration of 88.2 mg/kg. Comparison with previous studies shows that this measured concentration is almost 5 times higher than the Cr concentration measured in the proximity of an oil refinery in Spain and 4 times higher than the calculated values for the nearby area of JPRC [26]. The comparison also revealed that the measured values of Cr concentration in this study were in close agreement with the results of Banat et al. [18] and significantly lower than the Cr concentration in the Ankara region as measured by Yay et al. [23].

The calculated values of Cu concentration in the current study ranged from 9.2 to 57.1 mg/kg, with a mean concentration of 21.7 mg/kg. The comparison analysis revealed that the Cu values found in this study are much

lower than the previously stated concentration by Momani et al. [26]. These values are also lower than the reported Cu concentration for the Ankara region [23]. However, the means of concentrations of these results are still higher than the values measured by Al-Khashman [16].

The Ni concentrations in this study ranged from 41.9 to 600.5 mg/kg, with a mean concentration of 113.1 mg/kg. The comparison analyses revealed that the mean concentration of Ni in the current study is 40 times greater than the previously measured Ni concentration by Al-Khashman [16], but lower than 121.5 mg/kg, which is the value reported earlier in JPRC by Al-Shatnawi [25].

The Pb concentrations in the current study ranged from 5.7 to 166.7 mg/kg, with a mean concentration of 58.9 mg/kg. This value is slightly lower than the value calculated by Banat et al. [18]. However, the average concentration of Pb is significantly greater than the formerly reported values in other literature [16,24]. The values reported by Yay et al. [23] for the Ankara region were 3 times greater than the results of the present research.

The measured concentrations of Zn in this study ranged from 27.8 to 356.23 mg/kg with a mean value of 122.0 mg/kg. This mean value is in close agreement with the values reported by Al-Shatnawi [25], which was 127.5 mg/kg. However, when compared to the results obtained by Banat et al. [18] and Yay et al. [23] the measured concentrations of Zn in the current study are lower.

Table 7. Comparison of metal concentrations with literature

Metals	Results of this study	JPRC ^a	Cement ^b	Ind. Estate	Oil refinery	Ankara ^c
Cd	6.6	1.2	5.0		0.2	2.2
Cr	88.2	23.0	83.9		16.5	284.0
Cu	21.7	28.0		11.3		90.0
Mn	492.2				268.9	1100.0
Ni	113.1			4.2		81.0
Pb	58.9	21.0	62.2	11.2	37.8	189.0
Zn	122.0	104.0	146.9	13.1		181.0
Fe	18200	3755		43		858000

^a [26]; ^b [18]; ^c [16]; ^d [23-24]; ^e [22]

Probability Distribution

The Gaussian Distribution is a well-recognized technique for factor analysis and geostatistical analysis [27]. These techniques help in attaining the approximately normal data while the non-normality is apparent in the collected data. The shape and symmetry of distribution are measured by analyzing the Kurtosis and skewness of the distribution. The normal distribution is considered to be symmetric and has a zero value for its skewness. In this study, the obtained values of metals and values of soil properties were not normally distributed. Therefore, these values were normalized via logarithmic transformation to normalize the positively skewed distribution of heavy metal concentrations [28]. The Kolmogorov-Smirnov (K-S) test for normality was performed. The findings of this test are presented in Table 8.

The raw data showed positively skewed values for the obtained concentrations of all metals except for Mn. This result suggests that there are various processes such as mineralization and other pollutants that affect the concentration of these metals. The value of the K-S test for normality of Cr, Cu, Fe, Mn, and Pb ($p > 0.05$) indicates that their concentrations can be normalized. However, the values of Pb and Ni did not pass the K-S test for normality. The log-normal transformation was used to minimize data skewness. Fig. 2 illustrates the comparison of the skewed distribution of data before and after the log-transformation of the data.

Sources Identification

A factor analysis (FA) was conducted for the identification of the minimum number of common

factors that have the potential to impact the variance of heavy metal concentration in soil. There is no specific rule for the identification of factors and deciding how many factors should be included in FA. However, the common rule is to either keep factors with eigenvalues higher than 1.0 or keep all interpretable factors. The results of probability distribution and log transferred data were then analyzed under factor analysis, and then a varimax (orthogonal) rotation was also applied.

The factor analysis of the metals data set revealed that only the first three factors have eigenvalues higher than 1. The scree-test results also indicated that the first three factors are meaningful for source identification. The findings suggest that the first factor (FA1) explains 45.8% of the total variance. It was highly loaded with Zn (0.94) and Pb (0.94) and moderately loaded by Cu (0.71) and Cr (0.64). Since Pb, Cu, and Zn are identified as traffic markers by several authors, FA1 was assigned as a trafficking factor. The results showed that the second factor (FA2) explains 20.3% of the total variance. It was highly loaded with Ni (0.90) and moderately loaded by Fe (0.73). Moreover, Cr was distributed between FA1 and FA2. Ni has been identified as an important marker of oil combustion; therefore, this factor was assigned to oil refinery emission.

The third factor (FA3) (FA3) was highly loaded with Cd (0.85) and moderately loaded with Mn and Fe. Mn had high loadings on the first and third factors, 0.59 and 0.64, respectively, but was even higher on the third factor. Moreover, Fe (0.46) had comparatively significant loading in FA3. Fe and Mn are well recognized to be linked with industrial processes. The presence of Cd, along

Table 8. Shape statistics and results of the Kolmogorov-Smirnov (K-S) test for the raw and log-normally transformed data

Metal	Raw data			Log-normal transformed data		
	Skewness	Kurtosis	K-S p	Skewness	Kurtosis	K-S p
Cd	2.7	7.5	0.00	1.2	1.6	0.14
Cr	1.2	2.1	0.12	0.05	0.3	0.69
Cu	1.9	5.21	0.12	0.42	0.8	0.74
Fe	0.8	0.4	0.37	-0.15	-0.5	0.97
Mn	0.14	0.9	0.97	-1.8	5.45	0.24
Ni	2.7	6.5	0.00	1.6	1.45	0.00
Pb	0.37	1.6	0.39	-1.3	0.8	0.00
Zn	1.8	3.4	0.04	-0.02	0.5	0.79

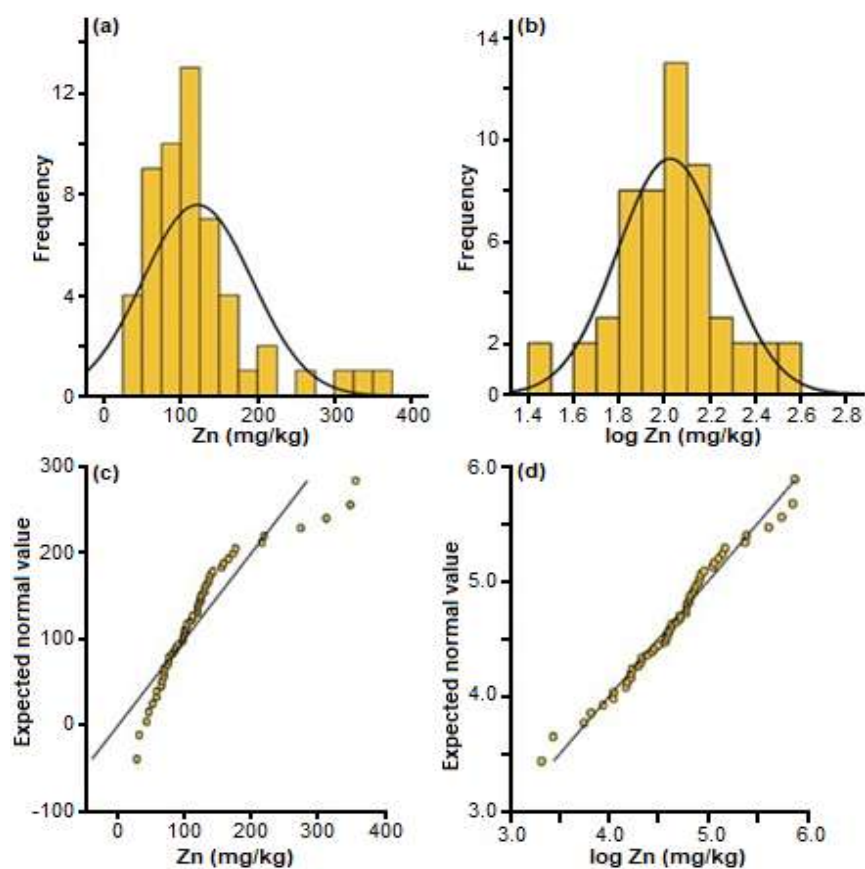


Fig 2. (a) Histogram of Zn concentrations in soil samples showing a skewed distribution, (b) Histogram of the log-transformed Zn concentrations showing normal distribution. (c) Q-Q plot of Zn concentrations showing a deviation from linearity, (d) Q-Q plot of the log-transformed Zn concentrations

Table 9. Correlation matrix of metals

	Cd	Cr	Cu	Fe	Mn	Ni	Pb
Cr	0.05						
Cu	0.05	0.53					
Fe	-0.33	0.61	0.29				
Mn	-0.24	0.47	0.35	0.43			
Ni	-0.13	0.42	0.20	0.52	0.11		
Pb	0.20	0.57	0.57	0.25	0.45	0.20	
Zn	0.20	0.57	0.57	0.25	0.45	0.20	1.00

Table 10. Factor loadings from factor analysis after rotation for the maximum variance

Elements	FA1	FA2	FA3	Communalities
Zn	0.94			0.90
Pb	0.94			0.90
Cu	0.71			0.54
Cr	0.64	0.57		0.74
Ni		0.90		0.82
Fe		0.73	0.46	0.79
Cd			0.85	0.80
Mn	0.59		0.64	0.76
Variance	45.8%	20.3%	12.1%	78.2%
Total Variance Explained, %				78.2

with these metals, indicates the occurrence of anthropogenic activities. Zarqa city has an industrial zone with four steel smelters [29]. Therefore, FA3 was assigned to mixed anthropogenic factors. The findings of factor analysis are presented in Table 9 and Table 10.

The outcomes of the factor analysis revealed that the chief sources of metals in topsoil include anthropogenic processes, oil burning, and emission from an oil refinery and steel industries.

The Spatial Distribution Analysis

The results obtained in this study present significant matching with earlier documented distribution patterns of Pb and Zn concentrations in Al-Zarqa city. The geochemical map shows that the distribution of the concentrations of these metals was lower than the maximum allowable limits in other countries, including Germany, UK, Japan, and Canada. It was also identified that the distribution of Cu was close to Pb and Zn concentrations. Factor analysis confirmed these results;

the first factor was highly loaded by Pb and Zn and moderately loaded by Cu and Cr. The results indicate that these heavy metals are uniformly distributed in the studied areas, and there were no major hotspots present for these elements as shown in Fig. 3. This homogeneous distribution pattern indicates that the sources for their emission are mobile sources. Therefore, automobile and vehicle emission was a major source for these elements.

The geochemical map showed that the studied area was significantly polluted with Cd as its measured concentration crossed the max allowable limits in the UK, Germany, Poland, and Australia (2 mg/kg). Moreover, a major hotspot was also identified in the new Al-Zarqa city with a Cd concentration of around 27.1 mg/kg. The other studied areas were less polluted while the northern outskirts were identified to have the lowest concentration of Cd (< 5.6 mg/kg). The same area was also identified for Cu hotspot as shown in Fig. 4. This distribution pattern indicates that there were Cd and Cu emitting sources present in the area. The topographic map

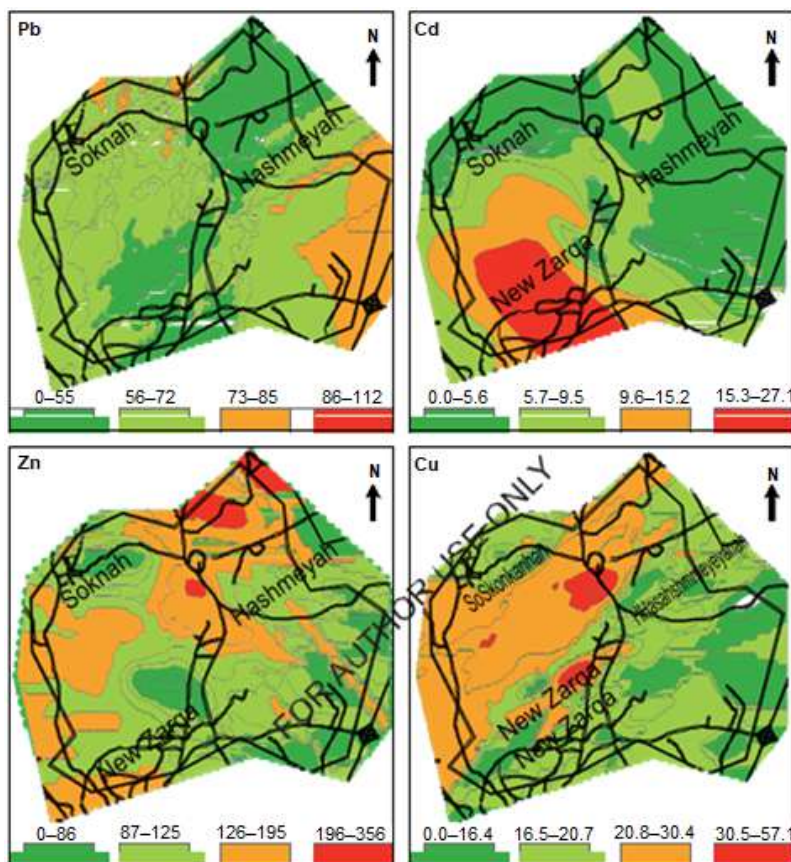


Fig 3. Spatial distribution of metals (Pb, Cd, Zn, Cu)

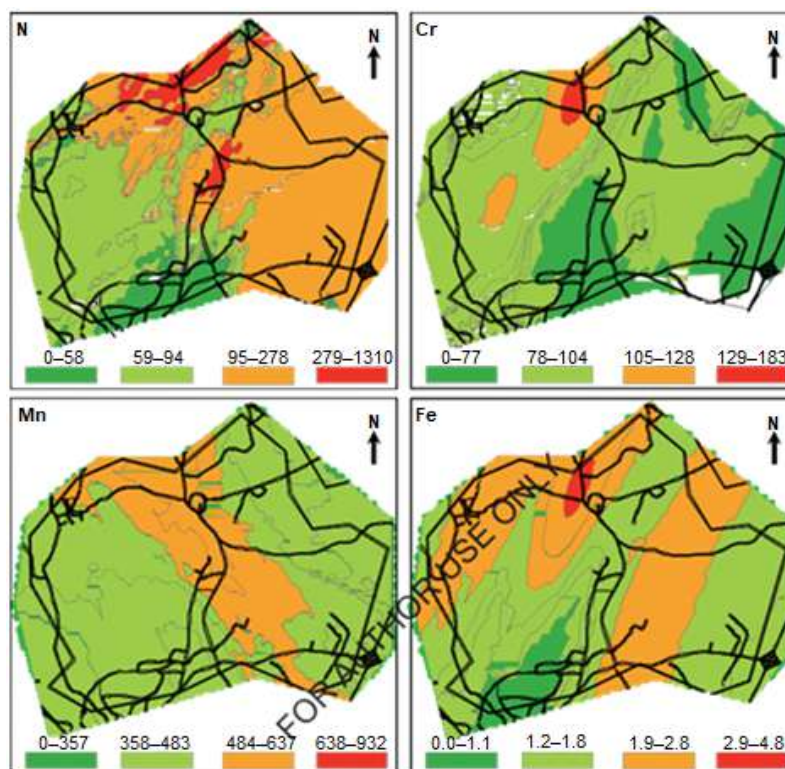


Fig 4. Spatial distribution of metals (Mn, Fe, Cr, Ni)

of this region suggests the presence of several industrial constructions; however, the nature of these industries was not identified.

These findings also revealed that the studied area was considerably polluted with Ni as its measured concentration was more than the maximum allowable limits in Australia, Poland, Canada, Japan, and Germany. The major hotspots for Ni concentration were seen in the east and north of the JPRC. There was no significant information about the distribution of industrial activities available; therefore, any correlation between the hotspot and their sources was difficult to identify. However, it is believed that the burning of oil was the major source of Ni concentration.

The findings also revealed that the studied area was significantly polluted with Cr, and its concentration was identified to be higher than the maximum allowable limits in the UK and Canada. However, the south-eastern area had a lower concentration of Cr, while the North-western area had a higher concentration. More hotspots were found in JPRC nearby locations. The factor analysis

further confirmed that JPRC was the key source for the emission of these metals.

The Geochemical maps of Fe and Mn revealed that the greater concentration of these two elements was clustered and not scattered. The widespread crust contribution of these elements attributes to their significantly higher concentrations. One major hotspot for higher concentrations of these metals was identified in the middle of the northern region of the studied area. The existence of human activities and the steel industry in that region was identified as the primary source of these elements. However, to validate this result, more information about these locations and meteorological data is needed.

CONCLUSION

Our results indicate that there is a higher degree of heavy metal pollution in Al-Zarqa city. The average values of the measured concentrations of identified metals were as follows; Cd (6.6), Cr (88.2), Cu (21.7), Ni (113.1), Pb (58.9), and Zn (122.0) mg/kg. The major

sources for the contribution of these elements in the studied area include traffic, emission from oil-refineries, and mixed anthropogenic sources. The distribution pattern of these metals and the pollution state in Al-Zarqa city were assessed by comparing the metal's concentrations with the maximum allowable limits (MAL) in different countries. Results showed that the average concentration of Cd was higher than the MAL in Australia, Poland, UK, and Germany. While the average concentration of Cr was higher than the MAL in Canada and the UK. Meanwhile, the average concentration of Cu was lower than the MAL in Australia, Canada, Poland, Japan, UK, and Germany. In addition, the average concentration of Ni was higher than the MAL in Australia, Canada, Poland, Japan, UK, and Germany. While the average concentration of Pb and Zn was lower than the MAL in Australia, UK, Canada, Poland, Japan, and Germany.

■ REFERENCES

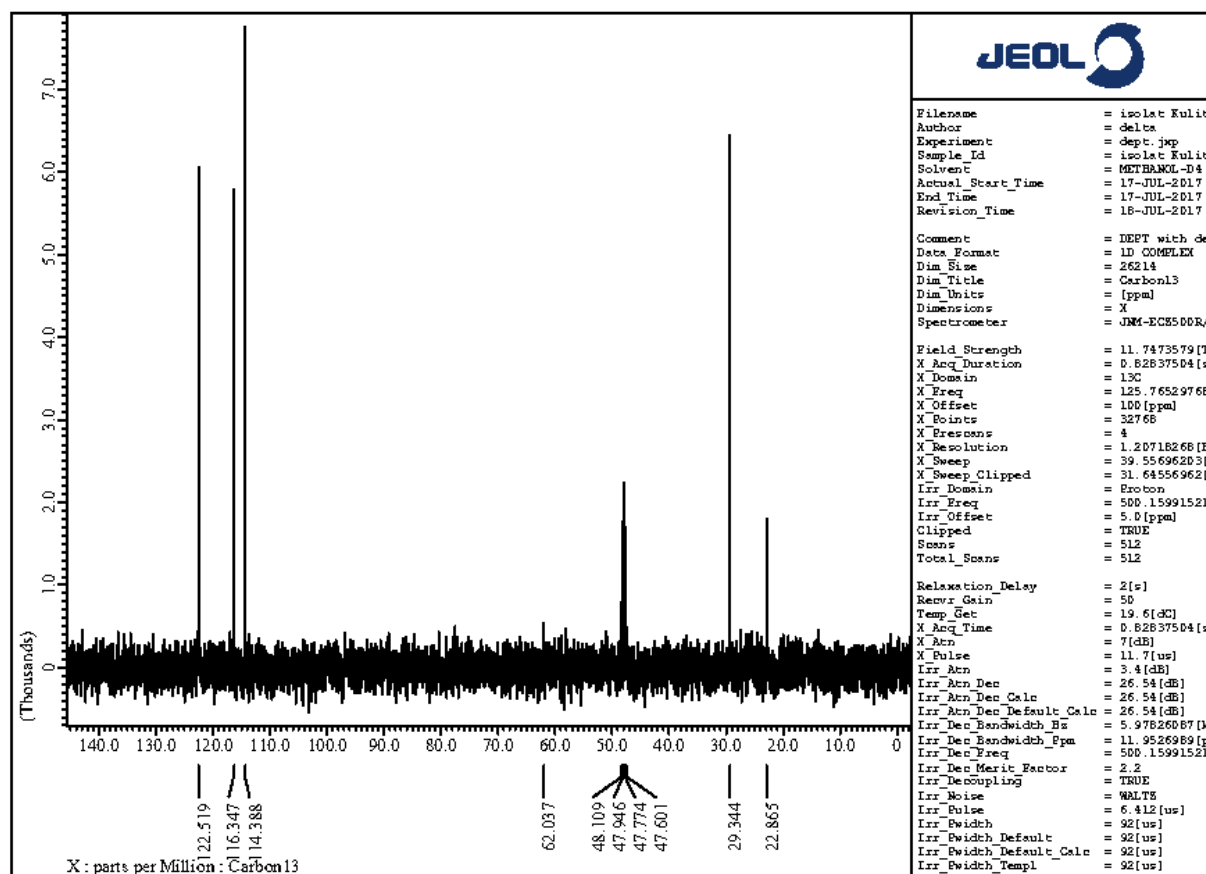
- [1] Li, Z., Ma, Z., van der Kuijp, T.J., Yuan, Z., and Huang, L., 2014, A review of soil heavy metal pollution from mines in China: Pollution and health risk assessment, *Sci. Total Environ.*, 468-469, 843–853.
- [2] El-Hasan, T., and Lataifeh, M., 2013, Field and dual magnetic susceptibility proxies for heavy metal pollution assessment in the urban soil of Al-Karak City, South Jordan, *Environ. Earth Sci.*, 69 (7), 2299–2310.
- [3] Fallahzadeh, R.A., Ghaneian, M.T., Miri, M., and Dashti, M.M., 2017, Spatial analysis and health risk assessment of heavy metals concentration in drinking water resources, *Environ. Sci. Pollut. Res.*, 24 (32), 24790–24802.
- [4] Zhang, X.Y., Lin, F.F., Wong, M.T., Feng, X.L., and Wang, K., 2009, Identification of soil heavy metal sources from anthropogenic activities and pollution assessment of Fuyang County, China, *Environ. Monit. Assess.*, 154 (1-4), 439.
- [5] Gao, X., and Chen, C.T.A., 2012, Heavy metal pollution status in surface sediments of the coastal Bohai Bay, *Water Res.*, 46 (6), 1901–1911.
- [6] Wang, S.L., Xu, X.R., Sun, Y.X., Liu, J.L., and Li, H.B., 2013, Heavy metal pollution in coastal areas of South China: A review, *Mar. Pollut. Bull.*, 76 (1-2), 7–15.
- [7] Ipeaiyeda, A.R., and Ayoade, A.R., 2017, Flame atomic absorption spectrometric determination of heavy metals in aqueous solution and surface water preceded by co-precipitation procedure with copper(II) 8-hydroxyquinoline, *Appl. Water Sci.*, 7 (8), 4449–4459.
- [8] Shan, Y., Tysklind, M., Hao, F., Ouyang, W., Chen, S., and Lin, C., 2013, Identification of sources of heavy metals in agricultural soils using multivariate analysis and GIS, *J. Soils Sediments*, 13 (4), 720–729.
- [9] Gworek, B., Dmuchowski, W., Koda, E., Marecka, M., Baczevska, A.H., Brągoszewska, P., and Osiński, P., 2016, Impact of the municipal solid waste Łubna landfill on environmental pollution by heavy metals, *Water*, 8 (10), 470.
- [10] Naser, H.A., 2013, Assessment and management of heavy metal pollution in the marine environment of the Arabian Gulf: A review, *Mar. Pollut. Bull.*, 72 (1), 6–13.
- [11] Yaseen, I.A.B., and Al-Hawari, Z., 2015, Assessment of heavy metal pollution of surface sediments in Wadi Shu'ayb, Jordan, *Jordan J. Civ. Eng.*, 9 (3), 303–313.
- [12] Al-Khashman, O.A., 2013, Assessment of heavy metals contamination in deposited street dusts in different urbanized areas in the city of Ma'an, Jordan, *Environ. Earth Sci.*, 70 (6), 2603–2612.
- [13] Li, F., Huang, J., Zeng, G., Yuan, X., Li, X., Liang, J., Wang, X., Tang, X., and Bai, B., 2013, Spatial risk assessment and sources identification of heavy metals in surface sediments from the Dongting Lake, Middle China, *J. Geochem. Explor.*, 132, 75–83.
- [14] Pan, H., Lu, X., and Lei, K., 2017, A comprehensive analysis of heavy metals in urban road dust of Xi'an, China: Contamination, source apportionment and spatial distribution, *Sci. Total Environ.*, 609, 1361–1369.
- [15] Al-Najjar, T., Al-Momani, R., Khalaf, M., Wahsha, M., Sbaihat, M., Khalaf, N., Khandra, K.A., and Magames, H., 2016, Levels of heavy metals in fishes (*Cheilinus trilobatus*) from the Gulf of Aqaba, Jordan, *Nat. Sci.*, 8 (6), 256–263.

- [16] Abderahman, N., and Abu-Rukah, Y.H., 2006, An assessment study of heavy metal distribution within soil in upper course of Zarqa River basin/Jordan, *Environ. Geol.*, 49 (8), 1116–1124.
- [17] Linnik, V.G., Minkina, T.M., Bauer, T.V., Saveliev, A.A., and Mandzhieva, S.S., 2019, Geochemical assessment and spatial analysis of heavy metals pollution around coal-fired power station, *Environ. Geochem. Health*, 2019, s10653-019-00361-z.
- [18] Barbeş, L., Bărbulescu, A., Rădulescu, C., Stih, C., and Chelarescu, E.D., 2014, Determination of heavy metals in leaves and bark of *Populus nigra* L. by atomic absorption spectrometry, *Rom. Rep. Phys.*, 66 (3), 877–886.
- [19] Soodan, R.K., Pakade, Y.B., Nagpal, A., and Katnoria, J.K., 2014, Analytical techniques for estimation of heavy metals in soil ecosystem: A tabulated review, *Talanta*, 125, 405–410.
- [20] Al-Taani, A.A., Batayneh, A.T., El-Radaideh, N., Ghrefat, H., Zumlot, T., Al-Rawabdeh, A.M., Al-Momani, T., and Taani, A., 2015, Spatial distribution and pollution assessment of trace metals in surface sediments of Ziqlab reservoir, Jordan, *Environ. Monit. Assess.*, 187 (2), 32.
- [21] Massadeh, A.M., and Al-Massaedh, A.A.T., 2018, Determination of heavy metals in canned fruits and vegetables sold in Jordan market, *Environ. Sci. Pollut. Res.*, 25 (2), 1914–1920.
- [22] Guo, G., Wu, F., Xie, F., and Zhang, R., 2012, Spatial distribution and pollution assessment of heavy metals in urban soils from southwest China, *J. Environ. Sci.*, 24 (3), 410–418.
- [23] Xie, Y., Chen, T., Lei, M., Yang, J., Guo, Q., Song, B., and Zhou, X.Y., 2011, Spatial distribution of soil heavy metal pollution estimated by different interpolation methods: Accuracy and uncertainty analysis, *Chemosphere*, 82 (3), 468–476.
- [24] Alloway, B.J., 1990, “Soil processes and behaviour of metals” in *Heavy Metals in Soil*, Eds. Alloway, B.J., Blackie and Son Ltd., London, 7–28.
- [25] Li, K., Gu, Y., Li, M., Zhao, L., Ding, J., Lun, Z., and Tian, W., 2018, Spatial analysis, source identification and risk assessment of heavy metals in a coal mining area in Henan, Central China, *Int. Biodeterior. Biodegrad.*, 128, 148–154.
- [26] Al-Khashman, O.A., 2004, Heavy metal distribution in dust, street dust and soils from the work place in Karak Industrial Estate, Jordan, *Atmos. Environ.*, 38 (39), 6803–6812.
- [27] Jaradat, Q.M., Masadeh, A., Zaitoun, M.A., and Maitah, B.M., 2005, Heavy metal contamination of soil, plant and air of scrapyard of discarded vehicles at Zarqa city, Jordan, *Soil Sediment Contam.*, 14 (5), 449–462.
- [28] Lü, J., Jiao, W.B., Qiu, H.Y., Chen, B., Huang, X.X., and Kang, B., 2018, Origin and spatial distribution of heavy metals and carcinogenic risk assessment in mining areas at You'xi County southeast China, *Geoderma*, 310, 99–106.
- [29] Banat, K.M., Howari, F.M., and Al-Hamad, A.A., 2005, Heavy metals in urban soils of central Jordan: Should we worry about their environmental risks?, *Environ. Res.*, 97, 258–273.
- [30] Al-Khashman, O.A., and Shawabkeh, R.A., 2006, Metals distribution in soils around the cement factory in southern Jordan, *Environ. Pollut.*, 140 (3), 387–394.
- [31] Pourjavid, M.R., Arabieh, M., Sehat, A.A., Rezaee, M., Hosseini, M.H., Yousefi, S.R., and Jamali, M.R., 2014, Flame atomic absorption spectrometric determination of Pb(II) and Cd(II) in natural samples after column graphene oxide-based solid phase extraction using 4-Acetamidothiophenol, *J. Braz. Chem. Soc.*, 25 (11), 2063–2072.
- [32] Al-Omari, A., Farhan, I., Kandakji, T., and Jibril, F., 2019, Zarqa River pollution: Impact on its quality, *J. Environ. Monit. Assess.*, 191 (3), 166.
- [33] Wedyan, M., Al Harahsheh, A., Muhaidat, R., Bsoul, E., and Qnais, E., 2016, Cd and Fe concentrations of the surface water of a stream in Jordan, *Pol. J. Environ. Stud.*, 25 (6), 2617–2621.
- [34] USEPA, 2004, *Soil and waste pH*, method 9045D. United States Environmental Protection Agency.
- [35] Al-Momani, I.F., and Shatnawi, W.M., 2017, Chemical characterization and source determination of trace elements in PM_{2.5} and PM₁₀ from an urban

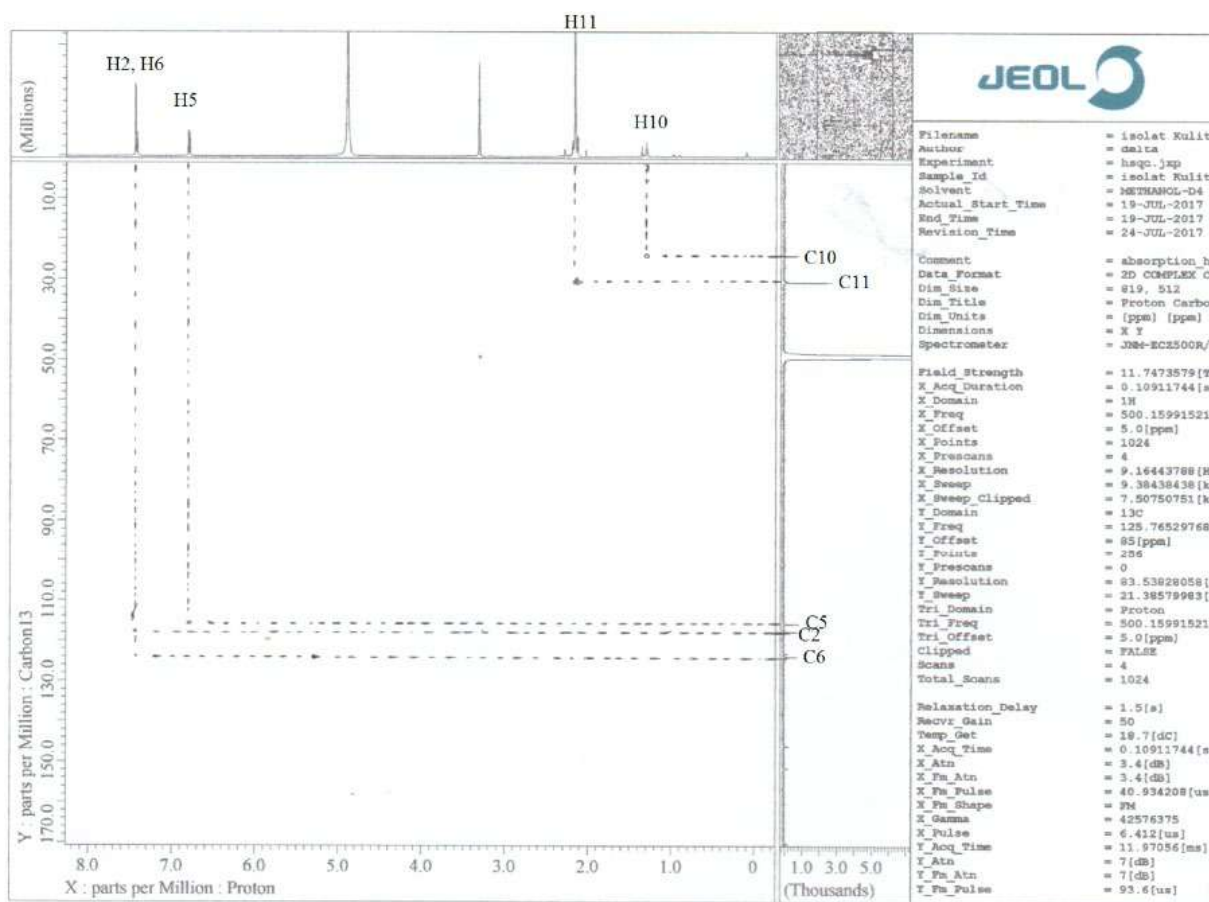
- area, Northern Jordan, *Int. J. Environ. Monit. Anal.*, 5 (4), 103–108.
- [36] Howari, F.M., Abu-Rukah, Y., and Goodell, P.C., 2004, Heavy metal pollution of soils along North Shuna-Aqaba Highway, Jordan, *Int. J. Environ. Pollut.*, 22 (5), 597–607.
- [37] Yay, D.O., Alagha, O., and Tuncel, G., 2008, Multivariate statistics to investigate metal contamination in surface soil, *J. Environ. Manage.*, 86 (4), 581–594.
- [38] Nadal, M., Schuhmacher, M., and Domingo, J.L., 2007, Levels of metals, PCBs, PCNs and PAHs in soils of a highly industrialized chemical/petrochemical area: Temporal trend, *Chemosphere*, 66 (2), 267–276.
- [39] Al-Shatnawi, S.Y., 2003, Geochemical study of selected toxic heavy metals associated with oil refinery in Al-Hashimeya area, North Jordan, *Thesis*, Yarmouk University, Jordan.
- [40] Momani, K.A., Jaradat, Q.M., Jbarah, A.Q., Omari, A.A., and Al-Momani, I.F., 2002, Water soluble species and heavy metal contamination of the petroleum refinery area, Jordan, *J. Environ. Monit.*, 4 (6), 990–996.
- [41] Zhang, C., 2006, Using multivariate analysis and GIS to identify pollutants and their patterns in urban soils in Galway, Ireland, *Environ. Pollut.*, 142 (3), 501–511.
- [42] Ghrefat, H.A., Abu-Rukah, Y., and Rosen, M.A., 2011, Application of geoaccumulation index and enrichment factor for assessing metal contamination in the sediments of Kafra Dam, Jordan, *Environ. Monit. Assess.*, 178 (1), 95–109.
- [43] DOS, 2006, *Statistical Yearbook*, Department of Statistics, Jordan.

Supplementary Data

This supplementary data is a part of paper entitled “Antioxidant Activities and Identification of an Active Compound from Rambutan (*Nephelium lappaceum* L.) Peel”.



Suppl. 1. DEPT spectrum



Suppl. 2. HSQC spectrum